論文 / 著書情報
Article / Book Information

題目(和文)	
Title(English)	Search for new phenomena in top-antitop quarks final states with additional heavy-flavour jets with the ATLAS detector
著者(和文)	山口大貴
Author(English)	Daiki Yamaguchi
出典(和文)	学位:博士(理学), 学位授与機関:東京工業大学, 報告番号:甲第10717号, 授与年月日:2018年3月26日, 学位の種別:課程博士, 審査員:陣内 修,久世 正弘,柴田 利明,河合 誠之,中村 隆司
Citation(English)	Degree:Doctor (Science), Conferring organization: Tokyo Institute of Technology, Report number:甲第10717号, Conferred date:2018/3/26, Degree Type:Course doctor, Examiner:,,,,
学位種別(和文)	博士論文
Type(English)	Doctoral Thesis

Ph.D Thesis

Search for new phenomena in top-antitop quarks final states with additional heavy-flavour jets with the ATLAS detector

Daiki Yamaguchi

Tokyo Institute of Technology, Department of Physics
Jinnouchi Lab.

Abstract

In the particle physics, in order to explain the shortcomings in the Standard Model (SM), physics models beyond the Standard Model (BSM) have been proposed. Some of them predict the existence of new particles such as vector-like quarks (VLQ), or enhancement of four-top-quark production. A search for new phenomena in top-antitop quarks final states with additional heavy-flavor jets has been carried out in this thesis. The analysis was executed for 36.1 fb^{-1} of $\sqrt{s}$ = 13 TeV proton-proton collisions data taken with the ATLAS detector at the LHC. The main target of this search is one of the VLQ, referred to as the vector-like top partner (VLT).

The signal events of VLQ and BSM four-top-quark production include boosted heavy particles such as Higgs bosons and top quarks. Introduction and optimisation of Higgs boson and top quark identifiers with the re-clustering technique are developed in this thesis. They improve the discrimination of signals from the SM backgrounds. Events are classified with jet, b-jet, Higgs-jet, and top-jet multiplicities and compared on the total energy in the transverse plane between the data and SM prediction. To improve the accuracy of the background estimation, a likelihood fit of the predicted backgrounds to the observed data is performed. Before searching for any excess of the data in the signal region, the background prediction is needed to be consistent with the data in the validation region. After the fit, the background predictions are confirmed to be consistent with the data within their uncertainty in the validation region. Therefore, any excess is searched for in the signal region.

As a result, no significant excess of events from the SM expectation is observed, hence the exclusion limits on the cross section for various BSM models are set. For the VLT signals, the cross section limits are interpreted as the lower VLT mass limits by comparing with the theoretical cross section. In the case of the fixed branching ratio of the VLT decaying into the Higgs boson and top quarks, $BR(T \rightarrow Ht) = 1$, the observed (expected) limit on the mass is set to be $m_{\text{VLT}} > 1.43$ (1.34) TeV. The observed (expected) mass limits for a weak-isospin doublet and singlet are set to be $m_{\text{VLT}} > 1.31$ (1.26) TeV and $m_{\text{VLT}} > 1.19$ (1.11) TeV, respectively. For the other branching ratios, the observed and expected mass limits are set, assuming $BR(T \rightarrow Ht) + BR(T \rightarrow Zt) + BR(T \rightarrow Wb) = 1$. As for the four-top-quark production, the observed (expected) cross section limit for a contact interaction in an effective field theory model is set to be 16.4 (30.9) fb. For two universal extra dimensions with the real projective plane, the Kaluza-Klein mass limits with the symmetric geometry case are set to be $m_{\text{KK}} > 1.8$ (1.73) TeV. These limits significantly exceed the previous results from similar experiments.

Declaration of author's contribution

The plots from Chapter 1 to Chapter 2 except Section 2.3 are necessary to understand the background of this dissertation. In the Section 2.3, the monitoring system for the Pixel detector has been developed at the beginning of Run2 in this dissertation. This development contributes to proper operation of the detector systems, which is most important in the experiment. The monitoring results are essential in understanding the conditions of the detector and foreseeing any failure. By using these monitoring results, the problematic data are excluded in order to assure the quality of the Run2 data.

From Chapter 3 to Chapter 5 except Section 3.1.1, the contents cover the basic information for the physics analysis about the physics objects, data, and simulation. The information reviewed here is common for the most of analyses in the ATLAS experiment. The plots are cited from the relevant references. In Section 3.1.1, the measurements of the impact parameter resolutions of tracks are performed. The procedure of the measurements is the same as was done in Run1, which is referred in the texts and bibliography. All the results and plots are made by the author. Since the tracks, which are trajectories of the charged particles, are the vital object for any physics analyses, the results are used for the performance measurements of other physics objects and propagated into their performances.

From Chapter 6, the analysis to search for new phenomena is described. The author and the analysis team decide the analysis flow and treatment of the systematic uncertainty for this search and validate all the results. All the plots are made by the author. Chapter 6 describes the introduction and optimisation of the Higgs boson and top quark identifiers specialised for this analysis. This is the main contribution of the author to improve the analysis. Chapter 7 shows the analysis strategy, which is the analysis flow from the event selection to discrimination of signals from backgrounds. The strategy used is similar to the one in Run1 except the event categorisation based on the Higgs bosons and top quarks taggers which is developed by the author. Chapter 8 reviews the systematic uncertainties considered in this dissertation. The systematic uncertainty on the multijet background is determined by the author, while the others are determined by the previous studies and confirmed by the author. Chapter 9 reviews the statistical treatment for the limit setting which is common for the fields of high energy physics. They are not developed or modified for this dissertation. The final results in Chapter 10 and discussion in Chapter 11 are produced by the author.

Contents

Acronyms

pdf	probability density function
pp	proton-prton
vdM	van der Meer
AD	Antiproton Decelerator
ADD	Arkani-Hamed, Dimopoulos, and Dvali
AdS	Anti-de Sitter
ALFA	Absolute Luminosity For ATLAS
ATLAS	A Toroidal LHC Apparatus
BDT	Boosted Decision Tree
BR	Branching Ratio
BSM	Beyond the Standard Model
Cal	Calorimeter
CERN	European Organization for Nuclear Research
CL	Confidence Level
CMS	Compact Muon Solenoid
CSC	Cathode Strip Chamber
DT	Direct Tagging
ED	Extra-Dimensional models
EFT	Effective Field Theory
EM	Electromagnetic
EW	Electroweak
FCal	Forward Calorimeter
GUT	Grand Unified Theory
GWS	Glashow-Weinberg-Salam theory
HLT	High Level Trigger
IBL	Insertable B-Layer
ID	Inner Detector
JVT	Jet Vertex Tagger
KK	Kaluza-Klein
LAr	Liquid Argon
LEP	Large Electron-Positron Collider
LHC	Large Hadron Collider
LINAC2	Linear Accelerator 2
LINAC3	Linear Accelerator 3
LS1	Long Shutdown 1
LUCID	Luminosity measurement using Cerenkov Integrating Detector
L1	Level-1

MBST	Minimum Bias Trigger Scintillators
MC	Monte Carlo
MCC	Module Controller Chip
MDT	Monitored Drift Tube chamber
MIP	Minimum Ionizing Particle
MPI	Multiparton Interaction
MS	Muon Spectrometer
NLO	Next-to-Leading Order
NNLO	Next-to-Next-to Leading Order
NNLL	Next-to-Next-to Leading Logarithm
NGB	Nambu-Goldstone bosons
NP	Nuisance Parameter
PDF	Parton Density Function
PMT	Photomultiplier tube
PS	Proton Synchrotron
PV	Primary Vertex
QCD	Quantum Chromo-Dynamics
RF	Radio-Frequency
RMS	Root-mean square
ROD	Read Out Driver
RPC	Resistive Plate Chamber
RS	Randall and Sundrum
SCT	Semiconductor Tracker
SM	Standard Model
SPS	Super Proton Synchrotron
SR	Search Regions
SSB	Spontaneous Symmetry Breaking
TGC	Thin Gap Chamber
TRF	Tag-Rate-Function
TRT	Transition Radiation Tracker
ToT	Time over Threshold
UED	Universal Extra Dimensions
VEV	Vacuum Expectation Value
VLT	Vector-like top quark
VLQ	Vector-like quark
VR	Validation Regions
ZDC	Zero-Degree Calorimeter
2UED-RPP	2 Universal Extra Dimensions on the Real Projective Plane

1 Introduction

An elementary particle is the minimum entity of the nature, which is not able to be divided further. The dynamics of elementary particles are described by a theoretical model referred to as "Standard Model" (SM). In the nature, it is known that there are four forces: the strong force, electromagnetic force, weak force, and gravity. The SM describes all forces except the gravity based on the quantum field theory. The SM can explain most of the experimental results precisely, while it cannot explain the origin of the dark matter in the universe and has fundamental issues called hierarchy problem, which causes the divergence of the Higgs boson's mass. Thereby a number of physics models beyond the Standard Model (BSM) have been proposed. For years, many experiments have searched for the new phenomena motivated by the BSM scenarios. This section describes the overview of the SM and BSM at first, and then introduces some of the latest results of searches for new phenomena.

1.1 Standard Model

The SM describes the dynamics of twelve fermions consisting of six quarks and six leptons, four vector bosons, and one Higgs boson. The forces are explained by an exchange of the mediator between two particles ("interaction"). The dynamics are based on the gauge theory, and a mediator of the vector boson with spin 1 is called a gauge boson. The strong force which is a force to bind nucleons is described by the Quantum Chromo-Dynamics (QCD) [1]. The mediator particle is a gluon (g). The mediator of the electromagnetic force is photon (γ). The weak force whose mediators are W and Z bosons is a force to cause the β-decay of nuclei. The electromagnetic and weak forces are unified as the electroweak (EW) force described by Glashow-Weinberg-Salam theory (GWS) [2–4]. These kinds of interactions occurring between the particles have the charge related to the interaction. The particles having colour charge can interact via the strong interaction. The ones with electric and weak charge can interact via electromagnetic and weak interaction, respectively.

The fermions, matter particles, have a spin of $1/2$ and divided into two groups: quarks and leptons. The quarks have the colour charges, while the leptons do not have the colour charge. There are six kinds ("flavour") of quarks: up(u), down(d), charm(c), strange(s), top(t), and bottom(b). They are split into three generations: the first generation (u, d), the second generation (c, s), and the third generation (t, b). Since they interact each other via the strong interaction, they are bound and form a stable or unstable state referred to as *hadron*. The three-quark state is a baryon, which is, for instance, a proton composed of (uud). The quark-antiquark state is a meson, which is, for instance, a charged pion composed of $(u\bar{d})$. The leptons with electric charge, so-called charged lepton, are electron (e), muon (μ), and τ-lepton (τ). The leptons without electric charge, so-called neutrino, are electron neutrino (ν_e), muon neutrino (ν_μ), and τ neutrino (ν_τ). Since the neutrino does not have the electric charge, they interact only via weak interaction. The leptons are also similarly split into

Table 1.1: Elementary particles in the Standard Model. The first column shows the fermions of quarks and leptons, the second column shows the gauge bosons, and the last column shows the Higgs boson. The "charge" represents the electric charge.

Matter particle (fermion)					Force mediator		Higgs
Name	Charge	1st gen.	2nd gen.	3rd gen.	Force	boson	(scalar)
Quarks	$+\frac{2}{3}$	u (up)	c (charm)	t (top)	Strong	g	H
	$-\frac{1}{3}$	d (down)	s (strange)	b (bottom)	Electromagnetic	γ	
Leptons	0	ν_e	ν_μ	ν_τ	Weak	$W^\pm$	
	-1	e	μ	τ		Z	

three generations: the first generation (ν_e, e), the second generation (ν_μ, μ), and the third generation (ν_τ, τ). All the particles described above are summarised in Table 1.3.

Mathematically, the SM is based on the gauge invariance under the gauge group:

$$SU(3)_C \otimes SU(2)_L \otimes U(1)_Y, \tag{1.1}$$

where $SU(3)_C$ corresponds to the symmetry group of the strong interaction and $SU(2)_L \otimes U(1)_Y$ corresponds to that of the electroweak interaction. The Lagrangian of the SM $\mathcal{L}_{\mathrm{SM}}$ which describes the particles equations of motion can be expressed by:

$$\mathcal{L}_{\mathrm{SM}} = \mathcal{L}_{\mathrm{EW}} + \mathcal{L}_{\mathrm{QCD}}, \tag{1.2}$$

where $\mathcal{L}_{\mathrm{EW}}$ and $\mathcal{L}_{\mathrm{QCD}}$ correspond to the Lagrangian of the electroweak interaction and QCD, respectively. They are explained in the following.

1.1.1 Electroweak theory

The electroweak theory describes the electromagnetic and weak interactions. The weak interaction has $SU(2)$ symmetry with respect to the weak isospin I and interact with the left-handed particle. Then, the symmetry is denoted as $SU(2)_L$. The left- and right-handed components of a fermion is expressed by:

$$\psi_L = \frac{1}{2}(1 - \gamma^5)\psi \tag{1.3}$$

$$\psi_R = \frac{1}{2}(1 + \gamma^5)\psi \tag{1.4}$$

The gauge field of the gauge group is denoted as $\boldsymbol{W}_\mu = (W^0_\mu, W^1_\mu, W^2_\mu)$. The left-handed component is isospin-doublet with $I = 1/2$, while the right-handed component is isospin-singlet with $I = 0$.

$$f_L = \begin{pmatrix} \nu^i_L \\ l^i_L \end{pmatrix}, \begin{pmatrix} u^i_L \\ d^i_L \end{pmatrix} \tag{1.5}$$

$$f_R = l^i_R,\ u^i_R,\ d^i_R, \tag{1.6}$$

where u, d, ν, and l here are an up-type quark with the electric charge of $+2/3$, down-type quark with the electric charge of $-1/3$, neutrino, and charged lepton, respectively. The index i represents the generation: $i = 1, 2, 3$. The SM assumes absence of the right-handed neutrinos. Here, the hypercharge Y is introduced by the Gell-Mann Nishijima formula:

$$Q = I_3 + \frac{Y}{2}, \tag{1.7}$$

where Q is the electric charge, and I_3 is the third component of the isospin. For example, the left-handed lepton has the hyperchange of $Y = -1$, while the right-handed lepton has the hypercharge of $Y = -2$. The gauge filed coupling with the hypercharge of the $U(1)$ group is denoted as B_μ. The Lagrangian of the electroweak interaction can be described by:

$$\mathcal{L}_{\rm EW} = \sum \bar{f} i\gamma^\mu D_\mu f - \frac{1}{4}\boldsymbol{W}_{\mu\nu}\cdot\boldsymbol{W}^{\mu\nu} - \frac{1}{4}B_{\mu\nu}\cdot B^{\mu\nu}, \tag{1.8}$$

$$D_\mu = \partial_\mu + ig_W \boldsymbol{W}_\mu\cdot\boldsymbol{\tau} + ig_B\frac{Y}{2}B_\mu, \tag{1.9}$$

where $\boldsymbol{\tau}$ is the vector of Pauli matrices: $\boldsymbol{\tau} = (\sigma^0/2, \sigma^1/2, \sigma^2/2)$, g_W and g_B are the coupling constants to the W and B fields, and $\boldsymbol{W}_{\mu\nu}$ and $B_{\mu\nu}$ are defined as:

$$\boldsymbol{W}_{\mu\nu} = \partial_\mu \boldsymbol{W}_\nu - \partial_\nu \boldsymbol{W}_\mu - g\boldsymbol{W}_\mu \times \boldsymbol{W}_\nu, \tag{1.10}$$

$$B_{\mu\nu} = \partial_\mu B_\nu - \partial_\nu B_\mu. \tag{1.11}$$

The first term of Eq. (1.8) represents the kinetic term of fermions involving the interactions with the bosons. The second and third terms represent the kinetic term of the bosons. Then, W^0 and B are replaced with the two fields of Z and A defined as:

$$\begin{pmatrix} Z_\mu \\ A_\mu \end{pmatrix} = \begin{pmatrix} \cos\theta_W & -\sin\theta_W \\ \sin\theta_W & \cos\theta_W \end{pmatrix}\begin{pmatrix} W^0_\mu \\ B_\mu \end{pmatrix} \tag{1.12}$$

$$\cos\theta_W = \frac{g_W}{\sqrt{g_W^2 + g_B^2}} \tag{1.13}$$

$$\sin\theta_W = \frac{g_B}{\sqrt{g_W^2 + g_B^2}} \tag{1.14}$$

The θ_W is known as Weinberg angle. Assuming massless for all the particles, the interaction part of the Lagrangian can be written with A, Z, and Q as:

$$\mathcal{L} = -e\bar{f}\gamma^\mu A_\mu Q f + \frac{g_W}{\sqrt{2}}\bar{f}_L\gamma^\mu(W^+_\mu\tau^+ + W^-_\mu\tau^-)f_L + g_Z\bar{f}\gamma^\mu Z_\mu(I_{3L} - Q\sin^2\theta_W)f, \tag{1.15}$$

$$e = \frac{g_W g_B}{\sqrt{g_W^2 + g_B^2}}, \tag{1.16}$$

$$g_Z = \frac{e}{\sin\theta_W\cos\theta_W}, \tag{1.17}$$

where $W^\pm = (W^1 \mp iW^2)/\sqrt{2}$. The first term describes the interaction between fermions and the field A, corresponding to the photon, with the electric charge, corresponding to the electromagnetic

interaction. The second term describes the interaction between the left-handed fermions and the field W, corresponding to the charged weak current. The third term describes the interaction between the fermions and the field Z, corresponding to the neutral electroweak current.

Here, it is assumed that all the particles are massless. When introducing the non-zero mass, the Lagrangian breaks the local SU(2) symmetry. The assumption of the massless particles does not agree with the experimental results. Then it is necessary to introduce the mechanism that the particles obtain the masses without breaking the symmetry.

1.1.2 The Higgs-Englert-Brout mechanism

The mechanism to introduce the non-zero masses with Spontaneous Symmetry Breaking (SSB) is known as the Higgs-Englert-Brout mechanism. Here a new SU(2) doublet scalar field $\mathbf{\Phi}$ is introduced in $SU(2)_L \otimes U(1)_Y$ group:

$$\mathbf{\Phi} = \begin{pmatrix} \phi^+ \\ \phi^0 \end{pmatrix}, \tag{1.18}$$

where "+" and "0" represent the electric charge of the fields. The field $\mathbf{\Phi}$ has the isospin of $I = 1/2$. The Lagrangian for the field $\mathbf{\Phi}$ is assumed to be written as:

$$\mathcal{L}_\Phi = (D_\mu \mathbf{\Phi})^\dagger (D^\mu \mathbf{\Phi}) - V(\Phi), \tag{1.19}$$

where D_μ is defined in Eq. (1.9) and the $V(\Phi)$ is the potential term defined by:

$$V(\Phi) = \mu^2 \mathbf{\Phi}^\dagger \mathbf{\Phi} + \lambda (\mathbf{\Phi}^\dagger \mathbf{\Phi})^2. \tag{1.20}$$

The potential V depends on the two parameters of μ^2 and λ. In the case of negative values of $\lambda < 0$, the minimum of the potential is negative infinity, resulting in no stability. In the case of positive values of $\lambda > 0$ and positive $\mu^2 > 0$, the potential has the minimum energy at $|\mathbf{\Phi}| = 0$. The stable state with the minimum energy is the vacuum. It means that the Vacuum Expectation Value (VEV) is zero ($\langle 0|\Phi|0\rangle = 0$). In the case of positive values of $\lambda > 0$ and negative $\mu^2 < 0$, the potential gets the minimum at:

$$\mathbf{\Phi}^\dagger \mathbf{\Phi} = -\frac{\mu^2}{\lambda} \equiv \frac{v^2}{2} \tag{1.21}$$

It corresponds to have non-zero VEV of $\langle 0|\Psi|0\rangle = v/\sqrt{2}$. The field of $\mathbf{\Phi}$ can have any value which satisfies $\langle 0|\Psi|0\rangle = v/\sqrt{2}$. The complex fields of ϕ^+ and ϕ^0 can be written by the four real scalar fields ϕ_i ($i = 1,\ 2,\ 3,\ 4$):

$$\phi^+ = \frac{1}{\sqrt{2}}(\phi_1 + i\phi_2) \tag{1.22}$$

$$\phi^0 = \frac{1}{\sqrt{2}}(\phi_3 + i\phi_4). \tag{1.23}$$

Now if $\phi_1 = \phi_2 = \phi_4 = 0$ and $\phi_3 = v$, the vacuum is fixed and the rotational SU(2) symmetry in the ϕ_i space is broken. This is the spontaneous symmetry breaking, as shown in Fig. 1.1.

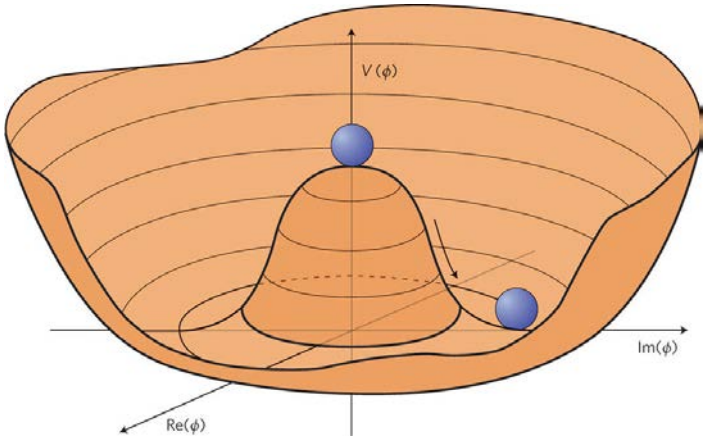

Figure 1.1: Higgs field potential $V(\phi)$. In case of $\lambda > 0$ and $\mu^2 > 0$, the vacuum which is the minimum energy state is the state at $\langle 0|\Phi|0\rangle = 0$. In case of $\lambda > 0$ and $\mu^2 < 0$, the vacuum is randomly chosen at the new lowest energy state at $\langle 0|\Psi|0\rangle = v/\sqrt{2}$. Cited from the reference [5].

The field at the vacuum Φ_0 is written as:

$$\Phi_0 = \frac{1}{\sqrt{2}} \begin{pmatrix} 0 \\ v \end{pmatrix} \tag{1.24}$$

Then, the field around the vacuum is expressed with the additional fluctuation component $H(x)$:

$$\mathbf{\Phi} = \frac{1}{\sqrt{2}} \begin{pmatrix} 0 \\ v + H(x) \end{pmatrix} \tag{1.25}$$

The field $H(x)$ describes the physical dynamics of the scalar field around the vacuum, corresponding to the "Higgs boson". The masses of the electroweak bosons are obtained from substitution of Eq. (1.24) into the kinetic term of Eq. (1.19):

$$(D_\mu \mathbf{\Phi})^\dagger (D^\mu \mathbf{\Phi}) \sim (0, v/\sqrt{2}) \frac{1}{2^2} \begin{pmatrix} g_W W^0 + g_B B & \sqrt{2} g_W W^+ \\ \sqrt{2} g_W W^- & -g_W W^0 + g_B B \end{pmatrix}^2 \begin{pmatrix} 0 \\ v/\sqrt{2} \end{pmatrix} \tag{1.26}$$

$$= \frac{v^2}{8} \left[2 g_W^2 W^- W^+ + (-g_W W^0 + g_B B)^2 \right] \tag{1.27}$$

$$= \left(\frac{g_W v}{2} \right)^2 W^- W^+ + \frac{1}{2} \left(\frac{g_Z v}{2} \right)^2 ZZ + 0 \cdot AA \tag{1.28}$$

The last side explicitly includes the term for the A field. Considering the difference of the coefficient between the neutral and charged bosons, the masses of W and Z are written as:

$$m_W = \frac{g_W v}{2}, \tag{1.29}$$

$$m_Z = \frac{g_Z v}{2}. \tag{1.30}$$

The mass of A remains to be zero. Regarding the mass of the scalar field, the Lagrangian for the scalar field can described by substituting Eq. (1.25) into Eq. (1.19):

$$\mathcal{L}_\Phi = \frac{1}{2} (\partial_\mu H)^2 - \lambda v^2 H^2 - (\lambda v H^3 + \frac{1}{4} \lambda H^4) + \cdots \tag{1.31}$$

From the second term, the mass of the scalar field is expressed by:

$$m_H = \sqrt{2\lambda v^2} = \sqrt{-2\mu^2} \tag{1.32}$$

Now we shall think to add the interaction between the scalar field and the fermions with the SU(2) symmetry around the vacuum preserved. Both $\mathbf{\Phi}$ and f_L have the isospin of $I = 1/2$, and then the $(\mathbf{\Phi}^\dagger f_L)$ and $(\bar{f_L}\mathbf{\Phi})$ are invariant with respect to the SU(2) isospin rotation. Thus, combining the isospin singlet f_R, the interaction can be described by using the Yukawa Lagrangian as:

$$\begin{aligned} \mathcal{L}_Y &= \sum -y_f[\bar{f}_R(\mathbf{\Phi}^\dagger f_L) + (\bar{f}_L\mathbf{\Phi})f_R] && (1.33)\\ &= \frac{y_f v}{\sqrt{2}}(\bar{f}_R f_L + \bar{f}_L f_R) - \frac{y_f}{\sqrt{2}}(\bar{f}_R f_L + \bar{f}_L f_R)H, && (1.34) \end{aligned}$$

where y_f is the coupling constant between the scalar field and the fermion. The masses of the fermion are written as:

$$m_f = \frac{y_f v}{\sqrt{2}}. \tag{1.35}$$

In addition, the interaction between the scalar field and fermions are also introduced.

In summary, considering that the parameter of μ^2 depends on the temperature or energy, the parameter μ^2 has positive values at high temperature such as the time of the early universe, and then the VEV is zero. As the temperature decreases, the parameter μ^2 obtains negative values below the critical temperature, and then the VEV has non-zero value. At the same time, the electroweak symmetry breaks and the particles obtain their masses.

1.1.3 Quantum Choromo-Dynamics

The QCD describes the strong interaction between the particles with the colour charge. The colour charge is one of the internal degree of freedom, which was introduced to explain the experimental results. The Δ^{++} baryon has the electric charge $Q = 2$ and the spin of $3/2$, leading to be composed of three up quarks as $u(\uparrow)u(\uparrow)u(\uparrow)$. But the state is not allowed by the spin statistics (Pauli exclusion principle). Then, the new quantum number, colour, is introduced to explain the existence of the baryon. The colour degree of freedom is named as red(R), green (G), and blue (B). The quark fields are expressed by:

$$q = \begin{pmatrix} q^R \\ q^G \\ q^B \end{pmatrix} \tag{1.36}$$

The Lagrangian of QCD can be described with SU(3) gauge group as:

$$\begin{aligned} \mathcal{L}_{\mathrm{QCD}} &= \bar{q}(i\gamma^\mu D_\mu)q - \frac{1}{4}G^a_{\mu\nu}G^{a\mu\nu}, && (1.37)\\ D_\mu &= \partial_\mu - ig_S T_a G^a_\mu, && (1.38) \end{aligned}$$

where a is the index $a = 1, \ldots, 8$, G is the gluon field, and T_a is the SU(3) operator, $T_a = \lambda_a/2$, written by the Gell-Mann matrices λ_a. The field strength tensor $G^a_{\mu\nu}$ is described as:

$$G^a_{\mu\nu} = \partial_\mu G^a_\nu - \partial_\nu G^a_\mu + g_S f_{abc} G^b_\mu G^c_\nu, \tag{1.39}$$

where f_{abc} is the structure constant of SU(3) gauge group . It describes the self-interaction of the gluon fields. The dependency of the coupling constant $\alpha_S = g_S^2/4\pi$ on the energy scale Q^2 can be expressed as:

$$\alpha_S(Q^2) = \frac{4\pi}{(11 - \frac{2}{3}n_f)\log\left(\frac{Q^2}{\Lambda^2_{\mathrm{QCD}}}\right)}, \tag{1.40}$$

where Λ_{QCD} is a cut-off scale named QCD scale, and n_f is the number of flavours of quarks:$n_f = 6$. According to Eq. (1.40), in the case of $Q^2 \to \infty$, the coupling strength decreases to zero, where the gluons and quarks behave like free particles, known as "Asymptotic freedom". The phenomenology of QCD with high Q^2 can be calculated perturbatively. On the other hand, in the case of $Q^2 \sim \Lambda^2_{\mathrm{QCD}}$, the coupling strength increase to infinity. The quarks and gluons interact each other very strongly and form hadrons with colour singlet, known as "colour confinement". If a quark is emitted with a certain momentum by some interaction, it emits gluons which split into quark-antiquark pairs, repeating the processes, and reduces its energy. At around the QCD scale, all the quarks form hadrons. From the experimental system, these hadrons go along the initial momentum direction like a hadron shower. This phenomena is called as "jet" in the high energy physics.

1.1.4 Experiment results on the Standard Model

For tens of years, a lot of experiments have verified the SM.

Especially, the collider experiments have provided the precise measurements for the electroweak sector. The W and Z boson masses can be predicted in the SM using the other measured parameters. The global fit using several experimental results is performed by the the Particle Data Group [6]. The SM expectation of these masses are obtained to be:

$$m_W^{\mathrm{exp}} = 80.361 \pm 0.006 \text{ GeV} \tag{1.41}$$
$$m_Z^{\mathrm{exp}} = 91.1880 \pm 0.0020 \text{ GeV}. \tag{1.42}$$

The CDF and D0 experiments at Tevatron combined the results of W boson mass measurements and provide the most precise value [7]:

$$m_W^{\mathrm{obs}} = 80.387 \pm 0.016 \text{ GeV} \tag{1.43}$$

The ALEPH, DELPHI, L3, OPAL experiments at LEP measure the Z boson resonance and provide the Z boson mass [8]:

$$m_Z^{\mathrm{obs}} = 91.1876 \pm 0.0021 \text{ GeV}. \tag{1.44}$$

The observed mass values are consistent with the SM expectations.

In addition, they determine the number of neutrino flavours by the measurements of the Z boson decay width. Since the partial width for the neutrino contribution can be extracted by the subtraction of the partial widths of charged leptons and hadronic decay modes: $\Gamma(\text{inv.}) = \Gamma(Z) - 3\Gamma(l^+l^-) - \Gamma(\text{had.})$. The number of neutrino flavour is obtained by dividing the partial width by the theoretical partial width:

$$N_\nu = \Gamma(\text{inv.})/\Gamma(\nu\nu)^{\text{theory}} = 2.992 \pm 0.007. \tag{1.45}$$

The Weinberg angle θ_W is measured by obtained by Tevatron experiments [9, 10]. the average value is obtained by combination of the results performed by the Particle Data Group [6]:

$$\sin^2\theta_W = 0.23185 \pm 0.00035. \tag{1.46}$$

The heaviest particle, top quark, was discovered at Tevatron experiments [11, 12] in 1995 and its property have been measured. The mass is combined by the Particle Data Group [6] using the results of Tevatron and LHC at $\sqrt{s} = 7$ TeV:

$$m_t = 173.1 \pm 0.6 \text{ GeV}. \tag{1.47}$$

As described in the previous sections, the Higgs-Englert-Brout mechanism introduces one scalar boson (Higgs boson) which are capable to be detected. A new scalar boson whose property is consistent with the SM Higgs boson was discovered by the ATLAS and CMS experiments at LHC in 2012, which are described later. In association with the discovery, Prof. Peter Higgs and Prof. François Englert won the Nobel prize in 2013. The mass of the Higgs boson is determined with the decay modes of $H \to \gamma\gamma$ and $H \to ZZ \to 4l$, where the four vectors of the decay products can be determined experimentally and the invariant mass can be reconstructed. The results in the ATLAS experiment at LHC $\sqrt{s} = 13$ TeV [13] are shown in Fig. 1.2, compared with the combined result of the ATLAS and CMS experiments at LHC Run1 [14]. The Higgs boson mass is found to be around 125 GeV.

The Higgs boson is expected to interact with all the SM bosons and fermions. The couplings to the fermions with Yukawa interaction are proportional to their masses. The coupling strength can be written as $\kappa_{F,i} \cdot y_{F,i}/\sqrt{2} = \kappa_{F,i} \cdot m_{F,i}/v$, where i is the index of the fermion flavours, $\kappa_{F,i}$ is the modification term of the cross section σ written as: $\kappa_{F,i} = \sigma_i/\sigma_i^{\text{SM}}$, and v is the vacuum expectation value: $v = 246$ GeV. In a similar way, the couplings to the weak bosons can be parameterised as $\sqrt{\kappa_{V,j} \cdot g_{F,j}/2v} = \sqrt{\kappa_{V,j}} \cdot m_{V,j}/v$, where j is the index of the weak bosons and $g_{V,j}$ is the gauge coupling strength between the Higgs boson and the weak boson. The measurements and searches for the Higgs coupling to the SM particles have been carried out at the LHC experiments. Figure 1.3 shows the Higgs boson couplings to the SM particles combined with the ATLAS and CMS experiments at the LHC Run1 [15]. It includes all the production and decay processes of the Higgs boson. The Higgs boson coupling to the top quark is determined from the production process since the mass of the top quark is heavier than the Higgs boson mass and the Higgs boson does not decay to the top quarks. The coupling to the muons has not been discovered yet due to its small branching ratio in both the ATLAS and CMS experiments. The coupling shown in Fig. 1.3 is obtained with the fit as the maximum likelihood value assuming no decay modes to BSM particles. It is found that the observed Higgs boson couplings agree with the SM prediction (blue dashed line).

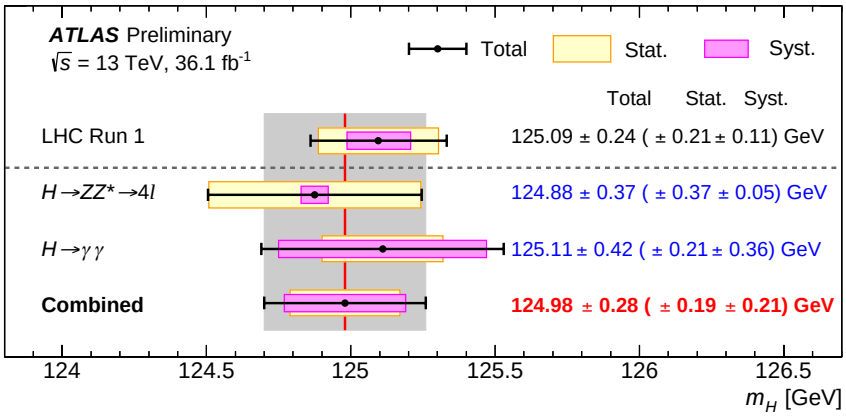

Figure 1.2: Higgs boson mass measurements from the individual and combined analyses in the ATLAS experiments [13]. The LHC Run1 represents the combined result of the ATLAS and CMS experiments [14]. The systematic (magenta-shaded bands), statistical line and corresponding (gray) shaded column indicate the central value and the total uncertainty of the combined measurement, respectively.

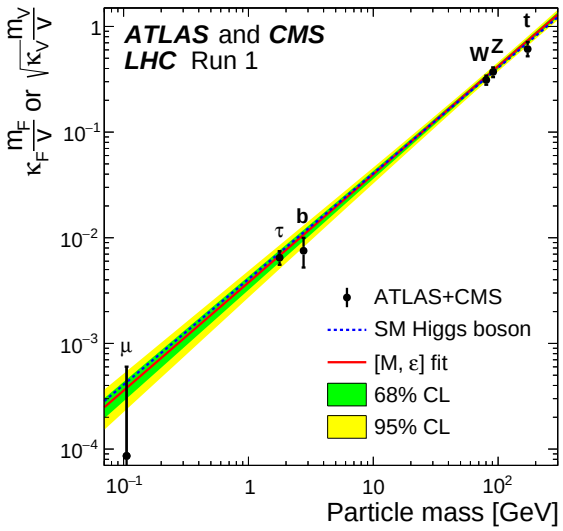

Figure 1.3: Best fit values of the couplings to the SM particles as a function of particle mass for the combination of the ATLAS and CMS data [15] in the case of the parameterisation described in the text, with parameters defined as $\kappa_F \cdot m_F/v$ for the fermions and as $\sqrt{\kappa_V} \cdot m_V/v$ for the weak vector bosons, where $v = 246$ GeV is the vacuum expectation value of the Higgs field. The dashed (blue) line indicates the predicted dependence on the particle mass in the case of the SM Higgs boson. The solid (red) line indicated the best fit results to the $[M, \epsilon]$ phenomenological model of Ref. [16] with the corresponding 68% and 95% confidence level bands.

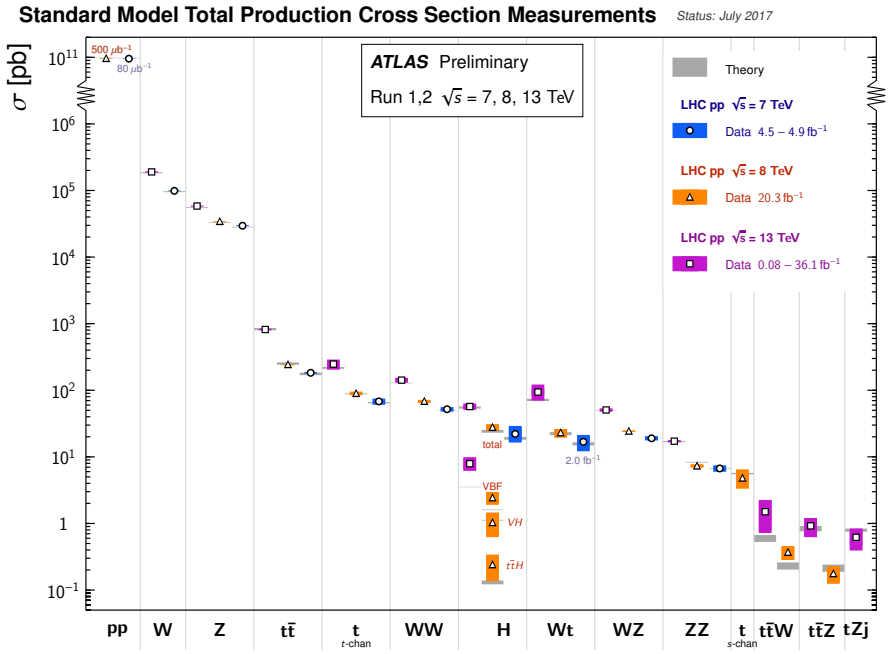

Figure 1.4: Summary of several Standard Model total production cross section measurements, compared to the corresponding theoretical expectations. All theoretical expectations were calculated at NLO or higher. The luminosity used for each measurement is indicated close to the data point. Uncertainties for the theoretical predictions are quoted from the original ATLAS papers [17].

The total cross sections of the various processes are measured in the ATLAS experiments at the LHC with $\sqrt{s}$ = 7, 8, 13 TeV, shown in Fig. 1.4. The theoretical physics processes are calculated with the Next-to-Leading Order (NLO) or higher, shown in gray bands. The luminosities used for the individual measurements are 4.5 - 4.9 fb^{-1} for $\sqrt{s}$ = 7 TeV (blue), 20.3 fb^{-1} for $\sqrt{s}$ = 8 TeV (orange), and 0.008 - 36.1 fb^{-1} for $\sqrt{s}$ = 13 TeV (purple). The observed cross sections agree with the SM predictions over 10^{12} orders of magnitude.

In spite of the successful descriptions of the elementary particle physics in the SM, there are several evidences that the SM framework is not the ultimate theory. One of the evidences is the existence of the dark matter. In 1933 Fritz Zwicky found that the velocity dispersion of galaxies in the Coma cluster was not supported by the luminous matter [18]. In 1970s, Vera Rubin and collaborators measured the rotation curves of galaxies [19, 20]. The dependency of the speed on the distance between the galaxy centre and a matter cannot be explained by the expectation in Newtonian dynamics with the masses and positions of the matter and the heavy and visible matter at the galaxy centre. It directly indicates the existence of the invisible (dark) matter. In addition, the evidence of the dark matter is indicated by another astronomical measurement using gravitational lensing. From the astronomy, the features of the dark matter are known as heavy, electrically neutral, and stable. The SM does not include the candidates of the dark matter, and then can not explain the phenomena. Over the past few decades, in the particle physics, the direct and indirect searches for the dark matter have been carried out, but

the evidence of the dark matter has not been observed.

Another fundamental problem is the hierarchy problem. As shown in Eq. (1.40), the coupling strength depends on the energy scale. The strong and electroweak coupling constants cross approximately at much higher energy scale of 10^{15} GeV than the electroweak energy scale of 246 GeV. The theorists have attempted to unify the strong and electroweak theories and describe the phenomena with one theoretical framework, "Grand Unified Theory (GUT)". The large difference of the energy scales does not seem to be natural and then is called the hierarchy problem. Such a large energy scale difference results in unnaturalness on the mass calculation of the Higgs boson. As described in the previous sections, the Higgs boson mass is expressed by Eq. (1.32). Since the accurate mass value is needed, the observed mass is calculated with the quantum correction. The observed mass m_H can be expressed by

$$m_H^2 = (m_{H_0})^2 + \Delta m_H^2, \tag{1.48}$$

where m_{H_0} is the bare mass expressed in Eq. (1.32) and Δm_H is the quantum correction on the Higgs mass. Considering the contribution of the fermions, the quantum correction is described by:

$$\Delta m_H^2 = -\frac{|y_f|^2}{16\pi^2}\left[2\Lambda^2 + O\left(m_f^2 \ln\frac{\Lambda}{m_f}\right)\right], \tag{1.49}$$

where y_f is the Yukawa coupling of the fermion f and Λ is a cut-off energy scale of the theory. If the SM is valid up to the GUT energy scale, the cut-off scale Λ^2 is 10^{30} GeV^2. It leads to the fact that the observed Higgs boson squared mass (10^4 GeV^2) should be obtained by the huge cancellation at 26 orders of magnitude. This enormous cancellation is known as *fine tuning*.

1.2 Beyond the Standard Model

For many years, in order to solve the fundamental problems in the SM, physics models beyond the Standard Model (BSM) have been proposed. In this section, several models related to the search for new phenomena with the $t\bar{t}$-plus-jets final state presented in this dissertation are reviewed.

1.2.1 Extra dimension

The SM describes the phenomena of particle physics with four dimensions spacetime composed of three spacial dimensions and one time dimension. The physics models to consider $4+\delta$ dimensions as the extension of the SM are called the Extra-Dimensional models (ED). The additional δ dimensions are denoted as extra dimensions. In 1920's, Theodor Kaluza and Oskar Klein attempted to unify the gravity and the other interactions with General Relativity based on 4 + 1 dimensions. The idea is to compact one spacial dimension in the small scale, known as Kaluza-Klein theory. Figure 1.5 illustrates the scheme of the spacetime dimensions. The vertical dimension represents the 3 + 1 dimensions with infinity size that we know well. The extra dimension is compactified on a circle of radius R with finite size. When a field propagates into the extra dimension, the extra dimension's component of the momentum is quantised in units of $1/R$, the compactification scale. In general,

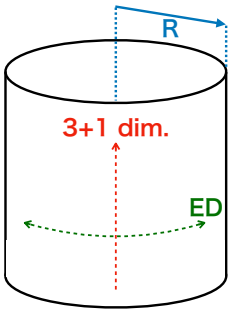

Figure 1.5: Representation of an extra dimension with a radius of R.

the particles propagating the extra dimensions appear as the Kaluza-Klein (KK) states in our 3 + 1 dimension. The KK states have infinite number of modes, referred to as "tower", in which the mass of the individual KK state corresponds to the quantised momentum in the extra dimensions. The ED models are classified with the compactifying geometry: flat and warped.

Flat-extra-dimensional models

In 1998, Arkani-Hamed, Dimopoulos, and Dvali (ADD) showed an interesting model that the SM is fixed in the 3 + 1 dimensions and only the graviton, a mediator of gravity, can propagate in the extra dimensions [21]. The extra dimensions are compactified in a radius of R. The energy scale unifying the gravity to the other forces, Planck scale, is approximately 10^{19} GeV order in the SM. The Planck scale M_{Pl} is effectively modified in the ADD model with n extra dimensions as:

$$M_{Pl}^2 \sim M_{Pl(4+n)}^{2+n} R^n, \tag{1.50}$$

where $M_{Pl(4+n)}$ is the Planck scale in the $4 + n$ dimensional model. If $n = 2$ and $R \sim 100$ μm, the Planck scale $M_{Pl(4+n)}$ is equivalent to the electroweak scale. From the experimental point of view, the lower limits are set on the Planck scale $M_{Pl(4+n)}$ of 7.7 TeV at $n = 2$ and 4.8 TeV at $n = 6$ [22], resulting in the higher Planck scale than the electroweak scale.

Another model is the Universal Extra Dimensions (UED) [23] assuming all the SM particles can propagate in the extra dimensions. It is known that the UED model with 4 + 2 dimensions on the real projective plane (2UED-RPP) is allowed experimentally and can produce the dark matter candidate [24, 25]. Each SM field can propagate the two extra dimensions and have KK states (towers) for each extra dimension. The towers are represented in tiers labelled by two integers (k, l) which correspond to the momenta along the extra dimensions. All the states are degenerated in a tier with the mass determined by:

$$m_{k,l}^2 = \frac{k^2}{R_5^2} + \frac{l^2}{R_6^2}, \tag{1.51}$$

where R_5 and R_6 are the compactification radii for each extra dimension. The coloured particles in the tier (1,0) and (0,1) can be produced at the LHC and decay into the lightest particle, which is the

dark matter candidate, with radiating the soft SM particles. Since the masses of the particles in the tier are degenerate, the radiated SM particles have very low momentum. Therefore, this analysis is not sensitive to the signature including missing and soft particles [26]. On the other hand, the tier (1,1) produces an interesting and targeting signature, four-top-quark production, described later. The observation of dark matter relic abundance using WMAP data prefers the range of the KK mass up to 1200 GeV [27].

Warped-extra-dimensional models

In 1999, Randall and Sundrum (RS) proposed an extra dimensional model using a warped geometry [28]. The RS model uses five dimensional Anti-de Sitter (AdS) spacetime with a compactification scale of TeV order. The RS model assumes two branes: one brane involving all the SM fields with $3+1$ dimensions and the other brane involving gravity. On the gravity brane, the gravity is very strong. The probability to find the graviton depends on the distance between the two branes and decrease exponentially at our brane. It explains the weakness of the gravity. Comparing to the ADD model, there are less strict constraint on this model because the observables depends on the AdS curvature. According to the AdS/CFT correspondence, the physics of the warped five extra dimensions can be interpreted to the four-dimensional-strongly-interacting theories [29]. The phenomenology is close to the composite models which are explained in the next section.

1.2.2 Compositeness

One solution of the hierarchy problem is to consider the Higgs boson as a composite state like pion in the QCD. When a symmetry breaks spontaneously, Nambu-Goldstone bosons, massless scalar particles, appear [30]. If the symmetry is not exact but approximate and breaks spontaneously, the Nambu-Goldstone bosons (NGB's) can obtain their masses. The bosons in this case are referred to as pseudo-Nambu-Goldstone bosons (pNGB's). The chiral symmetry in the QCD corresponds to the situation. If quarks do not have their masses, the symmetry is exactly conserved in which the left- and right-handed components are not mixed. However, since quarks have non-zero masses after the electroweak symmetry breaking, the chiral symmetry corresponds to the approximate symmetry. Then, the chiral symmetry breaks spontaneously, and the pNGB's appear. The pNGB's are pions, which have lower mass than the QCD energy scale. Above the QCD energy scale, the vectors and fermions appear as composite states of quarks. The idea of compositeness is analogous to the chiral symmetry breaking.

Higgs boson as a pseudo-Nambu-Goldstone boson

The BSM models such as Composite Higgs [31–33], and Little Higgs [34, 35] extend the SM by adding a the new strongly-interacting sector with a global symmetry. The Composite Higgs model proposed by Kaplan and Georgi in 1984 introduce a new strong sector with a global symmetry $\mathcal{G}$. At some energy scale f, the global symmetry is spontaneously broken to the symmetry group $\mathcal{H}$. The $\mathcal{H}$ contains the SM electroweak group $SU(2)_L \times U(1)_Y$. In the coset $\mathcal{G}/\mathcal{H}$, several NGB's emerge,

and then some of them are equivalent to the complex SU(2)-doublet Higgs field H. The NGB's are composite as the pion in the QCD. When gauging $SU(2)_L \times U(1)_Y$ and breaking the symmetry $\mathcal{G}$ explicitly, the Higgs field obtains its mass and behaves as the pNGB. This is an analogy to the pions as pNGB's. This idea can avoid the divergence of the Higgs boson mass because the Higgs boson does not exist above the energy scale f. The minimal composite Higgs model (MCHM) [36] is known as an minimal example. This model assumes that the symmetry $\mathcal{G} = SO(5) \times U(1)$ is broken to the symmetry $\mathcal{H} = SO(4) \times U(1)$. In the case, four real NGB's emerge in the coset $\mathcal{G}/\mathcal{H}$, which are equivalent to the components of the Higgs fields. This is the idea of the model proposed by Kaplan and Georgi. The other possibilities of the global symmetry [37] and the other models such as Little Higgs are studied. In general, the other resonances of hadrons in the QCD appear at the energy scale $m \sim g_\rho f$ where the coupling g_ρ in the strong sector ranges from 1 to 4π. One distinctive feature is the appearance of new fermions, vector-like quarks, which will be described in Section 1.3.1.

Top quark compositeness

The strongly-interacting gauge theories such as AdS/CFT correspondence of RS extra dimension [29] and Top partial compositeness [38] predict the SM top quark as a full or partial composite state [39–41]. The full composite state assumes that the top quark is made of new particles, while the partial compote state assumes that it is made of the top quark and the other new particles. The idea can explain the largest mass of the top quark in the SM. It is known that the electroweak precise measurements provides strong constraints on the compositeness of the left-handed top quark [42]. In this dissertation, it is assumed that only the right-handed top quark is a composite state. The top quark compositeness can be tested by the deviation on the couplings of $Zt\bar{t}$ and $Wt\bar{b}$ from the SM expectation. In addition, the compositeness predicts the enhancement of the four-top-quark production [39], which will be described later.

1.3 Signatures of the physics beyond the Standard Model

The BSM scenarios predicts new particles or deviations from the SM expectation. The new particles are usually heavy and unstable to decay immediately and detectable from the decay products. The scenarios reviewed in Section 1.2.1 and 1.2.2 predict new particles referred to as vector-like quark or enhancement of four-top-quark production. These new signatures can result in the final state including the top-antitop quark pair and additional jets. This section shows the phenomenology for the distinctive signatures.

1.3.1 Vector-like quark

The BSM models reviewed above predict new particles, vector-like quarks (VLQ's). They are fermions with the spin of $1/2$ under the $SU(3)_C$ gauge group and their left- and right-handed components have the same colour and electroweak quantum numbers. The VLQ's do not obtain their mass from the Yukawa couplings to the Higgs doublet field but the symmetry breaking at higher energy scale. These new quarks are known to mix with the SM particles with small mixing

Table 1.2: Possible SU(2) multiplet of the VLQ's. "Q" represents the electric charge. The SM multiplets are also shown as a reference.

Q	SM quarks	Vector-like quarks
+5/3		$\begin{pmatrix} X \\ T \end{pmatrix}$ $\begin{pmatrix} X \\ T \\ B \end{pmatrix}$
+2/3	$\begin{pmatrix} u \\ d \end{pmatrix}$ $\begin{pmatrix} c \\ s \end{pmatrix}$ $\begin{pmatrix} t \\ b \end{pmatrix}$	(T) $\begin{pmatrix} T \\ B \end{pmatrix}$ $\begin{pmatrix} T \\ B \\ Y \end{pmatrix}$
−1/3		(B) $\begin{pmatrix} B \\ Y \end{pmatrix}$
−4/3		

angles. From these features, the VLQ's are allowed experimentally. For instance, the introduction of the VLQ's result in the modification of the cross section on the Higgs boson at the LHC. In the gluon-fusion-production process ($gg \to H$), the cross section is known to increase by at most 6.4% with respect to the SM. In the di-photon decay process ($H \to \gamma\gamma$), the partial width decrease by at most 0.4% with respect to the SM [43]. The accuracy of the measurements for these values ranges at 20-30% at the ATLAS experiment in Run1 [44]. Even with an integrated luminosity of 3000 fb^{-1}, the accuracy is expected to be around 5-15% [45]. Thus, there is no severe constraints on the VLQ until now. The direct searches are the best way to verify the existence of VLQ's. However, the contribution of VLQ's into the Higgs boson process may be seen in the future LHC program. They can appear in seven gauge-covariant multiplets with SU(3)$_C$⊗SU(2)$_L$⊗U(1) quantum numbers [46]. The possible multiplets are shown in Table 1.2.

The VLQ fields T, B, X and Y have the electric charge of $+2/3$, $-1/3$, $+5/3$, and $-4/3$, respectively. For example, when a vector-like quark T is added into the SM, the mass eigenstates of the SM particles, (u, c, t) and T can have non-zero component of the weak eigenstate of the vector-like quark T^0. The VLQ's can have the flavour changing neutral current since they break the Glashow-Iliopoulos-Maiami mechanism [47]. It results in the deviation of the couplings in the SM such as the coupling of Z boson to the up quark. Considering the results on the precise measurements at LEP, it is reasonable to assume that only third generation quarks have sizeable T^0 component [43]. Therefore, this dissertation only consider the mixing to top and bottom quarks. The vector-like quark T (B) is often called top(bottom)-partner or vector-like top (bottom) quark, referred to as VLT(VLB), since the SM top (bottom) quark has the largest mixing with the T (B) quark. The mass eigenstate of the SM top quark and T quark can be written with the mixing angle θ^u as:

$$\begin{pmatrix} t_{L,R} \\ T_{L,R} \end{pmatrix} = \begin{pmatrix} \cos\theta^u_{L,R} & -\sin\theta^u_{L,R} e^{i\phi_u} \\ \sin\theta^u_{L,R} e^{-i\phi_u} & \cos\theta^u_{L,R} \end{pmatrix} \begin{pmatrix} t^0_{L,R} \\ T^0_{L,R} \end{pmatrix}, \tag{1.52}$$

where ϕ_u is the CP-violation phase. The mixing angles are constrained from the experimental results at the LEP and SLC [43] to be approximately $\sin\theta_{L,R} < 0.15$ for all the multiplets.

VLQ's are produced with strong or electroweak interaction at LHC. In the strong interaction, gluons originated from the protons are merged, and the VLQ and anti-VLQ are produced in pair as shown in Fig. 1.6 (a). The production cross section depends on only the mass of the VLQ. In the electroweak interaction, a VLQ is produced via W boson, shown in Fig. 1.6 (b). Since the interaction between the VLQ and W boson depends on the mixing angle to the corresponding SM quark, the production

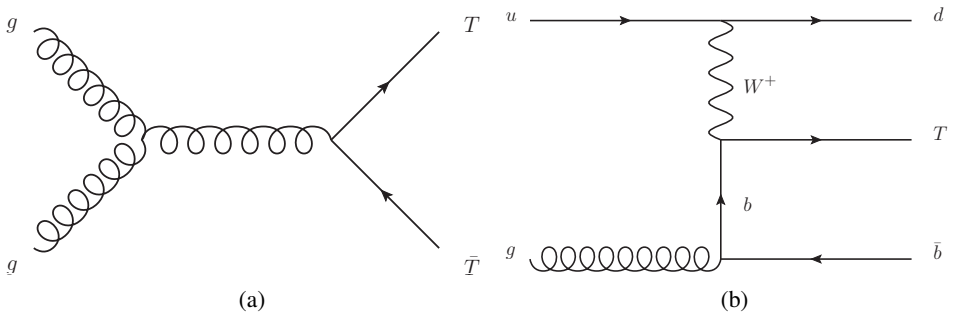

Figure 1.6: Feynman diagrams for VLQ production via (a) strong and (b) electroweak interaction. Only the productions of the vector-like top quark T are shown. Other VLQ's such as X, Y, B are expected to be produced in the same diagrams.

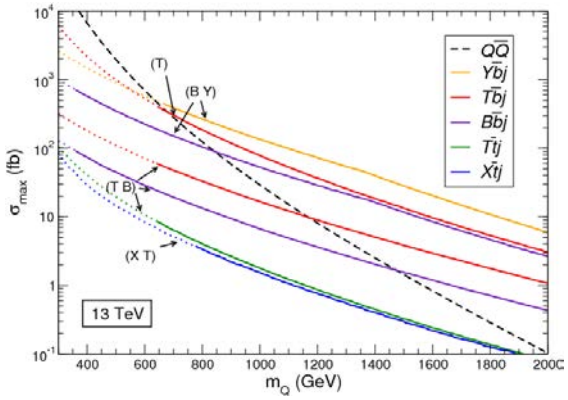

Figure 1.7: Production cross section of the VLQ via the strong (black dashed line) and electroweak (colour lines) interactions assuming a centre-of-mass energy of 13 TeV at the LHC. X, T, B, and Y stand for the VLQ's, and t, b, and j stand for the SM top, bottom, and light quark, respectively. The colour solid lines in the figure show the cross section with the maximum mixing angle allowed experimentally, while the experimentally excluded ranges are shown in dotted lines. Cited from [43].

cross section depends on the mass and mixing angle of the VLQ. Figure 1.7 shows the production cross section assuming the centre-of-mass energy of 13 TeV at the LHC for the strong (black dashed line) and weak interactions (colour solid and dotted lines) as a function of the mass of the VLQ. As described above, the cross section in the strong interaction depends only on the mass, while that in the electroweak interaction depends on the mass and mixing angle. The colour solid lines in the figure show the cross section with the maximum mixing angle allowed experimentally. In general, with small mixing angle, the cross section is less than that of larger mixing angle. The experimentally excluded ranges are shown in dotted lines. Comparing the maximum cross section in the electroweak interaction with that in the strong interaction, the pair production with the strong interaction is expected to be dominant for the mass below around 800 GeV, while the single production with the electroweak interaction is dominant for the higher mass range.

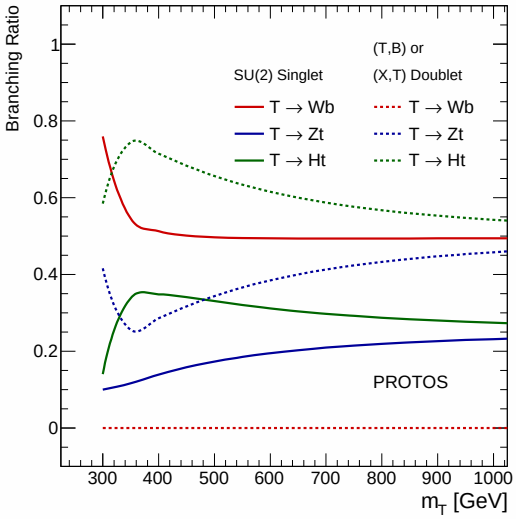

Figure 1.8: Branching ratio of vector-like top quark decaying to Wb (red), Zt (blue), and Ht (green) as a function of its mass with SU(2) singlet (solid line) and SU(2) doublet (dashed line).

The VLQ's decay directly to the SM top or bottom quarks with W, Z, or Higgs bosons because the precise measurements also lead to the constraints on the mass splitting of order 1 GeV for the VLQ's belonging to the same multiplet [43]. The X and Y quarks decay to W^+t and W^-b, respectively, due to their electric charge. The T quark can decays to W^+b, Zt, and Ht, while B quark can decays to W^-t, Zb, and Hb. The three branching ratios are not independent but have the relation:

$$BR(Q \to Wq') + BR(Q \to Zq) + BR(Q \to Hq) = 1, \tag{1.53}$$

where $(Q, q, q') = (T, t, b), (B, b, t)$. For the singlet case, a VLQ can decay to the three modes, while the doublet or triplet cases have constraints on the decay modes. In the case of (T, B) doublet, the two VLQ's interaction depends on the relative size of the up- and down-type mixing angles: θ^u and θ^d. If $\theta^u \sim \theta^d$, the two VLQ have the same decay modes as the singlet. If only the mixing between VLT and the SM top quark is large: $\theta^u \gg \theta^d$, the decay modes of $T \to W^+b$, $B \to Hb$, $B \to Zb$ are suppressed. In this dissertation, the latter case is considered. In the case of (X, T) doublet, it is known that the T quark does not decay to the bottom quark with W boson but decay to the top quark with Z and Higgs bosons [48]. In the triplet cases, the branching ratio is similar to the ones in the singlet or doublet cases. Figure 1.8 shows the branching ratio related with vector-like top quark as a function of the mass of the VLQ assuming the singlet and doublet cases. Eventually, this dissertation takes the singlet and doublet cases into account.

The analyses for the VLQ's are set by the ATLAS and CMS experiments with $\sqrt{s} = 13$ TeV at the LHC as of December 2017. In the ATLAS experiment, there are three analyses to search for the pair production of VLT's decaying to Wb, Zt,and Ht. The analysis for $T\bar{T} \to Ht + X$, where X stands for any of decay modes, sets the observed (expected) limits on the VLT mass to exclude the ranges of $m_{\mathrm{VLT}} < 1020$ (960) GeV for the singlet case, $m_{\mathrm{VLT}} < 1160$ (1110) GeV for the doublet case, $m_{\mathrm{VLT}} < 1200$ (1160) GeV for the case of $\mathrm{BR}(T \to Ht) = 1$, and $m_{\mathrm{VLT}} < 1100$ (1040) GeV

Table 1.3: Summary of the lower mass limits on the VLT.

Experiment	Analysis	Int. luminosity	Obs. (exp.) limit [GeV]	Branching ratio	Ref.
ATLAS	$T\bar{T} \to Ht + X$	13.2 fb^{-1}	$m_{\mathrm{VLT}} < 1200$ (1160)	BR$(T \to Ht) = 1$	[49]
	$T\bar{T} \to Zt + X$	36.1 fb^{-1}	$m_{\mathrm{VLT}} < 1160$ (1170)	BR$(T \to Zt) = 1$	[50]
	$T\bar{T} \to Wb + X$	36.1 fb^{-1}	$m_{\mathrm{VLT}} < 1350$ (1310)	BR$(T \to Wb) = 1$	[51]
CMS	$T\bar{T} \to WbWb$	35.8 fb^{-1}	$m_{\mathrm{VLT}} < 1295$ (1275)	BR$(T \to Wb) = 1$	[52]

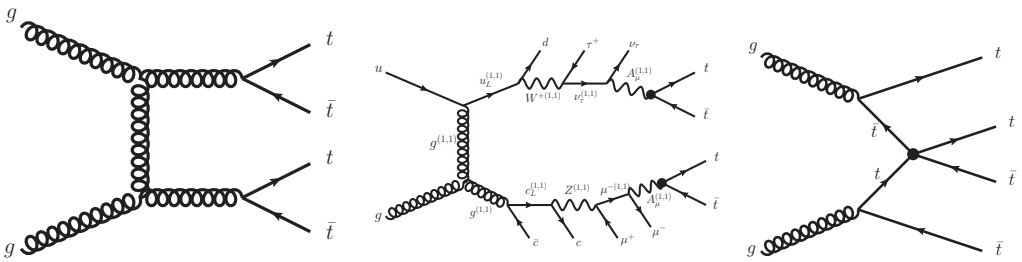

(a) (b) (c)

Figure 1.9: LO Feynman diagram of four-top-quark production in the SM (a), the BSM scenarios of 2UED-RPP (b) and contact interaction (c).

for the case of BR$(T \to Zt) = 1$ with 13.2 fb^{-1} of data [49]. The analysis for $T\bar{T} \to Zt + X$ sets the observed (expected) limits on the VLT mass to exclude the ranges of $m_{\mathrm{VLT}} < 870$ (890) GeV for the singlet case, $m_{\mathrm{VLT}} < 1050$ (1060) GeV for the doublet case, and $m_{\mathrm{VLT}} < 1160$ (1170) GeV for the case of BR$(T \to Zt) = 1$ with 36.1 fb^{-1} of data [50]. The analysis for $T\bar{T} \to Wb + X$ sets the observed (expected) limits on the VLT mass to exclude the ranges of $m_{\mathrm{VLT}} < 1170$ (1080) GeV for the singlet case and $m_{\mathrm{VLT}} < 1350$ (1310) GeV for the case of BR$(T \to Wb) = 1$ with 36.1 fb^{-1} of data [51]. In the CMS experiment, the analyses are split based on the final state signature. The analysis to search for the signature of $T\bar{T} \to WbWb$ sets the observed (expected) exclusion limits on the VLT mass to exclude the range of $m_{\mathrm{VLT}} < 1295$ (1275) GeV for the case of BR$(T \to Wb) = 1$ with 35.8 fb^{-1} of data [52]. A search for the pair production of the X quark with the same-sign dileptons sets the limits on the mass to exclude the range $m_{X_{5/3}} < 1160$ (1200) GeV for right handed X quark and $m_{X_{5/3}} < 1100$ (1150) GeV for left handed X quark with 35.9 fb^{-1} [53]. The lower VLT mass limits described above are summarised in Table 1.3.

1.3.2 Four-top-quark production

The production cross section of four-top-quark events in the SM shown in Fig. 1.9 (a) is estimated to be $\sigma_{t\bar{t}t\bar{t}} \simeq 9$ fb at $\sqrt{s} = 13$ TeV [54, 55]. This small cross section is useful to see any deviations originated from BSM models since the BSM models enhance the cross section. Figure 1.9 shows the leading order Feynman diagrams of four-top-quark production in the SM and the different BSM scenarios considered in this dissertation.

In the SM, the four-top-quark production has not been discovered yet due to its small cross section as described. The upper limits on the production cross section has been set in both the ATLAS and CMS experiments. In the ATLAS experiment, the observed (expected) limits are set to be 130 (110) fb with 13.2 fb^{-1} of data at $\sqrt{s}$ = 13 TeV [49]. In the CMS experiment, the observed (expected) limits are set to be 41.7 ($20.8^{+11.2}_{-6.9}$) fb with 35.9 fb^{-1} of data at $\sqrt{s}$ = 13 TeV [56].

In 2UED-RPP, the KK modes are represented with a tier shown in Eq. (1.51). As described in Section 1.2.1, the tier (1,0) and (0,1) produce the final state involving the missing energy and soft particles, which is difficult to be detected. The particles in tier (1,1) can be produced at the LHC and decay to the SM particles. As shown in Fig. 1.9 (b), the KK particles from the tier are produced in pair because of the symmetries of the model and decay into the lightest particle in this tier, the heavy photon $A^{(1,1)}$, with emitting SM particles. During the chain decay of KK particles, the out-going SM particles have very low momentum and are not detected since the KK particles are degenerate in mass. Then, the heavy photon $A^{(1,1)}$ is expected to decay to $t\bar{t}$ dominantly [26]. In the ATLAS experiment, the previous analysis provided the strongest exclusion limits. The observed (expected) limits are set to be in the range of $m_{KK} > 1.6$ (1.5) TeV with 13.2 fb $^{-1}$ of data with the centre-of-mass energy of 13 TeV [49]. The CMS experiment did not provide a corresponding result yet as of December 2017.

Other BSM models can contribute to the $t\bar{t} \to t\bar{t}$ scatter with exchanging new heavy vector particles within a very short distance. Since the interaction can occur with exchanging virtual bosons even at the LHC energy, the interaction is referred as contact interaction. It is possible to parameterise the new physics by using the effective field theory (EFT) approach similarly as the description of beta decay by Fermi using four-point interaction. This approach is used to describe the physics process for the composite top quark scenarios and RS models [57]. The Lagrangian for a four-point interaction is assumed as:

$$\mathcal{L}_{4t} = \frac{C_{4t}}{\Lambda^2}(\bar{t}_R\gamma^\mu t_R)(\bar{t}_R\gamma_\mu t_R), \tag{1.54}$$

where t_R is the right-handed top quark, Λ is the new physics energy scale and C_{4t} is the effective coupling constant. Here, only the interaction with right-handed top quarks is considered because the interaction with left-handed top quarks is constrained by the electroweak precise measurements [42]. In the previous analysis, the observed (expected) exclusion limits on the cross section is 51 (54) fb, corresponding to the limit on the free parameter of the model of $|C_{4t}|/\Lambda^2 < 2.9(3.0)$ TeV^{-2} [49]. Since top quarks have higher momentum in this scenario than the ones in the SM, the feature in the EFT leads to the difference of the limits between the EFT and SM. The CMS experiment did not provide a corresponding result yet as of December 2017.

2 The ATLAS Experiment at the Large Hadron Collider

The experimental equipments used for this dissertation are described in this section. In order to search for new phenomena described in the previous section, the high energy collider experiments are necessary. Such experiments consist of the collider and the detector. Section 2.1 describes the overview of the collider and its condition during data-taking period used for this dissertation. Section 2.2 shows the detector used in this dissertation. Section 2.3 describes results of the monitoring system for the Pixel detector developed in this dissertation.

2.1 Large Hadron Collider

The Large Hadron Collider (LHC) [58] is a circular hadron collider with 27 km in circumference located at European Organization for Nuclear Research (CERN) in Geneva, Switzerland. The accelerators are situated in the tunnel around 100 meters underground. It is designed to provide proton bunches containing 10^{11} protons with a beam energy of 7 TeV, which is the highest energy in the world, for precise measurements of the SM and search for new phenomena of BSM. As well as protons, heavy ions such as lead are possible to be accelerated to 2.76 TeV per nucleon for studies of the strong interaction in the high energy density. The LHC has four collision points where the experiments including the ATLAS experiment described later are carried out. This section describe how the LHC achieves the high energy with high instantaneous luminosity and the conditions in 2015 and 2016.

2.1.1 Accelerators

The energy of the particles is increased by several accelerating steps. Protons generated from hydrogen gas by applying electric field to detach the electrons from the hydrogen atom are guided into the Linear Accelerator 2 (LINAC2) and accelerated up to 50 MeV. The protons are injected into Proton Synchrotron Booster (PSB) where the protons are accelerated to 1.4 GeV and formed into bunches. The protons are accelerated up to 25 GeV in Proton Synchrotron (PS) which has a circumference of 628 m and contains 277 electromagnets. The PS can accelerate heavy ions which are injected from the accelerating chain of Linear Accelerator 3 (LINAC3) and Low Energy Ion Ring (LEIR). The PS provides the protons to further accelerating step of Super Proton Synchrotron (SPS) as well as other beam lines of Antiproton Decelerator (AD) and the neutron time-of-flight facility (n_TOF). The SPS has a circumference of around 7 km and contains 1317 electromagnets, and then accelerates protons to 450 GeV. From 1981 to 1991, it had operated as a proton-antiproton collider

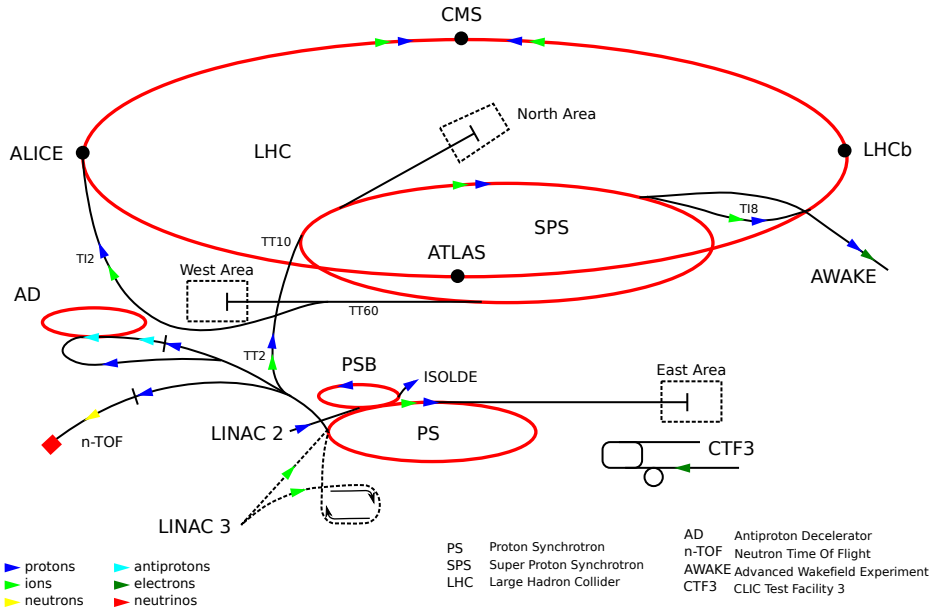

Figure 2.1: Scheme of the accelerating chain at CERN [63]. Protons are accelerated by a set of accelerators in following order: Linear Accelerator 2 (LINAC2), Proton Synchrotron Booster (PSB), Proton Synchrotron (PS), Super Proton Synchrotron (SPS), and LHC. Each accelerating step also provides particles to other various experiments. Heavy ions such as lead are also accelerated along Linear Accelerator 3 (LINAC3), Low Energy Ion Ring (LEIR), and then injected into PS.

where UA1 and UA2 experiments discovered W and Z bosons in 1983 [59–62]. Now it is used as the injector for the LHC, the fixed-target experiments, and the test beam facility. The LHC contains a series of superconducting magnets with 27 km long which are operated at a temperature below 2 K cooled by superfluid helium. The tunnel for the LHC was originally constructed for the Large Electron-Positron Collider (LEP) in which the LEP experiments precisely measured the electroweak interaction. The LHC is designed to obtain the beam energy of 7 TeV. The accelerators contain two beam lines in which the proton bunches go in opposite direction. They cross each other with a certain crossing angle at the four interaction points. These accelerating chains are shown in Fig. 2.1

2.1.2 The Design of the Large Hadron Collider

To increase the beam energy from 450 GeV to 7 TeV, protons are accelerated by a superconducting cavity system. Eight Radio-Frequency (RF) superconducting cavities accelerate the protons with the electric field oscillating with around 400 MHz. The field strength corresponds to 5.5 MV/m and then the energy gain is around 0.5 MeV per turn. A total of 1232 dipole superconducting magnets which are made of niobium-titanium (NbTi) and operated at 1.9 K apply 8.33 T at the maximum to bend the protons. A total of 858 quadrupole magnets are used for focusing the beams along the beam line.

The number of events per second generated by a certain physics process, N_{event}, is described by:

$$N_{\text{event}} = \sigma_{\text{process}} \cdot \mathcal{L}, \tag{2.1}$$

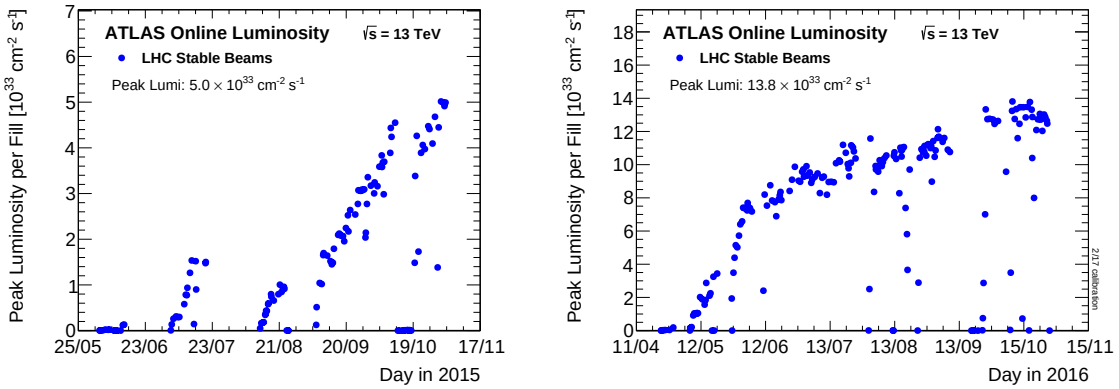

(a) (b)

Figure 2.2: Peak instantaneous luminosity delivered to the interaction point at the ATLAS detector in pp collisions during (a) 2015 and (b) 2016 [64]. The beam energy is 6.5 TeV each, and then the center-of-mass energy is 13 TeV. Each point represents one LHC fill. The stable beam represents ready for physics. The design value of the instantaneous luminosity is 1×10^{34} cm^{-2} s^{-1}.

where σ_{process} is the cross section of the physics process and $\mathcal{L}$ is the instantaneous luminosity. The cross section is determined by physics and the energy transfer, while the instantaneous luminosity depends on the beam parameters:

$$\mathcal{L} = \frac{N_{\text{b}}^2 n_b \gamma_r f_{\text{rev}}}{4\pi\epsilon_n \beta^*} F, \tag{2.2}$$

where N_{b} is the number of particles in a bunch: 1.15×10^{11}, n_b is the number of bunches per beam: 2808, γ_r is the proton beam energy in unit of its rest mass, f_{rev} is the revolution frequency: 11.2 kHz, ϵ_n is the normalised transverse beam emittance: 3.75 μm, β^* is the beta function at the collision point: 0.55 m, and F is the geometric luminosity reduction factor due to the crossing angle: 0.85. The parameters have been determined by the mechanical constraints or optimised to maximise the instantaneous luminosity for each interaction point. With the nominal set of the parameters, the instantaneous luminosity of 1×10^{34} cm^{-2} s^{-1} is obtained. The detail of the beam parameters and equipment are described in in Ref. [58].

Figure 2.2 shows the peak instantaneous luminosity delivered to the interaction point at the ATLAS detector which will be described later in pp collisions during (a) 2015 and (b) 2016. In 2015, the peak luminosity did not reach to the design value due to some of the electric board having radiation damages and worse vacuum condition. During the shutdown between 2015 and 2016, the electric boards were replaced and studies to improve the beam condition were carried out. In 2016, the LHC machine parameter was improved: the transverse emittance ϵ_n changed from 3.5 μm in 2015 to 2.0 μm in 2016 and the beta function β^* changed from 0.8 m in 2015 to 0.4 m in 2016. But the SPS had degradation in its dump vacuum, leading to constraints on the number of bunches per beam up to 2220. Including all the changes, the instantaneous luminosity reached the design value and increased up to 1.38×10^{34} cm^{-2} s^{-1} at the end of 2016.

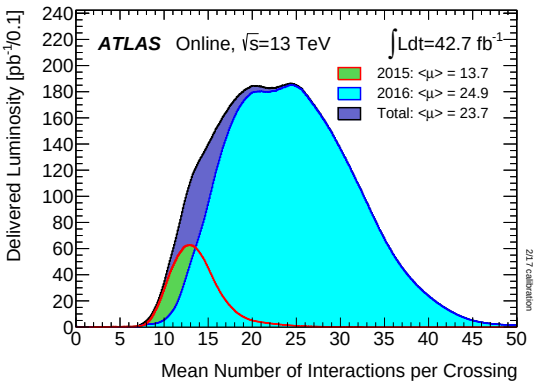

Figure 2.3: Mean number of interactions per crossing for the 2015 and 2016 pp collision data at 13 TeV [64].

Table 2.1: Summary of the physics runs showing the periods, the center-of-mass system energies ($\sqrt{s}$), and the integrated luminosities($\int \mathcal{L}dt$) delivered by the LHC. The long shutdown between the end of 2012 and the beginning of 2015 is called "Long Shutdown 1 (LS1)".

Physics Run	Year	$\sqrt{s}$ [TeV]	$\int \mathcal{L}dt$ [fb^{-1}]
Run1	2010	7	0.048
	2011	7	5.46
	2012	8	22.8
Run2	2015	13	4.2
	2016	13	38.5

Due to the high instantaneous luminosity, several protons can interact each other at one bunch crossing, referred to as "pile-up". The mean number of interaction per bunch crossing is shown in Fig. 2.3. The average pile-up values in 2015, 2016 and their combination are 13.7, 24.9, and 23.7, respectively

Table 2.1 shows the summary of the integrated luminosities during physics runs. The LHC started to provide the collisions for physics in 2010 as Run1. In 2012, the beam energy increased from 3.5 TeV to 4 TeV. Run1 finished at the end of 2012. The long shutdown between the end of 2012 and the beginning of 2015 is called "Long Shutdown 1 (LS1)". During the LS1, a few defects on the accelerator system were fixed. In 2015, the LHC started to provide the beams for physics as Run2 with increased the beam energy to 6.5 TeV. Run2 is planned to finish at the end of 2018.

2.2 ATLAS detector

A Toroidal LHC ApparatuS (ATLAS) experiment has been carried out for multiple purposes of measuring or searching for various physics phenomena in pp or heavy-ion collisions at LHC. In pp collisions, LHC provides rich phenomena to precisely measure the SM and search for new physics.

The search for the SM Higgs boson was one of the most important purposes and used as a benchmark to determine the specification and performances of each subdetector. In 2012 during Run1, a new scalar particle having a consistent property as the SM Higgs boson was successfully discovered by both the ATLAS and CMS experiments. From Run2, the measurements of the SM Higgs boson have been performed to probe the SM Higgs potential and measure the couplings more precisely. The couplings to the SM quarks are important to measure the properties of SM Higgs boson in the processes of $t\bar{t}H$, WH, and ZH with $H \to b\bar{b}$. In addition, pp collisions at LHC produce a lot of SM particles such as vector bosons, B mesons, and top quarks which have potential to study electroweak sector, CP-violation, and top quark property. As well as precise measurements of the SM, the search for new Higgs bosons beyond the SM are also important to be performed by any processes including τ-leptons or bottom quarks. In the supersymmetry models, it is known to produce a dark matter candidate. The particles such as neutrino in the SM and the dark matter candidate does not interact with the detector material, and then results in missing signature in the transverse plane. Thus it is also important to measure the visible particles as well as invisible particles from the momentum imbalance in the transverse plane.

The ATLAS detector shown in Fig. 2.4 is a cylindric detector with 25 meters in height, 44 meters in length, and 7000 tons in weight. In the order of the innermost part from the interaction point, it consists of the three subdetectors: the Inner Detector (ID), the electromagnetic and hadronic calorimeter (Cal), and the muon spectrometer (MS). The ID surrounded by the solenoid magnet is designed to reconstruct the trajectories of charged particles from the interaction point and measures the momenta by the curvature of a trajectory. The electromagnetic and hadronic calorimeters measure the energies of electrons or photons and hadrons, respectively, by measuring the showers formed by numerous interactions between the particles and their absorber materials. The MS embedded in the toroidal magnet measures trajectories and momentum of muons which penetrate the calorimeter volume. Each subdetector is designed to satisfy the requirements from the physics purposes described above. This section describes the overview of each detector component, the trigger system, and the data quality.

2.2.1 Coordinate system

The ATLAS experiment uses the right-handed coordinate system in which the x-axis points to the centre of LHC ring, y-axis points to the sky, and z-axis is along the beam line. In order to point the directions of out-going particles, the spherical coordinate system is used, in which the azimuthal angle ϕ is measured in the x-y plane and ranges from $-\pi$ to $+\pi$, the polar angle θ is measured with respect to z-axis in R-z plane, where R is the radius $R = \sqrt{x^2 + y^2}$, and ranges from 0 to $+\pi$. The origin is set to the centre of the detector where the collisions occur. The energy or momentum projected on the transverse plane (x-y plane) are often used since the energy and momentum should be conserved on the plane. The transverse energy (momentum) are denoted by:

$$E_{\mathrm{T}} = E \sin\theta \tag{2.3}$$

$$p_{\mathrm{T}} = \sqrt{p_x^2 + p_y^2} = |\vec{p}| \sin\theta \tag{2.4}$$

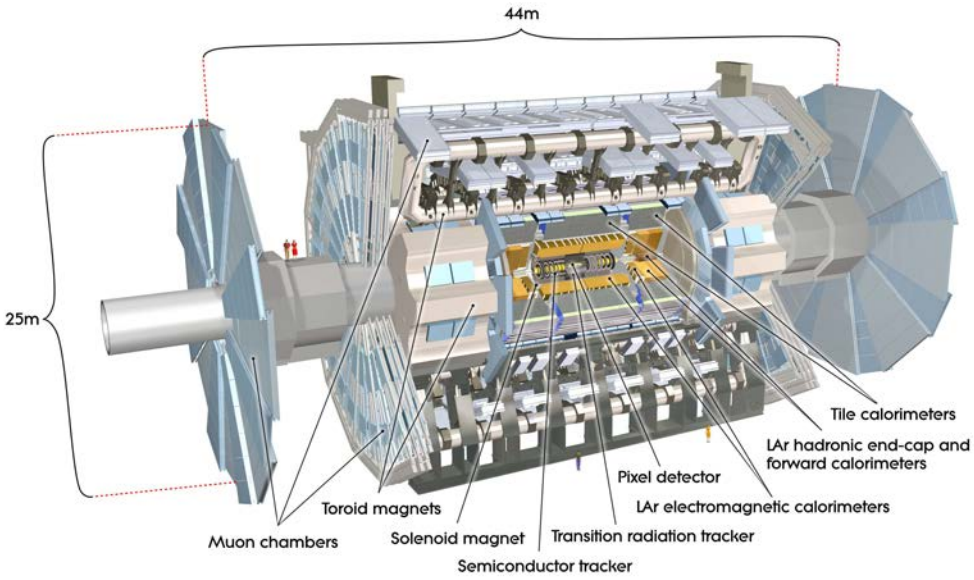

Figure 2.4: Overview of the ATLAS detector which is 25 m in height, 44 m in length, and 7000 tons in weight [65]. From the inner most, it consists of the Inner Detector (ID), electromagnetic and hadronic calorimeter, and muon spectrometer embedded in the toroid magnet. The solenoid magnet is located between the ID and electromagnetic calorimeter, producing the 2 T uniform magnetic field along the beam line.

The pseudo-rapidity η is often used instead of the polar angle θ in the high energy particle physics, defined by:

$$\eta = -\ln \tan(\theta/2) \tag{2.5}$$

To express the distance between particles, the angular distance ΔR is often used, defined by:

$$\Delta R = \sqrt{\Delta\eta^2 + \Delta\phi^2}, \tag{2.6}$$

where $\Delta\eta = \eta_i - \eta_j$ and $\Delta\phi = \phi_i - \phi_j$ for the particles i and j.

2.2.2 Magnet system

The magnet system provides the magnetic field which is necessary to measure the momentum of charged particles from the curvature of the trajectories. It consists of two components: the solenoid magnet [66] located between the ID and EM calorimeter and toroid magnets outside the hadron calorimeter, as shown in Fig. 2.5. These designs of the magnets has mainly three merits. The first merit is to be able to extend the pseudo rapidity coverage up to $|\eta| < 3$. The second merit is to keep the performance of the calorimeters without magnetic fields. The last one is to reduce the effect of multiple scattering in the magnet volume on the momentum resolution of muons thanks to the air-core design.

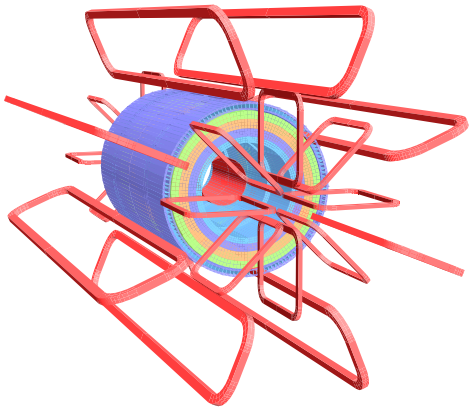

Figure 2.5: Overview of the ATLAS magnet system which is composed of the solenoid, the eight barrel toroid coils, and the eight end-cap toroid coils [65]. The solenoid is located inside the calorimeter. The barrel section of the hadron calorimeter is also shown in four layers and an outside return yoke.

The solenoid magnet provides a magnetic field of 2 T to the ID in parallel to the beam axis which bends charged particles in the transverse plane. It is 2.5 m in radius, 5.8 m in length. It is 4.5 cm thick, corresponding to around 0.66 radiation lengthss. It is designed to reduce the amount of materials as much as possible in front of the calorimeters. It is made of superconductor material (NbTi/Cu) and aluminium stabiliser with the cryostat shared with the EM calorimeter. The flux is returned via the steel of the hadron calorimeter.

The toroid magnets are designed to provide a magnetic fields in ϕ direction for bending muons for the measurement in the muon spectrometer. They are composed of the barrel section and end-cap section for each side. Both sections use similar materials for the conductor to the solenoid and have eight coils aligned in radial direction. The barrel section is 9.4 m and 20.1 m in inner and outer diameter and 25.3 m in length, while the end-carp section is 1.65 m and 10.7 m in inner and outer diameter and 5 m long. The end-cap section is established with an angle of 22.5° against the barrel section in order to obtain the uniform magnetic fields. For the barrel section, each coil has independent cryostat surrounded by the vacuum vessels, while for the end-cap section, the cryostat is shared with the forward calorimeter. The barrel and end-cap sections provide the magnetic fields of 0.5 T and 1 T, respectively.

2.2.3 The Inner Detector

The ID consists of three subdetectors in the order from inside, Pixel detectors, SemiConductor Tracker (SCT), and Transition Radiation Tracker (TRT). The overview of the ID in R-z plane is illustrated in Fig. 2.6. It also shows the Insertable B-Layer (IBL) [67] which was newly installed at the innermost layer during the long shutdown before Run2. The IBL employs a similar technology for the sensor and read-out system to the Pixel detectors, and then often categorised as a part of the Pixel detectors. To efficiently surround the interaction point with the detectors, the detectors consist of the barrel part and end-cap part. The Pixel detectors have 4 layers in the barrel including IBL and 3 disks for each

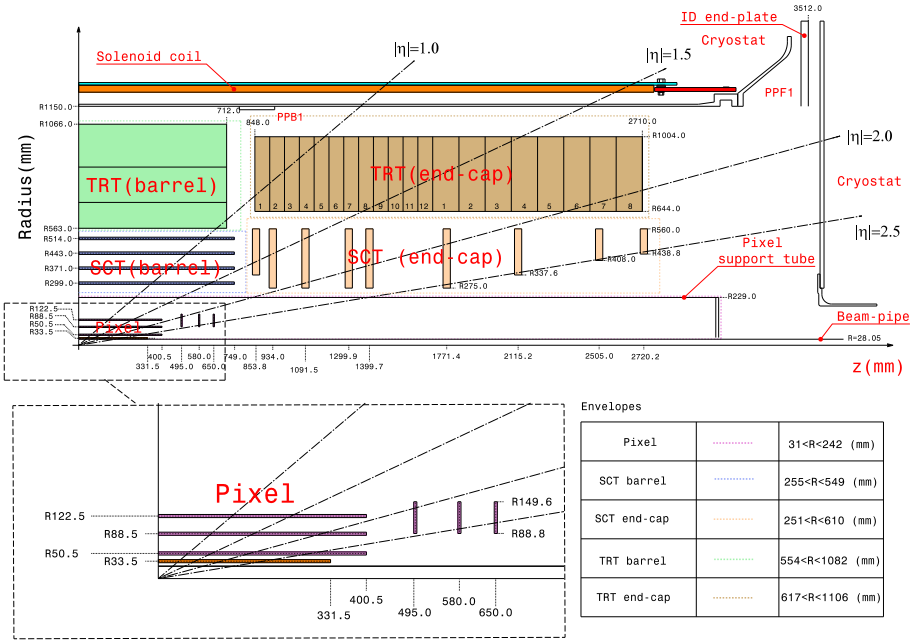

Figure 2.6: Overview of the ID in R-z plane ($z > 0$) [68]. The ID consists of IBL, Pixel, SCT and TRT in the oder of inner part from the interaction point. The IBL, the silicon pixel detector, was installed at a radius (R) of 33 mm before Run2. The Pixel detectors, the silicon pixel detector, have three layers ranged from R = 50.5 mm to R = 122.5 mm and three disks in each end-cap part. The SCT, the silicon micro-strip detector, has four layers ranged from R = 299.0 mm to R = 514.0 mm and nine disks in each end-cap part. The TRT, the gas drift tube detector, covers the radial range from R = 563.0 mm to R = 1066.0 mm and has 20 disks in each end-cap part.

end-cap side. The SCT has 4 layers in the barrel and 9 disks for each end-cap side. The TRT has 73 axial straw tubes in the barrel on which a charged particle is expected to deposit its energy at around 36 tubes on average. Each subdetector detects the electric signals induced by the charged particles penetrating the sensors, and then provides the hit information. All the combined hit information from the three subdetectors are used for reconstruction of the trajectories (track). The reconstruction algorithm and its performance are described in Section 3.1. This section describes each detector in the following.

Pixel detector

The Pixel detectors are located at the innermost part from the interaction point where the particle density is maximum in the ATLAS detector. In order to individually distinguish the particles, the Pixel detectors employ the silicon semiconductor material finely segmented like a rectangle (pixel). The barrel part is composed of four layers: IBL at R = 33.5 mm, B-Layer at R = 50.5 mm, Layer-1 at R = 88.5 mm, and Layer-2 at R = 122.5 mm, where R represents the radii from the origin. The IBL and the other three layers contain 224, 286, 494, 676 detector modules, respectively. Each end-cap

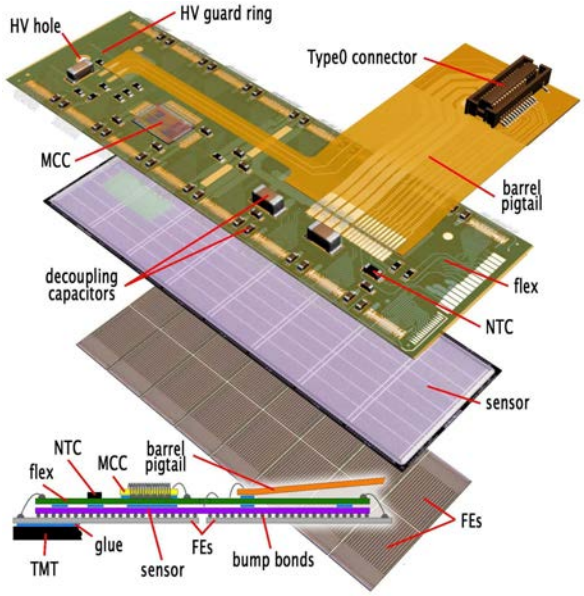

Figure 2.7: Scheme of the Pixel module used for others than IBL [65]. One module contains Module Controller Chip (MCC) on top of the flex which controls all the 16 front-end chips (FE-I3). The chips are bonded to the pixel sensor by bump bonds.

has three disks with a radius of 34 cm located at the positions along z-axis of $|z|$ =49.5, 58.0, 65.0 cm from the origin. Each disk contains 48 detector modules. One IBL module has one or two read-out (front-end) chips, referred to as FE-I4 [69–71] bonded to the pixel sensor whose pixel size is 50 μm wide in ϕ by 250 μm long along z-axis. One FE-I4 chip contains 26880 pixel segments with 336 rows in ϕ direction and 80 columns along z-axis. One pixel segment in the chip contains electric circuits to process the electric signals from the corresponding sensor pixel. The other Pixel module has 16 read-out chips which is different from FE-I4 but referred to as FE-I3 [72], bonded to the pixel sensor whose pixel size is 50 μm wide in ϕ by 400 μm long along z-axis. One FE-I3 chip contains 4096 pixel segments with 256 rows in ϕ direction and 16 columns along z-axis. The total number of pixels (read-out channel) is around 92 million. The spatial resolutions are around 10 μm in ϕ direction for both IBL and the other Pixel detectors and 60 μm and 96 μm along z-axis for IBL and the other Pixel detectors, respectively.

Each electrode in one pixel sensor detects the electrons generated by an incident charged particle inside the depletion zone in the silicon bulk, which are transferred into the read-out chip via bump bonding. The read-out chip stores the information of the pixel position, the value of Time-over-Threshold (ToT) corresponding to the collected charge. In case of IBL, the FE-I4 sends the data with additional information like the error flags into the central data acquisition system. In case of the other Pixel detectors, the read-out chips are controlled by Module Controller Chip (MCC) which sends the data including the chip identification number and similar hit information. The scheme of the module is shown in Fig. 2.7.

The silicon detectors are often operated with low temperature to reduce the thermal noise and mitigate

the effect of radiation damages. Concerning the operating temperature on each layer and disk, the IBL were operated with −10℃ in 2015, +15℃ from May to June in 2016, and +5 ℃ after June in 2016, while the other Pixel detectors were operated with −2℃ in 2015 and −10℃ in 2016 for the barrel layers, −7℃ in 2015 and −13℃ in 2016 for the end-cap disks. The operating temperature at IBL were set depending on the integrated luminosity to deal with the effect on the total ionisation doze.

The monitoring software for the Pixel detectors is developed in this dissertation. The performance and studies of the Pixel detectors from monitoring the data acquisition in 2015 and 2016 are described in Section 2.3.

Semiconductor Tracker

The SCT consists of the silicon micro-strip detector to provide the space points of hit position and covers larger area of 61.1 m^2 than the Pixel detectors. It is designed to provide four measurements for one charged particle in order to obtain precise measurements of momentum, impact parameters, and vertex positions. The SCT barrel uses four layers located at the radii of 299, 371, 443, and 514 mm. Each layer has 384, 480, 576, and 672 detector modules in the order from the inner part. One detector module consists of four detector components. One component is 6.36×6.40 cm^2 with 768 readout strips (electrodes) with 80 μm pitch. On each side of the module, the two detector components are wire-bonded to form 12.8 cm long strips. A pair of the bonded components are glued together back-to-back with a 40 mrad angle in order to provide the two-dimensional hit positions. The end-cap has 9 disks for each side located at the z positions of 853.8, 934.0, 1091.5, 1299.9, 1399.7, 1771.4, 2115.2, 2505.0, and 2720.2 mm, respectively. The end-cap module is constructed in the same way as the barrel module, but employs tapered strips. The SCT has 6.2 million readout channels in total. The spatial resolution is 16 μm in ϕ direction and 580 μm along z-axis.

Transition Radiation Tracker

The TRT consists of the straw detector fulfilled with gas. The TRT barrel section consists of 73 layers of the straws established in parallel to the beam axis. It has 52,544 straws in total and covers the larger area ranging from 560 mm to 1080 mm in radii and $|z| < 712$ mm along the z-axis. The end-cap section has 20 wheels in each side containing 8 layers of straws per wheel set perpendicular to the beam axis and covers the area ranging from 644 mm to 1004 mm in radii and from 827 mm to 2744 mm along z-axis. Each end-cap layer has 768 straws in R-ϕ plane. Each end cap section has 122,880 straws in total. One straw is 4 mm in diameter and made of carbon-fibre-reinforced kapton straw applied -1530 V and gold-plated tungsten ground wire at the centre. It is filled with a gas mixture of 70% of Xe, 27% of CO_2, and 3% of O_2. During Run2, the straws which had gas leaks in Run1 are filled with the argon-based mixture gas of 70% Ar, 27% CO_2, and 3% O_2. The xenon gas is used to absorb the transition radiation X-ray generated in the radiator material made from polypropylene or polyethylene to identify electrons. On the other hand, the argon gas has lower efficiency to absorb the transition radiation X-ray but has similar performances of tracking as the xenon gas. The radiator material is filled in the gap between the straws. The configuration of the gas is shown in Fig. 2.8. The acceptance of TRT is ranging $|\eta| < 2.0$.

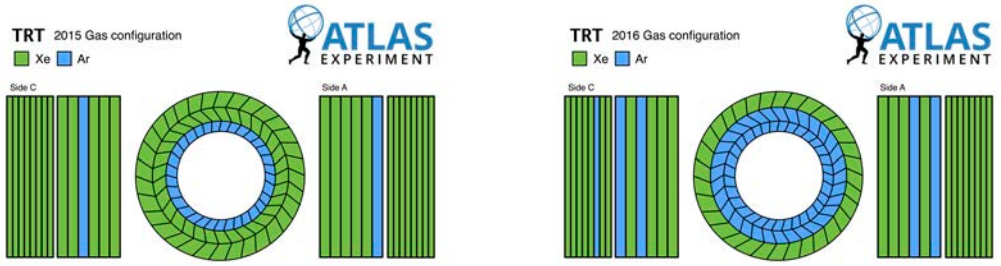

(a) (b)

Figure 2.8: Gas configuration in TRT during (a) 2015 and (b) 2016 [73]. The xenon-based and argon-based gas are shown in green and blue, respectively.

When a charged particle penetrates a straw, it deposits about 2.5 keV of energy in the gas, and then creates the electron-ion pairs. The electrons drifts to the central wire, creates cascades in strong electric field close to the wire and then produces the electric signals. The electric signals are amplified, shaped, and discriminated with respect to two thresholds: low level and high level. The low level threshold is used to measure the drift time between the incidence of a charged particle and detection of the electric signal and determine the position of an incident charged particle inside the straw. The position accuracy is estimated as around 120 μm for both data and simulation in Run2. The high level threshold is used to identify the large energy deposit from the transition radiation X-ray which has typically 6-15 keV. This threshold is used to discriminate electrons from charged pions.

2.2.4 The Calorimeters

To achieve the physics goals described above, it is necessary to accurately measure the energies of all the particles as well as the missing energy. The calorimeters are in charge of measuring the energies and identifying the particles. They consist of two sampling calorimeters: the electromagnetic (EM) calorimeter and hadron calorimeter. The EM calorimeter is designed to measure the energies of electrons and photons by using lead absorber and liquid argon scintillator (LAr). It covers the pseudo rapidity range of $|\eta| < 3.2$ and has high granularity to measure the shower development inside the calorimeter and identify the particle. The hadron calorimeter is designed to measure the energies of hadrons. The barrel sections for the pesudo rapidity range of $|\eta| < 1.7$ use the steel tile absorber and plastic scintillator. The endcap section for the range of $1.5 < |\eta| < 3.2$ use the copper plate absorber and liquid argon scintillator. The forward calorimeter covers the range of $3.1 < |\eta| < 4.9$ and is made of the copper and tungsten absorber and liquid argon scintillator. With the large coverage of η, the calorimeter is able to accurately measure the jet energy and missing energy.

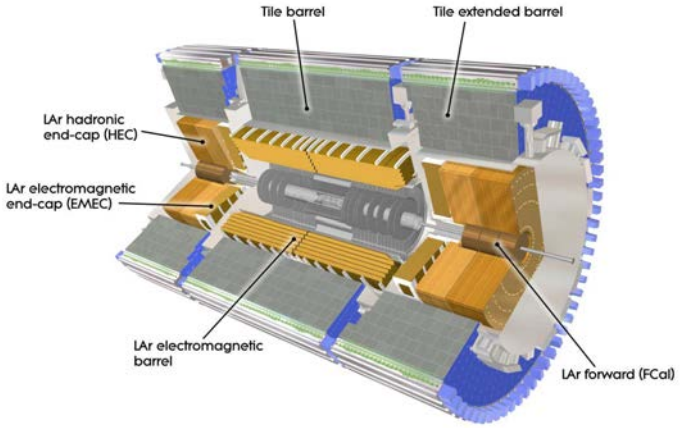

Figure 2.9: Cut-view of the calorimeter system which consist of the EM and hadron calorimeters [65]. The EM calorimeter uses liquid argon scintillator (LAr) and lead absorber and has two sections of the barrel and end-caps. The hadron calorimeter uses the combination of tile-shape plastic scintillator and steel absorber for the pseudo rapidity range of $|\eta| < 1.7$ and the combination of liquid argon and copper or tungsten absorber for the other range. It has four sections of the Tile barrel and extended barrel, LAr end-cap, and Forward calorimeter (FCal).

Electromagnetic calorimeter

The electromagnetic calorimeter is designed to measure the energy of electrons and photons precisely with liquid argon scintillator and lead absorber for the range of $|\eta| < 3.2$. The barrel part for the range of $|\eta| < 1.475$ and end-cap part for the range of $1.375 < |\eta| < 3.2$ employ the accordion-shape design of the absorber and the read-out electric circuits shown in Fig. 2.10 to achieve azimuthal uniformity and no instrumental gap. The modules for the range of $|\eta| < 2.5$ have three layers in radial direction while the ones for the other pseudo rapidity range have two layers. The inner strip layer has 0.0031×0.098 granularity in $\eta \times \phi$ plane to improve the particle identification. It has a thickness of 4.3 radiation lengthss. The middle layer has a 0.025×0.0245 granularity in $\eta \times \phi$ plane and a thickness of 16 radiation lengthss to measure most of the energy deposited in the calorimeter. The third layer has 0.05×0.0245 granularity in $\eta \times \phi$ plane and a thickness of 2 radiation lengthss to correct the energy beyond the calorimeter. For the central region in the range of $|\eta| < 1.8$, the additional layer so-called presampler is equipped directly in the inner side of the EM calorimeters. It consists of a single layer of the liquid argon scintillator without lead absorber to measure the energy before the calorimeter. In total, the EM calorimeter has a thickness of more than 22 radiation lengthss.

The relative energy resolution is expressed as:

$$\frac{\sigma}{E} = \frac{a}{\sqrt{E}} + \frac{b}{E} + c, \tag{2.7}$$

where a is the sampling term, b is the noise term, and c is the constant term. The sampling term contributes the resolution for lower energy. Its design value is $a \sim 9\% \times \sqrt{\text{GeV}}$. The noise term

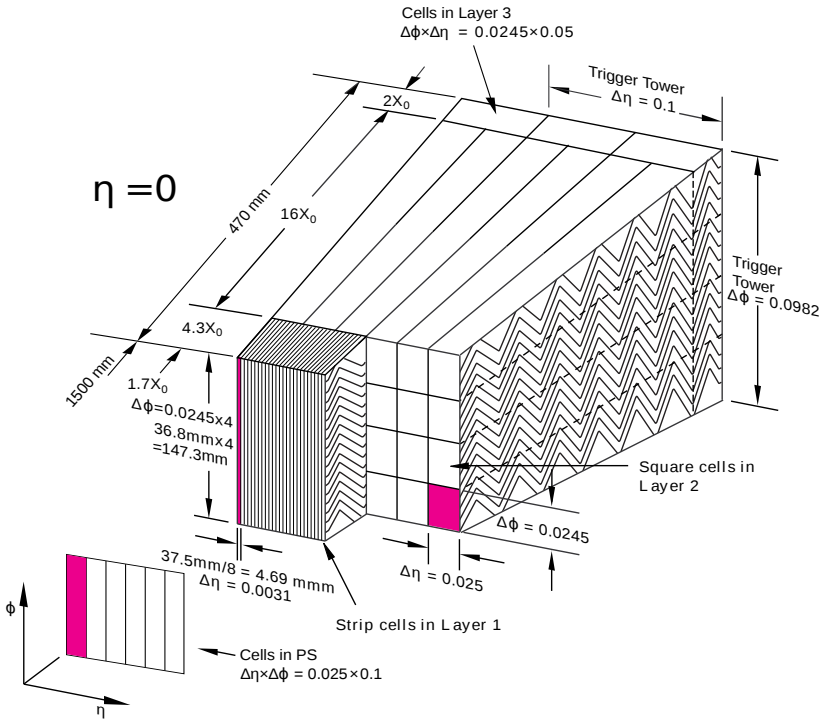

Figure 2.10: Accordion-shape EM calorimeter with three layers used for the pseudo rapidity range of $|\eta| < 2.5$ [65]. For the central region of $|\eta| < 1.8$, the presampler (PS) is equipped directly in the inner side of the EM calorimeters.

is around $350 \times \cosh \eta$ MeV for a cluster of 3×7 cells in $\eta \times \phi$ space in the barrel section. The constant term dominates for high energy. Its design value is 0.7%. In the pseudo rapidity range of $1.375 < |\eta| < 1.475$ where the barrel part is overlapped with the end-cap part, the energy resolution is worse than the other region.

Hadron calorimeter

The barrel section using the steel tile absorber so-called Tile Calorimeter is composed of the long barrel for the pseudo rapidity range of $|\eta| < 0.8$ and extended barrel for the range of $0.8 < |\eta| < 1.7$. The section has a length of 2.6 m along z-axis, an inner radius of 2.28 m, and an outer radius of 4.25 m. The hadrons come from the pp collisions generate the shower with nuclear interactions inside the calorimeter. The charged particles deposit the energy, and then generate the scintillation light. The lights are transferred into the photomultiplier tubes (PMT) located in the outer side of the module by the wavelength shifting fibres. All the fibres in one read-out cell are grouped into individual PMTs. The cells have a granularity of 0.1×0.1 in $\eta \times \phi$ space and are segmented as pointing the detector's centre according to the pseudo rapidity shown in Fig. 2.11. The barrel section is segmented in three layers in radial direction whose thicknesses are 1.5, 4.1, and 1.8 interaction lengths at the pseudo rapidity of $\eta = 0$. The end-cap section using the copper plate absorber and

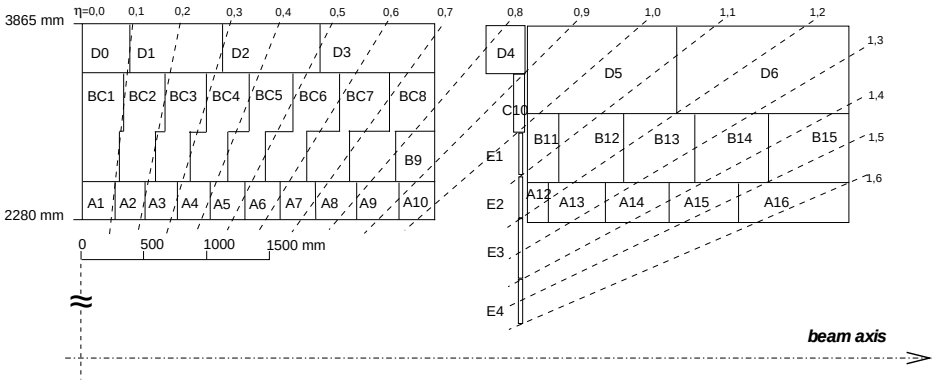

Figure 2.11: Segmentation of the long barrel (left) and extended barrel (right) in the Tile calorimeter in R-z plane [65]. The bottom side corresponds to the inner radius and the left side corresponds to the detector centre.

liquid argon consists of two wheels in each end-cap side. The wheels are located just after the EM calorimeters and overlapped with the Tile and forward calorimeters to reduce the effect on the energy measurement of the transition between the sections. The inner and outer wheel consist of 32 modules for each which are made of the copper plate with 25 mm and 50 mm thickness, respectively. The gaps of 8.5 mm between the plates are filled with liquid argon.

The forward calorimeter covers high pseudo rapidity range of $3.1 < |\eta| < 4.9$ and consists of three layers. The innermost layer is composed of the copper absorber and liquid argon and designed to precisely measure the energies of electrons and photons, while the other layer is composed of tungsten absorber and liquid argon and designed to measure the energies of hadrons. The total thickness is 10 interaction lengths. The combined energy resolution of the EM and Tile Calorimeters is evaluated by pion beams [74]. According to the parametrisation of Eq. (2.7), the sampling term is $(52.0 \pm 1.0)\% \times \sqrt{\text{GeV}}$, the noise term is 1.6 GeV $\pm 0.1\%$, and the constant term is $(3.0 \pm 0.1)\%$.

2.2.5 Muon spectrometer

The MS is designed to reconstruct the trajectories of muons and measure the momentum of muons from the curvatures of the trajectories in the magnetic field provided by the toroid magnets. It consists of four subdetectors for the different purposes: Monitored Drift Tube chambers (MDT's), Cathode Strip Chambers (CSC's), Resistive Plate Chambers (RPC's), and Thin Gap Chambers (TGC's). The cross section of the MS in R-z plane is shown in Fig. 2.12. The MDT provide the precise measurement on the momentum for the pseudo-rapidity range of $|\eta| < 2.7$. It has three layers: the inner, middle, and outer. Each layer has two chambers which contain drift tubes with 30 mm diameter and 1-6 m long filed with a gas mixture: 93% Ar and 7% CO_2, which detect the charged particle in similar way as the TRT. The position resolution of MDT is 80 μm per drift tube and 35 μm per chamber. The CSC is used for the innermost layer in the high pseudo-rapidity range of $2.0 < |\eta| < 2.7$ to deal with high rate measurements. It is a multi-wire proportional chamber whose spatial resolution is 60 μm in the bending plane.

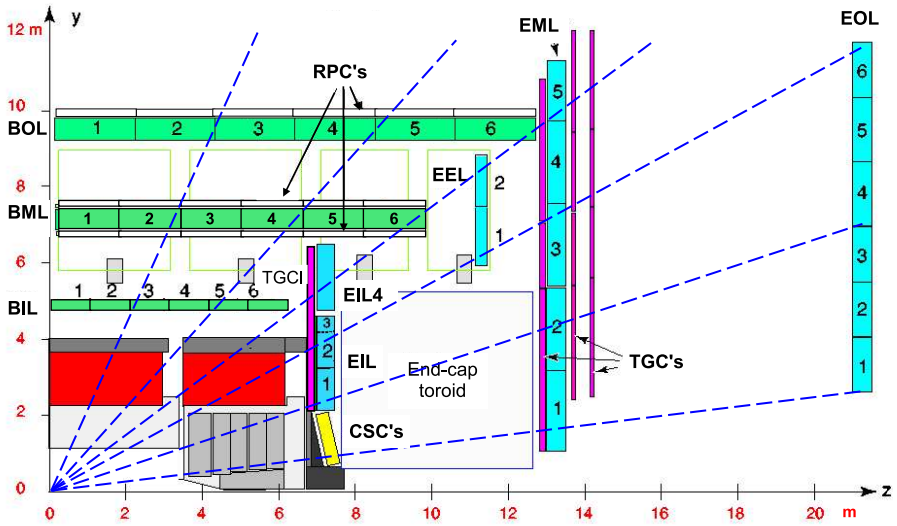

Figure 2.12: Cross section of the MS in R-z plane (bending plane) [65]. The MDT's are shown in green for the barrel (B) and blue for the end-cap (E). The second and third letters represent the layer name of the inner (I), middle (M), or outer (O) and their belonging sector of large (L) or small (S). The sequential number represents the sector number of a chamber. The "EEL" represents the End-cap Extra Large chamber located about 3-3.6 m away from the inner wheel. The CSC's (yellow) are located at the innermost layer for the pseudo-rapidity range of $2.0 < |\eta| < 2.7$. The RPC's (white box) are put on the sides of the middle and outer barrel layers of MDT. The TGC's (purple) are located in the end-cap section.

One more purpose of the MS is to provide triggers based on muon measurements. The trigger chambers are required to provide an electric signal within tens of nano-seconds just after a penetrating charged particle. The RPC covers the pseudo-rapidity range of $|\eta| < 1.05$ and TGC covers the range of $1.05 < |\eta| < 2.4$. The RPC has three layers and each module is a gaseous detector with electrode plates. It has a timing resolution of 1.5 ns. The TGC's are multi-wire proportional chambers and have four layers. It has a timing resolution of 4 ns.

2.2.6 Trigger system

While the proton bunches cross with 40 MHz, the event recording is limited up to 200 Hz due to the technical and resource constraints. It is necessary to reduce the amount of data without removing the events of interesting physics processes. The ATLAS trigger system is an online event selection system by using typical signatures in the interesting physics processes such as leptons, jets, or missing energy. The trigger system has two levels of selections: Level-1 (L1) and the High Level Trigger (HLT).

The L1 is implemented on the hardware to search for the events with high-p_{T} muons, large EM energy deposit, jets including hadronically decaying τ-lepton, or missing energy. It uses the electric signals from the RPC, TGC, the EM and hadron calorimeters with coarser granularity. The maximum L1

rate is 100 kHz. The L1 also provides the Regions-of-Interest (RoI's) where the trigger objects are located in a given event.

The HLT uses only the events passing the L1 trigger to reduce the amount of data to 1 kHz. It is implemented on the softwares to access the detector information within the RoI's to check if the variables such as the calorimeter cluster shape, the track-to-cluster matching, the energy and momentum, and isolations satisfy the criteria. Events are selected using the variables reconstructed with the fast reconstruction algorithm.

The events passing all the trigger criteria are stored in several groups determined by the fired trigger, so-called "data stream". The data used for physics analysis is stored in "PhysicsMain" stream containing all the events with relevant trigger sets. The data used for monitoring is stored in "express" stream which is picking up some of the events firing the triggers used for physics analysis in order to reconstruct the events quickly.

2.2.7 Luminosity detector

Measurement of the luminosity delivered to the ATLAS detector is performed with three detectors located far from the interaction point. The first detector is the LUminosity measurement using Cerenkov Integrating Detector (LUCID) located at ±17 m away from the interaction point along the beam line and around 10 cm in radial distance from the beam line, corresponding to the pseudo-rapidity of $|\eta| \sim 5.8$. It is the online monitor for the instantaneous luminosity and provider of the integrated luminosity. The detector consists of the twenty aluminium tubes filled with C_4F_{10} gas generating Cerenkov light. It detects the inelastic pp scattering, counts the number of particles, and then calculate the luminosity. The second detector is the Absolute Luminosity For ATLAS (ALFA) located at ±240 m away from the interaction point. It is intended to detect the elastic scattering at small angles to determine the luminosity. The detector is made of the scintillating fibres and designed to set 1 mili-meter close to the beam. The third detector is the Zero-Degree Calorimeter (ZDC) which is designed to determine the centrality of heavy-ion collisions. It is located at ±140 m away from the interaction point and measure the neutral particles with tungsten absorber and quartz rods for Cerenkov light generated by the shower.

The luminosity determination is calibrated by the van der Meer (*vdM*) method. The luminosity L when two proton bunches collide can be written by:

$$L = \frac{f_r n_1 n_2}{2\pi \Sigma_x \Sigma_y}, \tag{2.8}$$

where f_r is the bunch revolution frequency, $n_{1(2)}$ is the number of protons in the bench 1(2), and $\Sigma_{x(y)}$ is convolved beam size along x (y)-axis defined by:

$$\Sigma_x = \frac{1}{\sqrt{2\pi}} \frac{\int R_x(\delta) d\delta}{R_x(0)}, \tag{2.9}$$

where $R_x(\delta)$ is the luminosity in arbitrary units measured when the two beams are separated by the distance δ. The three parameters in the numerator in Eq. (2.8) are fixed beam parameters. Thus, the

luminosity can be determined when Σ_x and Σ_y are measured. In order to measure them, the *vdM* scan is performed. In the scan, the two bunches are displaced against each other along x or y-axis, and then the interaction rate is measured with the luminosity detectors. This measurement is performed several times. Then the beam profiles along x- and y-axes are obtained. After the calibration, the luminosity per bunch can be determined by:

$$L_b = \frac{\mu_{\mathrm{vis}}}{\mu_{\mathrm{vis}}^{\mathrm{MAX}}} \frac{f_r n_1 n_2}{2\pi \Sigma_x \Sigma_y}, \tag{2.10}$$

where μ_{vis} is the visible interaction rate per bunch crossing and μ_{vis} is the same variable as μ_{vis} except the value measured at the peak of the scan curve.

2.2.8 Operation and Data quality

Once the proton bunches are filled in the LHC ring from the SPS, the proton beams ramp up their energy. After squeezing the bunches to reduce the transverse emittance and longitudinal length, the beams are ready for data-taking ("stable beams"). When the stable beam is flagged, the ATLAS detector gets ready. Especially to avoid the possibility that the unstable beam conditions such as the beam hits the beam pipe and generates many particles going with very shallow angle affect the detector condition in the ID, the ID start getting ready from the outer side ("warm start"). Eventually, when the innermost layer of IBL is turned on, the data-taking starts.

During data-taking, the detector condition is monitored online by using reduced data to reconstruct quickly. The online monitor is used to find out the detector's defects and deal with them to reduce the amount of unrecoverable data. The further offline checks ("offline monitoring") are performed to use the reconstructed data of the express stream described in Section 2.2.6. The offline monitoring is carried out in each subdetector to identify the part of data which contain the significant detector failures which affect the physics analysis. These checks are performed again for the data of PhysicsMain stream used for the physics analysis after the full reconstruction. Only the data after removal of bad quality data is used for the physics analysis. Figure 2.13 shows the integrated luminosity delivered to (green) and recorded by (yellow) the ATLAS detector in (a) 2015 and (b) 2016. The sequential increase of the luminosity reflects the increase of the instantaneous luminosity shown in Fig. 2.2. In 2015 (2016), the ATLAS detector successfully recorded the total integrated luminosity of 3.9 (35.6) fb^{-1} with more than 90% efficiency against the delivered luminosity. For the data collected in 2015, the amount of data for physics analysis is 3.2 fb^{-1}. The largest impact of the reduction is come from the IBL which had been turned off for two data-taking runs, corresponding to 0.2 fb^{-1}, in order to deal with the increased low voltage current on the front-end chips [75]. For the data collected in 2016, the amount of data for physics analysis is 32.9 fb^{-1}. The leading reduction is originated from the turning-off of toroid magnet for one week due to recovering the cryostat, corresponding to 0.7 fb^{-1}.

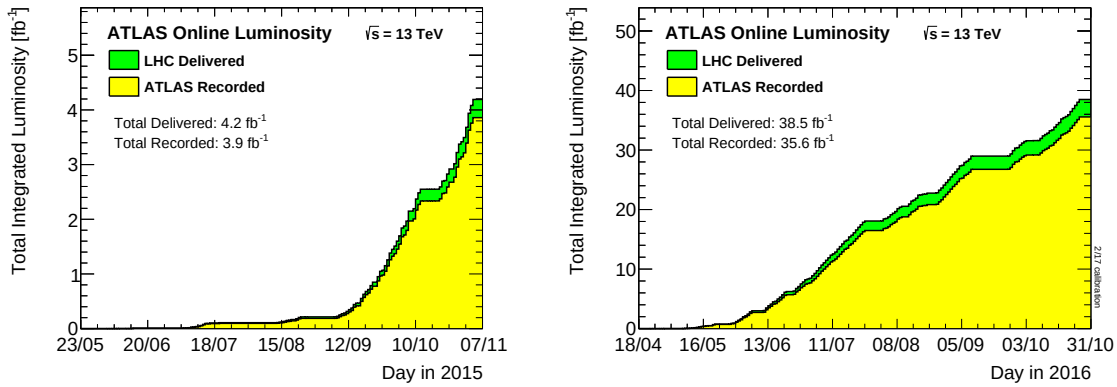

(a) (b)

Figure 2.13: Integrated luminosity as a function of data-taking time in (a) 2015 and (b) 2016 [64]. The luminosities delivered to (green) and recorded by (yellow) the ATLAS detector during stable beams for pp collisions at 13 TeV are shown. The recorded luminosity includes the inefficiencies by the warm start and data acquisition.

2.3 Studies of monitoring Pixel detector

Before the beginning of Run2, a few upgrades and maintenances for the Pixel detectors were carried out. The most remarkable upgrade was the installation of the new innermost layer, IBL as described in Section 2.2.3. In addition, the Pixel modules and read-out systems which had problems on the data acquisition were replaced with new ones. From these points of view, monitoring the Pixel detectors during taking data is very important to know whether they correctly record the hit information especially at the beginning of Run2. The monitoring software is developed in this dissertation to add the new functionalities on top of the one in Run1 to monitor IBL. The monitoring software is implemented in a part of the reconstruction framework, so-called Athena [76]. The Athena decodes the raw data with binary format from all the detector components, and reconstruct the tracks, electrons, muons, jets and missing energy. It runs in parallel to the data-taking and output the Analysis Object Data (AOD), the data format used for physics analysis. The monitoring software uses the information of the decoded detector hits and reconstructed objects and output histograms or graphs. This section shows some of the typical outputs from the monitoring software and describes the results.

Hit information

Figure 2.14 shows the typical pixel hit occupancy, the number of hits per pixel in an event, at IBL and B-Layer in the two dimensional space of module identifiers in data taken at the beginning of Run2. In the data-taking run, the highest number of interactions per bunch crossing (pileup) is 19.3. For the last three modules on each edge along η direction in IBL, the silicon sensor is thicker by 15% than the rest of the modules. For the edge region along η direction, charged particles penetrate the sensor with a shallow angle, and hence the cluster size is proportional to the sensor thickness. This

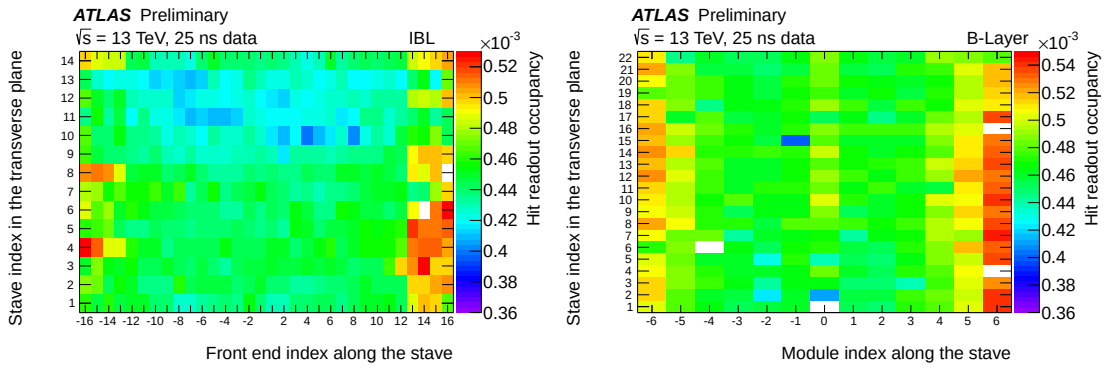

(a) (b)

Figure 2.14: Hit occupancy, the number of hits per pixel in an event, at (a) IBL and (b) B-Layer in the two dimensional space of module identifiers in one data-taking run at the beginning of Run2. In the data-taking run, the highest number of interactions per bunch crossing is 19.3. The (x, y, z) position of the beam spot for the run is $(-0.7, -0.5, -17.6)$ in unit of mili-meters. IBL and B-Layer have 2 and 4 disabled modules respectively.

is the reason why the modules have 15% higher hit occupancy than the rest of the modules. The (x, y, z) position of the beam spot for the run is $(-0.7, -0.5, -17.6)$ in unit of mili-meters. It causes the modulation along ϕ direction in IBL and asymmetry along z-axis in both IBL and B-Layer. The IBL and B-Layer have 2 and 4 disabled modules respectively which are set not to collect any hits due to problems such as connectivity. Some front-end chips have less occupancy due to dead pixels or higher occupancy due to noisy pixels or thicker volumes. It is found that the hit occupancy output from the monitoring software agrees with the expectations from the detector and beam conditions. The result ensures the software and pixel detectors work correctly.

Figure 2.15 shows the charge distribution collected by IBL. When a charged particle is injected into the boundary of pixels or with shallow angle, the electrons generated by the charged particle inside the sensor bulk are collected by multiple pixels. The neighbouring pixels recording hits are grouped into a cluster by a connected component analysis so-called digital clustering [77]. The collected charge values shown in the figure are the sum of the collected charge in a pixel of the cluster matched with a reconstructed track with $p_{\mathrm{T}} > 400$ MeV and $|\eta| < 2.5$. The cluster size represents the number of pixels in a cluster. In general, a minimum ionizing particle (MIP) generates about 80 electron-hole pairs per 1 μm along its path. Since the sensor of IBL is 200 μm thick, the MIP generates about 16,000 electron-hole pairs in the sensor when it penetrates the sensor at right angle, corresponding to a peak shown in the figure. For higher pseudo rapidity region, the charged particles penetrate the sensor with shallow angle. It causes more total charges and larger cluster size such as three or more pixels in a cluster. For the other layers, the charge distributions agree with their expectations. From the monitoring results, all the Pixel detectors are assured to correctly collect the data.

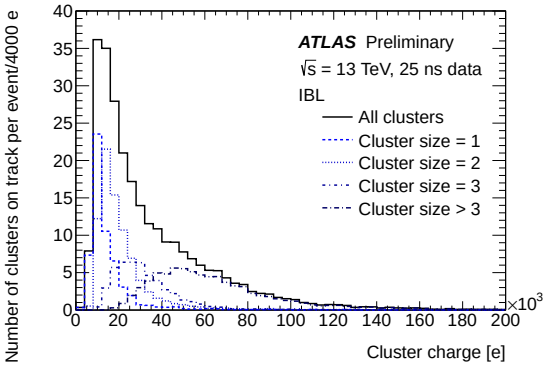

Figure 2.15: Charge distribution of clusters on tracks split by cluster size, the number of pixels in a cluster, for IBL. The tracks are reconstructed in Inner Detector with $p_{\mathrm{T}} > 400$ MeV and $|\eta| < 2.5$.

Pileup dependency of hit occupancy

Since the front-end chips have the limitation on how many hits they can store in their buffer, it is important to know whether the hit occupancy reaches the limitation at a certain number of interactions per bunch crossing since the hits after the full buffering are not recorded. The limitation of the buffer is approximately 1.9×10^{-3} and 0.8×10^{-3} hits per pixel in an event for IBL and other layers, respectively. Figure 2.16 shows the average hit occupancy in luminosity block units at B-Layer as a function of the number of interactions per bunch crossing in 2015. One luminosity block unit corresponds to approximately to one minute of data-taking. The data used here are taken by the mixture of triggers for the monitoring purpose. The black, red, and blue points show the occupancies at $\sqrt{s} = 8$ TeV with 50 nano-second bunch spacing in Run1, $\sqrt{s} = 13$ TeV with 25 and 50 nano-second bunch spacing in Run2, respectively. The difference between the black and blue is caused by the difference of centre-of-mass energy of 8 or 13 TeV. The hit occupancy can depend on the bunch spacing because of the time-walk effects from the previous bunch. The average hit occupancy increases from 4×10^{-4} at 15 interactions per bunch crossing to 5×10^{-4} at 20 interactions per bunch crossing. When the occupancy linearly extrapolates to more along x-axis, it was found that it reached to the buffer limitation at around 35 interactions per bunch crossing, where it was expected from the beam condition in 2016.

Based on the feedback about the hit occupancy from the monitoring results, the data-taking configuration at B-Layer was changed as shown in Table 2.2 during the shutdown from the end of 2015 to the beginning of 2016 in order to reduce the amount of hit information. The change of ToT range from 255 to 150 has the most impact to reduce the amount of hit information. To keep the sensitivity to heavy new particles with larger energy deposit, the setting in front-end chip is optimised so that the front-end chips output the 18 ToT with respect to the energy deposit of MIP. To reduce the noise contribution, the two kinds of thresholds with respect to the collected charge are optimised. One threshold is the analog threshold to determine the ToT. For example, if the analog threshold is set to be 5000 electrons and 5000 electrons are collected in a front-end chip, the hit is recorded as ToT= 1 by 50% probability. The other threshold is the digital threshold to decide if the hit is stored in its buffer or not. These changes reduce the hit occupancy by $\sim$ 30%. Further 10% reduction is performed by

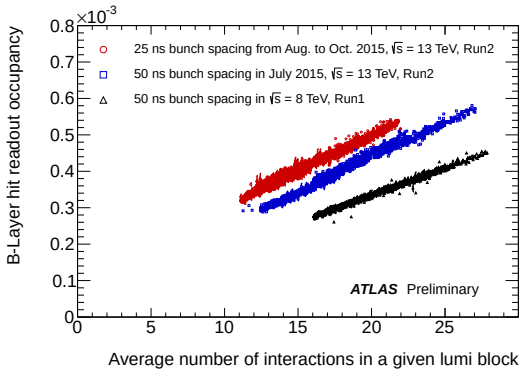

Figure 2.16: Average hit occupancy, the average number of hits per pixel per event, for B-Layer as a function of the average number of interactions per bunch crossing in luminosity block units (one luminosity block corresponds approximately to one minute of data-taking) in Run1 and Run2. The black, red, and green points show the occupancies at $\sqrt{s}$ = 8 TeV with 50 ns bunch spacing in Run1, $\sqrt{s}$ = 13 TeV with 25 ns and 50 ns bunch spacing in Run2, respectively.

Table 2.2: Parameters for data acquisition at B-Layer which are changed between the end of 2015 and the beginning of 2016. These changes are intended to reduce the amount of hit information in the front-end chip's buffer. In association with the reduction of ToT range, the ToT-to-charge calibration is changed to measure 18 ToT at the energy deposition of MIP from 30 ToT. The analog threshold is a threshold equivalent to record hits as 1 ToT by 50% probability. The digital threshold is a threshold that only hits above the threshold are stored in its buffer. The hit duplication is a copy mechanism to recover the hits which are not detected at proper time due to the time-walk effect.

Period	ToT range	Calib. at MIP	Analog threshold	Digital threshold	Hit dupl.
2015	255	30 ToT	Q > 3500 [e]	ToT > 3	On
2016	150	18 ToT	Q > 5000 [e]	ToT > 5	Off

removal of the hit duplication. It recovers the small ToT hits which are not detected at proper time due to the time-walk effect. All the changes tend to reduce the noise contribution. It is confirmed that there is no impact on the performance of reconstructed tracks.

Figure 2.17 shows the average hit occupancy for all the layers and disks in data taken with a zero-bias trigger in September and October in 2016. A zero-bias trigger fires when the trigger of EM calorimeter fired one LHC-orbit before, which results in a random trigger. The occupancy on the disk (purple plots) is calculated to take the average of the occupancies in all the disks. Comparing to Fig. 2.16, the occupancy on B-Layer is reduced by 50% in which the changes of the configuration contributes 40% and the different trigger scheme contributes by 10%. It also shows the linear fit results on each layer or disk whose parameters are shown in Table 2.3. It is found that the occupancy on B-Layer reaches the limitation at 60 interactions per bunch crossing, extended from 35 interactions.

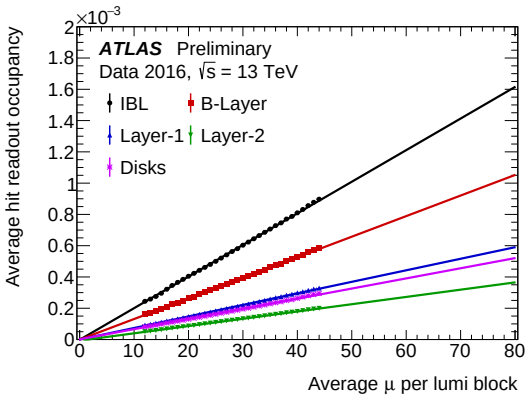

Figure 2.17: Average hit readout occupancy, i.e. the average number of hits per pixel per event, for IBL(black), B-Layer(red), Layer-1(blue), Layer-2(green), Disks(purple) as a function of the average number of interactions per bunch crossing (μ) for events collected by a zero-bias trigger in September and October in 2016. Each point corresponds to an average over four LHC fills (5339, 5393, 5394, and 5416). The solid lines show the linear extrapolation for each layer up to $\mu \sim 80$. The fit results of the occupancy are summarised in Table 2.3.

Table 2.3: Linear fit results of pile-up dependency of hit occupancy for all Pixel detectors in units of 10^{-5} hits per pixel in an event. The fit is performed for the data points shown in Fig. 2.17. The fit parameters of the slope and offset are shown in the table. The pile-up values (μ^{limit}) reaching the front-end chip's buffer limit from the linear extrapolation are shown in the last column. The hit buffer limits in units of hits per pixel in an event shown in the table are computed with the capability of the buffer and the ToT range. The values of (μ^{limit}) account only the buffer's limitation and do not include the other limitation from the data transfer and the read-out systems.

	Slope	Offset	μ^{limit}	Hit buffer limit
IBL	2.021 ± 0.002	-0.160 ± 0.050	94	1.9×10^{-3}
B-Layer	1.316 ± 0.001	-0.049 ± 0.032	99	1.3×10^{-3}
Layer-1	0.7378 ± 0.0007	-0.007 ± 0.017	108	0.8×10^{-3}
Layer-2	0.4650 ± 0.0005	-0.674 ± 0.012	172	0.8×10^{-3}
Disks	0.6489 ± 0.0007	-0.140 ± 0.015	123	0.8×10^{-3}

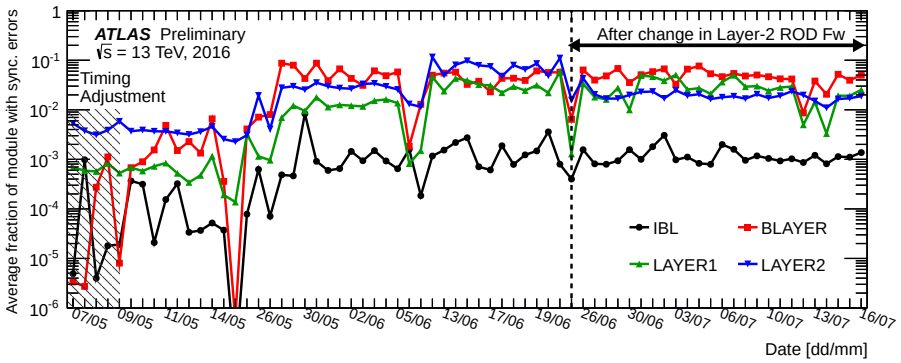

Figure 2.18: Average fraction of pixel and IBL modules with synchronisation errors per event in 2016 runs. Each point shows the average fraction in a given data-taking run. Different readout windows were used for Pixel and IBL in the first 5 runs due to timing adjustments. Runs until the middle of May were characterised by a low number of interactions per bunch crossing (< 25) and colliding bunches (< 1200). The effect of the subsequent increase in the number of interactions per bunch crossing and colliding bunches in the machine (up to approximately 32 and 2100 respectively) is visible until the end of June, when a change in the Layer-2 off-detector firmware (ROD Fw) was adopted, leading to a factor 10 decrease in the synchronisation error rate. At the same time the ATLAS trigger rate was raised from 70 kHz to 85 kHz, making the firmware modification even more relevant. Data used in this plot have been collected by a mixture of triggers used in the monitoring stream.

Synchronisation error rate

The monitoring software gives good feedbacks of hits as well as error flags. The most important error is a synchronisation error that is flagged when a discrepancy between the level-1 trigger or bunch crossing identifiers recorded in the front-end chips and those stored in the central acquisition system is detected. The hits associated with synchronisation errors are not used in the track reconstruction since the hit information on the front-end chip when it is accompanied by the errors is not reliable and can give biases on the reconstructed tracks. The error happens when charged particles penetrate the front-end chip and generate electrons to distort the electric signal on the circuit like flipping the digital signals, fluctuating the ground level, or changing the states in the memories. Figure 2.18 shows the average synchronisation error rate in a data-taking run for each layer in 2016. In the first 5 runs in May, the error rate largely fluctuates in IBL and B-Layer since the timing adjustment had been performed. For the period until the middle of May, the LHC provided the beams with low instantaneous luminosity and less colliding bunches. It causes less error rates for all the Pixel layers. In June, the error rates for all the layers increase since the LHC provides higher instantaneous luminosity corresponding to about 32 interactions per bunch crossing and more colliding bunches. At the end of June, the firmware of the read-out system, so-called Read Out Driver (ROD), at Layer-2 was improved, and then the error rate at Layer-2 decreased by a factor of 10. During the period, the level-1 trigger rate increased from 70 to 85 kHz. It ensures that the modification of the firmware is relevant.

This kind of the monitoring software output is also useful to know the performances of Pixel detectors and give good feedbacks to the developers of the read-out systems. In addition, the error rate is one

of the variables used to decide if the collected data can be used for the physics analysis. The figure ensures that the Pixel detector systems improve the availability of the data for physics analysis and keep it even with the high pileup events.

Summary

The monitoring software for the Pixel detectors was developed to know the performances of newly installed IBL detectors and other Pixel detectors. Several overviewing plots are shown in this dissertation. The hit occupancy map and collected charge distributions give a confirmation that the all the Pixel detectors collect the hit information as expected and the monitoring software works properly. The pileup dependency of hit occupancy shows the current availability of the buffers as well as the prediction of the availability at higher pileup. This feedback drove to the change of the data-taking configuration of B-Layer. It resulted in successful data-taking with higher pileup condition in 2016. In addition, the synchronisation error rate has been monitored to know the conditions for each layer and availability of the collected data for physics analysis. The monitoring output shows the effect on the error rate from the improvement of the read-out system's firmware and gave feedbacks to the developers of the read-out system. The monitoring results are also used to decide whether the collected data can be used for physics analysis.

3 Reconstruction of physics objects

The particles generated in pp collisions are detected in the ATLAS detector as described in Chapter 2. To use the information of the detectors, the information such as the direction and momenta of the particles are reconstructed. In addition, the kinds of particles are identified using the features of the particles such as the energy deposits and the lifetime. The reconstructed information is referred to as *physics object*. This chapter begins with the reconstruction of the trajectories of charged particles, which is the basic object for all the other objects. Afterwards, objects such as electrons and muons used in this analysis are described. In Section 3.1.1, measurements of the impact parameter resolutions of tracks performed in this dissertation are described.

3.1 Tracks

In the ID, the solenoid magnet produces an uniform magnetic field along the longitudinal direction. It bends charged particles produced in pp collisions in the transverse plane along a helicoidal trajectory with a radius $R[\mathrm{m}] = p_{\mathrm{T}}\ [\mathrm{GeV}]/(0.3 \cdot B[\mathrm{T}])$, where B and p_{T} are the magnitude of the magnetic flux density and the transverse momentum of the particle. Charged particles deposit their energy in the sensors of the detectors and induce electric signals which are read out as hit information. The hit information produces three-dimensional hit positions called, *space points*, which are used for track reconstruction and measurement of the momentum. The reconstructed tracks are the basic and important objects to identify most of particles like electron, muon, and b-hadrons as well as being used for pileup suppression of jets and $E_{\mathrm{T}}^{\mathrm{miss}}$. This section describes the track reconstruction algorithm and the study about the impact parameter resolutions of reconstructed tracks developed in this dissertation.

The track reconstruction is performed as the following steps:

1. Clusterisation
   When a charged particle penetrates the pixel or strip sensor, several pixels or strips can detect the electric signal and store the hit information. These multiple pixels or strips are grouped into a cluster with a connected component analysis (CCA) [78]. The cluster gives a space point which is used for the next steps.

2. Inside-out tracking

   a) Finding track candidates
      Track reconstruction starts from finding track seeds, sets of three space points, in the order of SCT-only, Pixel-only and the mixture of them. From the seeds, tracks are built by adding the space points in remaining pixel and SCT layers with a combinatorial Kalman

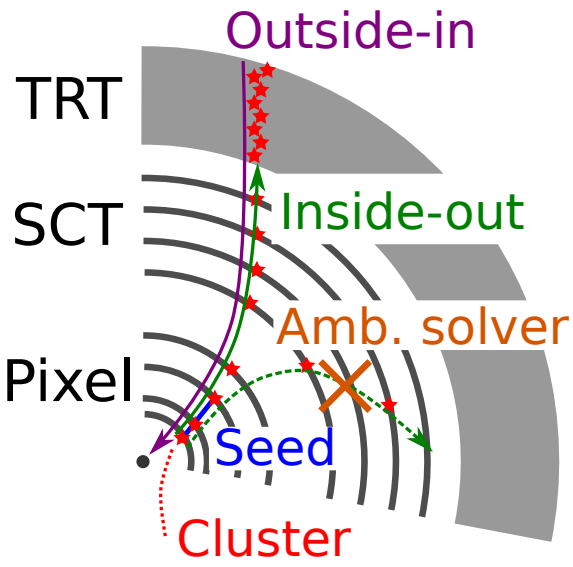

Figure 3.1: Illustration of the tracking procedure. A quarter of the cross section of the Inner Detector in the transverse plane is shown. The detector size and radius are not scaled correctly. Clusters (red stars) are used for the track reconstruction. From a track seed (blue line), track candidates are found. The ambiguity solver chooses good quality tracks. In this figure, the green dashed track candidate is excluded by the ambiguity solver due to many holes. After the TRT extension, the outside-in tracking is performed.

filter [79]. At this stage, one seed can have several track candidates. Then all the track candidates are passed to the ambiguity solver.

b) Ambiguity solving
The previous stage has a high number of the track candidates including fake tracks and tracks having shared clusters. The ambiguity solver determines the *track score* [80], representing track quality. For example, the score increases when clusters are assigned to a track. It decreases when a track has *holes*, which are not associated clusters in an active layer along the track. Also the χ^2 of track fit is considered in the score. Then, the tracks with good quality are used for further steps.

c) TRT extension
This step extends the track candidates from the silicon detectors into TRT. The silicon tracks are extrapolated into TRT hits without modification of the silicon tracks. Then, the tracks are refit with the combined silicon and TRT hits information.

3. Outside-in tracking
The inside-out tracking relies on a track seed found in the silicon detectors. But it may not work for tracks coming from the secondary vertices like K_s decays or photon conversions. Tracking from TRT to the silicon detectors is performed by using pattern recognition algorithms.

The tracking procedure is illustrated in Fig. 3.1. The detail of track reconstruction is described in Ref. [81, 82].

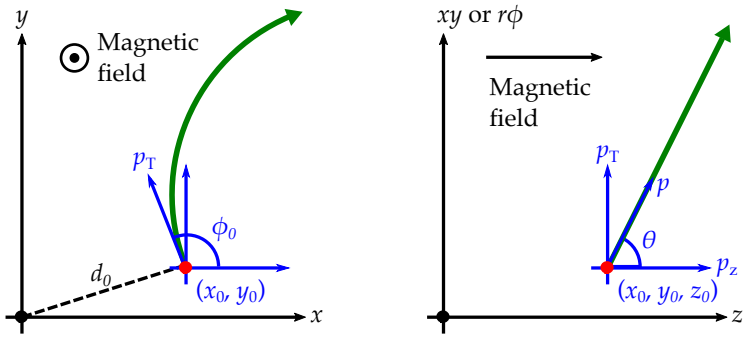

Figure 3.2: Definition of (a) the transverse and (b) longitudinal impact parameters wth respect to the detector's centre (black marker). Red marker is the closest point of the track (green). ϕ_0 and θ are the angles with respect to the x and z axis, respectively.

A reconstructed track is characterised by a set of five parameters:

$$(d_0, z_0, \phi_0, \theta, q/p), \tag{3.1}$$

where d_0 and z_0 are the distance of closest approach from the track to a reference point in the transverse plane and longitudinal direction, referred to as impact parameters. The ϕ_0, θ, and q/p are azimuthal angle, polar angle, and the charge divided by the momentum magnitude, respectively. The reference point for the impact parameters is often set to the primary vertex in the event. The definition of the impact parameters is illustrated in Fig. 3.2.

In ATLAS, to provide the common and robust quality and resolutions on tracks, the following baseline selection, so-called *Loose* selection, are applied for tracks:

- $p_T > 400$ MeV
- $|\eta| < 2.5$
- number of silicon hits ≥ 7
- number of shared modules ≤ 1
- number of silicon holes ≤ 2
- number of pixel holes ≤ 1

3.1.1 Study of impact parameter resolutions

This section shows the study about the impact-parameter resolutions developed in this dissertation. The impact parameters are important to discriminate tracks from primary vertices to the ones from secondary vertices for particle identification as well as searching for new particles. The first measurement of the intrinsic resolution of the track impact parameter is performed in both the simulation

and data in early 2015 at $\sqrt{s}$ = 13 TeV. The primary vertex which is defined as the one with the highest sum of squared track p_{T} associated to it is used as the reference point to measure the impact parameter in this section.

The results in this section use data collected in proton-proton collision at $\sqrt{s}$ = 13 TeV in June 2015, corresponding to an integrated luminosity of around 0.37 nb^{-1}. In this data taking period, the proton bunch spacing was set to 50 ns and μ was around 0.005. The events used here are triggered by the minimum bias trigger, which requires hits in the Minimum Bias Trigger Scintillators (MBTS) [83] mounted on the inner surface of electromagnetic end-cap calorimeter, corresponding to $2.08 < |\eta| < 3.75$.

To simulate the minimum bias events, the Pythia8.186 [84] generator with the ATLAS minimum-bias tune A2 [85] based on MSTW2008LO PDF [86] set is used. The detector response is simulated in a detail detector model implemented in Geant4 [87, 88].

The events in both simulation and data are required to pass the following criteria:

- Firing a MBTS trigger on at least one side of ATLAS detector
- Existing at least one reconstructed vertex associated with at least two tracks without any track selection
- Rejecting events having more than one vertices associated with four or more tracks
- Containing at least one track passing Loose track criteria

These criteria are designed to evaluate the performances with well-isolated tracks in events having only one pp collision. The simulated events are reweighed to match with data in track kinematics of (p_{T}, η) and the vertex position along z axis. Figure 3.3 shows the transverse and longitudinal impact parameter distributions with respect to the primary vertex in data and simulation for Loose tracks. Both d_0 and z_0 distributions show small discrepancy between data and simulation, which are discussed later.

We shall think to obtain the intrinsic resolutions of the impact parameters from the width of the distributions. Since the impact parameters are computed with respect to the primary vertex, the width includes mainly two components: the position resolution of vertexing and the intrinsic impact parameter resolution of tracks. These contributions are illustrated in Fig. 3.4

Removal of the former contribution is performed by using the iterative deconvolution procedure [90], which is used in the Run1 measurements. In the following, the basic idea of the procedure is described for an example of d_0. The measured distribution involving the two components can be written as:

$$R_{\mathrm{meas}}(d_0) = N \int \exp\left[-\frac{1}{2}\frac{d_0^2}{\sigma^2_{d_0,\mathrm{trk}} + \sigma^2_{d_0,\mathrm{PV}}}\right] P(\sigma_{d_0}, \mathrm{PV})\mathrm{d}\sigma_{d_0,\mathrm{PV}}, \tag{3.2}$$

where $\sigma_{d_0,\mathrm{trk}}$ and $\sigma_{d_0,\mathrm{PV}}$ are the contributions of tracks and primary vertex to the d_0 resolution, respectively, and N is the normalisation factor. For the first iteration, the distribution is made by

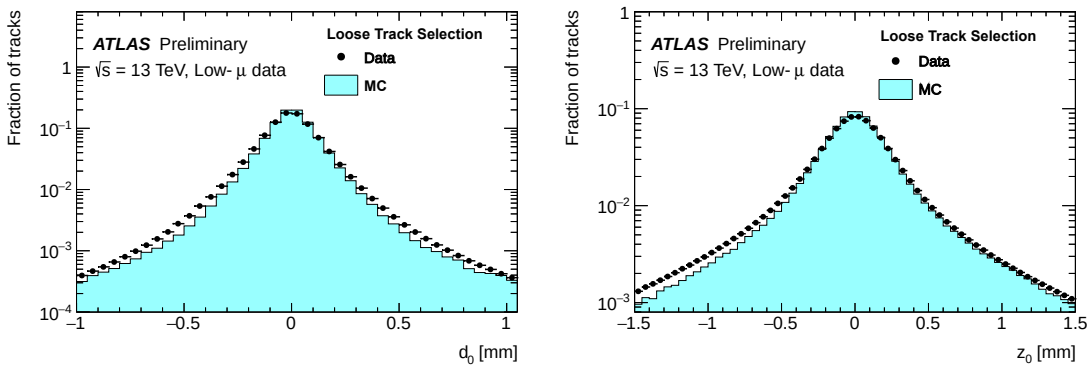

(a) (b)

Figure 3.3: (a) Transverse, d_0, (b) longitudinal, z_0, impact parameter distributions with respect to the primary vertex in data (black) and simulation (light blue). The tracks passing the Loose criteria are used. These plots are published in Ref. [89].

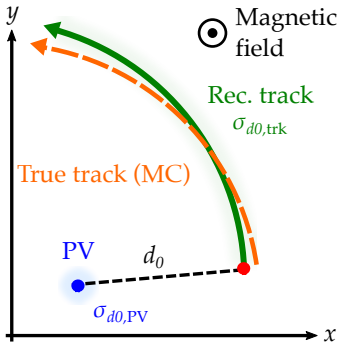

Figure 3.4: Illustration of contributions of the primary vertices (PV) $\sigma_{d_0,\mathrm{PV}}$ and reconstructed tracks $\sigma_{d_0,\mathrm{trk}}$ to the impact parameter resolution. The example of d_0 resolution is shown. In simulation, there are true trajectories shown as "True track", which can be used to calculate the intrinsic resolution of tracks.

filling the converted impact parameter d_0^{1st} defined by:

$$d_0^{\mathrm{1st}} = d_0 \cdot \left(\frac{(K^0_{\mathrm{trk}} \cdot \sigma_{d_0,\mathrm{trk,fit}})^2}{(K^0_{\mathrm{trk}} \cdot \sigma_{d_0,\mathrm{trk,fit}})^2 + (K_{\mathrm{PV}} \cdot \sigma_{d_0,\mathrm{PV,fit}})^2} \right)^{\frac{1}{2}}, \tag{3.3}$$

where $\sigma_{d_0,\mathrm{trk,fit}}$ and $\sigma_{d_0,\mathrm{PV,fit}}$ represent the position uncertainty of the track fit and of the vertexing, respectively. The scale factor K^0_{trk} is set to one at the first iteration and K_{PV} is the ratio of the vertexing uncertainty to the intrinsic vertexing resolution: $K_{\mathrm{PV}} = \sigma_{d_0,\mathrm{PV}}/\sigma_{d_0,\mathrm{PV,fit}}$, determined by the individual analysis dedicated for vertexing performance [91]. Substituting Eq. (3.3) into Eq. (3.2), the d_0^{1st} distribution can be written as:

$$R_{\mathrm{meas}}(d_0^{\mathrm{1st}}) = N \exp\left[-\frac{1}{2} \frac{(d_0^{\mathrm{1st}})^2}{(K^1_{\mathrm{trk}} \cdot \sigma_{d_0,\mathrm{trk}})^2} \right], \tag{3.4}$$

assuming $\int P(\sigma_{d_0}, \mathrm{PV}) \mathrm{d}\sigma_{d_0,\mathrm{PV}} = 1$. The new scale factor $K^1_{\mathrm{trk}} = (\sigma^2_{d_0,\mathrm{trk}} + \sigma^2_{d_0,\mathrm{PV}})/(\sigma^2_{d_0,\mathrm{trk,fit}} + \sigma^2_{d_0,\mathrm{PV}})$ is calculated approximately at the first order to $\sigma_{d_0,\mathrm{trk}}/\sigma_{d_0,\mathrm{trk,fit}}$. Thus, the intrinsic impact parameter resolution of tracks can be obtained from the width of the d_0^{1st} distribution approximately. Indeed, the new scale factor K^1_{trk} is obtained by comparing the distribution widths of the d_0^{1st} and the pseudo d_0. The pseudo d_0 is generated randomly according to a Gaussian function at the centre value of zero with $\sigma_{d_0,\mathrm{trk,fit}}$ wide. This procedure is performed iteratively, and the i-th converted d_0 is described as:

$$d_0^{i\mathrm{th}} = d_0 \cdot \left(\frac{(K^{i-1}_{\mathrm{trk}} \cdot \sigma_{d_0,\mathrm{trk,fit}})^2}{(K^{i-1}_{\mathrm{trk}} \cdot \sigma_{d_0,\mathrm{trk,fit}})^2 + (K_{\mathrm{PV}} \cdot \sigma_{d_0,\mathrm{PV,fit}})^2} \right)^{\frac{1}{2}}. \tag{3.5}$$

Result of the intrinsic resolutions In this analysis, the number of the iteration is set to be three. The width of the distribution is obtained by a fit using a Gaussian function twice. The first fit is performed without any constraints on the fit parameters. The second fit is performed within 2σ of the first fit result to suppress non-Gaussian components on the tails of the distribution. Then, the resolution is obtained as 1σ of the second fit result. Since the impact parameter resolutions depend on the track kinematics, the resolutions are computed in a (p_{T}, η) bin. In the MC simulation, the intrinsic resolutions of tracks can be computed by the difference of impact parameters between a reconstructed track and the trajectory of the true particle. This resolution is called as "MC-based" resolution here. Also, the resolutions are computed by the deconvolution procedure. The difference between the unfolded and MC-based resolutions is considered as the systematic uncertainty on the MC-based resolution. In the data, the intrinsic resolutions are obtained by the deconvolution procedure. The procedures in the data and MC simulation are summarised in Table 3.1.

Figure 3.5 shows the unfolded resolutions. In data, the resolutions before and after unfolding the intrinsic resolution with the iterative deconvolution procedure are shown in black and red, respectively. The MC-based resolution is shown in blue lines. The error bars in data and MC simulation are summarised in tab. 3.1. The discrepancies on d_0 between data and MC are observed for both low and high p_{T}, shown in Fig. 3.5 (a). For lower p_{T}, it is caused by the small differences of the material description at IBL in the detector simulation, which is known in a dedicated study [92]. The

Table 3.1: Summary of the procedures for calculation of the impact parameter resolutions. In the MC simulation, for instance, the intrinsic d_0 resolutions of tracks can be computed by the difference of impact parameters between a reconstructed track d_0^{Reco} and the trajectory of the true particle d_0^{True} ("MC-based"). In data, the resolutions are computed with the deconvolution procedure ("Unfolded"). The uncertainty on the resolutions in the simulation includes the statistical uncertainty and the difference between the MC-based and unfolded resolutions.

	Procedure	Uncertainty
Data	Deconvolution ("Unfolded")	stat.
Simulation	$d_0^{\mathrm{Reco}} - d_0^{\mathrm{True}}$ ("MC-based")	stat. $\oplus$ $(\sigma_{d_0}^{\mathrm{Unfolded}} - \sigma_{d_0}^{\mathrm{MC-based}})$

material effects is discussed later. For higher p_{T}, the known misalignment of detector components in simulation [93] contributes to the discrepancy in both d_0 and z_0. For the disagreement in high η shown in Fig. 3.5 (d), the simplified energy deposit model in simulation causes underestimation. Eventually, the differences between data and MC are taken into the systematic uncertainty on the impact parameter resolution. The other performance plots are shown in Ref. [94].

Comparison between Run1 and Run2 In order to cross check the resolutions, the results are compared with the data in Run1. The data in Run1 are collected in May 2012 at $\sqrt{s} = 8$ TeV with a mixture of jets, tau and $E_{\mathrm{T}}^{\mathrm{miss}}$ triggers. The same event selection except the requirement on MBTS is applied, and the resolutions are obtained by the same deconvolution procedure. Then, the intrinsic resolutions are found to be consistent with the previous results in Run1 [90]. The comparison of d_0 resolution as a function of track p_{T} between Run1 and Run2 data is shown in Fig. 3.6. The resolutions in Run2 data is $\sim$ 40% as small as those in Run1 data at track $p_{\mathrm{T}} \sim 400$ MeV. This significant reduction is caused by the installation of IBL at the innermost layer during long shutdown in 2015 and is consistent with the Technical Design Report of IBL [67]. Therefore, the comparison of the resolution shows the consistency of the unfolding procedure and improvement of the resolution by IBL.

Comparison between the material descriptions in the detector simulation The previous paragraph shows that the material description in the detector simulation causes the discrepancy of the resolution for lower p_{T} between the data and the simulation. The material description is independently studied by using secondary vertices of photon conversion and hadronic interaction with the detector material [92]. The study found out the missing materials at IBL in the detector simulation, which are mostly its front-end electronics. To know the impact of the material description at IBL, the d_0 resolution is compared between the detector simulations with and without correcting the material description at IBL. Figure 3.7 shows the unfolded d_0 resolution as a function of track p_{T} in data (black), the one in the detector simulation with (green) and without (blue) the correction for $|\eta| < 0.5$. The result indicates that the corrected geometry has better agreement with the data for lower p_{T} region, where the resolutions are determined by the multiple scattering inside the detector volume. For higher p_{T} region, the two simulations are consistent within the errors and inconsistent with the data due to

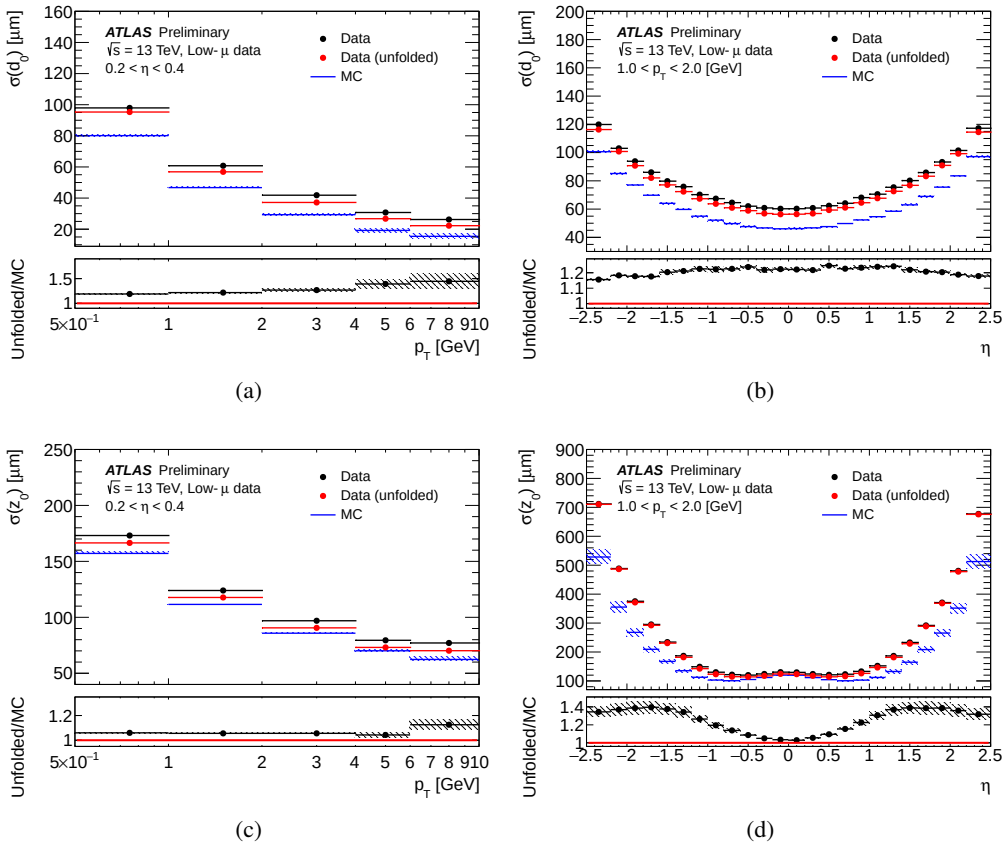

(a) (b)

(c) (d)

Figure 3.5: Impact parameter resolutions, d_0 resolution as a function of track (a) p_{T} and (b) η (b) and z_0 resolution as a function of track (c) p_{T} and (d) η, comparing between the data and MC simulation. The black and red graphs show the resolutions in the data before and after unfolding the intrinsic resolution with the iterative deconvolution procedure, respectively. The blue line shows the resolution computed by the difference of impact parameters between a reconstructed track and the truth in the MC simulation. These plots are published Ref. [94].

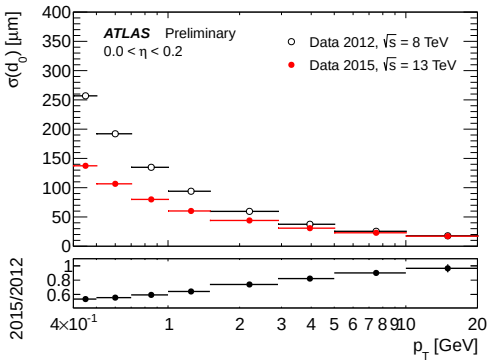

Figure 3.6: Intrinsic d_0 resolution as a function of track p_{T} in data in May 2012 (black) at $\sqrt{s}$ = 8 TeV and in 2015 (red) at $\sqrt{s}$ = 13 TeV for $|\eta| < 0.2$. The bottom panel shows the ratio of resolution in 2015 to that in 2012. This plot is published in Ref. [89].

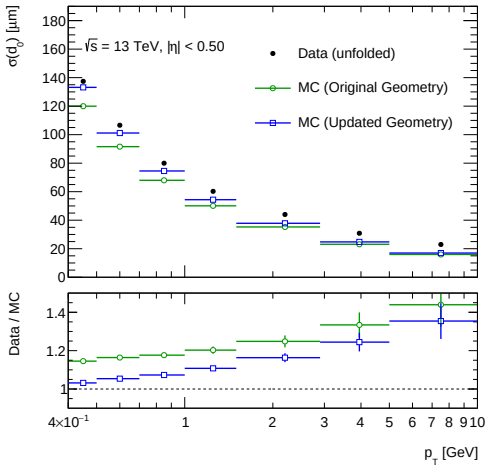

Figure 3.7: Intrinsic d_0 resolution as a function of track p_{T} in data (black) at $\sqrt{s}$ = 13 TeV, comparing with the ones in the detector simulations with (blue, "Updated Geometry") and without (green, "Original Geometry") correcting the material description at IBL for $|\eta| < 0.5$.

the common cause of the detector-alignment accuracy. Thus, this result is a qualitative cross-check to support the corrected geometry in central η region.

3.2 Primary vertices

The reconstruction of the interaction points, referred to as Primary Vertices (PV) is important to identify the hard-scattering process and reconstruct the physics objects from the process. The PV reconstruction is carried out by two steps with reconstructed tracks: *finding* and *fitting*. The

reconstructed tracks are selected to originate from the beam spot. The vertex seeds are determined by looking for the global maximum in the distribution of the track z_0 whose reference point is set to the beam spot. An *adaptive vertex fitting* algorithm [95] determines the vertex position using the seed position and tracks around it. The tracks which are not assigned to the vertex are used to find the next vertices. This procedure is performed iteratively [96]. In order to improve the spatial resolution of the vertex, the vertices having at least two tracks with $p_{\mathrm{T}} > 400$ MeV are considered. The vertex which has the highest sum of squared p_{T} of tracks associated to it is chosen as the hard-scattering PV in the event. The remaining vertices among the beam spot are considered as pile-up vertices. The ones incompatible with the beam spot are used as the secondary vertices for b-tagging, described in Section 3.6. The vertex-reconstruction efficiency is evaluated at $\sqrt{s} = 13$ TeV in data recorded in 2015 and simulation to be more than 99% for vertices having at least four tracks [97].

3.3 Leptons

This section describes the reconstruction and identification of electron and muon. In this analysis the τ-lepton is not identified nor used explicitly, and thus the reconstruction of τ-lepton is omitted.

3.3.1 Electrons

The reconstruction of electron candidates is performed by the following steps [98].

1. Seed clusters in the EM calorimeter are found by a sliding window with a size of 3×5 detector units in $\eta \times \phi$ space. This detector unit means the granularity of the modules at the middle layer in the EM calorimeter, corresponding to 0.025×0.025 in $\eta \times \phi$ space and contains energy measured in the longitudinal calorimeter layers, referred to as *longitudinal towers*. The seeds are required to have a total transverse energy of more than 2.5 GeV. The energy clusters around the seeds are formed using a clustering algorithm [99].

2. The track candidates are reconstructed in the ID as described in Section 3.1. This standard track reconstruction is carried out under pion hypothesis. In addition to it, the track reconstruction is performed with the new pattern recognition under electron hypothesis which allows to reconstruct the electrons losing larger energy by bremsstrahlung. These track candidates are fitted with the global χ^2 track fitter [100]. The candidates which fails the fit with pion hypothesis are refit with electron hypothesis.

3. The tracks extrapolated to EM clusters are matched to them using η and ϕ. Tracks associated to the cluster are refit with an optimised Gaussian Sum Filter [101] which considers the non-linear bremsstrahlung effects.

4. The matching of the tracks to the cluster is performed. Then, the electron cluster is re-formed with a size of 3×7 (5×5) longitudinal towers in the barrel (end-cap) regions. The energy of the clusters are calibrated to the true energy in the MC simulation.

Table 3.2: Input variables for the electron identification.

Type	Variable	Description
Track	n_{IBL}	Number of hits in the IBL
	n_{Pixel}	Number of hits in the Pixel detector
	n_{Si}	Number of hits in the Pixel and SCT detectors
	d_0	Transverse impact parameter with respect to the beam line
	d_0/σ_{d_0}	Transverse impact parameter significance
	$\Delta p/p$	Momentum lost
TRT	eProbabilityHT	Likelihood probability based on transition radiations in the TRT
Track-cluster matching	$\Delta\eta_1$	$\Delta\eta$ between the extrapolated track and the cluster in the strip EM layer
	$\Delta\phi_2$	$\Delta\phi$ between the extrapolated track and the cluster in the middle EM layer
	$\Delta\phi_{\mathrm{res}}$	Same definition as $\Delta\phi_2$ but tracks are rescaled to the cluster energy before the extrapolation
	E/p	Ratio of the cluster energy to the track momentum
EM Calorimeter (strip layer)	w_{stot}	Shower width
	E_{ratio}	Ratio of the energy difference between the largest and second largest energy deposits in the cluster over the sum of these energies
	f_1	Ratio of the energy in the strip layer to the total energy in the EM calorimeter
EM Calorimeter (middle layer)	$w_{\eta 2}$	Lateral shower width along η
	R_ϕ	Ratio of the energy in 3×3 cells over the energy in 3×7 cells
	R_η	Ratio of the energy in 3×7 cells over the energy in 7×7 cells
EM Calorimeter (back layer)	f_3	Ratio of the energy in the back layer to the total energy in the EM calorimeter
Hadronic leakage	R_{had1}	Ratio of E_{T} in the first layer of the Hadronic calorimeter to E_{T} in the EM calorimeter (used for the range of $\lvert\eta\rvert < 0.8$ or $\lvert\eta\rvert > 1.37$)
	R_{had}	Ratio of E_{T} in the Hadronic calorimeter to E_{T} in the EM calorimeter (used for the range of $0.8 < \lvert\eta\rvert < 1.37$)

For calculation of the four-momentum of the electron, the energy is derived from the calibrated cluster energy and the η and ϕ directions are determined from the associated track.

To discriminate the real electrons from backgrounds such as hadronic jets or converted photons, the electron identification algorithm is applied in the reconstructed electrons. The identification algorithm is the likelihood-based (LH) method which is a multivariate analysis technique to identify the object as either real electron (signal) or backgrounds using several input variables. The electron identification uses 20 input variables in total: 10 variables of track condition such as the impact parameter, the number of hits in the pixel detector, 9 variables of shower information in the calorimeter such as the shower width for each layer, and 1 variable of likelihood probability based on transition radiation in TRT. The detail of all the input variables is described in Table 3.2. In ATLAS, three operating points are available: *Loose*, *Medium*, and *Tight*. This analysis uses *Tight* criteria and requires $p_{\mathrm{T}} > 30$ GeV and $|\eta| < 2.47$ except for the calorimeter transition regions.

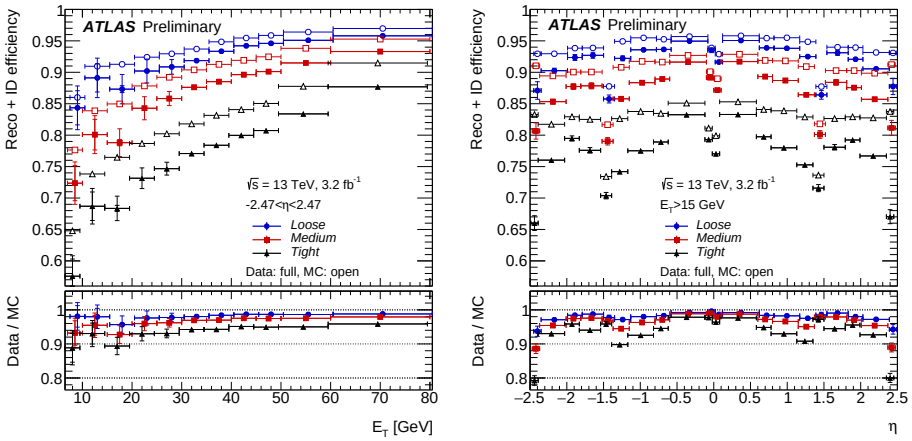

(a) (b)

Figure 3.8: Combined efficiency of reconstruction and identification as a function of E_{T} integrating over full η range (a) and as a function of η for $E_{\mathrm{T}} > 15$ GeV in $Z \to ee$ events of data (filled plots) and simulation (open plots). The inner (outer) error bars show the statistical (the combined statistical and systematic) uncertainty. Cited from [98].

In order to further discriminate real electrons from backgrounds such as the non-prompt electrons from hadron decay or those misidentified as electron, an isolation criteria is required. The isolation requires $p_{\mathrm{T}}^{\mathrm{varcone20}}/p_{\mathrm{T}}^{\mathrm{muon}} < 0.06$ for an electron, where the isolation variable $p_{\mathrm{T}}^{\mathrm{varcone20}}$ is defined as the sum of the transverse momenta of the reconstructed tracks passing the following requirements populated within a cone of size $\Delta R = \min(0.2, 10\ \mathrm{GeV}/p_{\mathrm{T}}^{\mathrm{electron}})$ around the electron, excluding the electron track.

- $p_{\mathrm{T}} > 1$ GeV
- Loose track requirements
- $|\Delta z_0 \sin\theta| < 3$ mm

The reconstruction and identification efficiency is measured in 3.2 fb^{-1} of data at $\sqrt{s} = 13$ TeV and simulation [98]. The tag-and-probe method is used in $Z \to ee$ and $J/\psi \to ee$ events. A set of strict identification requirements is applied for one electron candidate (*tag*) to ensure real electron. Looser requirements are applied for another electron candidate. The di-electron invariant mass is required around a well-known particle mass such as Z or J/ψ. Then, the looser electron candidate should be real electron and used to evaluate the performances (*probe*). The combined efficiencies of reconstruction and identification as a function of E_{T} and η in $Z \to ee$ events of data and simulation are shown in Figure 3.8. The efficiency for *Tight* is around $\geq 70\%$ for $E_{\mathrm{T}} > 15$ GeV integrating over η. The discrepancies between data and simulation by $\sim 5\%$ are used as the correction factor for MC in this analysis. The uncertainty of the correction factor is also computed as $\leq 2\%$ for $E_{\mathrm{T}} > 15$ GeV. It is considered as the systematic uncertainty on the electron object.

The electron energy scale and resolution after calibration are measured in $Z \to ee$ events of data and simulation [102]. The di-electron invariant mass shapes are compared in data and simulation, and then are translated into the energy scale. The energy scale is estimated at a level of 1%. The uncertainty on the energy scale is around $\leq 0.2\%$ at $E_{\mathrm{T}} \sim 40$ GeV. The energy resolution is derived from the width of the invariant mass distribution. It is estimated as $\leq 2\%$ for $E_{\mathrm{T}} \geq 40$ GeV and its relative uncertainty is around 10% for $E_{\mathrm{T}} \leq 50$ GeV increasing to $\sim 30\%$ at $E_{\mathrm{T}} \sim 200$ GeV. These uncertainties are taken into account as the systematic uncertainty on the electron object in this analysis.

3.3.2 Muons

The muons are reconstructed independently in the ID and MS, and then combined to identify the muons used in the analysis, referred to as *combined muon*. In the ID, the muon tracks are reconstructed in the same way as done for the other charged particles. In the MS, the muon candidates are reconstructed by four steps. The first step is to search for hit patterns inside each muon chamber to make segments. At the second step, the muon track candidates are formed to fit the local segments in different layers. One segment can have several track candidates at this step. Then, the third step assigns the best track to a segment. At the final step, the hits associated with the track are fitted with a global χ^2 fit.

The combined muons between the ID and MS are built with a global refit using hits in both the ID and MS. The muon identification requires a set of criteria to improve the identification efficiency and reduce the backgrounds like muons from in-flight decay of hadrons with a long lifetime such as charged pions. For instance, if a charged pion decays to $\mu\nu_\mu$, the corresponding trajectory is seen as the direction changes at the decay point ("kinked"). The backgrounds are prone to have a kinked trajectory and are characterised by worse fit quality and incompatible momentum measured in the ID and MS. To guarantee a robust momentum measurement, the following criteria, referred to as *Medium* muon are required for tracks in the ID and MS.

- ≥ 1 hits in the pixel detector
- ≥ 5 hits in SCT
- ≤ 2 holes in pixel or SCT
- $\geq 10\%$ hits in TRT assigned to the track for $0.1 < |\eta| < 1.9$
- ≥ 3 hits in ≥ 2 MDT layers for $|\eta| > 0.1$ or
  ≥ 1 MDT layers and ≤ 1 holes for $|\eta| < 0.1$
- q/p significance < 7

On top of these requirements, this analysis requires $p_{\mathrm{T}} > 30$ GeV and $|\eta| < 2.5$ for a muon.

In order to distinguish prompt muons from non-prompt muons from semileptonic decays of hadrons, further criteria on the isolation is required since muons from hadron decays are expected to accompany other particles associated with the decays. The isolation requires $p_{\mathrm{T}}^{\mathrm{varcone30}}/p_{\mathrm{T}}^{\mathrm{muon}} < 0.06$ for a

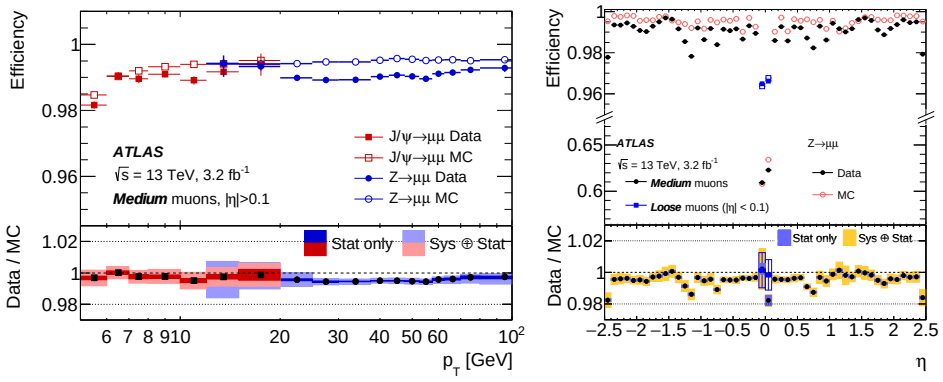

(a) (b)

Figure 3.9: Reconstruction efficiency of the combined muons as a function of p_{T} for $0.1 < |\eta| < 2.5$ (a) and of η for $p_{\mathrm{T}} > 10$ GeV (b) obtained by tag-and-probe method for $Z \to \mu^+\mu^-$ and $J/\psi \to \mu^+\mu^-$ events in data at $\sqrt{s} = 13$ TeV and simulation. Cited from [103].

muon, where the isolation variable $p_{\mathrm{T}}^{\mathrm{varcone30}}$ is the same definition with a different cone size $\Delta R = \min(0.3, 10\ \mathrm{GeV}/p_{\mathrm{T}}^{\mathrm{muon}})$ as electron.

The reconstruction efficiency for the *Medium* muons is measured in data and simulation using tag-and-probe method for $Z \to \mu^+\mu^-$ and $J/\psi \to \mu^+\mu^-$ events shown in Fig. 3.9 [103]. The efficiency for $p_{\mathrm{T}} > 30$ GeV is around 99%. The ratio of efficiency between data and MC is used as a scale factor to correct MC. The uncertainty of the efficiency is estimated to be $\leq 1\%$ for $p_{\mathrm{T}} > 30$ GeV and is considered as the systematic uncertainty on the muon reconstruction efficiency.

The momentum scale and resolution are derived from dimuon mass distributions in $Z \to \mu^+\mu^-$ and $J/\psi \to \mu^+\mu^-$ events [103]. In overall, the distributions are consistent between data and simulation. Only small disagreements are observed within the scale uncertainty of 0.05% in the barrel regions and 0.1% in high η regions $|\eta| \sim 2.5$ for $Z \to \mu^+\mu^-$ events. The momentum resolution is estimated to be about 2.3% (2.9%) in the barrel (end-cap) regions for $Z \to \mu^+\mu^-$ events.

3.4 Jets

In pp collisions, a number of quarks and gluons are generated. None of them can exist as a bare particle because of *confinement* of QCD. As soon as it is generated, it is hadronised and accompanying other hadrons along the momentum direction. The spray of hadrons are called as *jet* in high energy physics.

Jets are reconstructed with anti-k_{T} algorithm [104] using the energy clusters in the calorimeters, so-called *topological cluster* [105]. The topological clusters are built by two steps: collecting cells and cluster splitting. The first step is to find the cluster seed cells with $|E_{\mathrm{cell}}| > 4\sigma$, and incorporating the neighbouring cells with $|E_{\mathrm{cell}}| > 2\sigma$ and then the neighbouring cells with $|E_{\mathrm{cell}}| > 0\sigma$. The σ

represents the amplitude of the electronic noise and pile-up noise in a cell. But the first step does not contain the spatial information and can include several particles into one cluster. Then the second step splits the clusters around the local maxima in three dimensions. A collection of the topological clusters is the input of anti-k_{T} algorithm to reconstruct jets. The algorithm introduces the following distances d_{ij} and d_{iB} between inputs i and j:

$$d_{ij} = \min(k_{\mathrm{T}i}^{2p}, k_{\mathrm{T}j}^{2p}) \frac{\Delta_{ij}^2}{R^2}, \tag{3.6}$$

$$d_{iB} = k_{\mathrm{T}i}^{2p}, \tag{3.7}$$

$$\Delta_{ij} = (y_i - y_j)^2 + (\phi_i - \phi_j)^2 \tag{3.8}$$

where $k_{\mathrm{T}i}$, y_i, ϕ_i are the transverse momentum, rapidity and azimuthal angle of particle i, respectively. For anti-k_{T} algorithm, the parameter p is set to $p = -1$. The R parameter is set to 0.4 for the nominal jets. In addition, the topological cluster assumes massless. Then, the algorithm finds out the smallest distance from all the combination and if it is d_{ij}, it combines the inputs i and j iteratively until the smallest distance becomes d_{iB}. For instance, if there are no hard particles around one hard particle within a distance of $2R$, it combines all the soft components around the hard particle and forms a conical jet. The algorithm with $R = 0.4$ is used generally in ATLAS to reconstruct jets, referred to as small-R jets in order to distinguish explicitly from the large-radius jets. This analysis uses jets satisfying $p_{\mathrm{T}} > 25$ GeV and $|\eta| < 2.5$.

The sequential calibrations are performed in data and simulation [106]. After correction of pileup contribution, the measured energies of the jets are scaled to that of the particle level based on the simulation. Then, another calibration reduces the flavour dependence. In addition, a residual calibration, so-called *in situ* calibration is performed by balancing p_{T} of jets using 3.2 fb^{-1} of data at $\sqrt{s} = 13$ TeV in combination of di-jet, Z/γ+ jets, and multijet events. The jet energy scale is computed at a level of 4% at jet $p_{\mathrm{T}} = 20$ GeV and 2% at jet $p_{\mathrm{T}} = 1$ TeV. Its uncertainty is also derived around 4.5% at jet $p_{\mathrm{T}} = 20$ GeV and 1% at jet $p_{\mathrm{T}} = 1$ TeV. The jet energy resolution is also estimated as < 25% at jet $p_{\mathrm{T}} = 20$ GeV and 5% at jet $p_{\mathrm{T}} = 1$ TeV from the momentum balance [107] shown in Fig. 3.10. The uncertainty is computed at a level of 4% at jet $p_{\mathrm{T}} = 20$ GeV and 0.5% at jet $p_{\mathrm{T}} = 1$ TeV [108].

To suppress the pileup contamination into jets, the Jet Vertex Tagger (JVT) [109] is used. It is a multivariate analysis to show how much energy fraction in a jet originates from the hard-scatter vertex and designed to have higher (lower) values for a hard (pileup) jet. This analysis applies the JVT cuts JVT > 0.59 for jets with $p_{\mathrm{T}} < 60$ GeV and $|\eta| < 2.4$. The JVT selection efficiencies are measured in 13.3 fb^{-1} of data at $\sqrt{s} = 13$ TeV and simulation in Z+jets events [110]. The efficiency is above 90% for both data and simulation. The uncertainty is estimated at a level of 3% for jets with $20 < p_{\mathrm{T}} < 30$ GeV decreasing to around 1% for $50 < p_{\mathrm{T}} < 60$ GeV.

3.5 Large radius jets

The decay products from heavy particles with high momentum such as W/Z, Higgs boson, and top quark are detected close to each other along the momentum direction of the parent particle.

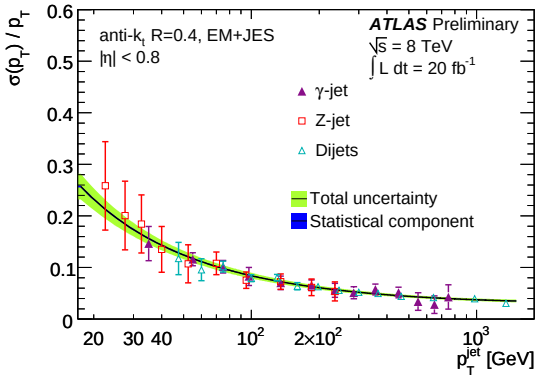

Figure 3.10: The jet resolution as a function of jet p_{T} ($p_{\mathrm{T}}^{\mathrm{jet}}$) for four different calibrations in $|\eta| < 0.8$. The final resolution curve combining all calibrations is also shown in black line with its associated statistical (blue fill) and total uncertainty (green fill). Cited from [107].

The angular separation between decay products can be expressed as $\Delta R = 2m/p$, where m and p are the mass and momentum of the parent particle, assumed that the masses of the decay products are negligible. Reconstruction of heavy particles as larger radius jets (large-R jets) is important for this analysis to identify signal-like events because SM heavy particles from VLT decays have higher momentum than SM physics processes and can be reconstructed by large-R jets. In order to reconstruct them, the jet re-clustering technique [111] is used in this analysis. The technique forms jets by anti-k_{T} algorithm with the radius parameter $R = 1.0$ from a collection of small-R jets as the input in the same way as small-R jets are built from a collection of the topological clusters in the calorimeters. All the kinematic variables of the large-R jets are derived from those of the calibrated small-R jets automatically, and then the technique does not need additional calibration. At the same time, the uncertainty of the large-R jets is also derived from those of small-R jets. In addition, the radius parameter R can be optimised for each analysis. The performances such as the mass resolution of the large-R jets with the re-clustering technique are similar to those of the different large-R jets reconstructed from the topological clusters which have been often used from Run1[1] [112].

In this analysis, the small-R jets with $p_{\mathrm{T}} > 25$ GeV and $|\eta| < 2.5$ after overlap removal with leptons described in Section 3.8 are used as the input of re-clustering. An additional requirement on p_{T} of a small-R jet more than 5% with respect to p_{T} of the large-R jet including the small-R jet is applied in order to suppress the pileup contribution and soft radiation. The small-R jets inside a large-R jet are referred to as *subjet* or *constituent* in the following.

Figure 3.11 shows the large-R jet mass distributions matching with hadronically decaying W bosons, Z bosons, or top quarks, or Higgs bosons decaying to the bottom quark pair in VLT signal events of SU(2)-singlet case with $m_{\mathrm{VLT}} = 1.0$ TeV. The matching criterion is to require the angular separation between a large-R jet and true particle $\Delta R < 0.75$. It shows clear mass peaks at the heavy particle masses and indicates that the large-R jets are able to reconstruct the heavy particles. In this analysis, the re-clustered large-R jets are used to identify the boosted top quarks and Higgs bosons from the

[1] This is large-R jets reconstructed from the topological clusters by anti-k_{T} algorithm with the radius parameter $R = 1.0$

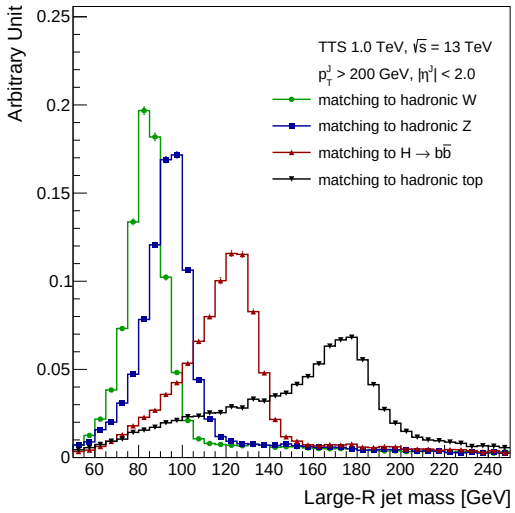

Figure 3.11: Large-R jet mass distributions matching with hadronically decaying W bosons (green), Z bosons (blue), or top quarks (black), or Higgs bosons decaying into the bottom quark pair in VLT signal events of SU(2)singlet case with $m_{\mathrm{VLT}} = 1.0$ TeV. The matching criterion is to require the angular separation between a large-R jet and the true particle $\Delta R < 0.75$. The large-R jets are required to have $p_{\mathrm{T}} > 200$ GeV and $|\eta| < 2.0$. Each distribution is normalised to unity and shows clear mass peak at the matching heavy particle mass.

kinematic variables which are distinctive of VLT decays. The optimisation of requirements and final selection are described in Section 6.

3.6 *b*-tagging

The identification of jets originating from b-hadron decays, so-called b-tagging, is important in this analysis since the heavy particles such as the Higgs bosons and top quarks decay into the bottom quarks. In ATLAS, the b-tagging algorithm [113] uses a multivariate analysis technique to combine the following individual tagging algorithms: the impact parameter based algorithm, the secondary vertex finding algorithm, and the decay chain multi-vertex algorithm.

- The impact parameter based algorithm: IP2D and IP3D
  The b-hadrons have long lifetime ($c\tau \sim 450$ μm) and result in at least one vertex displaced from the primary vertex where b-hadron is generated. The tracks from displaced vertices have larger impact parameters than those from primary vertices, shown in Fig. 3.12. This is distinct for b-hadrons and thus the basic idea to identify b-hadrons in this algorithm. Here, a sign of the impact parameters is assigned whether the displaced vertex is located in front of the primary vertex along the jet direction or behind, referred to as signed impact parameters. The d_0 significance d_0/σ_{d_0} is used as the discriminating variable in IP2D, while both d_0 and z_0 significances, d_0/σ_{d_0} and z_0/σ_{z_0}, are used in IP3D to make the two dimensional template using tracks satisfying the *Loose* criteria, $p_{\mathrm{T}} > 1$ GeV, $|d_0| < 1$ mm and $|z_0 \sin\theta| < 1.5$ mm.

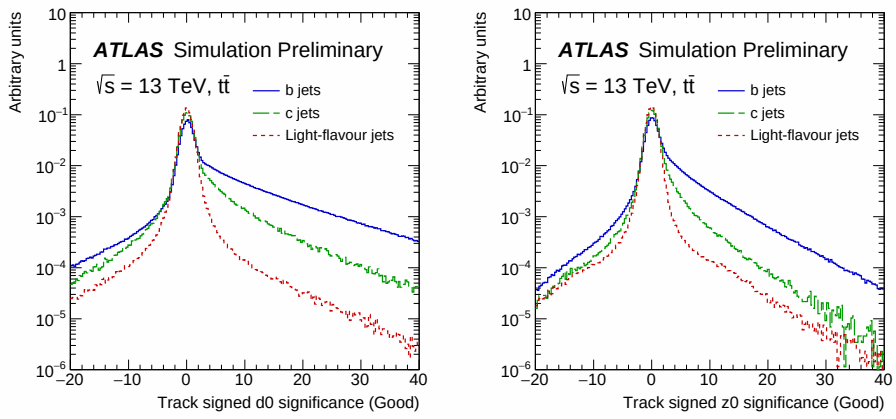

(a) (b)

Figure 3.12: (a) transverse and (b) longitudinal signed impact parameter significance of tracks in $t\bar{t}$ events for b (solid blue), c (dashed green) and light flavour (dotted red) jets. The *Good* in the x-title means tracks having neither holes, shared clusters, or split clusters associated to it. Cited from [113].

Then, the template PDFs, p_b and p_l, are made for b- and light-flavour jets hypotheses. A log-likelihood ratio $\sum_{i=1}^{N} \log\left(\frac{p_b}{p_l}\right)$ is computed as the final discriminating variable, where N is the number of tracks of a given jet. When using only IP3D, the light (c) -jet rejection is approximately 2.5% (30%) at the 77% b-tagging efficiency working point.

- The secondary vertex finding algorithm: SV
  The secondary vertex finding algorithm [114] reconstructs the secondary vertices characterised in b-hadron decays using tracks. The tracks used for vertex reconstruction are required to have less χ^2/NDF in the track fit than 3 and one more silicon hit for $|\eta| > 1.5$ on top of *Loose* selection. The tracks with low d_0 significance $d_0/\sigma_{d_0} < 2$ and high z_0 significance $z_0/\sigma_{z_0} > 6$ are discarded. At most 25 tracks ordered in the largest p_{T} are used. These criteria are designed to reduce the effects of material, fragmentation tracks, and pileup as well as to improve the reconstruction of secondary vertices.

  The following variables of reconstructed secondary vertices are used as the discriminating variables: two or three dimensional distance between the primary vertex and the secondary vertex, the invariant mass of secondary vertex, the energy fraction of tracks from the secondary vertices comparing to the energy of all tracks in the jet, the number of tracks associated to the vertex, and the number of two-track vertices inside a jet.

  The three dimensional distance significance is shown in Fig. 3.13 as an example. It shows that jets from b-hadrons have displaced vertices with long decay length. Thus it is a good discriminating variable.

- The decay chain multi-vertex algorithm: JetFitter
  The decay chain multi-vertex algorithm, so-called JetFitter [115], reconstructs the topology of b-hadron decay chain ($b \to c \to$ something) inside jets. It assumes that the vertices from

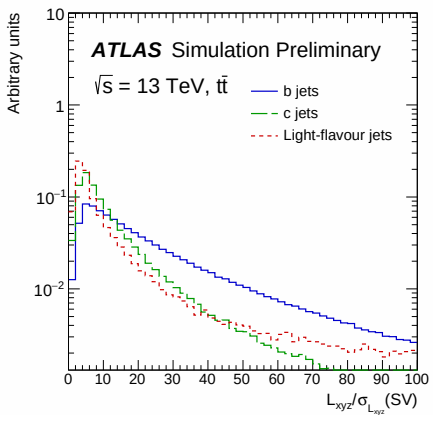

Figure 3.13: Three dimensional distance significance between the primary vertex and the secondary vertex along the jet direction in $t\bar{t}$ events for b (solid blue), c (dashed green) and light flavour (dotted red) jets. Cited from [113].

the decay chain (the primary vertex, the displaced vertices originating from b and c hadron decays) lie on a single common line along the b-hadron direction. It uses Kalman filter to find the common line. The discriminating variables are the vertex mass, the energy fraction of tracks from the displaced vertices compared to the energy of all tracks in the jet, and the flight length significance. The likelihood of these variables is used for the determination of b-hadrons.

The outputs from these algorithms are combined with a multivariate analysis based on a boosted decision tree (BDT) algorithm, so-called "MV2" and the BDT output value is used to discriminate b-flavour jets from light- and c-flavour jets. The training is performed with $t\bar{t}$ events. In ATLAS, three kinds of discriminant are available, MV2c00, MV2c10, and MV2c20 which differ in the fraction of c-flavour jet in the training sample. The light- and c-flavour jet rejections for each discriminant are shown in Fig. 3.14. The MV2c10 has similar light-flavour jet rejection comparing to the MV2c20 in 2015 configuration, while it has better c-flavour jets rejection at 77% b-flavour jet efficiency working point. This analysis uses MV2c10 with 77% b-flavour jet efficiency working point, corresponding to $\sim$ 130 light-flavour jet rejection and $\sim$ 6 c-flavour jet rejection. The jets tagged as b-flavour jets by the algorithm are referred to as b-jets in the following.

The dedicated calibration of b-tagging is performed similarly as done in Run1 [116]. It measures the efficiency to identify b-flavour jets and to misidentify light-flavour and c-flavour jets as b-flavour jets by several methods in the selected events.

In dijet events, the b-flavour jet samples can be obtained by selecting jets containing a muon. The b-tagging efficiency is estimated in both data and simulation by two method $p_{\mathrm{T}}^{\mathrm{rel}}$ and system8 [116] for lower p_{T} jets up to around 200 GeV. The $t\bar{t}$ events provide samples enriched with b-flavour jets. The events are selected by requiring one or two isolated leptons, $E_{\mathrm{T}}^{\mathrm{miss}}$, $m_{\mathrm{T}}^{\mathrm{W}}$, and at least four (two) jets with $p_{\mathrm{T}} > 25$ GeV and $|\eta| < 2.5$ for single(di)-lepton channel. Then, a few calibration methods are applied to extract b-tagging efficiency. Finally, the combination among all the methods is performed

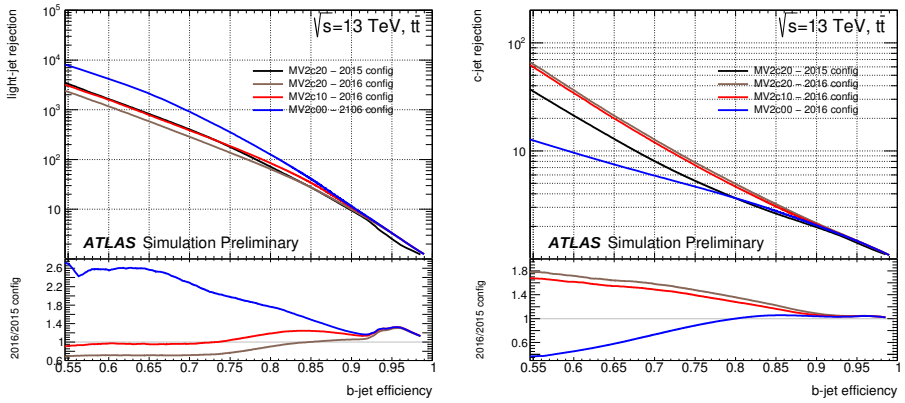

(a) (b)

Figure 3.14: (a) Light-flavour and (b) c-flavour jet rejection as a function of b-jet efficiency for the previous (2015 config) and the current configuration (2016 config) of the b-tagging algorithm evaluated on $t\bar{t}$ events. MV2c00, MV2c10, and MV2c20 represent the MV2 algorithm where the training sample contains 0%, 10%, and 20% c-jet contribution. Cited from [113].

to show good consistency of the individual measurements and obtain better calibration with less uncertainty.

For calibration of c-flavour jet tagging efficiency, the process of a W boson produced association with a single c quark, $gs \rightarrow W^{-}c$ and $g\bar{s} \rightarrow W^{+}\bar{c}$ is used to get highly pure c-flavour jets sample by requiring an isolated lepton from W boson and a soft muon from c-hadron decay with opposite sign compared to the lepton from W boson. The other method uses reconstruction of $D^{*+} \rightarrow D^{0}(K^{-}\pi^{+})\pi^{+}$ decay using tracks. After applying the invariant mass of D^{*+} and D^{0} mesons and subtracting b-flavour jets contribution, the c-flavour jet tagging efficiency is measured. The light-flavour jet tagging efficiency is evaluated in the dijet events to reverse the sign of the b-tagging discriminating variables in order to obtain mis-tagged samples, referred to as *negative tag* method [116].

The correction factor obtained by these calibrations is applied in this analysis. The uncertainty for the calibrations are propagated into the systematic uncertainty in this analysis, described in Section 8.

3.7 Missing transverse energy

The weakly interacting particles such as neutrino in the SM can penetrate the detector volume without any energy deposit in the sensitive part of the detector. They result in the imbalance of vectorial sum of the transverse momentum of all the reconstructed particles because of the conservation of momentum in the transverse plane. The imbalance is represented as the missing transverse energy, $E_{\mathrm{T}}^{\mathrm{miss}}$, in the following.

In ATLAS, $E_{\mathrm{T}}^{\mathrm{miss}}$ is reconstructed from the x and y components of the each hard object in an event [117]:

$$E_{x(y)}^{\mathrm{miss}} = E_{x(y)}^{\mathrm{miss},e} + E_{x(y)}^{\mathrm{miss},\mu} + E_{x(y)}^{\mathrm{miss},\tau} + E_{x(y)}^{\mathrm{miss},\gamma} + E_{x(y)}^{\mathrm{miss,jets}} + E_{x(y)}^{\mathrm{miss,soft}}, \tag{3.9}$$

where each component is computed by negative vectorial sum of momenta for the calibrated hard objects: electron (e), muon (μ), hadronically decaying tau-lepton (τ), photon (γ), jets, and soft term. The soft term stands for the reconstructed tracks originating from the primary vertex which are not associated with any physics objects in the event, referred to as track-based soft term (TST). For computation of TST, the tracks are required to pass *Loose* track selection and associate with the hard-scatter primary vertex. To avoid double-counting the tracks and the hard physics objects, the following selections[2] are applied to the tracks:

- Removing tracks within $\Delta R(\text{tracks, electron EM cluster}) < 0.05$
- Replacing tracks associated to combined or segment-tagged muons with the combined ID+MS fit
- Removing tracks associated with jets using the ghost-association technique [118]. In the technique, the tracks are treated as infinitesimally low p_{T} particles ("ghost") and added into the inputs of the jet algorithm. The ghosts does not affect the jet reconstruction due to their small p_{T}. After the jet algorithm, the tracks matching with the calorimeter clusters can be obtained.

In addition to them, tracks with larger momentum uncertainty than 40% are removed. The $E_{\mathrm{T}}^{\mathrm{miss}}$ and azimuthal angle ϕ^{miss} is calculated as:

$$E_{\mathrm{T}}^{\mathrm{miss}} = \sqrt{(E_x^{\mathrm{miss}})^2 + (E_y^{\mathrm{miss}})^2}, \tag{3.10}$$

$$\phi^{\mathrm{miss}} = \arctan(E_y^{\mathrm{miss}}/E_x^{\mathrm{miss}}). \tag{3.11}$$

In this analysis, hadronically decaying tau-lepton (τ) and photon (γ) are not selected, and therefore are accounted as jets inclusively.

The $E_{\mathrm{T}}^{\mathrm{miss}}$ performances are measured in data and simulation [117]. The $Z \to \mu\mu$ events are selected by requirements on the same sign lepton and the di-lepton invariant mass within Z mass. The $E_{\mathrm{T}}^{\mathrm{miss}}$ response is estimated by measurement of $E_{\mathrm{T}}^{\mathrm{miss}}$ against Z boson $\vec{p_{\mathrm{T}}}$ since it is sensitive to the momentum balance between the hard objects and the soft hadronic recoil. In $Z \to \mu\mu$ events, there is no genuine $E_{\mathrm{T}}^{\mathrm{miss}}$. Thus if the hard muons or objects are perfectly balanced against the other soft recoils, the $E_{\mathrm{T}}^{\mathrm{miss}}$ projected onto Z boson $\vec{p_{\mathrm{T}}}$ should be zero. The momentum axis of Z boson in the transverse plane is defined by

$$\vec{A}_Z = \frac{\vec{p_{\mathrm{T}}}^{\,l^+} + \vec{p_{\mathrm{T}}}^{\,l^-}}{|\vec{p_{\mathrm{T}}}^{\,l^+} + \vec{p_{\mathrm{T}}}^{\,l^-}|}, \tag{3.12}$$

where $\vec{p_{\mathrm{T}}}^{\,l^+}$ and $\vec{p_{\mathrm{T}}}^{\,l^-}$ are the transverse momenta of the leptons from the Z boson decay. Figure 3.15 (a) shows the mean value of $E_{\mathrm{T}}^{\mathrm{miss}}$ projected onto $\vec{A}_Z$ as a function of Z boson p_{T} ($\vec{p_{\mathrm{T}}}^{\,Z}$). It indicates

[2] In ATLAS, the tracks associated to τ-lepton are removed. However, this analysis does not use and reconstruct τ-lepton explicitly and thus this requirement is not described in the main composition.

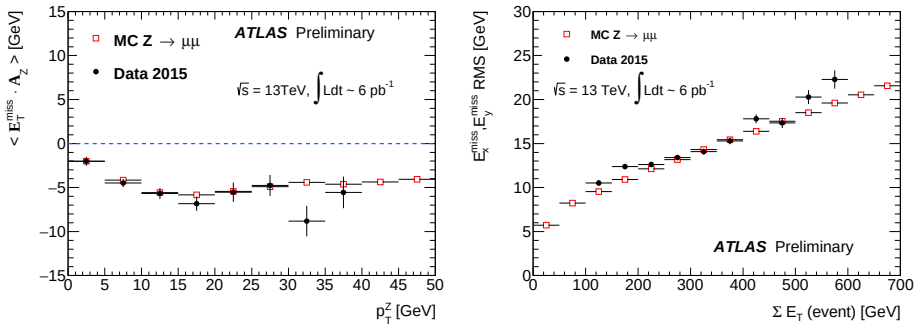

(a) (b)

Figure 3.15: (a) $E_{\mathrm{T}}^{\mathrm{miss}}$ scale as a function of p_{T}^{Z} and (b) $E_{x(y)}^{\mathrm{miss}}$ resolutions as a function of $\sum E_{\mathrm{T}}$ in $Z \to \mu\mu$ events of data (black circles) and simulation (red squares). Cited from [117].

a negative bias of $\sim$ 5 GeV due to underestimation of TST caused by the acceptance of the detector volume and neglection of neutral particles in TST. The resolution is estimated by the root-mean square (RMS) of combined values of E_x^{miss} and E_y^{miss} as a function of the scalar sum of the transverse momentum of all the hard objects and TST, shown in Fig. 3.15 (b). Both the scale and resolution estimated in simulation are consistent with those in data. The uncertainties are assigned as $\sim$ 10% and $\sim$ 20% for the resolution and the scale. The detail is described in Section 8.

3.8 Overlap removal

Since these physics objects can be double-counted, it is necessary to remove the overlaps among physics objects. For overlap removal between electron and muon objects, electrons within $\Delta R < 0.01$ between the electron and muon are removed to reduce the contribution of muon bremsstrahlung.

The overlap removal between electron and jets is performed at the next step. For instance, one isolated track having energy deposits in the calorimeter can be reconstructed as a jet and electron. In addition it can occur by the physics processes such as electron showering and non-prompt electrons from hadron decays. To reduce the former effect, the closest jet within $\Delta R < 0.2$ between the jet axis and the electron is removed. To reduce the latter effect, the electrons within $\Delta R < 0.4$ between the remaining jet axis and the electron are removed.

The final step is removal of overlap between the remaining jets and muons. Jets emerged from muon bremsstrahlung can be reconstructed and located close by the muon. Non-prompt muons from hadron decays can be overlapped with jets. If the remaining jets are located within $\Delta R < 0.4$ between the jet and the muon, the jets having at most 2 tracks are removed to suppress the former effect; otherwise the muons are removed to suppress the latter effect.

4 Data and Event simulations

In this section, the data and the simulation samples used in this analysis are described. To understand the observed data and search for new phenomena the comparison between data and simulation is essential. In the second part, the general methodology of the simulation is presented.

4.1 Data sample

The data sample used in this analysis was collected with the ATLAS detector in pp collisions at a centre-of-mass energy of 13 TeV during 2015 and 2016. The events were recorded with a single-lepton (electron and muon) trigger or a $E_{\mathrm{T}}^{\mathrm{miss}}$ trigger under stable beam conditions and after application of data quality requirements described in Section 2.2 correspond to an integrated luminosity of 36.1 fb^{-1}.

In 1-lepton channel, the events firing a single-lepton trigger are used. The single-lepton triggers with lower p_{T} threshold requires the isolation on the candidate lepton because there are numerous candidates to fire the trigger. The triggers with higher p_{T} threshold without any isolation requirement are also used. The p_{T} thresholds in 2015 and 2016 are summarised in Table 4.1. In 2016, the lowest p_{T} electron and muon trigger condition are changed to tighter identification criteria and higher p_{T} threshold, respectively.

In 0-lepton channel, the events firing $E_{\mathrm{T}}^{\mathrm{miss}}$ trigger are used. This dissertation focuses on the 1-lepton channel. The detail of the $E_{\mathrm{T}}^{\mathrm{miss}}$ trigger is described in elsewhere [49].

4.2 Simulation of pp collisions

The interesting physics process with high energy transfer can be written by Feynman diagrams and calculated with a perturbative theory. The final states often involve quarks or gluons (partons) which

Table 4.1: p_{T} thresholds in GeV for single-lepton trigger used in 1-lepton channel. The thresholds shown in bold fonts are required to pass the isolation criteria.

Data period	electron trigger	muon trigger
2015	**24**, 60, 120	**20**, 50
2016	**26**, 60, 140	**26**, 50

have colour charge and then result in emitting gluons, splitting quark-antiquark pair, repeating them until some energy scale (parton shower). Consequently they are hadronised into the stable and colour neutral particles. In addition to these processes, since protons are composite, the other partons than the hard scattering partons also interact each other. For these calculation of the non-perturbative phenomena, certain models and experimental results are used. Therefore, in order to simulate the proton-proton collision, several steps are needed to be taken into account. The first step simulates the hard scatter interaction written in Feynman diagrams by calculating the matrix element analytically at a fixed order. The second step simulates soft gluon radiation and parton showering by perturbative QCD up to hadronisation energy scale ($Q \sim 1$ GeV). The third step make use of the phenomenological models to simulate the hadronisation because it cannot be calculated analytically by perturbative QCD. On top of it, the underlying and pileup events are overlaid. The generated events are passed into the detector simulation to simulate interactions of particles with detector materials and the detector response from the particles. This section describes the overview of the procedures.

4.2.1 Event generation

The event simulation begins with the physics process associated with the high energy transfer. At the high energy, the partons can be described as asymptoticly free. The cross section of a physics process to produce a particle X from two partons a and b in the protons is described by:

$$\sigma_{pp\to X} = \sum_{a,b} \int_0^1 dx_a \int_0^1 dx_b f_a(x_a, \mu_F^2) f_b(x_b, \mu_F^2) \hat{\sigma}_{ab\to X}(x_a p_a, x_b p_b, \mu_R^2, \mu_F^2), \tag{4.1}$$

where $f_i(x_i, \mu_F^2)$ is the parton density function (PDF) for a parton i with the momentum fraction x_i, μ_F is the factorisation scale, μ_R is the renormalisation scale. This process is illustrated in Fig. 4.1. The sum computes over all the possible combination of partons a and b to produce the particle X. The PDF is the probability to find a parton i with the momentum xP in a proton with momentum P when a proton is probed at the energy scale μ_F. The PDF cannot be described by a perturbative theory but is determined by the experimental results. The PDF sets from the groups of CTEQ [119], NNPDF [120], and MSTW [121] are used exclusively in the LHC experiments. $\hat{\sigma}_{ab\to X}(x_a p_a, x_b p_b, \mu_R^2, \mu_F^2)$ is the cross section of partonic process involving the calculation of scattering matrix for the initial and final state at a fixed order. The total cross section depends on the factorisation scale μ_F and renormalisation scale μ_R. The factorisation scale is related to the boundary at low energy scale between the perturbative and non-perturbative theory in the QCD. The renormalisation scale is the scale at which physics quantities such as the running coupling constant is renormalised. These energy scales can vary the characteristic quantities in the physics process such as the sum of the momentum of the out-going particles. The uncertainty is estimated from the deviation of the cross section when the scales are varied.

The matrix element is calculated by the generators such as Powheg-Box [122–125]. The final state calculated on the generator includes partons with high energy scale Q. The initial scale Q is referred to as resummation scale. At such an energy scale, the partons can radiate gluons or partons. The gluons can radiate gluons or split into quark-antiquark pairs. The process ("parton shower") continues up to a certain energy scale referred to as hadronisation scale around 1 GeV. The hadronisation is not described with perturbative theory but with the phenomenological models in the LHC experiments:

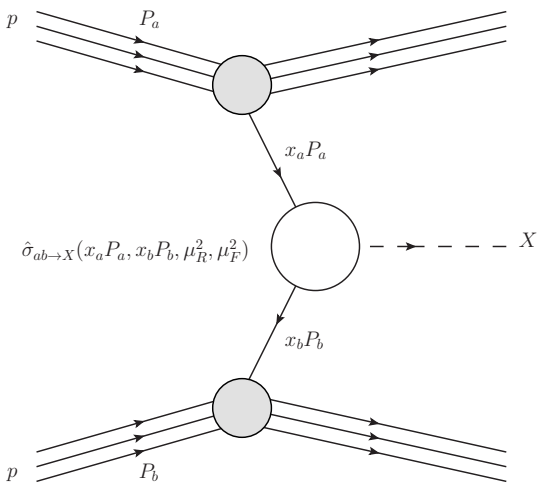

Figure 4.1: Illustration of a example of the hard process to generate a particle X from parsons a and b. A parton a (b) has a four-momentum $x_a P_a$ ($x_b P_b$) in a proton p with a momentum P_a (P_b).

Lund String Model [126, 127] or Cluster Model [128, 129]. The PYTHIA [130] generator is used to describe the parton shower and hadronisation with the string model, while the HERWIG generator [131] is used for the same purpose and employs the cluster model for the hadronisation. These generators also describe the other soft activities such as multiparton interaction (MPI) and pileup. The MPI is the interactions between the partons in the same protons which did not participate in the hard process. The pileup is the interactions between the other protons than the ones for the hard process in the same or neighbouring bunch crossing.

4.2.2 Detector simulation

The event generator produces four-vectors for all the generated particles referred to as generator level or true particles. In reality, these generated particles interact with the detector material including the sensors of all the subdetectors and their supporting structures. The interaction between the particles and the material is modelled with the GEANT4 simulation [87, 88]. It simulates the energy deposits of the particles in the detectors, which are converted into the digital information just exactly in the same way as the read-out system does. The digital information passes through the emulators of the central data acquisition system and trigger logic, and then stored as raw data in the same way as the observed data is done.

5 Signal and background modeling

This section describes various backgrounds and signals modelling in Monte Carlo simulation used for background estimation and interpretation of the final results to new physics theories beyond the standard model. The BSM scenarios considered in this analysis are the pair production of vector-like top quark and four-top-quark production. The detail of simulation is described in Section 5.1. After applying the preselection and event categorisation described in Section 7.1 and 7.2, the dominant background is $t\bar{t}$+jets. Other small contributions come from single-top production, a vector boson $V(V = W, Z)$ production associated with jets (V+jets), diboson (WW, WZ, ZZ) production and a vector boson or SM Higgs boson production associated with $t\bar{t}$ pair ($t\bar{t}V$, $t\bar{t}H$). Multijet production has also a small contribution to the backgrounds after preselection due to the misidentification of a jet or photon as an electron or the presence of non-prompt lepton from a heavy flavour hadrons containing bottom or charm quarks decaying semileptonically. This background is estimated by a data-driven method. The detail of background modelling is written in Section 5.2. In addition, all the common modelling to signal and background, e.g. the pileup contribution and detector simulation, are described in Section 5.3.

Table 5.1: List of the MC samples used in this analysis. The Sherpa generators for W/Z+jets and Diboson events employ the ME+PS@NLO prescription [132] and a dedicated parton shower tuning developed for Sherpa.

Process	Generator	Cross section	Tune	PDF set
VLQ	Protos	NNLO QCD, NNLL	A14	NNPDF2.3 LO
SM $t\bar{t}t\bar{t}$	Madgraph5	LO	A14	NNPDF2.3 LO
EFT $t\bar{t}t\bar{t}$	Madgraph5	LO	A14	NNPDF2.3 LO
2UED-RPP	Madgraph5/Bridge	LO	A14	NNPDF2.3 LO
$t\bar{t}$+jets	Powheg-Box	NNLO QCD, NNLL	P2012	CT10
W/Z+jets	Sherpa	NNLO QCD	Sherpa	NNPDF3.0NLO
t-channel t	Powheg-Box	NNLO	P2012	CT10f4
s/Wt-channels t	Powheg-Box	NNLO	P2012	CT10
Diboson	Sherpa	NLO	Sherpa	CT10
$t\bar{t} + V/H$	MG5_aMC	NLO	A14	NNPDF3.0NLO

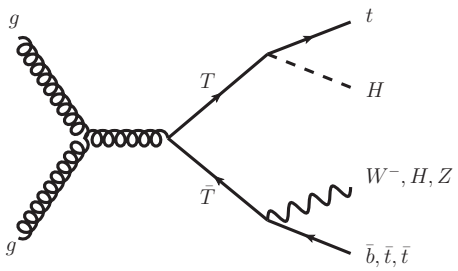

Figure 5.1: Feynman diagram for the main target of this search, where one vector-like top quark produced in pair via strong interaction decays to Higgs boson and SM top quark and the other decays to any pair of a boson and a third-generation quark.

5.1 Signal modeling

This section describes the simulation models of the BSM scenarios: the pair production of VLT and four-top-quark production.

5.1.1 Vector-like quark pair production

The cross section of the pair production depends on only the mass and is calculated by Top++ v2.0 [133] at next-to-next-to leading order (NNLO) in QCD including resummation of next-to-next-to-leading logarithmic (NNLL) soft gluon terms [134–138] with MSTW 2008 NNLO [121, 139] set of parton distribution functions (PDF) as shown in Figure 1.8 (a). It also shows that the cross section at $\sqrt{s}$ = 13 TeV increases drastically by a factor of more than 10 compared to that at $\sqrt{s}$ = 8 TeV for VLQ mass above 900 GeV. The cross section varies from 1.16 pb at the mass of 600 GeV to 11.7 fb the mass of 1.2 TeV with around 10% uncertainty. Theoretical uncertainties are derived from variations on the factorisation and renormalisation scales as from uncertainties on the PDF and α_S. The last two uncertainties are calculated by the PDF4LHC prescription [140] with the MSTW 2008 68% CL NNLO, CT10 NNLO [119, 141] and NNPDF2.3 5f FFN [120] PDF sets.

Figure 5.1 shows the Feynman diagram for the main target of this search, where one VLQ produced in pair decays to Higgs boson and SM top quark and the other decays to any pair of a boson and a third-generation quark. MC signal samples are generated with the LO generator Protos v2.2 [142] using the NNPDF2.3 LO [120] PDF set and Pythia 8.186 [84] for parton showering and fragmentation. The cross section is normalised to the Top++ prediction described above. For the underlying events description, the A14 [143] set of optimised parameters with the NNPDF2.3 LO PDF set for description of multiparton interaction and parton shower in Pythia8 is used. In the production step, VLT is set to decay to each mode Wb, Zt, Ht with artificial branching ratio of $1/3$ assuming SU(2)-singlet model. The signal events with desired branching ratio are obtained by reweighing events with BR($T \to X$) $\times$ BR($T \to Y$) $/(1/3 \cdot 1/3)$, where X and Y represent any decay mode of Wb, Zt or Ht.

On the other hand, in SU(2)-doublet or triplet cases where two or more VLQs are added into the SM, the event kinematics can differ from those in singlet. In the weak charged current, the additional

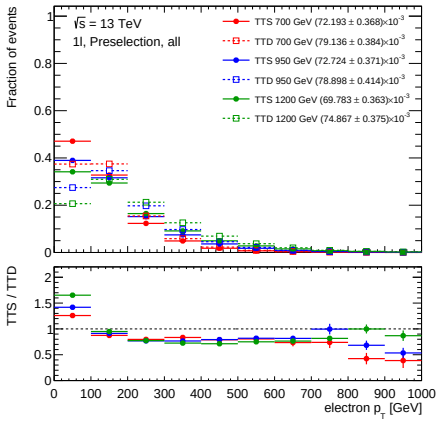

Figure 5.2: Electron p_{T} distribution for the m_{VLT} = 700, 950, 1200 GeV in SU(2) singlet and doublet models. The values in the legend represent the acceptance, the probability of a generated event to pass the preselection defined in Section 7.1. The bottom panel show the ratio of electron p_{T} between SU(2) singlet and doublet.

coupling with right-handed particle $T_{\mathrm{R}} \rightarrow W^{+}B_{\mathrm{R}}$ causes the different helicity of W boson, while it cannot occur in the singlet model since the singlet model introduces only one VLQ into the SM. At the centre-of-mass system of W boson, the W boson with the different helicity results in the reverse angular distribution of decay products from the W boson. Consequently the lepton and jet p_{T} and $E_{\mathrm{T}}^{\mathrm{miss}}$ in the doublet model can vary from those in the singlet model. In order to compare the event kinematics, additional signal samples with m_{VLT} = 700, 950, 1200 GeV assuming SU(2)-doublet model are generated. Figure 5.2 shows electron p_{T} distribution for the three mass points in the singlet and doublet models. The distribution varies especially for low p_{T} range as expected from the discussion above. Figure 5.2 also shows the acceptance of each mass point which represents the probability of a generated event to pass the preselection defined in Section 7.1. The acceptances are consistent among the singlet and doublet for each mass point. Other comparison plots are shown in Appendix A. All the comparisons conclude that the kinematic difference caused by the different chirality of singlet and doublet couplings is negligible because the final discriminating variable is the scalar sum of transverse momentum of all objects (see Section 7) and then not sensitive to the difference. Therefore, signal events with any branching ratio are obtained by the weights using SU(2)-singlet samples.

In all the samples including signals and backgrounds, SM top quark and Higgs boson masses are set to 172.5 GeV and 125 GeV, respectively.

5.1.2 Four-top-quark production

The four-top-quark production in several BSM scenarios involving a new heavy vector particle strongly coupled to the right-handed top quark like top quark compositeness [39–41] or Randall-Sumdram extra dimension [144] is simply described via an effective field theory (EFT) with a four-fermion contact interaction [57] (Figure 5.3 (b)).

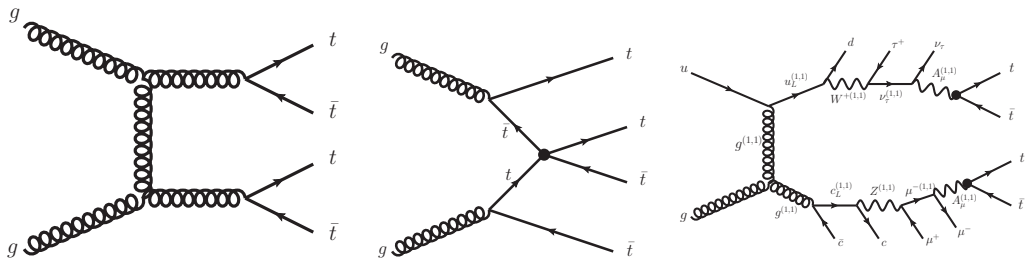

Figure 5.3: LO Feynman diagram of four-top-quark production in the SM (a), the BSM scenarios of contact interaction (b) and 2UED-RPP (c).

The samples of four-top-quark production shown in Fig. 5.3 are generated with the MADGRAPH5 [145] LO generator [1] and NNPDF2.3 LO PDF set passed to PYTHIA 8 [2] and A14 tune [146]. The production cross sections for SM and EFT are normalised to 9.2 fb and 928 fb assumed $|C_{4t}/\Lambda^2| = 4\pi$ TeV^{-2}, respectively. For 2UED-RPP, BRIDGE [147] generator is used to model the cascading decays of the pair-produced excitations from tier (1,1) generated by MADGRAPH5. Constraints for tier(2,0) and (0,2) can be derived from those for tier(1,1) together with the theoretical cross sections.

5.2 Background modeling

This section describes the simulation models of the SM backgrounds.

5.2.1 $t\bar{t}$+jets background

The $t\bar{t}$+jets events are generated with the next-to-leading order (NLO) generator POWHEG-BOX 2.0 [122–125] and CT10 PDF set [119]. The top quark mass m_{top} and decay mode are set to $m_{\text{top}} = 172.5$ GeV and $t \to Wb$, respectively. For the nominal samples, the h_{dump} parameter in POWHEG-BOX is set to m_{top}. This parameter is in charge of controlling the matrix element to parton shower matching and effectively regulates high-p_{T} radiation against $t\bar{t}$ system. This setting is known to show good agreement on the p_{T} of $t\bar{t}$ system between data and MC simulation at $\sqrt{s} = 7$ TeV [148]. The generated events are interfaced to the PYTHIA 6.428 [130] with CTEQ6L [149] PDF set and the parameter tune of parton shower and underlying events for PYTHIA, Pergia 2012 (P2012) tune [150]. The alternative $t\bar{t}$+jets samples are simulated to evaluate the systematic uncertainty, which are described in Section 8.4. The events are normalised to the theoretical cross section of 832^{+46}_{-51} pb computed with TOP++ at NNLO in QCD and resummation of NNLL soft gluon terms. $t\bar{t}$+jets events are orthogonally classified with the flavour content of the additional jets out of $t\bar{t}$ process into the one involving at least one b-flavour jet ($t\bar{t}$+≥1b), the one involving at least one c-flavour jet

[1] The versions of 2.2.2, 2.2.3 and 1.5.14 are used for the SM, EFT, and 2UED-RPP, respectively
[2] The versions of 8.186, 8.205 and 8.186 are used for the SM, EFT and 2UED-RPP, respectively

($t\bar{t}$+≥1c), and the remaining one including no additional jets ($t\bar{t}$+lights). The purpose of this classification is to apply further correction and treat the systematic uncertainty for different topologies. For $t\bar{t}$+≥1c and $t\bar{t}$+lights, the events are reweighed to top p_{T} distribution predicted at NNLO accuracy in QCD [151, 152]. For $t\bar{t}$+≥1b, the events are not applied with top p_{T} correction, which instead are reweighed to the NLO prediction in 4FNS of $t\bar{t}$+≥1b with parton showering [153], computed with Sherpa+OpenLoops [154, 155] and CT10 PDF set. The detail on the $t\bar{t}$+jets is described in Ref. [49].

5.2.2 W/Z+jets background

V+jets ($V = W/Z$) events are generated with the Sherpa v2.2 [154]. The matrix-element calculation is performed using up to two patrons at NLO and up to four partons at LO with the tree-level calculator Comix [156] and the scattering-amplitude calculator involving one loop OpenLoops [155]. The generated events are passed to the Sherpa parton shower [157] with ME+PS@NLO prescription [132]. The CT10 PDF tuned for Sherpa is used for the PDF information. V+jets events are separated into the one filtered with a b-jet (V+≥1b+jets), the one filtered with a c-jet and vetoing b-jets (V+≥1c+jets), and the one vetoed b- and c-jets (V+light-jets). The events are normalised to the NNLO theoretical cross section in QCD with FEWZ [158].

5.2.3 Single-top backgrounds

Single-top events are generated separately for each process of Wt, s-channel, and t-channel. The Wt and s-channel events are generated by the Powheg-Box 2.0 generator with CT10 PDF set. The Wt events can be double-counted with $t\bar{t}$ events beyond LO calculation. This overlap is avoided by removal of $t\bar{t}$ pair production from Wt process, so-called "diagram removal" scheme [159]. The detail of this procedure and systematic uncertainty are described in Section 8. The t-channel events are generated by the Powheg-Box 2.0 with the four-flavour scheme for calculation of the NLO matrix element and the fixed four-flavour CT10f4 PDF set [119]. These generated events are passed to the Pythia 6.425 with CTEQ6L1 PDF set and P2012 tune for modelling of parton shower, hadronisation, and the underlying events. The single-top samples are normalised to the approximate NNLO theoretical cross section [160–162].

5.2.4 Diboson background

The $WW/WZ/ZZ$+jets events are generated with Sherpa 2.1.1 and CT10 PDF set, involving at most four electroweak vertices. The matrix element calculation is performed with zero additional parton at NLO only for loop contribution and at most three additional partons at LO. In the final state, one of the vector bosons is set to decay leptonically and the other is set to decay hadronically. The samples are normalised to the NLO theoretical cross section provided by Sherpa.

5.2.5 $t\bar{t}$ + V and $t\bar{t}$ + H backgrounds

The $t\bar{t} + V$ and $t\bar{t} + H$ events are generated with MG5_aMC 2.3.2 with NLO matrix elements and the NNPDF3.0NLO PDF set [163]. The generated samples are interfaced to Pythia 8.210 and the A14 UE tune. The $t\bar{t} + V$ samples are normalised to the NLO cross section calculated with MG5_aMC. The $t\bar{t} + H$ samples are normalised with the NLO cross section [164–168] and the branching ratio of SM Higgs boson computed with Hdecay [169].

5.2.6 Multijet background

Multijet events produced via QCD can contribute to the backgrounds through the physics process or detector effects. For electron channel, non-prompt electrons from semileptonic decay of b- or c- hadrons or from photons decaying to electron-positron pair can pass the criteria of electron. In addition, jets with large fraction of their energy deposited in the electromagnetic calorimeter can be reconstructed and mis-identified as an electron. For muon channel, non-prompt muons from semileptonic decay of b- or c- hadrons or jets having very high momentum and penetrating the hadron calorimeter can be reconstructed and mis-identified as a muon. While the probability of these events to pass the preselection and event categorisation is very low, the production cross section of the multijet background is much higher than the main background processes listed above. Since it is difficult to simulate all the processes of multijet events that contribute to the total backgrounds with enough statistics, it is estimated by a data-driven method, called Matrix Method [170]. It estimates the multijet backgrounds by making use of the differences of lepton identification efficiency between real and "fake" leptons. To use it, the two samples have to be prepared: a tight sample which contains events with leptons passing the same criteria used in the analysis, and a loose sample which contains events with leptons passing looser criteria on the identification and isolation requirements described in Section 3.3 and is expected to include more fake leptons than the tight sample. The number of events in the tight sample and loose sample, N_{tight} and N_{loose} respectively, can be written as:

$$\begin{pmatrix} N_{\text{loose}} \\ N_{\text{tight}} \end{pmatrix} = \begin{pmatrix} 1 & 1 \\ \epsilon^{\text{real}} & \epsilon^{\text{fake}} \end{pmatrix} \begin{pmatrix} N_{\text{loose}}^{\text{real}} \\ N_{\text{loose}}^{\text{fake}} \end{pmatrix}, \tag{5.1}$$

where the variables are explained below.

- $N_{\text{tight(loose)}}$: The number of events in the tight (loose) sample
- $\epsilon^{\text{real(fake)}}$: The probability of a real (fake) loose lepton to pass the tight requirements. It depends on the lepton kinematics and event topology like jet multiplicity.
- $N_{\text{loose}}^{\text{real(fake)}}$: The number of events with a real (fake) lepton passing the loose requirements

The values of $\epsilon^{\text{real(fake)}}$ are computed with MC simulation, described later. Also, N_{tight} and N_{loose} are obtained in this analysis. Consequently, the estimated number of events with a tight and fake lepton($N_{\text{tight}}^{\text{fake}} \equiv \epsilon^{\text{fake}} \cdot N_{\text{loose}}^{\text{fake}}$), is determined by solving Eq. (5.1) analytically:

$$N_{\text{tight}}^{\text{fake}} = \frac{\epsilon^{\text{fake}}}{\epsilon^{\text{real}} - \epsilon^{\text{fake}}} \left(\epsilon^{\text{real}} \cdot N_{\text{loose}} - N_{\text{tight}} \right). \tag{5.2}$$

From this equation, $N_{\text{tight}}^{\text{fake}}$ is found to be obtained by summing events with the weight:

$$w_i = \frac{\epsilon^{\text{fake}}}{\epsilon^{\text{real}} - \epsilon^{\text{fake}}} \left(\epsilon^{\text{real}} - \delta_i\right), \tag{5.3}$$

where $\delta_i = 1(0)$ for the events with a tight (loose) lepton.

The efficiency ϵ^{real} is estimated from the MC simulation with the same SM processes as found in the preselection. The average ϵ^{real} is $\sim 97\%$ ($\sim 99\%$) for electrons (muons).

The efficiency ϵ^{fake} is estimated from the data with a control region. The requirements on an event for the control region are listed below:

- Containing exactly one lepton passing Loose criteria
- Containing no different flavour leptons passing Tight criteria
- Having $E_{\text{T}}^{\text{miss}} < 20$ GeV and $E_{\text{T}}^{\text{miss}} + m_{\text{T}}^{\text{W}} < 60$ GeV, where m_{T}^{W} is the transverse mass of $E_{\text{T}}^{\text{miss}}$ and the lepton computed as:

$$m_{\text{T}}^{\text{W}} = \sqrt{2p_{\text{T}}^{l} E_{\text{T}}^{\text{miss}}(1 - \cos\Delta\phi)}. \tag{5.4}$$

- Containing at least 4 jets and at least 1 b-jet

These requirements are designed in order to enrich the multijet background in the data. The efficiency ϵ^{fake} is inclusively derived from the control region, and then the average ϵ^{fake} is $\sim 77\%(73\%)$ for electrons (muons).

In order to validate the multijet background estimation, the data and the background estimation are compared. The events are required to contain one lepton, at least four jets, one b-jet, $E_{\text{T}}^{\text{miss}} < 20$ GeV and $E_{\text{T}}^{\text{miss}} + m_{\text{T}}^{\text{W}} < 60$ GeV. These requirements are designed to enrich the multijet background in data. Figure 5.4 shows comparison of lepton p_{T} between data and the background estimation. It is found that the estimated backgrounds are consistent with data within $\sim 10\%$ for both electron and muon channels. The validation of multijet background estimation is performed by selecting events with the number of jets and b-jets, values of $E_{\text{T}}^{\text{miss}}$ and m_{T}^{W}. Appendix B shows the set of validation plots comparing kinematic variables between data and the estimated backgrounds. It concludes that the multijet background is estimated within 50% accuracy and the multijet events can be neglected in the signal sensitive categories and higher m_{eff} range where the signal events are expected to populate. The uncertainty of the estimation is described in Section 8.

5.3 Common modelling and simulation to all the signals and backgrounds

All the signals and backgrounds samples use Photos 3.22 [171], Tauola [172], and EvtGen [173] to simulate photon radiation, τ decays, and heavy flavour hadron decays, respectively. Minimum-bias events are simulated with Pythia 8.186 generator with the MSTW 2008LO PDF set and the A2 tune. They are added after generation of events according to the luminosity profile of the recorded data. The

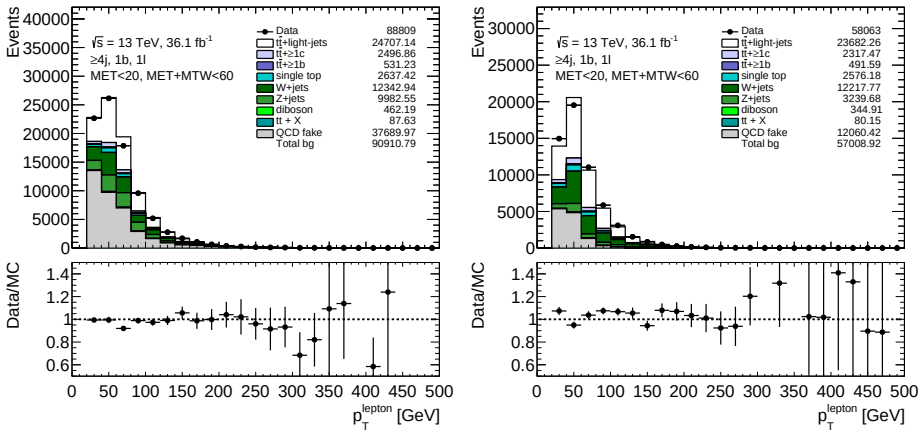

(a) Electron channel (b) Muon channel

Figure 5.4: (a) Electron and (b) muon p_{T} distribution in the events requiring at least four jets, one b-jet, $E_{\mathrm{T}}^{\mathrm{miss}} < 20$ GeV, $E_{\mathrm{T}}^{\mathrm{miss}} + m_{\mathrm{T}}^{\mathrm{W}} < 60$ GeV. The multijet background (gray) estimated by the Matrix Method and the other background estimation by MC (filled histograms) are consistent with data (black marker).

pileup contributions within the same bunch crossing as the hard-scatter process are taken into account in this way. The other pileup contributions within the neighbouring bunch crossings are modelled in the same way, but simulating the time response of the readout electronics. Produced samples are passed to the simulation of detector geometry and response with GEANT4. All the simulated samples are processed by the same reconstruction procedure as data and are applied with correction for the trigger and particle identification efficiency, energy scale and resolution to match with data.

5.4 Tag-rate-function method

This analysis requires a lot of jets and b-jets in an event. Normally only the events passing the requirements are used to estimate the backgrounds and signals. However this largely reduces the amount of MC statistics available for the background estimation. In the MC samples, there are not enough statistics for the parameter phase where the backgrounds are expected to be depleted while the signals are populated. It effectively leads to a loss of sensitivity for the signal due to the large statistical uncertainties, and it could also cause the bias in the estimation. In addition to them, with low statistics, the systematic uncertainty cannot be estimated precisely.

The problem is caused by the fact that the events which do not pass the requirements are not used for the estimation. The tag-rate-function (TRF) method is introduced to solves it. In TRF method, the probability of an event to pass the requirements is computed and applied in the event as weight, instead of retaining or discarding the event. Thus, all the events are utilised for the background estimation with TRF method. This analysis employs TRF method only for b-tagging criteria after applying kinematic cuts on jets. Indeed, the probability of an event to contain exactly one b-jet, P_{1b},

is computed by using the tagging efficiency ϵ for a given jet:

$$P_{1b} = \sum_{i=1}^{N} \epsilon_i \left(\prod_{j \neq i} (1 - \epsilon_j) \right), \tag{5.5}$$

$$\epsilon = \epsilon(p_{\mathrm{T}}^{\mathrm{jet}}, \eta^{\mathrm{jet}}, f^{\mathrm{truth}}), \tag{5.6}$$

where N is the number of jets in a given event. the tagging efficiency ϵ is parametrised by the jet p_{T} ($p_{\mathrm{T}}^{\mathrm{jet}}$), the jet η (η^{jet}), and the true jet flavour (f^{truth}).

The TRF does not use all the variables handled for the b-tagging algorithm such as impact parameters of tracks and displaced vertices in jets. Therefore it is necessary to check the difference of kinematic distributions between in TRF and in the normal way, referred to as direct tagging (DT). The validation is performed by using the dominant background of $t\bar{t}$+jets samples. Figure 5.5 shows the leading b-jet p_{T} in one background dominant category (0T, 0H, ≥6j, ≥4b) and one signal sensitive category (≥2H, ≥6j, ≥4b). The definition of these categories will be described in Section 7.2. The integrated luminosity of distributions are assumed to be 1 pb^{-1}. In the background dominant category, the event yield in TRF is different from the one in DT by $\sim$ 3% above its uncertainty. But the distribution shape are consistent with each other within a few percent. On the other hand, in the signal sensitive category, it is seen that TRF predicts the distribution smoothly and with less statistical fluctuation than the one in DT as expected.

In a few categories, the event yields are different between the TRF and DT. To know the impact of the difference to the fit results, several tests are performed. All the tests and comparison plots of the kinematic variables are shown in Appendix C. It is found that the fit results using TRF are consistent with those using DT since the differences between TRF and DT are only at a level of a few percent. At the same time, it is also found that TRF improves the sensitivity because of less statistical uncertainty. In this analysis, all the backgrounds except the multijet process are estimated with TRF.

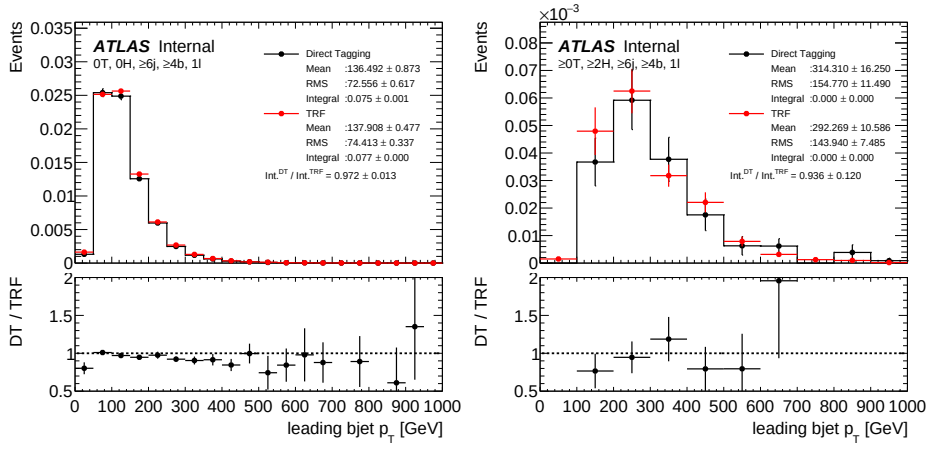

(a) (b)

Figure 5.5: Leading b-jet p_{T} distributions in one background dominant category (0T, 0H, ≥6j, ≥4b) and one signal sensitive category (≥2H, ≥6j, ≥4b). The definition of these categories are shown in Section 7.2. The mean, RMS, integral values for both TRF and DT are shown in the legend at top panel. The bottom panel shows the ratio of p_{T} in DT to TRF.

6 Optimisations of heavy object tagging and event categorisation

Until Run2 in 2015, this search has used an inclusive tagger for SM Higgs boson and top quark, requiring higher mass of large-R jets. On the other hand, the difference between VLQ signal and the dominant background of $t\bar{t}$+≥1b is the existence of boosted Higgs boson. A boosted Higgs boson tagger is promising to discriminate the signal from backgrounds and to improve the sensitivity. In the first part of this chapter, the exclusive Higgs boson and top quark taggers are defined and optimised. This analysis categorises events based on the multiplicity of jets, b-jets, Higgs-tagged jets and top-tagged jets before statistical analysis is carried out as described Chapter 7. Thus the categorising method also needed to be optimised, which are described in the last part of this chapter. Re-clustered large-R jets ($R = 1.0$) described in Section 3 are used as the inputs for the taggers.

In order to know the improvement of the sensitivity with a certain condition, the results with new conditions are compared with the one obtained with the same configuration as done in the previous analysis in 2016 [49]. The integrated luminosity used for the comparison is set to be common in the both configurations. The setting of the analysis is named here as *old configuration*.

6.1 Methodology of the optimisation

In order to determine the best requirements for the taggers, the requirements when they have the best sensitivity to signals are set. The benchmarks of the VLQ signals are set to be $m_{\mathrm{VLT}} = 950$ GeV for SU(2) singlet, $m_{\mathrm{VLT}} = 1.1$ TeV for SU(2) doublet, and $m_{\mathrm{VLT}} = 1.2$ TeV for the case of the fixed branching ratio of VLT: $\mathrm{Br}(T \to Ht) = 1$. These mass points are the expected exclusion limits on the VLT mass estimated using *old configuration*. The optimisation starts with the tentative requirements for the taggers and event categorisation determined from the characteristics of Higgs boson and top quark. When each requirement is varied for a certain range by a certain step, the sensitivity is computed at the various mass points from the fit including all the systematic uncertainties. Then, the best requirement which has the best sensitivity to signal is selected as the final configuration, assuming the requirements are independent and uncorrelated. The Higgs boson and top quark taggers are optimised in these steps. After the determination of the taggers, the event categorisation method is also optimised in the same way, starting from the tentative categorisation. The tentative requirements of taggers and event categorisation are shown in Table 6.1 and 6.2, respectively.

Table 6.1: List of the tentative requirements for the Higgs boson and top quark taggers. "Inclusive tagging" is the inclusive identifier of the Higgs bosons and top quarks used in the *old configuration*, which is shown as a reference.

Requirements	Higgs tagging	top tagging	Inclusive tagging
p_{T}	>250 GeV	>350 GeV	> 300 GeV
η	$\lvert\eta\rvert < 2.0$	$\lvert\eta\rvert < 2.0$	$\lvert\eta\rvert < 2.0$
mass	$95 < m < 140$ GeV	$m > 140$ GeV	$m > 100$ GeV
The number of constituents	$= 2(p_{\mathrm{T}} < 600$ GeV), $\leq 2(p_{\mathrm{T}} \geq 600$ GeV)	≥ 2	≥ 2
The number of b-jets	≥1	≥0	≥0

Table 6.2: Tentative event categorisation with the Higgs boson and top quark taggers. The names of categories are shown in the table, where the columns are the number of top-tagged jets (N_{top}) and the rows are the number of Higgs-tagged jets (N_{Higgs}). For instance, the "1T0H" category is a group of the events with one top-tagged jet and without any Higgs-tagged jets.

N_{Higgs} \ N_{top}	0	1	≥2
0	"0T0H"	"1T0H"	"2T0H"
1	"0T1H"	"≥1T≥1H"	
≥2	"0T2H"		

6.2 Optimisation of Higgs tagging

Higgs tagging is important to discriminate signals from background as discussed above. In this section, the Higgs boson tagger is defined with re-clustered jets having information of p_{T}, mass, and the number of constituents. The variables are illustrated in Fig. 6.1. Afterwards, the performances of acceptance, efficiency, and fake rate are shown.

6.2.1 Determination of Higgs tagging requirements

p_{T} requirement Assuming the Higgs boson decays to bottom quark pair, the angular separation ΔR between the bottom quarks becomes 1.0 at Higgs transverse momenta of $p_{\mathrm{T}} \sim 250$ GeV, according to calculation of $\Delta R = 2m/p$. Figure 6.2 (a) shows the ΔR between the bottom quarks as a function of the Higgs p_{T} calculated at the particle level of the MC generator in the VLT events with the mass of 1 TeV. The figure gives the confirmation that the ΔR becomes 1.0 (show in red dashed line) at Higgs transverse momenta of $p_{\mathrm{T}} \sim 250$ GeV. Thus, the p_{T} threshold should be set around 250 GeV. As the tentative p_{T} threshold of the Higgs boson

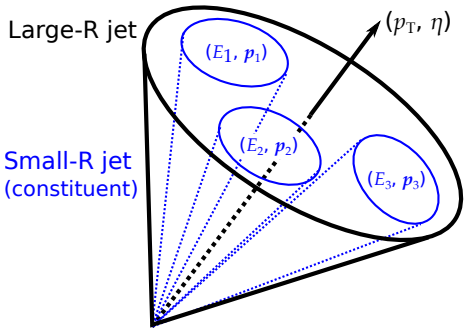

Figure 6.1: Variables of the large-R jets (black) used for the optimisation. The small-R jets (blue) composing the large-R jet are referred to as *constituent*. The invariant mass of the large-R jet is computed from the four-vectors of the small-R jets.

tagger is varied to $p_T > 200, 250, 300$ GeV, the sensitivity to signal is computed for each p_T threshold. The comparison of sensitivity among these requirements is shown in Fig. 6.2 (b). It shows the ratio of the upper limit at 95% confidence level (CL) on the production cross section for each setting to that of the result in the *old configuration* as a function of VLT mass with the same integrated luminosity of 30 fb^{-1}. In this plot, the smaller values along y-axis represent higher sensitivity to the signal. The detail of the calculation of sensitivity and the explanation of the confidence level is described in Chapter 9. The requirement of $p_T > 200$ GeV has the highest sensitivity to the signal for $m_{VLT} < 1.1$ TeV since it has higher signal acceptance, while for $m_{VLT} > 1.2$ TeV, the requirement of $p_T > 300$ GeV has better sensitivity to signal. The requirement of $p_T > 200$ GeV is chosen as the final configuration because our target on the VLT mass is around 900 GeV in case of SU(2)-singlet model and the improvement on the requirement of $p_T > 300$ GeV for higher mass points are negligible comparing to that for lower mass.

Mass requirement The large-R jet mass is a good discriminating variable of the targeting particle from the other particles. As shown in Fig. 3.11 in Section 3.5, the Higgs boson and top quark can be identified exclusively by the mass requirements such as $100 < m < 140$ GeV for the Higgs boson and $m > 140$ GeV for the top quark. In order to determine the best mass requirements, it is needed to compute the sensitivity in two dimensions: the mass requirement for the Higgs boson tagger and for the top quark tagger. To simplify the optimisation, the upper threshold for the Higgs boson tagger is set to be equal to the lower threshold for the top quark tagger. Consequently the two parameters of the lower threshold for the Higgs tagger and the lower threshold for the top quark tagger are scanned for the ranges from 75 GeV to 105 GeV and from 130 GeV to 150 GeV by a step of 5 GeV, respectively. Figure 6.3 shows the ratio of the upper limit on the production cross section in two dimensional plane of the lower threshold for the Higgs boson tagger in x-axis and the lower threshold for the top quark tagger in y-axis for several signal models. The color contour in z-axis represents the ratio of the upper limit. The Delaunay interpolation [174] is used to fill the intermediate area among the actual scan points. As discussed in the 'p_T requirement' section, smaller values along z-axis represent higher sensitivity to signal, comparing to the reference. In the cases of SU(2) doublet and

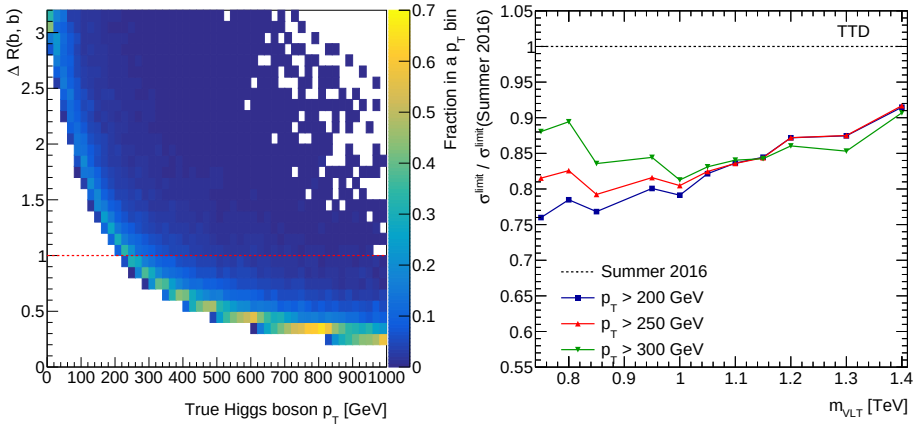

(a) (b)

Figure 6.2: (a) Angular separation ΔR between the bottom quarks from the Higgs boson decays as a function of the Higgs p_{T} calculated at the particle level of the MC generator in the VLT events with the mass of 1 TeV. The red dashed line shows $\Delta R = 1.0$ where the decay products can be reconstructed as large-R jets with the radius parameter $R = 1.0$. The values in each bin are normalised in a p_{T} bin. (b) Ratio of the upper limits at 95% CL on the production cross section with the various p_{T} thresholds to that with the *old configuration* ("Summer 2016", black dashed line) assuming the same integrated luminosity of 30 fb^{-1}. Blue, red, and green graphs show the sensitivity with the requirement of $p_{\mathrm{T}} > 200, 250, 300$ GeV, respectively. Smaller values along y-axis represent higher sensitivity to signal, compared to the reference.

BR(Ht) = 1, the sensitivity is the highest at $105 \leq m \leq 140$ GeV for the Higgs boson tagger and $m > 140$ GeV for the top quark tagger, while in the case of SU(2) singlet, the sensitivity is the highest at $85 \leq m \leq 140$ GeV for the Higgs boson tagger and $m > 140$ GeV for the top quark tagger. The difference of the branching ratio among signal models causes the difference of the minimum points. For BR(Ht) = 1, the signal events contain only the Higgs bosons and top quarks, while the background events contain W and Z bosons and top quarks. In order to reduce the background contamination, the lower mass threshold for the Higgs tagger is preferred to take higher values between Z boson and the Higgs boson masses. If the lower mass threshold is set to higher than 105 GeV, the statistics in the categories with at least one Higgs-tagged jet are too low to fit and compute the sensitivity stably. For SU(2) singlet or doublet, the signal events can contain W and Z bosons as well as the Higgs bosons and top quarks. The existence of these decay modes varies the best mass requirement to improve the signal acceptance. When comparing the improvement of the sensitivity between the lower threshold for the Higgs tagger of 85 GeV and 105 GeV with the lower threshold for the top quark tagger fixed at 140 GeV, the former requirement improves the sensitivity by $\sim 1\%$ for SU(2) singlet but loses the sensitivity by at least $\sim 2\%$ for SU(2) doublet and BR(Ht) = 1. The same set of plots are produced in VLT signals with the different mass points and in 2UED-RPP model with the different mass points, shown in Fig. D.1 in Appendix D. They show that the results in VLT signals with the different mass points have a similar tendency as shown in the figure and the requirements do not drastically affect the sensitivity to 2UED-RPP models. Thus, the requirement of $105 \leq m \leq 140$ GeV for the Higgs tagger and $m > 140$ GeV for the

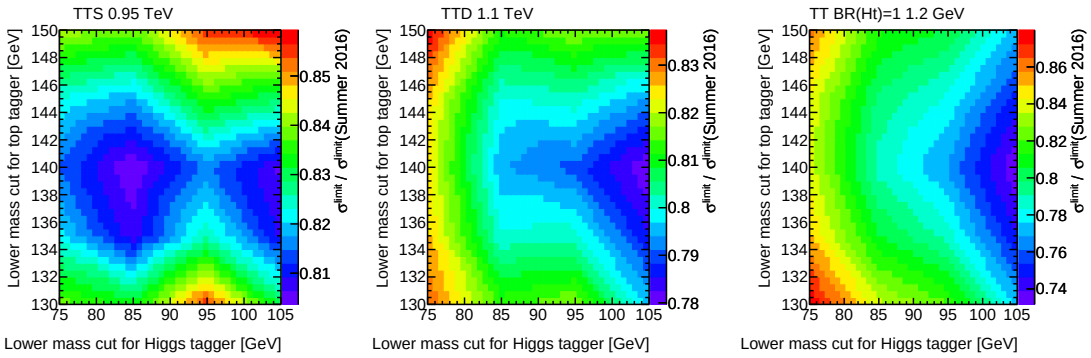

Figure 6.3: Ratio of the upper limits at 95% CL on the production cross section with various mass requirements to that with the *old configuration* ("Summer 2016") at the same integrated luminosity of 30 fb^{-1}. In order from left to right, the results with SU(2) singlet and m_{VLT} = 950 GeV, SU(2) doublet and m_{VLT} = 1.1 TeV, and BR(Ht) = 1 and m_{VLT} = 1.2 TeV are shown. The colour contour in z-axis represents the ratio of the upper limit. The lower threshold for the Higgs boson (top quark) tagger in $x(y)$-axis is scanned for the range from 75 (130) GeV to 105 (150) GeV by a step of 5 GeV. The Delaunay interpolation [174] is used to fill the intermediate area among the actual scan points.

top quark tagger is chosen as the final configuration.

The number of constituents requirement Considering the bottom quark pair decay of the Higgs boson, the large-R jet originating from the Higgs boson should have two constituents associated with the b-jets. The combinatorial backgrounds such as large-R jets formed by a few jets from pileup or radiations can have more than two constituents. Thus, the requirement on the number of constituents is effective in reducing the fake rate. As shown in Fig. 6.2 (a), the angular distance between the bottom quarks from the Higgs decays $\Delta R(b, \bar{b})$ is larger than 0.4 for $p_{\mathrm{T}} < 600$ GeV, resulting in two constituents inside the corresponding large-R jet. The value of 0.4 corresponds to the radius parameter of the small-R jet. Thus the two energy clusters with $\Delta R > 0.4$ are individually reconstructed as small-R jets. In contrast, for $p_{\mathrm{T}} > 600$ GeV, the $\Delta R(b, \bar{b})$ is less than 0.4. This situation leads to that the close-by two energy clusters are merged and reconstructed as one small-R jet, and then the corresponding large-R jet has only one constituent. This transition of constituent with the p_{T} in the signal events of SU(2) singlet and the mass of 1 TeV is shown in Fig. 6.4 (a). From this result, the requirements on the constituents should depend on p_{T}. Especially, the allowance of single constituent inside a large-R jet should improve the signal acceptance with highly boosted Higgs bosons.

To determine the best requirement, the sensitivity is computed with the various requirements shown in Table 6.3. Figure 6.4 (b) shows the ratio of the upper limit at 95% CL on the production cross section with the requirements as done in p_{T} threshold. The requirements B and C have worse sensitivity especially for higher mass signals in which the Higgs bosons from VLT decays have higher momentum. It is caused by losing highly boosted Higgs bosons which are reconstructed as single constituent large-R jets. The requirements A1 and A2, which allow for the single constituent only for high p_{T}, have higher sensitivity as expected. The requirement A2 is chosen as the final configuration since it has the best sensitivity for all the mass points.

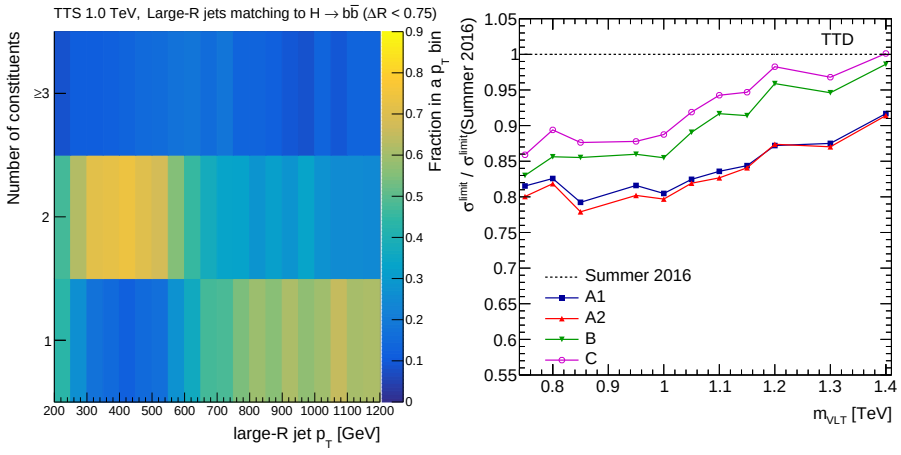

(a) (b)

Figure 6.4: (a) Number of constituents as a function of large-R jet p_{T} for the SU(2)-doublet VLT signal events with the mass of 1 TeV. In the signal events, the large-R jets are required to match to the Higgs boson decaying to the bottom quark pair by ΔR(large-R jet, Higgs boson) < 0.75. The values along z-axis are normalised to unity every p_{T} bin. (b) Ratio of the upper limits at 95% CL on the production cross section with the various requirements on the number of constituents to that of the *old configuration* ("Summer 2016"), setting the same integrated luminosity of 30 fb^{-1}. The detail of each requirement is described in the main body. The requirements of A1 (blue), A2 (red), B (green), and C (magenta) are shown in Table 6.3. The SU(2) doublet is used for calculation of the sensitivity.

Table 6.3: The various requirements on the number of constituents for the optimisation.

Name	The number of constituents
A1	$= 2$ for $p_{\mathrm{T}} < 600$ GeV ≤ 2 for $p_{\mathrm{T}} > 600$ GeV
A2	$= 2$ for $p_{\mathrm{T}} < 500$ GeV ≤ 2 for $p_{\mathrm{T}} > 500$ GeV
B	$= 2$
C	≥ 2

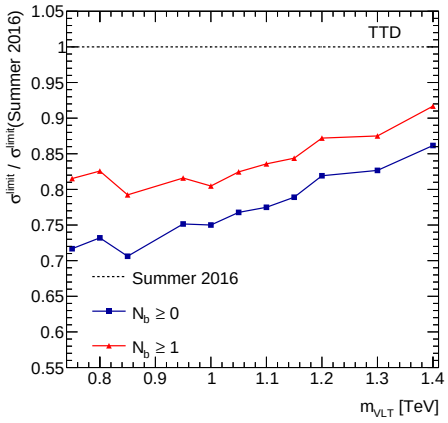

Figure 6.5: Ratio of the upper limits at 95% CL on the production cross section with and without the requirement of b-jet multiplicity to that with the *old configuration* (Summer 2016), assuming the same integrated luminosity of 30 fb^{-1}. The blue and red graphs show the sensitivities with no b-jet requirement and at least one b-jet inside the large-R jet. The SU(2) doublet is used for calculation of the sensitivity.

Requirement of b-jet multiplicity The large-R jets originating from the Higgs bosons can contain at most two b-jets. The requirements of b-jets inside a large-R jet can be helpful to reduce the fake backgrounds since the radiation or pileup jets do not often include b-jets. At the same time, the b-tagging efficiency is 77% and depends on small-R jet p_{T}; typically it decreases for high p_{T} range. It may result in the degradation of the sensitivity because of the reduced signal acceptance. Therefore it is necessary to check the sensitivity with or without the requirement of b-jet multiplicity. Then the comparison of the sensitivity between with $\geq$1 b-jet and without b-jet requirement is shown in Fig. 6.5. It shows removal of the requirement on b-jet multiplicity improves sensitivity to signal. As discussed above, without b-jet requirement, the tagger will have more fake backgrounds, while it can identify the Higgs boson from other hadronically decaying modes such as $H \to WW \to qqqq$. In total, the removal of b-jet requirement improves the signal acceptance and leads to better sensitivity.

Finally the requirements for the Higgs boson tagger are fixed by determining the best requirement for each variable as discussed above. Table 6.4 shows the final set of the requirements for the Higgs tagger.

6.2.2 Performance of the Higgs boson tagger

This section shows the performance of Higgs boson tagging defined in the previous section. The preselection of 1-lepton channel described in Section 7.1 is applied for all the results shown here. To avoid biases for the evaluation of the performances, the following requirements are applied in the Higgs boson at the particle level:

- $|\eta^{\mathrm{Higgs}}| < 2.0$
- $|\eta^{\mathrm{daughter}}| < 2.5$

Table 6.4: The set of requirements for the Higgs boson tagger.

Variable	Requirement
p_{T}	≥ 200 GeV
$\lvert\eta\rvert$	< 2.0
mass	$105 < m < 140$ GeV
Number of constituents	$= 2$ for $p_{\mathrm{T}} < 500$ GeV ≤ 2 for $p_{\mathrm{T}} > 500$ GeV
Number of b-jets	N/A

- ΔR(Higgs, others from VLQ decays) > 1.0

The first one requires that the Higgs boson distributes within the re-clustered jet coverage along $|\eta|$. The second one means that the decay products from Higgs bosons distributes within tracking coverage. In addition, if a Higgs boson exists nearby the other decay products of VLT such as boosted top quarks, the performance can have biases. Therefore, the third one requires the isolation among VLT decay products. The large-R jets satisfying the angular distance between the large-R jet and a Higgs boson ΔR(large-R jet, Higgs) < 0.75 are considered as the object matching to the Higgs boson. The target of this analysis is assumed to be Higgs bosons decaying to bottom quark pair. As the Higgs bosons have other decay modes like WW, $\tau\bar{\tau}$, the performances are separately presented for $b\bar{b}$ decay mode and the other modes.

Acceptance

The acceptance $\mathcal{A}$ is defined by:

$$\mathcal{A} = \frac{\text{Number of Higgs bosons matching with a large-}R\text{ jet}}{\text{Number of Higgs bosons}}. \tag{6.1}$$

It represents the probability to reconstruct a Higgs boson as a large-R jet. Figure 6.6 (a) shows the acceptance of Higgs bosons with some criteria for SU(2)-doublet VLT signal with the mass of 1.2 TeV. The large-R jets with only $|\eta|$ cut (black line) shows around 100% acceptance of $H \to b\bar{b}$ for $p_{\mathrm{T}} > 400$ GeV. Even for the other decay modes (Fig. 6.6 (b)), the acceptance is around 80% in the case of large-R jets with only $|\eta|$ cut. In total, around 90% Higgs bosons are inclusively reconstructed as a large-R jet. In the case of large-R jets satisfying the mass requirement shown in blue lines and all the Higgs tagging requirements shown in red lines, the acceptance is around 50% (30%) for the bottom quark pair decay (the other decays). By comparing the acceptances among the requirements, the mass requirement is found to decrease the Higgs boson tagging efficiency especially for the other decay modes. In the other decay modes, the large-R jets have higher possibility to be measured as lower mass than the tagging requirement because of the leptonic decay modes of W bosons or τ leptons. The detail of the efficiency is described in the 'tagging efficiency' part. Overall, $\sim$ 45% Higgs bosons are found to be identified as the Higgs-tagged jets.

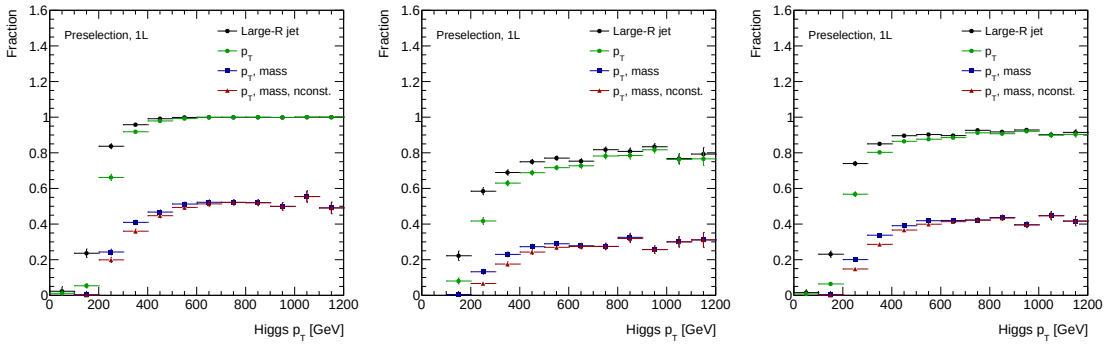

(a) (b) (c)

Figure 6.6: Acceptance of Higgs bosons, the probability to reconstruct a Higgs bosons as a large-R jet passing some criteria for VLT SU(2)-doublet signal with the mass of 1.2 TeV in (a) $H \to b\bar{b}$ decay mode, (b) the other decay modes such as $H \to WW$, and (c) all the decay modes as a function of Higgs boson p_{T}. The definition of the acceptance is shown in Eq. (6.1). Black, green, blue, and red graphs show the acceptance of the large-R jets with only $|\eta|$ cut, passing the p_{T} requirement, the p_{T} and mass requirements, and all the criteria of the Higgs boson tagger, respectively.

Tagging Efficiency

The tagging efficiency $\mathcal{E}$ is defined by:

$$\mathcal{E} = \frac{\text{Number of large-}R\text{ jets matching with a Higgs boson and tagged}}{\text{Number of large-}R\text{ jets matching with a Higgs boson}}. \tag{6.2}$$

It represents the probability that the large-R jets matching with Higgs bosons pass all the Higgs tagging requirements. Figure 6.7 shows the tagging efficiency for SU(2)-doublet VLT signals with the two masses of 1.0 and 1.2 TeV. For $p_{\mathrm{T}} > 400$ GeV, the efficiency is around 50% (45%) in $H \to b\bar{b}$ decay mode (the other decay modes) for both signal mass points. In addition, the p_{T} dependence of the efficiency is shown. The p_{T} dependence can be caused by the two requirements on the constituents and mass. In order to understand the p_{T} dependence, the efficiency is computed with separating the variables as follows.

To understand the p_{T} and constituent dependence of the efficiency, the efficiency is factorised with the number of constituents as below:

$$\mathcal{E} = \frac{N_{\mathrm{jets}}^{\mathrm{tagged}}}{N_{\mathrm{jets}}} = \sum_{i}^{\mathrm{const.}} \frac{N_{\mathrm{jets}(i)}}{N_{\mathrm{jets}}} \cdot \frac{N_{\mathrm{jets}(i)}^{\mathrm{tagged}}}{N_{\mathrm{jets}(i)}}, \tag{6.3}$$

where N_{jets} is the number of large-R jets matching with a Higgs boson, the number i reqresents the number of constituents, and "tagged" represents the large-R identified with the Higgs boson tagger. The first factor in the right side represents the probability of large-R jets to have i constituents, $N_{\mathrm{jets}(i)}/N_{\mathrm{jets}}$, which is shown in Fig. 6.4. From the plot, around 70% of the large-R jets matching with a Higgs boson have two constituents for $400 < p_{\mathrm{T}} < 500$ GeV and one constituent for $p_{\mathrm{T}} > 700$ GeV.

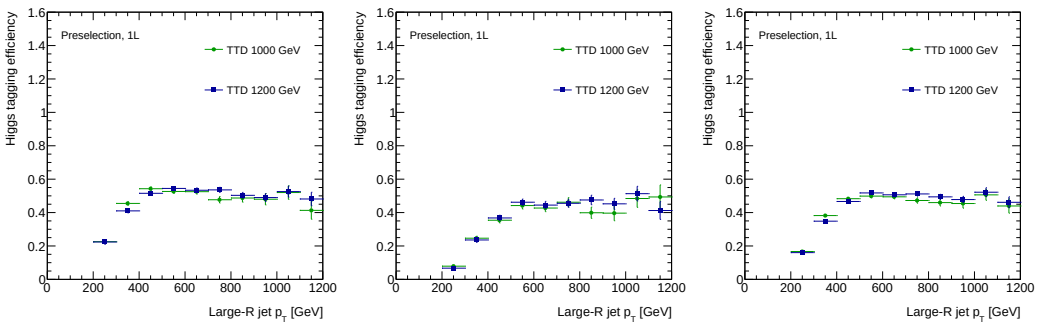

(a) (b) (c)

Figure 6.7: Tagging efficiency of the Higgs boson tagger, the probability that the large-R jets matching with Higgs bosons pass all the Higgs tagging requirements, as a function of large-R jet p_{T} in (a) $H \to b\bar{b}$ decay mode, (b) the other decay modes, and (c) all the decay modes. The definition of the tagging efficiency is shown in Eq. (6.2). The VLT signal events of SU(2) doublet with the two masses of 1.0 (blue) and 1.2 (red) TeV are used.

The second factor in the right side represents the probability of large-R jets with i constituents to be tagged as Higgs bosons, which is shown in Fig. 6.8 (a). In case of two constituents, the tagging efficiency shown in Fig. 6.8 (a) reaches at $\sim 80\%$ for $400 < p_{\mathrm{T}} < 600$ GeV and decreases for higher p_{T}, while in case of one constituent, the efficiency increases from $\sim 35\%$ at $p_{\mathrm{T}} = 500$ GeV to $\sim 70\%$ for $p_{\mathrm{T}} > 600$ GeV. Therefore, the combination of the two components is found to reproduce around 50% efficiency for the range of $400 < p_{\mathrm{T}} < 500$ GeV shown in Fig. 6.7.

To further understand the efficiency, the large-R jet mass distributions with the different p_{T} ranges and the different number of constituents are shown in Fig. 6.8 (b). The mass distributions have a peak at around 125 GeV expected from the Higgs boson mass and broader width than the mass requirements. The broader mass distribution is found to cause around 80% efficiency with two constituents. In addition, the mass distribution with one constituent for $800 < p_{\mathrm{T}} < 1000$ GeV (red) is similar to the one with two constituents for $400 < p_{\mathrm{T}} < 600$ GeV (green) because highly boosted Higgs bosons can be reconstructed as a large-R jet with single constituent. On the other hand, the mass distribution with two constituents for $800 < p_{\mathrm{T}} < 1000$ GeV (blue) is shifted to higher range compared to the others. It leads to lower efficiency for higher p_{T} in case of two constituents. This shift can be caused by a mixture with jets other than Higgs boson decays.

In order to investigate the mass shift, the large-R jets matching with a Higgs boson are classified by the following steps:

1. Classifying the large-R jets based on the number of the bottom quarks from Higgs boson decay at a particle level. Here, the particles at the MC generator level are referred to as *true* particles. The true particles satisfying the angular distance of $\Delta R < 1.0$ between a large-R jet axis and the true particle are considered as the ones matching with the large-R jet. In the classification, the angular distance between the true particles is also considered since the particles very close to each other are reconstructed as one small-R jet. For instance, the case of two true

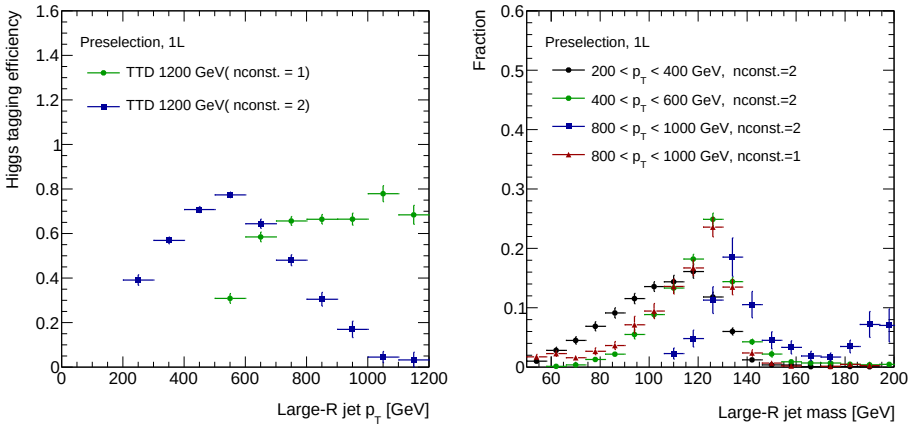

(a) (b)

Figure 6.8: (a) Higgs tagging efficiency with one (two) constituent(s) for VLT SU(2)-doublet signals with the mass of 1.2 TeV shown in green (blue) as a function of large-R jet p_{T}. (b) Large-R jet mass distribution with two constituents for the different p_{T} ranges of $200 < p_{\mathrm{T}} < 400$ GeV (black), $400 < p_{\mathrm{T}} < 600$ GeV (green), $800 < p_{\mathrm{T}} < 1000$ GeV (blue), and with one constituent for $800 < p_{\mathrm{T}} < 1000$ GeV(red) in the VLT signal events of SU(2) doublet and the mass of 1.2 TeV.

Table 6.5: Classification based on the number of bottom quarks from Higgs boson decays at a particle level and the number of constituents inside a large-R jet. "Merged" or "Resolved" classes are split by the angular distance between the true particles $\Delta R < 0.4$ or $\Delta R > 0.4$, respectively.

Number of true particles	Number of constituents
1	1
	≥ 2
2 (Resolved)	1
	2
	≥ 3
2 (Merged)	1
	≥ 2

particles contained inside a large-R jet is classified further into "Merged" or "Resolved" based on the angular distance between the true particles $\Delta R < 0.4$ or $\Delta R > 0.4$, respectively. This classification means whether the subjets are close to each other or well-separated.

2. Further classifying the large-R jets based on the number of constituents.

The classification has 7 classes in total and summarised in Table 6.5. Figure 6.9 illustrate the classification. In the following, only the $H \to b\bar{b}$ decay process is considered.

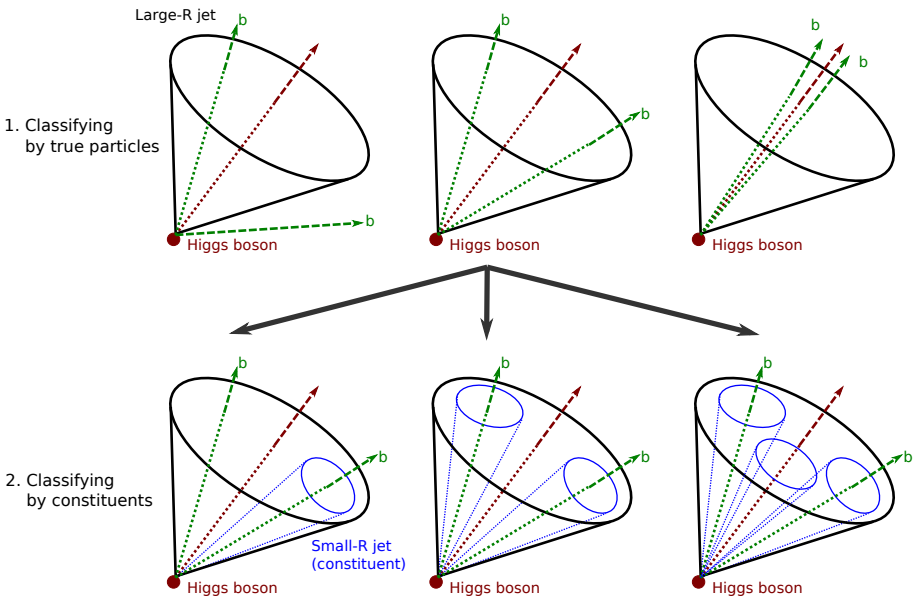

Figure 6.9: Illustration of the classification based on the true particles and constituents. Firstly, large-R jets are classified based on the true partons (green) as shown in top figures. Secondly, they are classified based on the constituents (blue) as shown in bottom figures. The classification of two "Resolved" partons is shown as an example.

Figure 6.10 (a) shows the large-R jet mass distributions of each class for the p_{T} range of $200 < p_{\mathrm{T}} < 1500$ GeV. Here, only the classes with two true particles are shown. Red graphs show the cases where large-R jets have the equivalent number of subjets corresponding to the two bottom quarks. They have a clear mass peak at the Higgs boson mass. Green and blue graphs show the cases where the large-R jets contain additional subjets and the case where they contain less subjets than the two bottom quarks, respectively. They have higher or lower mass contribution as expected. Figure 6.10 (b) shows the tagging efficiency of each class as a function of large-R jet p_{T} with the same color scheme as Fig 6.10 (a). The red graphs are found to have around 80% efficiency. By comparing Fig. 6.8 (a) and Fig. 6.10 (b), additional and missing jets cause the inefficiency. Especially, the efficiency of the red color with the two constituents decreases drastically for higher p_{T}. Consequently, the p_{T} dependence of the efficiency for high p_{T} range is not caused by the additional jets.

Figure 6.11 (a) shows the mass distributions of the jets with two "merged" true partons and one constituent for the different p_{T} ranges. Since the mass distributions are similar, the efficiency is assured to be stable for the high p_{T} range. Figure 6.11 (b) shows the mass distributions of the jets with two "resolved" true partons and one constituent for the different p_{T} ranges. In this case, the mass distribution for higher p_{T} range has high mass tail, compared to the one for lower p_{T} range. This tail can cause the inefficiency for the high p_{T} range. It can be caused by the p_{T} dependence of the mass calibration or resolution [112]. Measurements of the small-R jets such as mis-measurement of the momentum or direction, and contaminations of jets from other source also can lead to higher mass.

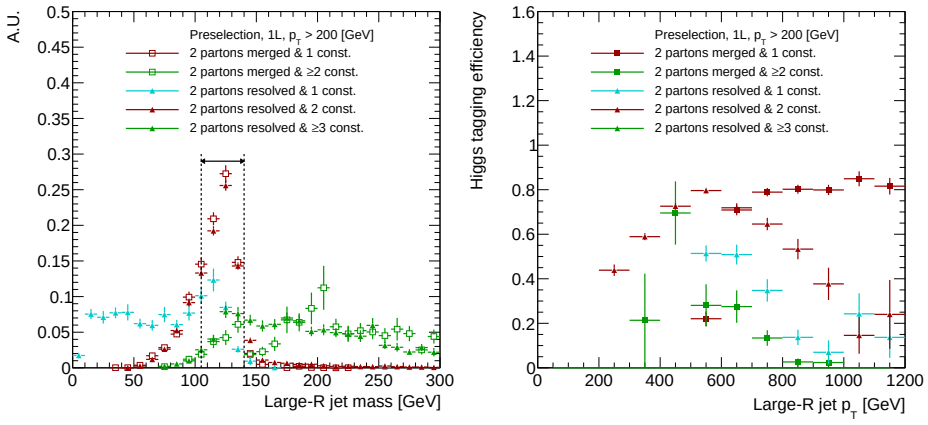

(a) (b)

Figure 6.10: (a) Large-R jet mass distribution for each class. Dashed lines show the mass requirement for the Higgs boson tagger. Red points show the cases where large-R jets have the equivalent number of subjets corresponding to the two bottom quarks. Green and blue points show the cases where the cases that the large-R jets contain additional subjets and the case that the they do not contain the two bottom quarks, respectively. (b) Higgs tagging efficiency for each class as a function of large-R jet p_{T} with the same color scheme as figure (b). The definition of each class is explained in Table 6.5.

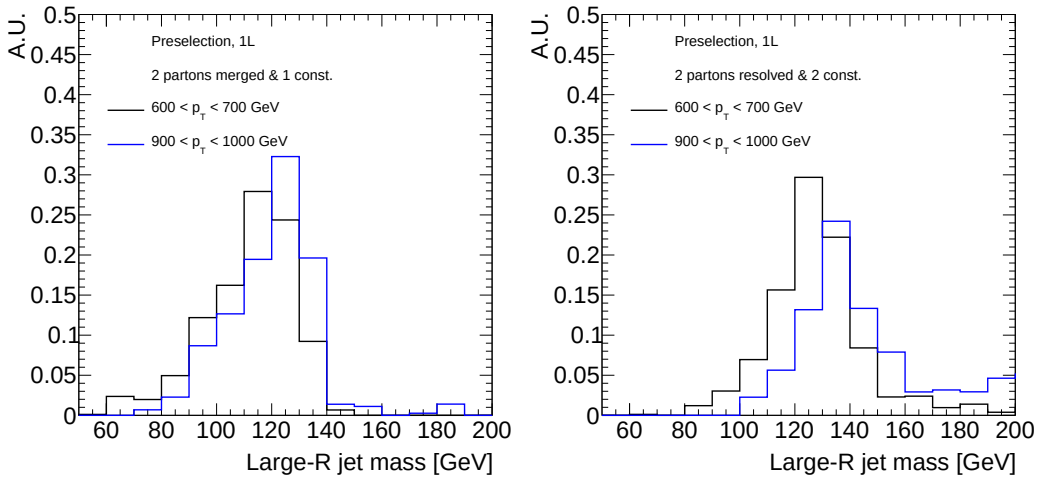

(a) (b)

Figure 6.11: Large-R jet mass distributions for the different p_{T} ranges of 600 < p_{T} < 700 GeV (black) and 900 < p_{T} < 1000 GeV (blue) for (b) the large-R jets containing two "Merged" particles and one constituent and (c) those containing two "Resolved" particles and two constituents.

In summary, the tagging efficiency is estimated to be around 50%. This is basically determined by the number of constituents and the mass distribution. For the constituents, large-R jets can have additional subjets originating from others than the Higgs boson decay. In addition, they can miss the jets from the Higgs boson decay products. These cause the inefficiency. For the mass distribution, large-R jets have higher mass tail for high p_{T} range due to the calibration or contamination of jets from other sources. This causes the inefficiency for the high p_{T} range.

Fake rate

The fake rate $\mathcal{F}$ is defined by:

$$\mathcal{F} = \frac{\text{Number of large-}R\text{ jets not matching with a Higgs boson and tagged}}{\text{Number of large-}R\text{ jets not matching with a Higgs boson}}. \tag{6.4}$$

It represents the probability that a large-R jet matching originating from other particles than Higgs bosons is identified as a Higgs boson. The large-R jets satisfying the criterion of the angular distance between the large-R jet axis and a Higgs boson, $\Delta R > 1.25$, are used for this calculation. Figure 6.12 (a) shows the fake rate as a function of large-R jet p_{T} for the dominant background of $t\bar{t}$+jets and VLT signals of SU(2) doublet with the two masses of 1.0 and 1.2 TeV. The fake rate is around 10% for $t\bar{t}$+jets background and around 15% for VLT signals for all the masses. The small differences of the fake rate between the background and the signals can be caused by the difference of the jet multiplicity, leading to more candidates of the combinatorial fakes in the signal events. Figure 6.12 (b) shows the fake origins in the $t\bar{t}$+jets background and VLT signal events with SU(2) doublet and the mass of 1.2 TeV, integrating over the p_{T} range. The dominant fake origin is found to be boosted hadronically decaying top quarks for both $t\bar{t}$ + jets background and the VLT signal events. The next dominant origins for $t\bar{t}$ + jets background are found to be boosted leptonically decaying top quarks and combination of other jets from $t\bar{t}$ decays such as the initial or final state radiation and parton showers. Those for the VLT signal are boosted Z boson and combination of jets from VLT decays.

Purity

The purity $\mathcal{P}$ is defined by:

$$\mathcal{P} = \frac{\text{Number of large-}R\text{ jets tagged and matching with a Higgs boson}}{\text{Number of large-}R\text{ jets tagged}}. \tag{6.5}$$

It represents the fraction of large-R jets originating from Higgs bosons out of large-R jets tagged as a Higgs boson. All the decay modes of the Higgs boson are considered in a computation of the purity. Figure 6.13 shows the purity of the Higgs boson tagger as a function of large-R jet p_{T} for SU(2)-doublet VLT signal events[1]. The purity is estimated to be around 70% for $p_{\mathrm{T}} > 600$ GeV in the signal events. The purity decreases for lower p_{T} range due to lower tagging efficiency.

[1] The purity is not estimated for $t\bar{t}$ + jets backgrounds since the backgrounds do not include the Higgs bosons.

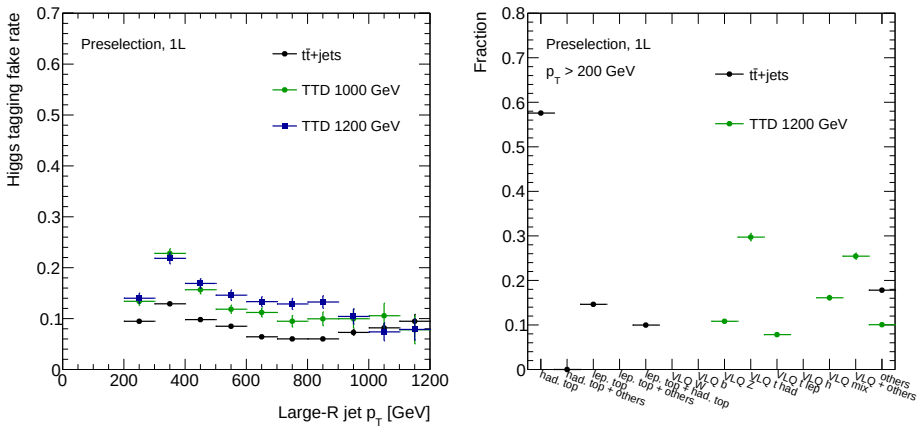

(a) (b)

Figure 6.12: (a) Fake rate as a function of large-R jet p_{T} for the dominant background of $t\bar{t}$ + jets (black) and the VLT signal of SU(2) doublet with the two masses of 1.0(blue) and 1.2(red) TeV. The definition of the fake rate is shown in Eq. (6.4). The large-R jets satisfying the criterion of the angular distance between the large-R jet axis and a Higgs boson $\Delta R > 1.25$ are used for this calculation. (b) Fake origins for $t\bar{t}$ + jets background (black) and the VLT signal of SU(2) doublet with the mass of 1.2 (green) TeV, integrating over the p_{T} range.

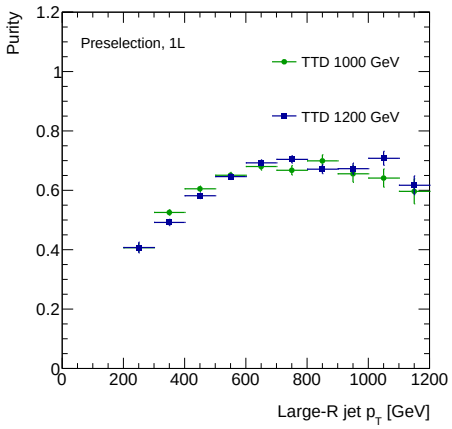

Figure 6.13: Purity of the Higgs boson tagger as a function of large-R jet p_{T} for the VLT signal of SU(2) doublet with the two masses of 1.0(green) and 1.2(blue) TeV.

6.3 Optimisation of the top quark tagger

This section shows the optimisation of requirements for the top quark tagger. It is performed in the same way as done for the Higgs boson tagger described in the previous section. After the optimisation is shown, the performances are described.

6.3.1 Determination of top tagging requirements

This section describes the optimisation of the requirements in order of Large-R jet p_{T}, its mass, and its constituents requirements.

p_{T} requirement A top quark decays to three quarks via hadronic W boson decay. In order to roughly estimate the width of the jets originating from top quarks, the maximum angular distance ΔR between the bottom quark and one of the quarks from W boson decay is displayed as a function of top quark p_{T} in Fig. 6.14 (a). It shows that the distance distributes broadly unlike that in $H \to b\bar{b}$ since the width depends on the kinematics of W boson. It is found that the width can be 1.0 at top quark $p_{\mathrm{T}} \sim 350$ GeV, where the decay products are reconstructed with a large-R jet. Eventually, the sensitivities are scanned for the various p_{T} thresholds around 350 GeV. Figure 6.14 (b) shows a comparison of the 95% upper limits on the production cross section with a few variations of p_{T} requirements of $p_{\mathrm{T}} > 300, 350, 400$ GeV. It indicates that the requirement of $p_{\mathrm{T}} > 300$ GeV has higher sensitivity to the signal for whole the mass range since it has higher signal acceptance. The requirement of $p_{\mathrm{T}} > 300$ GeV is chosen as the final configuration because our target on the VLT mass is around 900 GeV in case of SU(2)-singlet model.

Mass requirement In Section 6.2, the sensitivity is computed for each scan point in the two dimensional plane of the lower mass thresholds for the Higgs boson and top quark taggers. The result is shown in Fig. 6.3. It is found to have the best sensitivity at the threshold of $m > 140$ GeV for the top quark tagger in all the VLT signal models. Therefore the threshold of $m > 140$ GeV is chosen as the final configuration.

The number of constituents requirement As described in the previous section about the requirement on the constituents for Higgs tagging, allowance of one constituent inside a large-R jet can improve sensitivity to signal models whose events have highly boosted top quarks. Thus, the sensitivity is computed with the two configurations:

Option A At least two constituents for all large-R jet p_{T} range

Option B Exactly two constituents for large-R jet $p_{\mathrm{T}} < 800$ GeV and one or two constituents for the other p_{T} range

Comparison of the upper limits on the cross section between the two configurations is shown in Fig. 6.15. Figure 6.15 shows that sensitivity does not change significantly across the target signal mass range since the probability to have events with top $p_{\mathrm{T}} \geq 800$ GeV is very low even for our current targets. In addition, the uncertainty on the small-R jet mass was not available

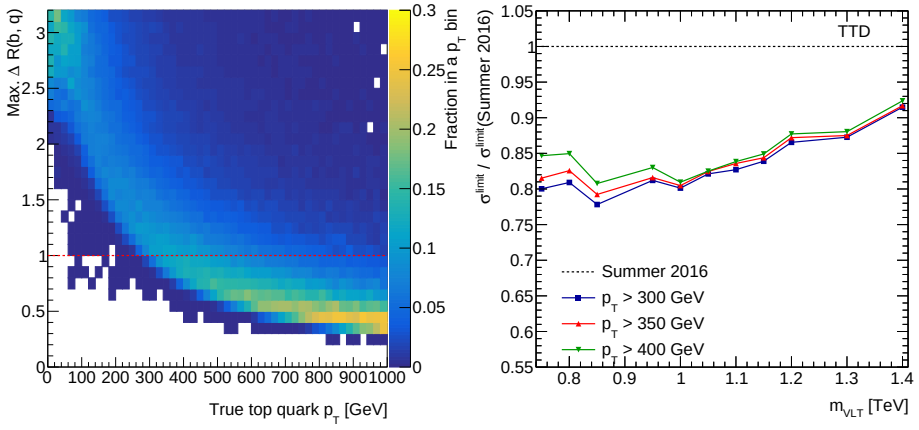

(a) (b)

Figure 6.14: (a) Maximum angular distance ΔR between the bottom quark and one of the quarks from W boson decay as a function of top quark p_{T} in the SU(2)-doublet VLT signal events with the mass of 1.2 TeV. The red line shows $\Delta R = 1$ where particles from a top quark decay can be reconstructed with a Large-R jet. (b) Ratio of the upper limits at 95% CL on the production cross section with the various p_{T} thresholds of $p_{\mathrm{T}} > 300$ (blue), 350 (red), 400 (green) GeV to that of the configuration in Summer 2016 in the same integrated luminosity of 30 fb^{-1}. The VLT signal events assuming SU(2) doublet are used.

Table 6.6: The set of requirements for the top quark tagger.

Variable	Requirement
p_{T}	$\geq$ 300 GeV
$\lvert\eta\rvert$	< 2.0
mass	$m >$ 140 GeV
Number of constituents	$\geq$2

for the whole mass range of $m > 140$ GeV. Therefore, the option A is chosen as the final configuration since, in the case, the mass is computed with the energies of the small-R jets[2].

The final requirements for the top quark tagger are determined. Table 6.6 shows the final set of the requirements for the top tagger.

6.3.2 Performance of the top tagger

This section shows the performance of the top quark tagger defined in the previous section. The same set of requirements are applied in the top quarks at a particle level as done for the Higgs tagging performance. The large-R jets satisfying the angular distance between the large-R jet axis and a top

[2] For the Higgs boson tagger, the small-R jet mass can be used. But the uncertainty on the mass for the small mass range can be derived from the Run1 measurement.

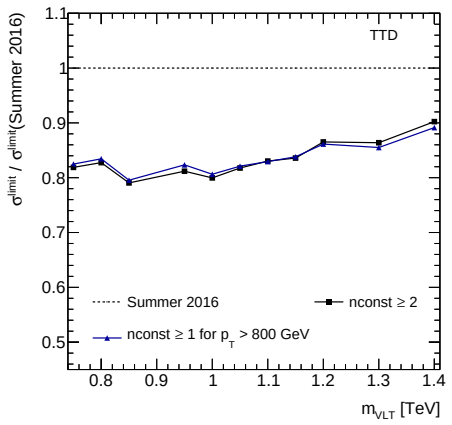

Figure 6.15: Ratio of the upper limits on the cross section at 95% CL computed with the two kinds of the requirement on the constituents comparing to that of Summer 2016 configuration in same integrated luminosity of 30 fb^{-1}.

quark ΔR(large-R jet, top) < 0.75 are considered as matching to the top quark. The target of the top quark tagger is to identify hadronically decaying top quarks. Therefore, the performances of the acceptance, efficiency, and fake rate are shown, separated to the hadronic decay mode and the others.

Acceptance

The acceptance, the probability to reconstruct a top quark as a large-R jet which is computed similarly as done in the Higgs bosons tagger (Eq. (6.1)), is shown in Fig. 6.16. The VLT signal events of SU(2) doublet with the mass of 1.2 TeV are used for the evaluation. The large-R jets with only $|\eta|$ cut (black graphs) have around 100% acceptance of hadronically decaying top quarks for $p_{\mathrm{T}} > 400$ GeV. They have around 80% acceptance of leptonically decaying top quarks for $p_{\mathrm{T}} > 400$ GeV. The inclusive acceptance of top quarks is around 90%. The top-tagged jets (red graphs) have around 80% acceptance at maximum and decrease for $p_{\mathrm{T}} > 700$ GeV. By comparing to the acceptance values between the large-R jets with only the p_{T} and the mass requirements (blue graphs) and with all the requirements (red graphs), the efficiency drop for higher p_{T} is found to be caused by the requirement on the number of constituents since a highly boosted top quark can be reconstructed as a small-R jet and a large-R jet with only one constituent. But this acceptance drop does not largely affect sensitivity to signals as described in Section 6.3.1. For the leptonically decaying top quarks, the acceptance is around 10%, and then the inclusive acceptance is at most 40%.

Tagging Efficiency

The tagging efficiency, the probability that the large-R jets matching with a top quark pass all the top tagging requirements, is computed similarly as done in the Higgs boson tagger (Eq. (6.2)) and is shown in Fig. 6.17. The VLT signal events of SU(2) doublet with various masses of 0.8, 1.0, and

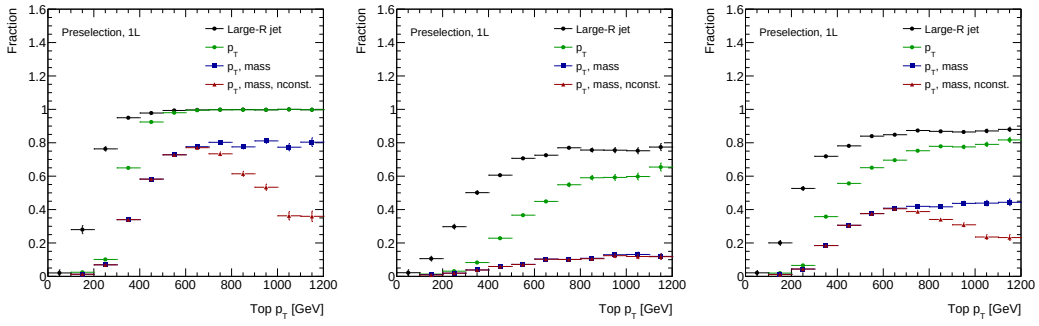

(a) (b) (c)

Figure 6.16: Acceptance of top quarks defined in Eq. (6.1) as a function of large-R jet p_{T} for VLT signals of SU(2) doublet with the mass of 1.2 TeV in (a) hadronic decay mode, (b) leptonic decay mode, and (c) all the decay modes. Black, green, blue, and red lines show the acceptance of large-R jets with only $|\eta|$ cut, passing p_{T} requirement, p_{T} and mass requirements, and all the criteria of the top quark tagger, respectively.

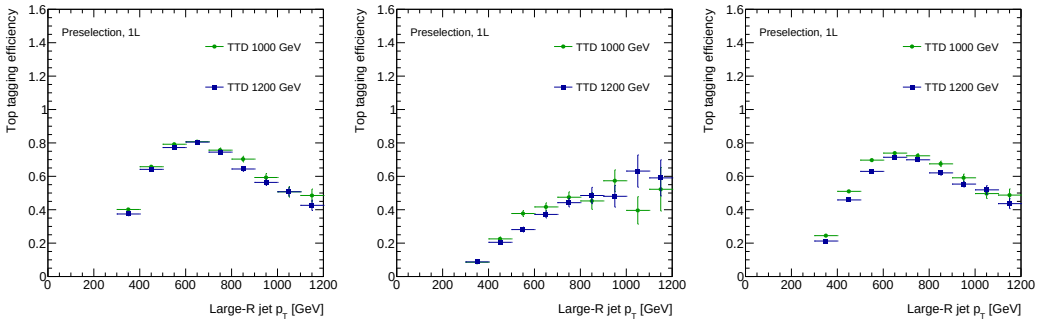

(a) (b) (c)

Figure 6.17: Tagging efficiency of the top quark tagger as a function of large-R jet p_{T} for VLT signals of SU(2) doublet with the various masses of 0.8 (green), 1.0 (blue), and 1.2 (red) TeV in (a) hadronic decay mode, (b) leptonic decay mode, and (c) all the decay modes. The efficiency is computed similarly in the Higgs boson tagger (Eq. (6.2)).

1.2 TeV are used. The efficiency for hadronically decaying top quarks is around 80% at maximum for $p_{\mathrm{T}} = 600$ GeV and decreases to $\sim$ 40% for high $p_{\mathrm{T}} > 700$ GeV due to the requirement on the constituent. Missing jets also causes the inefficiency, but the contribution does not significantly affect the efficiency. Since the top quark tagger does not have the upper requirements on the constituents and mass, the tagging efficiency does not decrease due to additional jets or higher mass contribution (see Appendix D). The efficiency for leptonically decaying top quarks is around 50%. In total, the inclusive efficiency is around 70% at maximum.

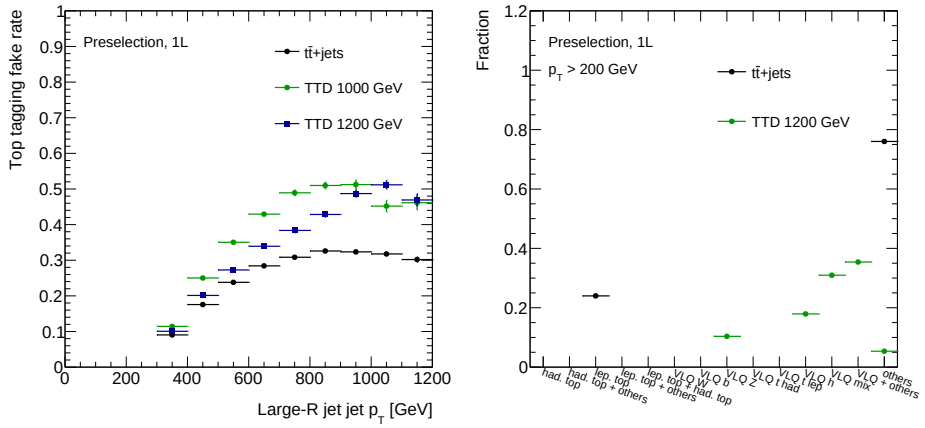

(a) (b)

Figure 6.18: (a) Fake rate as a function of large-R jet p_{T} for $t\bar{t}$ + jets background (black) and VLT signals of SU(2) doublet with the two masses of 1.0 (blue) and 1.2 (red) TeV. The fake rate represents the probability that a large-R jet originated from other particles than top quarks is identified as a top quark and computed in the same way as done for the Higgs boson tagger defined in Eq. (6.4). (b) fake origins of the top quark tagger for $t\bar{t}$ + jets background (black) and the VLT signal of SU(2) doublet with the mass of 1.2 (green) TeV.

Fake rate

The fake rate represents the probability that a large-R jet originating from other particles than top quarks is identified as a top quark and computed in the same way as done for the Higgs boson tagger defined in Eq. (6.4). Figure 6.18 (a) shows the fake rate as a function of large-R jet p_{T} for VLT signals of SU(2) doublet with the two masses of 1.0 and 1.2 TeV and the dominant background of $t\bar{t}$+jets including all the subprocesses of $t\bar{t}$+≥1b, $t\bar{t}$+≥1c, and $t\bar{t}$+lights. The fake rate for $t\bar{t}$ + jets background is estimated as around 30% for $p_{\mathrm{T}} > 600$ GeV, while that for VLT signals is estimated around 40% for the same p_{T} range. The signal events have higher jet multiplicity and more combinatorial fake sources, leading to the higher fake rate in the signal events. Figure 6.18 (b) shows the fake origin in $t\bar{t}$ + jets background and VLT signal of SU(2) doublet with the mass of 1.2 TeV, integrating over the full p_{T} range. The dominant fake origin is found to be other jets than top decays such as the initial and final state radiations and parton showers for $t\bar{t}$ + jets background. If several additional jets are distributed within the radius of $R = 1.0$, they can be identified as a top quark since top quark tagger does not require the upper limits on the mass and the number of constituents[3]. For the signal events, it is a mixture of jets from VLT decay products and others than VLT decays such as the QCD radiations. The next dominant components are leptonically decaying top quarks for $t\bar{t}$ + jets background and boosted vector bosons for VLT signals.

[3] For the top quark tagger, the upper thresholds of mass and constituents are not set in order to develop a high acceptance tagger with a minimum set of requirements.

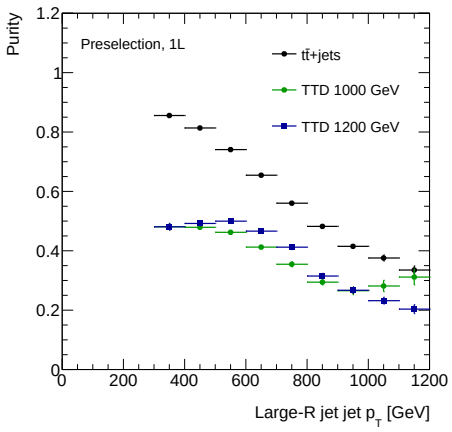

Figure 6.19: Purity of the top quark tagger as a function of large-R jet p_{T} for $t\bar{t}$ + jets background (black) and the VLT signal of SU(2) doublet with the two masses of 1.0 (green) and 1.2 (blue) TeV.

Purity

The purity represents the fraction of large-R jets originating from top quarks out of large-R jets tagged as a top quark and is computed in the same way as done for the Higgs boson tagger defined in Eq. (6.5). Hadronically decaying top quarks are considered in a computation of the purity. Figure 6.19 shows the purity of the top quark tagger as a function of large-R jet p_{T} for the $t\bar{t}$ + jets background and SU(2)-doublet VLT signal events. The purity is estimated to be $< 85\%$ ($< 50\%$) for the $t\bar{t}$ + jets background (the signal events). The purity decreases for higher p_{T} in both background and signal events. This is caused by two reasons. The one reason is the inefficiency for high p_{T} due to the requirement on constituents as shown in Fig. 6.17. The other reason is an increase of the fake rate for higher p_{T} due to no upper threshold on the mass as shown in Fig. 6.18.

6.4 Summary for determination of the taggers

The Higgs boson and top quark taggers are promising to improve the sensitivity to the VLT search owing to the distinctive feature of the boosted Higgs boson in the VLT signals. The requirements of the taggers are optimised by changing each requirement individually from the tentative requirements. The requirements are determined to have the best improvement of the final upper limits on the production cross section of VLT signals compared to that with the *old configuration*. The acceptance and tagging efficiency are evaluated in the VLT signal events of SU(2) doublet with various masses. The efficiencies of the Higgs boson and top quark taggers are around 55% and <80%, respectively. These values are determined by the large-R jet mass distribution and the fraction of the constituents. The fake rates are evaluated in both VLT signal and $t\bar{t}$ + jets background. The values of the Higgs boson and top quark taggers are around 10% and 30% respectively in $t\bar{t}$ + jets background events. The dominant fake origins for the Higgs boson and top quark taggers are hadronically decaying top quarks and the combinatorial fakes of other jets than top decays such as the initial and final state

Table 6.7: Summary of the definition and performances of the Higgs boson and top quark taggers.

	Higgs boson tagger	top quark tagger
p_{T}	> 200 GeV	> 300 GeV
$\lvert\eta\rvert$	< 2.0	< 2.0
mass	$105 < m < 140$ GeV	> 140 GeV
The number of constituents	$= 2 (p_{\mathrm{T}} < 500$ GeV) $\leq 2 (p_{\mathrm{T}} \geq 500$ GeV)	≥ 2
The number of b-jets	—	—
Tagging efficiency	$\sim 55\%$	$< 80\%$
Fake rate	$\sim 10\%$	$\sim 30\%$

radiations and parton showers. The summary of definitions and performances of the Higgs boson and top quark taggers are shown in Table 6.7.

6.5 Optimisation of event categorisation

In this analysis, the events after the preselection are divided into several groups by the event characteristics in order to enhance the discrimination of the signals from the backgrounds. After the categorisation, a likelihood fit of the MC prediction to the data is performed to further improve the background prediction. These detailed strategy is described in Chapter 7. In this section, the determination of the event categorisation is described.

The events passing the preselection are categorised based on the multiplicity of jets, b-jets, Higgs-tagged jets and top-tagged jets as described in Chapter 7. Regarding the categorisation based on the jet and b-jet multiplicity, this analysis follows the same categorisation strategy as that in the previous analysis [49]. First, events are divided into two groups by the number of jets per event, i.e., at least 6 jets or exactly 5 jets. They are named *search regions* (SR) and *validation regions* (VR), respectively. The search regions are sensitive to the signals and used in the fit, while the validation regions are not used in the fit but used for the validation of the fit by propagating the fit results in the search regions into them. Secondly, each of these categories are further divided into two groups by the number of b-jets per event, i.e., at least 4 b-jets or exactly 3 b-jets. Finally, each of these categories is further divided into several groups by the number of Higgs-tagged and top-tagged jets. This section shows the optimisation of the event categorisation of search regions and validation regions based on the number of Higgs-tagged jets and top-tagged jets in an event. In the last section, the final configuration of event categorisation is summarised.

6.5.1 Search regions

The search regions are used for the fit and most sensitive to signals. Thus, the event categorisation in search regions is optimised based on the sensitivity to signals as done in the optimisation of the Higgs

boson and top quark taggers. For the calculation of the ratio of cross section limits, the ratio shown in this section is computed after applying the Tag-rate-function method (TRF) for $t\bar{t}$ samples. The TRF is described in Section 5.4. The method allows to reduce the statistical uncertainty especially for the high m_{eff} bins while keeping the consistency of the background prediction. In association with the reduction of the statistical uncertainty, the m_{eff} binning is changed finer. The finer binning improves the signal sensitivity since it helps to distinguish the m_{eff} shape of the signals from the backgrounds. These two changes further improve the sensitivity to the signals, and then cause the difference between the figures shown in this section and Sections 6.2 and 6.3.

The signal events of VLT pair production have four boosted heavy particles of either, bottom quark, top quark, W, Z, or Higgs bosons. Those of the four-top-quark production have four top quarks. In 1-lepton channel, one of them is considered to decay leptonically and the others decay hadronically. At most three candidates to be identified with the Higgs boson or top quark taggers exist in the signal events. When events are divided by the number of Higgs-tagged and top-tagged jets of 0, 1, or $\geq$2 for each, then there are 9 categories in total, and the event yields for each category in the search regions with $\geq$4 b-jets are shown in Fig. 6.20. To simplify the naming convention, the Higgs-tagged and top-tagged jets are referred to as H and T, respectively. For instance, the category name of "1T, 0H" means the category including events with exactly one top-tagged jet and no Higgs-tagged jet per event. Figure 6.20 shows that most of the signal events are distributed in the categories with at least two Higgs-tagged or top-tagged jets, while most of the background events distribute in those with at most one Higgs-tagged or top-tagged jets as expected. At the same time, the categories with at least three Higgs-tagged or top-tagged jets are found to have not enough statistics even for the signal events. For instance, "$\geq$2T, $\geq$2H" category is expected to have less than one event even in the signal with an integrated luminosity of 36.1 fb^{-1}, and then it does not help to improve the sensitivity. In order to make the best of all the signal events, we shall think that the categories with small statistics are merged into the other categories. In the following, the method to merge the categories with at least three Higgs- or top-tagged jets ($N_{\text{higgs-tagged jets}} + N_{\text{top-tagged jets}} \geq 3$), which is named *the small stat. category group* here, is optimised.

In the same way as done in the optimisation of the taggers, the sensitivity is computed with the various merging methods. The best configuration is chosen from the candidates to be merged with the small stat. category group are following:

Option A "$\geq$1T, $\geq$1H"

This method merges three categories of "$\geq$2T, 1H", "1T, $\geq$2H", and "$\geq$2T, $\geq$2H" into "1T, 1H" category. Then, the merged "$\geq$1T, $\geq$1H" and "0T, $\geq$2H" categories are expected to be most sensitive to VLT signals, while "$\geq$2T, 0H" category is expected to be most sensitive to the signals of four-top-quark productions. It is the tentative categorisation shown in Table 6.2.

Option B: "$\geq$0T, $\geq$2H and $\geq$2T, 0-1H"

In this method, "$\geq$2T, 1H" category is combined into "$\geq$2T, 0H" named "$\geq$2T, 0-1H", and also "1T, $\geq$2H" and "$\geq$2T, $\geq$2H" categories are merged into "0T, $\geq$2H" category named "$\geq$0T, $\geq$2H". The method should have the same sensitivity as the case that "$\geq$2T, $\geq$2H" category is combined into "$\geq$2T, 0H" category since the category is expected to have only the 0.01 events even for signals and does not contribute to the sensitivity. Then, the merged "1T, 1H" and "$\geq$0T, $\geq$2H" categories are expected to be most sensitive to VLT signals, while "$\geq$2T, 0-1H"

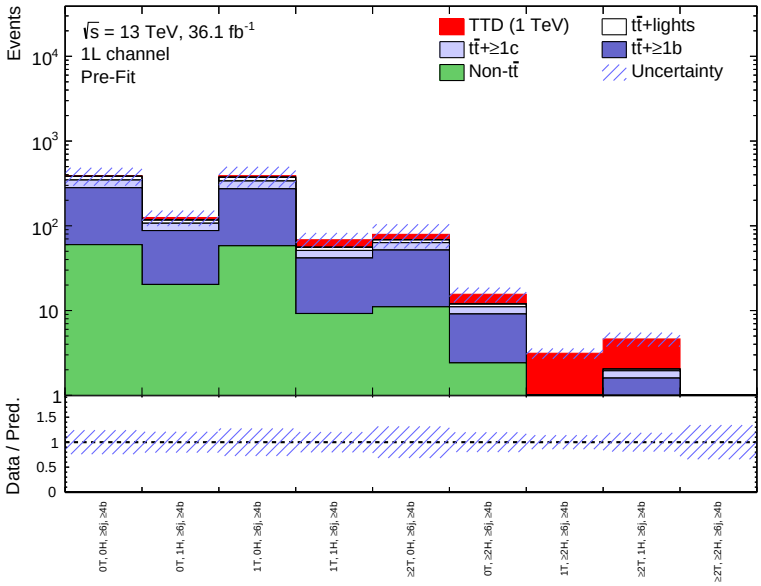

Figure 6.20: Expected event yields for each category in the search regions with ≥4 *b*-jets before the fit assuming an integrated luminosity of 36.1 fb^{-1}. The Higgs-tagged and top-tagged jets are referred to as H and T in the labels along x axis, respectively. Red, white, light blue, dark blue and green colors stand for the VLT signal of SU(2) doublet with the mass of 1 TeV, $t\bar{t}$+lights, $t\bar{t}$+≥1c, $t\bar{t}$+≥1b, and the other backgrounds, respectively. The shade shows the total uncertainty including the statistical and systematic uncertainties.

category is expected to be the most sensitive to the signals of four-top-quark productions. The categorisation is shown in Table 6.8.

Option C: "1T, ≥1H and ≥2T, ≥0H"

This method combines "1T, ≥2H" into "1T, 1H" named "1T, ≥1H". In addition, it merges "≥2T, 1H" and "≥2T, ≥2H" into "≥2T, 0H" named "≥2T, ≥0H". Similarly, the merged "1T, ≥1H" and "0T, ≥2H" categories are expected to be most sensitive to VLT signals, while "≥2T, ≥0H" category is expected to be most sensitive to the signals of four-top-quark productions. The effect of "1T, ≥2H" can be checked to compare the sensitivity between this method and "≥0T, ≥2H and ≥2T, 0-1H". The categorisation is shown in Table 6.9.

Option D: "≥3TH"

This method combines the three categories with at least 3 Higgs-tagged or top-tagged jets into one category named "≥3TH". The merged category is expected to help the sensitivity to all the signal scenarios. Comparison of the sensitivity between this method and the others gives the information of the effect for the three categories. The categorisation is shown in Table 6.10.

Option E: "≥1T, ≥2H"

This method merges "≥2T, ≥2H" category into "1T, ≥2H" category, named "≥1T, ≥2H". It is the same as "≥3TH" except not combining "1T, ≥2H" category into others. As seen in Fig. 6.20, The "1T, ≥2H" and "≥2T, ≥2H" categories are not expected to contain the backgrounds, and then the combination can have better or similar sensitivity compared to "≥3TH" categorisation.

Table 6.8: Option B (“≥0T, ≥2H and ≥2T, 0-1H”)

N_{Higgs} \ N_{top}	0	1	≥2
0	“0T, 0H"	“1T, 0H"	“≥2T, 0-1H"
1	“0T, 1H"	“1T, 1H"	
≥2	“≥0T, ≥2H"		

Table 6.9: Option C (“1T, ≥1H and ≥2T, ≥0H”)

N_{Higgs} \ N_{top}	0	1	≥2
0	“0T, 0H"	“1T, 0H"	“≥2T, ≥0H"
1	“0T, 1H"	“1T, ≥1H"	
≥2	“0T, ≥2H"		

Table 6.10: Option D (“≥3TH”)

N_{Higgs} \ N_{top}	0	1	≥2
0	“0T, 0H"	“1T, 0H"	“≥2T, 0H"
1	“0T, 1H"	“1T, 1H"	
≥2	“0T, ≥2H"	“3TH”	

Table 6.11: Option E (“≥1T, ≥2H”)

N_{Higgs} \ N_{top}	0	1	≥2
0	“0T, 0H"	“1T, 0H"	“≥2T, 0H"
1	“0T, 1H"	“1T, 1H"	“≥2T, 1H"
≥2	“0T, ≥2H"	“≥1T, ≥2H”	

Comparison between this method and “≥3TH” gives the effect on the sensitivity of “1T, ≥2H”. The categorisation is shown in Table 6.11.

Figure 6.21 shows the ratio of the upper limits on the production cross section at 95% CL with the various configurations listed above to that of the *old configuration*. The targets of this analysis are $m_{\text{VLT}} > 1.1$ TeV for VLT signals of SU(2) doublet and $m_{\text{KK}} > 1.5$ TeV for 2UED-RPP scenario. For all the signals, the option A (“≥1T, ≥1H”) is found to have the worst sensitivity. Comparing the sensitivities between option B (“≥0T, ≥2H and ≥2T, 0-1H”) and option C (“1T, ≥1H and ≥2T, ≥0H”), combining “1T, ≥2H” category into “0T, ≥2H” is found to help for improvement of the sensitivity to the VLT signals. This is because the “0T, ≥2H” category is expected to have less backgrounds than “1T, 1H” category. For SU(2)-doublet VLT signals, the three methods of option B (“≥0T, ≥2H and ≥2T, 0-1H”), option D (“≥3TH”), and option E (“≥1T, ≥2H”) have the better sensitivity. The option D (“≥3TH”) and option E (“≥1T, ≥2H”) have the best sensitivity for VLT signals with lower mass than 1.1 TeV where the signal processes have higher cross section, while the backgrounds are not expected to contribute to such a very high Higgs-tagged and top-tagged jet multiplicity. For the higher mass, these sensitivities are similar. On the other hand, for 2UED-RPP signal, option B (“≥0T, ≥2H and ≥2T, 0-1H”) has the best sensitivity because the signal events contains more top-tagged jets and less Higgs-tagged jets, and contribute to “≥2T, 0H” or “≥2T, 1H” categories most. This feature is the reason why the 2UED-RPP signal scenario has the best sensitivity with option B (“≥0T, ≥2H and ≥2T, 0-1H”). For the final configuration, the one option which has better sensitivities for both VLT and 2UED-RPP signals is compromised to be chosen. Consequently, the option B (“≥0T, ≥2H

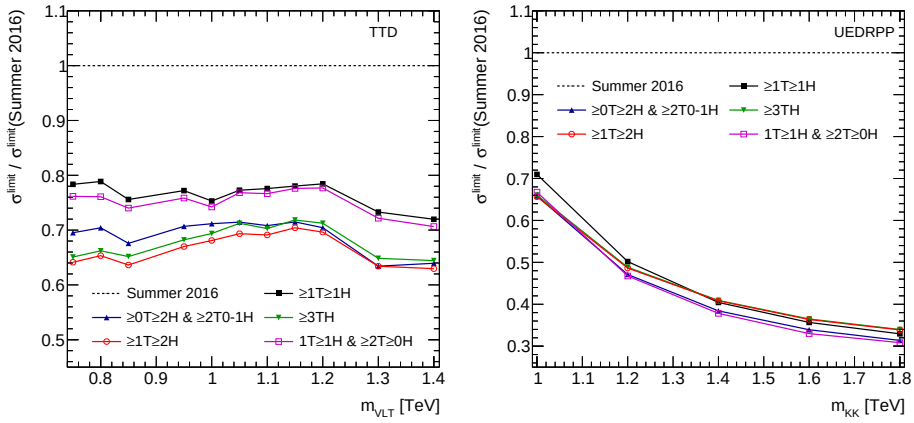

(a) (b)

Figure 6.21: Ratio of the upper limits on the cross section at 95% CL with various categorisations to that of the *old configuration* ("Summer 2016", black broken line) in same integrated luminosity. (a) and (b) show the ratio for SU(2)-doublet VLT and 2UED-RPP signals, respectively. Both figures show the ratio after applying TRF for $t\bar{t}$ samples and changing the m_{eff} binning finner. Black, blue, green, red, and purple graphs show the sensitivity with the option A ("≥1T≥1H"), option B ("≥0T≥2H and ≥2T0−1H"), option C ("1T≥1H and ≥2T≥0H"), option D ("≥3TH"), and option E ("≥1T≥2H"), respectively.

and ≥2T, 0-1H") is chosen as the final configuration.

6.5.2 Validation regions

Categories with 5 jets are used for the validation regions (VR), which are used to validate the fit results. The validation regions are necessary to satisfy the following requirements for the validation:

- Possibility to compare the kinematic variables in the similar event topology between the search and validation regions
- Having enough statistics in a category

In order to satisfy the first requirement, the categorisation in the validation regions employs the same categorisation based on the Higgs-tagged and top-tagged jet multiplicities as the search regions. Figure 6.22 shows the expected event yields for each category with 5 jets before the fit. In the categories with 3 b-jets, it is found that there are enough statistics to validate the fit results. Thus, the validation regions with 3 b-jets use the same categorisation as that in the search regions, and then there are 6 categories. In the categories with ≥4 b-jets, the three categories with at least two Higgs-tagged or top-tagged jets are expected to have only a few events, which are not enough to validate fit results. On the other hand, the categories with at most one Higgs-tagged or top-tagged jet have enough statistics to compare the kinematic distribution shape and validate the fit results.

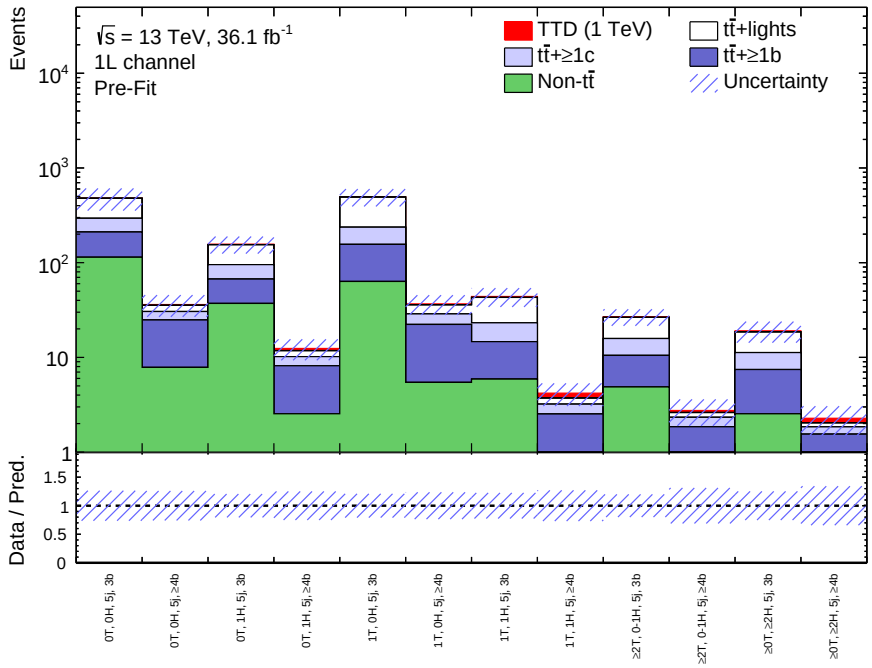

Figure 6.22: Event yields in a category of the validation regions expected with an integrated luminosity of 36.1 fb^{-1} before the fit. The Higgs-tagged and top-tagged jets are referred to as H and T in the labels along x axis, respectively. Red, white, light blue, dark blue and green colors stand for the VLT signal of SU(2) doublet with the mass of 1 TeV, $t\bar{t}$+lights, $t\bar{t}$+≥1c, $t\bar{t}$+≥1b, and the other backgrounds, respectively. The shade shows the total uncertainty including the statistical and systematic uncertainties.

To make the best of the categories with 5 jets, ≥4 b-jets, the categories at least 2 Higgs-tagged or top-tagged jets are merged into one category named "≥2TH, 5j, ≥4b". This satisfies the second requirement listed above. When merging the categories, the consistencies of the background compositions and kinematic distributions with the corresponding search regions are confirmed. Figure 6.23 shows the background compositions in the SR and VR categories with ≥4 b-jets. All the categories in both the search and validation regions contain $t\bar{t}$+≥1b background by around 50% or 60%, other backgrounds by around 15% each. Especially, the validation regions of "≥2T, 0H", "1T, 1H", and "0T, ≥2H" have similar background compositions as the corresponding SR categories. Consequently, the merged "≥2TH" category should have the same background compositions as "≥2T, 0H", "1T, 1H", and "0T, ≥2H" categories in the search regions. In addition, the background compositions in the other VR categories are assured to be similar to the corresponding SR categories.

Figure 6.24 shows comparisons of the lepton p_{T} distribution shape between the "≥2TH" validation region and the three corresponding search regions. All the distributions are normalised to unity. The mean and RMS values are shown in the legend. It is found that the lepton p_{T} distribution in "≥2TH" category is consistent with those in the corresponding SR categories within 10%. Comparisons of other kinematic variables are shown in Appendix H. In general, the variables of electron or muon p_{T}, $E_{\mathrm{T}}^{\mathrm{miss}}$, and $m_{\mathrm{T}}^{\mathrm{W}}$ which are not related to the jet multiplicity are consistent within 10% between the

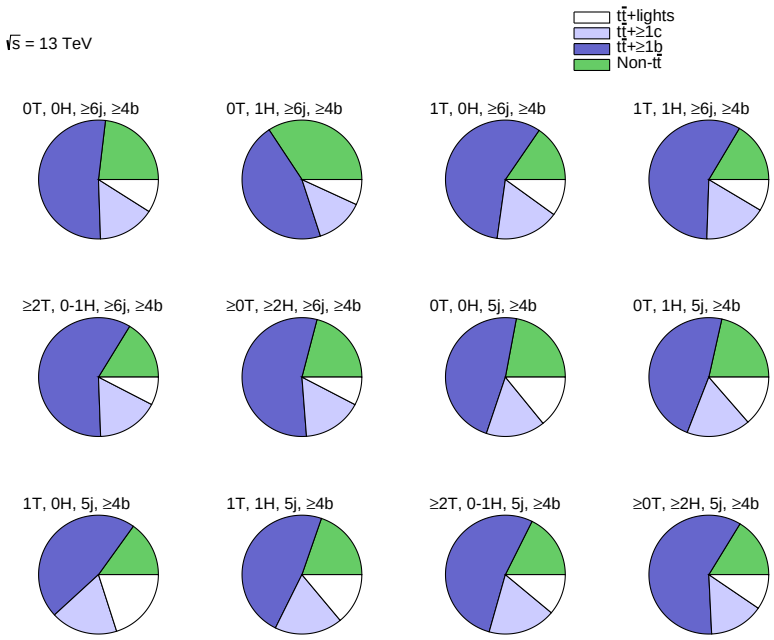

Figure 6.23: Fraction of background compositions with an integrated luminosity of 36.1 fb^{-1} in each category. Only the categories with at least 4 b-jets in both the search and validation regions are shown. The first six categories correspond to the search regions, and the others correspond to the validation regions. The Higgs-tagged and top-tagged jets are referred to as H and T, respectively. White, light blue, dark blue and green colors stand for the $t\bar{t}$+lights, $t\bar{t}$+≥1c, $t\bar{t}$+≥1b, and the other backgrounds, respectively.

search and validation regions. The mean and RMS values of leading jet p_{T} in the merged "≥2TH" category agree with those in the corresponding search regions by around 10%. The results assure that the merged "≥2TH" category has similar event topology to the corresponding SR categories. Therefore, the "≥2TH" category is used as the final configuration[4].

6.5.3 Summary for determination of the event categorisation

In this section, the event categorisation determined in the Section 6.5.1 and 6.5.2 is summarised. The event categorisation further improves the sensitivity to the signal models. The categorisation is based on the four variables: jet, b-jet, Higgs-tagged, and top-tagged jet multiplicities. The categorisation strategy based on jet and b-jet multiplicities follows that in Run1 [175] and the previous analysis in Run2 [49]. The strategy based on Higgs-tagged and top-tagged jet multiplicities is developed in this dissertation. The categorisation of search regions is determined to have the best sensitivity to the signal models considered, while that of validation regions is determined to properly validate the fit results. Table 6.12 shows the final configuration of the event categorisation. The search regions

[4] It is not necessary to check the sensitivity in this case because the validation regions are not used for searching for excesses of data but for the validation of the background estimation

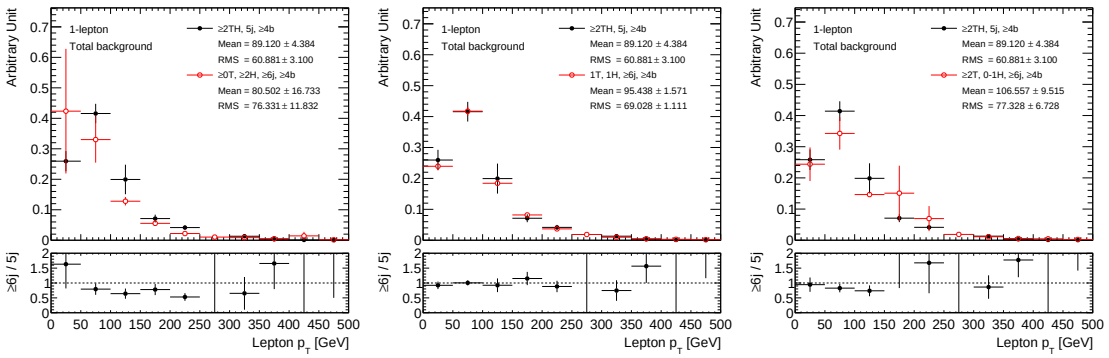

(a) (b) (c)

Figure 6.24: Lepton p_{T} distribution in "≥2TH, 5j, ≥4b" (black) compared to the category (red) of (a) "≥0T, ≥2H, ≥6j, ≥4b", (b) "1T, 1H, ≥6j, ≥4b", and (c) "≥2T, 0H, ≥6j, ≥4b". All the distributions are normalised to unity. The mean and RMS values are shown in the legend. The bottom panel shows the ratio between the 5 jets and ≥ 6 jets categories.

Table 6.12: Event categorisation used for the analysis. The search regions with ≥6 jets and 3/≥4 b-jets and validation regions with 5 jets and 3 b-jets have 6 categories each following the solid and dashed lines. Only the validation regions with 5 jets and ≥4 b-jets have 4 categories following solid lines and including the category merged from the 3 categories divided by dashed lines. In total, there are 12 and 10 categories in SR and VR, respectively.

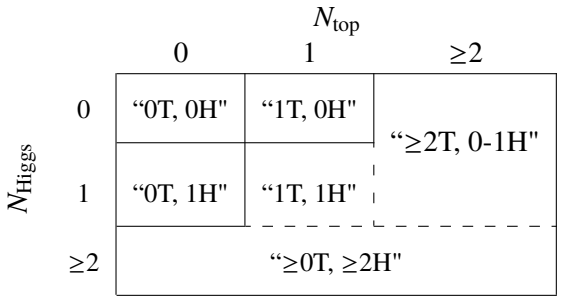

with ≥6 jets and 3/≥4 b-jets and validation regions with 5 jets and 3 b-jets have 6 categories each following the solid and dashed lines. Only the validation regions with 5 jets and ≥4 b-jets have 4 categories following solid lines and including the category merged from the 3 categories divided by dashed lines. In total 12 and 10 categories in SR and VR, respectively, are used in the analysis.

The sensitivity to VLT signals is compared between the *old configuration* and the final configuration after optimising the taggers and event categorisation. Figure 6.25 shows a comparison of significances between two configurations for SU(2)-singlet and SU(2)-doublet VLT signals. For the final configuration, the significances with the final configuration improve by around 30%, and therefore the evidence reaches on the VLT mass at 3σ significance are found to improve by around 80 GeV from the *old configuration*. Figure 6.26 shows a comparison of the expected upper limits on the

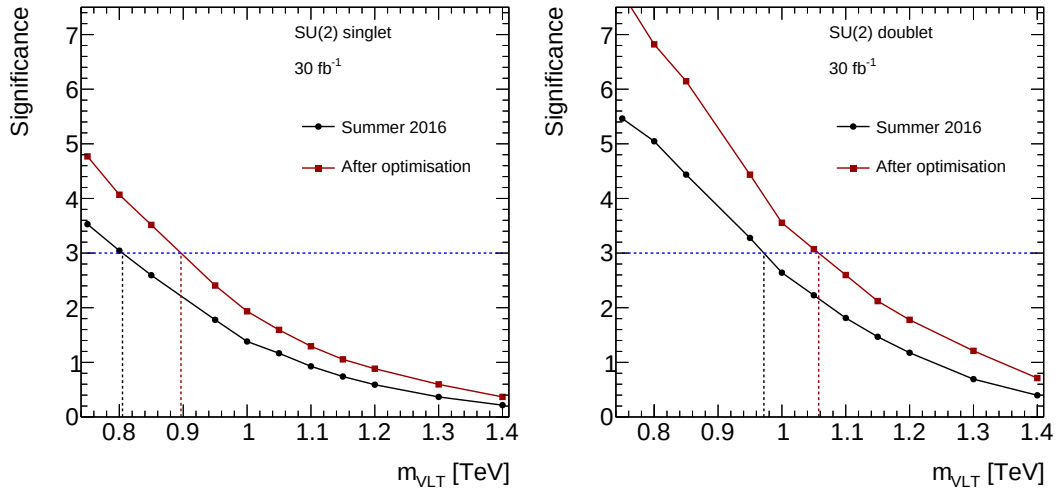

(a) (b)

Figure 6.25: Comparison of the significances between the *old configuration* (black, "Summer 2016") and the final configuration (red) after the optimisation for (a) SU(2)-singlet and (b) SU(2)-doublet VLT signals. The significances are computed assuming the integrated luminosity of 30 fb^{-1}. The evidence reaches, which are the VLT mass at 3σ significance (blue broken line), are shown in vertical broken lines for each configuration.

cross section between two configurations for SU(2)-singlet and SU(2)-doublet VLT signals. For the final configuration, the expected limits with the final configuration similarly improve by around 30%, and therefore the lower mass limits extend by around 70 GeV. These results indicate that introducing the Higgs boson and top quark taggers and optimising the event categorisation significantly improve sensitivities.

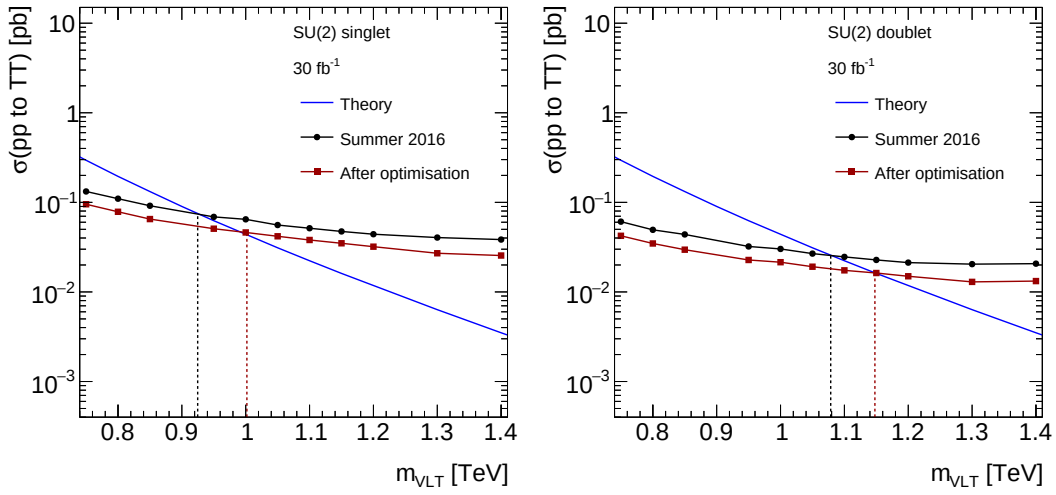

(a) (b)

Figure 6.26: Comparison of the expected upper limits on the cross section between the *old configuration* (black, "Summer 2016") and the final configuration (red) after the optimisation for (a) SU(2)-singlet and (b) SU(2)-doublet VLT signals. The cross section limits are interpreted into the lower mass limits by comparing the limits and the theory. The mass limits are shown in vertical broken lines.

7 Analysis strategy

This analysis is performed by the following three steps. The first step is to apply minimum requirements (preselection) to events in order to reduce unnecessary events for this analysis while keeping enough statistics for both background estimation and the search for signal. The second step is event classification by jets, b-jets, Higgs-tagged jets and top-tagged jets multiplicity to separate signals from backgrounds and improve signal sensitivity. Finally, in the third step MC prediction is fitted to data in m_{eff} distribution with their uncertainties taken into account. Here, m_{eff} is defined by the scalar sum of p_{T} of jets, lepton and $E_{\mathrm{T}}^{\mathrm{miss}}$:

$$m_{\mathrm{eff}} = \sum_{\mathrm{jet}} p_{\mathrm{T}}^{\mathrm{jet}} + p_{\mathrm{T}}^{\mathrm{lep}} + E_{\mathrm{T}}^{\mathrm{miss}}. \tag{7.1}$$

In the m_{eff} distribution after the fit ("postfit"), the search is performed to look for significant excess of data that is statistically inconsistent with the postfit MC prediction and their uncertainties. In this section, the detail of the analysis strategy is described.

7.1 Preselection

Data firing single-lepton trigger with different p_{T} thresholds are used in this analysis to maximise data acquisition efficiency.

Events after the trigger selection described in section 4.1 are required to have at least one reconstructed vertex with at least five associated tracks having $p_{\mathrm{T}} > 400$ MeV located in the beam spot in the transverse plane. This requirement assures that events originated from pp collisions.

Events are required to have exact one electron or muon satisfying the criteria described in Section 3.3. The lepton is required to match with the one firing the lepton tigger within $\Delta R < 0.15$. They are also required to have at least 5 jets and 2 b-jets. In addition to the requirements on jets and b-jets multiplicity, events are required to have $E_{\mathrm{T}}^{\mathrm{miss}} > 20$ GeV and $E_{\mathrm{T}}^{\mathrm{miss}} + m_{\mathrm{T}}^{\mathrm{W}} > 60$ GeV in order to suppress the multijet backgrounds. All the selections for the preselection are summarised in tab. 7.1.

Figure 7.1 shows the jet and b-jet multiplicities compared between the data and MC prediction after preselection. The bottom panel shows the ratio between the data and MC prediction. The errors stands for only statistical uncertainty. The systematic uncertainty is estimated around 25% at preselection level. The MC prediction agrees with the data within around 20%. The figures show that $t\bar{t}$+jets background is dominant for all the jet multiplicities, while the other backgrounds such as single top, V+jets and diboson have only small contribution of around 20% in total for lower b-jet multiplicity. The subprocess of $t\bar{t}$+lights is dominant in two b-jets and $t\bar{t}$+$\geq$1b is dominant for at least four b-jets.

Table 7.1: Preselection in 1-lepton channel.

	Requirement
Trigger	Single-lepton trigger
Lepton	1 isolated e or μ
N_{jets}	≥ 5
N_{bjets}	≥ 2
$E_{\text{T}}^{\text{miss}}$	$E_{\text{T}}^{\text{miss}} > 20$ GeV
$E_{\text{T}}^{\text{miss}} + m_{\text{T}}^{\text{W}}$	$E_{\text{T}}^{\text{miss}} + m_{\text{T}}^{\text{W}} > 60$ GeV

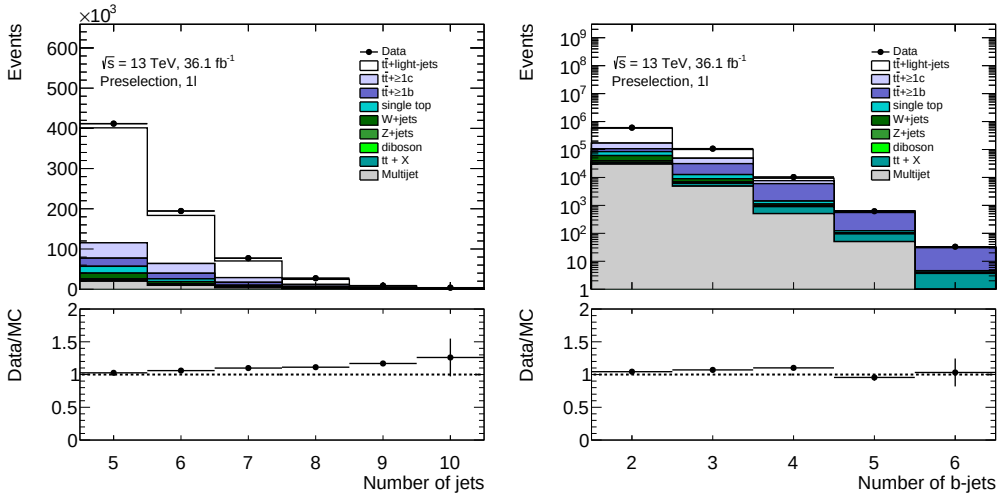

(a) (b)

Figure 7.1: Number of (a) jets and (b) b-jets in an event, compared between data and MC prediction at preselection in 1-lepton channel before fitting. The data and the MC prediction are shown in black marker and coloured fill, respectively. V+jets include all the subprocesses and $t\bar{t}$+X background includes all the processes of SM $t\bar{t}t\bar{t}$, $t\bar{t}$+V, and $t\bar{t}$+H. The bottom panel shows the ratio between the data and MC prediction. The error bar shows only the statistical uncertainty. The last bin includes the overflowing components.

All the subprocess of $t\bar{t}$+≥1b , $t\bar{t}$+≥1c , and $t\bar{t}$+lights have comparable contributions in the three b-jets categories due to the physics process with only one additional b-jet, inefficiency of b-tagging, mis-tagging of the strange and charm quarks as b-jets. For high b-jet multiplicity, $t\bar{t}$+X ($X = V, H, t\bar{t}$) have small contribution.

Figure 7.2 shows various kinematic variables compared between the data and MC prediction after preselection. As shown in the Fig. 7.1, the error bars include only the statistical uncertainty while the systematic uncertainty is estimated around 25%. Figure 7.2 (a) shows the lepton p_{T} distribution. The p_{T} threshold of 30 GeV for the lepton results in the lower yield in the first bin compared to the second bin. The MC prediction agrees with the data within 20%. For the region of $p_{\text{T}} > 400$ GeV,

the overestimation of the multijet background causes higher prediction than the data. Considering the systematic uncertainty of the multijet background by more than 50% which will be described in Section 8.8, the total MC prediction is consistent with the data. Figure 7.2 (b) shows the p_{T} distribution of the leading jet which is the jet with highest p_{T} in an event. As in the lepton p_{T}, the p_{T} threshold causes the low yield in the first bin. In general, the MC prediction agrees with the data within 20%. Also the discrepancy between the prediction and data is expected to be corrected by the fit from the previous analysis result [49]. Figure 7.2 (c) shows the $E_{\mathrm{T}}^{\mathrm{miss}}$ distribution. As in the lepton p_{T}, the criteria on $E_{\mathrm{T}}^{\mathrm{miss}}$ and $E_{\mathrm{T}}^{\mathrm{miss}} + m_{\mathrm{T}}^{\mathrm{W}}$ causes the low yield in the first bin. For the other ranges, the MC prediction agrees with data within 10%. Figure 7.2 (d) shows the m_{eff} distribution. The first four bins have less yields due to the kinematic thresholds of the physics objects and preselection. As in the leading jet p_{T}, the MC prediction is expected to be corrected by the fit with shifts according to their systematic uncertainties. In general, the MC prediction is consistent with the data and describes the event topology well.

7.2 Event classification

After applying the preselection, events are classified based on jets, b-jets, Higgs-tagged jets, and top-tagged jets multiplicities to enhance discrimination of signals from backgrounds. For VLQ signals, our target decay processes are $T\bar{T} \to HtHt$, $HtZt$, and $HtWb$. Concerning $T\bar{T} \to HtHt$ process, signal events can have 8 jets and 6 b-jets where one top quark decays hadronically into $Wb \to qq'b$, the other decays leptonically into $Wb \to l\nu b$, and the Higgs boson decays to $b\bar{b}$ dominantly. Even in the case of SU(2)-singlet, they can have 6 jets since SU(2)-singlet has larger branching ratio of $T \to Wb$ decay. For 2UED-RPP scenario, the signal events have four top quarks, and then around 10 jets and 4 b-jets. Thus, signal events have high jet and b-jet multiplicity while background events have in general lower jet and b-jet multiplicity as shown in Fig. 7.3 (a), (b).

Events are categorised into validation regions (VR) and search regions (SR) by requiring exactly 5 jets or ≥6 jets, respectively. For each, events are further categorised based on b-jet (2, 3, ≥4), Higgs-tagged (0, 1, ≥2), and top-tagged jet (0, 1, ≥2) multiplicities. As described in Section 6, signal events have high Higgs-tagged and top-tagged jet multiplicities since the decay products of signals have high momentum and can be reconstructed by large-R jets and tagged as Higgs bosons or top quarks. This feature is shown in Fig. 7.3 (c), (d). Event categorisation by Higgs-tagged (0, 1, ≥2), and top-tagged (0, 1, ≥2) jet multiplicities are optimised for VLQ signals, as described in Section 6.5. Table 7.2 shows the summary of events categorisation and naming convention for each category.

Figure 7.4 shows the ratios of $S/\sqrt{B}$ and S/B in each SR category for VLQ SU(2)-doublet VLT signals with the mass of 1 TeV. The four categories with the highest S/B ratio are shown in red colour, while the others are shown in blue colour. The categories having at least two Higgs-tagged or top-tagged jets and at least four b-jets are expected to have the highest sensitivities as expected. At the same time, the categories with low Higgs-tagged and top-tagged jet multiplicities have less sensitivity and then are useful to calibrate the background prediction in the fit. The ratios are computed with the number of events expected by the MC simulation before the fit. The expected signal yields for various signal scenarios and backgrounds in the red-colour categories with at least 4 b-jets shown in Fig. 7.4 are summarised in Table 7.3 and 7.4, respectively.

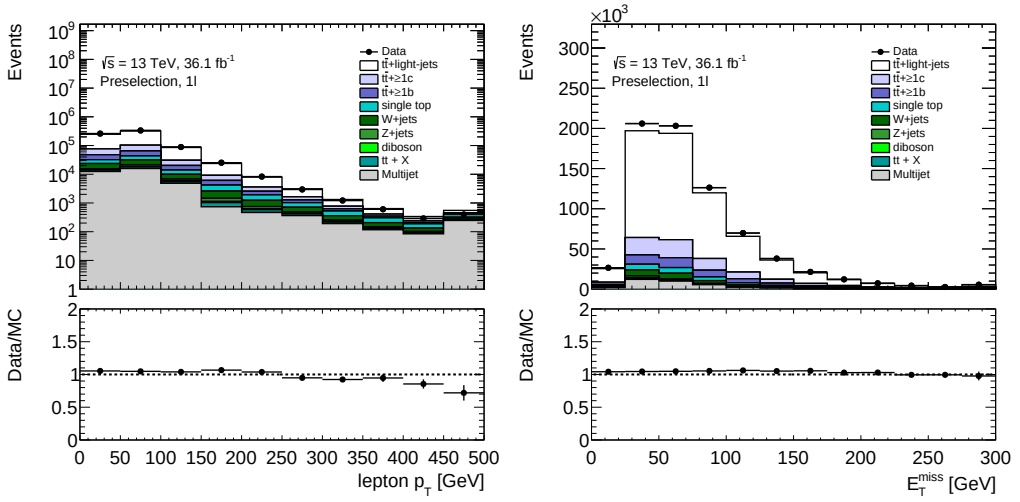

(a) Lepton p_{T} (b) $E_{\mathrm{T}}^{\mathrm{miss}}$

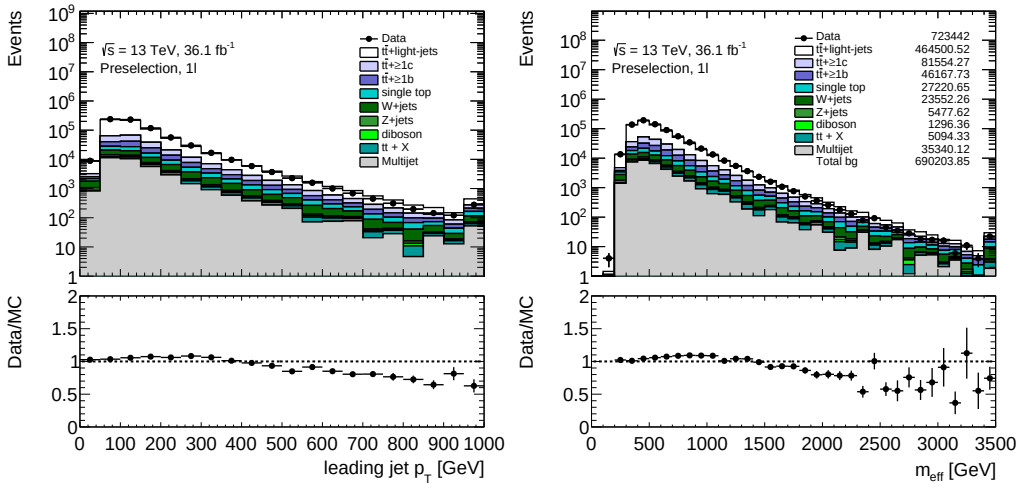

(c) Leading jet p_{T} (d) m_{eff}

Figure 7.2: Comparison of several kinematic variables between data and MC prediction at preselection in 1-lepton channel before fitting. V+jets include all the subprocesses and $t\bar{t}$+X background includes all the processes of SM $t\bar{t}t\bar{t}$, $t\bar{t}$+V, and $t\bar{t}$+H. In the m_{eff} distribution, the event yields of data (black marker) and the MC prediction (coloured fill) are shown in the legend. The bottom panel shows the ratio between the data and MC prediction. The error bar shows only the statistical uncertainty. The last bin includes the overflowing components.

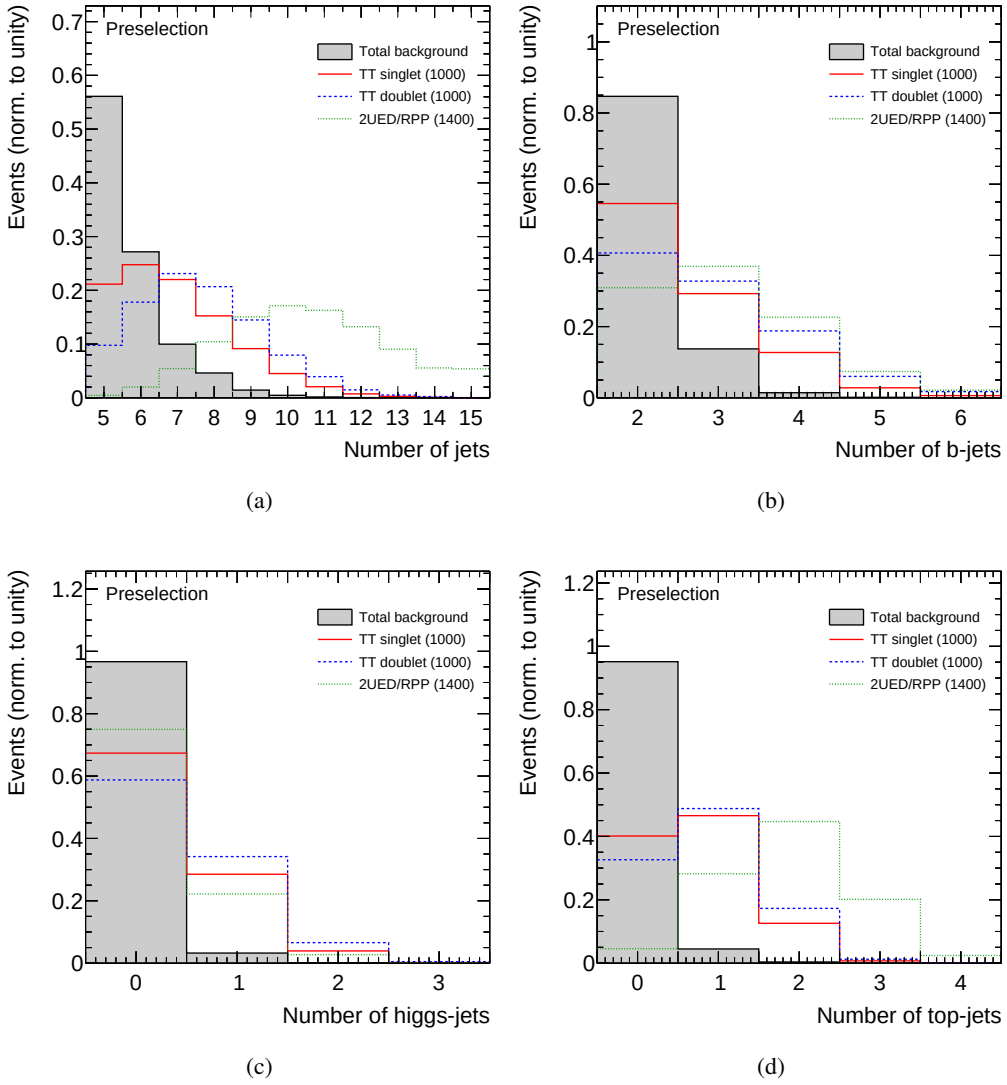

Figure 7.3: Shape comparison of (a) jet, (b) *b*-jet, (c) Higgs-tagged jet, and (d) top-tagged jet multiplicities between signals of VLQ SU(2)-singlet (red) and -doublet (blue) and 2UED-RPP (green) and backgrounds (gray) at the preselection before the fit. Each distribution is normalised to unity. The last bins include the overflowing components.

Table 7.2: Event categorisation and category name in search regions (SR) and validation region (VR). The SR and VR are classified by the jet multiplicity: exactly 5 or at least 6 jets.

Search region : $N_{\text{jet}} \geq 6$, $N_{b-\text{jet}} = 3$ (≥ 4)				
		$N_{\text{top-taggedjet}}$		
		0	1	≥ 2
$N_{\text{Higgs-taggedjet}}$	0	0T, 0H, ≥6j, 3b (≥4b)	1T, 0H, ≥6j, 3b (≥4b)	≥2T, 0-1H, ≥6j, 3b (≥4b)
	1	0T, 1H, ≥6j, 3b (≥4b)	1T, 1H, ≥6j, 3b (≥4b)	
	≥2	≥0T, ≥2H, ≥6j, 3b (≥4b)		
Validation region : $N_{\text{jet}} = 5$, $N_{b-\text{jet}} = 3$				
		$N_{\text{top-taggedjet}}$		
		0	1	≥ 2
$N_{\text{Higgs-taggedjet}}$	0	0T, 0H, 5j, 3b	1T, 0H, 5j, 3b	≥2T, 0-1H, 5j, 3b
	1	0T, 1H, 5j, 3b	1T, 1H, 5j, 3b	
	≥ 2	≥0T, ≥2H, 5j, 3b		
Validation region : $N_{\text{jet}} = 5$, $N_{b-\text{jet}} \geq 4$				
		$N_{\text{top-taggedjet}}$		
		0	1	≥ 2
$N_{\text{Higgs-taggedjet}}$	0	0T, 0H, 5j, ≥4b	1T, 0H, 5j, ≥4b	≥2TH, 5j, ≥4b
	1	0T, 1H, 5j, ≥4b		
	≥ 2			

Table 7.3: Predicted event yields in various signal models with an integrated luminosity of 36.1 fb^{-1}. TTS, TTD, and TTHtHt represesnt the VLT signals with SU(2) sinlet, doublet, and BR($T \to Ht$) = 1, respectively. The uncertainties are calculated by the sum in quadrature of the statistical and systematic uncertainties.

	≥0T, ≥2H, ≥6j, ≥4b	1T, 1H, ≥6j, ≥4b	≥2T, 0-1H, ≥6j, ≥4b
TTS (1.0 TeV)	2.18 ± 0.23	5.47 ± 0.62	5.51 ± 0.69
TTS (1.2 TeV)	0.58 ± 0.08	1.36 ± 0.17	1.45 ± 0.18
TTD (1.0 TeV)	5.96 ± 0.62	12.51 ± 1.36	13.32 ± 1.53
TTD (1.2 TeV)	1.66 ± 0.24	3.05 ± 0.35	3.46 ± 0.41
TTHtHt (1.0 TeV)	14.57 ± 1.99	24.30 ± 2.70	23.92 ± 2.85
TTHtHt (1.2 TeV)	4.39 ± 0.92	5.89 ± 0.71	6.56 ± 0.79
$t\bar{t}t\bar{t}$ (SM)	0.23 ± 0.07	1.12 ± 0.36	2.55 ± 0.82
$t\bar{t}t\bar{t}$ (EFT)	32.57 ± 6.37	170.10 ± 19.95	457.61 ± 62.09
2UED-RPP (1.4 TeV)	1.45 ± 0.32	3.69 ± 0.50	34.00 ± 3.75
2UED-RPP (1.6 TeV)	0.32 ± 0.07	0.79 ± 0.14	7.29 ± 0.80

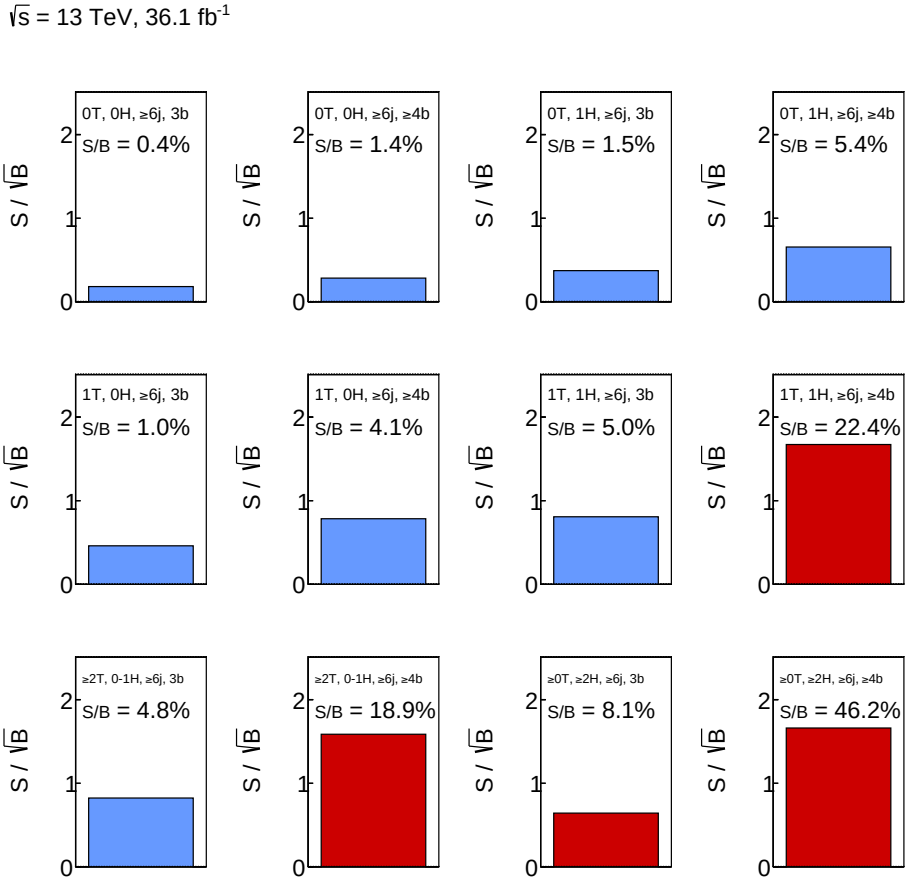

Figure 7.4: $S/\sqrt{B}$ and S/B in each category of SR for VLQ SU(2)-doublet signal with $m_{\mathrm{VLT}} = 1$ TeV. Red-colour categories have the highest signal-to-background ratio, corresponding to those with high b-jet, Higgs-tagged and top-tagged jet multiplicities which is distinctive in signal events. The other categories are shown in blue colour which have low b-jet, Higgs-tagged jet and top-tagged jet multiplicity and are populated by backgrounds largely.

Table 7.4: Predicted event yields from the backgrounds with an integrated luminosity of 36.1 fb^{-1} before the fit. The uncertainties are calculated by the sum in quadrature of the statistical and systematic uncertainties.

	≥0T, ≥2H, ≥6j, ≥4b	1T, 1H, ≥6j, ≥4b	≥2T, 0-1H, ≥6j, ≥4b
$t\bar{t}$ + lights$s$	0.99 ± 0.49	4.81 ± 2.37	5.38 ± 3.26
$t\bar{t}$+ ≥ 1c	2.08 ± 1.29	9.48 ± 5.64	11.85 ± 7.53
$t\bar{t}$+ ≥ 1b	7.13 ± 2.21	32.43 ± 9.50	41.82 ± 22.04
Single top	0.26 ± 0.21	1.69 ± 0.76	1.97 ± 0.95
W+light-jets	0.00 ± 0.00	0.00 ± 0.00	0.00 ± 0.00
W+≥1c+jets	0.01 ± 0.01	0.04 ± 0.03	0.05 ± 0.03
W+≥1b+jets	0.53 ± 0.48	0.65 ± 0.48	1.27 ± 0.70
Z+light-jets	0.00 ± 0.00	0.00 ± 0.00	0.00 ± 0.00
Z+≥1c+jets	0.00 ± 0.00	0.00 ± 0.00	0.01 ± 0.00
Z+≥1b+jets	0.06 ± 0.05	0.09 ± 0.07	0.13 ± 0.08
Dibosons	0.01 ± 0.04	0.11 ± 0.09	0.22 ± 0.14
$t\bar{t}V$	0.41 ± 0.10	1.73 ± 0.39	2.46 ± 0.53
$t\bar{t}H$	1.19 ± 0.20	3.79 ± 0.65	2.84 ± 0.62
$t\bar{t}t\bar{t}$ (SM)	0.23 ± 0.07	1.12 ± 0.36	2.55 ± 0.82
Multijet	0.00 ± 0.00	0.00 ± 0.00	0.00 ± 0.00

7.3 Signal-to-background discrimination

After the preselection and event categorisation described in the previous sections, the kinematic features of signal events helps to further discriminate signals from backgrounds. The variable of m_{eff} is good for the discrimination because high mass signal generates energetic particles in the final states. The variable corresponds to the total energy of a given event in the transverse plane. For instance, VLQ signal events have a peak at $m_{\text{eff}} \sim 2m_{\text{VLT}}$ since the signal events have two VLT's in the intermediate state while background events have lower values. For four-top-quark production, signal events are expected to have high m_{eff} especially in case of BSM scenarios. Figure 7.5 shows a comparison of m_{eff} shape between the signals and backgrounds at preselection level and illustrates the feature of several signal models. Consequently, m_{eff} is used as the final discriminating variable.

Searches for signal events are performed with a binned likelihood fit on m_{eff} distributions of the MC prediction to data in SR described in the previous section. The expected m_{eff} distributions in red-colour SR categories shown in Fig. 7.4 are shown in Fig. 7.6. In the figure, the SU(2)-doublet VLT signal with the mass of 1 TeV and the backgrounds expected with an integrated luminosity of 36.1 fb^{-1} before the fit are shown. In the categories with at least 4 b-jets, $t\bar{t}$+≥1b is dominant as expected. All the backgrounds are depleted in the highest m_{eff} bin, while the signal events are distributed. It is expected to observe the excess from the background prediction by a few events in the last bins if the data include the signals. The signal events are depleted in the first bin where is used for the validation of the fit using the blinded data. These figures assure that signal events are populated in high m_{eff} range in the regions with high b-jet, Higgs-tagged and top-tagged jet multiplicities. In the categories with at most one Higgs-tagged or top-tagged jet including both SR and VR, the additional

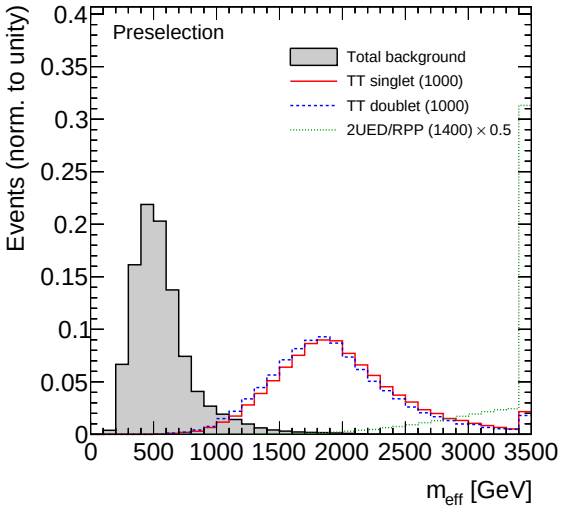

Figure 7.5: Shape comparison of m_{eff} between signals and backgrounds (gray) at preselection level. The signal models used here are SU(2)-singlet (red) and -doublet (blue) VLT signals with the mass of 1 TeV and 2UED-RPP signal with the KK mass of 1.4 TeV.

requirement of $m_{\text{eff}} > 1$ TeV is applied in order to minimise the effects from a possible mis-modelling on the m_{eff} distribution from the small backgrounds with large systematic uncertainties at lower m_{eff}. In the other categories, no other requirements on m_{eff} are applied.

The binning of m_{eff} distribution for each category are determined in order that a m_{eff} distribution has as many bins as possible in wide unit of 100 GeV. For the bins with low statistics, the bin widths are broadened to increase available statistics for calibrating the background prediction. Especially for the bins sensitive to signals, the bin widths are optimised to have good sensitivities to signals and expect at least one event in a bin[1] Therefore, the bin widths can be different among the categories.

7.4 Blinding strategy

Blind analysis techniques are often used in high energy physics experiments in order to avoid experimenters' biases on measurements from having the prior knowledge on the result, such as a further optimisation to enhance the signal events. This analysis applies blinding cuts to data at a validation step. After understanding data with the background prediction and its systematic uncertainty, we remove the blinding cuts and search for new phenomena in observed data.

The signal to background ratio S/B is computed as a function of m_{eff} for various branching ratio, SU(2)-singlet, SU(2)-doublet, and $BR(T \to Ht) = 1$ of the VLT signal with the mass of 1 TeV that is a typical lower limit on the mass in the previous analysis result [49]. Figure 7.7 shows the m_{eff}

[1] The bin widths are set to have at least one expected event because the asymptotic approximation in a fit may not be valid if the expected number of events are less than one.

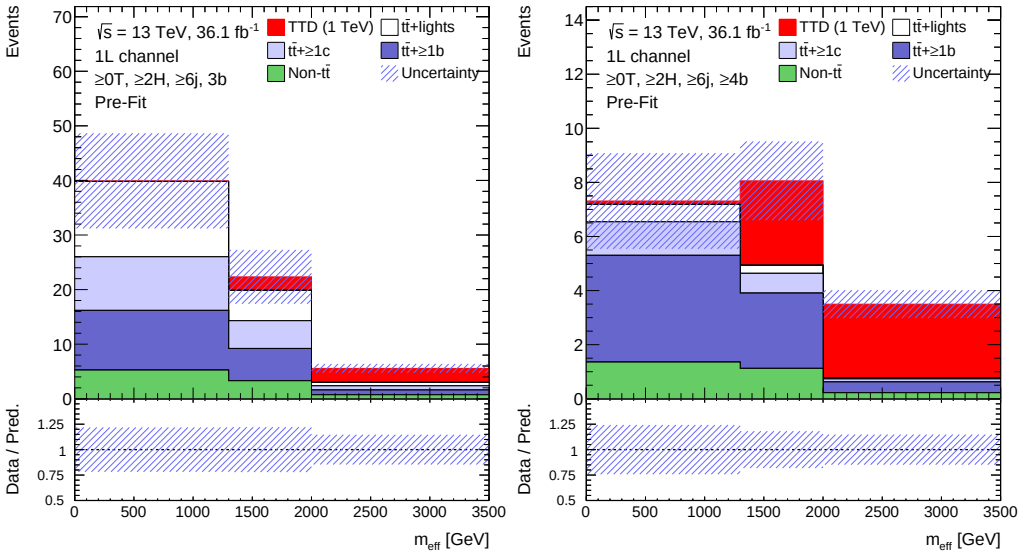

(a) ≥0T, ≥2H, ≥6j, 3b

(b) ≥0T, ≥2H, ≥6j, ≥4b

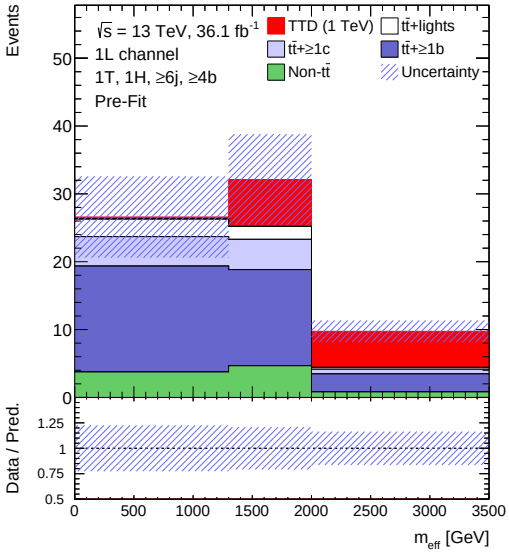

(c) 1T, 1H, ≥6j, ≥4b

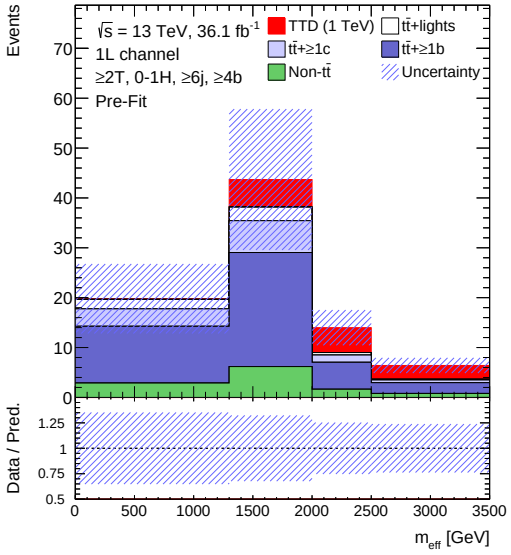

(d) ≥2T, 0-1H, ≥6j, ≥4b

Figure 7.6: m_{eff} distribution of the background prediction and signal (red) of SU(2)-doublet VLT with m_{VLT} = 1.0 TeV before the fit (Pre-fit) in the categories with the highest sensitivity shown in Fig. 7.4. $t\bar{t}$+lights, $t\bar{t}$+≥1c, and $t\bar{t}$+≥1b are shown in white, light blue, and dark blue histograms, respectively. "Non-$t\bar{t}$" (green) includes all the other backgrounds of single top, V+jets, diboson, $t\bar{t}+X$, and multijet processes. The uncertainty (shade) includes the statistical and systematic uncertainties which are computed by the sum in quadrature.

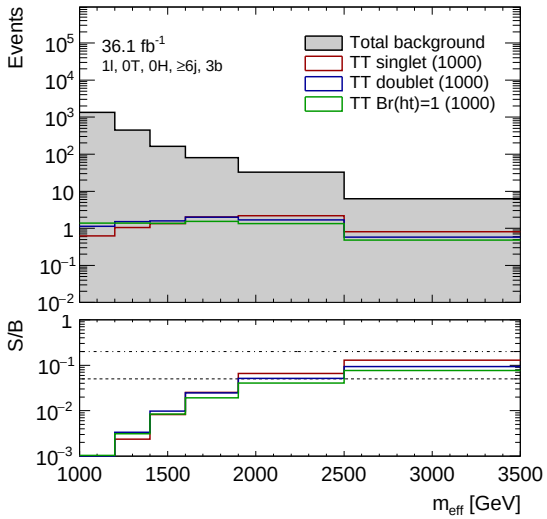

Figure 7.7: Expected m_{eff} distribution (top panel) and S/B (bottom panel) of VLT signals with $m_{\text{VLT}} = 1$ TeV and total backgrounds (gray) for "0T, 0H, 6j, 3b" category with 36.1 fb^{-1}. Various models of SU(2)-singlet (red), SU(2)-doublet (blue), and $BR(T \to Ht) = 1$ (green) are considered to determine the blind cuts.

distribution for the total background (gray) and signals (red, green, blue) in the top panel and the S/B of each m_{eff} bin in the bottom panel for "0T, 0H, 6j, 3b" category before the fit. The expected background distributes largely at low m_{eff} as seen in the one (Fig. 7.5) at the preselection level. On the other hand, the signal events are expected to have large contribution at high m_{eff}. Then, the S/B increases for high m_{eff} for all the signal models. In addition, it shows that the upper cuts on m_{eff} can blind the data for the specific range where the signals can contaminate. To keep the contamination minimum, the upper cuts satisfying $S/B < 5\%$ (dashed line) are determined in each category as the blind cuts. The cuts are determined conservatively based on the models with the smallest contribution in the three models. The upper cuts after simplifying are summarised in Table 7.5. All the computed S/B in each category are shown in Appendix E. The data blinded for the region above the cuts are referred to as blinded data. Here, the BSM four-top-quark production signals are not used to determine the blind cuts since the signal events are expected to contribute to higher m_{eff} than the VLT signals. The figure also shows the other dashed line in the bottom panel corresponding to $S/B = 20\%$. This looser criteria is used for the further validation which will be described in section 10.3.

7.5 Data-to-MC comparison in blinded regions

Comparisons of m_{eff} distributions between the data and MC prediction after applying the preselection, event categorisation, and blind cuts in the SR categories with the highest sensitivity are shown in Fig. 7.8. The blind cut in these categories is 1.3 TeV on m_{eff}, and then the figures show only one bin in the region of $m_{\text{eff}} < 1.3$ TeV. The MC prediction agrees with the data within two standard deviation of its uncertainty which is computed by the sum in quadrature of the statistical and systematic

Table 7.5: Blinding cuts on m_{eff} in 1-lepton channel determined by the $S/B < 5\%$ based on the model having the smallest contribution in the three models. The m_{eff} distributions for all the categories are shown in Appendix E. In several categories with 3b-jets where the backgrounds dominate and the signals are depleted, the blind cut is 1.9 TeV. For the other categories, the cut is 1.3 TeV.

Category	Blinding m_{eff} cuts ($S/B < 5\%$) [TeV]
1T, 0H, 5j, 3b 0T, 0H, $\geq$ 6j, 3b 1T, 0H, $\geq$ 6j, 3b $\geq$ 2T, 0 $-$ 1H, $\geq$ 6j, 3b	1.9
Others	1.3

uncertainties. Appendix F shows the m_{eff} and the other kinematic variables distributions in the other categories including VR. In general, the MC predictions for all the categories for both SR and VR agree with the data within two standard deviation before the fit. For the jet p_{T}, the discrepancy between the data and MC prediction is seen. A likelihood fit of the MC prediction to the data recovers the discrepancy to shift the prediction within their systematic uncertainties of the modelling and all the other components taken into account. This step is also important for the $t\bar{t}$+$\geq$1b normalisation, which is known to be underestimated in the simulation [49]. The results are shown in Section 10.3. Details of fit and systematic uncertainties are described in Section 9 and Section 8, respectively.

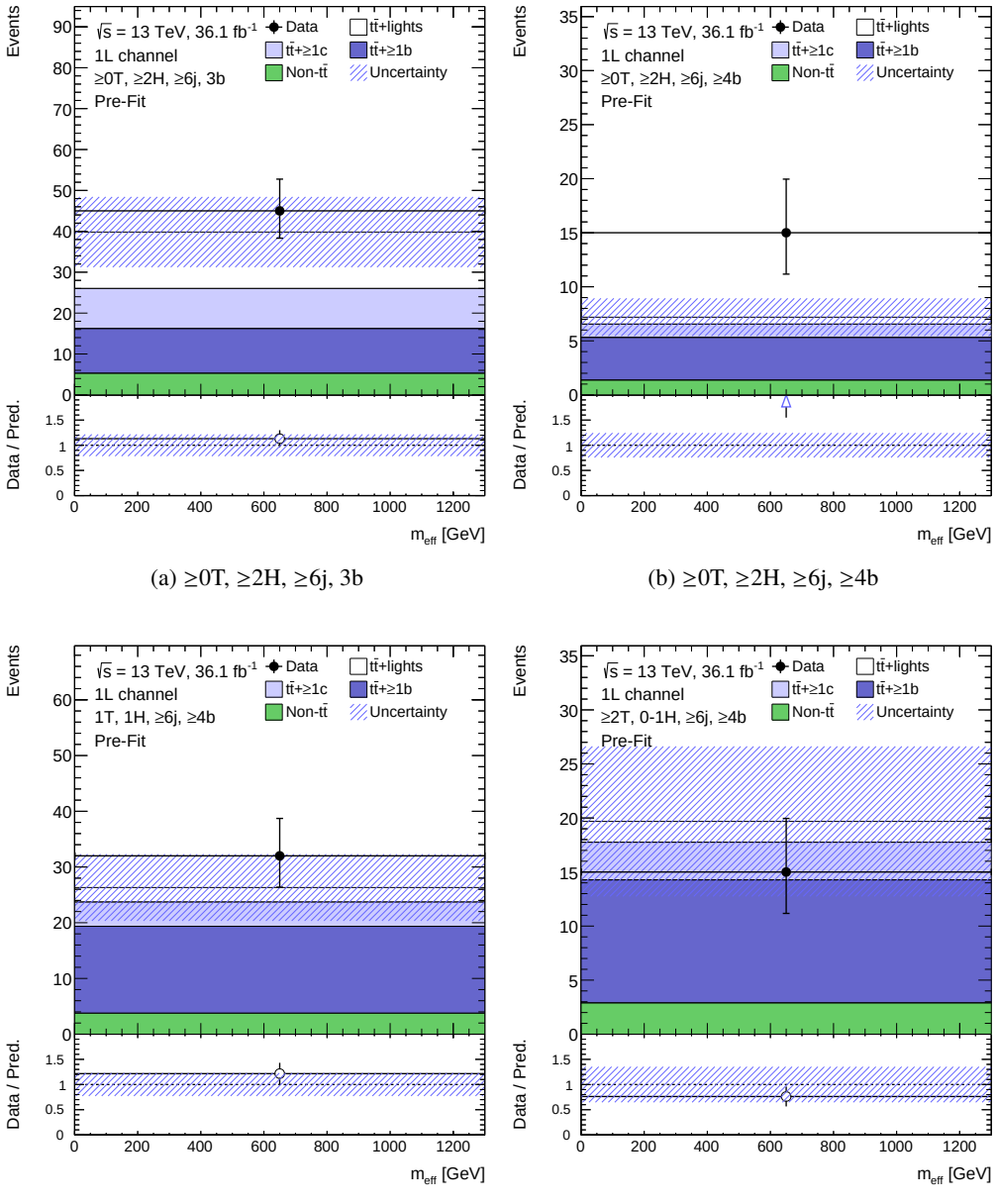

(a) ≥0T, ≥2H, ≥6j, 3b

(b) ≥0T, ≥2H, ≥6j, ≥4b

(c) 1T, 1H, ≥6j, ≥4b

(d) ≥2T, 0-1H, ≥6j, ≥4b

Figure 7.8: m_{eff} distribution of the blinded data and background prediction before the fit (Pre-fit) in the categories with the highest sensitivity shown in Fig. 7.4. The blind cut in these categories is 1.3 TeV on m_{eff}. $t\bar{t}$+lights, $t\bar{t}$+≥1c , and $t\bar{t}$+≥1b are shown in white, light blue, and dark blue histograms, respectively. "Non-$t\bar{t}$" (green) includes all the other backgrounds of single top, V+jets, diboson, $t\bar{t}+X$, and multijet processes. The uncertainty (shade) includes the statistical and systematic uncertainties which are computed by the sum in quadrature.

8 Systematic uncertainties

This section describes the systematic uncertainty in this analysis. The sources of systematic uncertainties are considered: the physics objects and simulation modelling. The systematic uncertainties affect the normalisation, the m_{eff} shape, or both of them. All the systematic uncertainties are estimated without correlation among them and listed in the table 8.1. During fit procedure, the correlations among the systematics are resolved. Each systematic uncertainty is described in the following.

8.1 Luminosity

The uncertainty on the integrated luminosity for the dataset in 2015 and 2016 is 2.1%. It is derived from a calibration of the luminosity scale using x-y beam-separation scans, so-called van der Meer scan, performed in August 2015 and May 2016. The detail of the methodology is described in Ref. [176]. For the multijet background, it is not taken into account since the background is estimated by a data-driven method.

8.2 Pileup

The uncertainty on the pileup is estimated from a variation in the pileup reweighing of MC, which covers the uncertainty on the ratio between the predicted and measured inelastic cross section in the fiducial volume defined by a certain range of the hadronic system [177].

8.3 Physics objects

This section describes the systematic uncertainties for all the physics objects. In general, the systematic uncertainties are obtained by the measurements in individual analysis for each physics object. Each measurement is described in Chapter 3.

8.3.1 Lepton

The measurements of the reconstruction, identification, and isolation are performed based on the tag-and-probe method. The systematic uncertainties on the method are obtained by varying the tag-and-probe selection, the fitting procedure, and the criteria for the signal counting. The uncertainty on reconstruction scale factor is assigned to be $\leq 2\%$ for $E_{\text{T}} > 25$ GeV. The uncertainties on the

Systematic uncertainty	Type	Components
Luminosity	N	1
Pileup reweighting	SN	1
Reconstructed Objects		
Electron trigger+reco+ID+isolation	SN	5
Electron energy scale+resolution	SN	2
Muon trigger+reco+ID+isolation	SN	6
Muon momentum scale+resolution	SN	3
Jet vertex tagger	SN	1
Jet energy scale	SN	21
Jet energy resolution	SN	1
Jet mass scale	SN	4
Jet mass resolution	SN	1
Missing transverse momentum	SN	3
b-tagging efficiency	SN	6
c-tagging efficiency	SN	4
Light-jet tagging efficiency	SN	17
b-tagging extrapolation	SN	2
Background Model		
$t\bar{t}$ cross section	N	1
$t\bar{t}$+HF: normalisation	N	2
$t\bar{t}$+$\geq 1b$: NLO Shape	SN	10
$t\bar{t}$ modelling: residual Radiation	SN	3
$t\bar{t}$ modelling: residual NLO generator	SN	3
$t\bar{t}$ modelling: residual parton shower+hadronisation	SN	3
$t\bar{t}$ NNLO reweighting	SN	2
V+jets normalisation	N	39
Single top cross-section	N	42
Single top model	N	1
Diboson normalisation	N	13
$t\bar{t}V$ cross section	N	1
$t\bar{t}H$ cross section	N	1
SM $t\bar{t}t\bar{t}$ cross section	N	1
Multijet normalisation	N	12

Table 8.1: List of systematic uncertainties, where “N” (“SN") represent the type of the systematic uncertainty which is taken as normalisation-only (both shape and normalisation) for all processes and categories. The component represents the number of nuisance parameters considered in the fit. Some of the systematic uncertainties are split into several components with categories or processes for a more accurate treatment.

identification, isolation, and trigger are assigned at a level of 1%. The uncertainty on the electron energy scale is around $\leq 0.2\%$ at $E_{\mathrm{T}} \sim 40$ GeV. The uncertainty on the electron energy resolution is estimated to be around 10% for $E_{\mathrm{T}} \leq 50$ GeV increasing to around 30% at $E_{\mathrm{T}} \sim 200$ GeV. In total, seven nuisance parameters are taken into account in the fit.

The uncertainty on the combination of muon reconstruction and identification is $\leq 1\%$ for $p_{\mathrm{T}} > 30$ GeV, which is at a similar level of the uncertainty on the isolation. The uncertainty on the momentum scale is 0.05% in the barrel and 0.1% at the pseudo-rapidity of $|\eta| \sim 2.5$. The measurements of momentum resolution has a systematic uncertainty of $\sim 10\%$ and statistical uncertainty up to 30% for high p_{T}. The uncertainty on the muon trigger is measured in Run1 as 0.6% [178]. The nine nuisance parameters corresponding to each uncertainty component are considered in the fit.

8.3.2 Jets

The systematic uncertainties on the jets originate from the measurements on the JVT, energy scale, and energy resolution. The uncertainty on the JVT efficiency is estimated at a level of 3% for jets with $20 < p_{\mathrm{T}} < 30$ GeV, decreasing to around 1% for $50 < p_{\mathrm{T}} < 60$ GeV. The jet energy scale is measured by combination of a few individual measurements using different physics processes, and has 80 systematic uncertainty components. The ones of *in situ* calibrations originate from the MC simulations, sample statistics, and uncertainties propagated from other physics objects such as leptons and photon energies. The uncertainties are combined into eight effective uncertainties ("EffectiveNP") with the original largest correlations among the components kept. The effect of loss of the small correlations is limited in certain kinematic phase space and negligible in this analysis. The remaining systematic uncertainties originate from the six classes: η-inter-calibration, pileup, jet flavour, punch through, non-closure in the detector simulation, and single hadron response. The measurement on the η-inter-calibration has two systematic uncertainties of MC modelling and non-closure in the range of $2.0 < |\eta| < 2.6$ and statistical uncertainty. These uncertainty affects at most 2% in the most sensitive categories. The pileup correction has four uncertainties: pileup modelling, modelling of the number of primary vertices, modelling of the event p_{T} density, and the residual p_{T} dependence. The third component affects the m_{eff} distribution in the most sensitive categories by around 4%, while the others affect by less than 1%. The jet flavour has three systematic uncertainties: the flavour composition in a jet between quarks and gluons, the response of jets originating by gluons, and the response of jets initiated by the bottom quarks. The systematic uncertainty affects from low p_{T} jets by around 10%, deceasing to high p_{T}. The uncertainty for the punch through correction in the calibration steps using the hits in the muon spectrometer is also taken into account. The uncertainty is obtained by the difference of the jet response between the data and MC simulation. The effect of the uncertainty is negligible in the sensitive categories. An uncertainty is derived from the difference between the detector simulations of nominal one and faster simulation called Atlfast-II [88], affecting <1% in all the categories. The systematic uncertainty from the test-beam measurement on the single-particle response with high p_{T} is around <0.1% in all the categories. The 21 corresponding nuisance parameters are considered in the fit.

The uncertainty on the jet energy resolution is derived from the *in situ* measurements in Run1 [179] and the extrapolation from Run1 to Run2 [108]. The total uncertainty is around 4% for low p_{T} and

less than 1% for high p_{T} for a jet. It corresponds to an effect of around 1% for low m_{eff} and up to 4% for high m_{eff}. This nuisance parameter is considered in the fit.

In addition, the systematic uncertainties on the small-R jet mass are considered. The mass scale was measured in Run1 by using the dijet events [180]. The uncertainty is derived from the comparison of the mass between the jets made of energy clusters in the calorimeter and ones made of tracks reconstructed in the ID. It has four systematic components: the MC modelling, calibration of the mass in the calorimeter, track measurements, and statistical uncertainty. They affect the m_{eff} distribution in the sensitive categories by at most 1%. A relative 20% mass resolution uncertainty is assigned. It affects only 4% in the sensitive categories. In total five nuisance parameters are considered in the fit.

8.3.3 Missing Transverse Energy

The systematic on $E_{\mathrm{T}}^{\mathrm{miss}}$ is propagated from uncertainties of all the other physics objects of leptons and jets. Other contributions from MC modelling associated with the track soft term are also taken into account. The systematic uncertainties of the scale and resolutions affect the m_{eff} distribution in the sensitive categories by at most 1%. The three nuisance parameters are considered in the fit.

8.3.4 Large-R jets

As described in Section 3.5, the large-R jets are reclustered from the small-R jets. The systematic uncertainties on the large-R jets are propagated from the uncertainties on the small-R jets.

8.3.5 Flavor tagging

The efficiency to identify the b- and c-jets and misidentify light-jets are calibrated by several individual measurements. A number of systematic uncertainties for the measurements including MC modelling and the uncertainties on the other physics objects are combined by the diagonalisation method. In the different p_{T} bin, the covariance matrix of the scale factors is diagonalised. The eigenvectors correspond to the variations of the systematic uncertainties. Six eigenvectors are considered to describe the systematic uncertainty on the b-tagging efficiency. The same procedure is applied in the light- and c-tagging efficiencies, and seventeen and four eigenvectors are considered for the light- and c-tagging efficiencies, respectively. The first eigenvector for the b-jets tagging affects the m_{eff} distribution in the sensitive categories by around 10%. The first eigenvectors for the c-jets tagging and light-jets mis-tagging affect the m_{eff} distribution in the sensitive categories by around 3%. An additional uncertainty on the extrapolation to high p_{T} is assigned. Since the individual measurements with data are carried out for certain momentum ranges, the extrapolation of the scale factors is derived from a variation of the efficiency when changing the variables affecting the b-tagging efficiency. The uncertainty on the extrapolation affects approximately 5% for the highest m_{eff} and 1% for lower m_{eff}. In absence of a direct measurement in data, for τ-jets, the c-jet scale factor is used. The extrapolation from c-jets to τ-jets is taken into account in the fit as a nuisance parameter. This uncertainty affects by only less than 1%.

8.4 $t\bar{t}$+jets background

In this section, the uncertainties on the modelling of $t\bar{t}$+jets background is described. In $t\bar{t}$+jets background, the $t\bar{t}$+≥1b background is treated differently from $t\bar{t}$+≥1c and $t\bar{t}$+lights background to describe the background better. The systematic uncertainties on the common generator of the $t\bar{t}$+jets backgrounds are described in the next paragraph. The additional systematic uncertainties for $t\bar{t}$+≥1b and others are described afterwards.

Common uncertainties for all the $t\bar{t}$+jets samples The uncertainty of the inclusive $t\bar{t}$ production cross section is +5.1%/−6.1%. It is driven from the theoretical calculations varying the factorisation and renormalisation scales and the other uncertainties on the PDF, α_S, and the top quark mass. The effects of the initial and final state radiation are estimated from the two Powheg+Pythia samples with the different parameter sets. One sample gives more radiation, which is generated with the h_{dump} parameter of $2 \cdot m_{\text{top}}$, the renormalisation and factorisation scales of half the nominal values, and the P2012 radHi tune. The other sample gives less radiation, which is generated with the h_{dump} parameter of m_{top}, the renormalisation and factorisation scales of twice the nominal values, and the P2012 radLo tune. The uncertainty of the radiation is driven by the difference between each sample and the nominal sample. The effects of the generator for the hard scattering process and the parton showering model are derived from two alternative samples. One sample is produced by the MG5_aMC generator interfaced into Herwig++ [131] for parton showering. The other sample is produced by the Powheg-Box generator interfaced into Herwig++ for parton showering. The uncertainty of the generator is estimated by the difference between the two alternative samples, while the uncertainty of the parton showering model is estimated by the difference between the latter alternative sample and the nominal sample.

The uncertainties for $t\bar{t}$+≥1b samples The uncertainty is assigned to all the $t\bar{t}$+jets backgrounds of $t\bar{t}$+≥1b, $t\bar{t}$+≥1c, and $t\bar{t}$+lights. As shown in Fig. 7.2 (f), the background prediction in the categories dominated by $t\bar{t}$+≥1b is underestimated. It is known from the cross section measurements of $t\bar{t}$+≥1b at $\sqrt{s}$ = 8 TeV [181, 182]. The difference between data and the prediction is compatible with the large uncertainties on the $t\bar{t}$+≥1b production. Since the $t\bar{t}$+≥1b production cross section at $\sqrt{s}$ = 13 TeV has not been measured, the $t\bar{t}$+≥1b normalisation factor floats freely in the fit to avoid biases and then is determined by the fit.

The $t\bar{t}$+≥1b samples are weighted to match the NLO prediction by Sherpa+OpenLoop as described in section 5.2.1. Thus, the uncertainties related to Sherpa+OpenLoop are described in this paragraph. The nominal samples are configured by the three parameters of the renormalisation scale μ_{R}, factorisation scale μ_{F}, and resummation scale μ_{Q} as $\mu_{\text{R}} = \mu_{\text{CMMPS}}$ and $\mu_{\text{F}} = \mu_{\text{Q}} = H_{\text{T},t}/2$, where $\mu_{\text{CMMPS}} = \prod_{t,\bar{t},b,\bar{b}} E_{\text{T},i}^{1/4}$ and $H_{\text{T},t} = E_{\text{T},t} + E_{\text{T},\bar{t}}$. The uncertainty on the choice of the parameters is estimated by three kinds of the parameter setting. One is to vary the renormalisation scale by a factor of two up and down("scale"). Another is configured to vary only the factorisation and resummation scales to softer scale μ_{CMMPS}("glosoft"). The last one is configured to vary only the resummation scale to softer scale μ_{CMMPS} ("Q-CMMPS"). These parameter settings are summarised in Table 8.2. Another alternative sample is generated with a different shower recoil model scheme

Table 8.2: Different scale variations considered in the NLO prediction for $t\bar{t}$+≥1b from SHERPA+OPENLOOP. The renormalisation, factorisation and resummation scales are represented by μ_R, μ_F, and μ_Q, respectively, where $\mu_{CMMPS} = \prod_{t,\bar{t},b,\bar{b}} E_{T,i}^{1/4}$ and $H_{T,t} = E_{T,t} + E_{T,\bar{t}}$.

Scale variable	nominal	"scale"	"glosoft"	"Q-CMMPS"
μ_R	μ_{CMMPS}	$\mu_{CMMPS} \times/\div 2$	μ_{CMMPS}	μ_{CMMPS}
μ_F	$H_{T,t}/2$	$H_{T,t}/2$	μ_{CMMPS}	$H_{T,t}/2$
μ_Q	$H_{T,t}/2$	$H_{T,t}/2$	μ_{CMMPS}	μ_{CMMPS}

("CSS KIN") [157]. Also the uncertainties of PDF set are derived from the other PDF sets of MSTW and NNPDF. The fraction of $t\bar{t}$+≥1b subprocess depends on the multiple parton interaction (MPI) and the final-state radiation from the top decay products. The former contribution is studied in Run1 to compare the samples with different UE, and results in a normalisation uncertainty of 25%(50%) for MPI b ($b\bar{b}$) category [183]. The uncertainty of the latter contribution is assessed by the comparison of different parameter settings of POWHEG+PYTHIA, which is described above.

The additional systematic uncertainties on the choice of the NLO generator is assigned. The one uncertainty ("4F PY8") is derived from the comparison between the NLO prediction of MADGRAPH5_aMC@NLO+PYTHIA 8 and nominal prediction of SHERPA+OPENLOOP. The other uncertainty ("4F PS") is computed from the comparison between the MADGRAPH5_aMC@NLO+PYTHIA 8 and MADGRAPH5_aMC@NLO+HERWIG++.

Uncertainties for $t\bar{t}$+≥1c and $t\bar{t}$+lights samples The $t\bar{t}$+≥1c normalisation uncertainty is assigned to be 50% conservatively since this analysis is not sensitive enough to determine the value by the fit. The uncertainties on the generator, radiation, and parton showering are considered as described above. In addition, the systematic uncertainty on the NNLO prediction is taken from the difference between applying and not applying the reweighing.

8.5 W/Z+jets background

The uncertainty on the normalisation of V+jets background is estimated from all the subprocesses of V+≥1b+jets, V+≥1c+jets, and V+light-jets to be 30% [49]. Additional uncertainty of 30% is conservatively assumed for V+≥1b+jets, V+≥1c+jets since these subprocesses are underestimated in the MC prediction. The uncertainty is treated to be uncorrelated across the event categorisation with top-tagged and Higgs-tagged jet multiplicity. In total, twelve corresponding nuisance parameters are considered in the fit.

8.6 Single top backgrounds

The total normalisation uncertainty on the single top background is estimated as 20%. It includes the theoretical uncertainty on the total cross section in t-, Wt- and s-channels (+5%/−4%) [160–162] and the contributions from the variation of the parameter sets regulating the radiation as done in $t\bar{t}$+jets background. For the t- and Wt-channel processes, an uncertainty of the parton shower and hadronisation model is derived by comparing events produced by the Powheg generator interfaced to Pythia or Herwig++. The total uncertainty is computed by the sum in quadrature of all the uncertainties at the preselection level.

Additional uncertainty ("DR/DS") on Wt process about the removal scheme of double-counting the events with $t\bar{t}$ process is estimated by the difference between the nominal sample and alternative sample with the different removal scheme, so-called "diagram subtraction" scheme [184]. The difference significantly affects m_{eff} shape by 50% at m_{eff} = 1 TeV, increasing up to 90% at m_{eff} = 3.5 TeV. The corresponding six nuisance parameters, uncorrelated among the event categorisation with the top-tagged and Higgs-tagged jet multiplicity, are taken into the fit.

8.7 Other backgrounds

The uncertainty on the NLO theoretical cross section for the diboson process is 5% [185], which is estimated in the events with ≥2 jets. To estimate the uncertainty for higher jet multiplicity, it is extrapolated based on the comparison among various algorithms [186]. Consequently, the uncertainty of 48% is considered in the events with at least 6 jets. The uncertainty is taken to be uncorrelated across the categories with the top-tagged and Higgs-tagged jet multiplicity.

For $t\bar{t}V$, $t\bar{t}H$, the uncertainties on the NLO theoretical cross sections are estimated 15% [187, 188], +9%/−13% [189], respectively. Finally, an uncertainty of 30% is estimated for the NLO prediction of the SM $t\bar{t}t\bar{t}$ cross section [190]. Other additional modelling uncertainties are not taken into account for these backgrounds.

8.8 Multijet background

The uncertainty of the multijet background originates from the uncertainty on the efficiency and fake rate in the data-driven MM. It is expected to be large in the events with high jet and b-jet multiplicities because of lack of the available statistics for determination of the rates. In order to estimate the uncertainty on the background, the MC prediction is compared with the data in the multijet-rich regions. From the results, the normalisation uncertainty in electron channel is assumed 50% for $|\eta| < 1.0$ and 100% for $|\eta| > 1.0$, and that in muon channel is assumed 50% for all η range. Since the source of fake leptons is different between electron and muon, and also the dominant source can depend on the event topology, the corresponding NPs are taken to be uncorrelated among electron, muon, and the event categorisation with the top-tagged and Higgs-tagged jet multiplicity.

In total twelve NPs are taken into the fit. While the uncertainties may be too conservative, it does not affect the signal sensitivity since the background is negligible in the signal-sensitive categories.

9 Statistical analysis

Statistical processing of data allows to quantitatively test an existence or an absence of the signal in observed data. A binned likelihood is used in the fitting procedure. In this section, the detail of the methodology in statistical treatment is described.

In order to search for signals of the new phenomena in physics, two hypotheses are tested:

- Null hypothesis
  It is the hypothesis, referred as H_0. In this analysis, it is denoted as b-only hypothesis where data does not include any signals but only backgrounds.
- Test hypothesis
  It is the one to be true when the null hypothesis is rejected, known as H_1. In this analysis, it is denoted as $s + b$ hypothesis that data includes both signals and backgrounds.

The two hypotheses are distinguished by the parameter μ, signal strength, which corresponds to b-only hypothesis for $\mu = 0$ and $s + b$ hypothesis for $\mu = 1$. In case that the p-value, which is a probability under b-only hypothesis to observe as many events as the one observed in data, is low, which means the data is not explained by the background only prediction, it allows us to state about the presence of the new signals. p-value is often converted into significance expressing in a unit of standard deviation of the Gaussian distribution. In high energy particle physics experiments, the following statements are conventionally used based on p-value and significance:

- Evidence
  It is stated when p-value is less than 1.35×10^{-3} corresponding to a significance of $>3\sigma$.
- Discovery
  It is stated when p-value is less than 2.87×10^{-7} corresponding to a significance of $>5\sigma$.

When the p-value is higher than the criteria above, it cannot exclude b-only hypothesis due to the small significance. In the absence of the signals, the signal models considered are excluded at some confidence level by using the similar probability under $s + b$ hypothesis. The detailed procedure will be discussed later.

9.1 Likelihood function and profile likelihood ratio

The probability to observe as many events as measured in data is described with the likelihood function $\mathcal{L}$. Here, we shall consider the simplest example that we observe n_i^{obs} events at the i-th bin in a histogram with $n_i^{\text{exp}} = \mu \cdot s_i + b_i$ events expected from MC prediction, where s_i and b_i stand for the expected number of events for the signal and backgrounds in the bin, respectively, and μ is the

signal strength. The probability to observe n_i^{obs} events under the expectation of n_i^{exp} events, $P_i(\mu)$, can be expressed with Poisson distribution:

$$P_i(\mu) = \frac{(n_i^{\text{exp}})^{n_i^{\text{obs}}}}{n_i^{\text{obs}}!} e^{-n_i^{\text{exp}}} = \frac{(\mu \cdot s_i + b_i)^{n_i^{\text{obs}}}}{n_i^{\text{obs}}!} e^{-(\mu \cdot s_i + b_i)}. \tag{9.1}$$

Thus, the likelihood, the probability to observe data in all histogram bins is computed as:

$$\mathcal{L}(\mu) = \prod_i^{\text{bins}} P_i(\mu). \tag{9.2}$$

In reality, any experiments have statistical and systematic errors, and measurements can fluctuate with them. We have to take into account the effect of errors in the likelihood function. The effects are described as nuisance parameters θ. The expected number of events s_i and b_i are affected by the nuisance parameters and can be written as a function of θ: $s_i(\theta)$, $b_i(\theta)$. The variations for each nuisance parameters are added into the likelihood function assuming a probability density function (pdf), $\rho(\theta)$, referred to as *penalty term* or *prior* on θ:

$$\mathcal{L}(\mu, \theta) = \prod_i^{\text{bins}} P_i(\mu) \prod_j^{\text{NP}} \rho(\theta_j) \tag{9.3}$$

The form of pdf is chosen depending on the property of the nuisance parameter. In this analysis, the following pdfs are used:

- Free float
  It means that no constraint is applied in the likelihood function. $t\bar{t}$+≥1b normalisation factor is free floated since it has not been measured precisely at $\sqrt{s} = 13$ TeV.

$$\rho(\theta) = 1 \tag{9.4}$$

- Gamma (Poisson) distribution
  It is used for the statistical uncertainty related to the number of MC events in a bin since it can describe the probability in the cases of both large and small statistics. Here, we shall think that N events are entered in a histogram bin by a certain probability p when n events are generated by a MC simulation: $n \cdot p = N$. The probability to observe θ events is expressed by using Poisson distribution:

$$\rho(\theta) = \frac{(N)^{\theta}}{\theta!} e^{-N}. \tag{9.5}$$

- Log-normal distribution
  It is a Gaussian distribution with the variable $\theta \to \ln\theta$ which are bounded in positive θ. Thus, the pdf for the normalisation uncertainty can be written by Log-normal distribution as following since it is not allowed to take negative values.

$$\rho(\theta) = \frac{1}{\sqrt{2\pi}\ln(\sigma)} \exp\left(-\frac{(\ln(\theta/\hat{\theta}))^2}{2(\ln(\sigma))^2}\right) \tag{9.6}$$

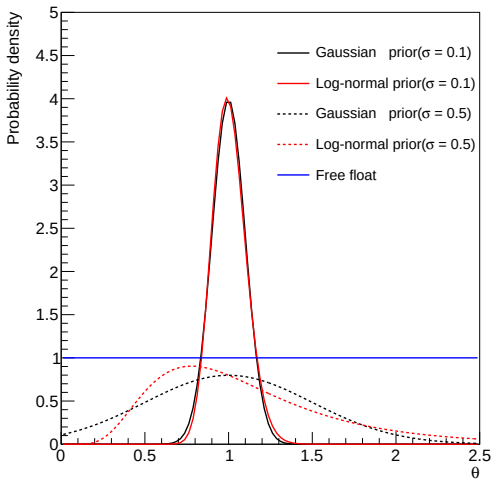

Figure 9.1: Probability densitiy functions used for prior, Gaussian (black), Log-normal(red) with the mean $\hat{\theta} = 1$ and different uncertainty $\sigma = 0.1$ (solid line) and 0.5 (broken line).

- Gaussian distribution
  It is commonly used for the other systematic uncertainties.

$$\rho(\theta) = \frac{1}{\sqrt{2\pi}\sigma}\exp\left(-\frac{(\theta-\hat{\theta})^2}{2\sigma^2}\right) \tag{9.7}$$

Figure 9.1 shows a comparison among the pdf listed above except Poisson distribution. As described above, in case of larger uncertainty, it is shown that Log-normal pdf falls down to zero near around $\theta = 0$ and be bounded positive while Gaussian pdf does not. On the other hand, for smaller uncertainty, Log-normal distribution is similar to Gaussian distribution.

To make it easy and simple to understand the fit results, all the NPs are represented to be zero at the center and with a width of one. For instance, a NP θ with the uncertainty σ and the mean $\hat{\theta}$ can be expressed as:

$$\theta' = \frac{\theta - \hat{\theta}}{\sigma} \tag{9.8}$$

When data does not have enough sensitivity to access a NP or enough statistical power to pull the NP and reduce the original uncertainty, the post-fit NP distributes around zero and with a width of one. If nominal MC prediction or systematic uncertainties are mis-modelled or mis-estimated like $t\bar{t}$+≥1b modelling, the central value of a post-fit NP distribution is shifted far from zero and then post-fit data / MC agreement becomes better. In case that the original uncertainty is assigned too large or has correlations among other NPs, fit can reduce the post-fit uncertainty of the NP. In particular, establishing the correlation among NPs during fit process reduces the total uncertainty.

Each background process has hundreds of NPs, and then one fit takes quite long time to scan all the NPs and find the maximum of the likelihood. In order to speed up a fit, the NPs which have a very

small effect on normalisation or m_{eff} shape are pruned without drastically changing the fit results. The pruning algorithm detects the systematic variation on m_{eff} from nominal expectation. If the variation on normalisation (shape) in a NP is less than 1%, the NP is not used in the fit as normalisation (shape) uncertainty.

In this analysis, the profile likelihood ratio is used as the test statistic q_μ:

$$q_\mu = -2 \ln \frac{\mathcal{L}(\mu, \hat{\hat{\theta}}_\mu)}{\mathcal{L}(\hat{\mu}, \hat{\theta})}, \tag{9.9}$$

where $\hat{\mu}$ and $\hat{\theta}$ are the parameters that maximise the likelihood function and $\hat{\hat{\theta}}$ is the parameter that maximise the likelihood function with a given signal strength μ. In order to test b-only hypothesis, μ in the denominator is set to zero: $q_0 = -2 \ln \mathcal{L}(\mu = 0, \hat{\hat{\theta}}_0)/\mathcal{L}(\hat{\mu}, \hat{\theta})$. For example, if data prefers b-only hypothesis, $\mathcal{L}(\mu = 0, \hat{\hat{\theta}}_0)$ becomes as large as the denominator $\mathcal{L}(\hat{\mu}, \hat{\theta})$ and then q_0 becomes ~ 0. If not, $\mathcal{L}(\mu = 0, \hat{\hat{\theta}}_0)$ becomes small compared to the denominator $\mathcal{L}(\hat{\mu}, \hat{\theta})$ and then q_0 becomes large. The test statistic is known to be expressed with Wald's approximation [191]:

$$q_\mu = \frac{(\mu - \hat{\mu})^2}{\sigma^2} + O(1/\sqrt{N}), \tag{9.10}$$

where $\hat{\mu}$ follows a Gaussian distribution with a mean μ' and standard deviation σ, when the data are distributed according to a parameter of μ'. Assuming the term $O(1/\sqrt{N})$ can be neglected, the pdf for the test statistic q_μ can be described with a non-central chi-square distribution [192]:

$$f(q_\mu|\mu') = \frac{1}{2\sqrt{q_\mu}} \frac{1}{\sqrt{2\pi}} \left[\exp\left(-\frac{1}{2}(\sqrt{q_\mu} + \frac{\mu - \mu'}{\sigma})^2 \right) + \exp\left(-\frac{1}{2}(\sqrt{q_\mu} - \frac{\mu - \mu'}{\sigma})^2 \right) \right], \tag{9.11}$$

In the case of $\mu = \mu'$, the distribution $f(q_\mu|\mu)$ is written as:

$$f(q_\mu|\mu) = \frac{1}{\sqrt{2\pi}} \frac{1}{\sqrt{q_\mu}} e^{-q_\mu/2}. \tag{9.12}$$

Finally, the p-value can be computed by:

$$p_\mu = \int_{q_{\mu,\text{obs}}}^{\infty} f(q_\mu|\mu) dq_\mu. \tag{9.13}$$

Figure 9.2 illustrates the pdfs for the test statistic q_0 assuming background-only and signal-plus-background hypotheses. In both hypotheses, the parameter μ is set to be zero. If the test statistic is observed to be the median on the dataset under the signal-plus-background hypothesis, the expected p_0 is computed by integrating the pdf under background-only hypothesis from the median to positive infinity. When the upper limits on the signal strength μ are computed, the μ is scanned, and then the upper limit is determined to be the value for which the p-value is $p_\mu = \alpha$ at a confidence level $\text{CL} = 1 - \alpha$.

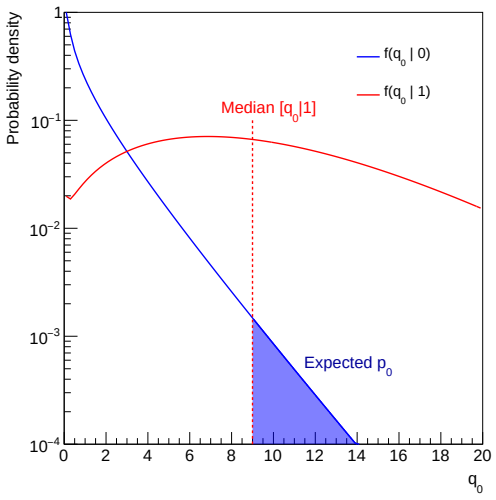

Figure 9.2: Test statistic q_0 distribution under the background-only (blue) and signal-plus-background (red) hypotheses. The shaded area corresponds to an expected p_0 if the observed q_0 is the median on the dataset under the signal-plus-background hypothesis.

9.2 Confidence level

Here, we shall think statistical test to compute the compatibility of observed data with the two hypotheses. Assuming that the test-statistic probability density distributions for b-only and $s + b$ hypothesis are obtained by a number of toy experiments, the compatibility of the test-statistic value observed in data $q_\mu^{\rm obs}$ with the hypotheses can be represented quantitatively by the following *confidence levels*:

- 1-$\mathrm{CL_b}$
  It is the compatibility of the observed test-statistic value with b-only hypothesis obtained by the integral of probability density distribution of q_0 from negative infinity to the observed test-statistic value $q_\mu^{\rm obs}$. It means background p-value, the probability to get the observed test-statistic value under b-only hypothesis.

- $\mathrm{CL_{s+b}}$
  It is the compatibility of the observed test-statistic value with $s + b$ hypothesis obtained by the integral of probability density distribution of q_1 from the observed test-statistic value $q_\mu^{\rm obs}$ to positive infinity. It means the probability to get the observed test-statistic value under $s + b$ hypothesis.

Figure 9.3 illustrates an example of test-statistic probability density distribution for b-only (red line) and $s + b$ (blue line) hypothesis and the test-statistic observed in data $q_\mu^{\rm obs}$ (black line). 1-$\mathrm{CL_b}$ and $\mathrm{CL_{s+b}}$ are shown in red and blue area.

First, we shall think whether we discovered signals by using the compatibility of data with b-only hypothesis $\mathrm{CL_b}$, which is the integral of the pdf from $q_\mu^{\rm obs}$ to positive infinity. If the value of 1-$\mathrm{CL_b}$

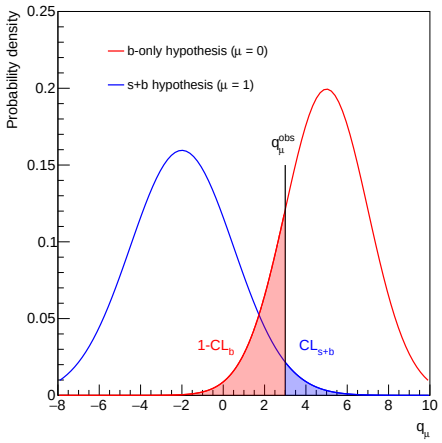

Figure 9.3: An example of test-statistic probability density distribution for b-only (red line) and $s + b$ (blue line) hypothesis and the test-statistics value observed in data $q_\mu^{\rm obs}$ (black line). This is not an experimental result but only a sketch showing the idea of confidence levels, 1-CL$_{\rm b}$(red area) and CL$_{\rm s+b}$(blue area).

is as small as the borders, 1.35×10^{-3} (3σ) or 2.87×10^{-7} (5σ), it is possible to claim evidence or discovery of signal events as written at the beginning of this section. If not, data do not contain significant amount of signal events and is consistent with background prediction. In the case, we show that the signal models are excluded with 95% confidence level, where the value of 95% is used commonly in high energy physics experiments. For exclusion, CL$_{\rm s+b}$ can be used in principle, but it is not used because the signal model can be excluded due to a downward fluctuation of data with respect to the mean value of b-only expected distribution in spite of small sensitivity when difference of probability density distributions between $s + b$ and b-only hypotheses is not clear and overlapped largely with each other. One solution to prevent this issue is CL$_{\rm s}$ method [193] that defines CL$_{\rm s}$, the ratio of the two p-values:

$$\mathrm{CL_s} = \frac{\mathrm{CL_{s+b}}}{\mathrm{CL_b}} \tag{9.14}$$

In case of CL$_{\rm s} < 0.05$, the signal model can be excluded with 95% confidence level. In this analysis, the upper limits of cross section for signal models with a certain mass and branching ratio are calculated. For 2UED-RPP and VLQ signals, the mass range having higher cross section values than 95% upper limits are excluded finally.

10 Results

This chapter shows all the results of the fits using several kinds of configurations. As described in Chapter 7, a likelihood fit to data further improves the background prediction and constraints the systematic uncertainty. Before describing the fit results, the fit procedure is explained in Section 10.1. First, the fit is performed using the pseudo dataset generated with MC for the evaluation of the expected fit performance. Secondly, the fit is performed using the observed data with the blind cut, referred to as "blinded data", in which the backgrounds dominate. It is important to verify whether the background estimation is consistent with the observed data before searching for an excess in data. After the validation, the fit is performed again using the full data, called as "unblinded data", to search for an excess in the data originating from the new physics. This procedure is illustrated in Fig. 10.1. If an excess is observed, its significance is computed with respect to the background estimation, and then what kinds of signal scenarios can make the excess is discussed. If no excess is observed, some parameter space in the signal scenarios considered can be excluded since the events expected from the signal are not observed. In this case, the upper limits on the production cross section for the various signal models are set.

10.1 Fit procedure

In this analysis, the profile likelihood approach is employed, which scans over all the nuisance parameters for each signal strength hypothesis to find the parameter set maximising the likelihood. In the approach, the nuisance parameters can be pulled, and the uncertainties can be reduced. These features result in the improvement of background predictions and of sensitivities due to the smaller uncertainties. When the systematic variation is not compatible with the variation allowed by the statistical uncertainty on the data, the systematic uncertainties are individually constrained. If several systematic uncertainties have similar effects, the total effect of the uncertainties may be larger than the statistical uncertainty of the data. In the case, to adjust the total systematic uncertainty to be a level of the data statistical uncertainty, a correlation or anti-correlation is established. If a systematic variation is much smaller than the statistical uncertainty on the data, the pull and error on the uncertainty are not changed from the input variables. This section shows several examples to explain the fitting procedure.

Fit to a toy data generated without including signal

This fitting process is explained with a simple example using a toy data in following. Here, the following setup is assumed:

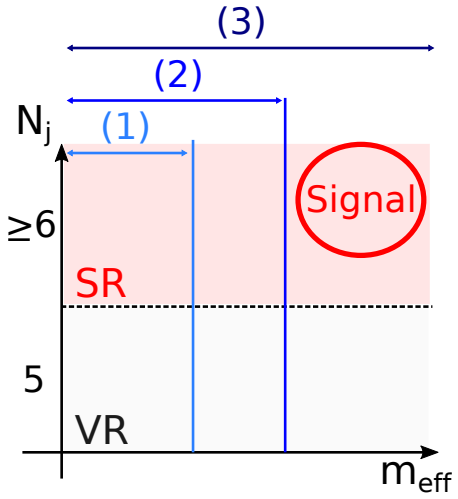

Figure 10.1: Illustration of the fit procedure using the observed data. The x- and y-axes stand for the m_{eff} and the number of jets per event, respectively. After checking the fit performance using the pseudo dataset, three kinds of fits are performed. At the first step (1), the fit with the blinded data ($S/B < 5\%$) is performed. The fit uses only lower m_{eff} range where the backgrounds dominate in order to check whether the background models are correct. At the second step (2), the fit with the blinded data ($S/B < 20\%$) is performed. The looser blind cuts allow to check the background models for higher m_{eff} range. After the two validations, the final fit (3) using whole m_{eff} range is performed to search for an excess of data.

- Searching for a signal in a region named "Region 1"
- The region "Region 1" is dominated by one background process which is estimated with the simulation
- The final discriminating variable is named "X"
- The background is dominant in lower X range, while the signal is expected to populate in higher X range
- Considering two systematic uncertainties on the background: the normalisation uncertainty by 1% and X scale uncertainty

Then, the example shows that the background prediction is fitted to the data.

Figure 10.2 (a) shows the predicted (blue) and observed (black markers) X distribution in Region 1 before the fit. The expectation of the signal is overlaid as a reference. The background prediction agree with the data within one standard deviation of its uncertainty. But the prediction has discrepancies with the data by around 10% at the first two bins.

Then, we shall think to maximise the likelihood described in Eq. (9.3). As described above, the two systematic uncertainties are considered. In the fit, the two nuisance parameters which correspond to the systematic uncertainties are taken into account. The normalisation uncertainty is estimated to be 1%. Since this uncertainty is too smaller than the statistical uncertainty on the data, it is not expected to be constrained. On the other hand, the X scale uncertainty is expected to have

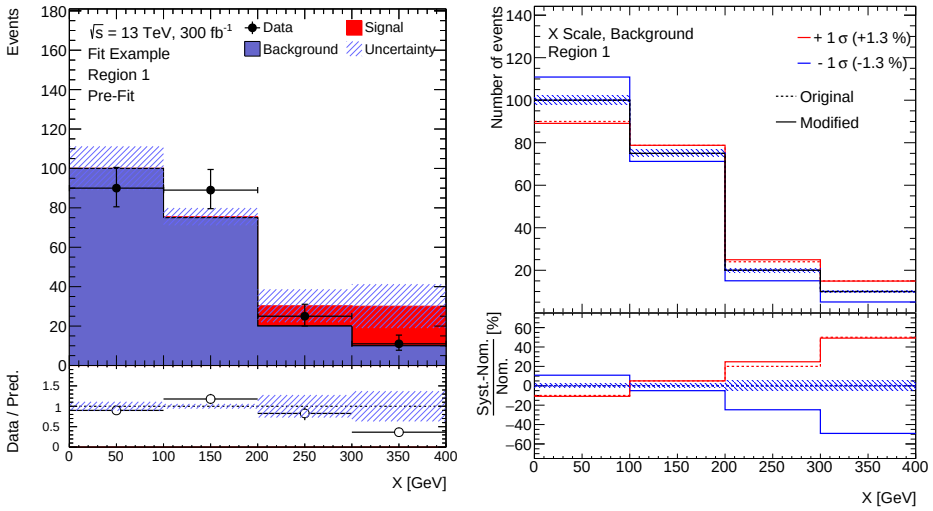

(a) (b)

Figure 10.2: (a) X distribution for a fit example. In Region 1, the background (blue) is dominant for lower X range, while the signal (red) is expected to populate for higher X range. The background prediction agrees with data (black markers) within its uncertainty (shaded area). (b) Systematic variations of X scale uncertainty. The variations by $+1\sigma$ and -1σ are shown in red and blue lines, respectively. They are symmetrised with respect to the nominal prediction. The variations after this modification ("Modified") are shown in solid lines, while the variations before this modification ("Original") are shown in broken lines.

larger deviation for high X range as shown in Fig. 10.2 (b). By comparing the systematic variations with the data, when the systematic variation on the X scale uncertainty is pulled by around $+1\sigma$, the background prediction can naively expected to agree with the data. Since the variation of this systematic uncertainty is larger than the statistical error on the data, the uncertainty is expected to be constrained.

Figure 10.3 (a) shows the pulls and constraints on the systematic uncertainties after the fit. The normalisation uncertainty is not pulled, and its uncertainty keeps the input variation as expected. The nuisance parameter of the X scale uncertainty is pulled by around $+1\sigma$, and this uncertainty is constrained as expected. This pull should improve the agreements between the prediction and the data. Figure 10.3 (b) shows X distributions after the fit, and the post-fit background prediction agrees with the data. As a result, no excess of the data is observed. This is the fitting procedure under the background-only hypothesis. If the data includes the signal, an excess of the data should be seen. The case where the data includes the signal is considered in following.

Fit to a toy data generated with including signal

This section shows the case where a toy data is generated with including the signal. The background prediction and its uncertainties are the same as the ones used in the previous example. Figure 10.4

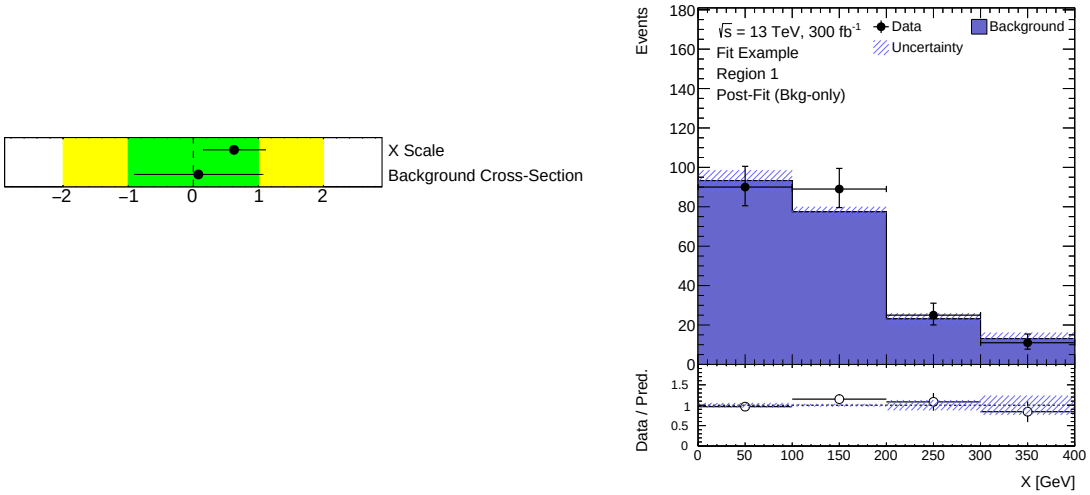

(a) (b)

Figure 10.3: (a) Pulls and uncertainties of the nuisance parameters considered in the fit. (b) Observed and predicted X distributions after the fit. The post-fit background prediction (blue) agrees with data (black markers) within its uncertainty (shaded area).

shows the observed and predicted X distributions before the fit. In this example, this data has more events for high X range than the one shown in Fig. 10.2 (a).

Since the discrepancy between the data and the pre-fit prediction is larger for high X range, the nuisance parameter of the X scale uncertainty is expected to be pulled by more than 1σ. When this nuisance parameter is pulled by much more than 1σ, the discrepancy between the data and the prediction for low X range becomes larger, hence the likelihood value becomes smaller. The penalty term also contributes to decrease the likelihood value due to large pulls. These features are effectively the upper limits of the pulls.

Figure 10.5 (a) shows the pulls and uncertainties of the nuisance parameters after the fit under the background-only hypothesis. The nuisance parameter of the X scale uncertainty is pulled by around 2σ. This significant change of the pulls is caused by the signal contribution. The 2σ pull of the X scale uncertainty attempts to correct the prediction for high X range. Figure 10.5 (b) shows the observed and the predicted X distributions after the fit. At the lowest X bin, the worse agreement between the prediction and the data is seen. And a significant excess of the data is observed at the highest X bin.

As described above, in the fit under the background-only hypothesis, the signal contributions are seen as excesses of the data. In the case where the data include the signal, several nuisance parameters

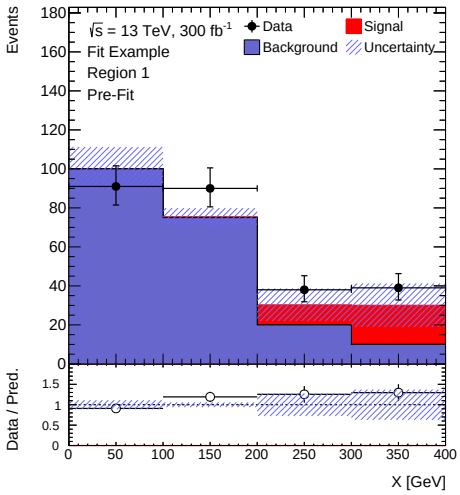

Figure 10.4: Observed and predicted X distributions before the fit. In Region 1, the background (blue) is dominant for lower X range, while the signal (red) is expected to populate for higher X range. The background prediction including the signal agrees with data (black markers) within its uncertainty (shaded area). The toy data is generated with including the signal.

are pulled in order to correct the prediction. Thus, differences of the pulls are seen in the fit results between using only the background dominant regions and all the regions including the signal sensitive regions. These differences also indicate the signal contributions.

In this example, if the fit is performed under the signal-plus-background hypothesis, the post-fit prediction should result in better agreements with the data than the one under the background-only hypothesis. Figure 10.6 (a) shows the pulls and uncertainties of the nuisance parameters after the fit under the signal-plus-background hypothesis. The pulls of the nuisance parameters are within 1σ and similar to the ones in the fit to the toy data without including the signal. Since the data include the signal, these pulls are consistent with the expectation. The best-fit value of the signal strength μ is estimated to be 1.11 ± 0.46. Since the signal strength does not have the penalty term in the likelihood, this uncertainty is determined by the accuracy of the background estimation. The fit result prefers non-zero contributions of the signal.

Figure 10.6 (b) shows the observed and predicted X distributions after the fit under the signal-plus-background hypothesis. The post-fit prediction including the signal has better agreements with the data than the one shown in Fig. 10.5 (b).

The two examples shown above illustrate the fit procedure. The nuisance parameters corresponding to the systematic uncertainty can be pulled in order to correct the background prediction within their uncertainties and maximise the likelihood. The uncertainties can be constrained by using the data statistics. Without any signals in the data, the nuisance parameters are pulled, and then the background prediction is consistent with the data after the fit under the background-only hypothesis. If the data include the signal, the signal contribution can be observed as an excess of the data. By comparing fit results between using the background dominant regions and using the signal sensitive

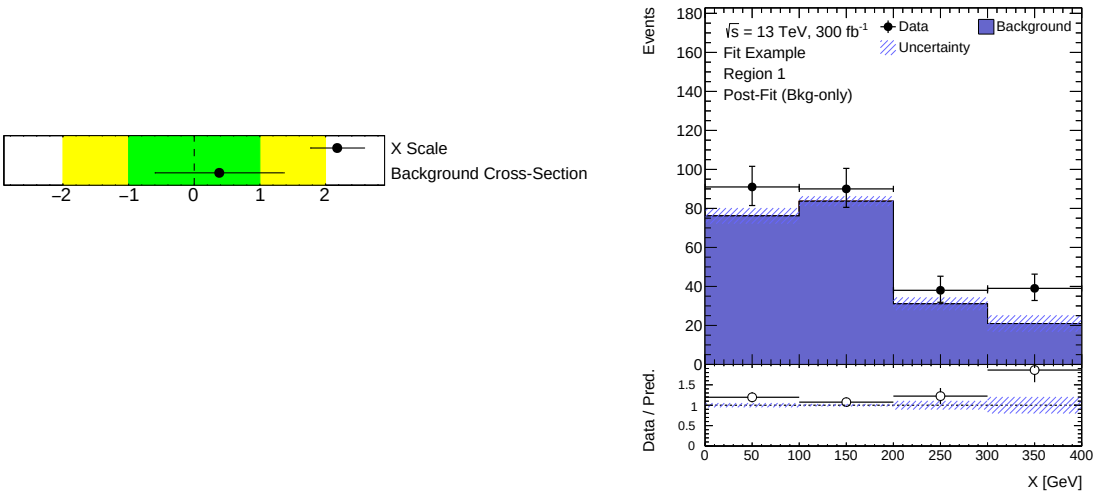

(a) (b)

Figure 10.5: (a) Pulls and uncertainties of the nuisance parameters considered in the fit under the background-only hypothesis. (b) Observed and predicted X distributions after the fit. The post-fit background prediction (blue) agrees with data (black markers) within its uncertainty (shaded area).

regions, the signal contributions can be seen in the nuisance parameters' pulls. In the fit under the signal-plus-background hypothesis, the signal strength parameter μ is determined. If the data include the signal, the fitted μ value is estimated to be non-zero value with an uncertainty.

10.2 Expected fit performance

In order to understand beforehand the fit behaviour such as the pull and constraints on the nuisance parameters (NP) after the fit, the fit is performed to the artificial data so-called "Asimov data" generated under the background-only hypothesis. In other words, the event yields of Asimov data are exactly equivalent with the expected total background prediction[1]. The Asimov data has only statistical uncertainties with respect to the expected number of events in each bin, as the observed data has.

Figure 10.7 shows the pulls and constraints on the nuisance parameters in the fit to the Asimov dataset under the background-only hypothesis with an integrated luminosity of 36.1 fb^{-1}. For each

[1] The Asimov data used here is not randomly generated with the expected uncertainty but is equal to the total background prediction.

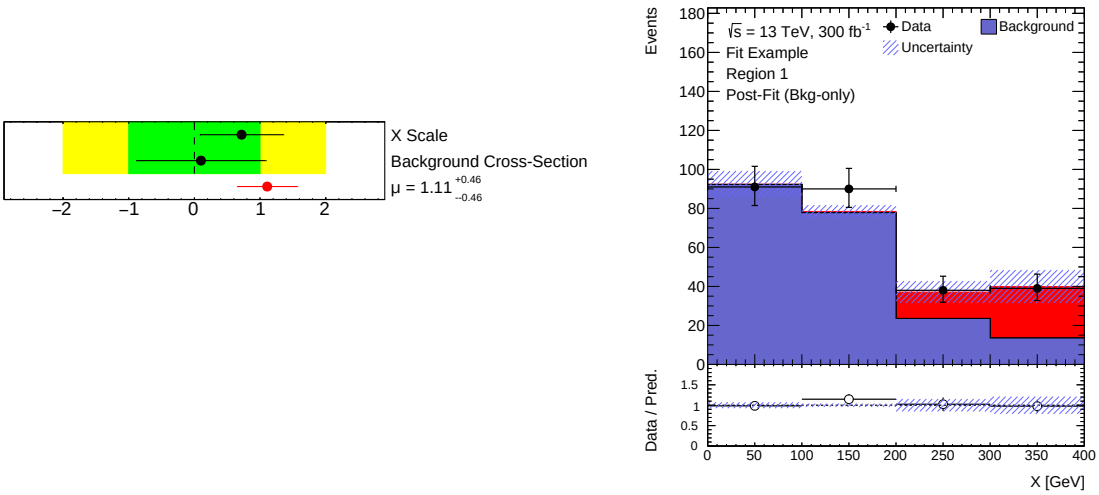

(a) (b)

Figure 10.6: (a) Pulls and uncertainties of the nuisance parameters considered in the fit under the signal-plus-background hypothesis. The signal strength μ (red) is estimated to be 1.11 ± 0.46 by the fit. (b) Observed and predicted X distributions after the fit. The post-fit background prediction (blue) agrees with data (black markers) within its uncertainty (shaded area).

NP, the fitted value represents the preferred shift with respect to the prediction in a unit of its prior uncertainty, and the fitted error represents the uncertainty after the fit in a unit of its prior uncertainty. As described above, the Asimov dataset agrees perfectly with the total background prediction. It results in that all the central values are distributed at zero since the NPs are needed to be shifted within their uncertainty. If this analysis does not have sensitivity to a NP or the NP is not correlated to another NP, the fitted error should be one since nothing constrains the uncertainty. The $t\bar{t}$+≥1b normalisation floated freely in the fit is determined as 1.0 ± 0.27 by the statistics. Since the NP of the $t\bar{t}$+≥1c normalisation is determined to be 0.0 ± 0.747, the $t\bar{t}$+≥1c normalisation is determined to be 1.0 ± 0.37 after the fit. The larger uncertainty on $t\bar{t}$+≥1c normalisation is caused by less sensitivity of this analysis for the $t\bar{t}$+≥1c background. For instance, in all the SR categories, $t\bar{t}$+≥1c background is not dominant while the categories with 4 b-jets are dominated by $t\bar{t}$+≥1b background. It results in less constraints on the $t\bar{t}$+≥1c nomalisation uncertainty. Most of the NPs have the errors of one, while a few NPs have reduced errors after the fit. The uncertainties on the pileup and related to the jet energy resolution contribute to lower jet p_{T} region which corresponds to lower m_{eff} region where there are a lot of statistics. This feature results in the errors less than one. The nominal modelling uncertainties related to $t\bar{t}$+jets background can be overestimated because they are estimated by the theoretical comparisons between the extreme parameter settings of the generators. In addition, the

NPs related to modelling uncertainties can be correlated with another NP. These features result in the constraints on the NPs of $t\bar{t}$+≥1b modelling. The correlation matrix among the NPs is built during the fit (Fig. G.1 in Appendix G.1) and shows around 20% (anti-)correlations among the NPs of $t\bar{t}$+jets modelling. It results in the constraints on these NPs. The other NPs have only a few percent correlations in general. The uncertainties on the multijet background are constrained in the "0T0H" and "0T1H" categories since the prior uncertainty is overestimated. The total uncertainty on the event yield in a category is reduced from around 20% to around 10%.

To understand the impact of each NP on the signal strength μ, a fit to the Asimov dataset generated under the background-only hypothesis is performed under the signal-plus-background hypothesis and evaluate the impact from the variation of μ when each NP varies by $\pm 1\sigma$ with respect to its prior uncertainty. Figure 10.8 shows the leading 10 uncertainties according to the impact on μ after the fit assuming the VLT signal events of SU(2) doublet with the mass of 1 TeV. The leading uncertainty is those related to $t\bar{t}$+≥1b modelling such as the generator, parton shower, and radiation as well as the b-tagging extrapolation uncertainty which are not constrained by the fit. These leading uncertainties depend on the m_{eff} ranges which are sensitive to the signal model considered. Similar plots with different signal models are shown in Appendix G.3 and indicate that the same uncertainties have the largest impact on μ for whole m_{eff} ranges and all the sensitive categories in general. For the other uncertainties, the $t\bar{t}$+≥1b normalisation and $t\bar{t}$+≥1c NNLO uncertainties also have the impact in lower and higher m_{eff} range, respectively. In order to understand the effect to the signal estimation, the similar plots are made with the signal event being injected into the Asimov dataset (Fig. G.2 in Appendix G.3). It turns out that the uncertainties of the leading b-tagging eigen-vector components and b-tagging extrapolation affect the signal prediction.

Finally, the fit will be performed to the observed data. The observed data can fluctuate from the background prediction, which may lead to unreliable results if the fit condition is unstable since numerous NPs are fitted simultaneously over many categories. To validate the fit condition, several Asimov datasets are generated with some NPs or signal events injected. The set of fits is performed under both background-only and signal-plus-background hypotheses, and then the consistency of the fit result with the alternative Asimov dataset is confirmed. All the test items and results are shown in Appendix G.2. It is concluded that all the fit results are consistent with the expectations and the fit stably works.

10.3 Fits to blinded dataset

A fit to the blinded data as defined in Section 7.4 is performed under the background-only hypothesis. The results of the pulls and constraints on the NPs and correlation matrix among NPs are shown in Appendix G.4. In general, most of NPs have the values of zero and the errors expected from the fit to the Asimov dataset. The shifts at most $+1\sigma$ of the NPs related with $t\bar{t}$+jets modelling improve the agreement of the prediction. The $t\bar{t}$+≥1b normalisation factor is determined to be 1.24 ± 0.32 whose relative uncertainty increases because the blind cut limits the available statistics. The correlations among the NPs are also consistent with the expectation from the fit to the Asimov dataset.

Figure 10.9 shows the event yields in the search and validation regions after the fit ("post-fit"). All the categories have good agreements between the post-fit background prediction and observed data.

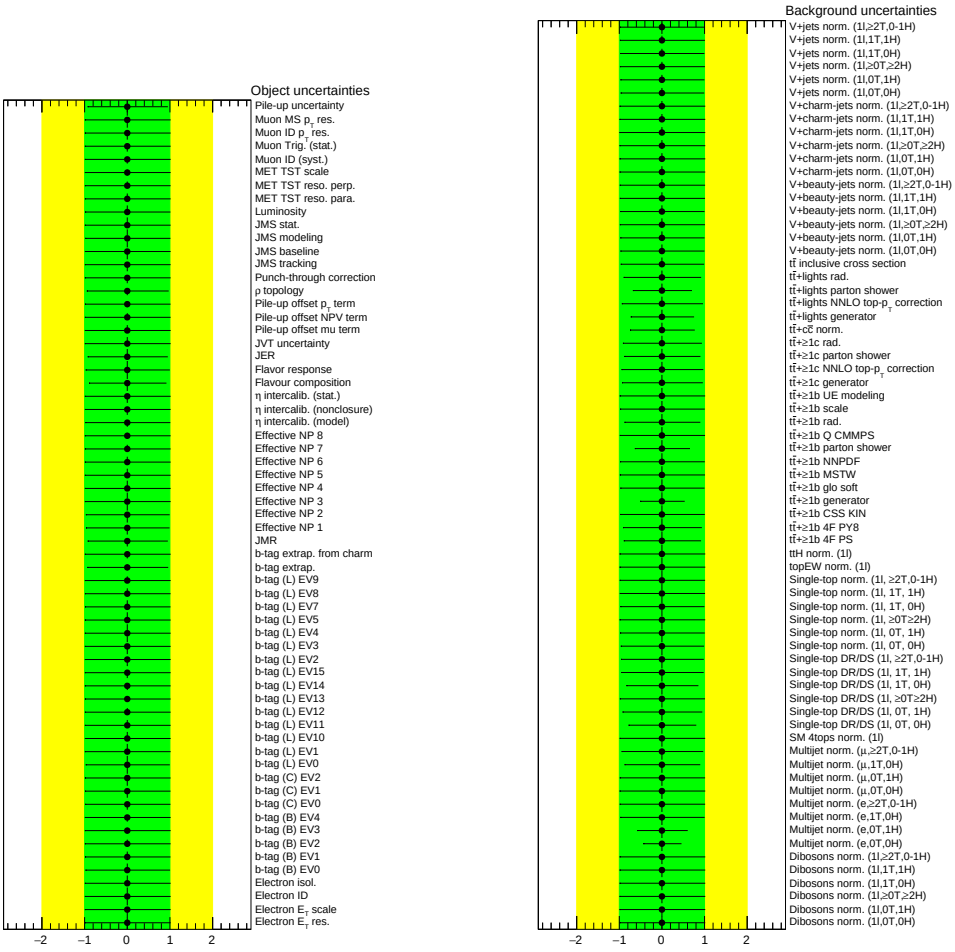

(a) (b)

Figure 10.7: Pulls and constraints on the fitted nuisance parameters related to (a) the luminosity, pileup, and physics objects and (b) background modelling in simulation and the normalisation uncertainty of multijet background by the data-driven estimation. The $t\bar{t}$+≥1b normalisation is not displayed since it is floated freely in the fit. The fit is performed to the Asimov dataset generated under the background hypothesis with an integrated luminosity of 36.1 fb^{-1}. For each NP, the fitted value represents the preferred shift with respect to the prediction in a unit of its prior uncertainty, and the fitted error represents the uncertainty after the fit in a unit of its prior uncertainty. All the values are distributed at zero since the background prediction perfectly agrees with the Asimov dataset and it does not need to improve the prediction by shifting the NPs.

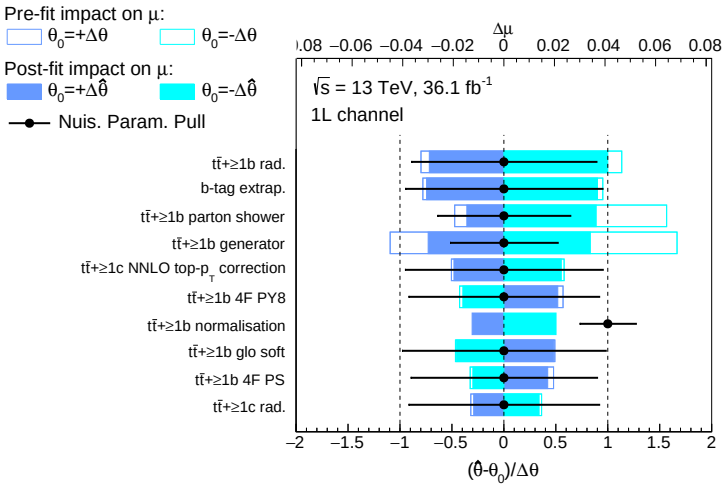

Figure 10.8: Impact on the signal strength μ of each uncertainty obtained from the fit under the signal-plus-background hypothesis to the Asimov dataset generated under the background-only hypothesis. The signal model used here is the VLT signal of SU(2) doublet with the mass of 1 TeV. The leading 10 uncertainties according to the impact on μ after the fit are shown. In the figure, there are two independent x-axes in the top and bottom. Black points which are plotted according to the bottom x-axis represent the deviation of each fitted nuisance parameter ($\hat{\theta}$) from the nominal value (θ_0) in a unit of its prior uncertainty ($\Delta\theta$). The uncertainties are sorted according to the impact of it after the fit (hashed blue area) plotted according to the top x-axis. The impact of each uncertainty on μ is calculated by the difference of μ when a fit is performed with the corresponding nuisance parameter fixed at $\hat{\theta} \pm \sigma_\theta$. The $t\bar{t}$+≥1b normalisation floated freely in the fit is set to be one. The uncertainty of $t\bar{t}$+≥1b radiation has the most impact on μ for the signal.

The post-fit prediction in "≥0T, ≥2H, ≥6j, ≥4b" category (the right end bin) also agrees with the data within 2σ and is not related to any signal models since the excess distributes at $m_{\text{eff}} < 1.3$ TeV (Fig. G.6 (h) in Appendix G.4). Especially the yields of the post-fit prediction in the validation regions agree with data. It indicates that the fitted NP corrects the background prediction properly. Comparison of all the m_{eff} distributions between the post-fit prediction and the data is shown in Figs. G.6 and G.7 in Appendix G.4. It is found that the post-fit prediction also agrees with the blinded data in the m_{eff} range.

As discussed in Chapter 7.4, when the blind cut determined by the S/B threshold of 5% is applied, the m_{eff} distributions in both the search and validation regions do not include the high m_{eff} region even in the signal-depleted categories such as "0T, 0H" and "1T, 0H" categories. In order to validate the fit results further, the fit to the data with the S/B threshold loosened from 5% to 20% is performed under the background-only hypothesis. The looser cut allows to validate the high m_{eff} regions in the signal-depleted categories. All the fit results are shown in Appendix G.5. The pulls and constraints on the NPs are consistent with the fit to the blinded data with the tighter blind cut ($S/B < 5\%$). The $t\bar{t}$+≥1b normalisation is determined to be 1.12 ± 0.29, which is consistent with the fit result (1.24 ± 0.32) to the blinded data with the 5% threshold. The pulls, constraints, and correlations of the NPs are also consistent with them. The event yields and m_{eff} distributions of the post-fit background prediction agree with the data within 2σ in both the search and validation regions. For the signal-depleted categories, the m_{eff} distributions have good agreement between the post-fit prediction and

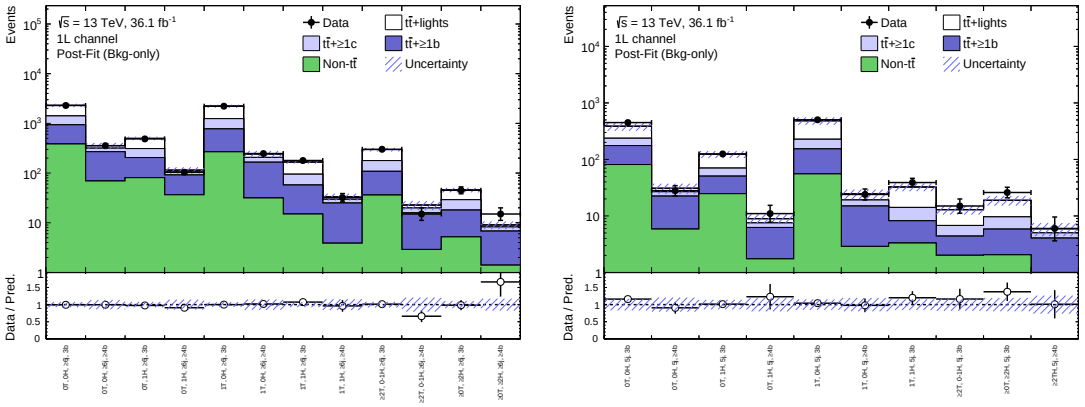

(a) (b)

Figure 10.9: Event yields in (a) the search regions (≥6 jets) and (b) validation regions (5 jets) after the fit ("Post-fit") to the data (black dots) with the blind cut applied. The fit to the blinded data is performed under the background-only hypothesis (Bkg-only) using only the search regions. The fit result in the search regions is propagated into the background prediction in the validation regions. The backgrounds of V+jets, diboson, single-top, ttV and ttH which have small contributions are combined into a single background named "Non-$t\bar{t}$". The hashed area represents the total uncertainty on the post-fit background prediction, which is computed by the sum in quadrature of all the statistical and systematic uncertainties with correlations among NPs taken into account.

observed data in the whole range as shown in Fig. 10.10 (a) and (b).

These validation results assure that the fit properly works for whole m_{eff} range and the systematic uncertainties and their nuisance parameters include no significant problems.

10.4 Fits to unblinded dataset

Before going to the detail in this section, the fit results described above are summarised briefly. From the fit results with the Asimov dataset, the fit procedure is validated and confirmed to work properly. The two validation steps of the fits with the blinded data show good agreements of the background prediction with the blinded data for both lower and higher m_{eff} ranges. Consequently the blinded data is understood. Then, in this section, the data is unblinded, and then the search for new phenomena is performed.

A fit to the data without any blind cut is performed under the background-only hypothesis. The pulls and constraints of the NPs are shown in Fig. 10.11, which show similar results to those obtained in the fit to the blinded data. In followings, the effects of the pulls on the high m_{eff} are discussed.

Jet uncertainties The NPs related with the jet uncertainty have small shifts by at most $\pm 0.5\sigma$. They come from $t\bar{t}$+lights for lower m_{eff} range in the signal-depleted categories with 3 b-jets. The "ρ topology" and "Flavour composition" are shifted by around $+0.3\sigma$. They affect the high

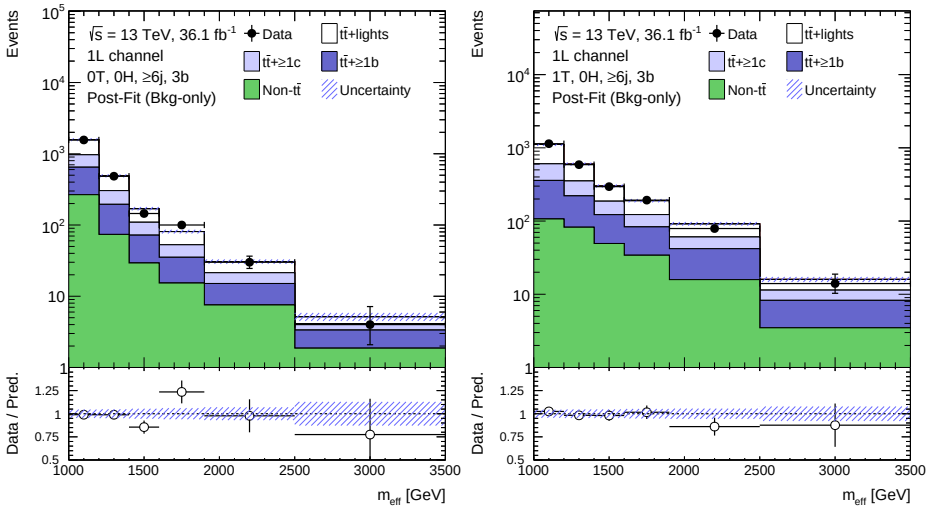

(a) (b)

Figure 10.10: Predicted and observed m_{eff} distributions in the signal-depleted categories of (a) "0T, 0H, ≥6j, 3b", (b) "1T, 0H, ≥6j, 3b" after the fit to the data under the background-only hypothesis. In these categories, the whole m_{eff} spectrums are compared because of less sensitivity to signal under the looser blind cut ($S/B < 20\%$). The bottom panel shows the ratio between the data and total background prediction ("Pred.").

m_{eff} only by at most +3% in the signal-sensitive categories. The pull on the "Effective NP2" by -0.5σ affect only −1% in the signal-sensitive categories. The pull on the "JMR" by $+0.5\sigma$ affect only around +2% in the signal-sensitive categories. The effects of these uncertainties are too small to affect the background prediction as well as the signal sensitivity.

***b*-tagging uncertainties** The NPs related with the b-tagging eigen-vector of the uncertainty and b-tagging extrapolation have small shifts by -0.3σ and -0.7σ, respectively. The leading eigen-vector component of the b-tagging (B) and c-tagging (C) has -0.3σ shift, which result in a small effect by around 1.5% and 3% for 3 and ≥4b-jets categories, respectively, in $t\bar{t}$+≥1b prediction. The uncertainty corresponding to the leading b-tagging does not have a large effect on the m_{eff} shape but the normalisation, leading to anti-correlation with $t\bar{t}$+≥1b normalisation. The uncertainty of b-tagging extrapolation affects the m_{eff} shape by −1% at lowest m_{eff} increasing to around −4% at the highest m_{eff}. The shift originates from "0T, 0H, ≥6j, ≥4b" category which has enough statistics at higher p_{T}.

***tt̄*+jets modelling uncertainties** The uncertainties are constrained as expected from the fit to the Asimov dataset. These pulls are caused by $t\bar{t}$+lights in the signal-depleted categories which have high statistics. Eventually the pulls correct the m_{eff} shape of the background prediction. In the preselection, the pre-fit background prediction is overestimated for higher m_{eff} range with respect to the data as shown in Fig. 7.5. The NPs like $t\bar{t}$+lights generator correct the higher m_{eff} tail as shown in Fig 10.12 (a). Pulls of these NPs result in less events in lower m_{eff} range. In order to compensate the event yields in this range, the NP of $t\bar{t}$+lights parton shower, whose

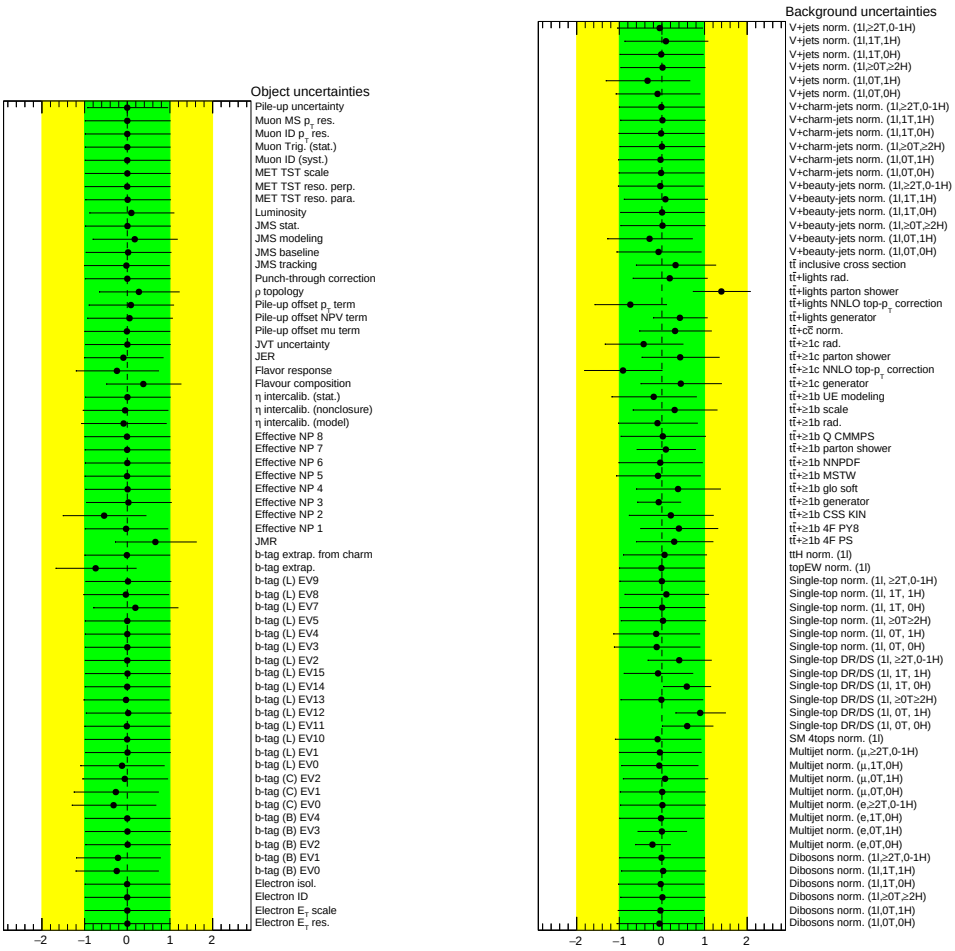

(a) (b)

Figure 10.11: Pulls and constraints on the fitted nuisance parameters related to (a) the luminosity, pileup, and physics objects and (b) background modelling in simulation and the normalisation uncertainty of multijet background by the data-driven estimation. The $t\bar{t}$+≥1b normalisation is not displayed since it is floated freely in the fit. The fit is performed to the dataset without any blind cuts. For each NP, the fitted value represents the preferred shift with respect to the prediction in a unit of its prior uncertainty, and the fitted error represents the uncertainty after the fit in a unit of its prior uncertainty.

systematic variation increases the event yields as shown in Fig 10.12 (b), is pulled largely such as 1.40 ± 0.67.

After the fit, the $t\bar{t}$+≥1b and $t\bar{t}$+≥1c normalisation factors are estimated as 1.04 ± 0.27 and 0.30 ± 0.42, respectively, which are also consistent with the fit result with the blinded data. The correlations among the NPs shown in Appendix G.6 are similar to those in the fits with the blinded data.

The event yields of the post-fit background prediction in the signal-depleted categories are shown in Table 10.1. In the categories with 3 b-jets, the $t\bar{t}$+lights background is dominant and then has around

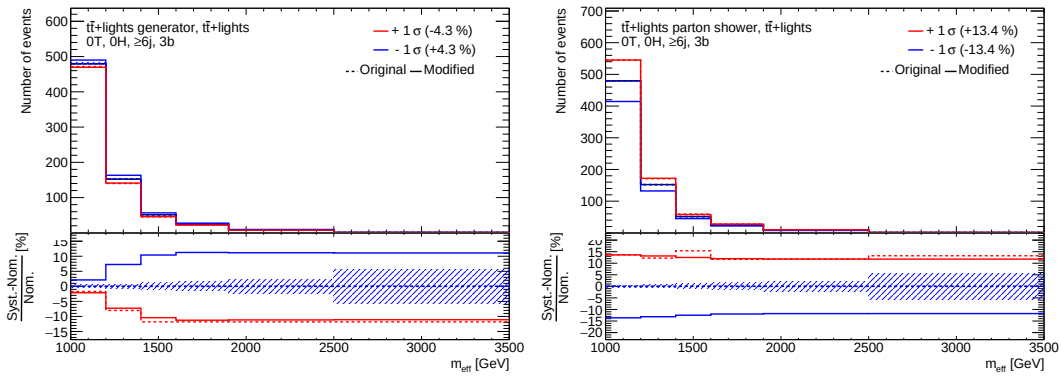

(a) (b)

Figure 10.12: (a) generator and (b) parton shower systematic uncertainties of $t\bar{t}$+lights in "0T, 0H, 6j, 3b" category. The systematic variations by $\pm 1\sigma$ are shown. The "Modified" (solid line) uncertainty is the variation of the uncertainty after smoothing the "Original" (broken lines) uncertainty. The shaded area shows the uncertainty on the $t\bar{t}$+lights prediction. The values in round brackets show the systematic effect on the total event yield in this category.

15% uncertainty on the total event yield. In the categories with ≥4 b-jets, the $t\bar{t}$+≥1b background is dominant and then has around 13% uncertainty on the total event yield. And the multijet background is negligible in the ≥4 b-jets categories. The total events of the post-fit prediction in the signal-depleted categories agree with those of the observed data within the uncertainty, which is calculated by the sum of the systematic and statistical uncertainties on the yield with the correlations among the NPs taken into account. This is the reason why the uncertainty on the total event yield is less than the quadratic sum of the individual background component. The event yields of the post-fit prediction in the validation regions shown in Appendix G.6 also agree with those of the data within the uncertainties.

The event yields of the post-fit background prediction in the signal sensitive categories are shown in Table 10.2. The dominant background component is $t\bar{t}$+≥1b in the categories with ≥4 b-jets as expected. The multijet background is negligible even in the categories with 3 b-jets. In most of the categories, the predicted yields after the fit agree with those of the data within their uncertainties. In "≥0T, ≥2H, ≥6j, ≥4b" category, the observed yield slightly exceeds the prediction. In order to verify the excess, it is necessary to compare the m_{eff} distributions between the data and prediction.

The m_{eff} distributions of the data and post-fit prediction in the sensitive categories are shown in Fig. 10.13. In general, the prediction agrees with the data within 2σ of its uncertainty. In "≥0T, ≥2H, ≥6j, ≥4b" category, the excess by around 2σ is seen in the lowest bin. This contributes to the slight excess of the event yield in this caegory. Since the lowest bin ranges m_{eff} up to only 1.3 TeV, where the signal events are not expected to distribute a lot as shown in Fig 7.6, it is not related to the signal events. Before the fit, the data exceeds by around 2σ of the total uncertainty without any constraints as shown in Fig. F.13 (h). Therefore, the excess is not explained by the expected total uncertainty. This excess can be due to the statistical fluctuation. Especially, the last bins for

Table 10.1: Predicted and observed event yields in the signal-depleted categories. The background prediction is shown after the fit to the data under the background-only hypothesis. The uncertainties are calculated by the sum in quadrature of the statistical and systematic uncertainties with the correlations among the nuisance parameters taken into account.

	0T, 0H, ≥6j, 3b	0T, 0H, ≥6j, ≥4b	0T, 1H, ≥6j, 3b
$t\bar{t}$ + lights	908.40 ± 131.20	51.96 ± 14.57	257.10 ± 38.76
$t\bar{t}+ \geq 1c$	502.15 ± 181.87	65.48 ± 24.50	150.41 ± 54.52
$t\bar{t}+ \geq 1b$	579.89 ± 96.76	246.05 ± 28.70	170.95 ± 29.51
$t\bar{t}V$	39.47 ± 6.78	10.95 ± 2.10	12.59 ± 2.21
$t\bar{t}H$	21.74 ± 2.79	12.05 ± 1.95	10.66 ± 1.31
W+light-jets	0.67 ± 0.47	0.01 ± 0.01	0.16 ± 0.11
W+≥1c+jets	9.90 ± 4.91	0.42 ± 0.23	2.39 ± 1.20
W+≥1b+jets	79.67 ± 33.45	9.17 ± 4.06	22.75 ± 9.66
Z+light-jets	0.08 ± 0.06	0.00 ± 0.00	0.02 ± 0.02
Z+≥1c+jets	1.11 ± 0.54	0.05 ± 0.03	0.25 ± 0.13
Z+≥1b+jets	14.07 ± 6.18	1.85 ± 0.86	3.19 ± 1.55
Single top	99.64 ± 24.88	15.17 ± 4.09	16.78 ± 4.91
Dibosons	12.21 ± 6.25	2.03 ± 1.15	2.59 ± 1.39
Multijet	77.12 ± 46.68	28.90 ± 15.32	51.82 ± 25.18
$t\bar{t}t\bar{t}(SM)$	4.29 ± 1.30	3.44 ± 1.09	1.60 ± 0.49
Total	2350.41 ± 98.56	447.52 ± 22.92	703.25 ± 32.48
Data	2325	454	691

	0T, 1H, ≥6j, ≥4b	1T, 0H, ≥6j, 3b	1T, 0H, ≥6j, ≥4b
$t\bar{t}$ + lights	13.66 ± 3.91	995.08 ± 152.18	55.05 ± 15.18
$t\bar{t}+ \geq 1c$	20.10 ± 7.47	472.67 ± 172.59	66.46 ± 24.34
$t\bar{t}+ \geq 1b$	73.82 ± 9.55	542.88 ± 91.54	245.48 ± 29.81
$t\bar{t}V$	3.35 ± 0.67	47.10 ± 8.07	12.32 ± 2.33
$t\bar{t}H$	6.85 ± 1.06	28.31 ± 3.67	16.44 ± 2.64
W+light-jets	0.00 ± 0.00	0.40 ± 0.29	0.01 ± 0.01
W+≥1c+jets	0.11 ± 0.06	6.17 ± 3.00	0.29 ± 0.16
W+≥1b+jets	2.72 ± 1.22	60.73 ± 26.24	8.72 ± 4.21
Z+light-jets	0.00 ± 0.00	0.06 ± 0.04	0.00 ± 0.00
Z+≥1c+jets	0.01 ± 0.01	0.68 ± 0.34	0.03 ± 0.02
Z+≥1b+jets	0.30 ± 0.15	8.03 ± 3.54	1.02 ± 0.48
Single top	2.81 ± 1.27	64.41 ± 17.01	11.07 ± 3.33
Dibosons	0.21 ± 0.15	8.36 ± 4.20	1.04 ± 0.56
Multijet	30.14 ± 10.90	59.49 ± 33.70	0.00 ± 0.00
$t\bar{t}t\bar{t}(SM)$	1.25 ± 0.40	6.07 ± 1.84	5.05 ± 1.60
Total	155.33 ± 12.24	2300.43 ± 82.51	422.99 ± 22.01
Data	144	2309	428

Table 10.2: Predicted and observed event yields in the signal sensitive categories. The background prediction is shown after the fit to the data under the background-only hypothesis. The uncertainties are calculated by the sum in quadrature of the statistical and systematic uncertainties with the correlations among the nuisance parameters taken into account.

	1T, 1H, ≥6j, 3b	1T, 1H, ≥6j, ≥4b	≥2T, 0-1H, ≥6j, 3b
$t\bar{t}$ + lights	128.80 ± 24.18	7.09 ± 2.20	141.32 ± 35.36
$t\bar{t}+ \geq 1c$	68.49 ± 26.07	9.58 ± 3.68	74.78 ± 31.57
$t\bar{t}+ \geq 1b$	76.99 ± 15.43	36.05 ± 6.65	90.44 ± 19.90
$t\bar{t}V$	7.61 ± 1.37	1.95 ± 0.40	10.31 ± 1.78
$t\bar{t}H$	6.42 ± 0.81	4.09 ± 0.63	5.28 ± 0.74
W+light-jets	0.04 ± 0.03	0.00 ± 0.00	0.07 ± 0.05
W+≥1c+jets	1.07 ± 0.60	0.05 ± 0.03	1.26 ± 0.68
W+≥1b+jets	7.90 ± 3.76	0.79 ± 0.53	8.70 ± 4.16
Z+light-jets	0.01 ± 0.01	0.00 ± 0.00	0.01 ± 0.01
Z+≥1c+jets	0.08 ± 0.05	0.00 ± 0.00	0.17 ± 0.11
Z+≥1b+jets	0.81 ± 0.60	0.07 ± 0.06	1.24 ± 0.61
Single top	12.62 ± 4.33	1.89 ± 0.74	9.95 ± 3.39
Dibosons	0.96 ± 0.52	0.16 ± 0.12	2.02 ± 1.15
Multijet	0.00 ± 0.00	0.00 ± 0.00	3.58 ± 4.90
$t\bar{t}t\bar{t}(SM)$	1.31 ± 0.40	1.14 ± 0.36	2.80 ± 0.85
Total	313.11 ± 14.45	62.86 ± 5.52	351.93 ± 19.99
Data	331	60	353

	≥2T, 0-1H, ≥6j, ≥4b	≥0T, ≥2H, ≥6j, 3b	≥0T, ≥2H, ≥6j, ≥4b
$t\bar{t}$ + lights	8.61 ± 3.04	26.17 ± 4.61	1.37 ± 0.46
$t\bar{t}+ \geq 1c$	11.63 ± 4.97	16.67 ± 6.26	2.29 ± 0.93
$t\bar{t}+ \geq 1b$	46.81 ± 9.28	19.03 ± 3.39	7.96 ± 1.43
$t\bar{t}V$	2.67 ± 0.52	1.64 ± 0.30	0.46 ± 0.10
$t\bar{t}H$	3.17 ± 0.58	1.85 ± 0.24	1.26 ± 0.20
W+light-jets	0.00 ± 0.00	0.01 ± 0.01	0.00 ± 0.00
W+≥1c+jets	0.06 ± 0.03	0.17 ± 0.14	0.01 ± 0.01
W+≥1b+jets	1.35 ± 0.71	2.77 ± 1.40	0.70 ± 0.52
Z+light-jets	0.00 ± 0.00	0.00 ± 0.00	0.00 ± 0.00
Z+≥1c+jets	0.01 ± 0.01	0.02 ± 0.01	0.00 ± 0.00
Z+≥1b+jets	0.14 ± 0.08	0.43 ± 0.44	0.06 ± 0.04
Single top	1.54 ± 0.63	2.64 ± 1.30	0.32 ± 0.23
Dibosons	0.26 ± 0.16	0.21 ± 0.28	0.01 ± 0.03
Multijet	0.00 ± 0.00	0.00 ± 0.00	0.00 ± 0.00
$t\bar{t}t\bar{t}(SM)$	2.62 ± 0.83	0.27 ± 0.09	0.23 ± 0.07
Total	78.86 ± 7.64	71.89 ± 4.57	14.65 ± 1.49
Data	78	76	18

$m_{\text{eff}} > 2$ TeV are most sensitive to signals. In all categories shown in the figure, there are no excess of data there, and instead the data is observed less than the prediction by around 1σ.

In summary of the fit results with the unblinded data, the fit results about the pulls, constraints, and correlations of the NPs are consistent with the validation results of the fits with the blinded data. Unfortunately, no excess of data is observed in the high m_{eff} ranges where this analysis has the most sensitivity to the signal models considered. Therefore, as described at the beginning of this chapter, the exclusion limits on the cross section for the VLT signals and four-top-quark productions are set in Section 10.5 and 10.6, respectively.

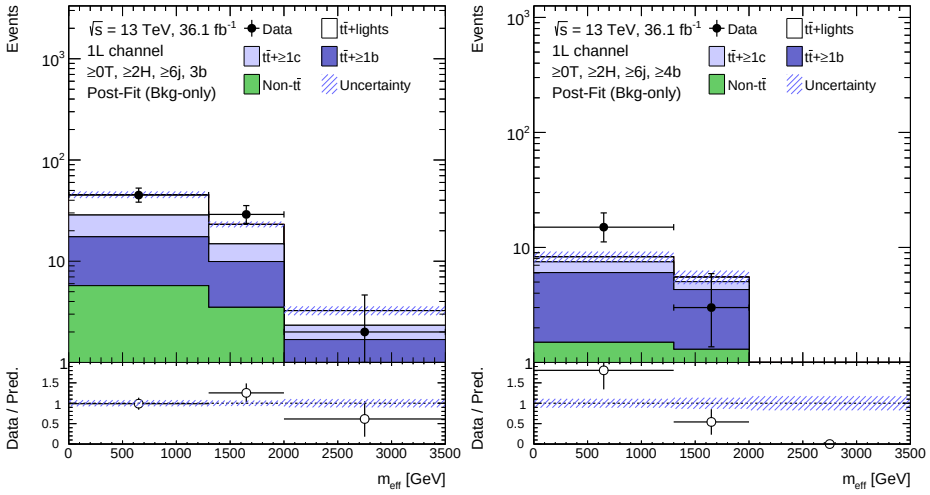

(a)

(b)

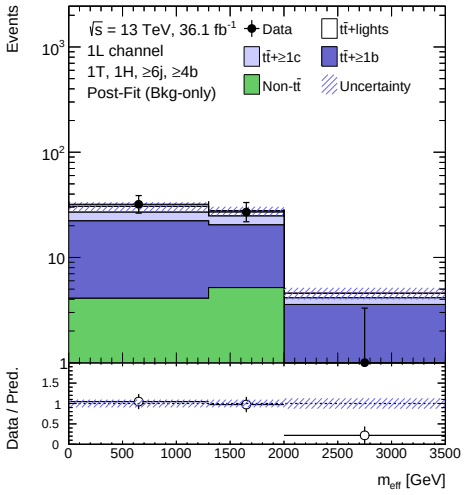

(c)

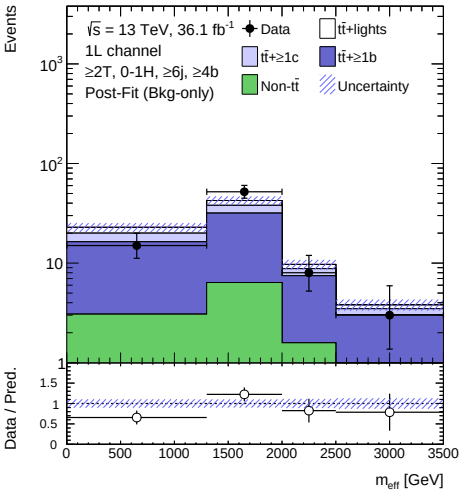

(d)

Figure 10.13: Predicted and observed m_{eff} distributions in the sensitive categories of (a) "≥0T, ≥2H, ≥6j, 3b", (b) "≥0T, ≥2H, ≥6j, ≥4b", (c) "1T, 1H, ≥6j, ≥4b", and (d) "≥ 2T, 0-1H, ≥6j, ≥4b" after the fit to the data under the background-only hypothesis. The bottom panel shows the ratio between the data and total background prediction ("Pred."). In the last bin in "≥ 0T, ≥2H, ≥6j, ≥4b" shown in the figure (b), the events with $m_{\text{eff}} > 2$ TeV are not observed in the data.

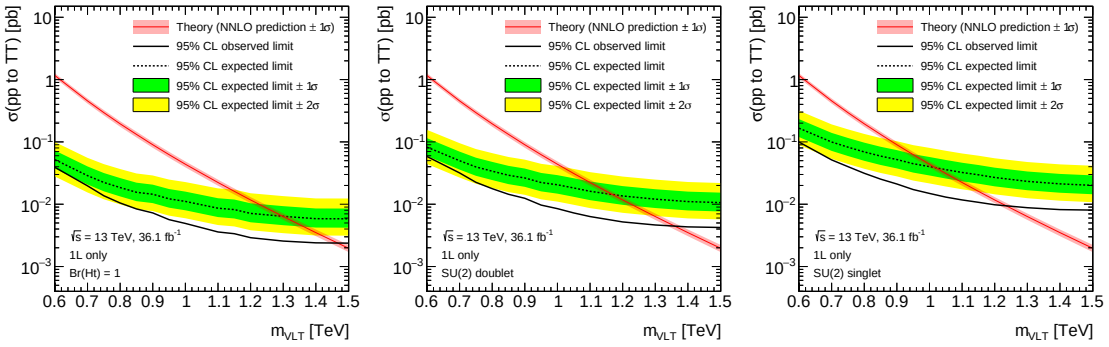

(a) (b) (c)

Figure 10.14: Observed (solid line) and expected (dashed line) upper limits on the cross section of the pair production of vector-like top quarks at 95% CL in the benchmarks of (a) BR($T \to Ht$) = 1, (b) SU(2) doublet, and (c) SU(2) singlet. The green and yellow shaded area correspond to ±1 and ±2 standard deviation around the expected limit, respectively. The red line and band show the theoretical prediction and its ±1 standard deviation uncertainty.

10.5 Cross section limits for pair production of vector-like top quark

Since no significant excess of data is observed, the upper limits on the cross section of the pair production of vector-like top quarks at 95% CL are set in the various benchmarks. The upper limits are calculated by the fit to the observed data under the signal-plus-background hypothesis. The 1-lepton channel has the best sensitivity to the case of the fixed branching ratio: BR($T \to Ht$) = 1. It also has better sensitivity to SU(2) doublet but less sensitivity to SU(2) singlet. The model dependence of the sensitivity or limits is caused by the acceptance of this analysis. For instance, the analysis requires high jet and b-jet multiplicities while the VLT decay to W boson and bottom quark results in less jet and b-jet multiplicities. The other selections such as the number of leptons, $E_{\mathrm{T}}^{\mathrm{miss}}$, heavy object taggers are optimized for the fixed branching ratio: BR($T \to Ht$) = 1.

Figure 10.14 shows the upper limits as a function of vector-like top quark mass (m_{VLT}) in the benchmarks of BR($T \to Ht$) = 1 (a), SU(2) doublet (b), and SU(2) singlet (c). The expected and observed limits are computed using the post-fit prediction and observed data, respectively. The observed limit has around 3σ deficit with regard to the expected limit, originating from the sum of less observed events than the prediction in each signal sensitive category. The systematic analysis and reason are discussed in Chapter 11. By comparing the upper limits on the cross section with the theoretical cross section, a certain range of the VLT mass can be excluded at 95% CL. For BR($T \to Ht$) = 1, the observed (expected) lower limit on the mass is set to 1.47 (1.30) TeV. For SU(2) doublet, the expected (observed) limit is set to 1.36 (1.16) TeV. For SU(2) singlet, the expected (observed) limit is set to 1.23 (1.02) TeV. The theoretical error is not taken into account in computations of these mass limits.

By varying the branching ratio, the exclusion limits on the VLT mass can be displayed in the two dimensional plane of BR($T \to Ht$) vs. BR($T \to Wb$). The observed and expected exclusion limits

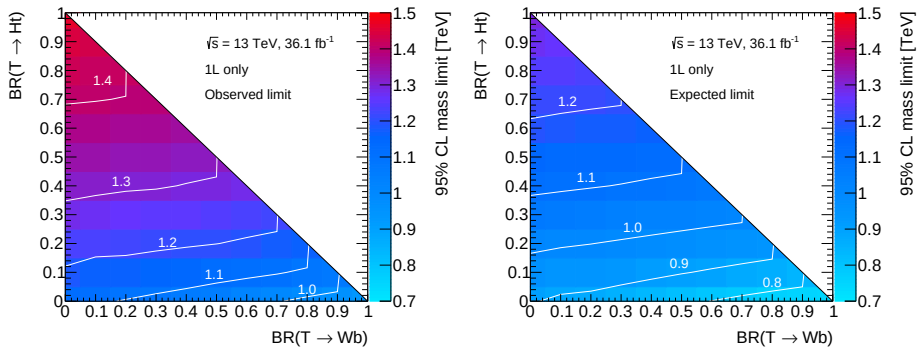

(a) (b)

Figure 10.15: (a) Observed and (b) expected lower limits on the vector-like top quark mass at 95% CL in the two dimensional plane of BR($T \to Ht$) and BR($T \to Wb$).

are shown in Fig. 10.15. From the observed data (expectation), the lower mass limits range from 0.94 (0.75) TeV to 1.47 (1.30) TeV for all possible branching ratio. The possibility of masses below 0.94 GeV is excluded for any branching ratio.

10.5.1 Overview of 0-lepton channels

The detail of 0-lepton analysis and its result are not described in this dissertation, while this dissertation shows the interpretation of the results combining 0- and 1- lepton analyses. This section briefly describes the overview of the 0-lepton analysis. The 0-lepton analysis requires the similar preselection and event categorisation as done in 1-lepton channels. The main differences are to require at least 7 jets for the search regions and to categorise events based on the kinematic variable of $m^{\mathrm{b}}_{\mathrm{T,min}}$ which is the minimum transverse mass between $E^{\mathrm{miss}}_{\mathrm{T}}$ and the one of the leading three b-jets, in addition to the same categorisation with the Higgs-tagged and top-tagged jet multiplicity. The variable allows to distinguish the signal events from $t\bar{t}$+jets background because of the kinematic difference. The same set of the validations using the data with the looser and tighter blind cuts is performed and shows good agreements between the post-fit background prediction and observed data. After fitting the MC prediction to the full data without any blind cuts, the comparison between the post-fit prediction and data shows no significant excess in data.

10.5.2 Combination of 1-lepton and 0-lepton channels

The fit is performed using both 1- and 0- lepton channels under the signal-plus-background hypothesis to obtain the upper limits on the cross section. Figure 10.16 shows the upper limits on the cross section at 95% CL for the VLT pair production as a function of the VLT mass after the combination of 0- and 1-lepton analyses. The 0-lepton analysis categorises the events by using $E^{\mathrm{miss}}_{\mathrm{T}}$, and then enhance the sensitivity to BR($T \to Zt$) = 1. Thus, the observed and expected limits are drastically

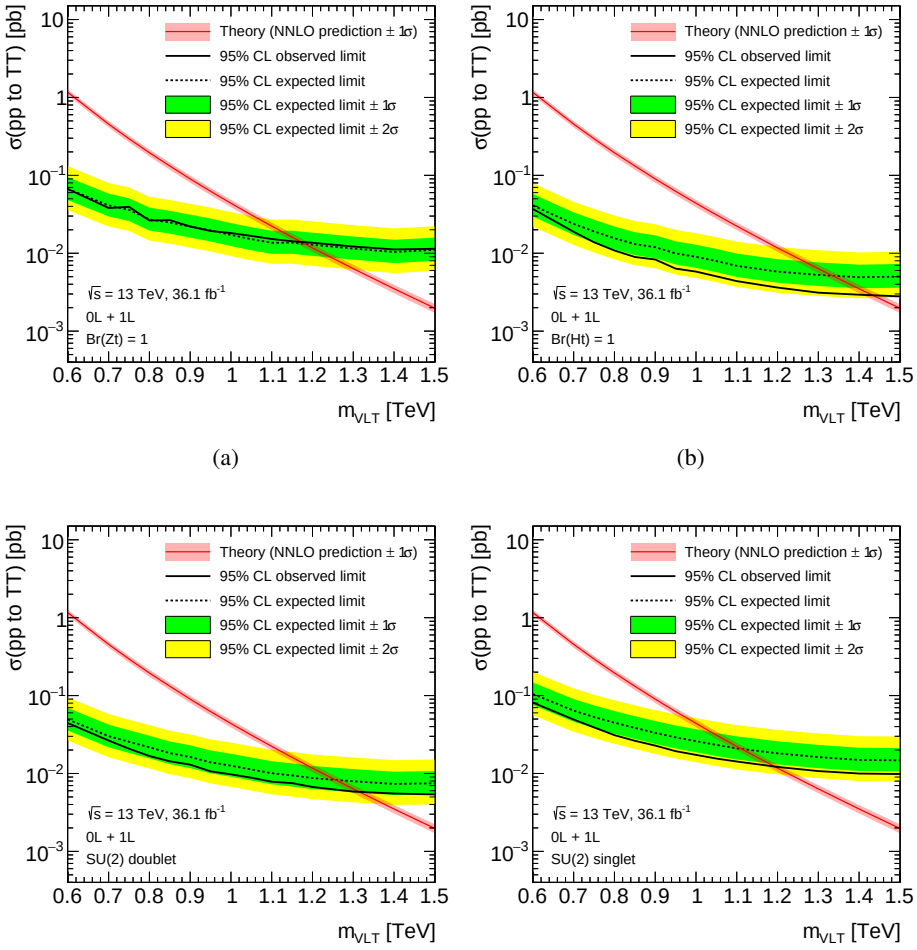

Figure 10.16: Observed (solid line) and expected (dashed line) upper limits on the cross section of the pair production of vector-like top quarks at 95% CL in the benchmarks of (a) BR($T \to Zt$) = 1, (b) BR($T \to Ht$) = 1, (c) SU(2) doublet, and (d) SU(2) singlet using both 1-lepton and 0-lepton channels. The green and yellow shaded area correspond to ±1 and ±2 standard deviation around the expected limit, respectively. The red line and band show the theoretical prediction and its ±1 standard deviation uncertainty.

improved for BR($T \to Zt$) = 1, compared to the result in only 1-lepton analysis. The expected limit is improved from that in only 1-lepton analysis by more than 20% for other benchmarks. Only in the 0-lepton analysis, the observed data has more events than the post-fit prediction, and then leads to 1 $\sim 2\sigma$ excess in the observed limits. The 1-lepton analysis has more statistics than that in the 0-lepton analysis, and then the combined observed limit is 1 $\sim 2\sigma$ lower compared to the expected limit. The limits are translated to the observed (expected) lower limits on the VLT mass of 1.43 (1.34) TeV for BR($T \to Ht$) = 1, 1.17 (1.18) TeV for BR($T \to Zt$) = 1, 1.31 (1.26) TeV for SU(2) doublet, and 1.19 (1.11) TeV for SU(2) singlet.

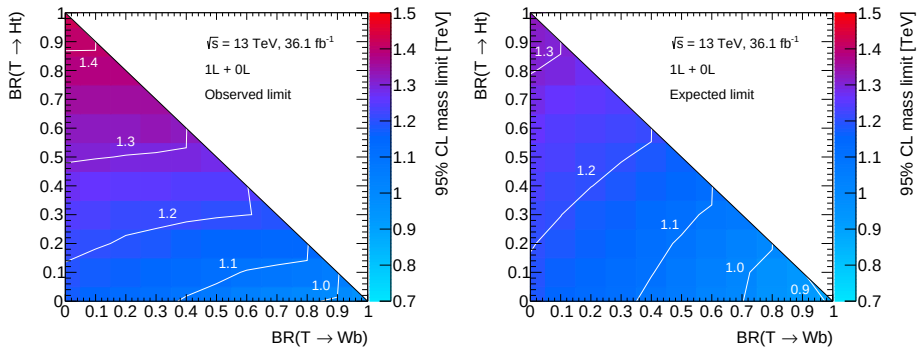

(a) (b)

Figure 10.17: (a) Observed and (b) expected lower limits on the vector-like top quark mass at 95% CL in the two dimensional plane of BR($T \to Ht$) and BR($T \to Wb$) using both 1-lepton and 0-lepton channels.

In the same way as done in the 1-lepton channel, the lower limits on the VLT mass at 95% CL are set in the two dimensional plane of BR($T \to Ht$) vs. BR($T \to Wb$) as shown in Fig. 10.17. For all the possibilities of the branching ratio, the combination improves the reach on the VLT mass, compared to the result only in 1-lepton analysis. Even after combining the 0-lepton analysis, the sensitivity for BR($T \to Wb$) = 1 is the lowest in the 2D plane because the 0-lepton channel also requires high jet and b-jet multiplicity and then results in less sensitivity to the signal events having low jet and b-jet multiplicity.

The values of the mass limits for the benchmarks are summarised in Table 10.3 together with the previous result with 13.2 fb^{-1} of the integrated luminosity [49]. Comparing the results between this analysis and the previous one, the expected limits are improved by around 150 GeV due to the introduction of the new categorisation based on the Higgs-tagged and top-tagged jet multiplicity and an increase of the integrated luminosity. As described in Section 6.5.3, the former improvement extends the expected limits by around 70 GeV. The latter improvement contributes the extension of limits by around 80 GeV.

10.6 Cross section limits for four-top production

Similarly to the case of the VLT signals, the upper limits on the cross section of the four-top-quark production are set in the various signal models. For the production in the SM, the observed (expected) upper limit on the production cross section at 95% CL is set to 53.0 (72.8) fb, corresponding to 5.7 (7.9) times the SM prediction. The expected sensitivity is improved by a factor of 2, compared to the previous search [49]. The increase of the integrated luminosity mainly helps the improvement.

In the production via an EFT with the four-top-quark contact interaction, the observed (expected) upper limit on the production cross section at 95% CL is set to 16.4 (30.9) fb. The values are stronger than the limits in case of the SM four-top-quark production because the events in this scenario contains

Table 10.3: Summary of observed (expected) lower limits on the VLT mass (in TeV) at 95% CL for the 1L and 0L channels, as well as their combination, under different benchmarks on the decay branching ratios. The corresponding limits obtained by the previous ATLAS Run 2 search (13.2 fb^{-1}) [49] are also shown.

Observed (expected) 95% CL lower limits on the VLT mass [TeV]				
Search	BR($T \to Ht$) = 1	BR($T \to Zt$) = 1	Doublet	Singlet
1L channel	1.47 (1.30)	1.12 (0.91)	1.36 (1.16)	1.23 (1.02)
0L channel	1.11 (1.20)	1.12 (1.17)	1.12 (1.19)	0.99 (1.05)
Combination	1.43 (1.34)	1.17 (1.18)	1.31 (1.26)	1.19 (1.11)
Previous ATLAS Run 2 search (13.2 fb^{-1}) [49]				
1L channel	1.18 (1.12)	0.74 (0.82)	1.06 (1.00)	0.90 (0.88)
0L channel	1.09 (1.07)	1.06 (1.01)	1.09 (1.06)	0.95 (0.89)
Combination	1.20 (1.16)	1.10 (1.04)	1.16 (1.11)	1.02 (0.96)

harder top quarks and then result in higher m_{eff} values where the backgrounds are depleted. The upper limits are interpreted into the free parameter of the model: $|C_{4t}|/\Lambda^2 < 1.7$ (2.3) TeV^{-2}.

In 2UED-RPP scenario, Figure 10.18 shows the upper limit on the four-top-quark production cross section as a function of KK mass m_{KK} for the symmetric case $\xi = R_4/R_5 = 1$ and production by tier(1,1) alone. The observed (expected) limit on the cross section times the branching ratio is set to around 1 (2) fb at $m_{\text{KK}} = 1.8$ TeV. The observed (expected) limit is translated into the lower limit on the KK mass of 1.80 (1.73) TeV by comparison with the LO theoretical cross section. The cross section limits are improved by a factor of 3 from previous search [49] due to the increase of the integrated luminosity and introduction of the Higgs boson and top quark taggers.

The cross section limits for 2UED-RPP scenario are much smaller than that for the EFT scenario. In the EFT scenario, the momentum of top quarks are lower than that in 2UED-RPP, and hence top quarks cannot be identified with the top quark tagger. Then, the signal events are broadly distributed in the categories with different top-tagged jets multiplicity. Also the m_{eff} distribution expected in the EFT scenario is lower than that in 2UED-RPP. On the other hand, the signal events in 2UED-RPP scenario contain top quarks with higher momentum and hence are predominantly distributed at higher m_{eff} in the categories with at least two top-tagged jets. The difference between the two signal models is shown in Fig. 10.19. Assuming that the EFT scenario has the same cross section as the 2UED-RPP, "≥2T, 0-1H, ≥6j, ≥4b" category is most sensitive for both signals[2]. The highest m_{eff} bin is most sensitive to both signals, but the significance for the EFT scenario at the bin is much less than that for 2UED-RPP due to differences of the m_{eff} shape and the yields. The differences of the signal models cause the different cross section limits[3].

[2] "≥2T, 0-1H, ≥6j, 3b" category is also most sensitive to 2UED-RPP model. The significances for both categories are similar.

[3] Even if the cross section for 2UED-RPP scenario is set to be 16 fb, which corresponds to the cross section limit for the

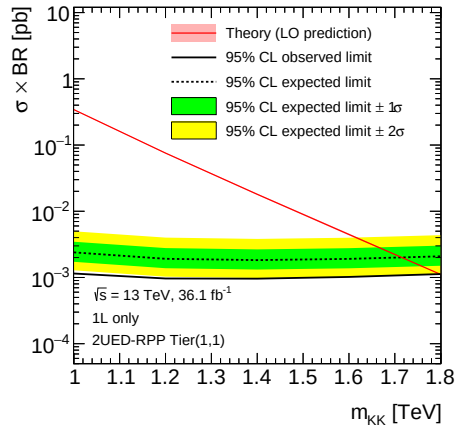

Figure 10.18: Observed (solid line) and expected (dashed line) upper limits on the cross section times branching ratio of the four-top-quark production at 95% CL in 2UED-RPP scenario as a function of KK mass m_{KK} for the symmetric case $\xi = R_4/R_5 = 1$ and production by tier(1,1) alone. The m_{KK} corresponds to the compact scale of the extra dimensions. The green and yellow shaded area correspond to ±1 and ±2 standard deviation around the expected limit, respectively. The red line and band show the theoretical prediction and its ±1 standard deviation uncertainty.

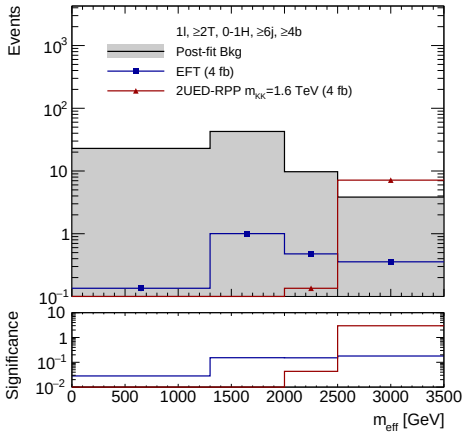

Figure 10.19: Expected m_{eff} distributions for post-fit background prediction (gray), EFT signal model (blue), and 2UED-RPP (red) in "≥2T, 0-1H, ≥6j, ≥4b" category. The EFT signal is normalised to the cross section of 4 fb, which is equivalent with the theoretical prediction of 2UED-RPP with the KK mass of 1.6 TeV.. The bottom panel shows the significance for each signal model, computed as $\sqrt{2((s+b)\ln(1+s/b)-s)}$, where s and b are the number of event in a bin for the signal and background, respectively.

EFT, the same result is obtained.

11 Discussion

In Chapter 10, no excess of the data is observed, and then the upper limits on the cross section for various signal models are set. The limits in both only 1-lepton channel and combined channel of 1- and 0-lepton are consistent with the data within three standard deviations of their expected uncertainty. However, the discrepancy by around 3σ on the limits in only 1-lepton channel may be caused by other potential issues than statistical fluctuations. In this chapter, to investigate potential issues, the systematic analyses for the 3σ discrepancies are carried out and summarised. The discrepancy on the limits can be caused by the fact that the data is observed less than the post-fit prediction at the last bins in the most sensitive categories as shown in Fig. 10.13. After the categories causing the discrepancy are identified, the detailed studies are performed.

11.1 Categories causing the discrepancy

In order to identify the categories which cause the discrepancy, a set of the cross section limits is calculated in the situation where the post-fit background prediction (the Asimov data) is used instead of the observed data in a category. By comparing the nominal and an alternative limits, the effect of the deficits of data on the cross section limits can be quantitatively computed. The categories considered here are listed below:

- "≥0T, ≥2H, ≥6j, 3/≥4b"
- "1T, 1H, ≥6j, 3/≥4b"
- "≥2T, 0-1H, ≥6j, 3/≥4b"

Figure 11.1 shows the observed upper limits on the cross section divided by the expected limits as a function of the VLT mass in case of the SU(2)-doublet signal. The "Nominal" limits (black) use the observed data for all SR categories, which correspond to the ones shown in Fig. 10.14. Thus, the "Nominal" limits show the 3σ discrepancy with respect to the expected limits. For instance, the "blind 0T2H6j4b" limits (purple) are computed using the post-fit prediction (the Asimov data) for "≥0T, ≥2H, ≥6j, ≥4b" category and the observed data for the other categories. Therefore, the difference between the "Nominal" and "blind 0T2H6j4b" limits is caused by the deviation of the data from the post-fit prediction in the category. In "≥0T, ≥2H, ≥6j, ≥4b" category, no event is observed at the last m_{eff} bin as shown in Fig. 10.13 (b). This deficit of events is found to affect the cross section limits by around 0.5σ from Fig. 11.1 (a).

According to the Fig. 11.1, the discrepancy for each category is found to affect the final limit by at most one standard deviation. Especially the categories having the largest difference from the "Nominal" limits are listed below:

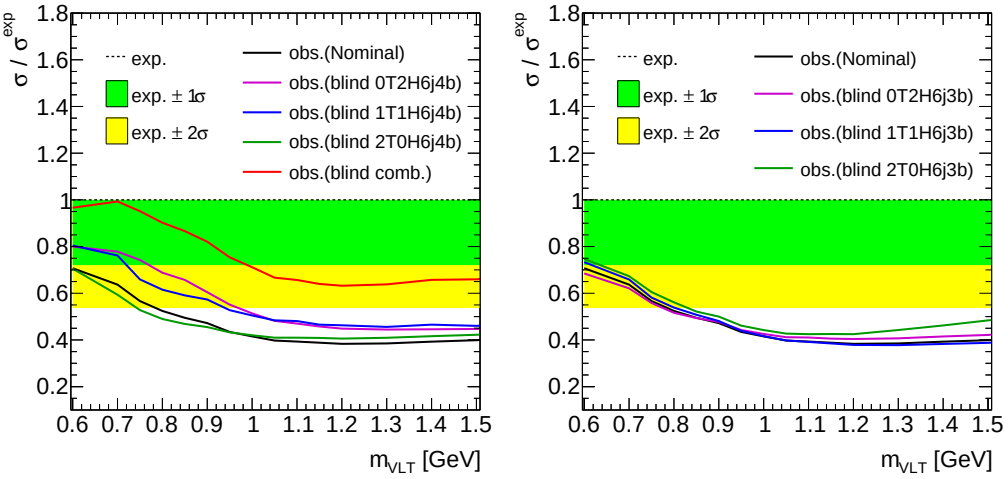

(a) (b)

Figure 11.1: Observed upper limits on the cross section divided by the expected limits as a function of the VLT mass, compared to several cases in which the Asimov data (post-fit prediction) for a SR category is used instead of the observed data. "Nominal" limit uses the observed data for all SR categories, which is same as the final limit. Another limit is computed using the Asimov data ("blind"), which is equivalent with the post-fit prediction, for the SR category and the observed data for the other categories. The difference between "Nominal" and another shows the effect of deficits of data on the cross section limits. Figure (a) and (b) show the effect on the cross section limits with using the Asimov data in each ≥4 and 3 *b*-jets category, respectively. In the case of "blind comb." (red) shown in the figure (a), the Asimov data is used for the three categories having the largest differences from the "Nominal". The signal used here is SU(2)-doublet VLT.

- ≥0T, ≥2H, ≥6j, ≥4b
- 1T, 1H, ≥6j, ≥4b
- ≥2T, 0-1H, ≥6j, 3b

These categories largely affect the observed cross section limits, and hence are named *the largest impact category group* in this chapter for the convenience. The "≥0T, ≥2H, ≥6j, ≥4b" and "1T, 1H, ≥6j, ≥4b" categories contribute to the 3σ discrepancy by less than one standard deviation as expected from the deficits of data at the highest m_{eff} bin shown in Figs. 10.13 (b) and (c), respectively. The "≥2T, 0-1H, ≥6j, 3b" category affects the discrepancy by less than one standard deviation especially for the higher mass range. This is caused by the deficit of data at the highest m_{eff} bins with respect to the post-fit prediction in the category. In the other categories, the post-fit prediction agrees with the data, hence the difference of the limits between "Nominal" and another is small. The limits using the Asimov data for *the largest impact category group* (red line in Fig. 11.1 (a)) are consistent with the expected limits with in two standard deviations. This result indicates that all the small contributions for each category result in the 3σ discrepancy in total. To understand the details, the systematic studies for the categories are performed as follows.

Table 11.1: Configuration of the m_{eff} binning. The neighboring bins shown in bold fonts are merged into one m_{eff} bin. The binning after merging is used in the test for validity of the asymptotic approximation.

Category	Before	After
"0T, 1H, ≥6j, 3b"	[1000,1100,1300,1700,2100,**2500**,3500]	[1000,1100,1300,1700,2100,3500]
"0T, 1H, ≥6j, ≥4b"	[1000,1300,1700,**2100**,3500]	[1000,1300,1700,3500]
"≥0T, ≥2H, ≥6j, ≥4b"	[0,1300,**2000**,3500]	[0,1300,3500]
"≥2T, 0-1H, ≥6j, ≥4b"	[0,1300,2000,**2500**,3500]	[0,1300,2000,3500]
"1T, 1H, ≥6j, ≥4b"	[0,1300,**2000**,3500]	[0,1300,3500]

Table 11.2: Comparison of the cross section limits with two methods: asymptotic approximation and pseudo experiments. The pseudo-experiments generated with toy MC by 100,000 times. Only the statistical uncertainty is taken into account in the limits. The values shown here is the observed and expected cross section limits (σ^{lim}) divided by the theoretical cross section (σ^{th}). For the expected limits, the $\pm 1\sigma$ errors are shown.

	Observed limit ($\sigma^{\text{lim}}/\sigma^{\text{th}}$)	Expected limit ($\sigma^{\text{lim}}/\sigma^{\text{th}}$)
Asymptotic	0.190	$0.376^{+0.140}_{-0.104}$
Pseudo Exp.	0.185	$0.374^{+0.140}_{-0.100}$

11.2 Validity of the asymptotic approximation

As seen in the previous section, the deficits in the highest m_{eff} bins affect the limits by around one standard deviation in each category. But still there is more than 1σ deficit for the mass range of $m_{\text{VLT}} > 1$ TeV. As described in Chapter 9, the limits are computed with the asymptotic approximation. The approximation is known to be invalid in case of small statistics [192]. This section discusses the validity of the asymptotic approximation. As shown in Fig. 10.13, the last m_{eff} bins are expected to have a few events in both the data and simulation. In order to check the validity of the approximation, the results of the fit with the several bins merged are shown in this section.

In the test, the highest m_{eff} bins for the categories with $\sim 1\sigma$ deficit are merged. The configuration of the bins is summarised in Table 11.1. The fit is performed with the same conditions as the final result except the binning. Figure 11.2 shows the result of the observed limits. The limits with the merged bins are found to be consistent with the final limit within 10%. It indicates that the asymptotic approximation is valid in the analysis.

To cross check the fit results, the exclusion limits are computed by the pseudo-experiments generated with toy MC by 100,000 times. Only the statistical uncertainty is taken into account in the limits. The signal strength is scanned for the range from 0.1 to 0.5 by a step of 0.1. The results are summarised in Table 11.2. Since the result with the different method is consistent with the asymptotic method, it is concluded that the deficit is not caused by the asymptotic approximation.

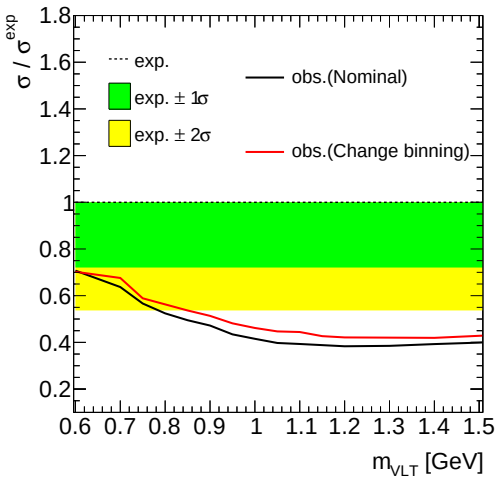

Figure 11.2: Observed upper limits on the cross section divided by the expected limits as a function of the VLT mass, comparing to the fit result with changing the binning summarised in Table 11.1. The signal used here is SU(2)-doublet VLT.

11.3 TRF Closure

If the background expectation predicted with TRF method has a non-closure to the one predicted in the ordinary way ("Direct tagging"), this can be a bias for the background prediction. As described in Section 5.4, both methods have consistency on the background prediction. Especially, for *the largest impact category group*, Figs. 11.3 show the m_{eff} distributions comparing both TRF and Direct tagging method. It assures that the TRF method is consistent with the Direct tagging method, and then TRF method does not affect the deficit.

11.4 Fit with combined categories

There is a possibility that some systematic uncertainty missing in this analysis causes the small deficit in the categories. In order to check systematic effects on the m_{eff} distributions with large statistical power, the fit is performed with combining categories as following:

- "0T, 1H, 5/≥6j, 3/≥4b" + "1T, 0H, 5/≥6j, 3/≥4b"
  → "1THex, 5/≥6j, 3/≥4b"

- "≥0T, ≥2H, 5/≥6j, 3/≥4b" + "1T, 1H, 5/≥6j, 3/≥4b" + "≥2T, 0-1H, 5/≥6j, 3/≥4b"
  → "2THin, 5/≥6j, 3/≥4b"

The merging processes are applied for all the SR and VR categories, hence there are six categories in each SR and VR. The other conditions in the fit are the same as the final limits. If there are missing uncertainties, more significant discrepancies are expected than the results before merging.

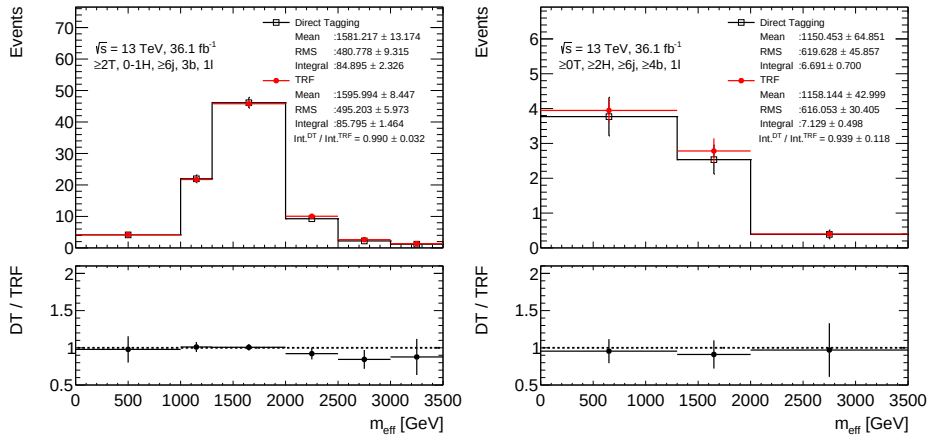

Figure 11.3: m_{eff} distributions in *the largest impact category group* which includes (a) "≥2T, 0-1H, ≥6j, 3b", (b) "≥0T, ≥2H, ≥6j, ≥4b", and (c) "1T, 1H, ≥6j, ≥4b", and (d) "≥2T, 0-1H, ≥6j, ≥4b" category comparing between the Direct tagging (black) and TRF (red) for $t\bar{t}$+≥1b background.

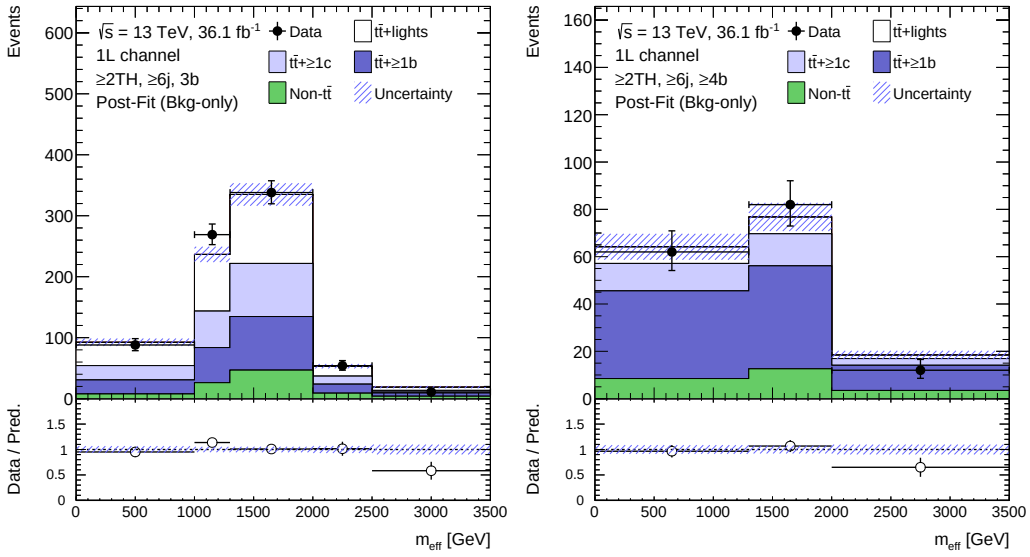

Figure 11.4: Post-fit predicted and observed m_{eff} distributions in the "2THin, ≥6j" categories. The categories with exact 3 and at least 4 b-jets are shown in (a) and (b), respectively. The bottom panel shows the ratio between the data and total background prediction ("Pred.").

The post-fit m_{eff} distributions are shown in Fig. 11.4. In the last m_{eff} bins, the post-fit prediction is consistent with the data and the results before merging. The result indicates that this analysis does not miss any large systematic uncertainty.

In the 1-lepton channel, the categories with 2 b-jets are not used in neither SR nor VR. These categories are dominated with the $t\bar{t}$+lights background. In order to check the mis-modelling of the background, the fit is performed with adding the "2b" categories as validation regions and combining the categories described above. If there are problems in the modelling and uncertainty of the $t\bar{t}$+lights background, the significant deficit of data with respect to the post-fit prediction should be seen in the "2THin, ≥6j, 2b" category. Figure 11.5 shows the post-fit m_{eff} distribution in "2THin, ≥6j, 2b" category. The post-fit prediction is found to be consistent with the data within its uncertainty. The result means that the modelling and its uncertainty of the $t\bar{t}$+lights background are described well and properly propagated into the most sensitive categories. Therefore the modelling of $t\bar{t}$+lights background is unlikely to be a cause of the discrepancy.

11.5 Correlation scheme of the systematic uncertainties

In this section, further tests to check the potential background mis-modelling are performed with different correlation schemes for the background modelling uncertainties. Two kinds of correlation schemes are tested:

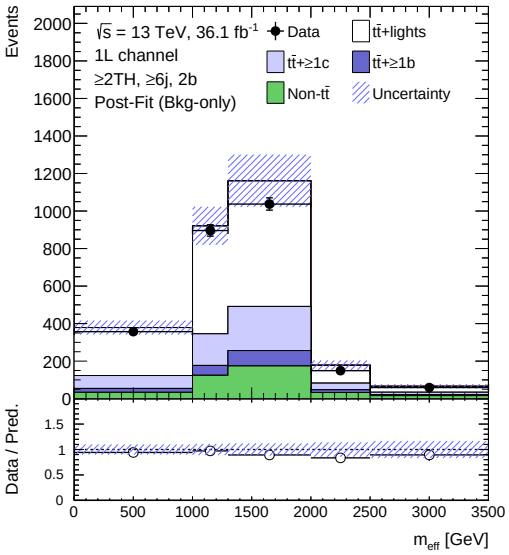

Figure 11.5: Post-fit predicted and observed m_{eff} distribution in "2THin, ≥6j, 2b" category where the $t\bar{t}$+lights background (white) is dominant. The category is used as VR in the fit.

Scheme A: Correlate $t\bar{t}$+jets modelling uncertainties across all the $t\bar{t}$+jets subprocesses.
The generator, radiation, and parton shower uncertainties for the $t\bar{t}$+jets backgrounds are dominant components for the high m_{eff} range as shown in Fig 10.8. By default, these uncertainties are taken into account in the fit assuming that they are uncorrelated across the subprocesses of $t\bar{t}$+≥1b , $t\bar{t}$+≥1c , and $t\bar{t}$+lights. On the other hand, in this scheme, they are assumed to be correlated across all the subprocesses. This scheme allows to check whether the pulls for $t\bar{t}$+lights are propagated to predictions of $t\bar{t}$+≥1c and $t\bar{t}$+≥1c, and then whether the background prediction in the last m_{eff} bins is corrected or not. If the uncertainties for $t\bar{t}$+≥1c and $t\bar{t}$+≥1b are wrong, the corresponding pulls and the background prediction are expected to change.

Scheme B: Correlate the DR/DS uncertainty for single-top background across all the Higgs-tagged and top-tagged jets categories. The diagram subtraction (DS) method predicts much less single-top background especially for the high m_{eff} range. This uncertainty is taken into account in the fit assuming non-correlation across all the Higgs-tagged and top-tagged jets categories. In this scheme, the corresponding pulls in the categories with higher statistics are propagated into *the largest impact category group*. Therefore, if the correlation scheme for this uncertainty is wrong, the corresponding pulls are expected to change and the post-fit prediction agree with data better.

In addition, the combination of the scheme A and B ("Scheme A+B") is also checked.

Figure 11.6 shows the m_{eff} distributions in "1T, 1H, ≥6j, ≥4b" category for the nominal and alternative correlation schemes. The post-fit predictions with the schemes A, B, and A+B are found to be consistent with the nominal scheme. The post-fit predictions in the other categories are also consistent

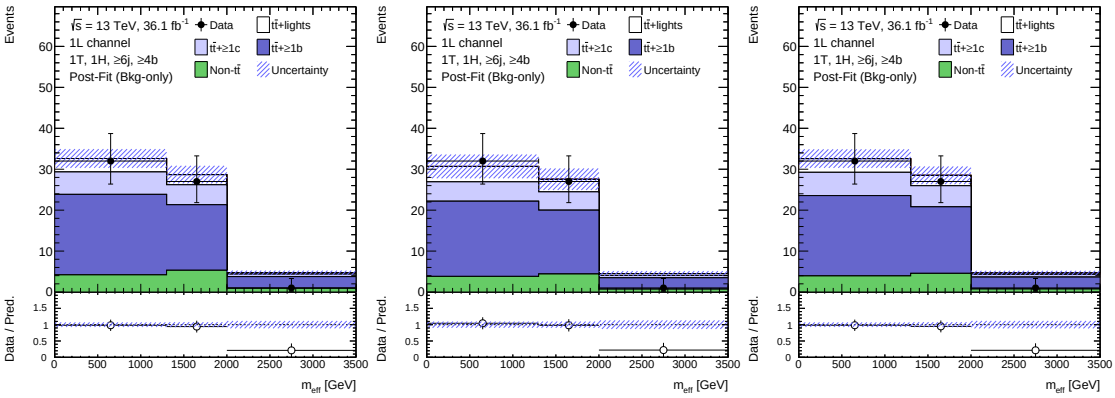

(a) (b) (c)

Figure 11.6: Post-fit predicted and observed m_{eff} distribution in "1T, 1H, ≥6j, ≥4b" category with (a) the correlation scheme A, (b) scheme B, and (c) combination of scheme A and scheme B.

with the nominal scheme. From the results, the correlation scheme for these uncertainties are unlikely to be a cause of the discrepancy on the limits.

11.6 Post-fit kinematic variables at the preselection level

In order to confirm which kinematic variable affects the discrepancy, the kinematic variables at the preselection level after the fit are checked in this section. The preselection regions are not used for the fit, but used as the validation regions. All the systematic uncertainties in the preselection are propagated from the search regions. As the cut of $m_{\text{eff}} > 1$ TeV is applied for most categories, the same cut is required at the preselection just for the consistency.

Figure 11.7 shows the leading jet p_{T}, $E_{\text{T}}^{\text{miss}}$, electron p_{T}, and muon p_{T} distributions at the preselection after the fit. In general, the post-fit predictions on the all the kinematic variables agree with the data within two standard deviation of their uncertainty. Especially for the $E_{\text{T}}^{\text{miss}}$, electron p_{T}, and muon p_{T}, the background prediction is consistent with the data within one standard deviation. The results indicate that these variables are modelled well. For the leading jet p_{T}, small systematic deficits are seen for $p_{\text{T}} > 500$ GeV. In the next section, this is investigated.

11.7 Reweighing leading jet p_{T}

In the previous section, the tendency of the small deficits for high leading jet p_{T} range is seen at the preselection after the fit. This may be a cause of the discrepancy on the limits. In this section, the following items are investigated:

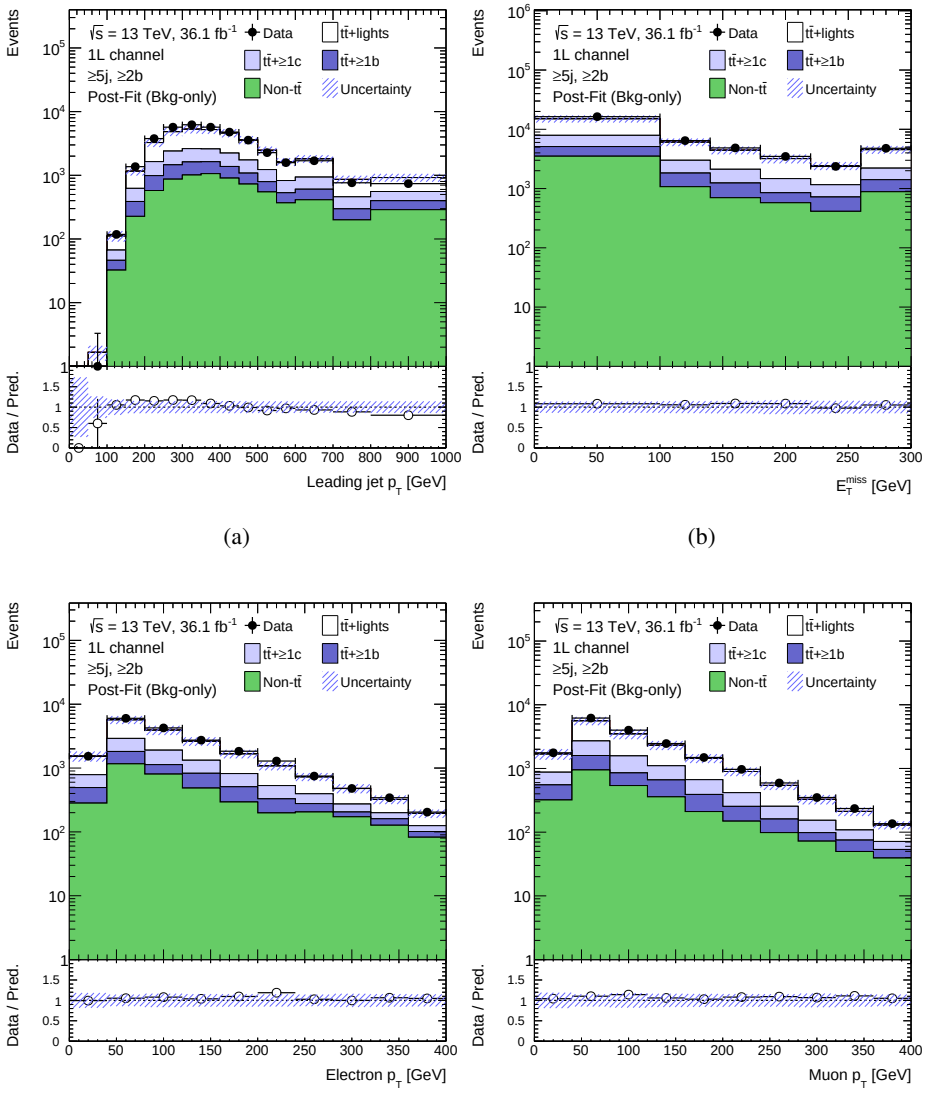

Figure 11.7: Post-fit predicted and observed kinematic variables distribution at the preselection. (a) leading jet p_{T}, (b) $E_{\mathrm{T}}^{\mathrm{miss}}$, (c) electron p_{T}, and (d) muon p_{T} are shown. In these plots, the cut of $m_{\mathrm{eff}} > 1$ TeV is applied for the consistency with the other fit results.

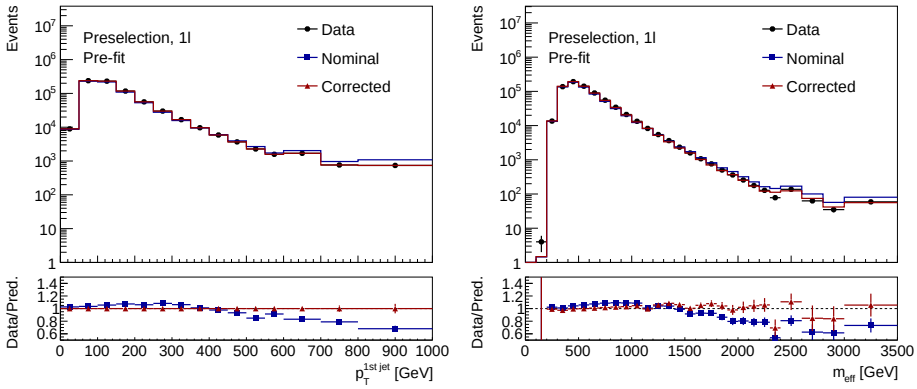

(a) (b)

Figure 11.8: (a) Leading jet p_{T} and (b) m_{eff} distributions at the preselection before the fit. "Nominal" (blue) represents the nominal background prediction, and "Corrected" (red) represents the background prediction corrected with the correction factor $w^{\mathrm{corr}}(p_{\mathrm{T}}^{\mathrm{1st.jet}})$.

1. Correlation between the leading jet p_{T} and m_{eff} at the preselection.
2. Correlation between the leading jet p_{T} at the preselection and m_{eff} in *the largest impact category group*.
3. Whether the tendency is covered by the systematic uncertainties.

In order to check the first item, the background predictions are weighted to correct the leading jet p_{T} distribution to the data with the correction factor $w^{\mathrm{corr}}(p_{\mathrm{T}}^{\mathrm{1st.jet}})$ defined by:

$$w^{\mathrm{corr}}(p_{\mathrm{T}}^{\mathrm{1st.jet}}) = \frac{N^{\mathrm{data}}(p_{\mathrm{T}}^{\mathrm{1st.jet}}) - N^{\mathrm{Multijet}}(p_{\mathrm{T}}^{\mathrm{1st.jet}})}{N^{\mathrm{MC}}(p_{\mathrm{T}}^{\mathrm{1st.jet}})}, \tag{11.1}$$

where $N^{\mathrm{data}}(p_{\mathrm{T}}^{\mathrm{1st.jet}})$ represents the number of events for the leading jet p_{T} value ($p_{\mathrm{T}}^{\mathrm{1st.jet}}$) in the data, "Multijet" represents the multijet background estimated by the data-driven Matrix Method, and "MC" represents all the other backgrounds estimated by simulations. The correction factor $w^{\mathrm{corr}}(p_{\mathrm{T}}^{\mathrm{1st.jet}})$ is applied for each event for MC simulations.

Figure 11.8 shows the leading jet p_{T} and m_{eff} distributions at the preselection before the fit, comparing the background prediction with (red) and without (blue) the correction factor $w^{\mathrm{corr}}(p_{\mathrm{T}}^{\mathrm{1st.jet}})$. Figure 11.8 (a) indicates that the background prediction with the correction factor is perfectly consistent with the data by definition. With the correction factor, the m_{eff} distribution of the pre-fit background prediction agrees with the data as shown in Fig. 11.8 (b). From the results, the leading jet p_{T} is found to be correlated with the m_{eff}.

For the second item, the correction factor is propagated into each category. Here, to reduce the statistic uncertainty, the merged categories shown in 'Fit with combined categories' section are used. Figure 11.9 shows the m_{eff} distribution in "2THin, ≥6j, 3/≥4b" categories before the fit. After

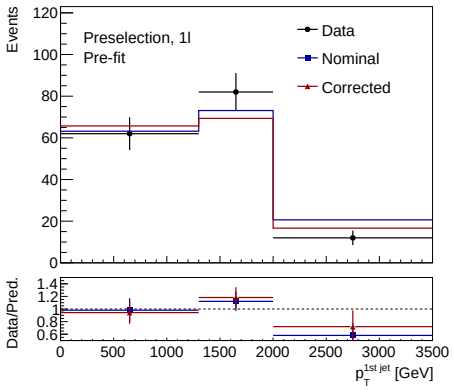

Figure 11.9: Pre-fit m_{eff} distributions in "2THin, ≥6j, 3/≥4b" categories. "Nominal" (blue) represents the nominal background prediction, and "Corrected" (red) represents the background prediction corrected with the correction factor $w^{\text{corr}}(p_{\text{T}}^{\text{1st.jet}})$.

application of the correction factor, the background prediction is improved only by $\sim$ 10%. The correction factor does not have large improvement in the signal sensitive categories. Therefore, the observed deficits on m_{eff} in *the largest impact category group* are not directly related with the discrepancy on the leading jet p_{T} at the preselection.

For the last item, the pulls of the systematic uncertainties are checked. The high m_{eff} range at the preselection is dominated with $t\bar{t}$+lights background. Figure 11.10 shows the variations of the NNLO and parton shower uncertainties of $t\bar{t}$+lights background in "0T, 0H, 5j, 3b" category. These uncertainties have the largest impact on the higher m_{eff} range. The spontaneous pulls of them are -0.63σ and 1.02σ, respectively, and then these pulls correct high m_{eff} range by around 40%. The difference of m_{eff} distributions between the nominal and leading jet p_{T} corrected predictions is found to be covered by these pulls.

Figure 11.11 shows the m_{eff} distributions at the preselection before and after the fit. The pre-fit m_{eff} distribution indicates the deficits related with the discrepancy on the leading jet p_{T} as shown in Fig. 11.8. On the other hand, the post-fit m_{eff} distribution is corrected by the simultaneous pulls of the systematic uncertainties. From these results, the discrepancy on the leading jet p_{T} is covered with the systematic uncertainties and corrected by the fit, hence it is not the cause of the deficits on the limits.

To summarise, in order to investigate the small deficits on the leading jet p_{T} at the preselection observed in the previous section, several tests are performed. The m_{eff} distributions after applying the correction factor for the leading jet p_{T} are found to be improved. But the improvements in the signal sensitive categories are less than that at the preselection. Also the difference of m_{eff} distributions between with and without the correction factor can be covered by the systematic uncertainties of $t\bar{t}$+lights background. Therefore, no evidence of the potential issue on the modelling of the leading jet p_{T} is found.

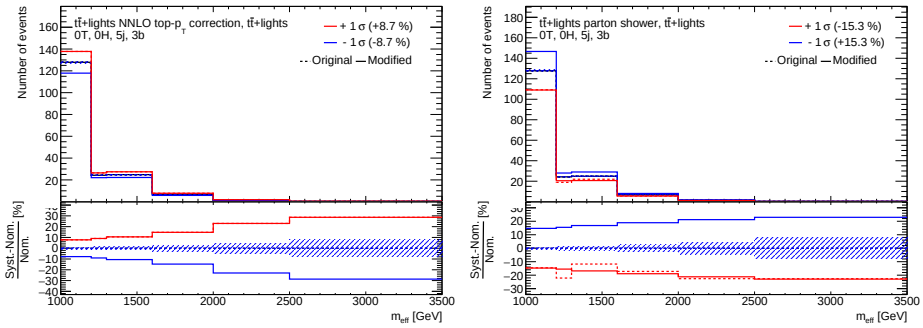

(a) (b)

Figure 11.10: (a) NNLO and (b) parton shower systematic uncertainties of $t\bar{t}$+lights in "0T, 0H, 5j, 3b" category. The systematic variations by $\pm 1\sigma$ are shown. The "Modified" (solid line) uncertainty is the variation of the uncertainty after smoothing the "Original" (broken lines) uncertainty. The shaded area shows the uncertainty on the $t\bar{t}$+lights prediction. The values in round brackets show the systematic effect on the total event yield in this category. The pulls of the NNLO and parton shower uncertainties are -0.74σ and 1.40σ, respectively. In total, these uncertainties affect high m_{eff} range by around 40%.

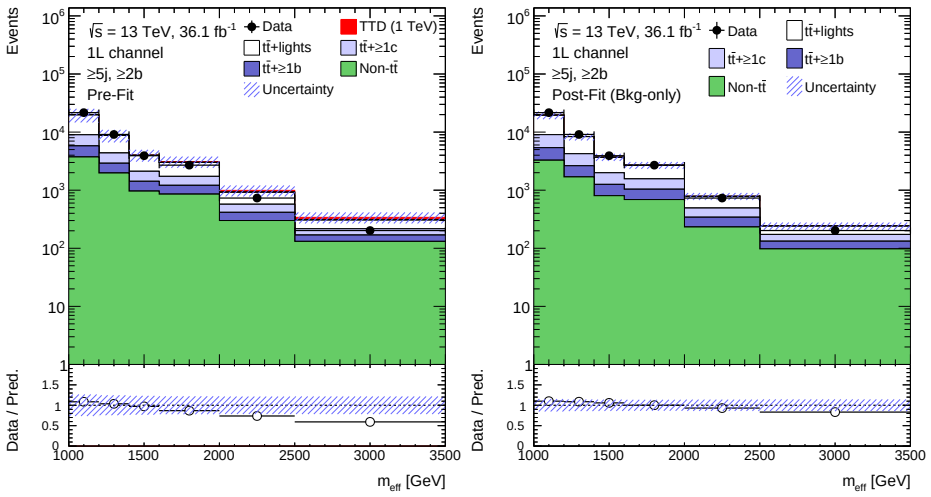

(a) (b)

Figure 11.11: (a) Pre-fit and (b) Post-fit predicted and observed m_{eff} distribution at the preselection. The simultaneous pulls of the systematic uncertainties correct the high m_{eff} tail after the fit.

11.8 Summary

In general, the observed limits on the cross section in 1-lepton only channel are consistent with the expected limits within 3σ of their uncertainties. But the discrepancies may be caused by the potential issues in this analysis. In order to investigate the potential issues, the several tests are performed in this chapter. First, the three categories to contribute to the deficits most are identified. Then, the possible candidates causing the deficit are checked: the calculation method of the limits, the background estimating method, the dominant background modelling and its uncertainty, and the model of the kinematic variables. The results show no evidence of the potential issues in this analysis. If the background modeling or its systematic uncertainties are wrong, the deficits should be seen in the 0-lepton channel. However the deficits and potential issues are not found. The deficits on the limits can be originated from the statistical fluctuations.

12 Prospect

The ATLAS experiment will continue to acquire the collision data until the end of 2018 in Run2. The total amount of data in Run2 will correspond to an integrated luminosity of 100 fb^{-1}. After Run2, Run3 will begin in 2020 and end in 2023. The amount of data combining Run2 and Run3 corresponds to 300 fb^{-1}. At the same time, the instantaneous luminosity is going to increase and the number of interactions per bunch crossing will be around 80. In this chapter, the sensitivities with 100 and 300 fb^{-1} are shown. In addition, the study to keep the sensitivity for high pileup condition, is performed.

12.1 Sensitivity for high luminosity

This section shows the sensitivities of this analysis for higher integrated luminosity. The significances or the expected limits on the cross section are computed for various BSM models with changing only the integrated luminosity. The computation does not use the unblinded fit results shown in Section 10.4 but use the Asimov data which is equivalent with the pre-fit total background prediction, for simple estimations.

Figure 12.1 (a) shows the significance for VLT signals with the fixed branching ratio of $BR(T \rightarrow Ht) = 1$ as a function of the VLT mass. The evidence reach on the VLT mass at 3σ significance is estimated to be 1.23 TeV for 36.1 fb^{-1}. For 100 and 300 fb^{-1}, the evidence reaches on the VLT mass are 1.33 and 1.43 TeV, respectively. Figure 12.1 (b) shows the 95% CL upper limits on the cross section for VLT signals with the fixed branching ratio of $BR(T \rightarrow Ht) = 1$ as a function of the VLT mass. By comparing the expected limit with the theoretical cross section, the lower limit on the VLT mass is estimated to be 1.31 TeV for 36.1 fb^{-1}. For 100 and 300 fb^{-1}, the lower mass limits are 1.41 and 1.51 TeV, respectively. Thus, the evidence reaches for the VLT signal and the limits improve by 100 and 200 GeV with the integrated luminosity at the end of Run2 and Run3, respectively.

Table 12.1 shows the significances or the expected 95% CL upper limits on the cross section for SM and EFT four-top-quark production. For both cases, the significance and the expected limit improve by a factor of two with 300 fb^{-1} from the ones with 36.1 fb^{-1}. But for the SM case, the current analysis will not discover this physics process due to its small cross section and the sensitivity of this analysis. The CMS experiment searches for this process with better sensitivity using both the same-sign dilepton and at least 3 leptons [56]. In order to improve the sensitivity to the SM four-top-quark production, introducing and combining multi-lepton channels can be efficient for the future analysis.

Figure 12.2 shows the significance for 2UED-RPP scenario as a function of the KK mass. The evidence reach on the VLT mass is estimated to be 1.69 TeV for 36.1 fb^{-1}. For 100 and 300 fb^{-1},

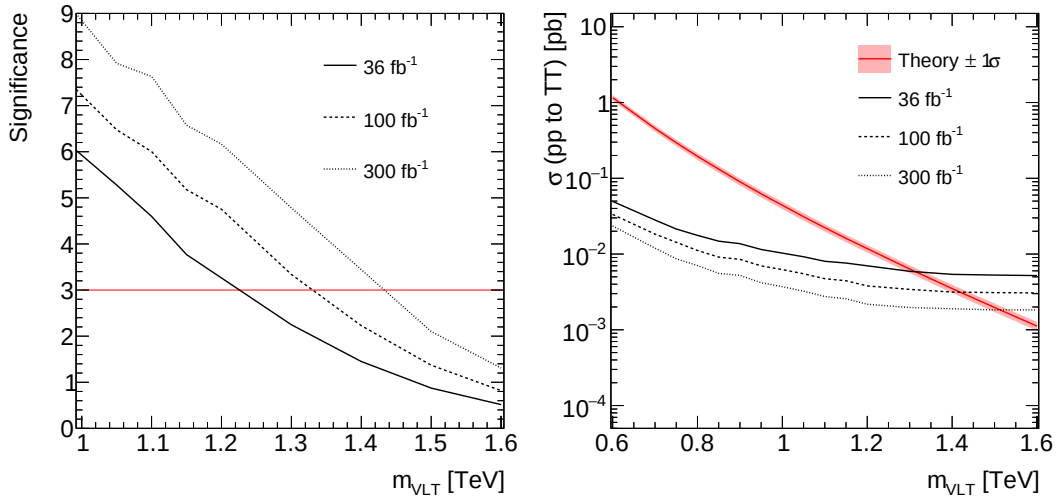

(a) (b)

Figure 12.1: (a) Significances and (b) expected upper limits on the cross section for VLT signals with the fixed branching ratio of $BR(T \rightarrow Ht) = 1$ as a function of the VLT mass. The solid, dashed, and dotted lines represents the significances or the upper limits with 36, 100, and 300 fb^{-1}, respectively. In the figure (a), the evidence reaches on the VLT mass are seen as intersections of each significance line and the red line (significance = 3σ). In the figure (b), the theoretical cross section at NNLO is shown in the red line, and its uncertainty is shown in the red band.

Table 12.1: Significances or the expected 95% CL upper limits on the cross section for SM and EFT four-top-quark production with the integrated luminosities of 36, 100, and 300 fb^{-1}.

Signal	Variable	Integrated luminosity [fb^{-1}]		
		36	100	300
SM $t\bar{t}t\bar{t}$	Significance	0.26	0.37	0.55
	Limit $\sigma/\sigma_{\mathrm{SM}}$	8.0	5.6	3.9
EFT $t\bar{t}t\bar{t}$	Limit σ [fb]	32	22	16

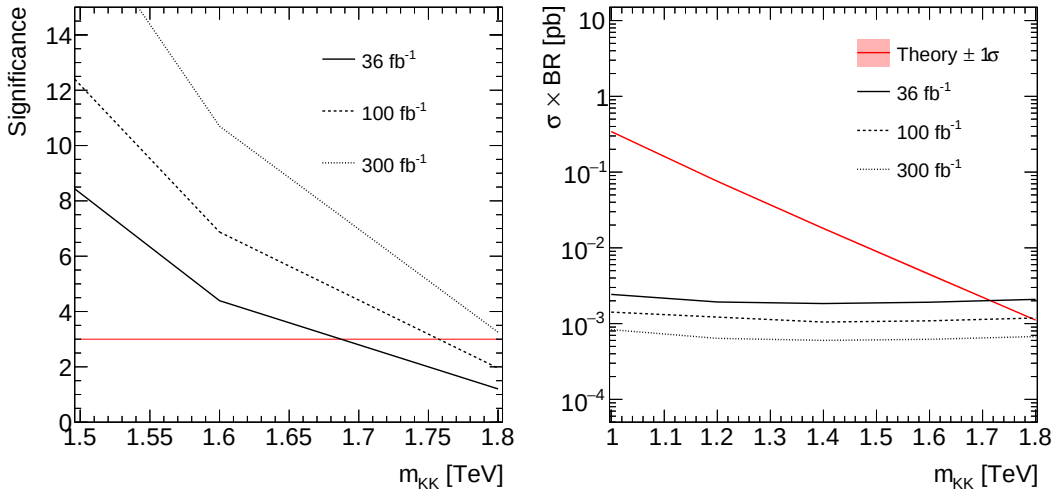

(a) (b)

Figure 12.2: (a) Significances and (b) expected limits on the cross section for 2UED-RPP scenario as a function of the KK mass. The solid, dashed, and dotted lines represents the significances or the upper limits with 36, 100, and 300 fb^{-1}, respectively. The actual KK mass points used for computing significances are 1.0, 1.2, 1.4, 1.6, and 1.8 TeV. For the intermediate range, the significance values are linearly interpolated. In the figure (a), the evidence reaches on the VLT mass are seen as intersections of each significance line and the red line (significance = 3σ). In the figure (b), the theoretical cross section at LO is shown in the red line.

the evidence reaches on the VLT mass are 1.75 and 1.80 TeV, respectively. Thus, the evidence reach for the 2UED-RPP scenario improves by 60 and 110 GeV with the integrated luminosity at the end of Run2 and Run3, respectively. Figure 12.2 (b) shows the 95% CL upper limits on the cross section for 2UED-RPP scenario as a function of the KK mass. By comparing the expected limit with the theoretical cross section, the lower limit on the KK mass is estimated to be 1.69 TeV for 36.1 fb^{-1}. For 100 and 300 fb^{-1}, the lower mass limits are 1.78 TeV and more than 1.8 TeV, respectively. Thus, the evidence reaches for 2UED-RPP scenario and the KK mass limits improve by at least 60 GeV with the integrated luminosity at the end of Run2.

12.2 Performances of Higgs boson and top quark taggers

The Higgs boson and top quark taggers are important to enhance the discrimination of the signals from the backgrounds. As described in Section 6.4, one of the dominant fake origins are other jets than the VLT or top quark decay processes such as gluon radiations or parton showers. These sources can depend on the pileup. Therefore, the tagging performance, especially fake rate, can increase for the higher pileup condition.

In order to qualitatively check the performance for the higher pileup condition, the efficiencies and fake rates are shown as a function of pileup in Fig. 12.3. For the Higgs boson tagger, the efficiency

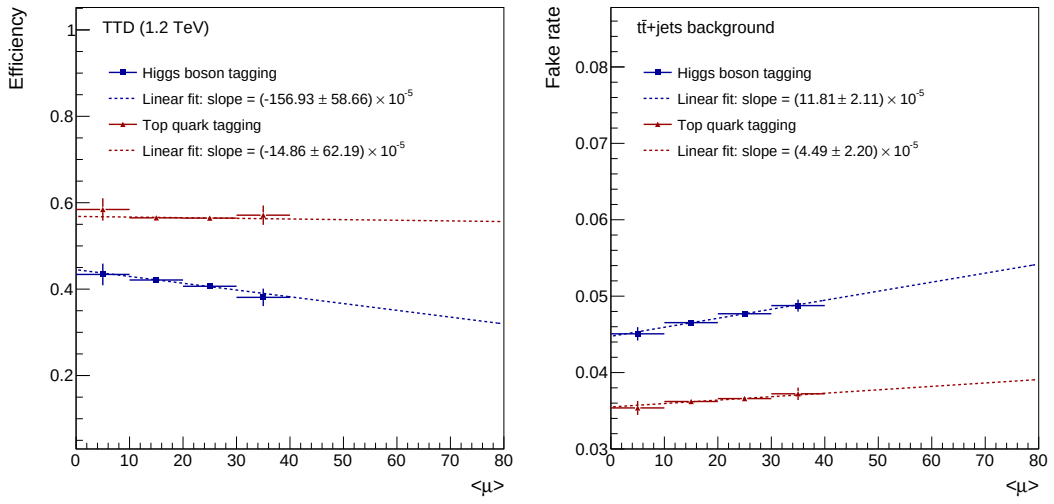

(a) (b)

Figure 12.3: (a) Efficiencies and (b) fake rates of the Higgs boson and top quark taggers as a function of the number of interaction per bunch crossing (μ). For the efficiency, the VLT signal events with the mass of 1.2 TeV are used, while for the fake rates, $t\bar{t}$+jets backgrounds are used.

decreases for higher pileup. In the high pileup condition, large-R jets originating from the Higgs bosons can be contaminated with additional jets from other sources. This leads to higher large-R jet masses and causes the efficiency drop. To solve the issue, the jets with a smaller radius parameter like $R = 0.2$ can be useful to individually reconstruct two b-jets in the future analysis. This new technique is described in Ref. [194], and is not discussed in this dissertation. For the top quark tagger, the efficiency seems to be stable. The fake rates for both the Higgs boson and top quark taggers increase for higher pileup. This feature indicates that the sensitivity of this analysis can decrease in higher pileup condition.

To mitigate the increase of fake rates, the following requirements are considered:

- For the Higgs boson tagger, requiring larger angular distance between a signal lepton and a large-R jet ($\Delta R(\text{lep}, \text{J}) > 1.0$)
- For the top quark tagger, requiring that a large-R jet contains at least one b-jet.

The first requirement is expected to mitigate fakes originating leptonically decaying top quarks which are ones of the leading fake origins as shown in Fig. 6.12. When top quarks leptonically decay, boosted b-jets from the decay and other jets can be reconstructed as large-R jets and identified as Higgs bosons. This fake can be rejected by requiring the angular distance between a lepton and a large-R jet. The second is expected to mitigate the fake originating from other jets than $t\bar{t}$ decays because these additional jets have less probability to include bottom quarks.

After changing the requirements, the efficiencies and fake rates are estimated as shown in Fig. 12.4 and 12.5. For the Higgs boson tagger, the additional requirement on a lepton is found to reduce the

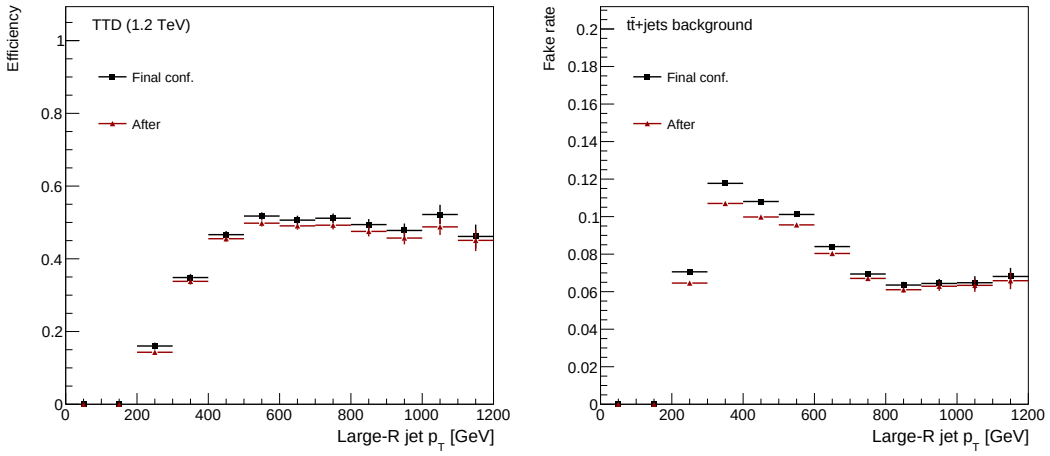

(a) (b)

Figure 12.4: (a) Efficiency and (b) fake rate of the Higgs boson tagger as a function of large-R jet p_{T} after changing the requirements (red), compared to the ones with the final configuration (black) shown in Table 6.7. For the efficiencies, the SU(2)-doublet VLT signal with the mass of 1.2 TeV is used. For the fake rates, the $t\bar{t}$+jets background is used.

fake rate by around 10% with keeping the efficiency as shown in Fig. 12.4. This improvement is expected to gain sensitivities to VLT signals. For the top quark tagger, the efficiency (Fig. 12.5 (a)) decreases by around 20%, while the fake rate (Fig. 12.5 (b)) significantly decreases by around 70% due to the b-tagging requirement. These changes can improve sensitivities to signals.

Figure 12.6 shows the ratio of the upper limit at 95% CL on the production cross section after changing the requirements to the one with the final configuration. In a fit and computation of the limits, only the dominant $t\bar{t}$ background and the statistical uncertainty are considered[1]. The VLT signal with fixing the branching ratio of $BR(T \to Ht) = 1$ is used. These additional requirements are found to improve the sensitivity by around 5%. These simple solutions are useful for the future analysis.

[1] The other small backgrounds and all the systematic uncertainties are not taken into a fit and a limit to simplify the computation.

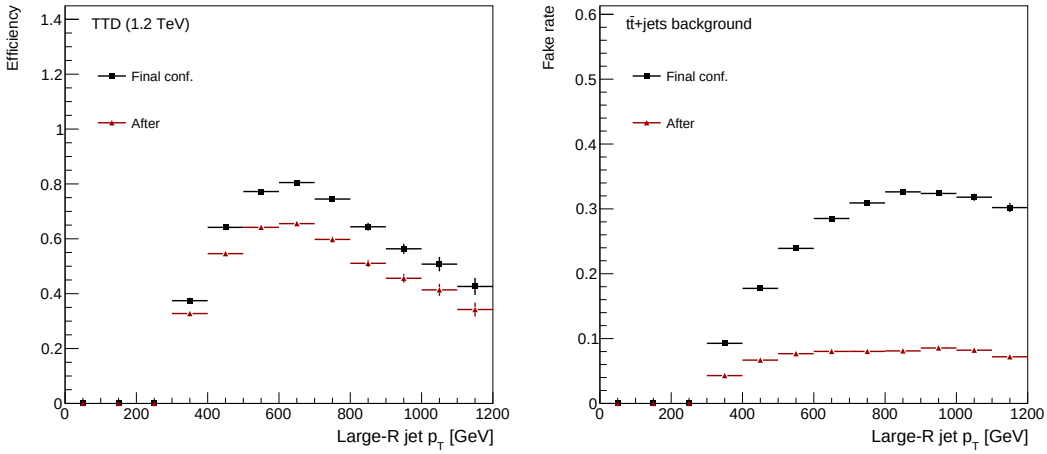

(a) (b)

Figure 12.5: (a) Efficiency and (b) fake rate of the top quark tagger as a function of large-R jet p_{T} after changing the requirements (red), compared to the ones with the final configuration (black) shown in Table 6.7. For the efficiencies, the SU(2)-doublet VLT signal with the mass of 1.2 TeV is used. For the fake rates, the $t\bar{t}$+jets background is used.

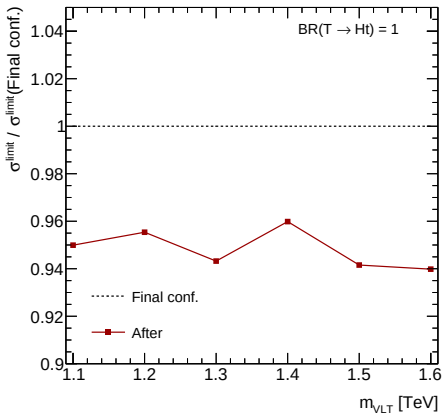

Figure 12.6: Ratio of the upper limits at 95% CL on the production cross section after changing the requirements (red) to the one with the final configuration (black). Only the dominant $t\bar{t}$ background and the statistical uncertainty are considered. The VLT signal with fixing the branching ratio of $BR(T \rightarrow Ht) = 1$ is used.

13 Conclusion

The Standard Model (SM) in the particle physics can precisely explain most the experimental results, while it has fundamental problems. The physics models beyond the Standard Model (BSM) have been proposed to solve the problems. Many BSM models predict new phenomena of the existence of the new particles called vector-like quark (VLQ) and enhancement of the four-top-quark production. This dissertation presents a search for the new phenomena in top-antitop final states with additional heavy-flavor jets with 36.1 fb^{-1} of data at $\sqrt{s}$ = 13 TeV taken in 2015 and 2016 by the ATLAS detector. Especially, one of the VLQ referred to as vector-like top quark (VLT) is considered as the main target in this analysis.

Before the data analysis, high-quality data taking is the most important work. The monitoring tools for the Pixel detector are developed in this dissertation and enable to properly understand the detector condition. By using the tools, the potential issue on the B-Layer about the hit occupancy in 2015 was identified. The prompt feedbacks to the data taking group contributes to the smooth data-taking in 2016 and later.

The physics objects reconstructed from the hit information collected in the ATLAS detector are the bases of the physics analyses. Tracks, which are trajectories of the charged particles in the Inner Detector, are one of the most basic objects. The distance between tracks and collision points, which is so-called impact parameter, is a characteristic parameter to distinguish the tracks associated with secondary vertices from those associated with the primary vertex. Measurements of the impact parameter resolutions with the data taken in early 2015 are presented in this dissertation. The results show that the observed resolutions are improved compared with those in Run1 as expected from the installation of the new innermost Pixel layer (IBL). The resolutions and their uncertainties are propagated into the other performance measurements for the other physics objects.

In this physics analysis, the features of the signal events are used for the determination of the analysis strategy. The VLT's are expected to be produced in pair via the strong interaction and decay into three modes of Wb, Zt, and Ht. This analysis searches for the events in which one VLT decays into Ht and the other decays into any of three decay modes. Also the events are assumed to include one electron or muon. All the SM backgrounds except the multijet background are predicted using the Monte Carlo simulations. The multijet background is estimated with the data-driven Matrix Method. Thus, to reduce the SM backgrounds, the events are required to have many jets and b-jets, and one electron or muon.

After the selection, the dominant SM background is the pair production of top quarks with additional jets. The feature of VLT signal events is the existence of the boosted Higgs bosons. And the BSM four-top-quark production predicts the existence of the boosted top quarks. In order to improve the discrimination of the signals from the backgrounds, the boosted Higgs boson and top quark taggers are developed in this dissertation. The event categorisation based on the Higgs-tagged and top-tagged

jet multiplicities is found to improve the sensitivity to the signal models. Therefore, the events after the selection are categorised with jets, b-jets, Higgs-tagged jets, and top-tagged jets multiplicities. For further improvement of this analysis, a likelihood fit of the SM background prediction to the data is performed. The fitting procedure is validated to work properly. At several validation steps with the blind cuts, the background prediction after the fit is confirmed to be consistent with the data in the validation regions close to the signal sensitive regions.

Finally, in the most signal sensitive regions, no excess of data from the SM background prediction after the fit is observed. The exclusion limits on the cross section for the various signal models are set at 95% confidence level in both 1-lepton only channel and the combination of 0- and 1-lepton channels. For the VLT signals, the cross section limits are interpreted into the VLT mass limits by comparing the theoretical prediction. In the case of the fixed branching ratio of the VLT decaying the Higgs boson and top quarks, $BR(T \rightarrow Ht) = 1$, the observed (expected) limit on the mass is set to be $m_{\mathrm{VLT}} > 1.43$ (1.34) TeV. The observed (expected) mass limits for a weak-isospin doublet and singlet are set to be $m_{\mathrm{VLT}} > 1.31$ (1.26) TeV and $m_{\mathrm{VLT}} > 1.19$ (1.11) TeV, respectively. Also for the other branching ratio, the observed and expected mass limits are set, assuming $BR(T \rightarrow Ht) + BR(T \rightarrow Zt) + BR(T \rightarrow Wb) = 1$. For the four-top-quark production, the observed (predicted) cross section limits for a contact interaction in an EFT model are set to be 16.4 (30.9) fb. For 2UED-RPP model, the Kaluza-Klein mass limits with the symmetric geometry case are set to be $m_{\mathrm{KK}} > 1.8$ (1.73) TeV.

A small discrepancy on the observed limits are seen in 1-lepton channel. Since it may be due to potential issues in this analysis, all the possibilities are discussed. The test results show that no evidence of issues is observed. Therefore, the deficits on the observed events are concluded to be originated from the statistical fluctuation.

This analysis does not discover new phenomena. However, improvements of sensitivities by an increase of the integrated luminosity and development of the taggers can significantly extend the mass coverage of the VLT signal by around 150 GeV from the previous analysis result in the ATLAS experiment. The limits set in this analysis extend constraints in the parameter space in signal models. At the end of Run3, the mass coverage can extend by around 200 GeV. This analysis has good potentials to further search for VLT signals.

At last, the prospects for future experiments are shown. In the future, the LHC will be upgraded to increase the instantaneous and integrated luminosities with the centre-of-mass energy of 14 TeV. Then, the amount of data after operating over ten years will correspond to 3000 fb^{-1}. In the case, the discovery reach (lower mass limit) on on the VLT mass is expected to extend to 1.5 (1.8) TeV [195]. If the pp collision data are taken at the centre-of-mass energy of 100 TeV, the cross section on the pair production of VLT with the mass of 7 TeV is estimated to be around 1 fb, which may be covered by experiments [196]. Since future experiments will significantly improve sensitivities to signals, potentials to discover VLT signals will widen more.

Acknowledgements

I would like to sincerely thank my supervisor, Associate Professor Osamu Jinnouchi. His supervising over six years has driven my interest to the particle physics. Numeraous discussions with him about the physics and detectors help me to understand the physics experiments deeper. He has supported not only for the physics but also for important things to study at CERN especially about interactions with researchers at CERN. Thank to all the support, I could smoothly progress my studies with actively having good discussions with numerous researchers at CERN.

Doctor Loic Valery, who worked as the convener of the the ATLAS Exotic-HQT Ht+X analysis group, gave me a good guidance of understanding the analysis detail step by step and had many discussions about my studies. In addition, he supported and corrected my presentations every time. Without his supervision, I could not progress my analysis. Moreover, I would like to thank all the members of the ATLAS Exotic-HQT Ht+X analysis group for discussions and advices, with special mention: Prof. Aurelio Juste Rozas, Trisha Farooque, and Mirkoantonio Casolino.

Assistant Professor Yosuke Takubo, who worked as the convener of the ATLAS Pixel Data Quality group, supervised me for the monitoring studies of the Pixel detector. Thanks to his many supports, I successfully developed and updated the monitoring system. And, he taught me the detector operation, and I could understand the data acquisition and reconstruction. I would like to thank all the member of the ATLAS Pixel detector group for discussions and feedbacks, with special mention: Didier Ferrere, Mario Giordani, Kerstin Lantzsch, Hideyuki Oide, and Soshi Tsuno.

I would like to thank all the members of the ATLAS Inner Detector Tracking group, with special mention: Anthony Morley, Heather Gray, Shih-Chieh Hsu, and Simone Pagan Griso. Thanks to all the technical advices and discussions, I could measure the impact parameter resolutions in both the data and simulation and provide the performance for all the other ATLAS groups.

I would like to thank Professor Masahiro Kuze for many discussions in all the seminars and lectures. The discussions are interesting and help me to understand the particle physics.

I would like to thank all the people related with Jinnouchi group, especially Minoru Hirose, Yohei Yamaguchi, Ryo Nagai, Nora Petterson, Kazuki Motohashi, Kazuki Todome, and all the other members for many interesting discussions. I would also like to thank people at CERN. Takuya Nobe supported me for my stay as well as discussions about the physics. I would like to thank one of my best friends, Mutsuto Hagihara, for mental supports and refreshing me. Thanks to good Golf players, Naoki Ishijima, Satoshi Higashino, Shohei Shirabe, I could refresh and concentrate on my studies. I would like to thank Masahiro Tanaka for his physical support of picking me up by his car.

I would like to thank my family for many financial and mental supports of my life. Without all the helps, my thesis would not have been possible. I also thank my puppy, Honey, for giving me a lot

of happiness. I would like to thank Chika Ogasawara, who is my fiancée, for her supports of my life over years.

Appendix

A Signal chirality study

This section shows the comparison plots between SU(2)-singlet and doublet models. The detail explanation is shown in Section 5.1. A comparison of m_{eff} distribution is made for particular decay modes ($T\bar{T} \to HtHt$, $HtWb$, $HtZt$, $ZtZt$, $WbZt$, or $WbWb$) and different selections. Three different vector-like top quark masses are considered: 700, 950 and 1200 GeV. Singlet and doublet samples of the same mass are normalized to the same cross-section. Figure A.1 shows the comparison of the signal acceptance and the shape of the m_{eff} distribution at the preselection level. Figures A.2–A.13 show the comparison in each of the search regions. The search regions are defined in Section 7.2. In general the shape of the m_{eff} spectrum is found to be consistent between both singlet and doublet models, while there are $\sim$10% differences in yields, which are expected to have a negligible impact on the final result.

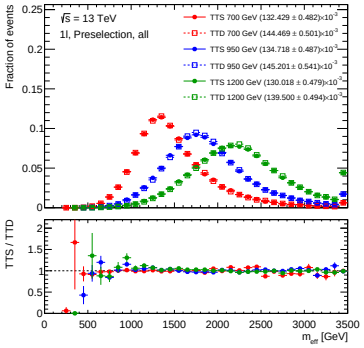

(a) all

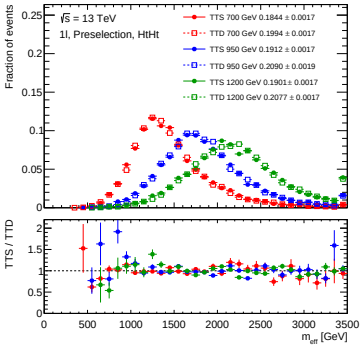

(b) HtHt

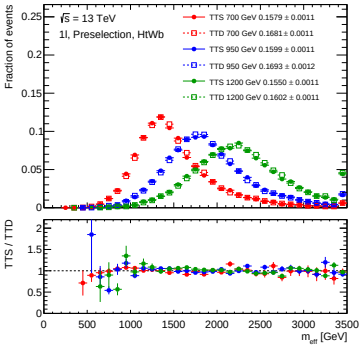

(c) HtWb

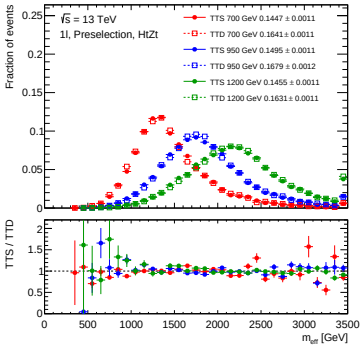

(d) HtZt

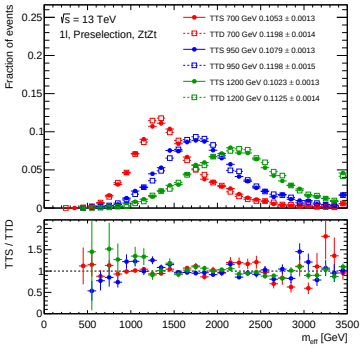

(e) ZtZt

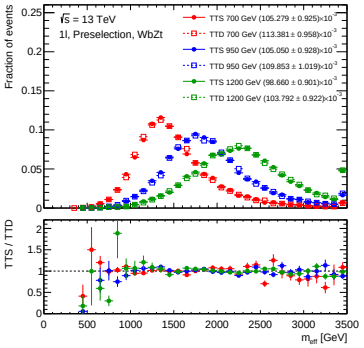

(f) WbZt

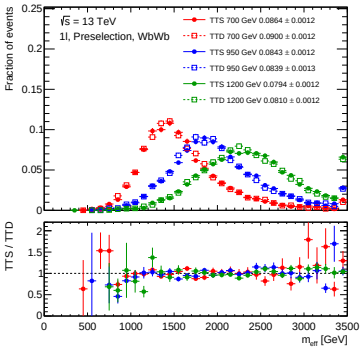

(g) WbWb

Figure A.1: Comparison of the signal acceptance and shape of the m_{eff} spectrum between the signalsamples produced in the singlet (full symbols) and doublet (open symbols) configurations for different decay modes and masses of 700 (red), 950 (blue), and 1200 GeV (green) at the preselection.

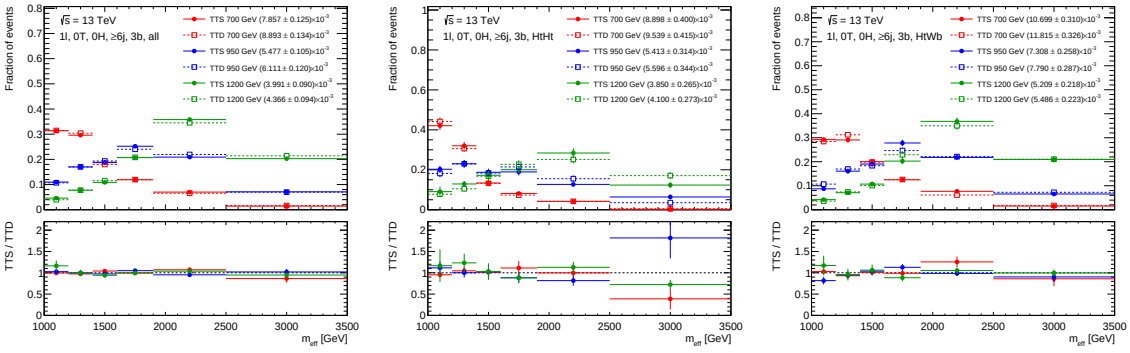

(a) all

(b) HtHt

(c) HtWb

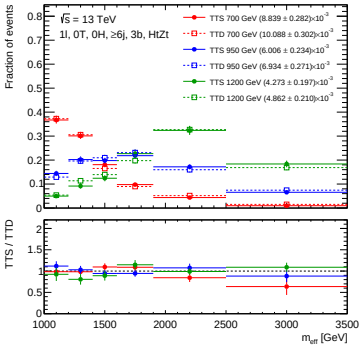

(d) HtZt

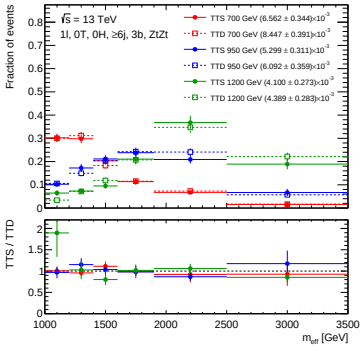

(e) ZtZt

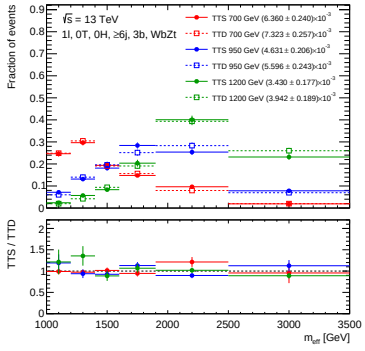

(f) WbZt

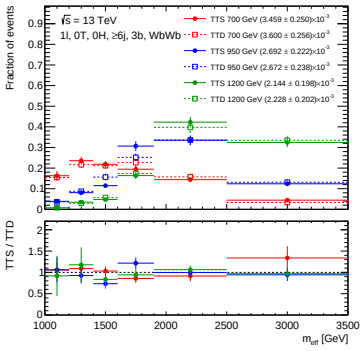

(g) WbWb

Figure A.2: Comparison of the signal acceptance and shape of the m_{eff} spectrum between the signalsamples produced in the singlet (full symbols) and doublet (open symbols) configurations for different decay modes and masses of 700 (red), 950 (blue), and 1200 GeV (green) in "0T, 0H, ≥6j, 3b" category.

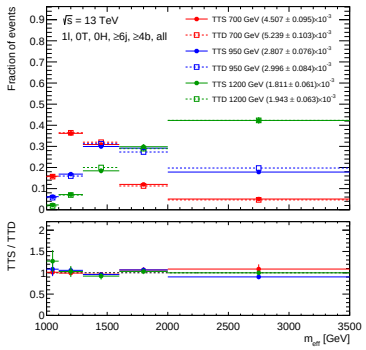

(a) all

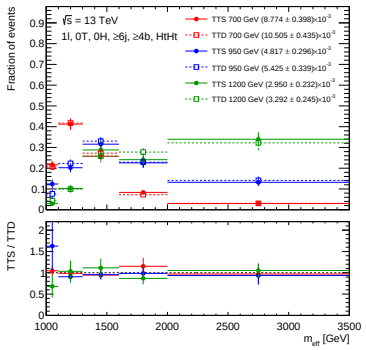

(b) HtHt

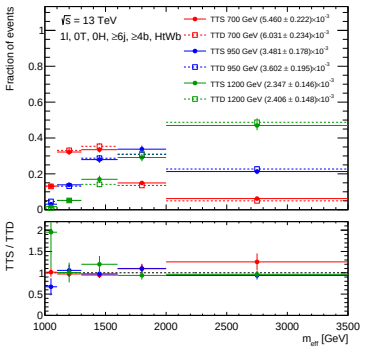

(c) HtWb

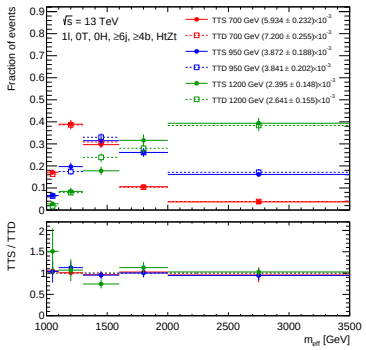

(d) HtZt

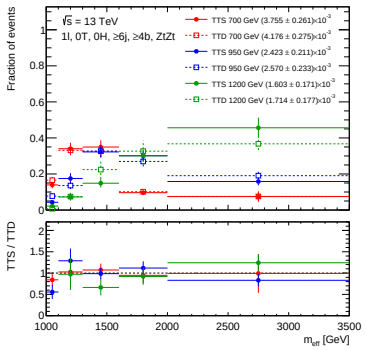

(e) ZtZt

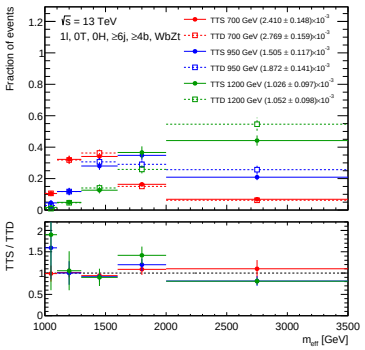

(f) WbZt

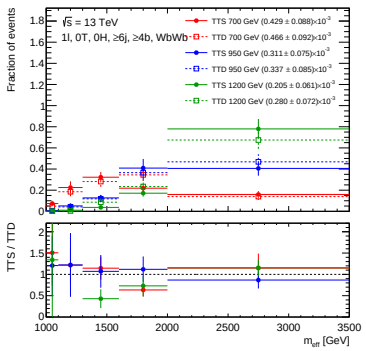

(g) WbWb

Figure A.3: Comparison of the signal acceptance and shape of the m_{eff} spectrum between the signalsamples produced in the singlet (full symbols) and doublet (open symbols) configurations for different decay modes and masses of 700 (red), 950 (blue), and 1200 GeV (green) in "0T, 0H, ≥6j, ≥4b" category.

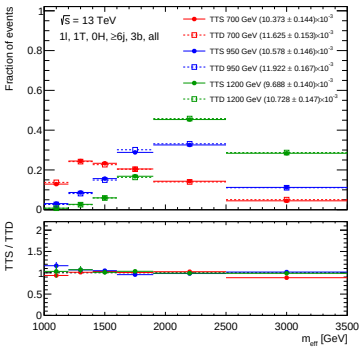

(a) all

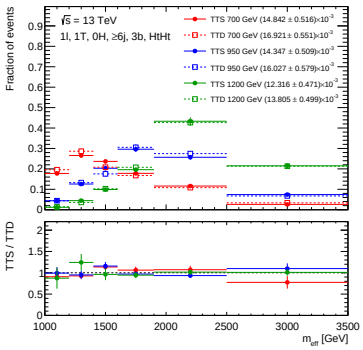

(b) HtHt

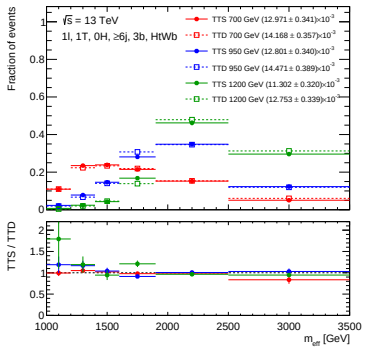

(c) HtWb

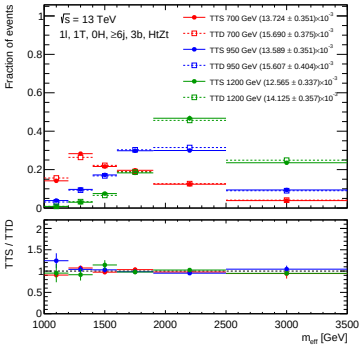

(d) HtZt

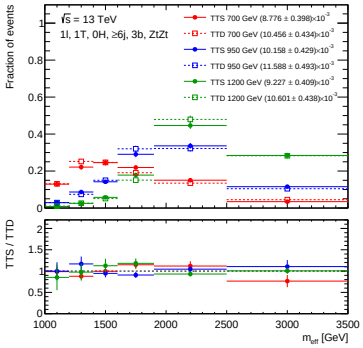

(e) ZtZt

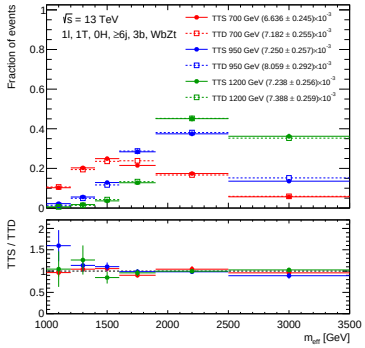

(f) WbZt

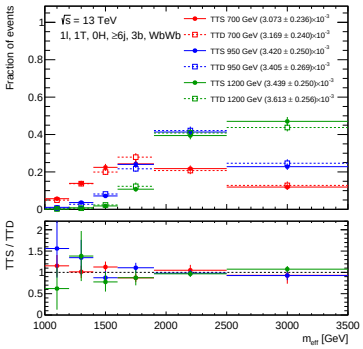

(g) WbWb

Figure A.4: Comparison of the signal acceptance and shape of the m_{eff} spectrum between the signalsamples produced in the singlet (full symbols) and doublet (open symbols) configurations for different decay modes and masses of 700 (red), 950 (blue), and 1200 GeV (green) in "1T, 0H, ≥6j, 3b" category.

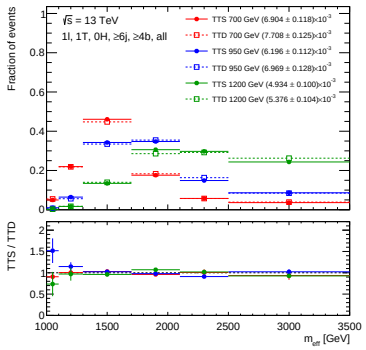

(a) all

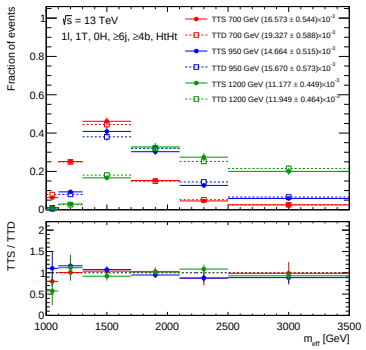

(b) HtHt

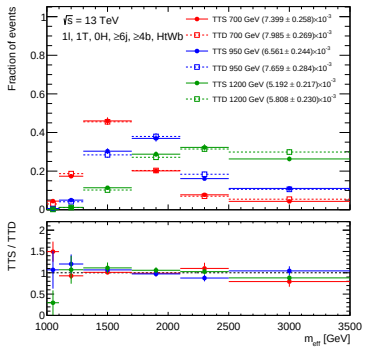

(c) HtWb

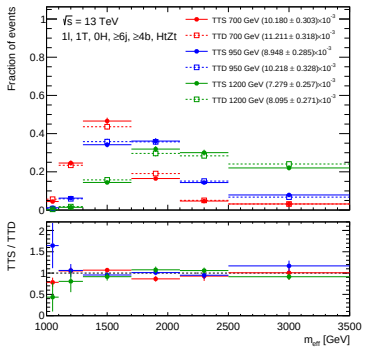

(d) HtZt

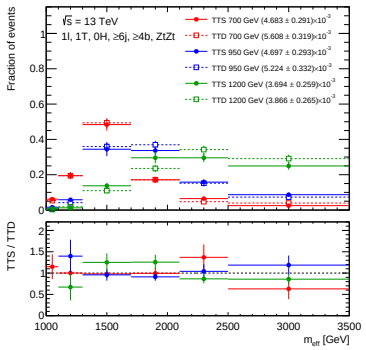

(e) ZtZt

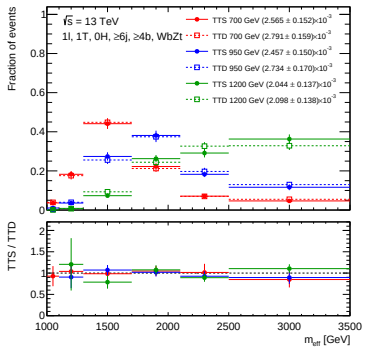

(f) WbZt

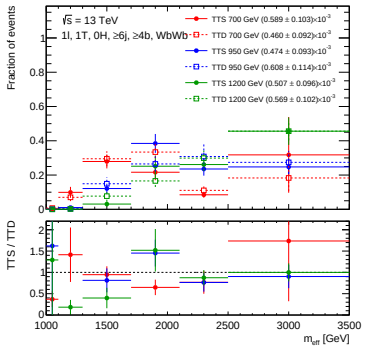

(g) WbWb

Figure A.5: Comparison of the signal acceptance and shape of the m_{eff} spectrum between the signalsamples produced in the singlet (full symbols) and doublet (open symbols) configurations for different decay modes and masses of 700 (red), 950 (blue), and 1200 GeV (green) in "1T, 0H, ≥6j, ≥4b" category.

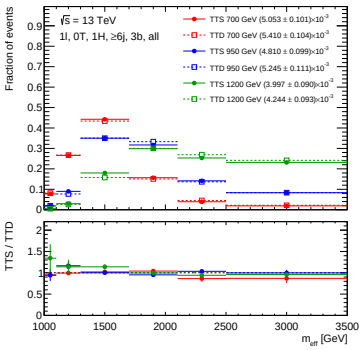

(a) all

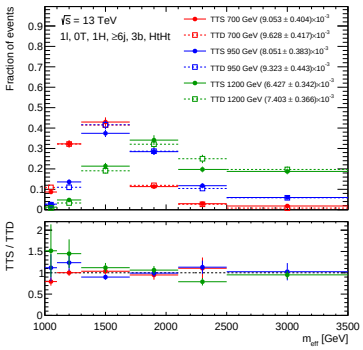

(b) HtHt

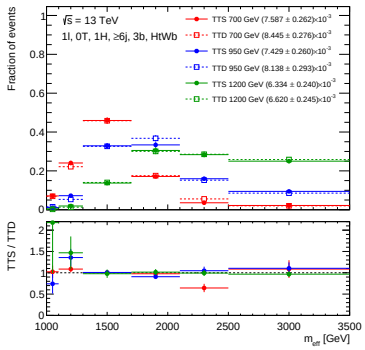

(c) HtWb

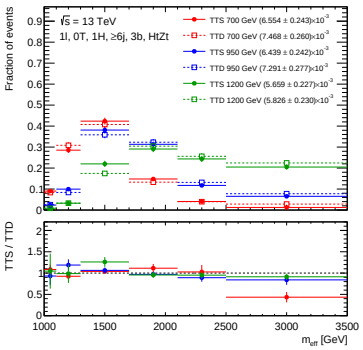

(d) HtZt

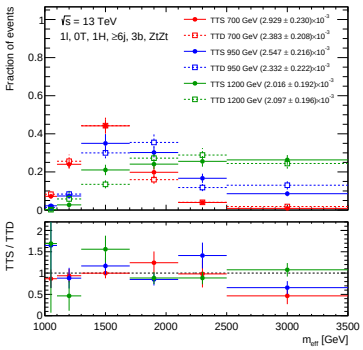

(e) ZtZt

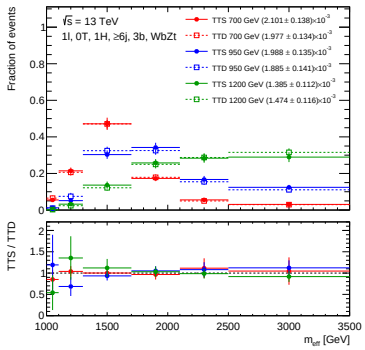

(f) WbZt

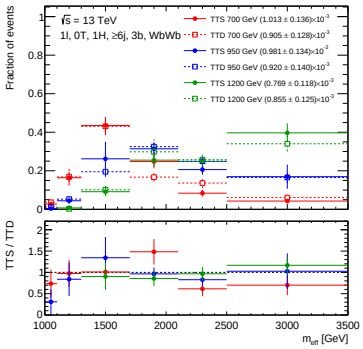

(g) WbWb

Figure A.6: Comparison of the signal acceptance and shape of the m_{eff} spectrum between the signalsamples produced in the singlet (full symbols) and doublet (open symbols) configurations for different decay modes and masses of 700 (red), 950 (blue), and 1200 GeV (green) in "0T, 1H, ≥6j, 3b" category.

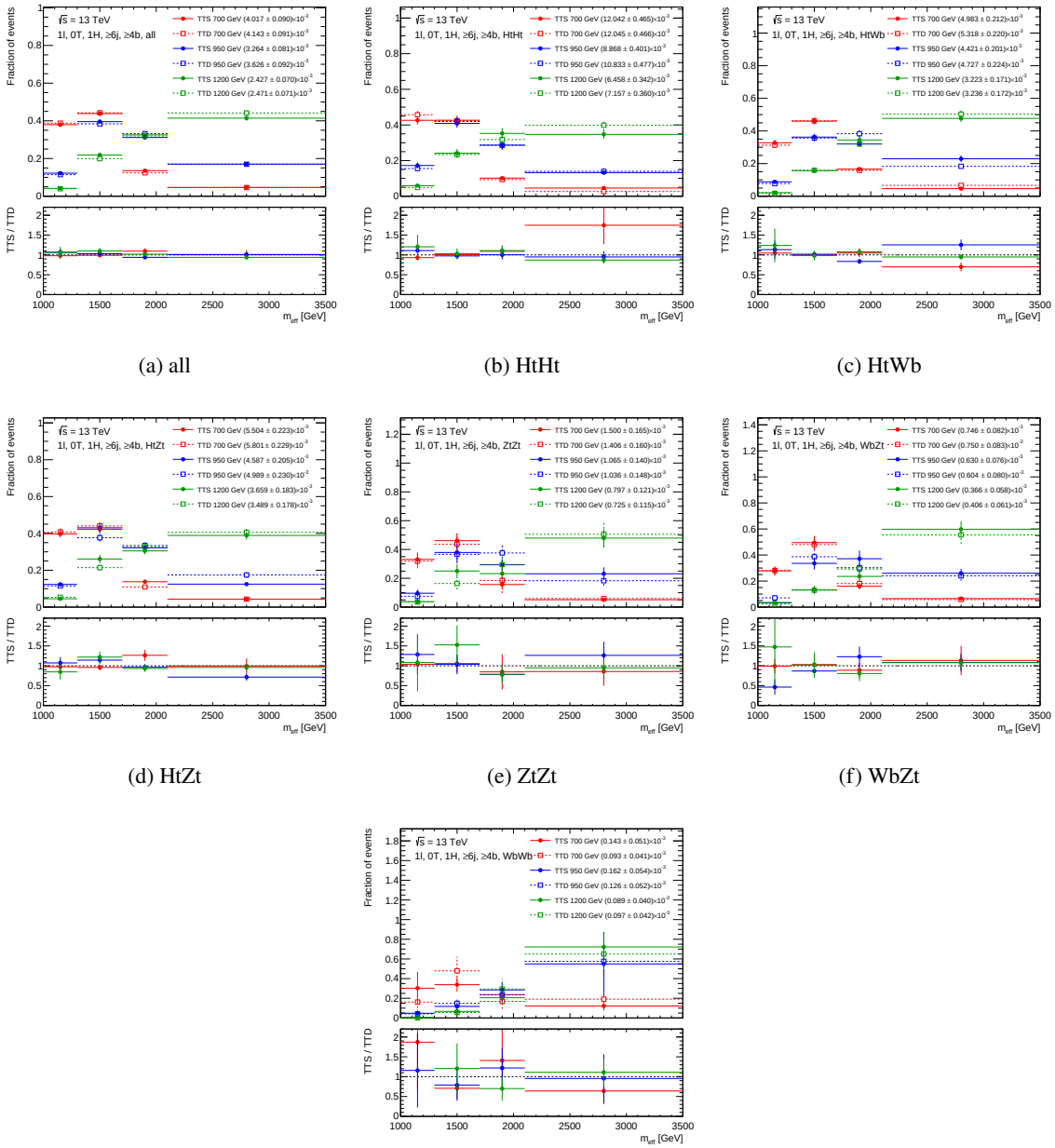

(a) all (b) HtHt (c) HtWb

(d) HtZt (e) ZtZt (f) WbZt

(g) WbWb

Figure A.7: Comparison of the signal acceptance and shape of the m_{eff} spectrum between the signalsamples produced in the singlet (full symbols) and doublet (open symbols) configurations for different decay modes and masses of 700 (red), 950 (blue), and 1200 GeV (green) in "0T, 1H, ≥6j, ≥4b" category.

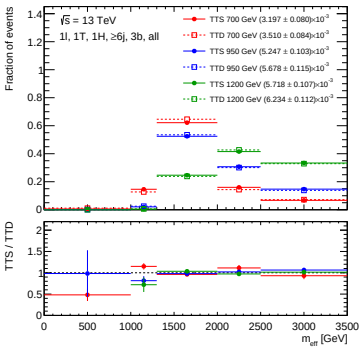

(a) all

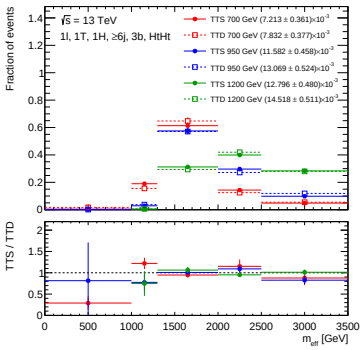

(b) HtHt

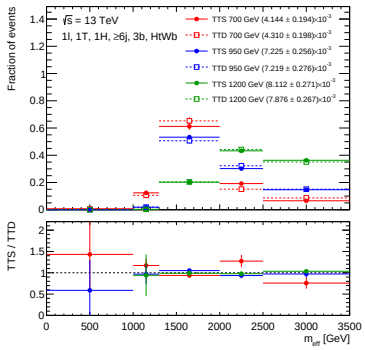

(c) HtWb

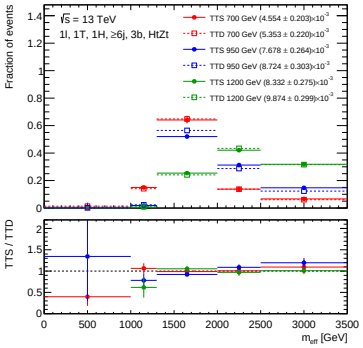

(d) HtZt

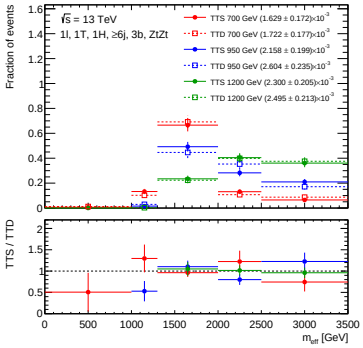

(e) ZtZt

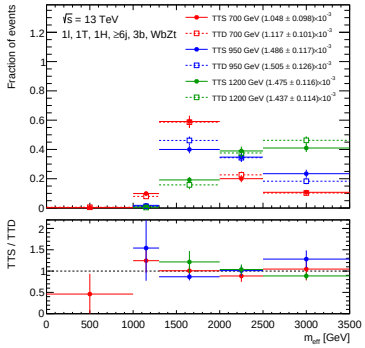

(f) WbZt

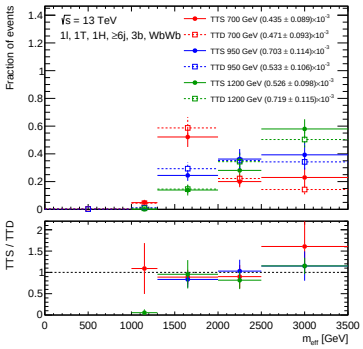

(g) WbWb

Figure A.8: Comparison of the signal acceptance and shape of the m_{eff} spectrum between the signalsamples produced in the singlet (full symbols) and doublet (open symbols) configurations for different decay modes and masses of 700 (red), 950 (blue), and 1200 GeV (green) in “1T, 1H, ≥6j, 3b” category.

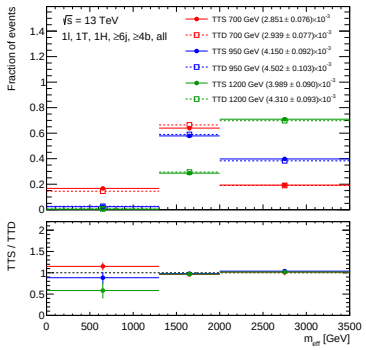

(a) all

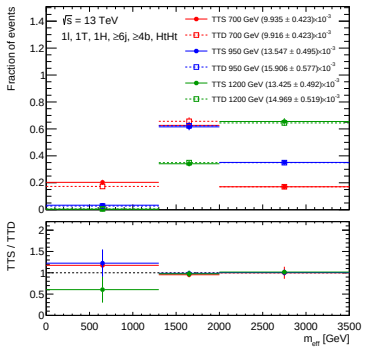

(b) HtHt

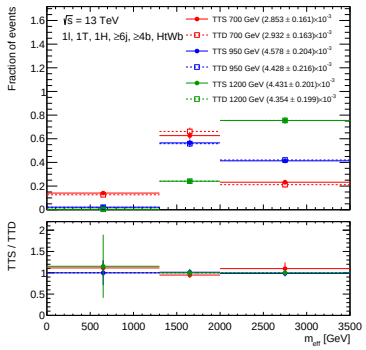

(c) HtWb

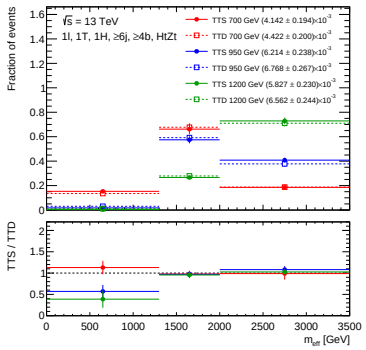

(d) HtZt

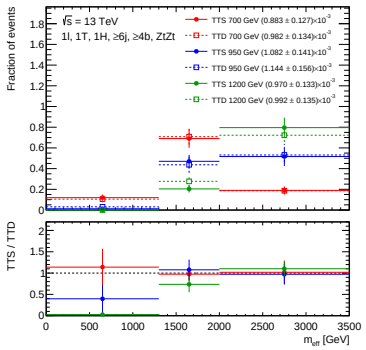

(e) ZtZt

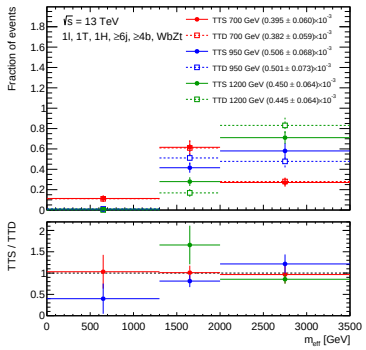

(f) WbZt

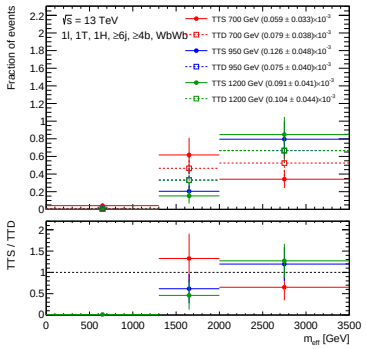

(g) WbWb

Figure A.9: Comparison of the signal acceptance and shape of the m_{eff} spectrum between the signalsamples produced in the singlet (full symbols) and doublet (open symbols) configurations for different decay modes and masses of 700 (red), 950 (blue), and 1200 GeV (green) in "1T, 1H, ≥6j, ≥4b" category.

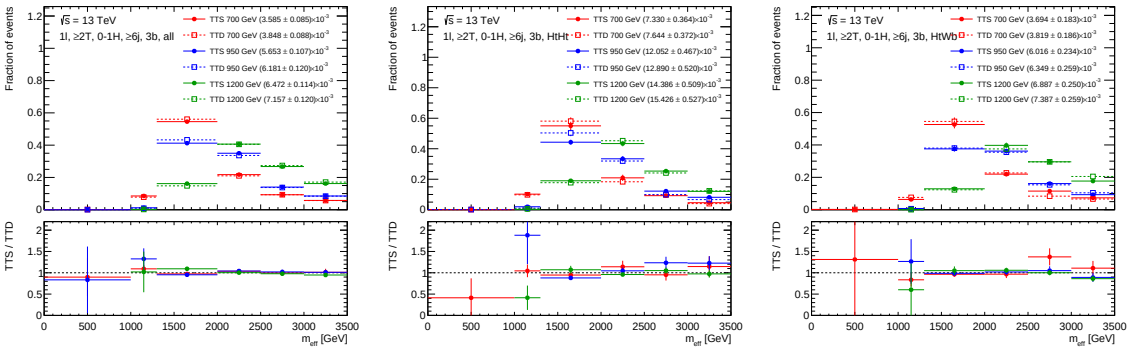

(a) all

(b) HtHt

(c) HtWb

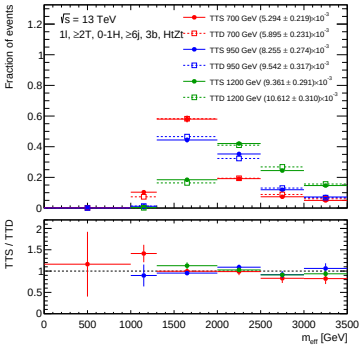

(d) HtZt

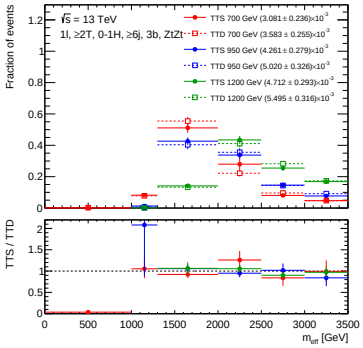

(e) ZtZt

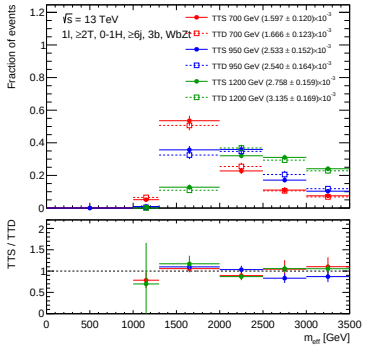

(f) WbZt

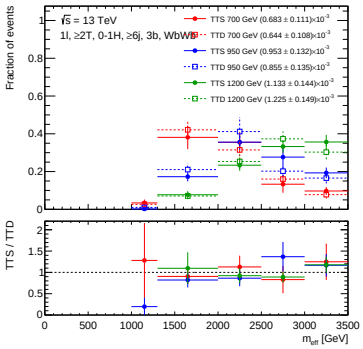

(g) WbWb

Figure A.10: Comparison of the signal acceptance and shape of the m_{eff} spectrum between the signalsamples produced in the singlet (full symbols) and doublet (open symbols) configurations for different decay modes and masses of 700 (red), 950 (blue), and 1200 GeV (green) in "≥2T, 0-1H, ≥6j, 3b" category.

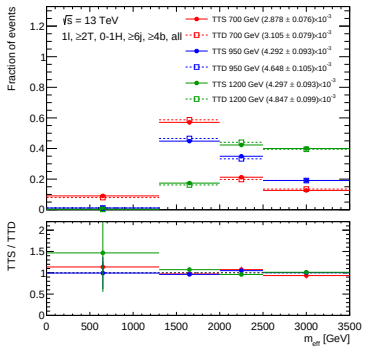

(a) all

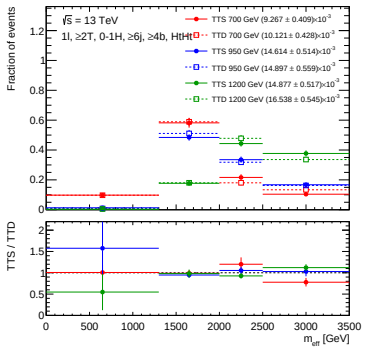

(b) HtHt

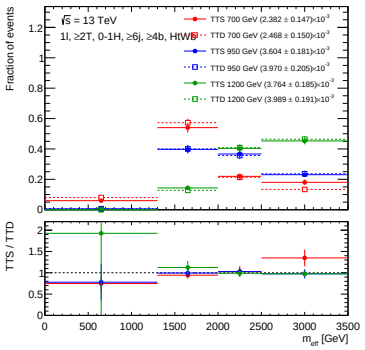

(c) HtWb

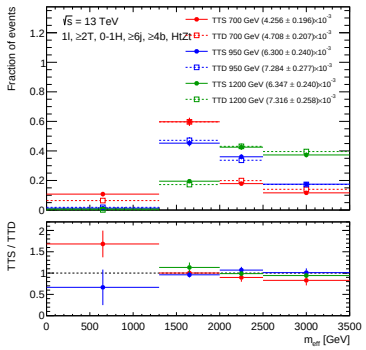

(d) HtZt

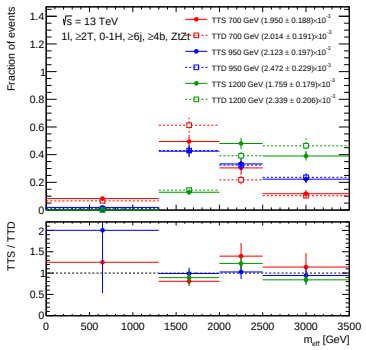

(e) ZtZt

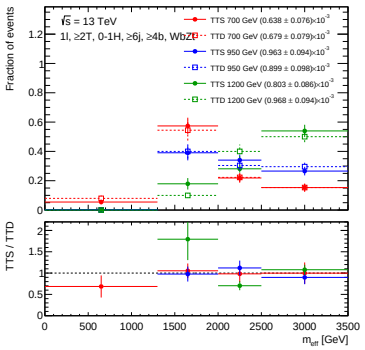

(f) WbZt

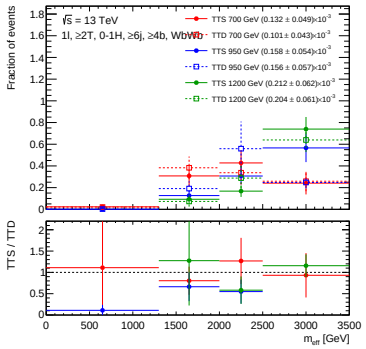

(g) WbWb

Figure A.11: Comparison of the signal acceptance and shape of the m_{eff} spectrum between the signalsamples produced in the singlet (full symbols) and doublet (open symbols) configurations for different decay modes and masses of 700 (red), 950 (blue), and 1200 GeV (green) in "≥2T, 0-1H, ≥6j, ≥4b" category.

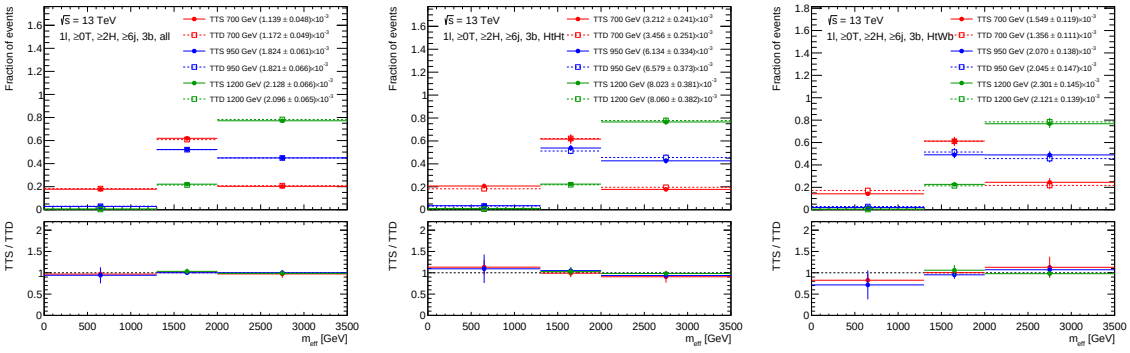

(a) all

(b) HtHt

(c) HtWb

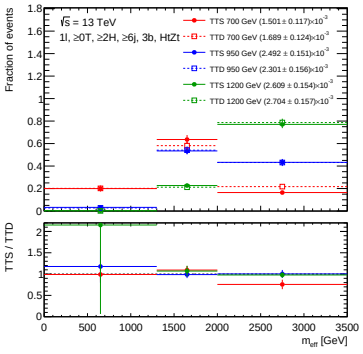

(d) HtZt

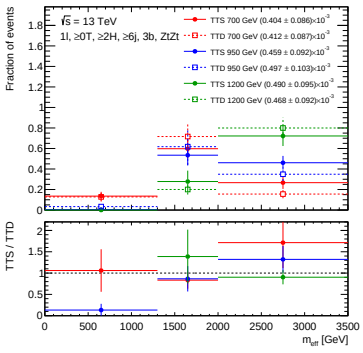

(e) ZtZt

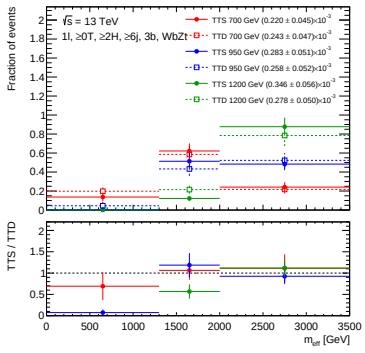

(f) WbZt

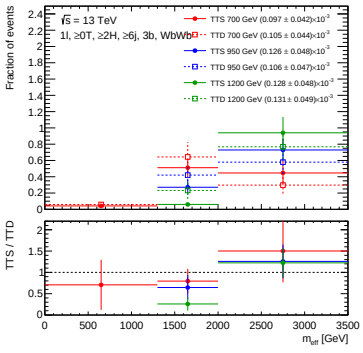

(g) WbWb

Figure A.12: Comparison of the signal acceptance and shape of the m_{eff} spectrum between the signalsamples produced in the singlet (full symbols) and doublet (open symbols) configurations for different decay modes and masses of 700 (red), 950 (blue), and 1200 GeV (green) in "≥0T, ≥2H, ≥6j, 3b" category.

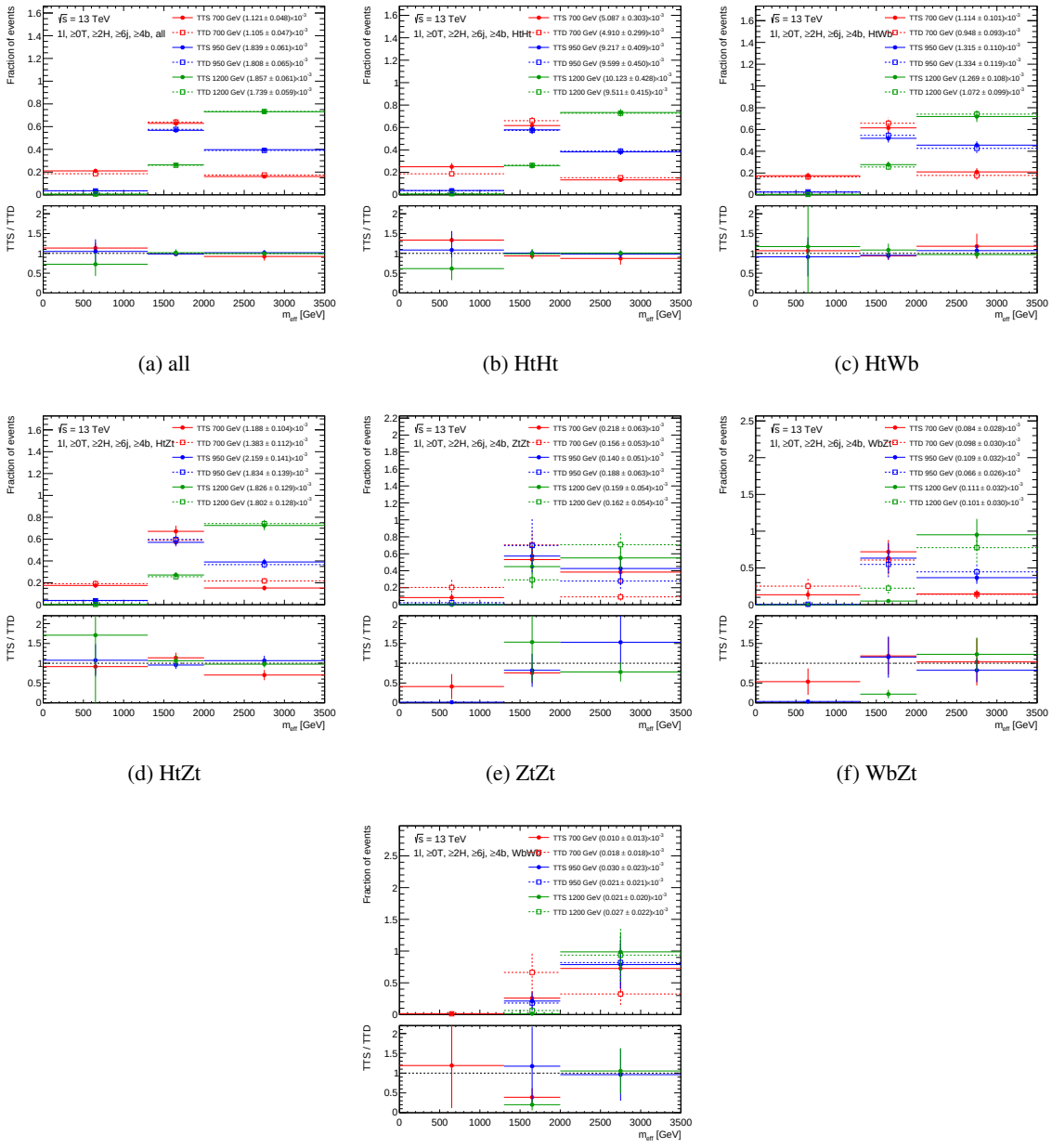

(a) all (b) HtHt (c) HtWb

(d) HtZt (e) ZtZt (f) WbZt

(g) WbWb

Figure A.13: Comparison of the signal acceptance and shape of the m_{eff} spectrum between the signalsamples produced in the singlet (full symbols) and doublet (open symbols) configurations for different decay modes and masses of 700 (red), 950 (blue), and 1200 GeV (green) in "≥0T, ≥2H, ≥6j, ≥4b" category.

B Validation plots for the multijet background estimation

This section shows the kinematic variables comparing the background prediction and data before the fit for validation of the multijet background estimation. For the validation, the preselection is not used. Instead, to enhance the multijet background contribution, the events are require to have at least four jets and at least one b-jets. Then, to validate the estimation step by step, the special validation regions are defined with $E_{\mathrm{T}}^{\mathrm{miss}}$, $m_{\mathrm{T}}^{\mathrm{W}}$, and b-jet multiplicity as shown in Table B.1. The region "1b, low $E_{\mathrm{T}}^{\mathrm{miss}}$, low $m_{\mathrm{T}}^{\mathrm{W}}$" is expected to contain much multijet background. In the region, good agreements between the background prediction and data are observed. In another regions with higher $E_{\mathrm{T}}^{\mathrm{miss}}$ and $m_{\mathrm{T}}^{\mathrm{W}}$, the background predictions are consistent with the data. For regions with more b-jets per event, small discrepancy between the prediction and data is observed. Around 50% uncertainty in the multijet background can cover it.

Table B.1: Special validation regions used for the validation of the multijet background estimation. Each region is classified with $E_{\mathrm{T}}^{\mathrm{miss}}$ and $m_{\mathrm{T}}^{\mathrm{W}}$ in units of GeV and the number of b-jets per event (N_b).

		$E_{\mathrm{T}}^{\mathrm{miss}}$ and $m_{\mathrm{T}}^{\mathrm{W}}$			
		$E_{\mathrm{T}}^{\mathrm{miss}} < 20$, $m_{\mathrm{T}}^{\mathrm{W}} < 60$	$m_{\mathrm{T}}^{\mathrm{W}} < 60$	N/A	$E_{\mathrm{T}}^{\mathrm{miss}} > 20$, $m_{\mathrm{T}}^{\mathrm{W}} > 60$
N_b	1	"1b, low $E_{\mathrm{T}}^{\mathrm{miss}}$, low $m_{\mathrm{T}}^{\mathrm{W}}$"	"1b, low $m_{\mathrm{T}}^{\mathrm{W}}$"	"1b"	"1b, high $E_{\mathrm{T}}^{\mathrm{miss}}$, high $m_{\mathrm{T}}^{\mathrm{W}}$"
	≥1	"≥1b, low $E_{\mathrm{T}}^{\mathrm{miss}}$, low $m_{\mathrm{T}}^{\mathrm{W}}$"	"≥1b, low $m_{\mathrm{T}}^{\mathrm{W}}$"	"≥1b"	"≥1b, high $E_{\mathrm{T}}^{\mathrm{miss}}$, high $m_{\mathrm{T}}^{\mathrm{W}}$"
	2	"2b, low $E_{\mathrm{T}}^{\mathrm{miss}}$, low $m_{\mathrm{T}}^{\mathrm{W}}$"	"2b, low $m_{\mathrm{T}}^{\mathrm{W}}$"	"2b"	"2b, high $E_{\mathrm{T}}^{\mathrm{miss}}$, high $m_{\mathrm{T}}^{\mathrm{W}}$"
	≥2	"≥2b, low $E_{\mathrm{T}}^{\mathrm{miss}}$, low $m_{\mathrm{T}}^{\mathrm{W}}$"	"≥2b, low $m_{\mathrm{T}}^{\mathrm{W}}$"	"≥2b"	"≥2b, high $E_{\mathrm{T}}^{\mathrm{miss}}$, high $m_{\mathrm{T}}^{\mathrm{W}}$"

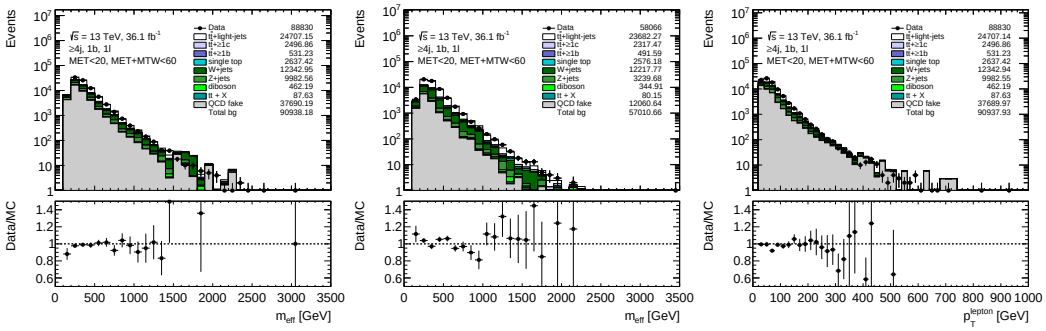

(a) m_{eff} in el

(b) m_{eff} in mu

(c) electron p_{T}

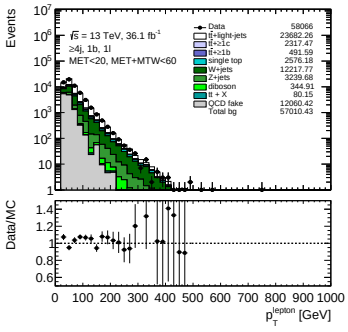

(d) muon p_{T}

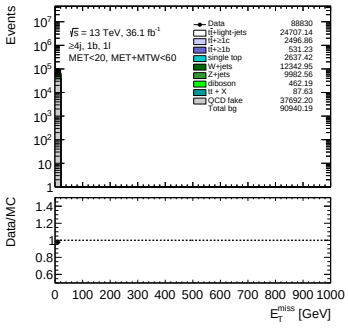

(e) $E_{\text{T}}^{\text{miss}}$ in el

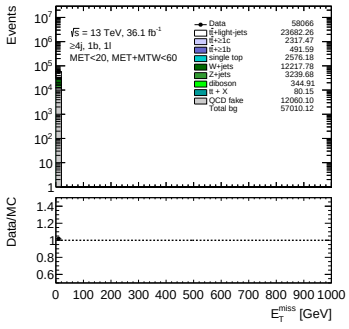

(f) $E_{\text{T}}^{\text{miss}}$ in mu

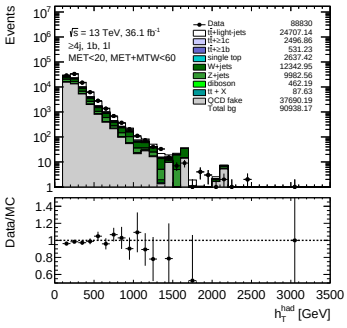

(g) $H_{\text{T}}^{\text{had}}$ in el

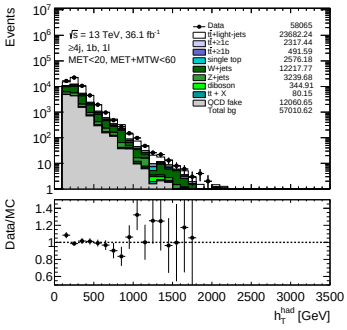

(h) $H_{\text{T}}^{\text{had}}$ in mu

Figure B.1: Kinematic variables for validation of the multijet background estimation in "≥ 4j, 1b, low $E_{\text{T}}^{\text{miss}}$, low m_{T}^{W}" region

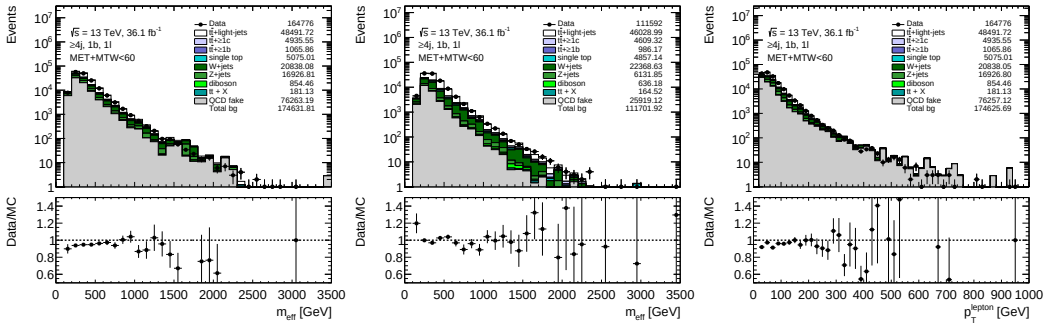

(a) m_{eff} in el (b) m_{eff} in mu (c) electron p_{T}

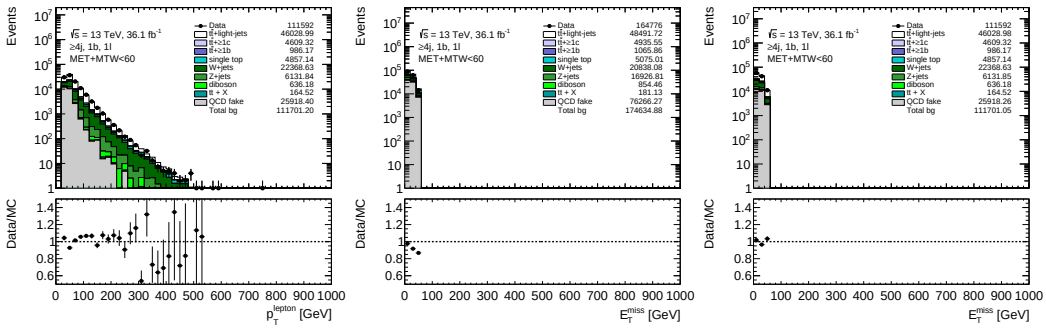

(d) muon p_{T} (e) $E_{\text{T}}^{\text{miss}}$ in el (f) $E_{\text{T}}^{\text{miss}}$ in mu

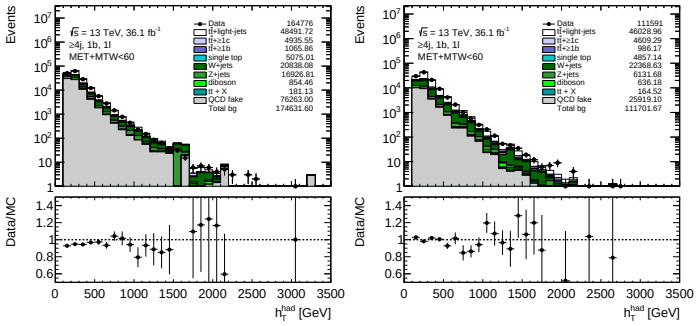

(g) $H_{\text{T}}^{\text{had}}$ in el (h) $H_{\text{T}}^{\text{had}}$ in mu

Figure B.2: Kinematic variables for validation of the multijet background estimation in "≥ 4j, 1b, low m_{T}^{W}" region

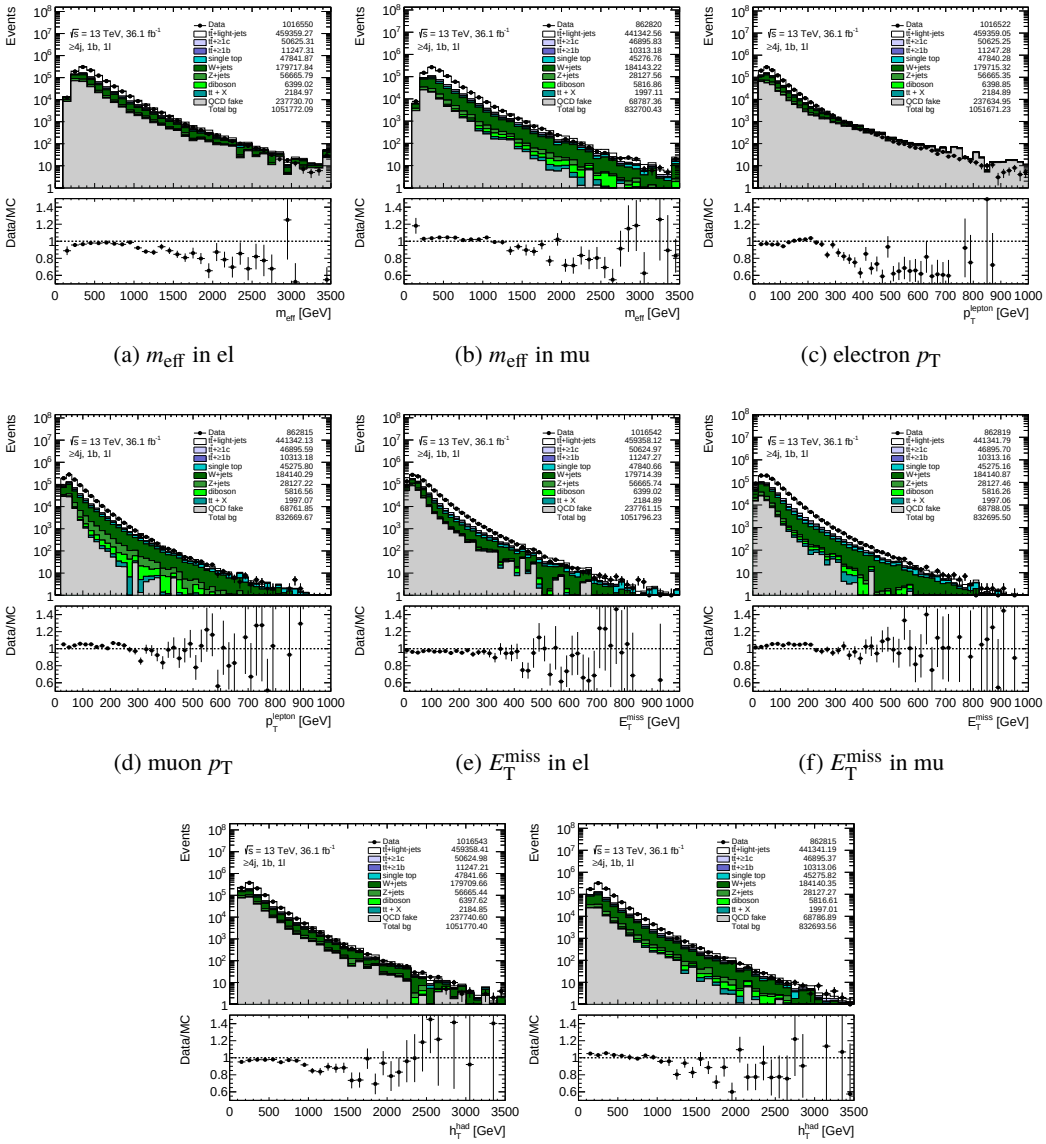

(a) m_{eff} in el (b) m_{eff} in mu (c) electron p_{T}

(d) muon p_{T} (e) $E_{\mathrm{T}}^{\mathrm{miss}}$ in el (f) $E_{\mathrm{T}}^{\mathrm{miss}}$ in mu

(g) $H_{\mathrm{T}}^{\mathrm{had}}$ in el (h) $H_{\mathrm{T}}^{\mathrm{had}}$ in mu

Figure B.3: Kinematic variables for validation of the multijet background estimation in "≥ 4j, 1b" region

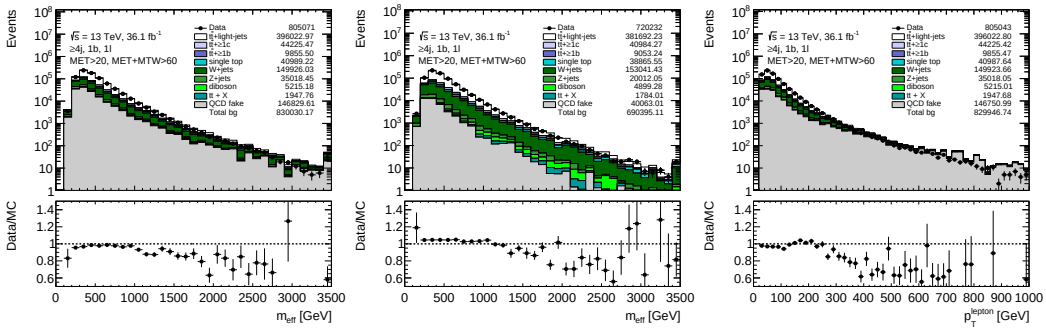

(a) m_{eff} in el (b) m_{eff} in mu (c) electron p_{T}

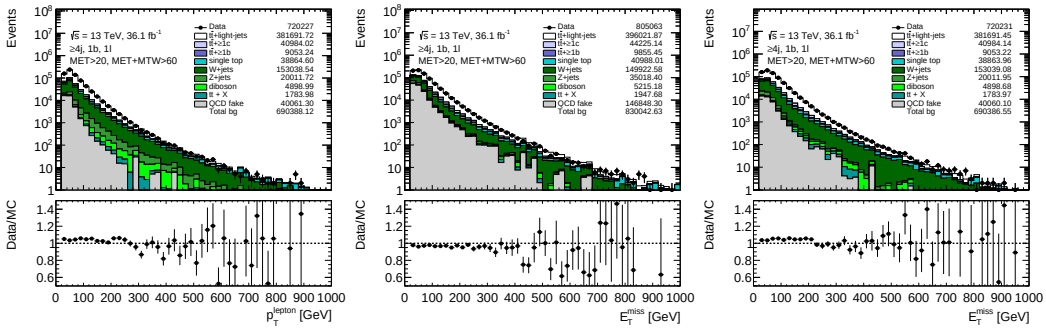

(d) muon p_{T} (e) $E_{\text{T}}^{\text{miss}}$ in el (f) $E_{\text{T}}^{\text{miss}}$ in mu

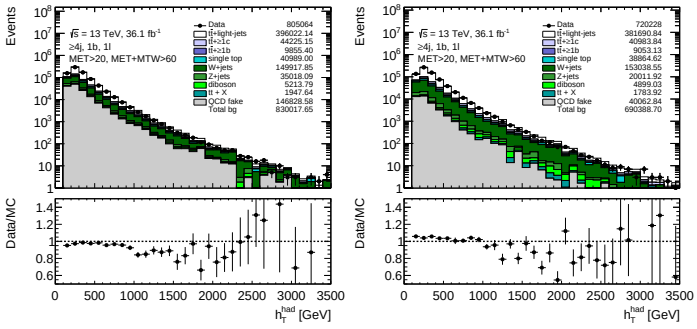

(g) $H_{\text{T}}^{\text{had}}$ in el (h) $H_{\text{T}}^{\text{had}}$ in mu

Figure B.4: Kinematic variables for validation of the multijet background estimation in "≥ 4j, 1b, high $E_{\text{T}}^{\text{miss}}$, high m_{T}^{W}" region

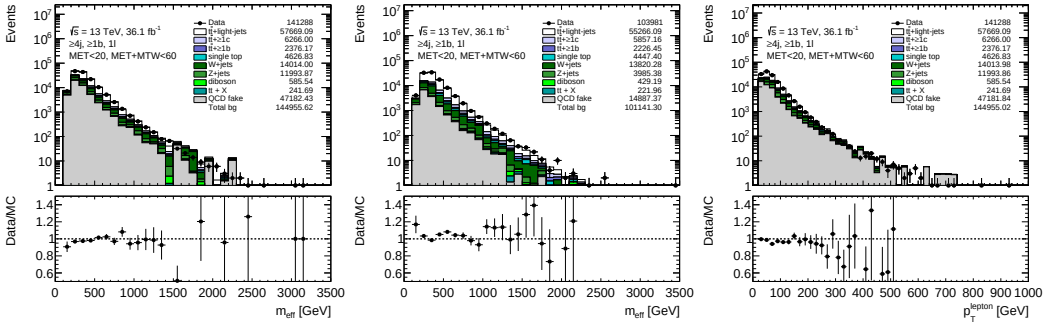

(a) m_{eff} in el

(b) m_{eff} in mu

(c) electron p_{T}

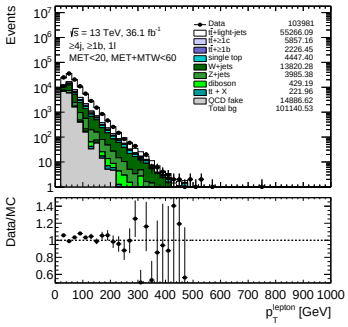

(d) muon p_{T}

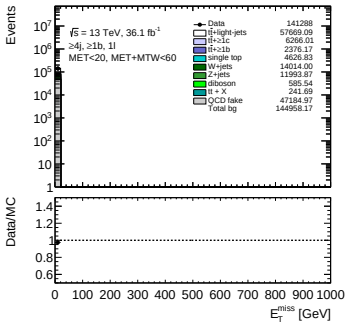

(e) $E_{\mathrm{T}}^{\mathrm{miss}}$ in el

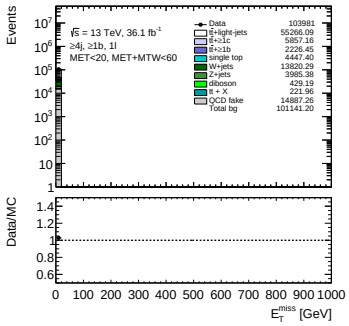

(f) $E_{\mathrm{T}}^{\mathrm{miss}}$ in mu

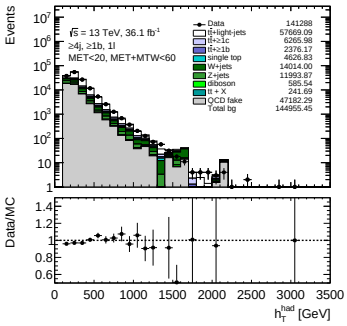

(g) $H_{\mathrm{T}}^{\mathrm{had}}$ in el

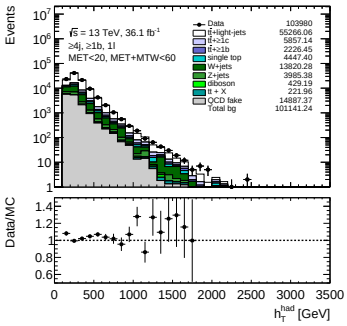

(h) $H_{\mathrm{T}}^{\mathrm{had}}$ in mu

Figure B.5: Kinematic variables for validation of the multijet background estimation in "≥ 4j, ≥ 1b, low $E_{\mathrm{T}}^{\mathrm{miss}}$, low $m_{\mathrm{T}}^{\mathrm{W}}$" region

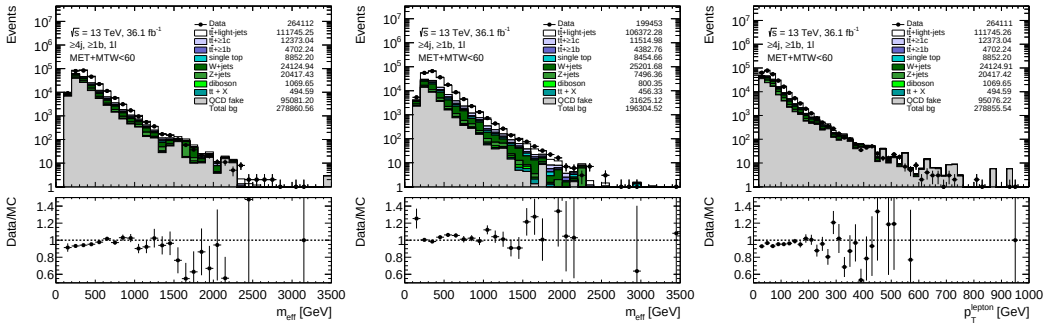

(a) m_{eff} in el (b) m_{eff} in mu (c) electron p_{T}

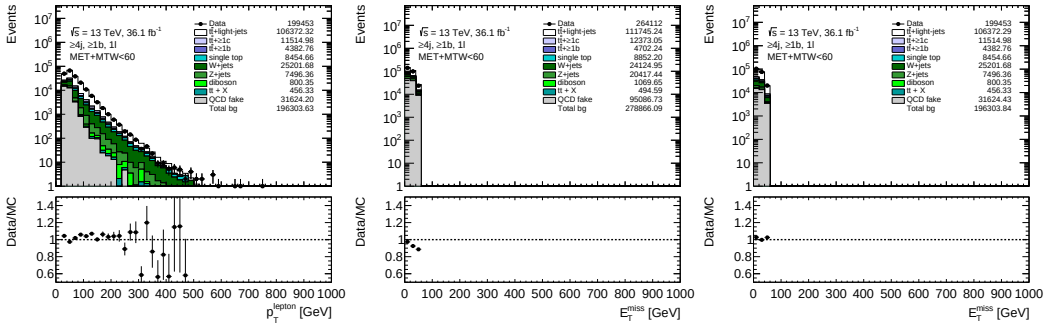

(d) muon p_{T} (e) $E_{\text{T}}^{\text{miss}}$ in el (f) $E_{\text{T}}^{\text{miss}}$ in mu

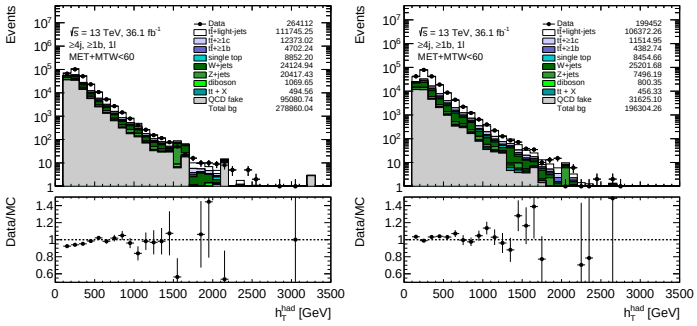

(g) $H_{\text{T}}^{\text{had}}$ in el (h) $H_{\text{T}}^{\text{had}}$ in mu

Figure B.6: Kinematic variables for validation of the multijet background estimation in "≥ 4j, ≥ 1b, low m_{T}^{W}" region

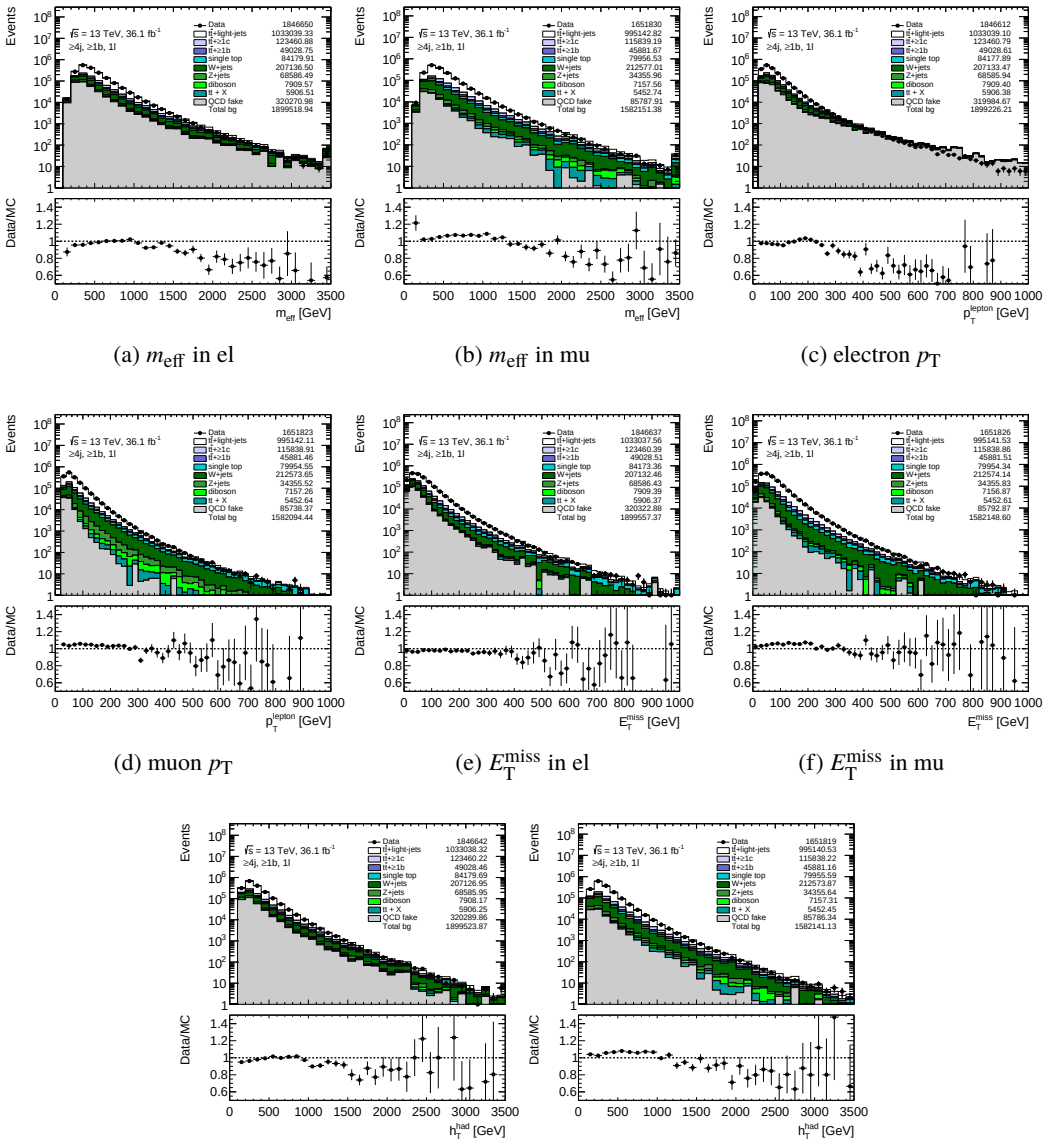

(a) m_{eff} in el (b) m_{eff} in mu (c) electron p_{T}

(d) muon p_{T} (e) $E_{\text{T}}^{\text{miss}}$ in el (f) $E_{\text{T}}^{\text{miss}}$ in mu

(g) $H_{\text{T}}^{\text{had}}$ in el (h) $H_{\text{T}}^{\text{had}}$ in mu

Figure B.7: Kinematic variables for validation of the multijet background estimation in "≥ 4j, ≥ 1b" region

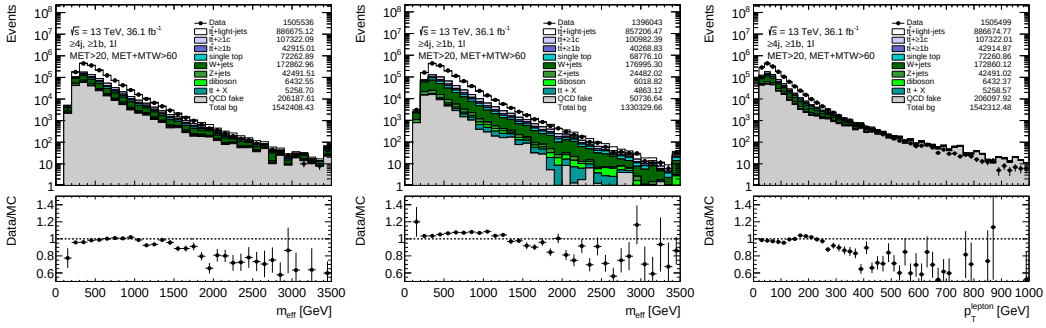

(a) m_{eff} in el (b) m_{eff} in mu (c) electron p_{T}

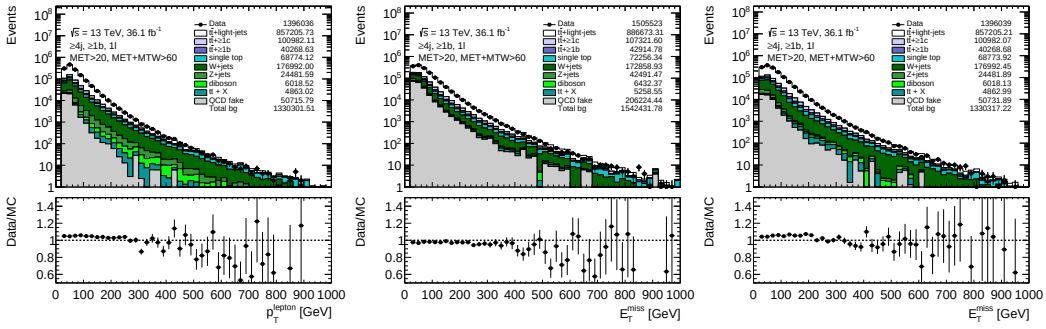

(d) muon p_{T} (e) $E_{\text{T}}^{\text{miss}}$ in el (f) $E_{\text{T}}^{\text{miss}}$ in mu

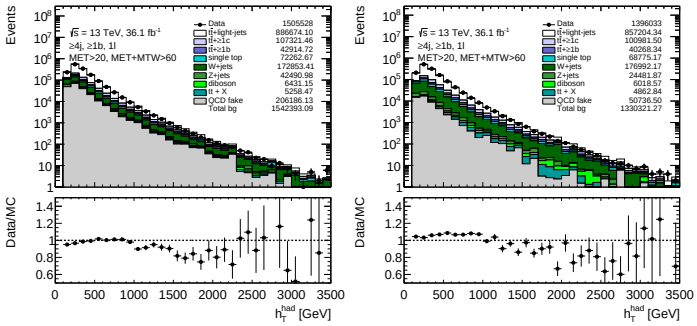

(g) $H_{\text{T}}^{\text{had}}$ in el (h) $H_{\text{T}}^{\text{had}}$ in mu

Figure B.8: Kinematic variables for validation of the multijet background estimation in "≥ 4j, ≥ 1b, high $E_{\text{T}}^{\text{miss}}$, high m_{T}^{W}" region

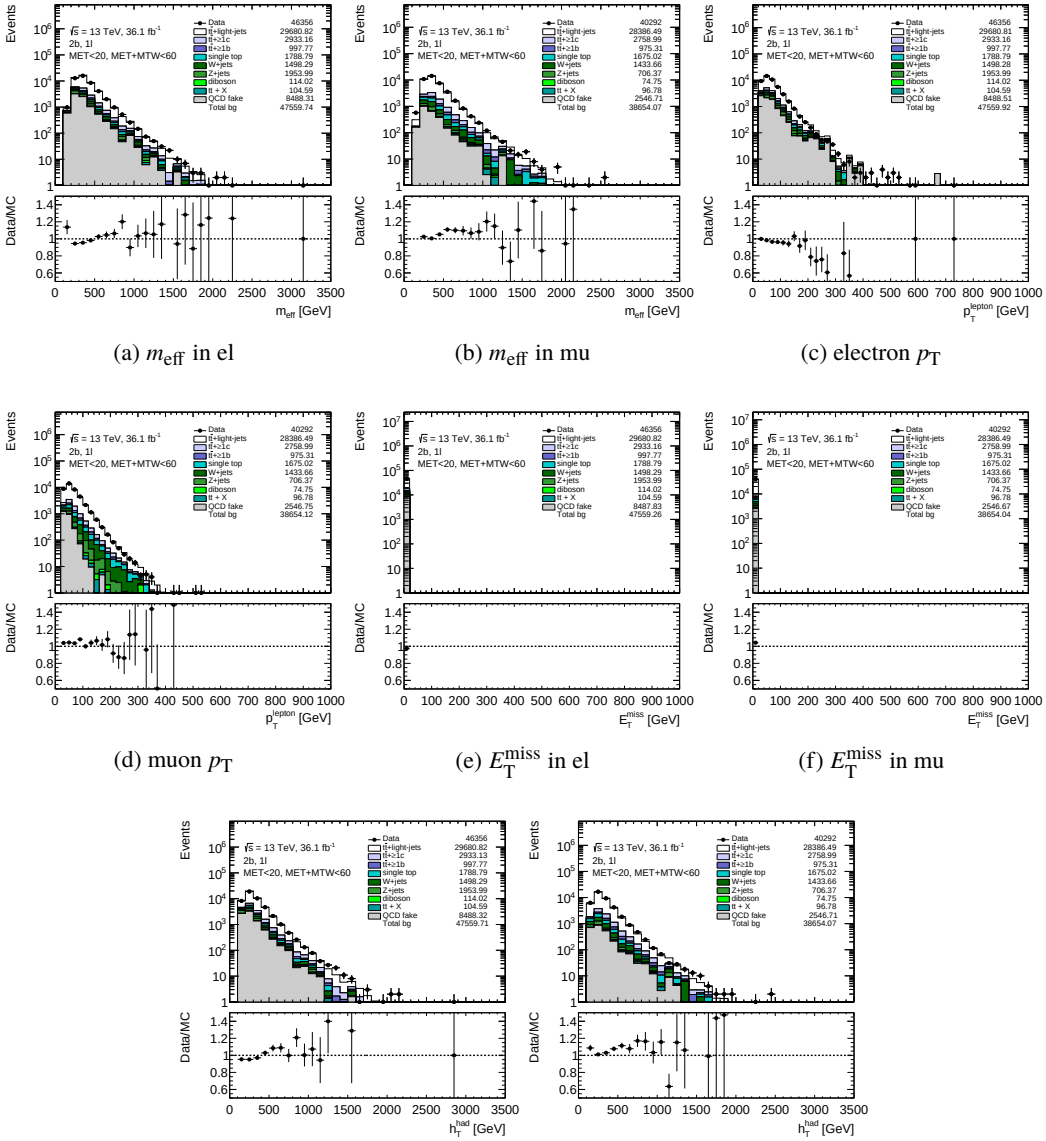

(a) m_{eff} in el (b) m_{eff} in mu (c) electron p_{T}

(d) muon p_{T} (e) $E_{\text{T}}^{\text{miss}}$ in el (f) $E_{\text{T}}^{\text{miss}}$ in mu

(g) $H_{\text{T}}^{\text{had}}$ in el (h) $H_{\text{T}}^{\text{had}}$ in mu

Figure B.9: Kinematic variables for validation of the multijet background estimation in "≥ 4j, 2b, low $E_{\text{T}}^{\text{miss}}$, low m_{T}^{W}" region

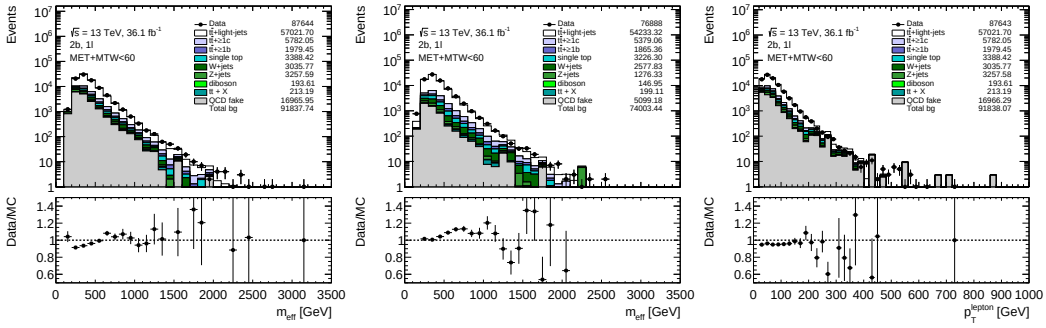

(a) m_{eff} in el (b) m_{eff} in mu (c) electron p_{T}

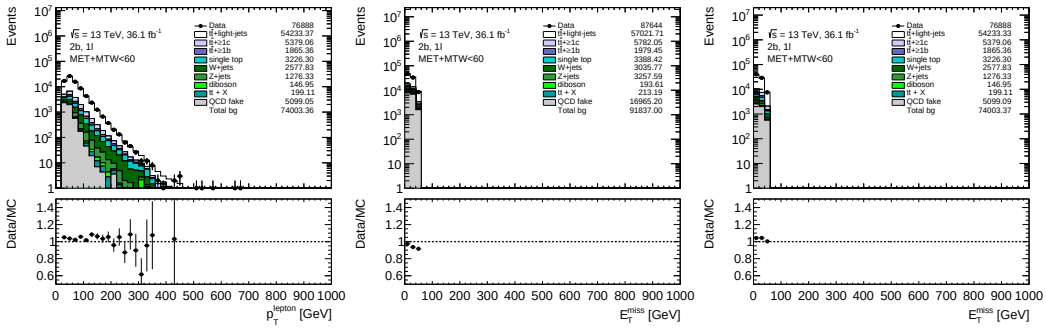

(d) muon p_{T} (e) $E_{\text{T}}^{\text{miss}}$ in el (f) $E_{\text{T}}^{\text{miss}}$ in mu

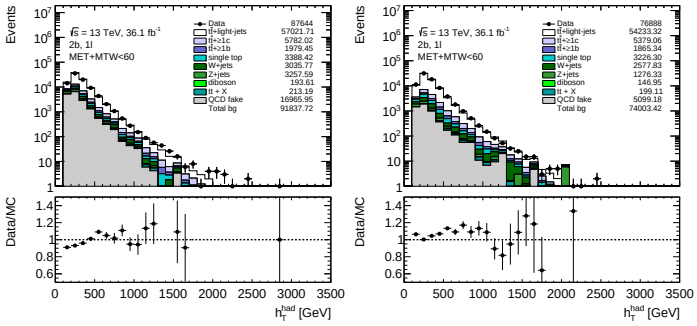

(g) $H_{\text{T}}^{\text{had}}$ in el (h) $H_{\text{T}}^{\text{had}}$ in mu

Figure B.10: Kinematic variables for validation of the multijet background estimation in "≥ 4j, 2b, low m_{T}^{W}" region

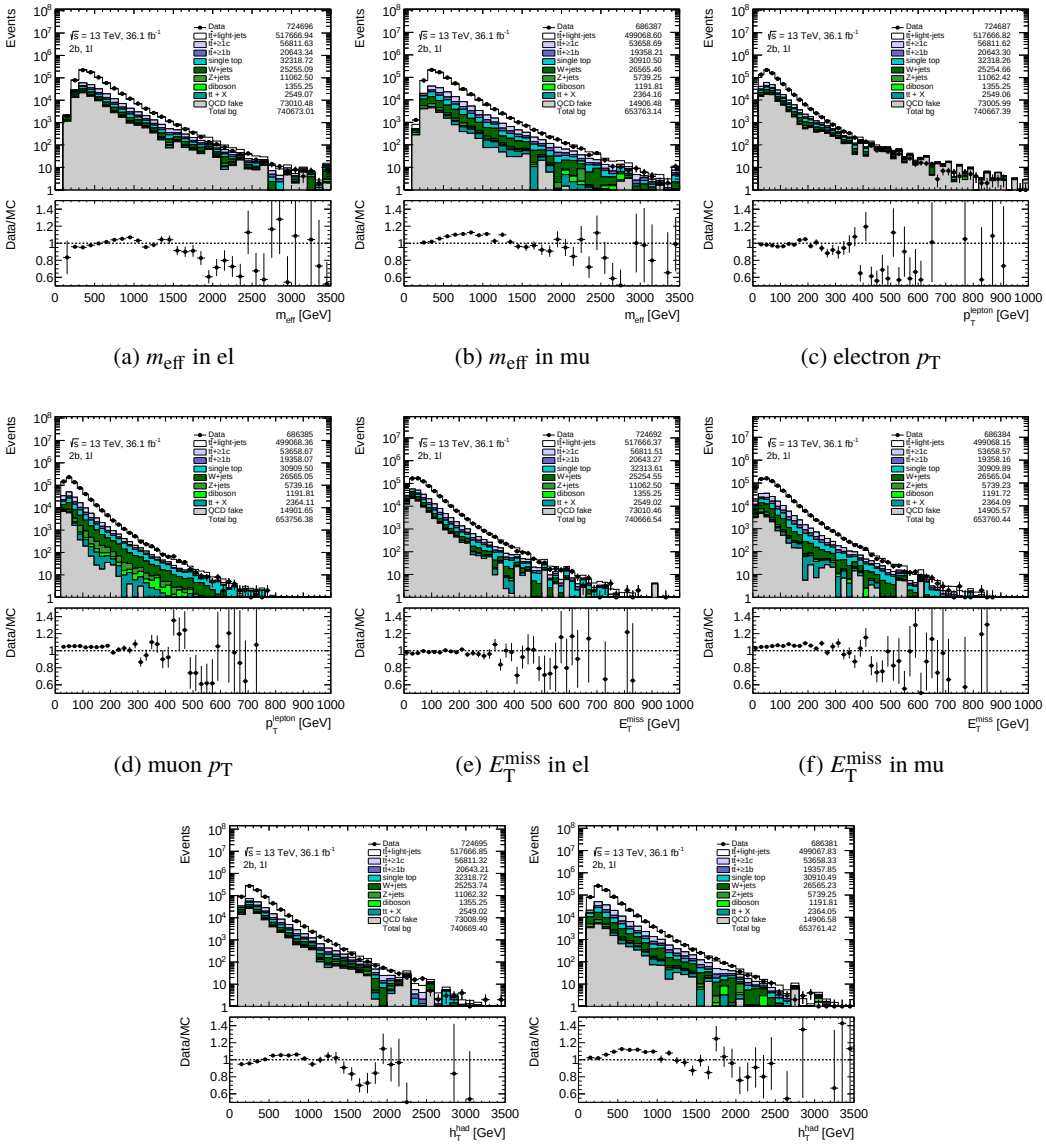

(a) m_{eff} in el (b) m_{eff} in mu (c) electron p_{T}

(d) muon p_{T} (e) $E_{\text{T}}^{\text{miss}}$ in el (f) $E_{\text{T}}^{\text{miss}}$ in mu

(g) $H_{\text{T}}^{\text{had}}$ in el (h) $H_{\text{T}}^{\text{had}}$ in mu

Figure B.11: Kinematic variables for validation of the multijet background estimation in "≥ 4j, 2b" region

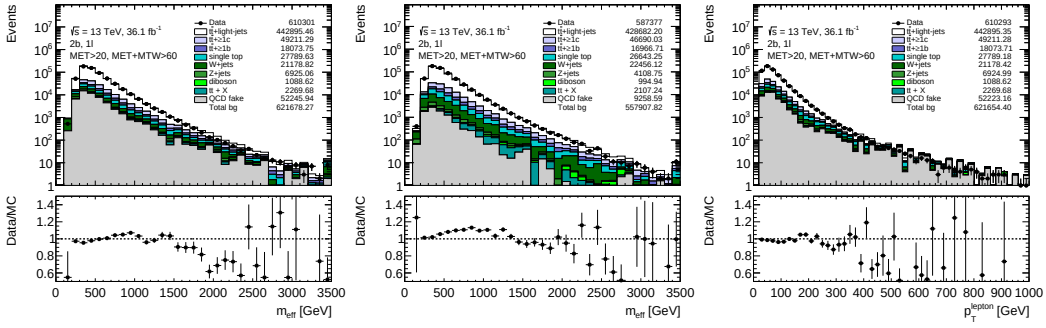

(a) m_{eff} in el (b) m_{eff} in mu (c) electron p_{T}

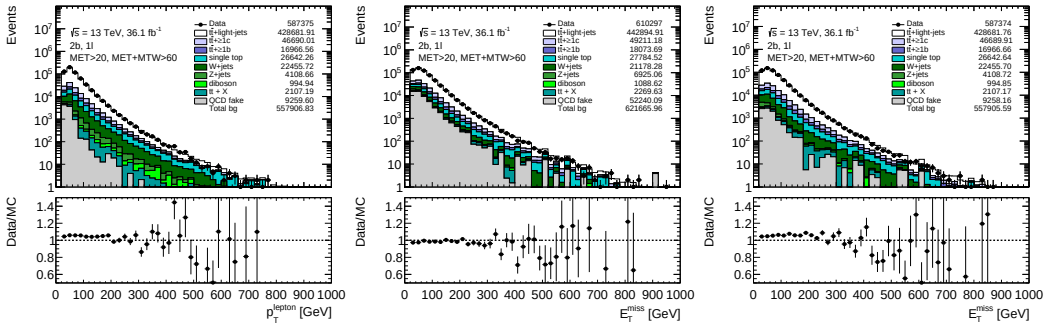

(d) muon p_{T} (e) $E_{\text{T}}^{\text{miss}}$ in el (f) $E_{\text{T}}^{\text{miss}}$ in mu

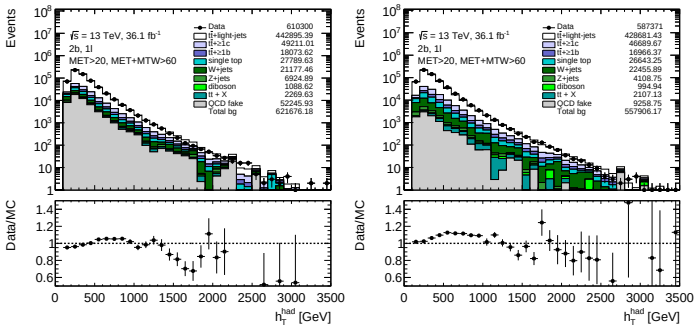

(g) $H_{\text{T}}^{\text{had}}$ in el (h) $H_{\text{T}}^{\text{had}}$ in mu

Figure B.12: Kinematic variables for validation of the multijet background estimation in "≥ 4j, 2b, high $E_{\text{T}}^{\text{miss}}$, high m_{T}^{W}" region

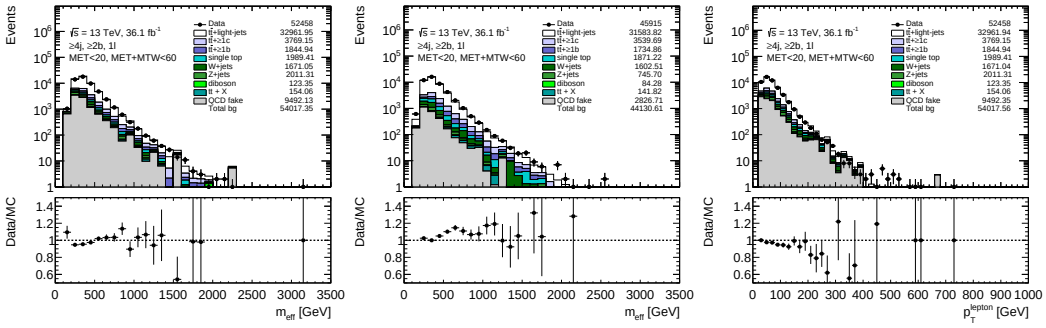

(a) m_{eff} in el

(b) m_{eff} in mu

(c) electron p_{T}

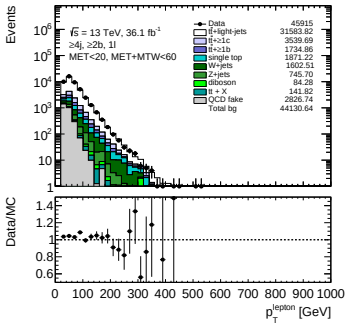

(d) muon p_{T}

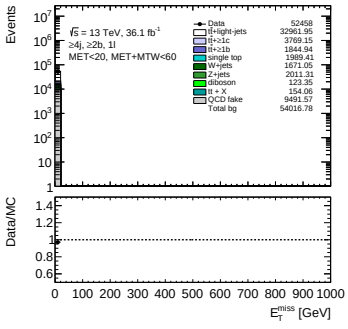

(e) $E_{\text{T}}^{\text{miss}}$ in el

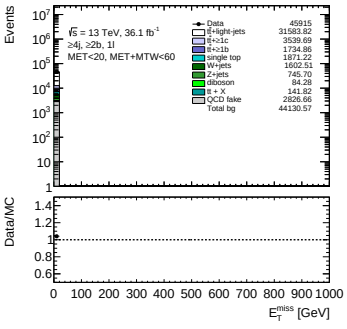

(f) $E_{\text{T}}^{\text{miss}}$ in mu

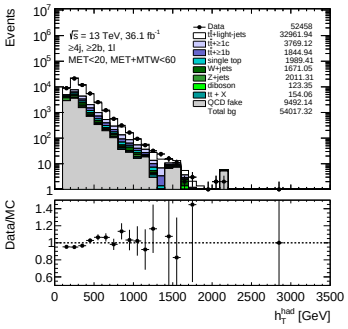

(g) $H_{\text{T}}^{\text{had}}$ in el

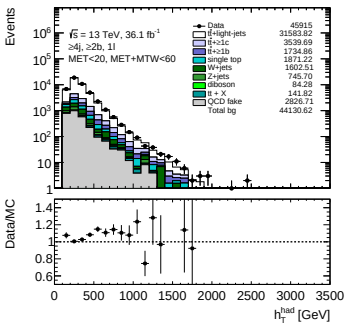

(h) $H_{\text{T}}^{\text{had}}$ in mu

Figure B.13: Kinematic variables for validation of the multijet background estimation in "≥ 4j, ≥ 2b, low $E_{\text{T}}^{\text{miss}}$, low m_{T}^{W}" region

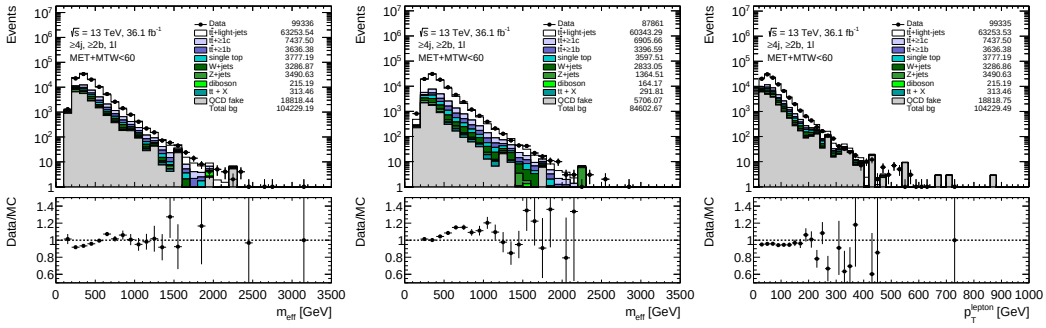

(a) m_{eff} in el (b) m_{eff} in mu (c) electron p_{T}

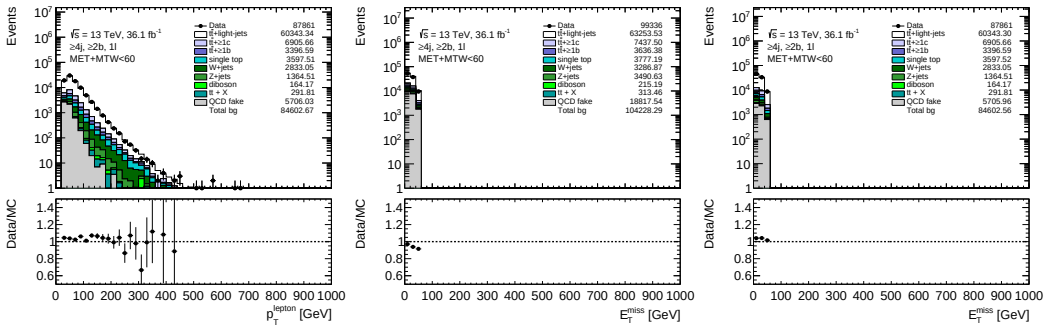

(d) muon p_{T} (e) $E_{\text{T}}^{\text{miss}}$ in el (f) $E_{\text{T}}^{\text{miss}}$ in mu

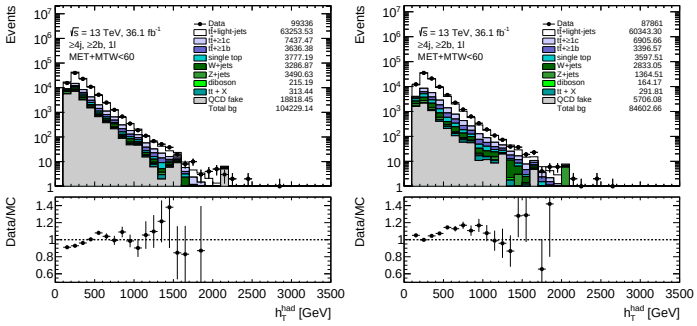

(g) $H_{\text{T}}^{\text{had}}$ in el (h) $H_{\text{T}}^{\text{had}}$ in mu

Figure B.14: Kinematic variables for validation of the multijet background estimation in "≥ 4j, ≥ 2b, low m_{T}^{W}" region

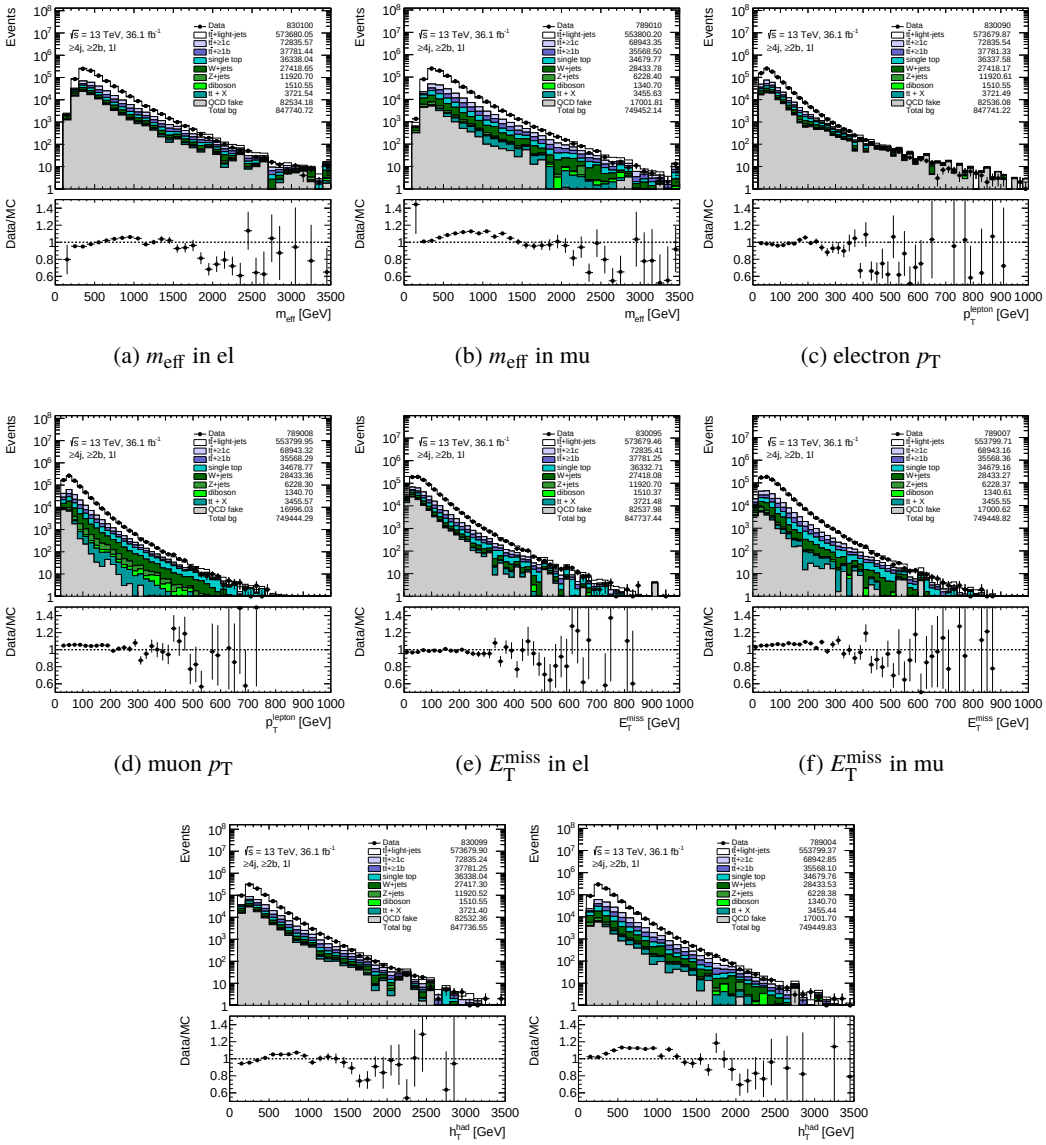

(a) m_{eff} in el (b) m_{eff} in mu (c) electron p_{T}

(d) muon p_{T} (e) $E_{\text{T}}^{\text{miss}}$ in el (f) $E_{\text{T}}^{\text{miss}}$ in mu

(g) $H_{\text{T}}^{\text{had}}$ in el (h) $H_{\text{T}}^{\text{had}}$ in mu

Figure B.15: Kinematic variables for validation of the multijet background estimation in "≥ 4j, ≥ 2b" region

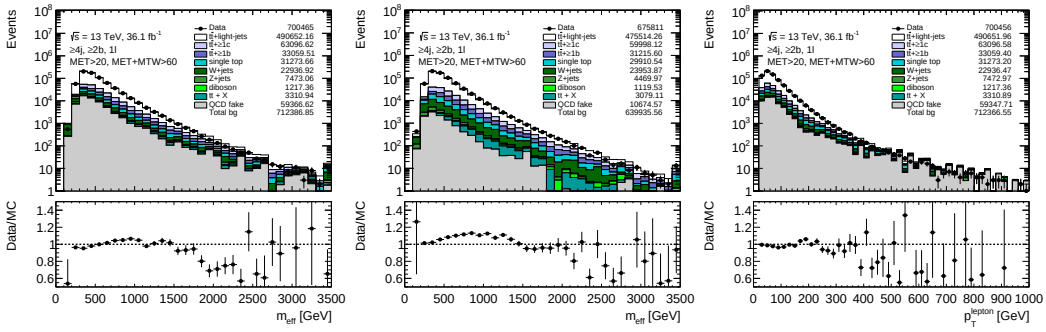

(a) m_{eff} in el (b) m_{eff} in mu (c) electron p_{T}

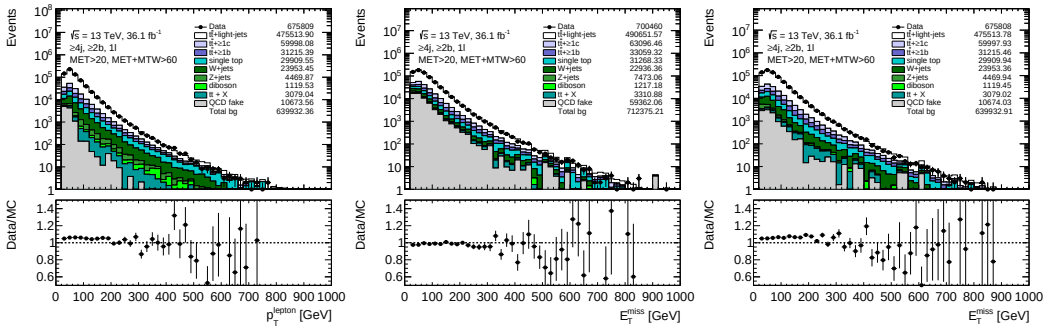

(d) muon p_{T} (e) $E_{\text{T}}^{\text{miss}}$ in el (f) $E_{\text{T}}^{\text{miss}}$ in mu

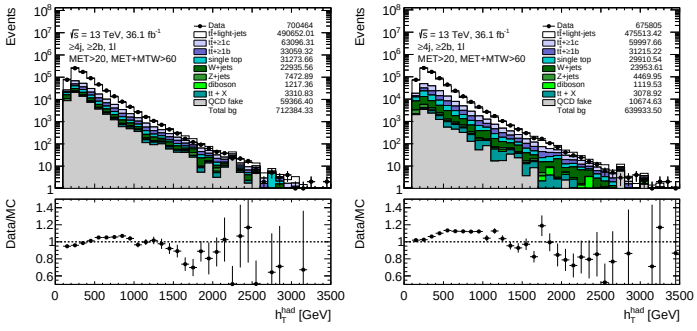

(g) $H_{\text{T}}^{\text{had}}$ in el (h) $H_{\text{T}}^{\text{had}}$ in mu

Figure B.16: Kinematic variables for validation of the multijet background estimation in "≥ 4j, ≥ 2b, high $E_{\text{T}}^{\text{miss}}$, high m_{T}^{W}" region

C TRF closure tests

The Tag Rate Function (TRF) method is employed in this analysis to increase MC statistics for the ranges where the backgrounds are expected to be depleted, as described in Section 5.4. Since TRF does not use the substracture varibales inside jets, it is necessary to check the consistency between the TRF and nominal way (Direct Tagging). In this chapter, auxiliary materials for the TRF are shown. m_{eff} distributions between TRF and Direct Tagging in each $t\bar{t}$+jets subprocess are compared in folllowing. In general, the prediction with TRF is consistent with the one with DT.

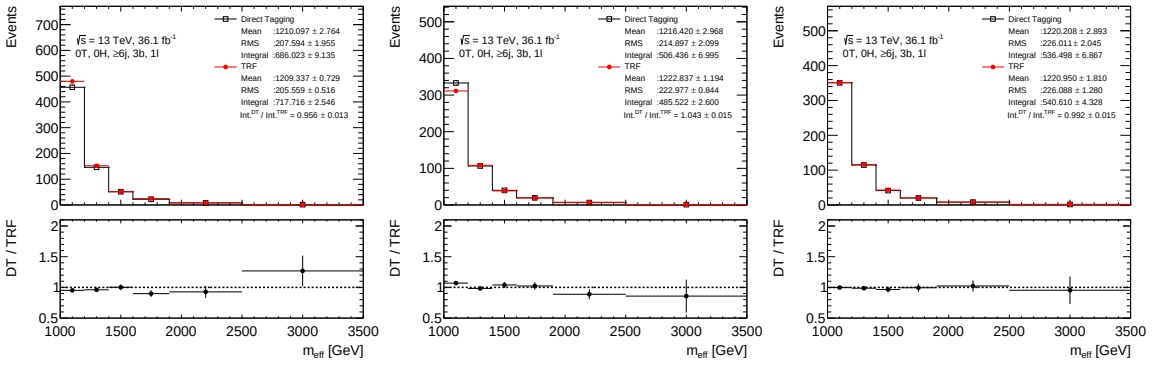

(a) (b) (c)

Figure C.1: m_{eff} distributions with the Direct Tagging (black) and TRF (red) before the fit in "0T, 0H, ≥6j, 3b" category of the 1L channel: (a) $t\bar{t}$+lights, (b) $t\bar{t}$+≥1c, (c) $t\bar{t}$+≥1b, (d) $t\bar{t}$ inclusive The mean, root mean square (RMS), and integral values are shown in the legend.

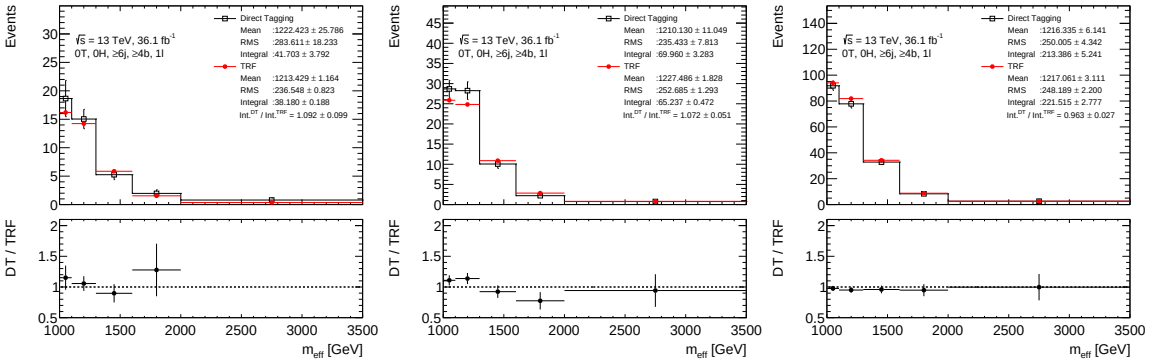

(a) (b) (c)

Figure C.2: m_{eff} distributions with the Direct Tagging (black) and TRF (red) before the fit in "0T, 0H, ≥6j, ≥4b" category of the 1L channel: (a) $t\bar{t}$+lights, (b) $t\bar{t}$+≥1c, (c) $t\bar{t}$+≥1b, (d) $t\bar{t}$ inclusive The mean, root mean square (RMS), and integral values are shown in the legend.

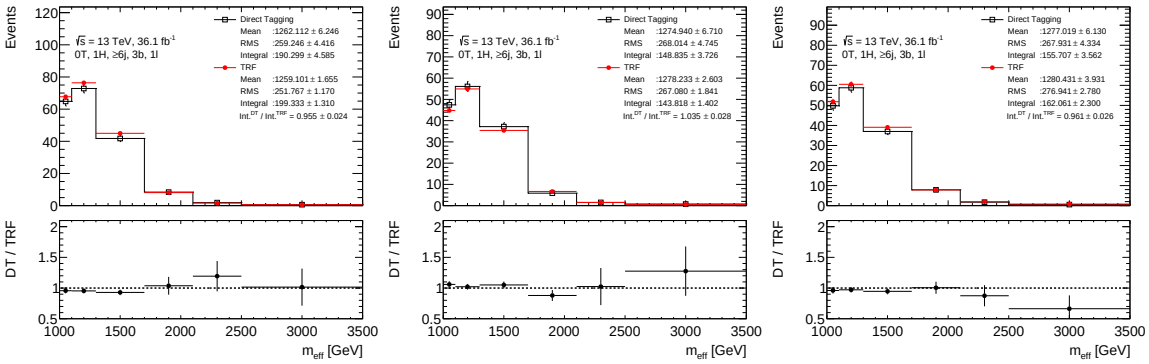

(a) (b) (c)

Figure C.3: m_{eff} distributions with the Direct Tagging (black) and TRF (red) before the fit in "0T, 1H, ≥6j, 3b" category of the 1L channel: (a) $t\bar{t}$+lights, (b) $t\bar{t}$+≥1c, (c) $t\bar{t}$+≥1b, (d) $t\bar{t}$ inclusive The mean, root mean square (RMS), and integral values are shown in the legend.

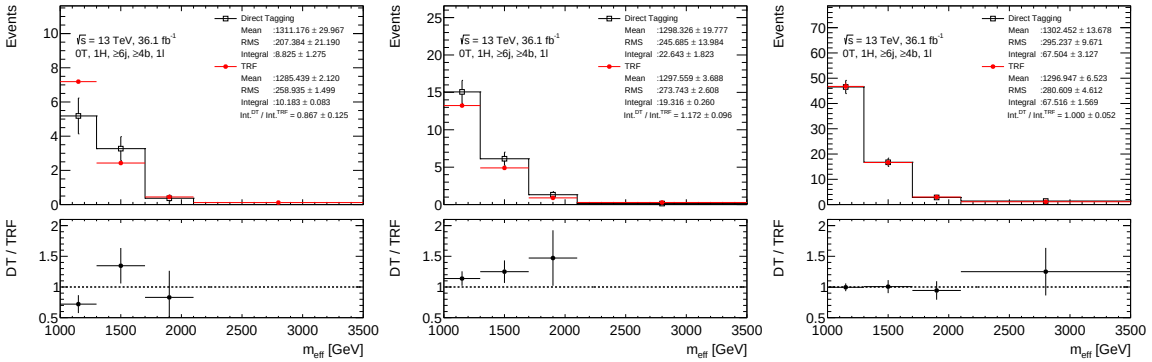

(a) (b) (c)

Figure C.4: m_{eff} distributions with the Direct Tagging (black) and TRF (red) before the fit in "0T, 1H, ≥6j, ≥4b" category of the 1L channel: (a) $t\bar{t}$+lights, (b) $t\bar{t}$+≥1c, (c) $t\bar{t}$+≥1b, (d) $t\bar{t}$ inclusive The mean, root mean square (RMS), and integral values are shown in the legend.

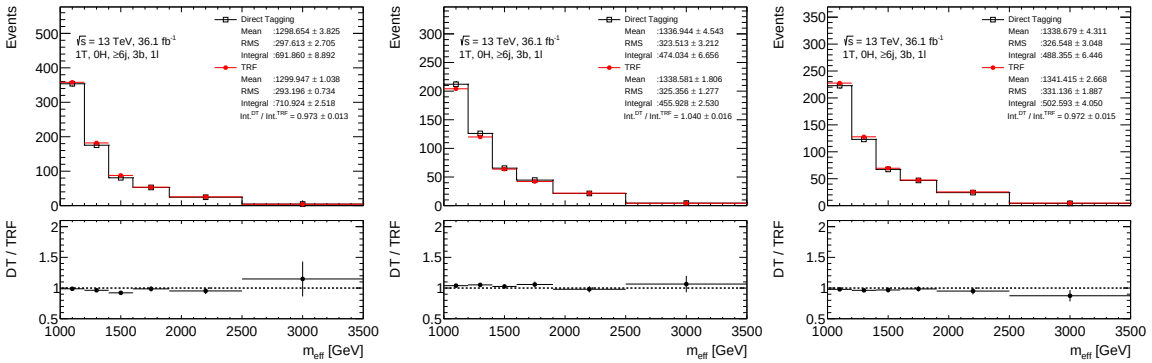

(a) (b) (c)

Figure C.5: m_{eff} distributions with the Direct Tagging (black) and TRF (red) before the fit in "1T, 0H, ≥6j, 3b" category of the 1L channel: (a) $t\bar{t}$+lights, (b) $t\bar{t}$+≥1c, (c) $t\bar{t}$+≥1b, (d) $t\bar{t}$ inclusive The mean, root mean square (RMS), and integral values are shown in the legend.

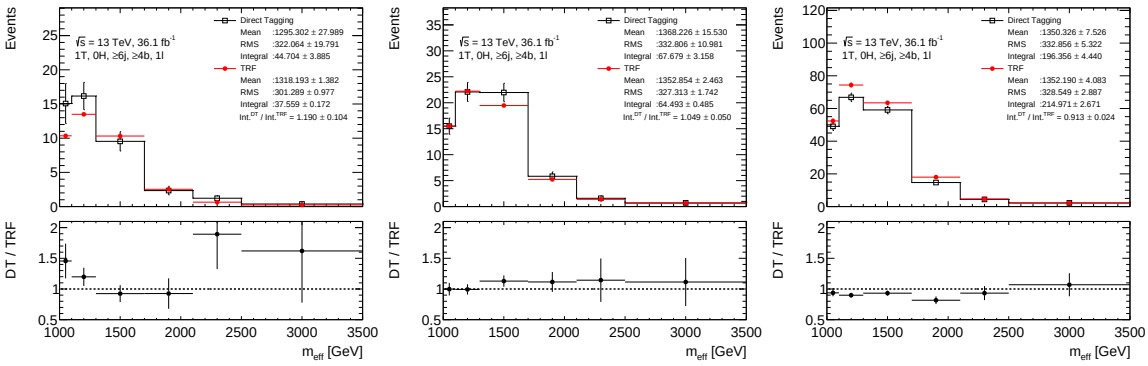

(a) (b) (c)

Figure C.6: m_{eff} distributions with the Direct Tagging (black) and TRF (red) before the fit in "1T, 0H, ≥6j, ≥4b" category of the 1L channel: (a) $t\bar{t}$+lights, (b) $t\bar{t}$+≥1c, (c) $t\bar{t}$+≥1b, (d) $t\bar{t}$ inclusive The mean, root mean square (RMS), and integral values are shown in the legend.

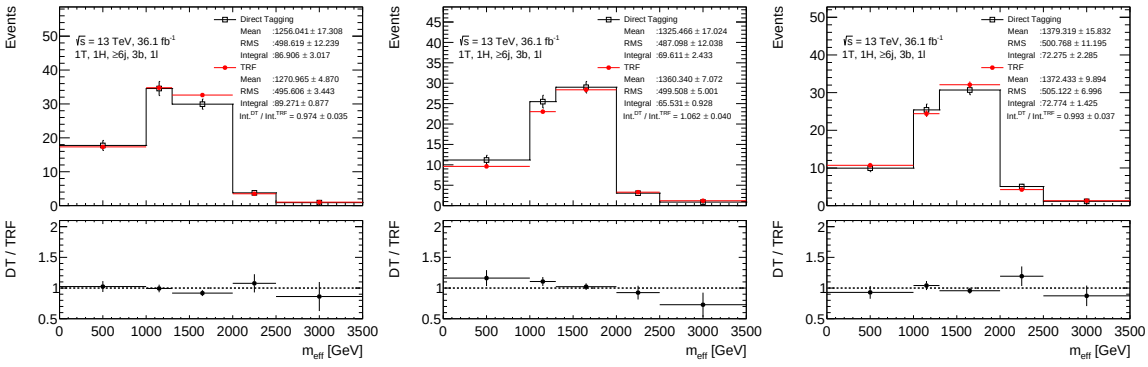

(a) (b) (c)

Figure C.7: m_{eff} distributions with the Direct Tagging (black) and TRF (red) before the fit in "1T, 1H, ≥6j, 3b" category of the 1L channel: (a) $t\bar{t}$+lights, (b) $t\bar{t}$+≥1c, (c) $t\bar{t}$+≥1b, (d) $t\bar{t}$ inclusive The mean, root mean square (RMS), and integral values are shown in the legend.

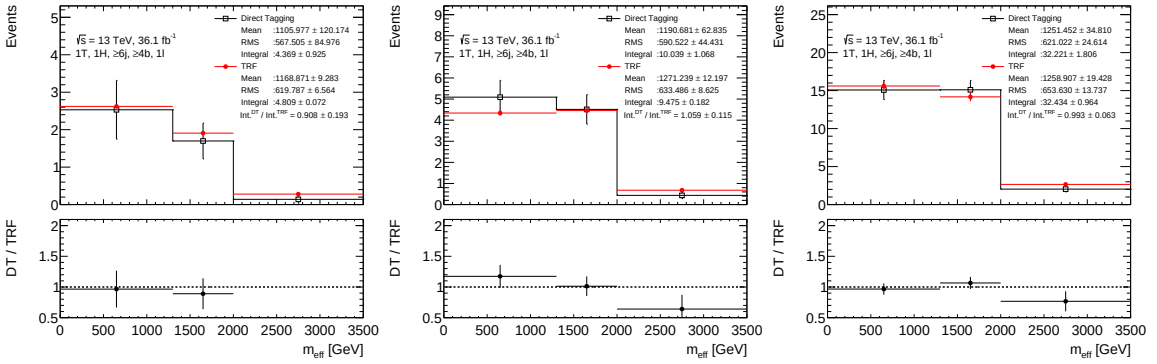

(a) (b) (c)

Figure C.8: m_{eff} distributions with the Direct Tagging (black) and TRF (red) before the fit in "1T, 1H, ≥6j, ≥4b" category of the 1L channel: (a) $t\bar{t}$+lights, (b) $t\bar{t}$+≥1c, (c) $t\bar{t}$+≥1b, (d) $t\bar{t}$ inclusive The mean, root mean square (RMS), and integral values are shown in the legend.

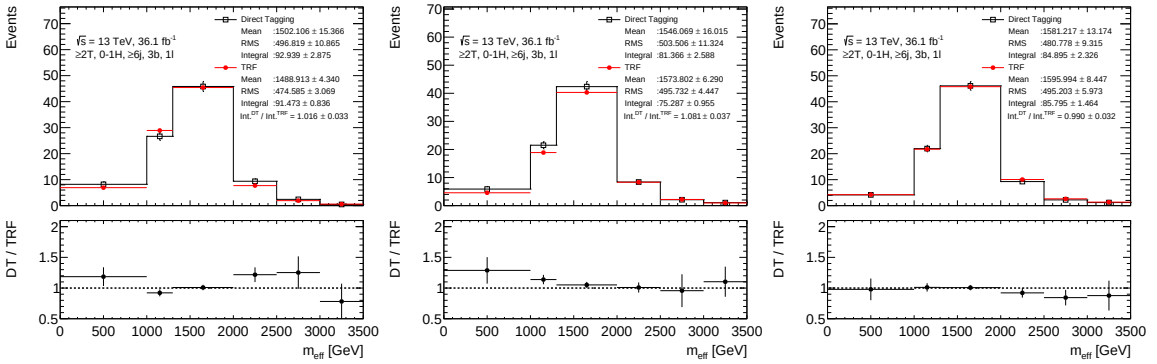

(a) (b) (c)

Figure C.9: m_{eff} distributions with the Direct Tagging (black) and TRF (red) before the fit in "≥2T, 0-1H, ≥6j, 3b" category of the 1L channel: (a) $t\bar{t}$+lights, (b) $t\bar{t}$+≥1c, (c) $t\bar{t}$+≥1b, (d) $t\bar{t}$ inclusive The mean, root mean square (RMS), and integral values are shown in the legend.

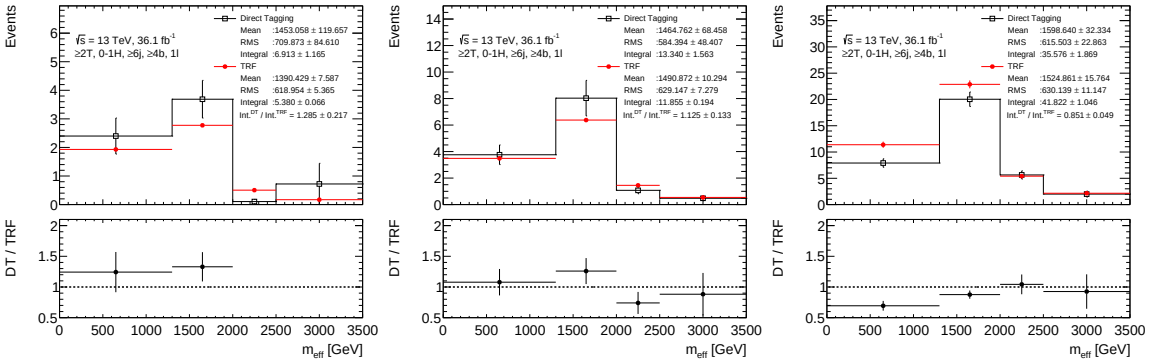

(a) (b) (c)

Figure C.10: m_{eff} distributions with the Direct Tagging (black) and TRF (red) before the fit in "≥2T, 0-1H, ≥6j, ≥4b" category of the 1L channel: (a) $t\bar{t}$+lights, (b) $t\bar{t}$+≥1c, (c) $t\bar{t}$+≥1b, (d) $t\bar{t}$ inclusive The mean, root mean square (RMS), and integral values are shown in the legend.

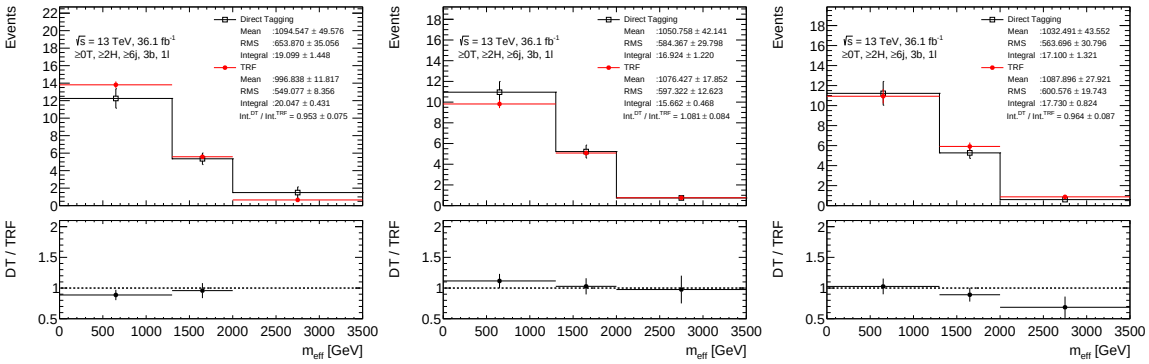

(a) (b) (c)

Figure C.11: m_{eff} distributions with the Direct Tagging (black) and TRF (red) before the fit in "≥0T, ≥2H, ≥6j, 3b" category of the 1L channel: (a) $t\bar{t}$+lights, (b) $t\bar{t}$+≥1c, (c) $t\bar{t}$+≥1b, (d) $t\bar{t}$ inclusive The mean, root mean square (RMS), and integral values are shown in the legend.

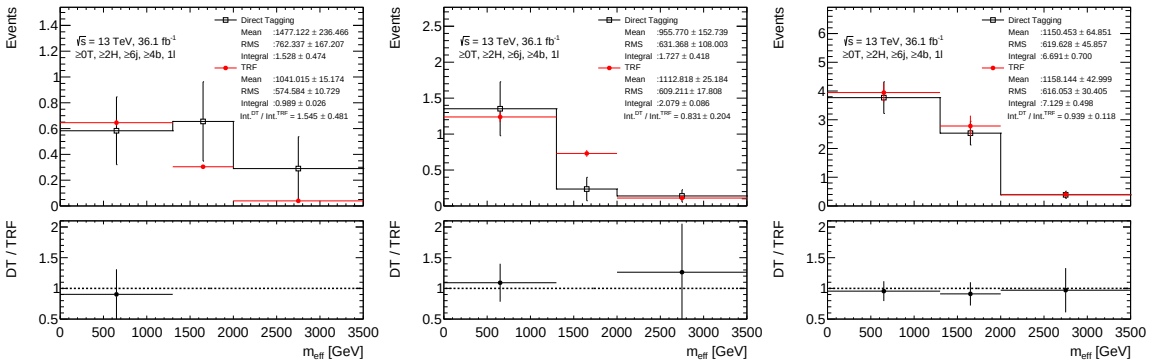

(a) (b) (c)

Figure C.12: m_{eff} distributions with the Direct Tagging (black) and TRF (red) before the fit in "≥0T, ≥2H, ≥6j, ≥4b" category of the 1L channel: (a) $t\bar{t}$+lights, (b) $t\bar{t}$+≥1c, (c) $t\bar{t}$+≥1b, (d) $t\bar{t}$ inclusive The mean, root mean square (RMS), and integral values are shown in the legend.

D Auxiliary materials for the optimisation

In this chapter, the auxiliary materials for the optimisation described in Chapter 6 are shown.

Figure D.1 shows the ratio of the upper limits comparing to the one with the *old* configuration for various signal models including 2UED-RPP model. Especially in 2UED-RPP model, the category having $\geq$ 2 top-tagged jets and 0 Higgs-tagged jets is the most sensitive because the signal model has four boosted top quarks and does not have Higgs boson in the final state. Therefore the tightest mass requirement of higgs tagging results in better sensitivity to 2UED-RPP model since signal has higher probability to be categorised in 0 Higgs-tagged jet category.

Table D.1 shows the classification for the investigating the top-quark tagging efficiency. The classification is carried out in the same way as done in the Higgs bosons tagger.

Figure D.2 shows the fraction of each class, large-R jet mass distributions, and the efficiency as a function of large-R jet p_{T}. In summary, missing constituents causes inefficiency on the top quark

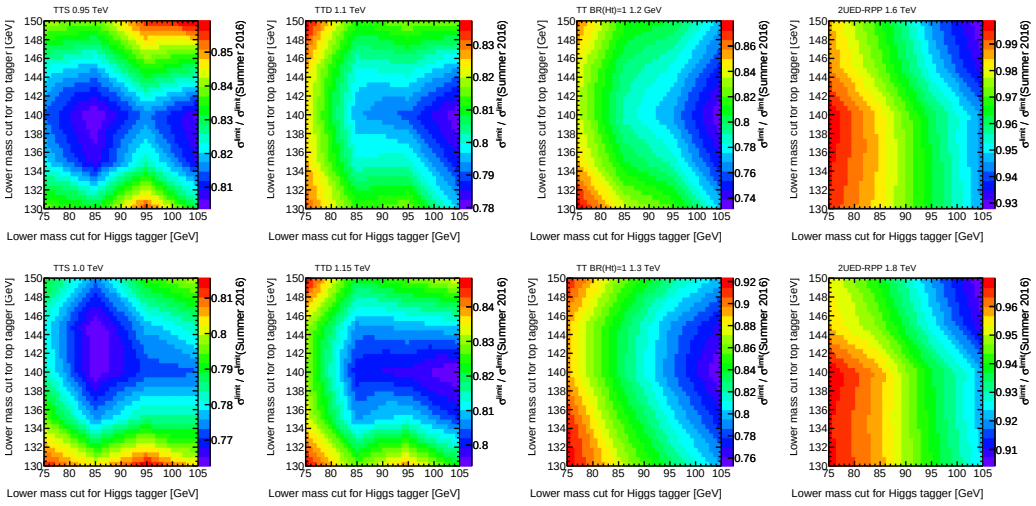

Figure D.1: Ratio of the upper limits at 95% CL on the production cross section with various mass requirements to that with the *old* configurationat the same integrated luminosity of 30 fb^{-1}. In order from left to right, the results with SU(2) singlet and m_{VLT} = 900 GeV(top), 1000 GeV(bottom), SU(2) doublet and m_{VLT} = 1100 GeV(top), 1150 GeV(bottom), BR(Ht) = 1 and m_{VLT} = 1200 GeV(top), 1300 GeV(bottom), and 2UED-RPP and m_{KK} = 1600 GeV(top), 1800 GeV(bottom) are shown. The colour contour in z-axis represents the ratio of the upper limit. The lower threshold for the Higgs boson (top quark) tagger in $x(y)$-axis is scanned for the range from 75 (130) GeV to 105 (150) GeV by a step of 5 GeV. The Delaunay interpolation is used to fill the intermediate area among the actual scan points.

Table D.1: Classification based on the number of MC true particles out of the three quarks from a hadronic top decay and the number of constituents inside a large-R jet. The three classes of "Resolved", "Fully merged" and "Partially merged" are defined by the angular distance ΔR among three true particles: the minimum ΔR between two quarks larger than 0.4 (min.$\Delta R > 0.4$), all the ΔR between the top quark axis and the true particle less than 0.4 ($\Delta R(\text{top}, \text{q}) < 0.4$, and the others, respectively.

Number of truth particles	Number of constituents
1	1
	≥ 2
2 (Resolved)	1
	2
	≥ 3
2(Merged)	1
	≥ 2
3 (Resolved)	≤ 2
	3
	≥ 4
3 (Partially merged)	1
	2
	≥ 3
3(Fully merged)	1
	≥ 2

tagger, while additional jets does not causes inefficiency because the top quark tagger does not require the upper thresholds on the mass and constituents. And the fully merged cases have large contributions for high p_{T} range of $p_{\text{T}} > 800$ GeV. Since the top quark tagger does not allow single constituent, the tagging efficiency drops.

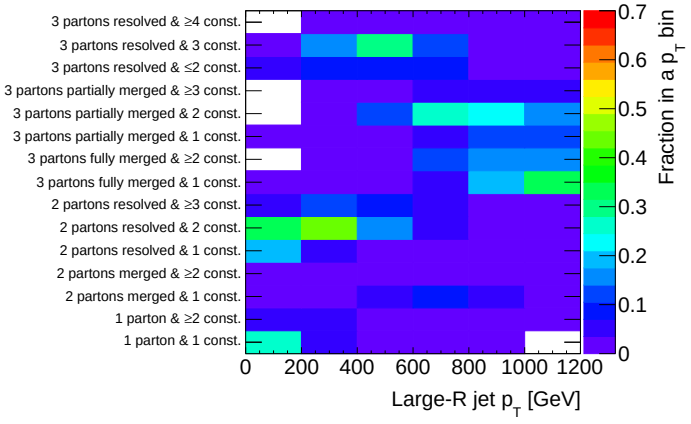

(a)

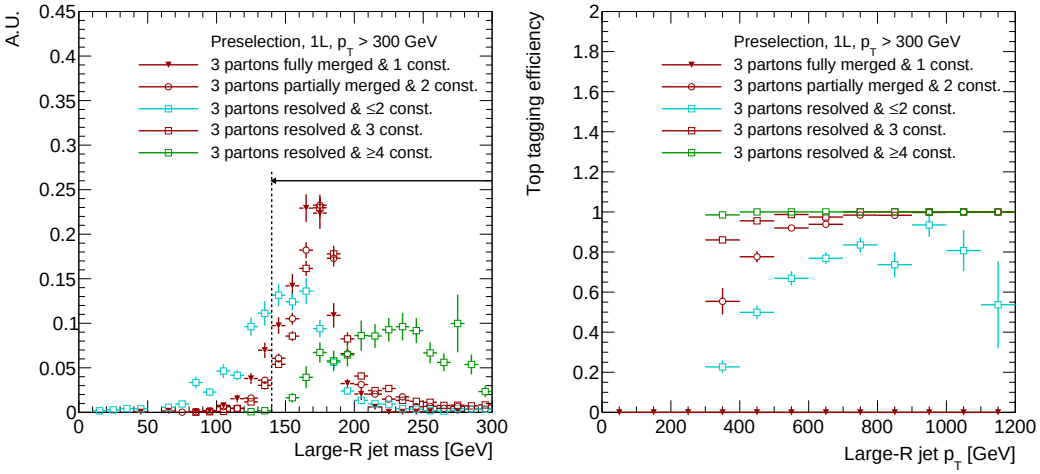

(b) (c)

Figure D.2: (a) Fraction of each class in a p_{T} bin. Each class is defined in Table D.1. (b) Reclustered jet mass distribution for the classes including three true particles. Dashed lines show the mass threshold for top quark tagging. (c) Top quark tagging efficiency for the classes including three true particles. For (b) and (c), the case of reclustered jets with same truth particles as the expected number of constituents is shown in red, and those with more(less) truth particles than the expected number of constituents are shown in blue (green).

E Blind cuts on m_{eff}

This chapter shows the set of m_{eff} distributions in each category for determination of blind cuts. Figure E.1 and E.2 shows the m_{eff} distributions in SR ($\leq$6 jets) and VR (5 jets), respectively. The top panel show the expected m_{eff} distributions of background (gray) and VLT signals with the mass of 1 TeV before the fit, and the bottom panel shows the signal-to-background ratio, S/B, in each m_{eff} bin. The two kinds of blind cuts are used in this dissertation, shown in dashed lines in the bottom panel: loose and tight. The tight blind cut requires the S/B less than 5%, while the loose blind cut requires S/B less than 20% for the validation.

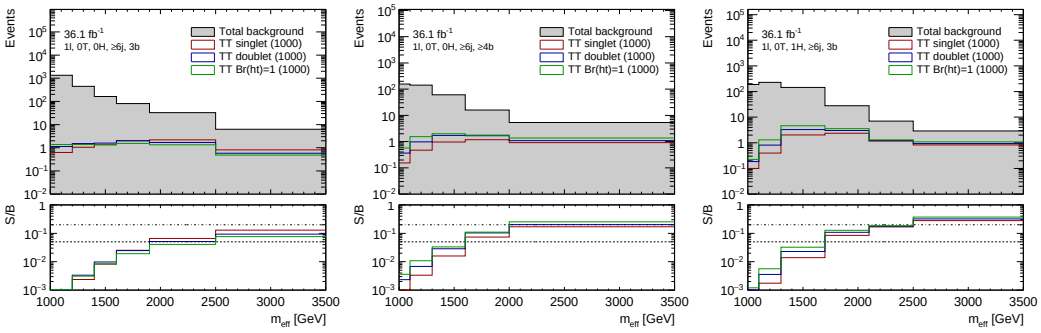

(a) 0T, 0H, ≥ 6j, 3b

(b) 0T, 0H, ≥ 6j, ≥ 4b

(c) 0T, 1H, ≥ 6j, 3b

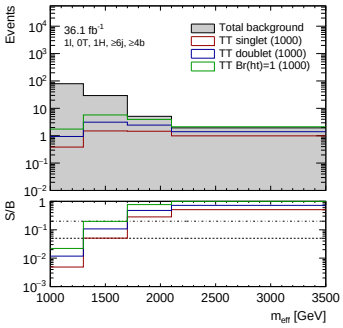

(d) 0T, 1H, ≥ 6j, ≥ 4b

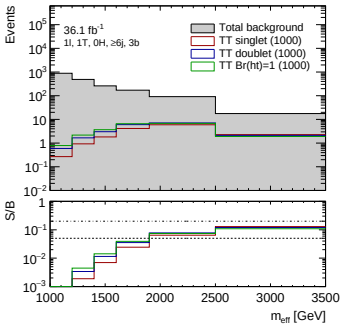

(e) 1T, 0H, ≥ 6j, 3b

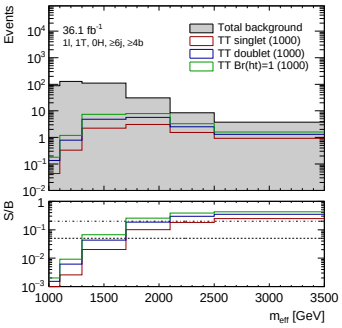

(f) 1T, 0H, ≥ 6j, ≥ 4b

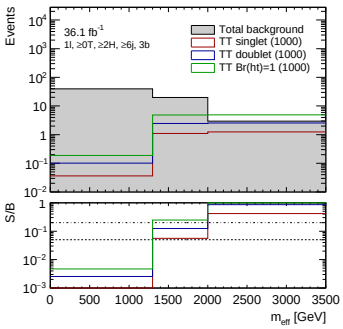

(g) ≥ 0T, ≥ 2H, ≥ 6j, 3b

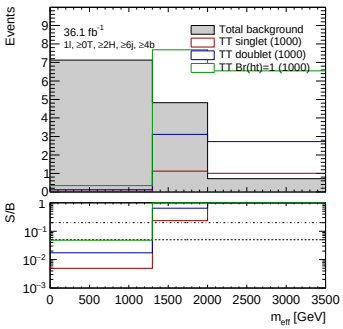

(h) ≥ 0T, ≥ 2H, ≥ 6j, ≥ 4b

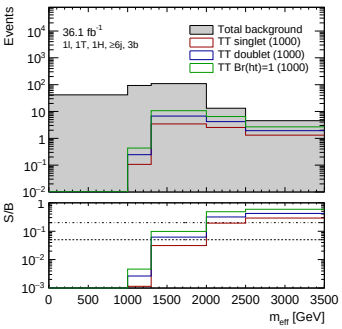

(i) 1T, 1H, ≥ 6j, 3b

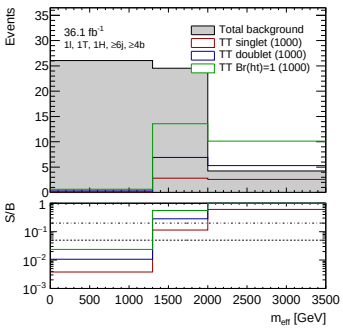

(j) 1T, 1H, ≥ 6j, ≥ 4b

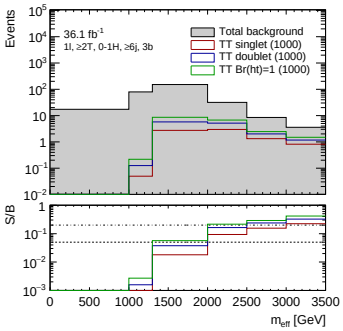

(k) ≥ 2T, 0 − 1H, ≥ 6j, 3b

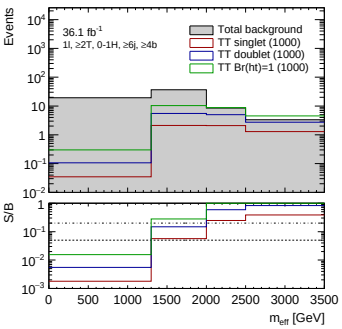

(l) ≥ 2T, 0 − 1H, ≥ 6j, ≥ 4b

Figure E.1: Expected m_{eff} distribution (top panel) and S/B (bottom panel) of VLT signals with the mass of $m_{\text{VLT}} = 1$ TeV and backgrounds for each category with 36.1 fb^{-1} in Search regions.

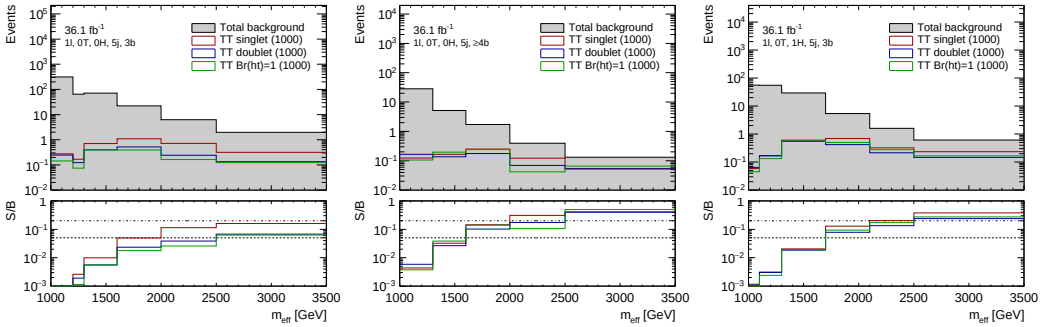

(a) 0T, 0H, 5j, 3b

(b) 0T, 0H, 5j, ≥ 4b

(c) 0T, 1H, 5j, 3b

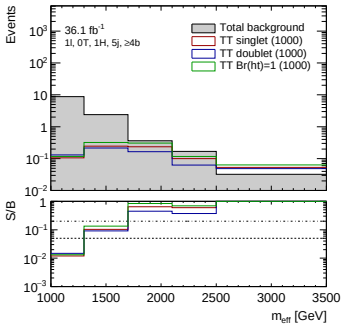

(d) 0T, 1H, 5j, ≥ 4b

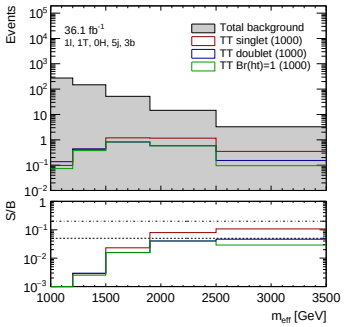

(e) 1T, 0H, 5j, 3b

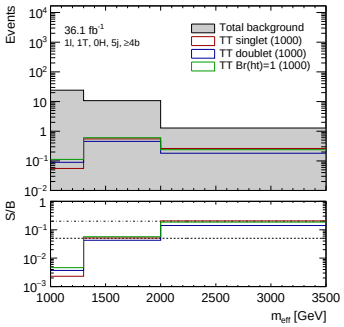

(f) 1T, 0H, 5j, ≥ 4b

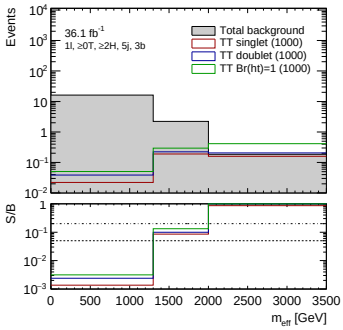

(g) ≥ 0T, ≥ 2H, 5j, 3b

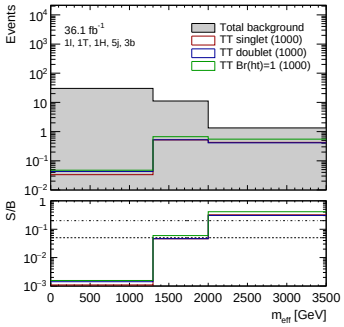

(h) 1T, 1H, 5j, 3b

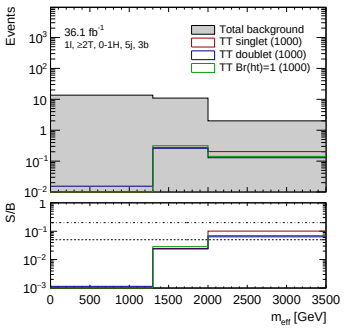

(i) ≥ 2T, 0 – 1H, 5j, 3b

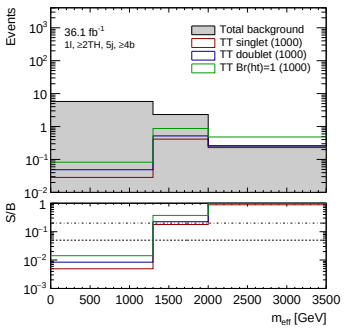

(j) ≥ 2TH, 5j, ≥ 4b

Figure E.2: Expected m_{eff} distribution (top panel) and S/B (bottom panel) of VLT signals with the mass of $m_{\text{VLT}} = 1$ TeV and backgrounds for each category with 36.1 fb^{-1} in Validation regions.

F Data / MC comparison in blinded regions

This chapter shows the various kinematic distributions compared between the data and MC prediction before the fit (Pre-fit). Figures F.1 – F.12 show the jet and b-jet multiplicity, leading jet p_{T}, lepton p_{T} and η, and $E_{\mathrm{T}}^{\mathrm{miss}}$ in each category. Figure F.13 and F.14 show the m_{eff} distributions comparing between the Pre-fit background prediction and the data.

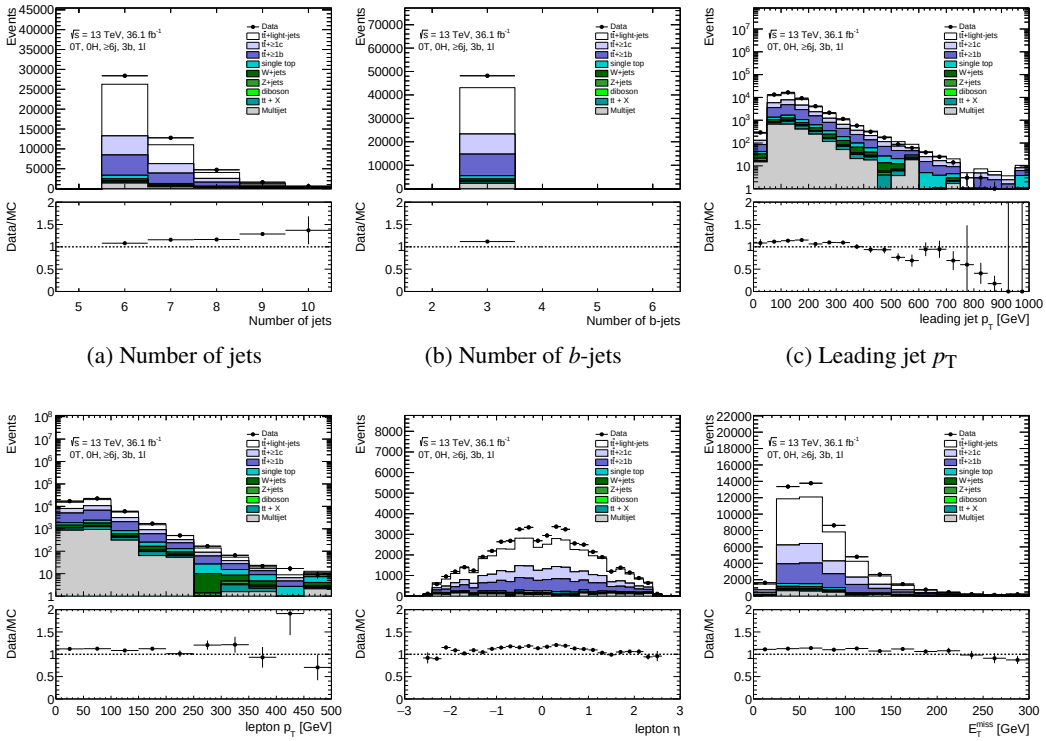

(a) Number of jets (b) Number of b-jets (c) Leading jet p_{T}

(d) Lepton p_{T} (e) Lepton η (f) $E_{\mathrm{T}}^{\mathrm{miss}}$

Figure F.1: Comparison of several kinematic variables between data and MC prediction in "0T, 0H, ≥ 6j, 3b" before fitting.

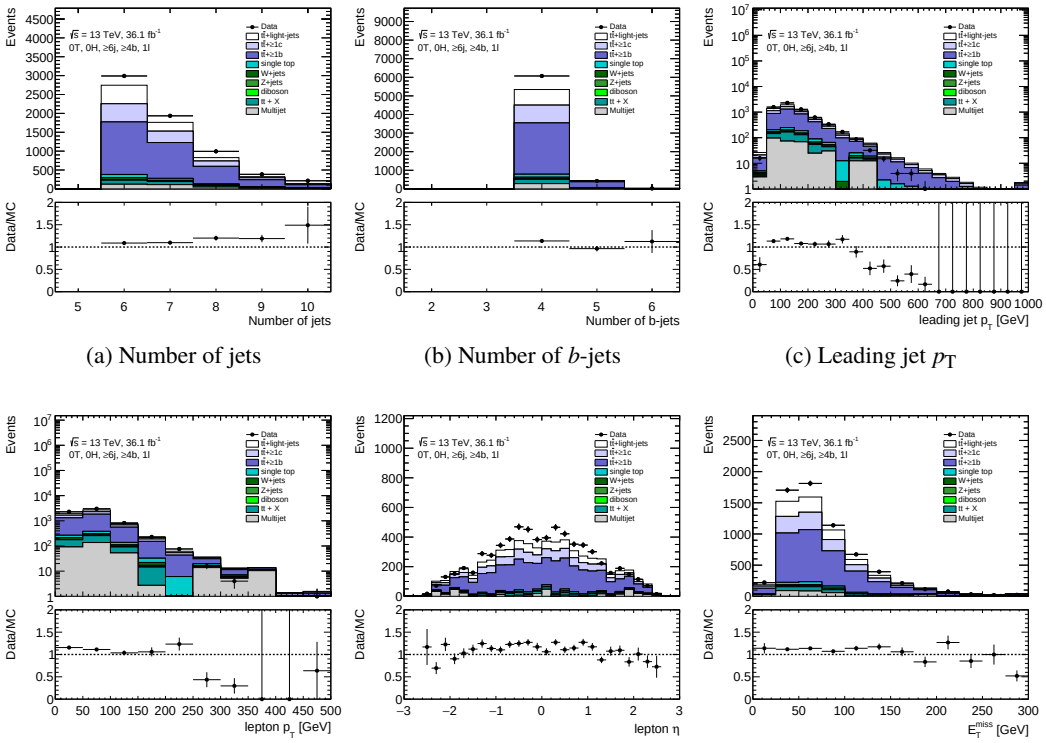

(a) Number of jets (b) Number of b-jets (c) Leading jet p_{T}

(d) Lepton p_{T} (e) Lepton η (f) $E_{\mathrm{T}}^{\mathrm{miss}}$

Figure F.2: Comparison of several kinematic variables between data and MC prediction in "0T, 0H, ≥ 6j, ≥ 4b" before fitting.

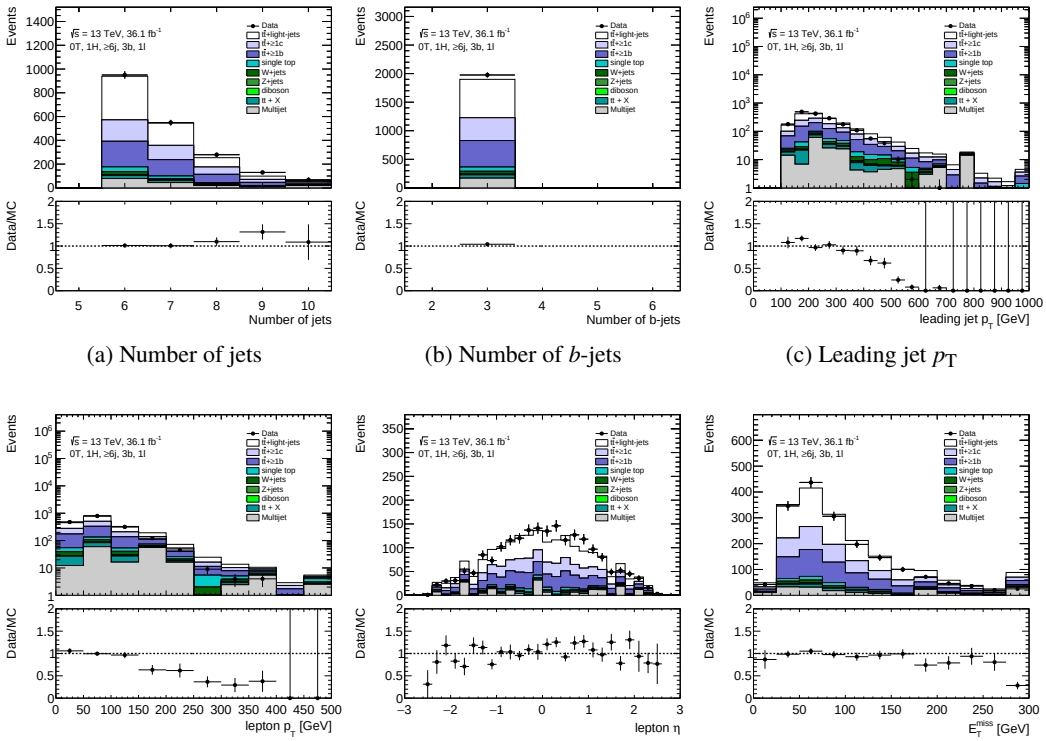

(a) Number of jets (b) Number of b-jets (c) Leading jet p_{T}

(d) Lepton p_{T} (e) Lepton η (f) $E_{\mathrm{T}}^{\mathrm{miss}}$

Figure F.3: Comparison of several kinematic variables between data and MC prediction in "0T, 1H, ≥ 6j, 3b" before fitting.

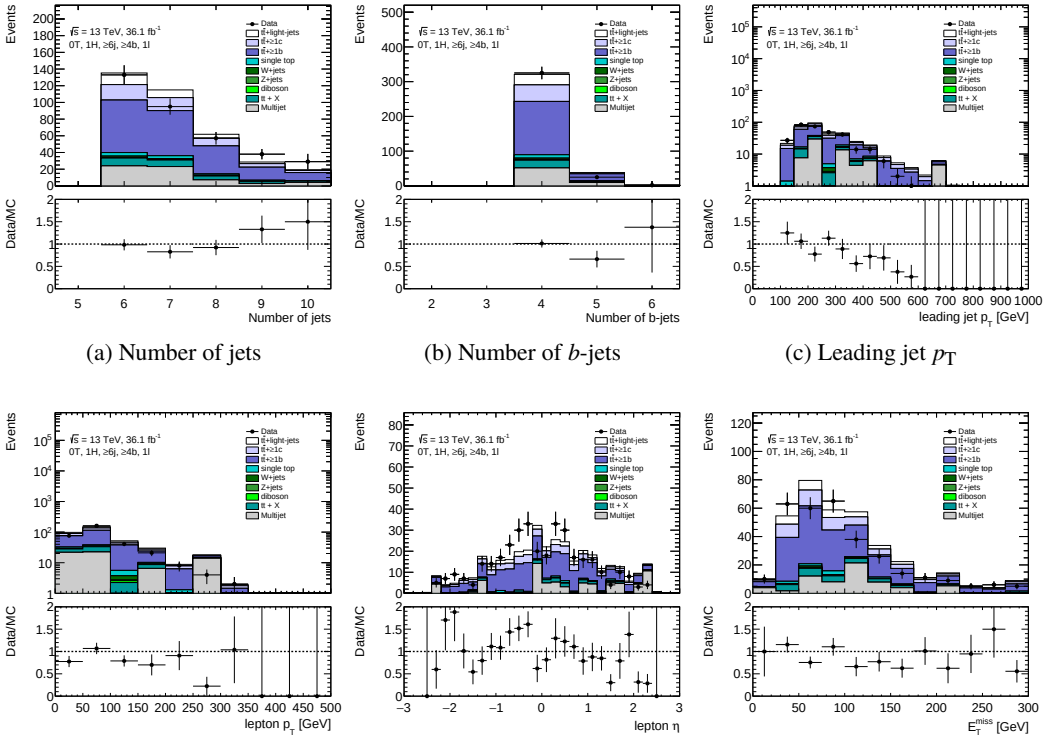

(a) Number of jets (b) Number of b-jets (c) Leading jet p_{T}

(d) Lepton p_{T} (e) Lepton η (f) $E_{\mathrm{T}}^{\mathrm{miss}}$

Figure F.4: Comparison of several kinematic variables between data and MC prediction in "0T, 1H, ≥ 6j, ≥ 4b" before fitting.

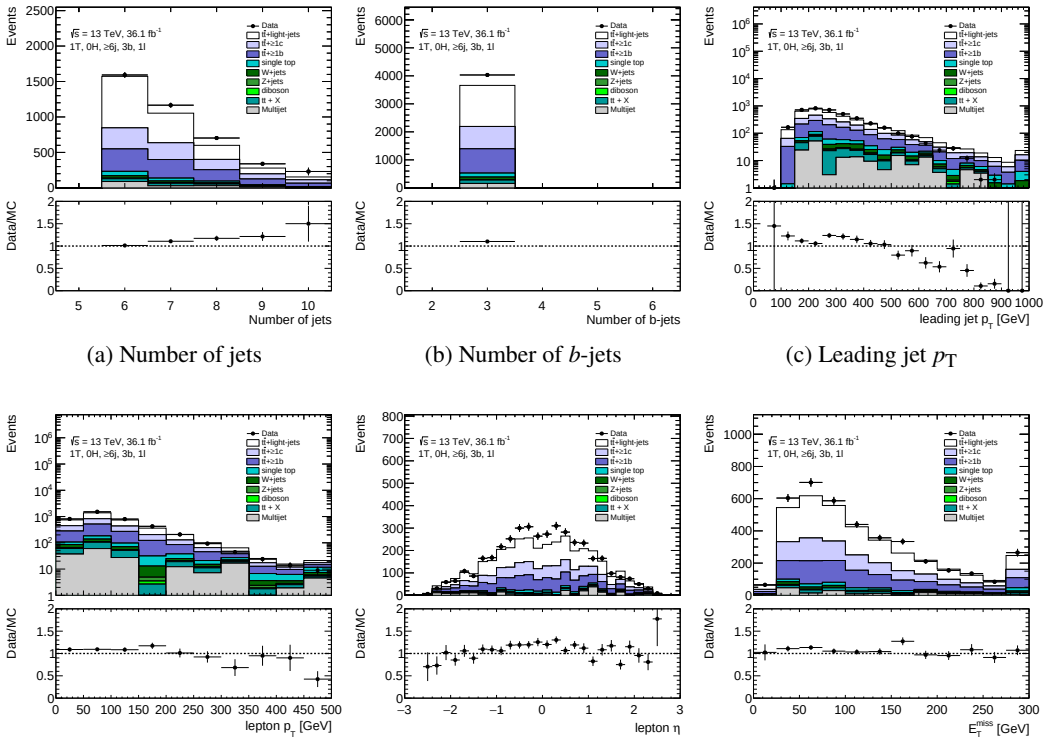

(a) Number of jets (b) Number of b-jets (c) Leading jet p_{T}

(d) Lepton p_{T} (e) Lepton η (f) $E_{\mathrm{T}}^{\mathrm{miss}}$

Figure F.5: Comparison of several kinematic variables between data and MC prediction in "1T, 0H, ≥ 6j, 3b" before fitting.

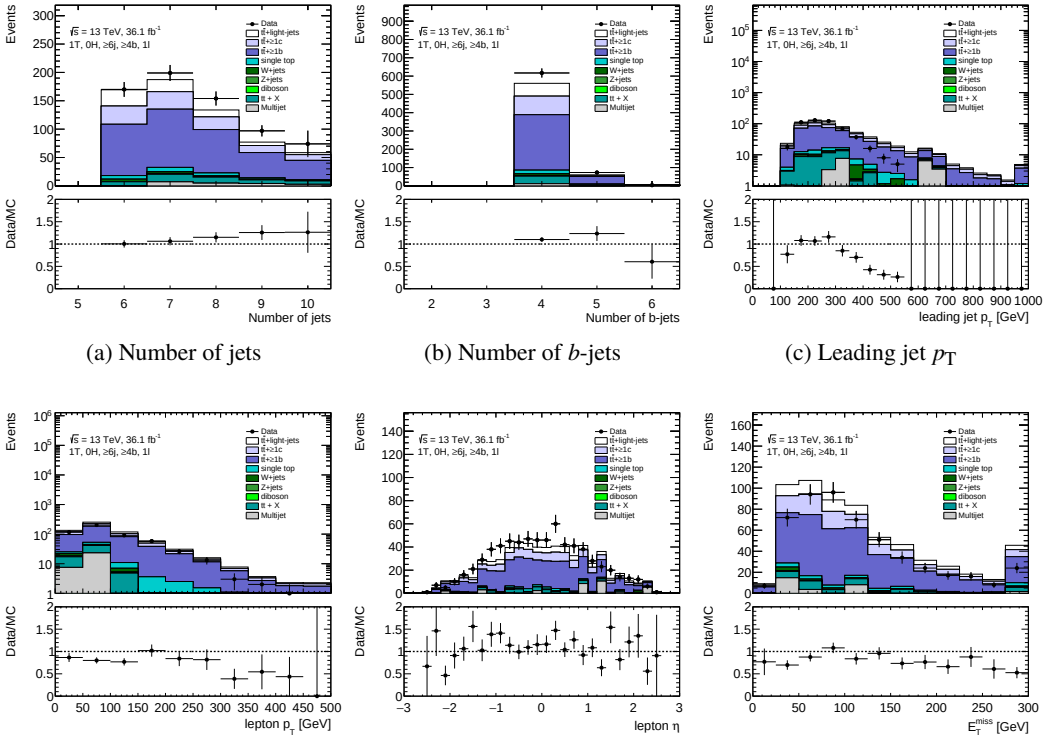

(a) Number of jets (b) Number of b-jets (c) Leading jet p_{T}

(d) Lepton p_{T} (e) Lepton η (f) $E_{\mathrm{T}}^{\mathrm{miss}}$

Figure F.6: Comparison of several kinematic variables between data and MC prediction in "1T, 0H, ≥ 6j, ≥ 4b" before fitting.

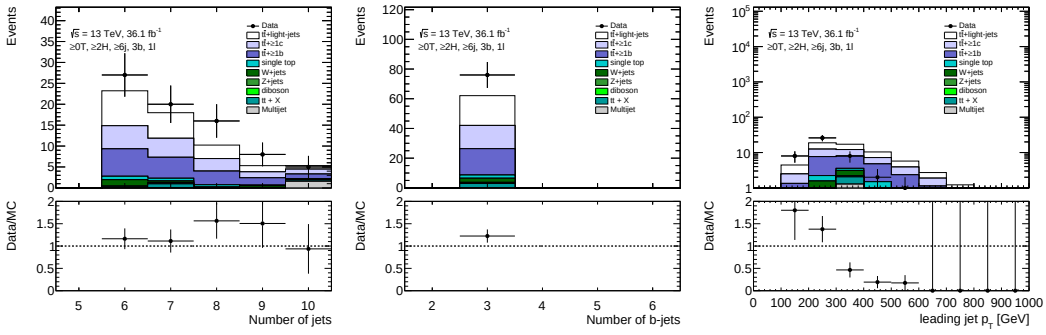

(a) Number of jets (b) Number of b-jets (c) Leading jet p_{T}

(d) Lepton p_{T} (e) Lepton η (f) $E_{\mathrm{T}}^{\mathrm{miss}}$

Figure F.7: Comparison of several kinematic variables between data and MC prediction in "≥0T, ≥2H, ≥ 6j, 3b" before fitting.

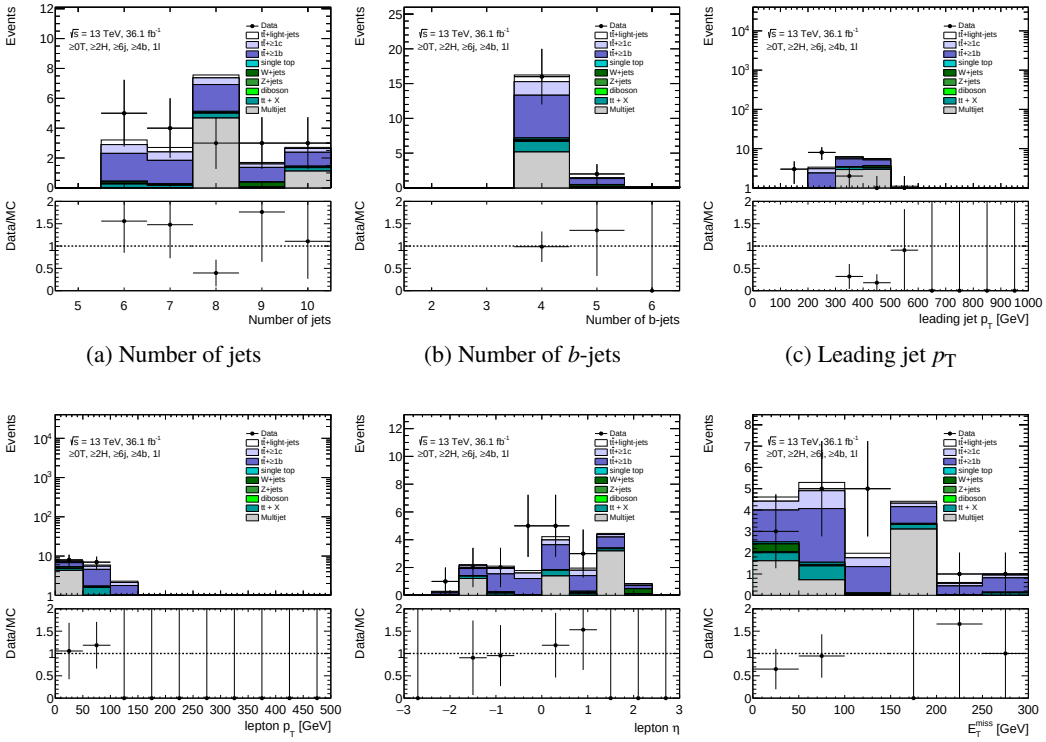

(a) Number of jets (b) Number of b-jets (c) Leading jet p_{T}

(d) Lepton p_{T} (e) Lepton η (f) $E_{\mathrm{T}}^{\mathrm{miss}}$

Figure F.8: Comparison of several kinematic variables between data and MC prediction in "≥0T, ≥2H, ≥ 6j, ≥ 4b" before fitting.

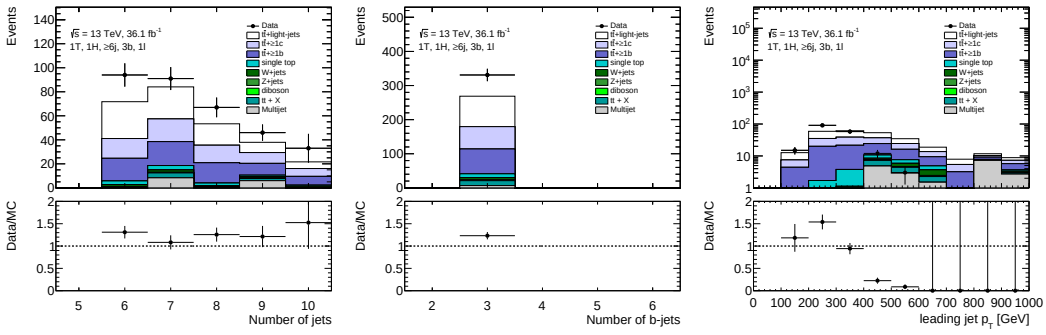

(a) Number of jets (b) Number of b-jets (c) Leading jet p_{T}

(d) Lepton p_{T} (e) Lepton η (f) $E_{\mathrm{T}}^{\mathrm{miss}}$

Figure F.9: Comparison of several kinematic variables between data and MC prediction in "1T, 1H, ≥ 6j, 3b" before fitting.

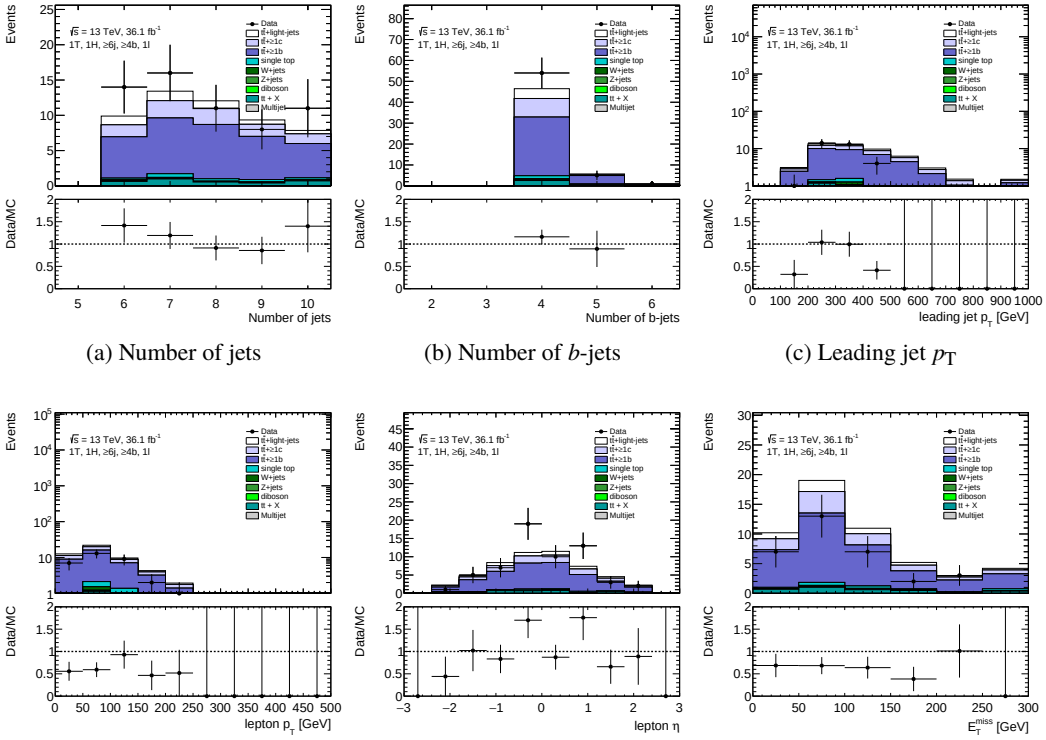

(a) Number of jets (b) Number of b-jets (c) Leading jet p_{T}

(d) Lepton p_{T} (e) Lepton η (f) $E_{\mathrm{T}}^{\mathrm{miss}}$

Figure F.10: Comparison of several kinematic variables between data and MC prediction in "1T, 1H, $\geq$ 6j, $\geq$ 4b" before fitting.

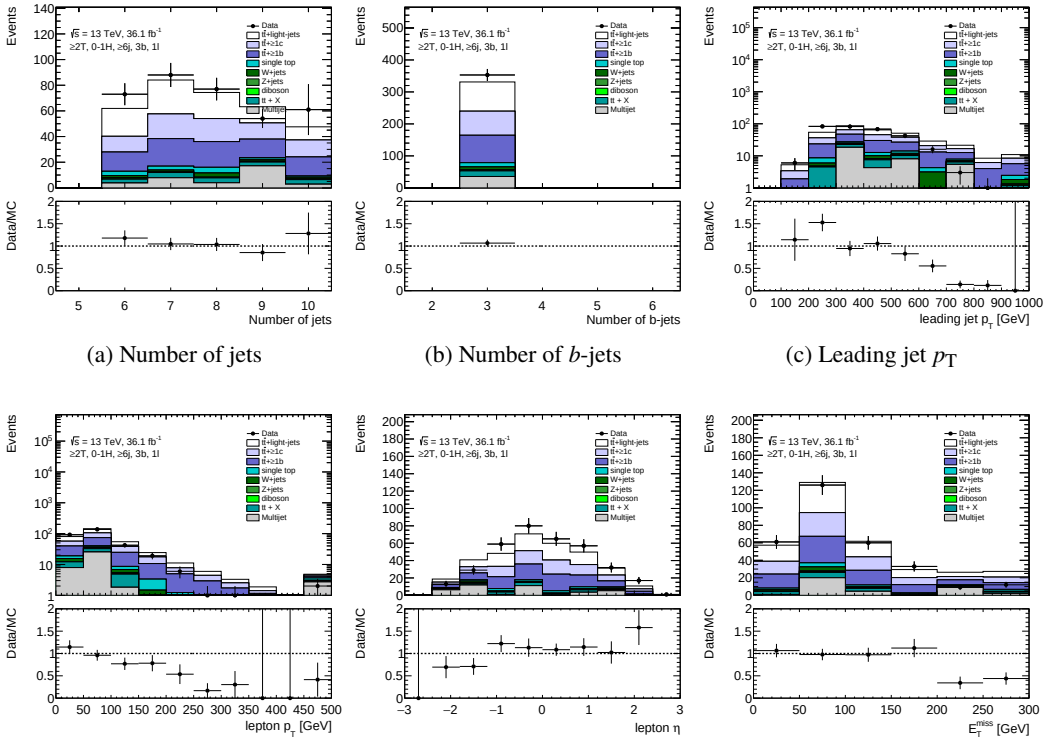

(a) Number of jets (b) Number of b-jets (c) Leading jet p_{T}

(d) Lepton p_{T} (e) Lepton η (f) $E_{\mathrm{T}}^{\mathrm{miss}}$

Figure F.11: Comparison of several kinematic variables between data and MC prediction in "≥2T, 0-1H, ≥ 6j, 3b" before fitting.

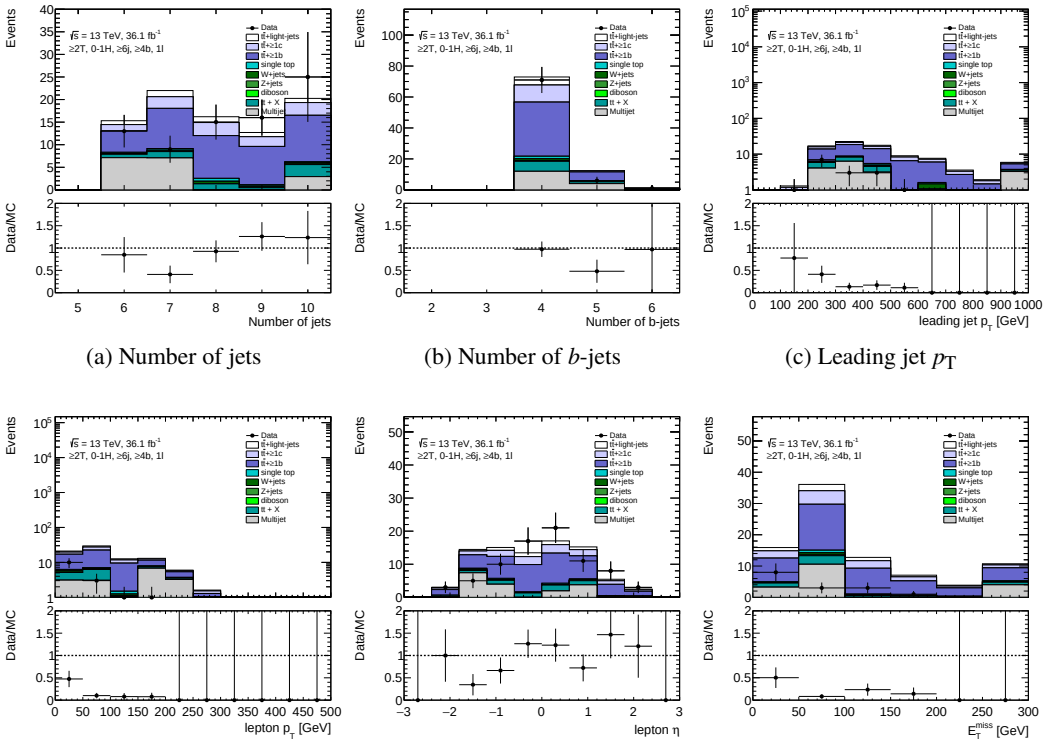

(a) Number of jets (b) Number of b-jets (c) Leading jet p_{T}

(d) Lepton p_{T} (e) Lepton η (f) $E_{\mathrm{T}}^{\mathrm{miss}}$

Figure F.12: Comparison of several kinematic variables between data and MC prediction in "≥2T, 0-1H, ≥ 6j, ≥ 4b" before fitting.

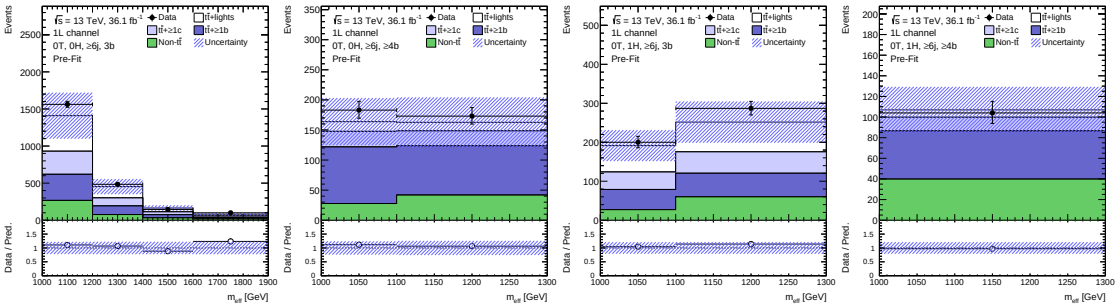

(a) 0T, 0H, ≥6j, 3b (b) 0T, 0H, ≥6j, ≥4b (c) 0T, 1H, ≥6j, 3b (d) 0T, 1H, ≥6j, ≥4b

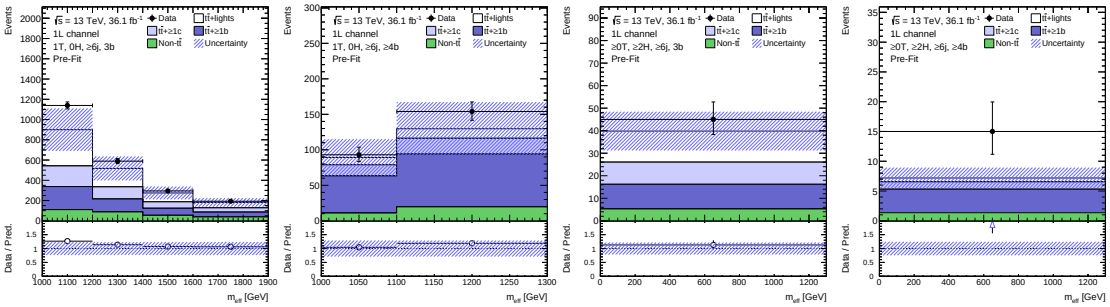

(e) 1T, 0H, ≥6j, 3b (f) 1T, 0H, ≥6j, ≥4b (g) ≥0T, ≥2H, ≥6j, 3b (h) ≥0T, ≥2H, ≥6j, ≥4b

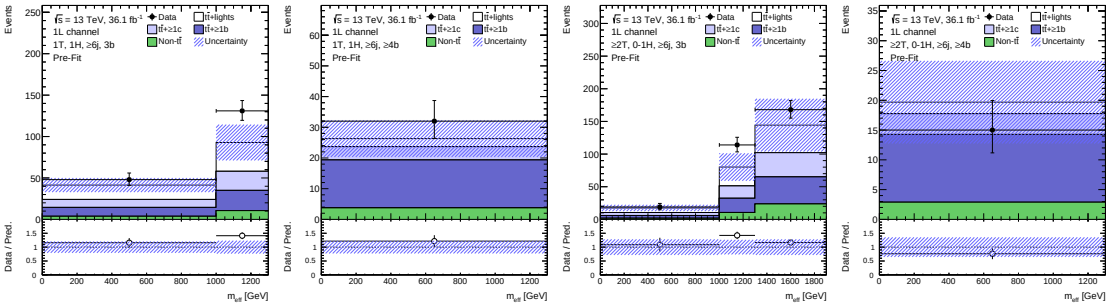

(i) 1T, 1H, ≥6j, 3b (j) 1T, 1H, ≥6j, ≥4b (k) ≥2T, 0-1H, ≥6j, 3b (l) ≥2T, 0-1H, ≥6j, ≥4b

Figure F.13: m_{eff} distribution of background prediction and data before fit in blinded region for each category of Search region.

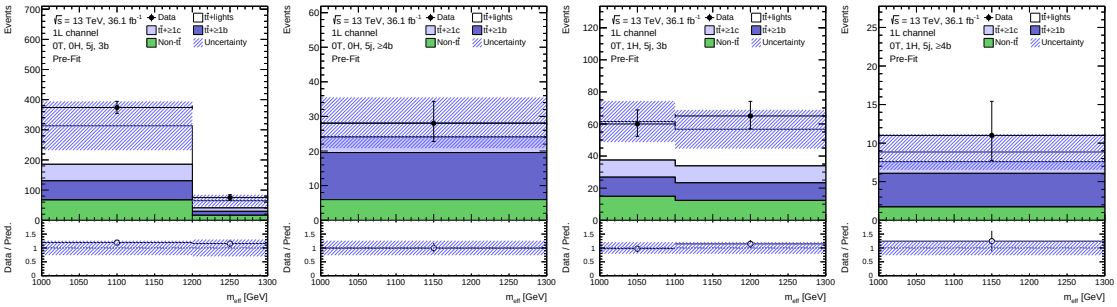

(a) 0T, 0H, 5j, 3b

(b) 0T, 0H, 5j, ≥4b

(c) 0T, 1H, 5j, 3b

(d) 0T, 1H, 5j, ≥4b

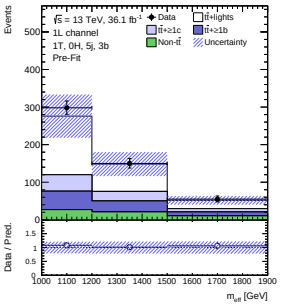

(e) 1T, 0H, 5j, 3b

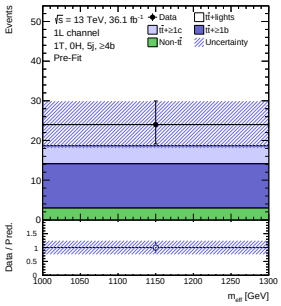

(f) 1T, 0H, 5j, ≥4b

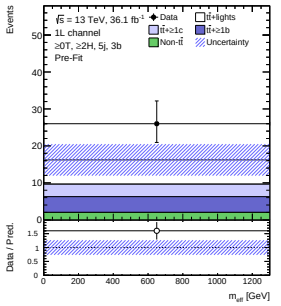

(g) ≥0T, ≥2H, 5j, 3b

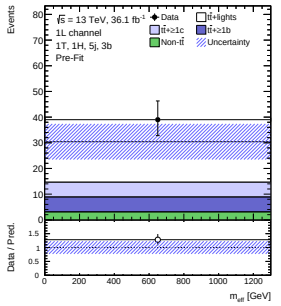

(h) 1T, 1H, 5j, 3b

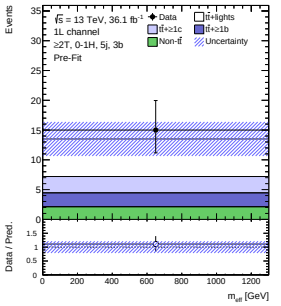

(i) ≥2T, 0-1H, 5j, 3b

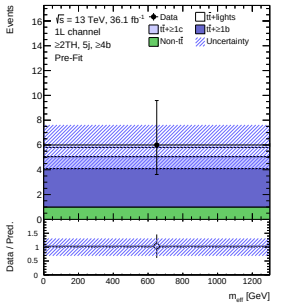

(j) ≥2TH, 5j, ≥4b

Figure F.14: m_{eff} distribution of background prediction and data before fit in blinded region for each category of Validation region.

G Auxiliary materials for the fit results

In this chapter, the auxiliary materials for the fit results described in Chapter 10 are shown.

G.1 Plots in the fit to the Asimov dataset

This section shows the materials for the fit to the Asimov dataset under the background-only hypothesis assuming an integrated luminosity of 36.1 fb^{-1}. Figure G.1 shows the correlation matrix among the nuisance parameters in the fit. The $t\bar{t}$+≥1b normalisation has around 45% correlation with the leading component of b-tagging eigenvector.

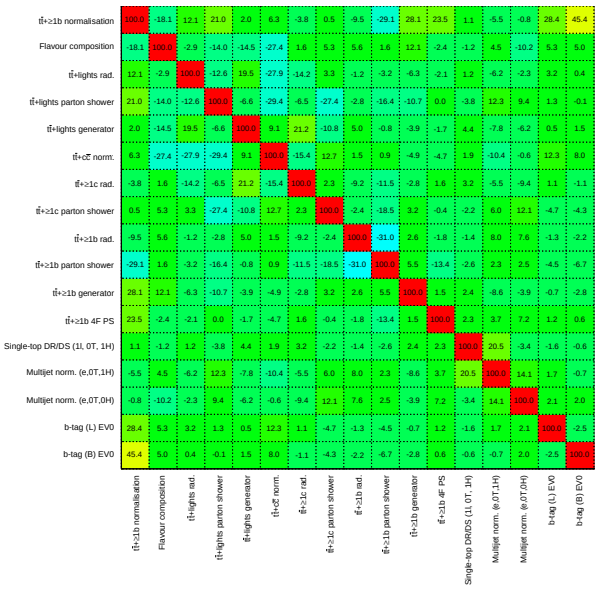

Figure G.1: Correlation matrix among the nuisance parameters in the fit to the Asimov dataset under the background-only hypothesis assuming an integrated luminosity of 36.1 fb^{-1}. Only the nuisance parameters which have above 20% correlations to another are shown.

Table G.1: Detail of the validation tests for the fit stability. The Asimov datasets are generated with some NPs or signal events injected. The fits are performed under both background-only ("b-only") and signal-plus-background ("s+b") hypotheses.

No.	Settings of the Asimov dataset	Fit hypothesis	Post-fit pulls and constraints
0	Nominal	b-only	—
1	Nominal	s+b	No difference
2-1	Injected $t\bar{t}$+≥1b norm. by 1.3	b-only	$t\bar{t}$+≥1b norm. = 1.30 ± 0.32
2-2	Injected b-tag (L) EV0 by -1σ	b-only	b-tag (L) EV0 = −0.19 ± 0.86
2-3	Injected b-tag (C) EV0 by -1σ	b-only	b-tag (C) EV0 = −0.05 ± 0.96
2-4	Injected $t\bar{t}$+≥1b norm. by 1.3 b-tag (L) EV0 by -1σ b-tag (C) EV0 by -1σ	b-only b-only b-only	$t\bar{t}$+≥1b norm. = 1.43 ± 0.34 b-tag (L) EV0 = −0.23 ± 0.89 b-tag (C) EV0 = −0.10 ± 0.96
3-1	Injected $t\bar{t}$+≥1b norm. by 1.3	s+b	$t\bar{t}$+≥1b norm. = 1.30 ± 0.32
3-2	Injected b-tag (L) EV0 by -1σ	s+b	b-tag (L) EV0 = −0.18 ± 0.88
3-3	Injected b-tag (C) EV0 by -1σ	s+b	b-tag (C) EV0 = −0.05 ± 0.96
3-4	Injected $t\bar{t}$+≥1b norm. by 1.3 b-tag (L) EV0 by -1σ b-tag (C) EV0 by -1σ	s+b s+b s+b	$t\bar{t}$+≥1b norm. = 1.43 ± 0.34 b-tag (L) EV0 = −0.23 ± 0.89 b-tag (C) EV0 = −0.10 ± 0.96
4	Injected $t\bar{t}$+≥1b norm. by 1.3 b-tag (L) EV0 by -1σ b-tag (C) EV0 by -1σ signal	s+b	$t\bar{t}$+≥1b norm. = 1.43 ± 0.33 b-tag (L) EV0 = −0.23 ± 0.89 b-tag (C) EV0 = −0.11 ± 0.96 $\hat{\mu}$ = 1.01 ± 0.33

G.2 Fit stability test

As described in Section 10.2, the observed data can be fluctuated from the background prediction, which may leads to unreliable results if the fit condition is unstable since numerous NPs are fitted simultaneously over many categories. All the validation items and results are listed in Table G.1. Several Asimov datasets are generated with some NPs or signal events injected. In addition, the set of fits is performed under both background-only and signal-plus-background hypotheses. All the validation tests show the expected pulls and no unexpected results. Therefore, the fit is assured to stably work even with systematic fluctuations in the data.

G.3 Impact on μ for various signal models

This section shows the leading 10 uncertainties according to the impact on μ after the fit in the different situations from Fig. 10.8. Figure G.2 shows the leading 10 uncertainties having the largest impact on the signal estimation. It is computed in the fit to the Asimov dataset generated with injecting the

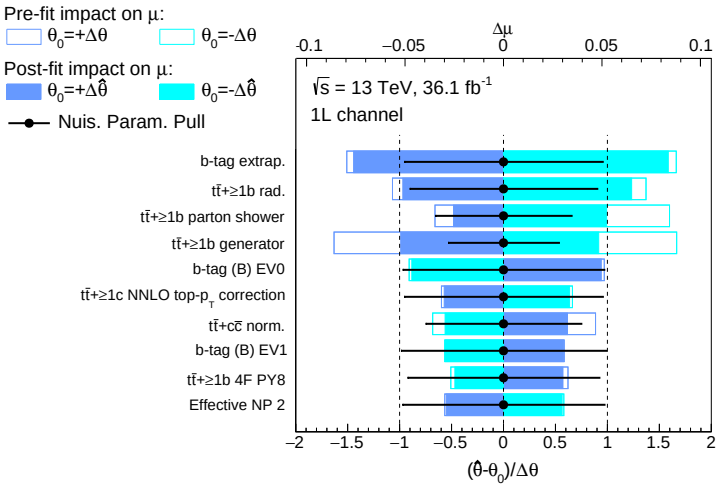

Figure G.2: Impact on the signal strength μ for each uncertainty on the signal estimation obtained from the fit under the signal-plus-background hypothesis to the Asimov dataset generated under the signal-plus-background hypothesis. The signal model used here is the VLT signal of SU(2) doublet with the mass of 1 TeV. The leading 10 uncertainties according to the impact on μ after the fit are shown. Black points which are plotted according to the bottom scale represent the deviation of each fitted nuisance parameter ($\hat{\theta}$) from the nominal value (θ_0) in a unit of its prior uncertainty ($\Delta\theta$). The uncertainties are sorted according to the impact of it after the fit (hashed blue area) plotted according to the top scale. The impact on μ for each uncertainty is calculated by the difference of μ when a fit is performed with the corresponding nuisance parameter fixed at $\hat{\theta} \pm \sigma_\theta$.

SU(2)-doublet VLT signal events ($m_{\mathrm{VLT}} = 1.0$ TeV). It turned out that the uncertainties of the leading b-tagging eigenvector components and b-tagging extrapolation affect the signal prediction.

Figure G.3 shows the leading 10 uncertainties having the largest impact on the background estimation. The signal model used here is the SU(2)-doublet VLT with the mass of 1.3 TeV. The mass point is higher than the one in Fig. 10.8. Thus, the leading uncertainties shown here have large impacts on μ for higher m_{eff} range, comparing to Fig. 10.8.

G.4 Plots in the fit to the Blinded data

In this section, the plots in the fit to the blinded data are shown. Here, the blind cut on m_{eff} corresponding to $S/B < 5\%$ is applied in all the categories.

Figure G.4 shows the pulls and constraints on the nuisance parameters. Most of NPs have the values of zero and the errors expected from the fit to the Asimov dataset. The shifts at most $+1\sigma$ of the NPs related with $t\bar{t}$+jets modelling improve the agreement of the prediction. The $t\bar{t}$+≥1b normalisation factor is determined 1.24 ± 0.32 whose relative uncertainty increases because the blind cut limits the available statistics.

Figure G.5 shows the correlation matrix among the nuisance parameters. Basically, all the correlations are similar to the ones in the fit to the Asimov dataset.

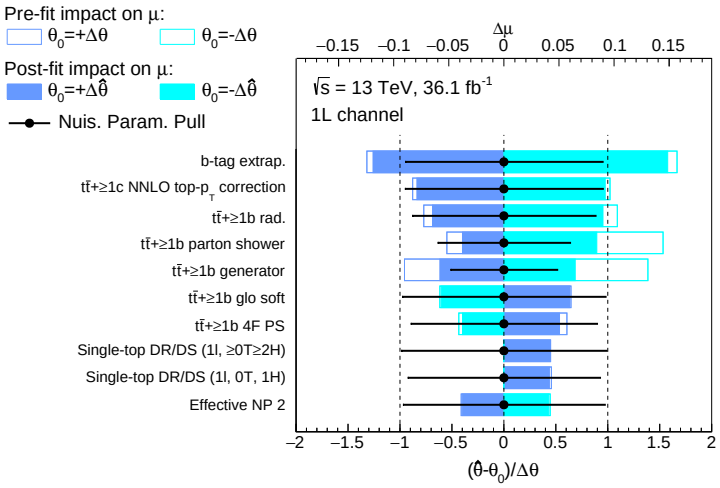

Figure G.3: Impact on the signal strength μ for each uncertainty obtained from the fit under the signal-plus-background hypothesis to the Asimov dataset generated under the background-only hypothesis. The signal model used here is the VLT signal of SU(2) doublet with the mass of 1.3 TeV. The leading 10 uncertainties according to the impact on μ after the fit are shown. Black points which are plotted according to the bottom scale represent the deviation of each fitted nuisance parameter ($\hat{\theta}$) from the nominal value (θ_0) in a unit of its prior uncertainty ($\Delta\theta$). The uncertainties are sorted according to the impact of it after the fit (hashed blue area) plotted according to the top scale. The impact on μ for each uncertainty is calculated by the difference of μ when a fit is performed with the corresponding nuisance parameter fixed at $\hat{\theta} \pm \sigma_\theta$.

Figure G.6 and G.7 show the post-fit m_{eff} distributions in the search and validation regions, respectively. With the blind cuts, the post-fit background prediction is consistent with the data within two standard deviation of its uncertainty in both SR and VR.

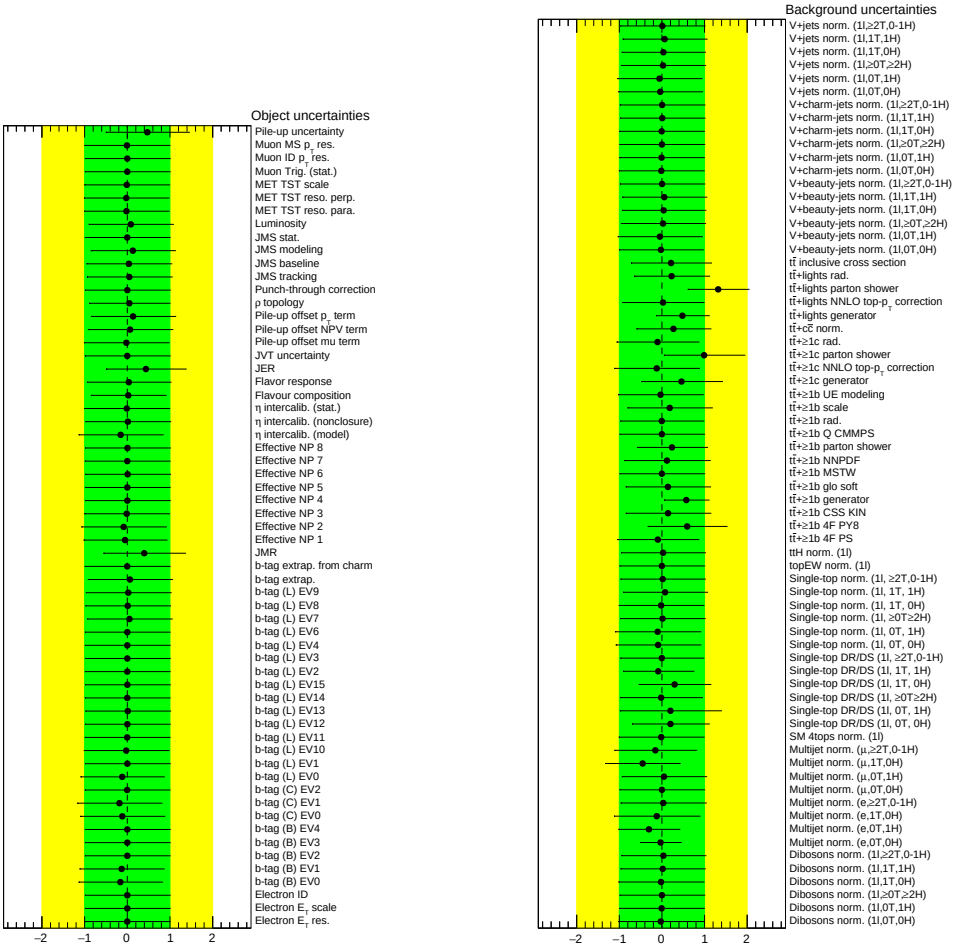

(a) (b)

Figure G.4: Pulls and constraints on the fitted nuisance parameters related to (a) the luminosity, pileup, and physics objects and (b) modelling. The fit is performed to the observed data applied the blind cut defined in Section 7.4. For each NP, the fitted value represents the preferred shift with respect to the prediction in a unit of its prior uncertainty, and the fitted error represents the uncertainty after the fit in a unit of its prior uncertainty.

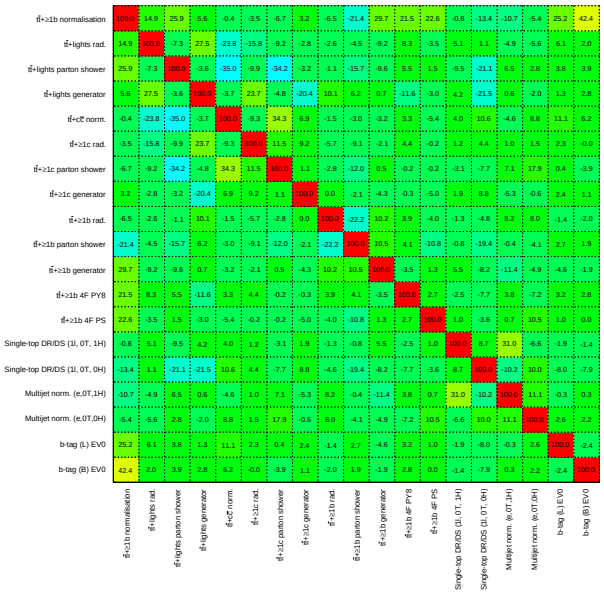

Figure G.5: Correlation matrix among the nuisance parameters in the fit to the data applied the blind cut defined in Section 7.4. Only the nuisance parameters which have above 20% correlations to another are shown.

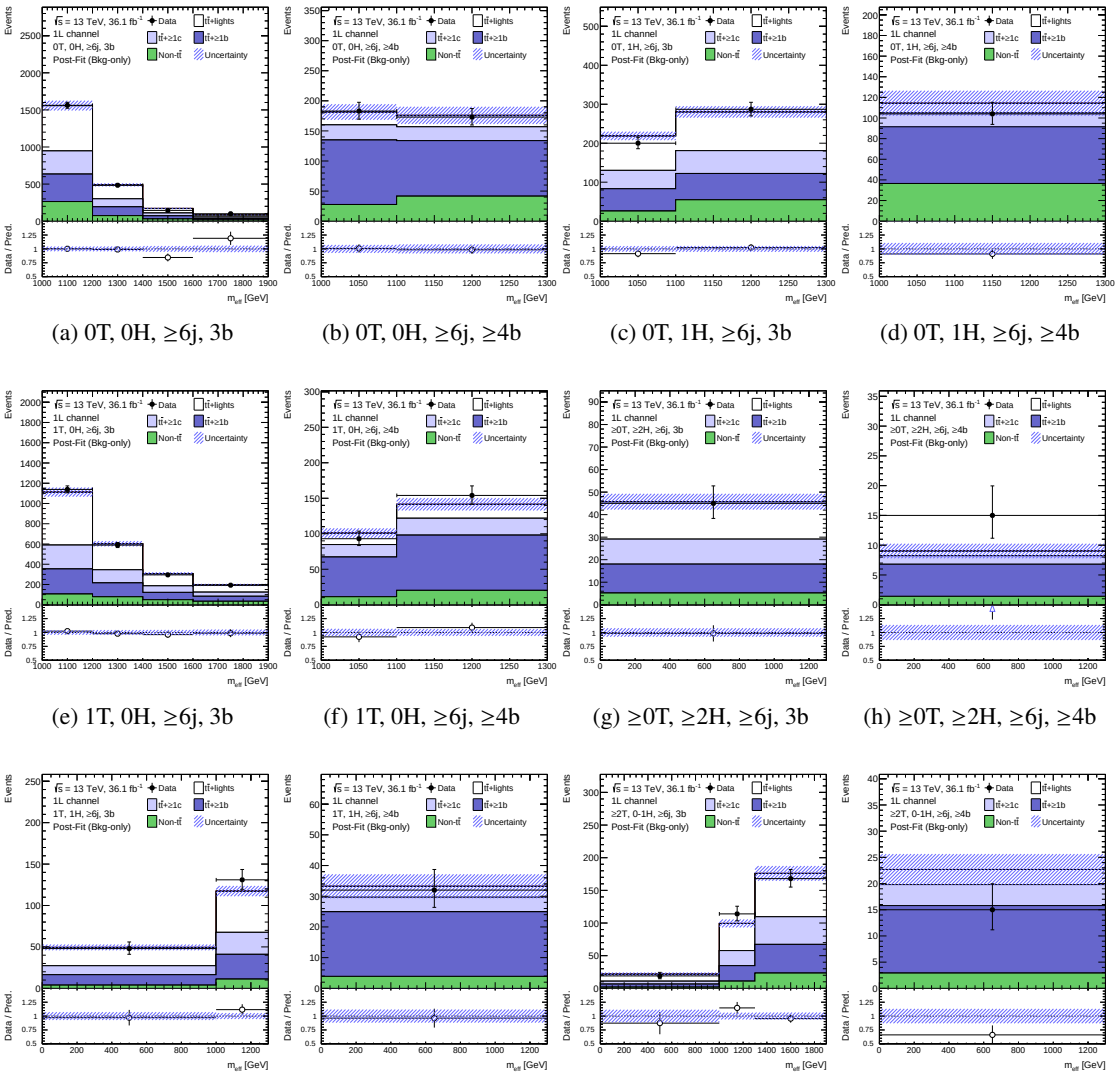

(a) 0T, 0H, ≥6j, 3b (b) 0T, 0H, ≥6j, ≥4b (c) 0T, 1H, ≥6j, 3b (d) 0T, 1H, ≥6j, ≥4b

(e) 1T, 0H, ≥6j, 3b (f) 1T, 0H, ≥6j, ≥4b (g) ≥0T, ≥2H, ≥6j, 3b (h) ≥0T, ≥2H, ≥6j, ≥4b

(i) 1T, 1H, ≥6j, 3b (j) 1T, 1H, ≥6j, ≥4b (k) ≥2T, 0-1H, ≥6j, 3b (l) ≥2T, 0-1H, ≥6j, ≥4b

Figure G.6: m_{eff} distribution of backgrounds after the fit to the blinded data for each category of Search region.

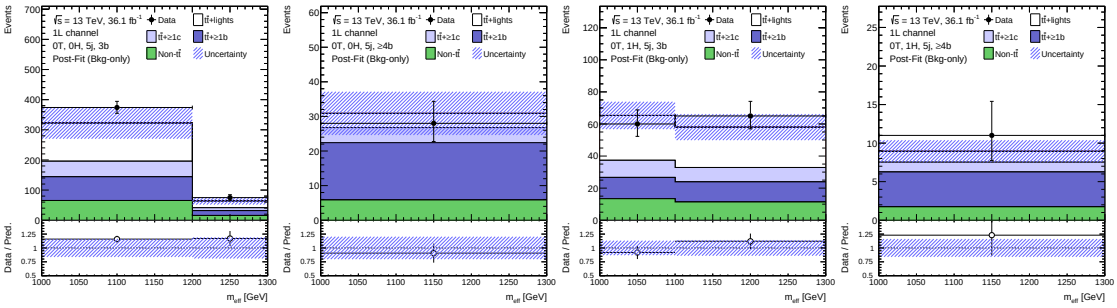

(a) 0T, 0H, 5j, 3b

(b) 0T, 0H, 5j, ≥4b

(c) 0T, 1H, 5j, 3b

(d) 0T, 1H, 5j, ≥4b

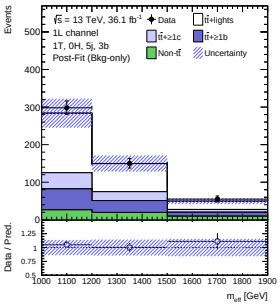

(e) 1T, 0H, 5j, 3b

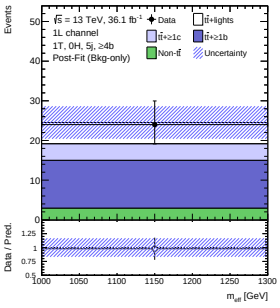

(f) 1T, 0H, 5j, ≥4b

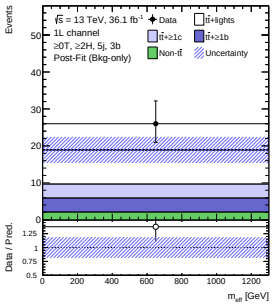

(g) ≥0T, ≥2H, 5j, 3b

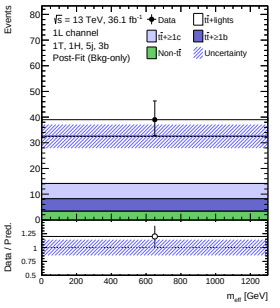

(h) 1T, 1H, 5j, 3b

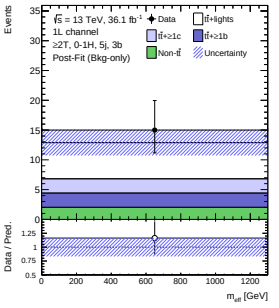

(i) ≥2T, 0-1H, 5j, 3b

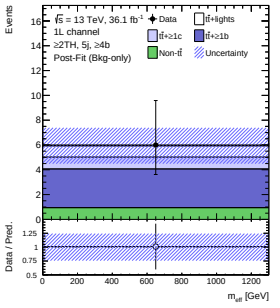

(j) ≥2TH, 5j, ≥4b

Figure G.7: m_{eff} distribution of backgrounds after the fit to the blinded data for each category of Validation region.

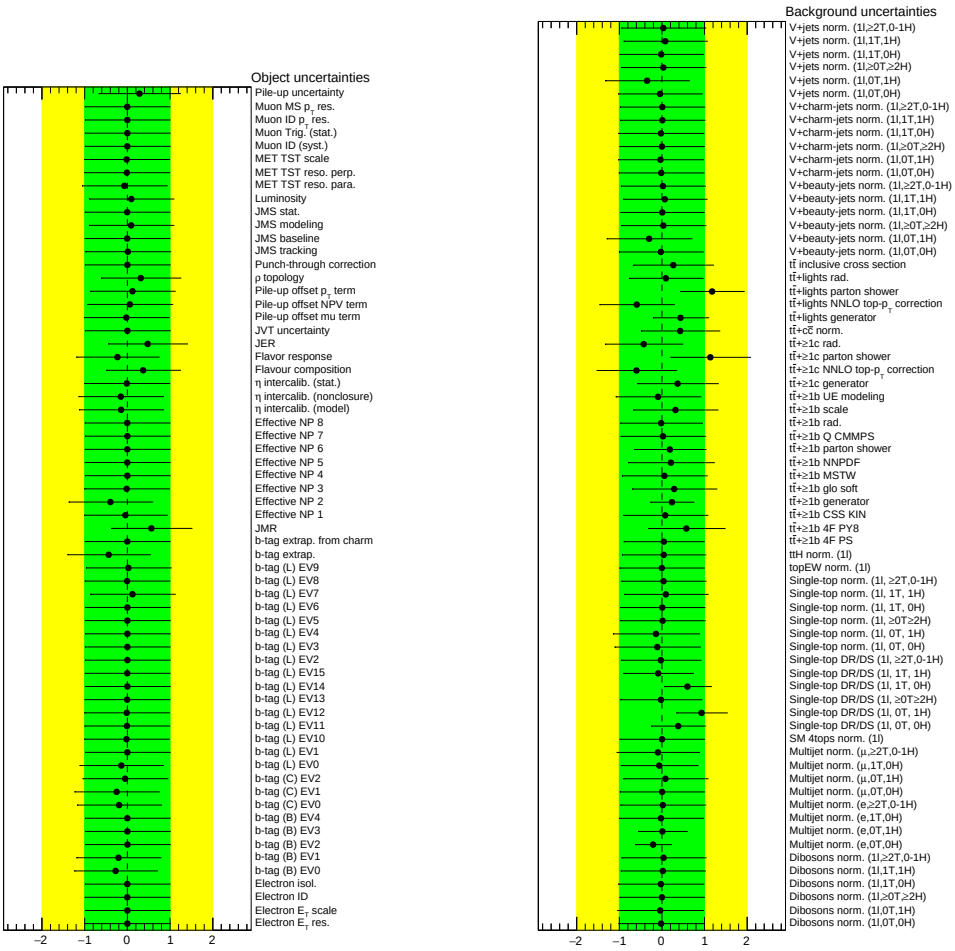

(a) (b)

Figure G.8: Pulls and constraints on the fitted nuisance parameters related to (a) the luminosity, pileup, and physics objects and (b) modelling. The fit is performed to the observed data applied the looser blind cut ($S/B < 20\%$). For each NP, the fitted value represents the preferred shift with respect to the prediction in a unit of its prior uncertainty, and the fitted error represents the uncertainty after the fit in a unit of its prior uncertainty.

G.5 Plots in the fit to the partially unblinded data

In this section, the plots in the fit to the blinded data are shown. Here, the blind cut on m_{eff} corresponding to $S/B < 20\%$ is applied in all the categories.

Figure G.8 shows the pulls and constraints on the nuisance parameters. All the pulls and constraints are consistent with the fit result using the tighter blinded data shown in the previous section.

Figure G.9 shows the correlation matrix among the nuisance parameters. All the correlations are

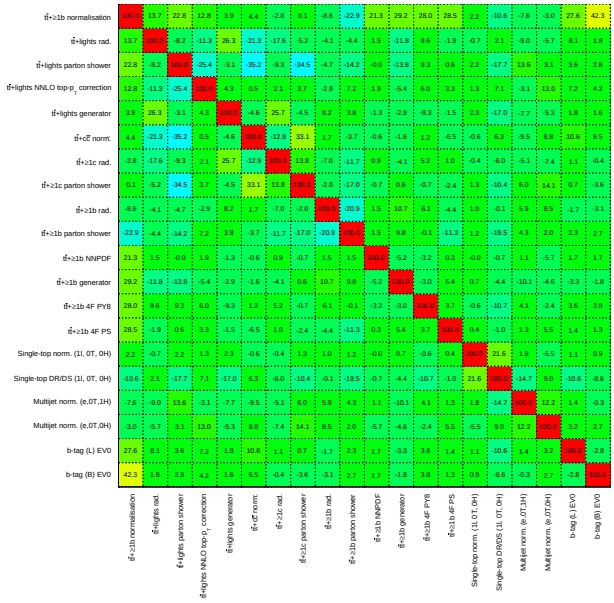

Figure G.9: Correlation matrix among the nuisance parameters in the fit to the data applied the looser blind cut ($S/B < 20\%$). Only the nuisance parameters which have above 20% correlations to another are shown.

assured to be consistent with the fit results with the Asimov dataset and the tighter blinded data.

Figure G.10 shows the event yields in each category. In the validation regions, the post-fit predicted event yields are consistent with the data within their uncertainties. This result assures that the systematic uncertainties are correctly taken into account in the fit and properly propagated into the validation regions.

Figure G.11 and G.12 show the post-fit m_{eff} distributions in the search and validation regions, respectively. With the looser blind cuts, the SR and VR include the higher m_{eff} range in the fit. The post-fit background predictions are found to agree with the data. From this result, the systematic uncertainty and its model for high m_{eff} range are validated.

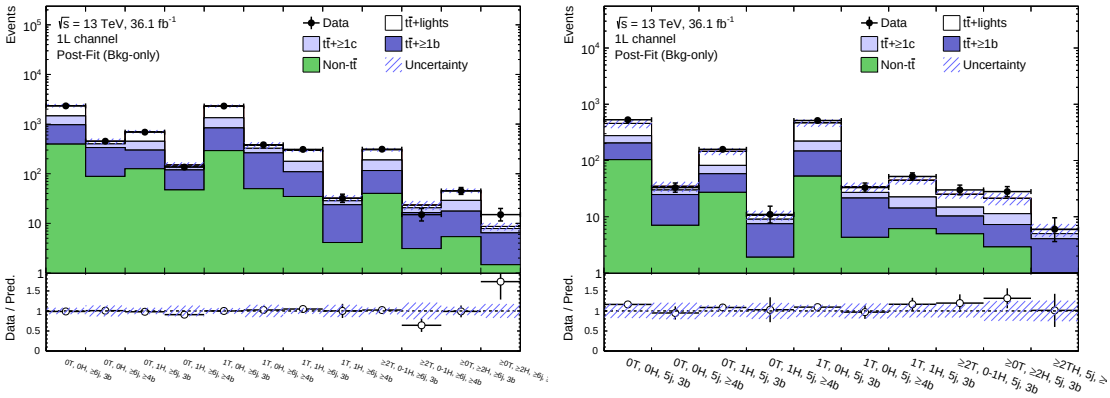

(a) (b)

Figure G.10: Event yields in (a) the search regions (≥6 jets) and (b) the validation regions (5 jets) after the fit ("Post-fit") to the data (black dots) with the looser blind cut ($S/B < 20\%$) applied. The fit to the blinded data is performed under the background-only hypothesis only in the search regions. The fit result in the search regions is propagated into the background prediction in the validation regions. The backgrounds of V+jets, diboson, single-top, ttV and ttH which have small contributions are combined into a single background named "Non-$t\bar{t}$. The hashed area represents the total uncertainty on the post-fit background prediction.

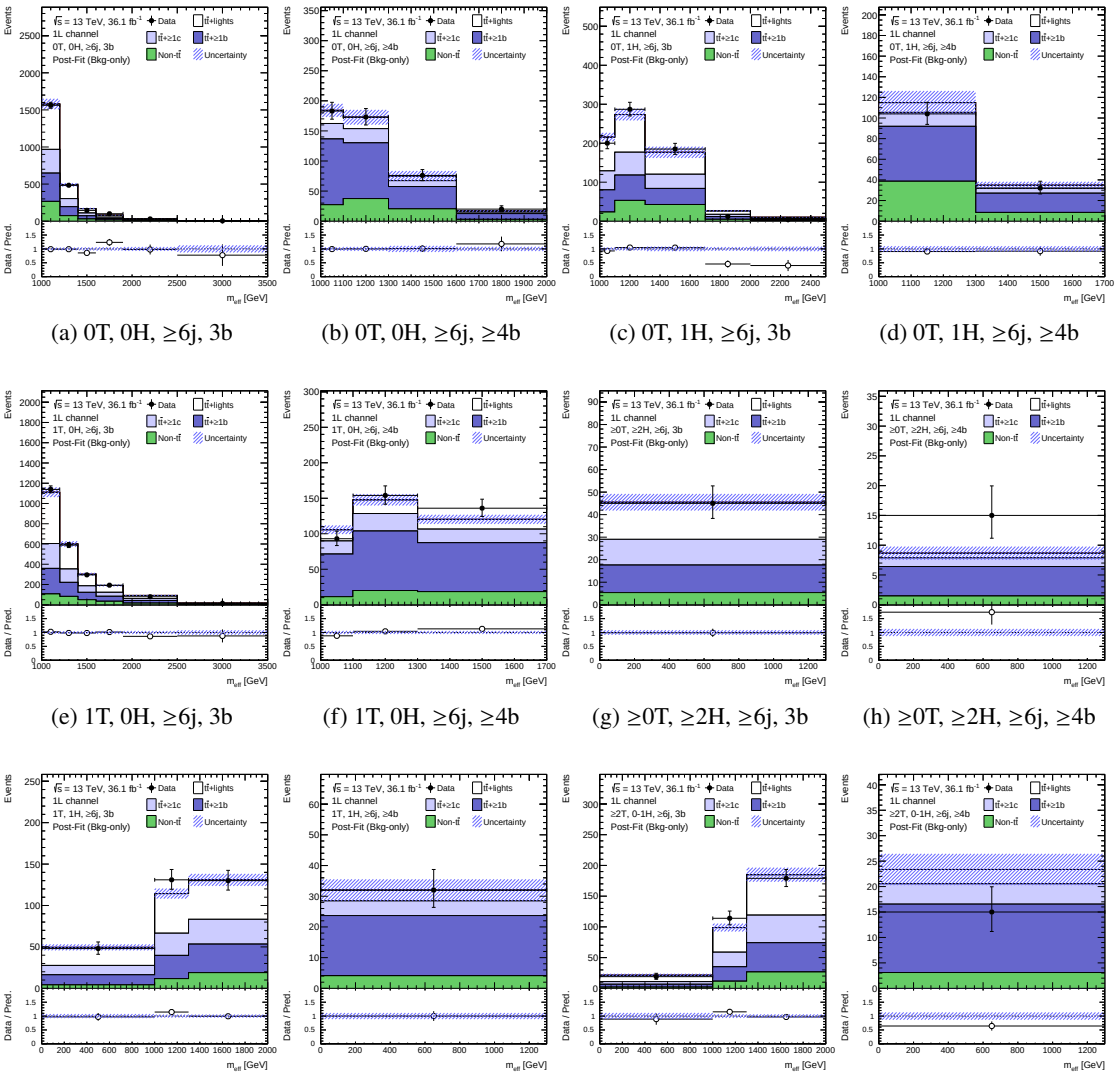

(a) 0T, 0H, ≥6j, 3b (b) 0T, 0H, ≥6j, ≥4b (c) 0T, 1H, ≥6j, 3b (d) 0T, 1H, ≥6j, ≥4b

(e) 1T, 0H, ≥6j, 3b (f) 1T, 0H, ≥6j, ≥4b (g) ≥0T, ≥2H, ≥6j, 3b (h) ≥0T, ≥2H, ≥6j, ≥4b

(i) 1T, 1H, ≥6j, 3b (j) 1T, 1H, ≥6j, ≥4b (k) ≥2T, 0-1H, ≥6j, 3b (l) ≥2T, 0-1H, ≥6j, ≥4b

Figure G.11: m_{eff} distribution of backgrounds after the fit to the blinded data for each category of Search region.

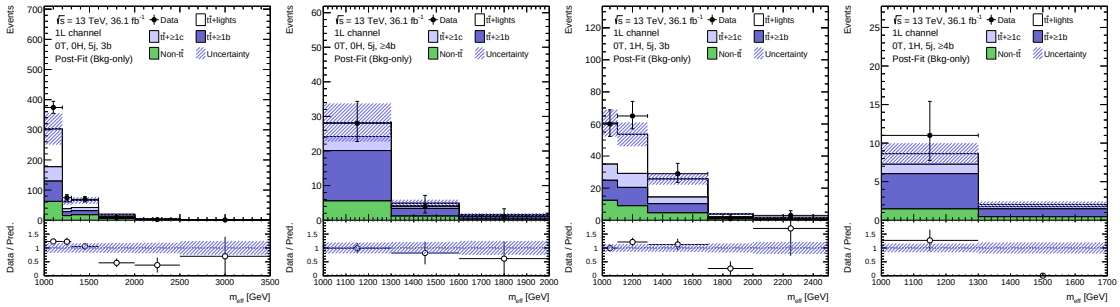

(a) 0T, 0H, 5j, 3b

(b) 0T, 0H, 5j, ≥4b

(c) 0T, 1H, 5j, 3b

(d) 0T, 1H, 5j, ≥4b

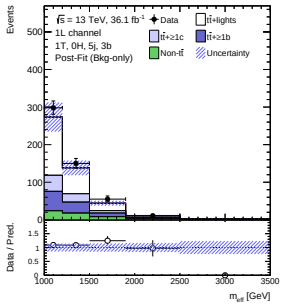

(e) 1T, 0H, 5j, 3b

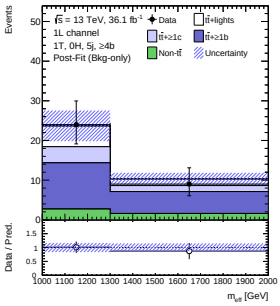

(f) 1T, 0H, 5j, ≥4b

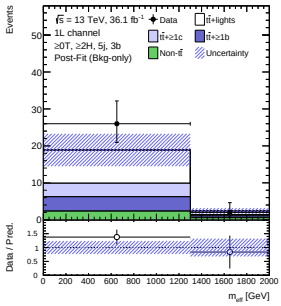

(g) ≥0T, ≥2H, 5j, 3b

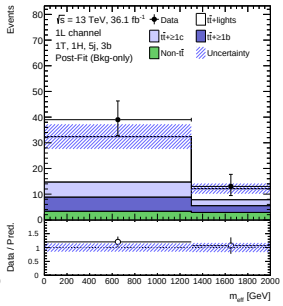

(h) 1T, 1H, 5j, 3b

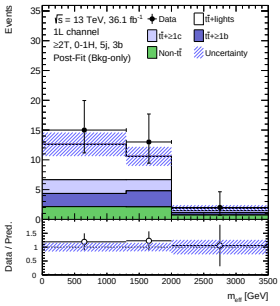

(i) ≥2T, 0-1H, 5j, 3b

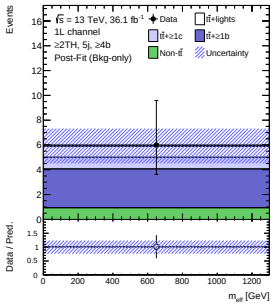

(j) ≥2TH, 5j, ≥4b

Figure G.12: m_{eff} distribution of backgrounds after the fit to the blinded data for each category of Validation region.

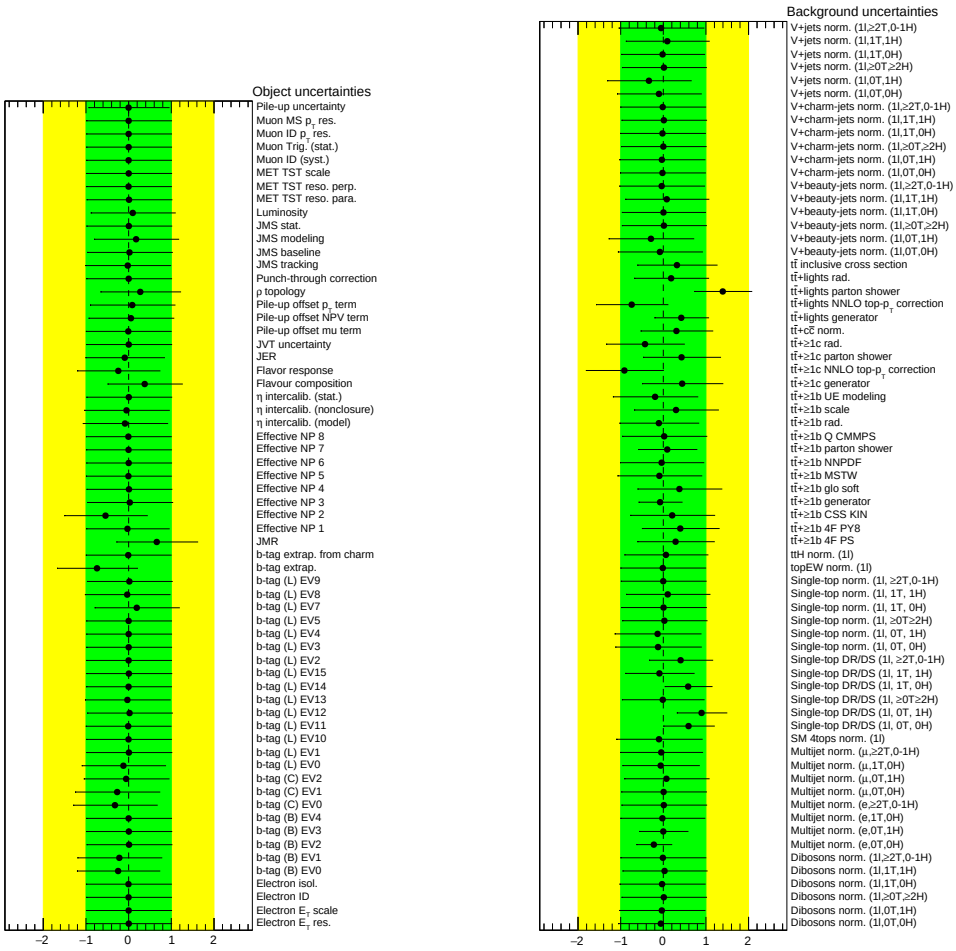

(a) (b)

Figure G.13: Pulls and constraints on the fitted nuisance parameters related to (a) the luminosity, pileup, and physics objects and (b) modelling. The fit is performed to the observed data without the blind cut. For each NP, the fitted value represents the preferred shift with respect to the prediction in a unit of its prior uncertainty, and the fitted error represents the uncertainty after the fit in a unit of its prior uncertainty.

G.6 Plots in the fit to the unblinded data

This section shows the plots in the fit to the unblinded data. Figure G.13 shows the pulls and constraints of the nuisance parameters. They are found to be consistent with the fit results using the blinded data.

Figure G.14 shows the correlation matrix among the nuisance parameters. It is consistent with the other fit results using the Asimov dataset and blinded data.

Table G.2 and G.3 show the number of events of the post-fit prediction and data in the singal depleted

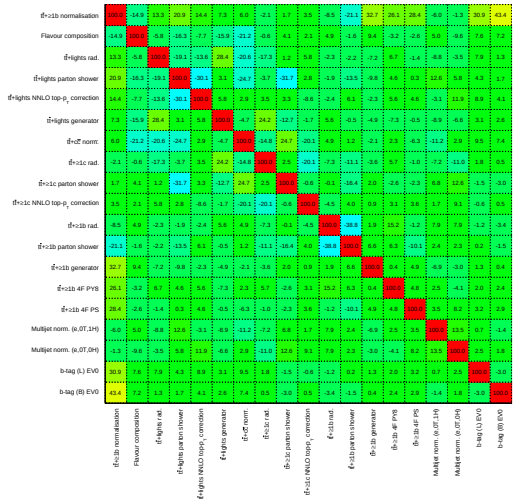

Figure G.14: Correlation matrix among the nuisance parameters in the fit to the data without the blind cut. Only the nuisance parameters which have above 20% correlations to another are shown.

and sensitive categories, respectively.

Table G.2: Predicted and observed event yields in the signal depleted VR categories. The background prediction is shown after the fit to the data under the background-only hypothesis. The uncertainties are calculated by the sum in quadrature of the statistical and systematic uncertainties with the correlations among the nuisance parameters taken into account.

	0T, 0H, 5j, 3b	0T, 0H, 5j, ≥4b	0T, 1H, 5j, 3b
$t\bar{t}$ + lights	170.38 ± 54.85	4.71 ± 1.95	60.69 ± 13.92
$t\bar{t}$+ ≥ 1c	93.00 ± 59.71	6.98 ± 5.94	27.76 ± 12.23
$t\bar{t}$+ ≥ 1b	93.66 ± 29.96	16.91 ± 4.72	30.49 ± 8.12
$t\bar{t}V$	6.43 ± 1.13	0.92 ± 0.18	2.52 ± 0.44
$t\bar{t}H$	2.61 ± 0.35	0.65 ± 0.11	1.92 ± 0.25
W+light-jets	0.26 ± 0.19	0.00 ± 0.00	0.06 ± 0.04
W+≥1c+jets	3.40 ± 1.80	0.07 ± 0.04	0.79 ± 0.38
W+≥1b+jets	24.51 ± 10.50	1.37 ± 0.61	6.91 ± 3.37
Z+light-jets	0.04 ± 0.03	0.00 ± 0.00	0.01 ± 0.01
Z+≥1c+jets	0.33 ± 0.17	0.01 ± 0.00	0.07 ± 0.04
Z+≥1b+jets	3.22 ± 1.69	0.19 ± 0.11	1.01 ± 0.50
Single top	43.46 ± 10.86	2.79 ± 0.85	7.31 ± 2.23
Dibosons	3.97 ± 2.08	0.33 ± 0.24	0.76 ± 0.42
Multijet	0.96 ± 1.63	0.00 ± 0.00	6.85 ± 4.52
$t\bar{t}t\bar{t}(SM)$	0.06 ± 0.02	0.02 ± 0.01	0.03 ± 0.01
Total	446.30 ± 78.68	34.93 ± 7.52	147.19 ± 18.94
Data	530	33	159
	0T, 1H, 5j, ≥4b	1T, 0H, 5j, 3b	1T, 0H, 5j, ≥4b
$t\bar{t}$ + lights	1.61 ± 0.55	236.45 ± 50.47	6.66 ± 2.20
$t\bar{t}$+ ≥ 1c	1.91 ± 0.86	83.70 ± 38.16	6.80 ± 3.33
$t\bar{t}$+ ≥ 1b	6.20 ± 1.57	95.14 ± 24.24	18.19 ± 4.15
$t\bar{t}V$	0.36 ± 0.08	8.14 ± 1.39	1.03 ± 0.20
$t\bar{t}H$	0.68 ± 0.12	3.70 ± 0.48	1.09 ± 0.18
W+light-jets	0.00 ± 0.00	0.12 ± 0.09	0.00 ± 0.00
W+≥1c+jets	0.02 ± 0.01	1.80 ± 0.91	0.04 ± 0.02
W+≥1b+jets	0.35 ± 0.17	14.63 ± 6.27	0.83 ± 0.38
Z+light-jets	0.00 ± 0.00	0.02 ± 0.01	0.00 ± 0.00
Z+≥1c+jets	0.00 ± 0.00	0.14 ± 0.07	0.00 ± 0.00
Z+≥1b+jets	0.07 ± 0.04	1.20 ± 0.65	0.05 ± 0.03
Single top	0.47 ± 0.25	20.80 ± 5.52	1.49 ± 0.55
Dibosons	0.03 ± 0.02	1.96 ± 1.04	0.11 ± 0.07
Multijet	0.00 ± 0.00	0.00 ± 0.00	0.00 ± 0.00
$t\bar{t}t\bar{t}(SM)$	0.01 ± 0.00	0.07 ± 0.02	0.02 ± 0.01
Total	11.70 ± 1.85	467.90 ± 63.08	36.32 ± 5.48
Data	12	514	34

Table G.3: Predicted and observed event yields in the signal sensitive VR categoris. The background prediction is shown after the fit to the data under the background-only hypothesis. The uncertainties are calculated by the sum in quadrature of the statistical and systematic uncertainties with the correlations among the nuisance parameters taken into account.

	1T, 1H, 5j, 3b	≥2T, 0-1H, 5j, 3b	≥0T, ≥2H, 5j, 3b
$t\bar{t}$ + lights	22.66 ± 4.40	10.01 ± 1.95	10.34 ± 2.42
$t\bar{t}+ \geq 1c$	9.09 ± 3.82	5.04 ± 2.07	4.58 ± 2.52
$t\bar{t}+ \geq 1b$	9.54 ± 3.30	5.65 ± 1.70	5.21 ± 1.58
$t\bar{t}V$	1.11 ± 0.20	0.98 ± 0.18	0.37 ± 0.12
$t\bar{t}H$	1.07 ± 0.16	0.51 ± 0.08	0.46 ± 0.08
W+light-jets	0.01 ± 0.01	0.01 ± 0.01	0.00 ± 0.00
W+≥1c+jets	0.14 ± 0.08	0.15 ± 0.09	0.07 ± 0.04
W+≥1b+jets	1.07 ± 0.51	1.72 ± 0.99	0.51 ± 2.64
Z+light-jets	0.00 ± 0.00	0.00 ± 0.00	0.00 ± 0.00
Z+≥1c+jets	0.04 ± 0.03	0.00 ± 0.00	0.01 ± 0.00
Z+≥1b+jets	0.19 ± 0.10	0.15 ± 0.11	0.08 ± 0.10
Single top	2.82 ± 1.30	1.03 ± 0.45	0.93 ± 0.44
Dibosons	0.22 ± 0.14	0.04 ± 0.03	0.14 ± 0.10
Multijet	0.00 ± 0.00	0.00 ± 0.00	0.00 ± 0.00
$t\bar{t}t\bar{t}(SM)$	0.01 ± 0.01	0.01 ± 0.01	0.00 ± 0.00
Total	47.97 ± 7.08	25.30 ± 3.72	22.70 ± 4.00
Data	52	30	29

	≥2TH, 5j, ≥4b
$t\bar{t}$ + lights	1.17 ± 0.37
$t\bar{t}+ \geq 1c$	1.58 ± 0.68
$t\bar{t}+ \geq 1b$	4.94 ± 1.76
$t\bar{t}V$	0.31 ± 0.07
$t\bar{t}H$	0.76 ± 0.15
W+light-jets	0.00 ± 0.00
W+≥1c+jets	0.01 ± 0.00
W+≥1b+jets	0.14 ± 0.13
Z+light-jets	0.00 ± 0.00
Z+≥1c+jets	0.00 ± 0.00
Z+≥1b+jets	0.01 ± 0.01
Single top	0.36 ± 0.18
Dibosons	0.01 ± 0.01
Multijet	0.00 ± 0.00
$t\bar{t}t\bar{t}(SM)$	0.01 ± 0.00
Total	9.30 ± 1.98
Data	8

H Kinematic variables in Validation regions

This chapter shows the kinematic variables in the validation regions, comparing to the corresponding search regions. Figure H.1 – H.12 show the distributions of m_{eff}, the leading jet p_{T}, electron and muon p_{T}, $E_{\text{T}}^{\text{miss}}$, and m_{T}^{W}. In general, the variables of electron or muon p_{T}, $E_{\text{T}}^{\text{miss}}$, and m_{T}^{W} which are not related to the jet multiplicity are consistent within 10% between the search and validation regions. The mean and RMS values of leading jet in the merged "≥2TH" category agree with those in the corresponding search regions by around 10%. The results assure that the merged "≥2TH" category has similar event topology to the corresponding SR categories. Eventually, the "≥2TH" category is used as a final configuration[1].

[1] It is not necessary to check the sensitivity in this case because the validation regions are not used for the searching for excesses of data but for the validation of the background estimation

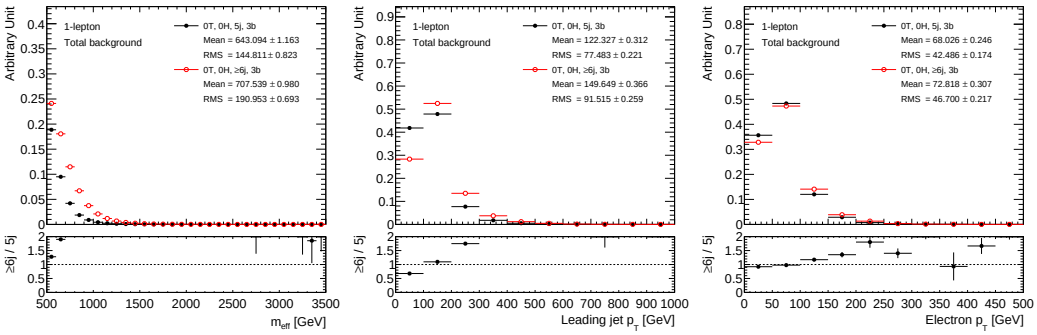

(a) m_{eff} (b) Leading jet p_{T} (c) Electron p_{T}

(d) Muon p_{T} (e) $E_{\text{T}}^{\text{miss}}$ (f) m_{T}^{W}

Figure H.1: Comparison of various kinematic variables between "0T, 0H, 5j, 3b category" (black) and "0T, 0H, ≥6j, 3b category" (red) for total background before fitting.

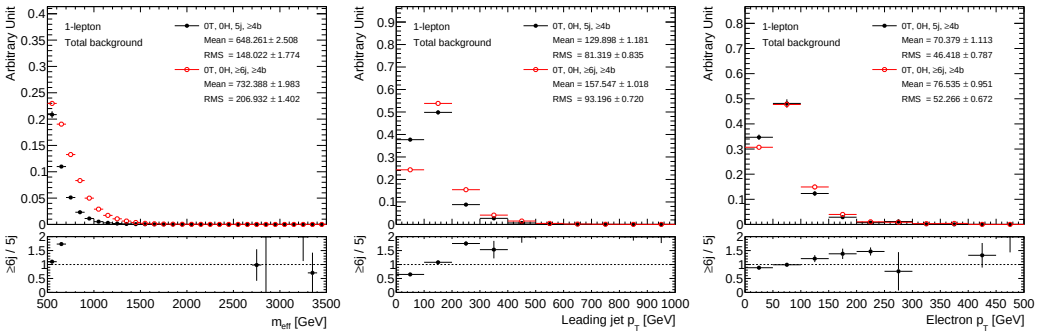

(a) m_{eff} (b) Leading jet p_{T} (c) Electron p_{T}

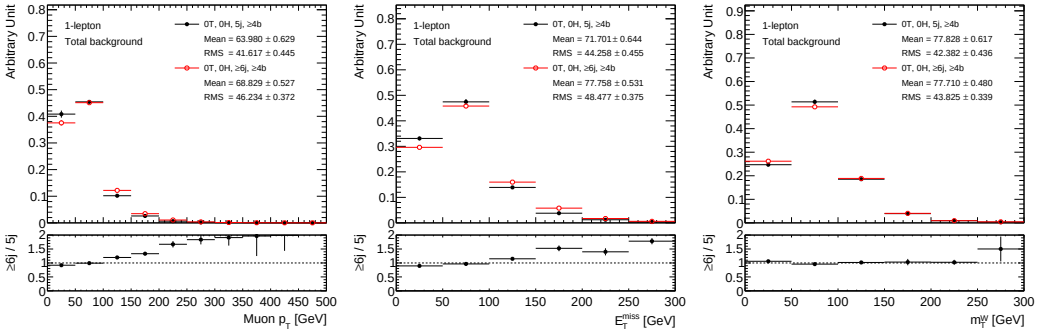

(d) Muon p_{T} (e) $E_{\text{T}}^{\text{miss}}$ (f) m_{T}^{W}

Figure H.2: Comparison of various kinematic variables between “0T, 0H, 5j, ≥4b category” (black) and “0T, 0H, ≥6j, ≥4b category” (red) for total background before fitting.

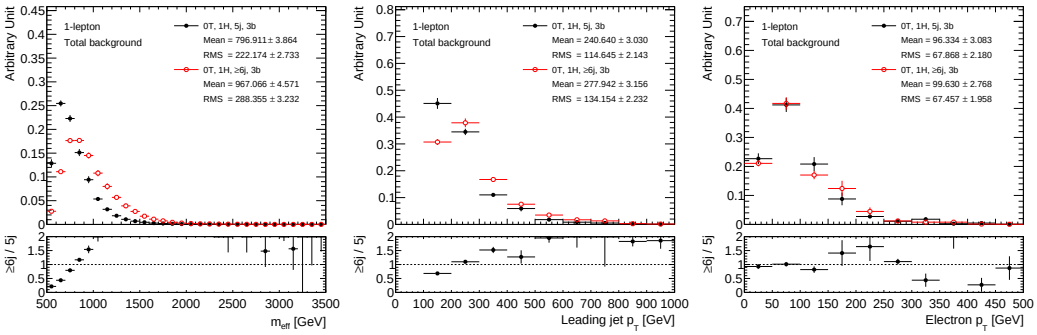

(a) m_{eff} (b) Leading jet p_{T} (c) Electron p_{T}

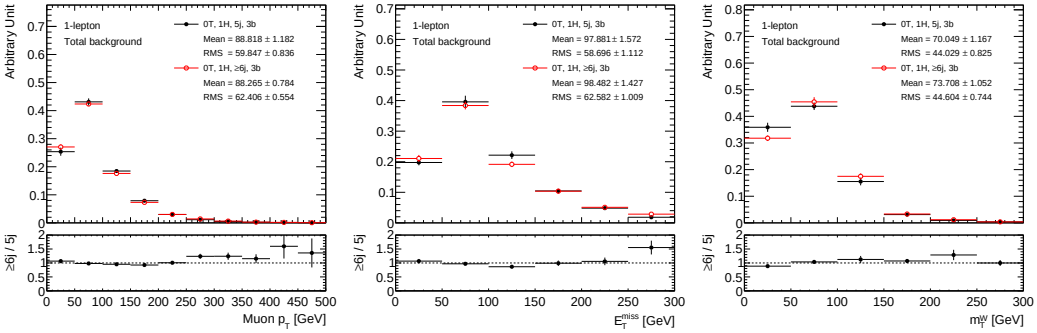

(d) Muon p_{T} (e) $E_{\text{T}}^{\text{miss}}$ (f) m_{T}^{W}

Figure H.3: Comparison of various kinematic variables between "0T, 1H, 5j, 3b category" (black) and "0T, 1H, ≥6j, 3b category" (red) for total background before fitting.

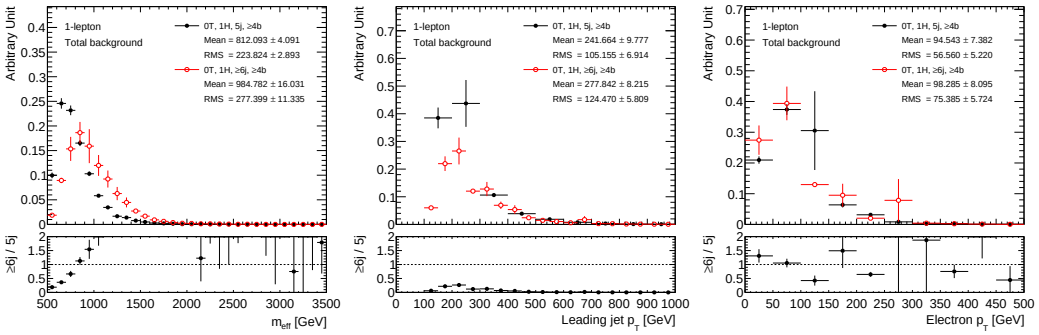

(a) m_{eff} (b) Leading jet p_{T} (c) Electron p_{T}

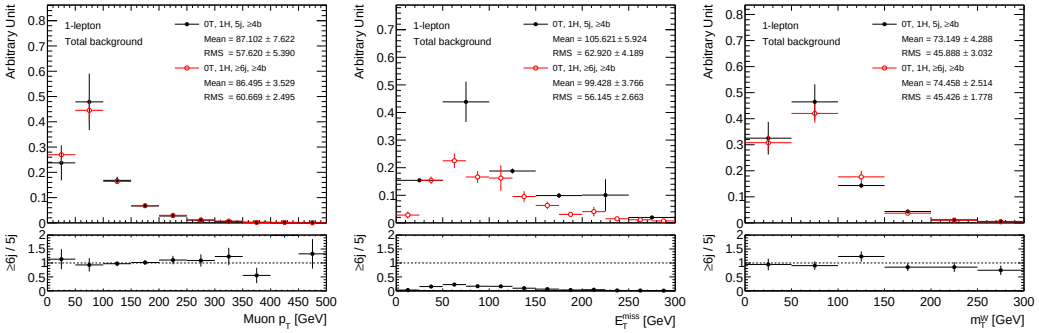

(d) Muon p_{T} (e) $E_{\text{T}}^{\text{miss}}$ (f) m_{T}^{W}

Figure H.4: Comparison of various kinematic variables between “0T, 1H, 5j, ≥4b category” (black) and “0T, 1H, ≥6j, ≥4b category” (red) for total background before fitting.

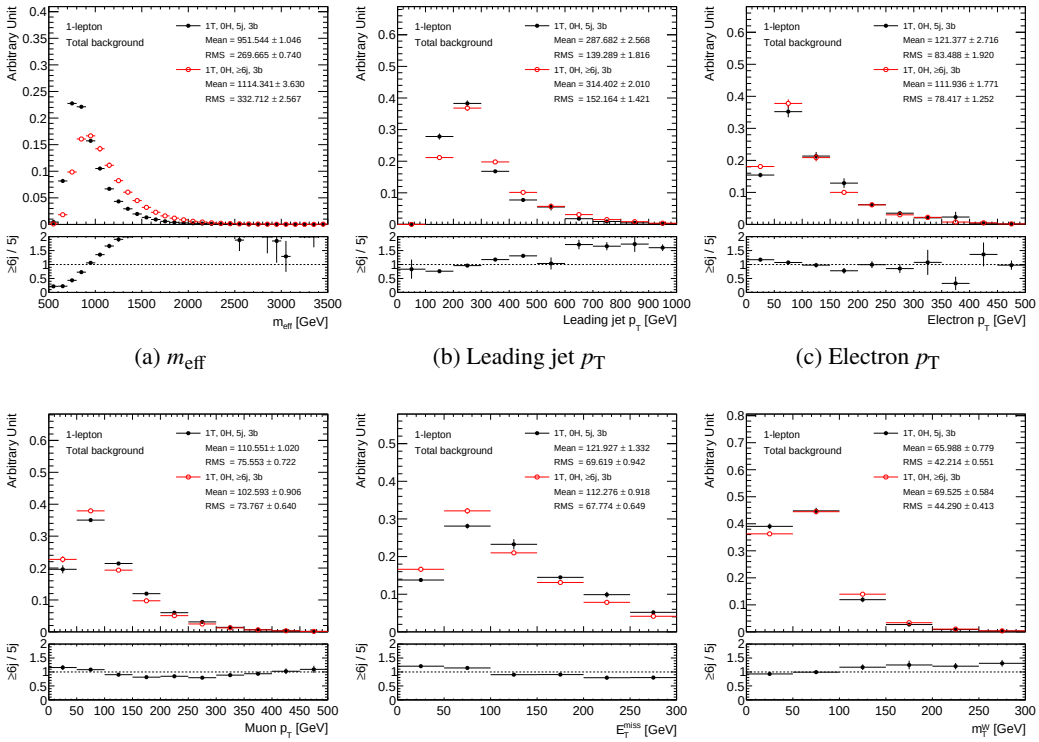

(a) m_{eff} (b) Leading jet p_{T} (c) Electron p_{T}

(d) Muon p_{T} (e) $E_{\text{T}}^{\text{miss}}$ (f) m_{T}^{W}

Figure H.5: Comparison of various kinematic variables between "1T, 0H, 5j, 3b category" (black) and "1T, 0H, ≥6j, 3b category" (red) for total background before fitting.

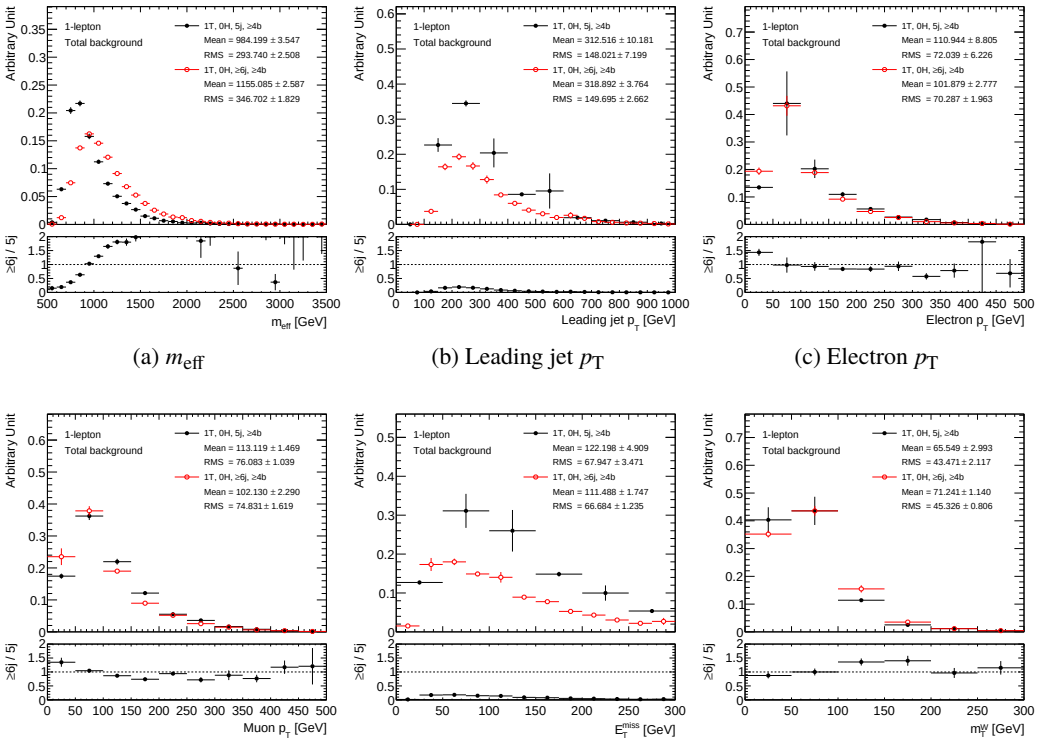

(a) m_{eff} (b) Leading jet p_{T} (c) Electron p_{T}

(d) Muon p_{T} (e) $E_{\text{T}}^{\text{miss}}$ (f) m_{T}^{W}

Figure H.6: Comparison of various kinematic variables between "1T, 0H, 5j, ≥4b category" (black) and "1T, 0H, ≥6j, ≥4b category" (red) for total background before fitting.

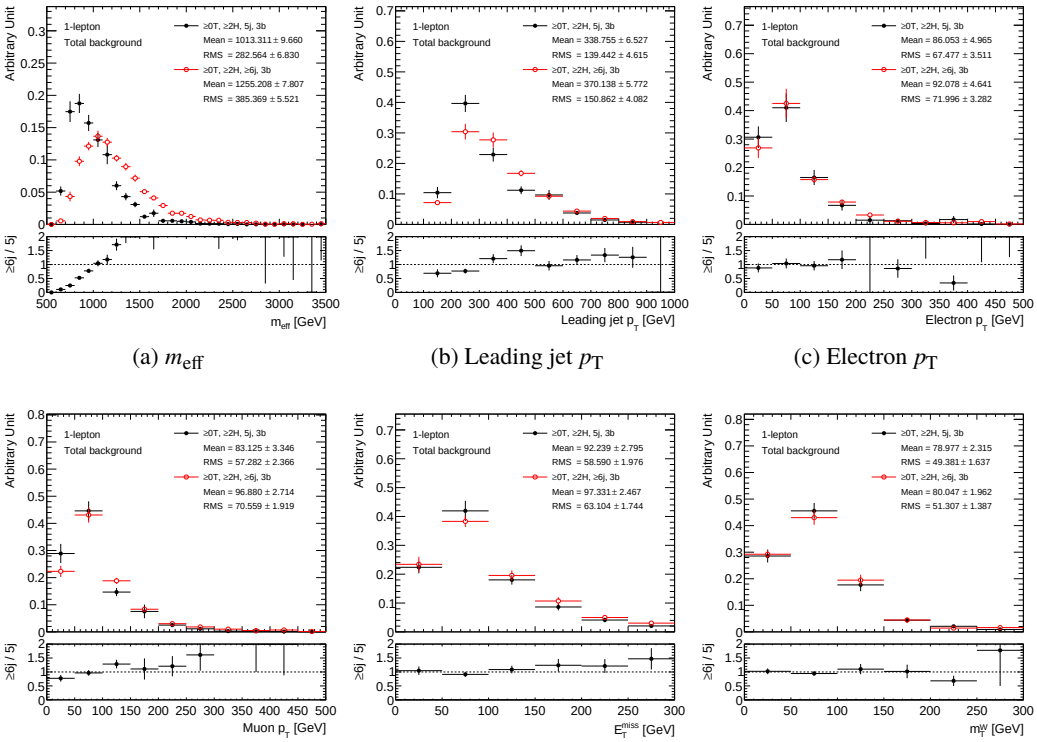

(a) m_{eff} (b) Leading jet p_{T} (c) Electron p_{T}

(d) Muon p_{T} (e) $E_{\text{T}}^{\text{miss}}$ (f) m_{T}^{W}

Figure H.7: Comparison of various kinematic variables between "≥0T, ≥2H, 5j, 3b category" (black) and "0T, 1H, ≥6j, 3b category" (red) for total background before fitting.

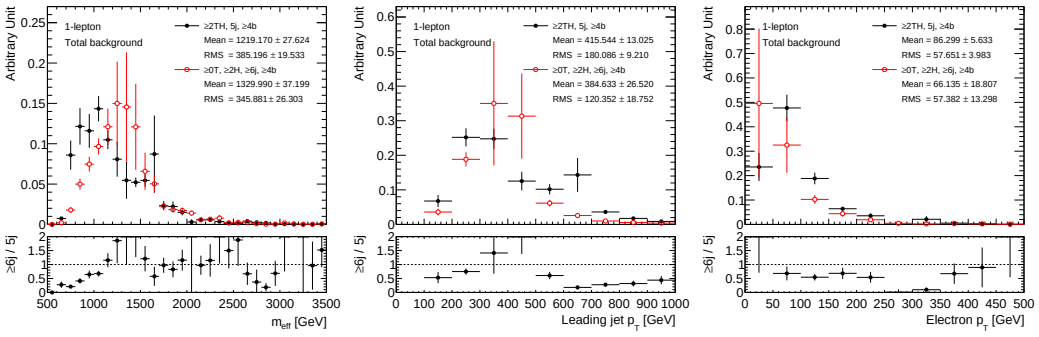

(a) m_{eff} (b) Leading jet p_{T} (c) Electron p_{T}

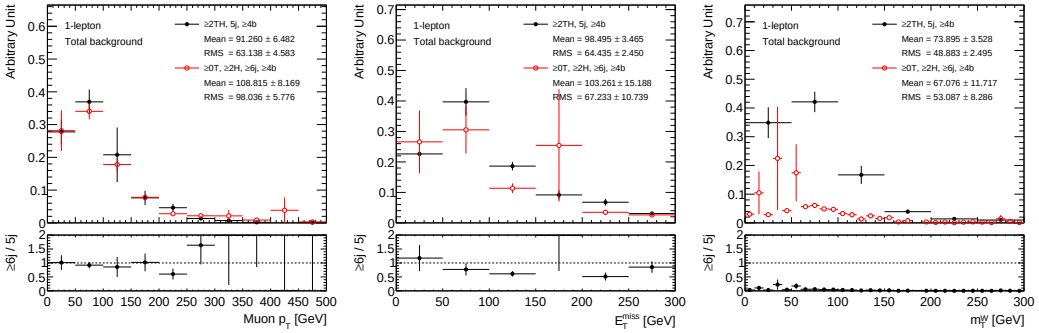

(d) Muon p_{T} (e) $E_{\text{T}}^{\text{miss}}$ (f) m_{T}^{W}

Figure H.8: Comparison of various kinematic variables between "≥2TH, 5j, ≥4b category" (black) and "≥0T, ≥2H, ≥6j, ≥4b category" (red) for total background before fitting.

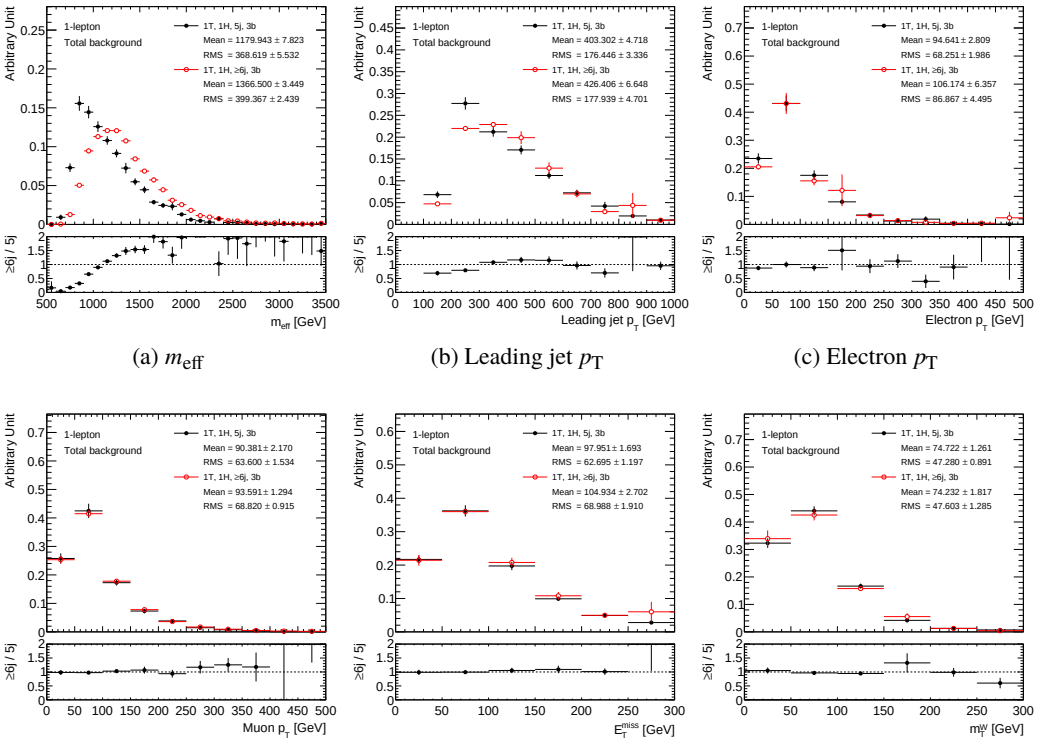

(a) m_{eff} (b) Leading jet p_{T} (c) Electron p_{T}

(d) Muon p_{T} (e) $E_{\mathrm{T}}^{\mathrm{miss}}$ (f) $m_{\mathrm{T}}^{\mathrm{W}}$

Figure H.9: Comparison of various kinematic variables between "1T, 1H, 5j, 3b category" (black) and "1T, 1H, ≥6j, 3b category" (red) for total background before fitting.

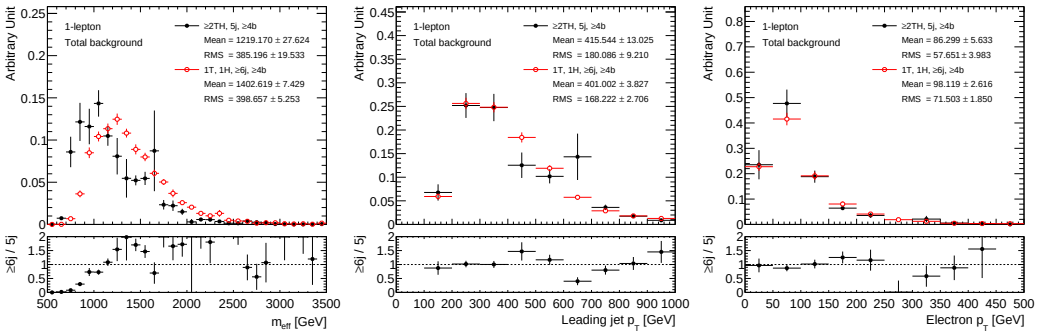

(a) m_{eff} (b) Leading jet p_{T} (c) Electron p_{T}

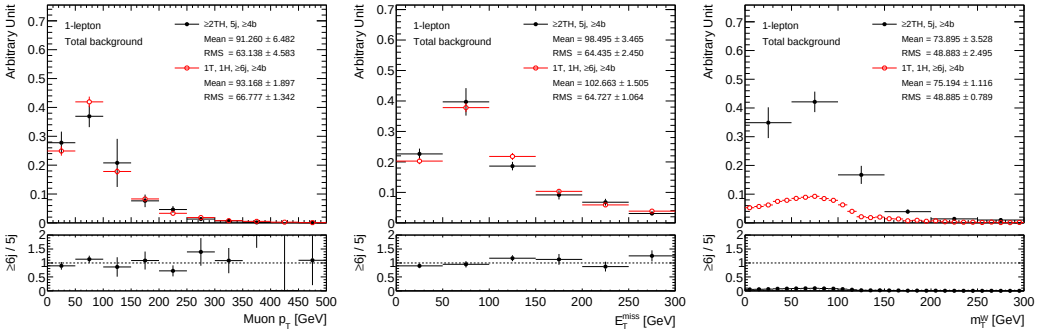

(d) Muon p_{T} (e) $E_{\text{T}}^{\text{miss}}$ (f) m_{T}^{W}

Figure H.10: Comparison of various kinematic variables between "≥2TH, 5j, ≥4b category" (black) and "1T, 1H, ≥6j, ≥4b category" (red) for total background before fitting.

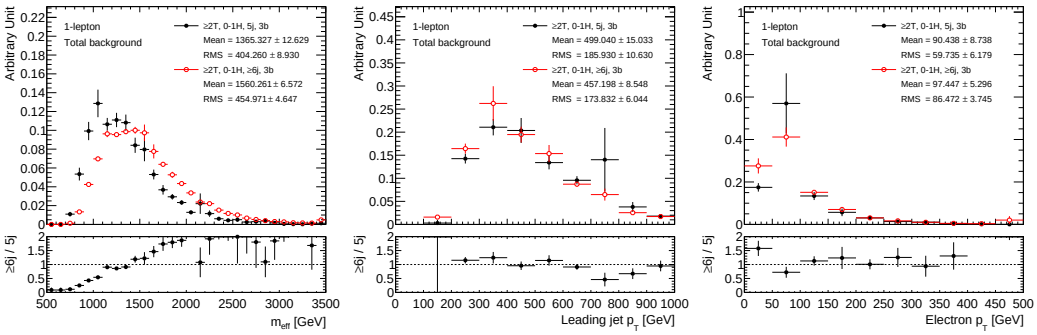

(a) m_{eff} (b) Leading jet p_{T} (c) Electron p_{T}

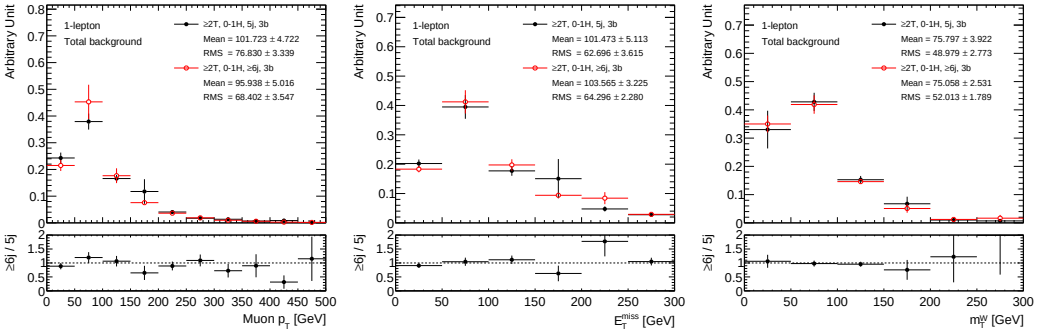

(d) Muon p_{T} (e) $E_{\text{T}}^{\text{miss}}$ (f) m_{T}^{W}

Figure H.11: Comparison of various kinematic variables between "≥2T, 0-1H, 5j, 3b category" (black) and "≥2T, 0-1H, ≥6j, 3b category" (red) for total background before fitting.

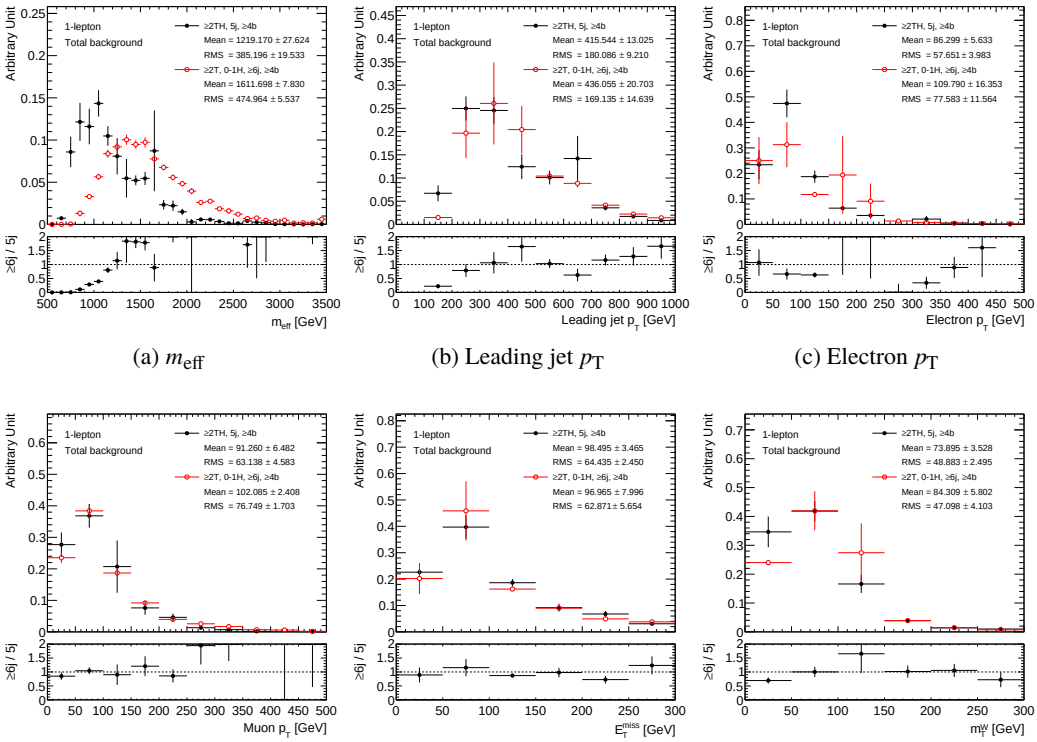

(a) m_{eff} (b) Leading jet p_{T} (c) Electron p_{T}

(d) Muon p_{T} (e) $E_{\text{T}}^{\text{miss}}$ (f) m_{T}^{W}

Figure H.12: Comparison of various kinematic variables between "≥2TH, 5j, ≥4b category" (black) and "≥2T, 0-1H, ≥6j, ≥4b category" (red) for total background before fitting.

Bibliography

[1] M. Gell-Mann, *A Schematic Model of Baryons and Mesons*, Phys. Lett. **8** (1964) 214.

[2] S. Weinberg, *A Model of Leptons*, Phys. Rev. Lett. **19** (1967) 1264.

[3] A. Salam, *Weak and Electromagnetic Interactions*, Conf. Proc. **C680519** (1968) 367.

[4] S. L. Glashow, J. Iliopoulos and L. Maiani,
Weak Interactions with Lepton-Hadron Symmetry, Phys. Rev. **D2** (1970) 1285.

[5] L. Álvarez-Gaumé and J. Ellis, *Eyes on a prize particle*, Nature Physics **7** (2010) 2,
URL: http://dx.doi.org/10.1038/nphys1874.

[6] C. P. et al., Chin. Phys. C **40** (2016) 10001.

[7] T. A. Aaltonen et al., *Combination of CDF and D0 W-Boson Mass Measurements*,
Phys. Rev. **D88** (2013) 052018, arXiv: 1307.7627 [hep-ex].

[8] *Precision electroweak measurements on the Z resonance*, Physics Reports **427** (2006) 257 ,
ISSN: 0370-1573, URL:
http://www.sciencedirect.com/science/article/pii/S0370157305005119.

[9] V. M. Abazov et al.,
Measurement of the Effective Weak Mixing Angle in $p\overline{p} \to Z/\gamma^* \to e^+e^-$ Events,
Phys. Rev. Lett. **115** (4 2015) 041801,
URL: https://link.aps.org/doi/10.1103/PhysRevLett.115.041801.

[10] T. Aaltonen et al., *Indirect measurement of $\sin^2\theta_W$ (or M_W) using $\mu^+\mu^-$ pairs from γ^*/Z bosons produced in $p\overline{p}$ collisions at a center-of-momentum energy of 1.96 TeV*,
Phys. Rev. D **89** (7 2014) 072005,
URL: https://link.aps.org/doi/10.1103/PhysRevD.89.072005.

[11] F. Abe et al., *Observation of Top Quark Production in $\overline{p}p$ Collisions with the Collider Detector at Fermilab*, Phys. Rev. Lett. **74** (14 1995) 2626,
URL: https://link.aps.org/doi/10.1103/PhysRevLett.74.2626.

[12] S. Abachi et al., *Observation of the Top Quark*, Phys. Rev. Lett. **74** (14 1995) 2632,
URL: https://link.aps.org/doi/10.1103/PhysRevLett.74.2632.

[13] 'Measurement of the Higgs boson mass in the $H \to ZZ^* \to 4\ell$ and $H \to \gamma\gamma$ channels with $\sqrt{s}$=13TeV pp collisions using the ATLAS detector', tech. rep. ATLAS-CONF-2017-046,
CERN, 2017, URL: http://cds.cern.ch/record/2273853.

[14] G. Aad et al., *Combined Measurement of the Higgs Boson Mass in pp Collisions at $\sqrt{s} = 7$ and 8 TeV with the ATLAS and CMS Experiments*, Phys. Rev. Lett. **114** (2015) 191803,
arXiv: 1503.07589 [hep-ex].

[15] ATLAS and CMS Collaborations, *Measurements of the Higgs boson production and decay rates and constraints on its couplings from a combined ATLAS and CMS analysis of the LHC pp collision data at $\sqrt{s}$ = 7 and 8 TeV*, JHEP **08** (2016) 045, arXiv: 1606.02266 [hep-ex].

[16] J. Ellis and T. You, *Updated Global Analysis of Higgs Couplings*, JHEP **06** (2013) 103, arXiv: 1303.3879 [hep-ph].

[17] ATLAS Collaboration, 'Summary plots from the ATLAS Standard Model physics group', 2017 (accessd December, 2017), URL: https://atlas.web.cern.ch/Atlas/GROUPS/PHYSICS/CombinedSummaryPlots/SM/.

[18] F. Zwicky, *Spectral displacement of extra galactic nebulae*, Helv. Phys. Acta **6** (1933) 110.

[19] V. C. Rubin and W. K. Ford Jr., *Rotation of the Andromeda Nebula from a Spectroscopic Survey of Emission Regions*, Astrophys. J. **159** (1970) 379.

[20] V. C. Rubin, W. K. Ford Jr. and N. Thonnard, *Rotational properties of 21 SC galaxies with a large range of luminosities and radii, from NGC 4605 /R = 4kpc/ to UGC 2885 /R = 122 kpc/*, Astrophys. J. **238** (1980) 471.

[21] N. Arkani-Hamed, S. Dimopoulos and G. R. Dvali, *The Hierarchy problem and new dimensions at a millimeter*, Phys. Lett. **B429** (1998) 263, arXiv: hep-ph/9803315 [hep-ph].

[22] M. Aaboud et al., *Search for dark matter and other new phenomena in events with an energetic jet and large missing transverse momentum using the ATLAS detector*, (2017), arXiv: 1711.03301 [hep-ex].

[23] T. Appelquist, H.-C. Cheng and B. A. Dobrescu, *Bounds on universal extra dimensions*, Phys. Rev. **D64** (2001) 035002, arXiv: hep-ph/0012100 [hep-ph].

[24] G. Burdman, B. A. Dobrescu and E. Ponton, *Resonances from two universal extra dimensions*, Phys. Rev. **D74** (2006) 075008, arXiv: hep-ph/0601186 [hep-ph].

[25] G. Cacciapaglia, A. Deandrea and J. Llodra-Perez, *A Dark Matter candidate from Lorentz Invariance in 6D*, JHEP **03** (2010) 083, arXiv: 0907.4993 [hep-ph].

[26] G. Cacciapaglia et al., *Four tops on the real projective plane at LHC*, JHEP **1110** (2011) 042, arXiv: 1107.4616 [hep-ph].

[27] A. Arbey et al., *Dark Matter in a twisted bottle*, JHEP **01** (2013) 147, arXiv: 1210.0384 [hep-ph].

[28] L. Randall and R. Sundrum, *Large Mass Hierarchy from a Small Extra Dimension*, Phys. Rev. Lett. **83** (17 1999) 3370, URL: https://link.aps.org/doi/10.1103/PhysRevLett.83.3370.

[29] R. Contino et al., *Warped/composite phenomenology simplified*, JHEP **05** (2007) 074, arXiv: hep-ph/0612180 [hep-ph].

[30] J. Goldstone, A. Salam and S. Weinberg, *Broken Symmetries*, Phys. Rev. **127** (1962) 965.

[31] D. B. Kaplan and H. Georgi, *SU(2) x U(1) Breaking by Vacuum Misalignment*, Phys. Lett. **136B** (1984) 183.

[32] D. B. Kaplan, H. Georgi and S. Dimopoulos, *Composite Higgs Scalars*, Phys. Lett. **136B** (1984) 187.

[33] H. Georgi and D. B. Kaplan, *Composite Higgs and Custodial SU(2)*, Phys. Lett. **145B** (1984) 216.

[34] N. Arkani-Hamed, A. G. Cohen and H. Georgi, *Electroweak symmetry breaking from dimensional deconstruction*, Phys. Lett. **B513** (2001) 232, arXiv: hep-ph/0105239 [hep-ph].

[35] N. Arkani-Hamed et al., *The Littlest Higgs*, JHEP **07** (2002) 034, arXiv: hep-ph/0206021 [hep-ph].

[36] K. Agashe, R. Contino and A. Pomarol, *The Minimal composite Higgs model*, Nucl. Phys. **B719** (2005) 165, arXiv: hep-ph/0412089 [hep-ph].

[37] J. Mrazek et al., *The Other Natural Two Higgs Doublet Model*, Nucl. Phys. **B853** (2011) 1, arXiv: 1105.5403 [hep-ph].

[38] D. B. Kaplan, *Flavor at ssc energies: A new mechanism for dynamically generated fermion masses*, Nuclear Physics B **365** (1991) 259 , ISSN: 0550-3213, URL: http://www.sciencedirect.com/science/article/pii/S0550321305800215.

[39] A. Pomarol and J. Serra, *Top Quark Compositeness: Feasibility and Implications*, Phys. Rev. D **78** (2008) 074026, arXiv: 0806.3247 [hep-ph].

[40] B. Lillie, J. Shu and T. M. P. Tait, *Top Compositeness at the Tevatron and LHC*, JHEP **0804** (2008) 087, arXiv: 0712.3057 [hep-ph].

[41] K. Kumar, T. M. P. Tait and R. Vega-Morales, *Manifestations of Top Compositeness at Colliders*, JHEP **0905** (2009) 022, arXiv: 0901.3808 [hep-ph].

[42] H. Georgi et al., *Effects of top quark compositeness*, Phys. Rev. D **51** (7 1995) 3888, URL: https://link.aps.org/doi/10.1103/PhysRevD.51.3888.

[43] J. A. Aguilar-Saavedra et al., *Handbook of vectorlike quarks: Mixing and single production*, Phys. Rev. **D88** (2013) 094010, arXiv: 1306.0572 [hep-ph].

[44] ATLAS Collaboration, *Measurements of the Higgs boson production and decay rates and coupling strengths using pp collision data at $\sqrt{s} = 7$ and 8 TeV in the ATLAS experiment*, Eur. Phys. J. C **76** (2016) 6, arXiv: 1507.04548 [hep-ex].

[45] C. ATLAS, 'Letter of Intent for the Phase-II Upgrade of the ATLAS Experiment', tech. rep. CERN-LHCC-2012-022. LHCC-I-023, Draft version for comments: CERN, 2012, URL: http://cds.cern.ch/record/1502664.

[46] F. del Aguila, M. Perez-Victoria and J. Santiago, *Effective description of quark mixing*, Phys. Lett. **B492** (2000) 98, arXiv: hep-ph/0007160 [hep-ph].

[47] S. L. Glashow, J. Iliopoulos and L. Maiani,
Weak Interactions with Lepton-Hadron Symmetry, Phys. Rev. D **2** (7 1970) 1285,
URL: https://link.aps.org/doi/10.1103/PhysRevD.2.1285.

[48] J. A. Aguilar-Saavedra, *Identifying top partners at LHC*, JHEP **0911** (2009) 030,
arXiv: 0907.3155 [hep-ph].

[49] ATLAS Collaboration, *Search for new phenomena in $t\bar{t}$ final states with additional heavy-flavour jets in* 13.2 fb^{-1} *of pp collisions at* $\sqrt{s}$ = 13 *TeV with the ATLAS detector*, ATLAS-CONF-2016-104, 2016, URL: https://cds.cern.ch/record/2220371.

[50] M. Aaboud et al.,
Search for pair production of vector-like top quarks in events with one lepton, jets, and missing transverse momentum in $\sqrt{s}$ = 13 *TeV pp collisions with the ATLAS detector*,
JHEP **08** (2017) 052, arXiv: 1705.10751 [hep-ex].

[51] M. Aaboud et al., *Search for pair production of heavy vector-like quarks decaying to high-p_T W bosons and b quarks in the lepton-plus-jets final state in pp collisions at* $\sqrt{s}$ = 13 *TeV with the ATLAS detector*, JHEP **10** (2017) 141, arXiv: 1707.03347 [hep-ex].

[52] A. M. Sirunyan et al., *Search for pair production of vector-like quarks in the $bW\bar{b}W$ channel from proton-proton collisions at* $\sqrt{s}$ = *13 TeV*, (2017), arXiv: 1710.01539 [hep-ex].

[53] 'Search for heavy vector-like quarks decaying to same-sign dileptons',
tech. rep. CMS-PAS-B2G-16-019, CERN, 2017,
URL: https://cds.cern.ch/record/2256747.

[54] V. D. Barger, A. L. Stange and R. J. N. Phillips, *Four heavy quark hadroproduction*,
Phys. Rev. D **44** (1991) 1987.

[55] V. Barger, W.-Y. Keung and B. Yencho, *Triple-Top Signal of New Physics at the LHC*,
Phys. Lett. B **687** (2010) 70, arXiv: 1001.0221 [hep-ph].

[56] 'Search for the standard model production of four top quarks with same-sign and multilepton final states in proton-proton collisions at $\sqrt{s}$ = 13 TeV',
tech. rep. CMS-PAS-TOP-17-009, CERN, 2017,
URL: https://cds.cern.ch/record/2284599.

[57] C. Degrande et al., *Non-resonant New Physics in Top Pair Production at Hadron Colliders*,
JHEP **03** (2011) 125, arXiv: 1010.6304 [hep-ph].

[58] L. Evans and P. Bryant, *LHC Machine*, Journal of Instrumentation **3** (2008) S08001,
URL: http://stacks.iop.org/1748-0221/3/i=08/a=S08001.

[59] *"Experimental Observation of Isolated Large Transeverse Energy Electrons with Associated Missing Energy at* $\sqrt{s}$ = 540 *GeV"*, Phys. Lett. **122B** (1983).

[60] *"Observation of Single Isolated Electrons of High Transeverse Momentum in Events with Missing Transeverse Energy at the CERN $\bar{p}p$ Collider"*, Phys. Lett. **122B** (1983).

[61] *"Experimental Observation of Lepton Pairs of Invariant Mass around 95 GeV/c^2 at the CERN SPS Collider"*, Phys. Lett. **126B** (1983).

[62] *"Evidence for $Z^0 \to e^+e^-$ at the CERN $\bar{p}p$ Collider"*, Phys. Lett. **129B** (1983).

[63] J. Haffner, *The CERN accelerator complex. Complexe des accélérateurs du CERN*, (2013), General Photo, URL: https://cds.cern.ch/record/1621894.

[64] ATLAS Collaboration, 'Luminosity Public Results Run2', 2017 (accessd December, 2017), URL: https://twiki.cern.ch/twiki/bin/view/AtlasPublic/LuminosityPublicResultsRun2.

[65] ATLAS Collaboration, *The ATLAS Experiment at the CERN Large Hadron Collider*, JINST **3** (2008) S08003.

[66] A. Yamamoto et al., *The ATLAS central solenoid*, Nucl. Instrum. Meth. **A584** (2008) 53.

[67] M Capeans et al., 'ATLAS Insertable B-Layer Technical Design Report', tech. rep. CERN-LHCC-2010-013. ATLAS-TDR-19, 2010, URL: https://cds.cern.ch/record/1291633.

[68] 'Studies of the ATLAS Inner Detector material using $\sqrt{s}$ =13 TeV pp collision data', tech. rep. ATL-PHYS-PUB-2015-050, CERN, 2015, URL: https://cds.cern.ch/record/2109010.

[69] M. Barbero et al., *A new ATLAS pixel front-end IC for upgraded LHC luminosity*, Nucl. Instrum. Meth. **A604** (2009) 397.

[70] M. Garcia-Sciveres et al., *The FE-I4 pixel readout integrated circuit*, Nucl. Instrum. Meth. **A636** (2011) S155.

[71] D. Arutinov et al., *Digital Architecture and Interface of the New ATLAS Pixel Front-End IC for Upgraded LHC Luminosity*, IEEE Transactions on Nuclear Science **56** (2009) 388, ISSN: 0018-9499.

[72] G Aad et al., *ATLAS pixel detector electronics and sensors*, Journal of Instrumentation **3** (2008) P07007, URL: http://stacks.iop.org/1748-0221/3/i=07/a=P07007.

[73] ATLAS Collaboration, 'TRT performance results from 13 TeV collision data (2015/2016)', 2016 (accessd December, 2017), URL: https://atlas.web.cern.ch/Atlas/GROUPS/PHYSICS/PLOTS/TRT-2016-001/.

[74] S. Akhmadaliev et al., *Results from a new combined test of an electromagnetic liquid argon calorimeter with a hadronic scintillating-tile calorimeter*, Nuclear Instruments and Methods in Physics Research Section A: Accelerators, Spectrometers, Detectors and Associated Equipment **449** (2000) 461 , ISSN: 0168-9002, URL: http://www.sciencedirect.com/science/article/pii/S0168900200001534.

[75] 'Drift of IBL LV current and its consequence in IBL distortion', tech. rep. ATL-INDET-PUB-2015-002, CERN, 2015, URL: https://cds.cern.ch/record/2105528.

[76] *ATLAS Computing: technical design report*, Technical Design Report ATLAS, CERN, 2005, URL: https://cds.cern.ch/record/837738.

[77] A. Rosenfeld and J. L. Pfaltz, *Sequential Operations in Digital Picture Processing*, J. ACM **13** (1966) 471, ISSN: 0004-5411, URL: http://doi.acm.org/10.1145/321356.321357.

[78] A. Rosenfeld and J. L. Pfaltz, *Sequential Operations in Digital Picture Processing*, J. ACM **13** (1966) 471, ISSN: 0004-5411, URL: http://doi.acm.org/10.1145/321356.321357.

[79] R. Frühwirth, *Application of Kalman filtering to track and vertex fitting*, Nuclear Instruments and Methods in Physics Research Section A: Accelerators, Spectrometers, Detectors and Associated Equipment **262** (1987) 444 , ISSN: 0168-9002, URL: http://www.sciencedirect.com/science/article/pii/0168900287908874.

[80] D. Wicke, *A New Algorithm For Solving Track Ambiguities*, (1998).

[81] T. Cornelissen et al., *Concepts, Design and Implementation of the ATLAS New Tracking (NEWT)*, (2007), ed. by A. Salzburger.

[82] M. Aaboud et al., *Performance of the ATLAS Track Reconstruction Algorithms in Dense Environments in LHC run 2*, (2017), arXiv: 1704.07983 [hep-ex].

[83] A. Sidoti, *Minimum Bias Trigger Scintillators in ATLAS Run II*, Journal of Instrumentation **9** (2014) C10020, URL: http://stacks.iop.org/1748-0221/9/i=10/a=C10020.

[84] T. Sjostrand, S. Mrenna and P. Z. Skands, *A Brief Introduction to PYTHIA 8.1*, Comput. Phys. Commun. **178** (2008) 852, arXiv: 0710.3820 [hep-ph].

[85] ATLAS Collaboration, *Further ATLAS tunes of Pythia 6 and Pythia 8*, ATL-PHYS-PUB-2011-014, 2011, URL: https://cds.cern.ch/record/1400677.

[86] A. Sherstnev and R. S. Thorne, *Parton Distributions for LO Generators*, Eur. Phys. J. **C55** (2008) 553, arXiv: 0711.2473 [hep-ph].

[87] S. Agostinelli et al., *GEANT4: A Simulation toolkit*, Nucl. Instrum. Meth. **A506** (2003) 250.

[88] ATLAS Collaboration, *The ATLAS Simulation Infrastructure*, Eur. Phys. J. C **70** (2010) 823, arXiv: 1005.4568 [hep-ex].

[89] ATLAS Collaboration, 'Impact Parameter Resolution', 2015 (accessd December, 2017), URL: https://atlas.web.cern.ch/Atlas/GROUPS/PHYSICS/PLOTS/IDTR-2015-007/.

[90] ATLAS Collaboration, *Tracking Studies for b-tagging with 7 TeV Collision Data with the ATLAS Detector*, ATLAS-CONF-2010-070 (2010), https://cds.cern.ch/record/1281352.

[91] ATLAS Collaboration, *Vertex Reconstruction Performance of the ATLAS Detector at* $\sqrt{s} = 13$ *TeV*, ATL-PHYS-PUB-2015-026 (2015), https://cds.cern.ch/record/2037717.

[92] M. Aaboud et al., *Study of the material of the ATLAS inner detector for Run 2 of the LHC*, (2017), arXiv: 1707.02826 [hep-ex].

[93] ATLAS Collaboration, *Early Inner Detector Tracking Performance in the 2015 data at* $\sqrt{s} = 13$ *TeV*, ATL-PHYS-PUB-2015-051 (2015), https://cds.cern.ch/record/2110140.

[94] ATLAS Collaboration,
Track Reconstruction Performance of the ATLAS Inner Detector at $\sqrt{s}$ = 13 TeV,
ATL-PHYS-PUB-2015-018 (2015), https://cds.cern.ch/record/2037683.

[95] R. Fruhwirth, W. Waltenberger and P. Vanlaer, *Adaptive vertex fitting*,
J. Phys. **G34** (2007) N343.

[96] ATLAS Collaboration, *Performance of primary vertex reconstruction in proton-proton collisions at $\sqrt{s}$ = 7 TeV in the ATLAS experiment*,
ATLAS-CONF-2010-069 (2010), https://cds.cern.ch/record/1281344.

[97] ATLAS Collaboration, *A search for R-parity-violating scalar top decays in all-hadronic final states with the ATLAS detector in $\sqrt{s}$ = 8 TeV pp collisions*, ATLAS-CONF-2015-026, 2015, URL: https://cds.cern.ch/record/2037653.

[98] ATLAS Collaboration, *Electron efficiency measurements with the ATLAS detector using the 2015 LHC proton–proton collision data*, ATLAS-CONF-2016-024, 2016,
URL: https://cds.cern.ch/record/2157687.

[99] W Lampl et al., 'Calorimeter Clustering Algorithms: Description and Performance',
tech. rep. ATL-LARG-PUB-2008-002. ATL-COM-LARG-2008-003, CERN, 2008,
URL: https://cds.cern.ch/record/1099735.

[100] T. G. Cornelissen et al., *The global χ^2 track fitter in ATLAS*,
Journal of Physics: Conference Series **119** (2008) 032013,
URL: http://stacks.iop.org/1742-6596/119/i=3/a=032013.

[101] ATLAS Collaboration, *Improved electron reconstruction in ATLAS using the Gaussian Sum Filter-based model for bremsstrahlung*, ATLAS-CONF-2012-047, 2012,
URL: https://cds.cern.ch/record/1449796.

[102] G. Aad et al.,
Electron and photon energy calibration with the ATLAS detector using LHC Run 1 data,
Eur. Phys. J. **C74** (2014) 3071, arXiv: 1407.5063 [hep-ex].

[103] G. Aad et al., *Muon reconstruction performance of the ATLAS detector in proton–proton collision data at $\sqrt{s}$ =13 TeV*, Eur. Phys. J. **C76** (2016) 292, arXiv: 1603.05598 [hep-ex].

[104] M. Cacciari, G. P. Salam and G. Soyez, *The Anti-k(t) jet clustering algorithm*,
JHEP **04** (2008) 063, arXiv: 0802.1189 [hep-ph].

[105] G. Aad et al.,
Topological cell clustering in the ATLAS calorimeters and its performance in LHC Run 1,
Eur. Phys. J. **C77** (2017) 490, arXiv: 1603.02934 [hep-ex].

[106] M. Aaboud et al.,
Jet reconstruction and performance using particle flow with the ATLAS Detector,
Eur. Phys. J. **C77** (2017) 466, arXiv: 1703.10485 [hep-ex].

[107] ATLAS Collaboration, *Monte Carlo Calibration and Combination of In-situ Measurements of Jet Energy Scale, Jet Energy Resolution and Jet Mass in ATLAS*,
ATLAS-CONF-2015-037, 2015, URL: https://cds.cern.ch/record/2044941.

[108] ATLAS Collaboration, *Jet Calibration and Systematic Uncertainties for Jets Reconstructed in the ATLAS Detector at sqrts = 13 TeV*, ATL-PHYS-PUB-2015-015, 2015, URL: https://cds.cern.ch/record/2037613.

[109] ATLAS Collaboration, *Tagging and suppression of pileup jets with the ATLAS detector*, ATLAS-CONF-2014-018, 2014, URL: https://cds.cern.ch/record/1700870.

[110] ATLAS Collaboration, *JVT Public Plots for ICHEP 2016*, JETM-2016-011, 2016, URL: https://atlas.web.cern.ch/Atlas/GROUPS/PHYSICS/PLOTS/JETM-2016-011/.

[111] B. Nachman et al., *Jets from Jets: Re-clustering as a tool for large radius jet reconstruction and grooming at the LHC*, JHEP **02** (2015) 075, arXiv: 1407.2922 [hep-ph].

[112] ATLAS Collaboration, *Jet reclustering and close-by effects in ATLAS Run 2*, ATLAS-CONF-2017-062, 2017, URL: https://cds.cern.ch/record/2275649.

[113] ATLAS Collaboration, *Optimisation of the ATLAS b-tagging performance for the 2016 LHC Run*, ATL-PHYS-PUB-2016-012, 2016, URL: https://cds.cern.ch/record/2160731.

[114] ATLAS Collaboration, *Commissioning of the ATLAS high performance b-tagging algorithms in the 7 TeV collision data*, ATLAS-CONF-2011-102, 2011, URL: https://cds.cern.ch/record/1369219.

[115] G Piacquadio and C Weiser, *A new inclusive secondary vertex algorithm for b-jet tagging in ATLAS*, Journal of Physics: Conference Series **119** (2008) 032032, URL: http://stacks.iop.org/1742-6596/119/i=3/a=032032.

[116] G. Aad et al., *Performance of b-Jet Identification in the ATLAS Experiment*, JINST **11** (2016) P04008, arXiv: 1512.01094 [hep-ex].

[117] ATLAS Collaboration, *Performance of missing transverse momentum reconstruction with the ATLAS detector in the first proton–proton collisions at $\sqrt{s}$ = 13 TeV*, ATL-PHYS-PUB-2015-027, 2015, URL: https://cds.cern.ch/record/2037904.

[118] M. Cacciari and G. P. Salam, *Pileup subtraction using jet areas*, Phys. Lett. **B659** (2008) 119, arXiv: 0707.1378 [hep-ph].

[119] H.-L. Lai et al., *New parton distributions for collider physics*, Phys. Rev. **D82** (2010) 074024, arXiv: 1007.2241 [hep-ph].

[120] R. D. Ball et al., *Parton distributions with LHC data*, Nucl. Phys. **B867** (2013) 244, arXiv: 1207.1303 [hep-ph].

[121] A. D. Martin et al., *Parton distributions for the LHC*, Eur. Phys. J. **C63** (2009) 189, arXiv: 0901.0002 [hep-ph].

[122] S. Frixione, P. Nason and G. Ridolfi, *A Positive-weight next-to-leading-order Monte Carlo for heavy flavour hadroproduction*, JHEP **0709** (2007) 126, arXiv: 0707.3088 [hep-ph].

[123] P. Nason, *A New method for combining NLO QCD with shower Monte Carlo algorithms*, JHEP **0411** (2004) 040, arXiv: hep-ph/0409146.

[124] S. Frixione, P. Nason and C. Oleari,
Matching NLO QCD computations with Parton Shower simulations: the POWHEG method,
JHEP **0711** (2007) 070, arXiv: 0709.2092 [hep-ph].

[125] S. Alioli et al., *A general framework for implementing NLO calculations in shower Monte Carlo programs: the POWHEG BOX*, JHEP **1006** (2010) 043,
arXiv: 1002.2581 [hep-ph].

[126] B. Andersson et al., *Parton Fragmentation and String Dynamics*, Phys. Rept. **97** (1983) 31.

[127] T. Sjostrand, *Jet Fragmentation of Nearby Partons*, Nucl. Phys. **B248** (1984) 469.

[128] B. Webber, *A QCD model for jet fragmentation including soft gluon interference*,
Nuclear Physics B **238** (1984) 492 , ISSN: 0550-3213,
URL: http://www.sciencedirect.com/science/article/pii/055032138490333X.

[129] G. Marchesini and B. Webber,
Monte Carlo simulation of general hard processes with coherent QCD radiation,
Nuclear Physics B **310** (1988) 461 , ISSN: 0550-3213,
URL: http://www.sciencedirect.com/science/article/pii/0550321388900892.

[130] T. Sjöstrand, S. Mrenna and P. Z. Skands, *PYTHIA 6.4 Physics and Manual*,
JHEP **0605** (2006) 026, arXiv: hep-ph/0603175.

[131] M. Bahr et al., *Herwig++ Physics and Manual*, Eur. Phys. J. **C58** (2008) 639,
arXiv: 0803.0883 [hep-ph].

[132] S. Höche et al., *QCD matrix elements + parton showers: The NLO case*,
JHEP **04** (2013) 027, arXiv: 1207.5030 [hep-ph].

[133] M. Czakon and A. Mitov,
Top++: A Program for the Calculation of the Top-Pair Cross-Section at Hadron Colliders,
Comput. Phys. Commun. **185** (2014) 2930, arXiv: 1112.5675 [hep-ph].

[134] M. Cacciari et al., *Top-pair production at hadron colliders with next-to-next-to-leading logarithmic soft-gluon resummation*, Phys. Lett. **B710** (2012) 612,
arXiv: 1111.5869 [hep-ph].

[135] P. Bärnreuther, M. Czakon and A. Mitov, *Percent Level Precision Physics at the Tevatron: First Genuine NNLO QCD Corrections to $q\bar{q} \to t\bar{t} + X$*, Phys. Rev. Lett. **109** (2012) 132001,
arXiv: 1204.5201 [hep-ph].

[136] M. Czakon and A. Mitov, *NNLO corrections to top-pair production at hadron colliders: the all-fermionic scattering channels*, JHEP **12** (2012) 054, arXiv: 1207.0236 [hep-ph].

[137] M. Czakon and A. Mitov,
NNLO corrections to top pair production at hadron colliders: the quark-gluon reaction,
JHEP **01** (2013) 080, arXiv: 1210.6832 [hep-ph].

[138] M. Czakon, P. Fiedler and A. Mitov,
Total Top-Quark Pair-Production Cross Section at Hadron Colliders Through $O(\alpha_S^4)$,
Phys. Rev. Lett. **110** (2013) 252004, arXiv: 1303.6254 [hep-ph].

[139] A. D. Martin et al., *Uncertainties on alpha(S) in global PDF analyses and implications for predicted hadronic cross sections*, Eur. Phys. J. **C64** (2009) 653,
arXiv: 0905.3531 [hep-ph].

[140] M. Botje et al., *The PDF4LHC Working Group Interim Recommendations*, (2011), arXiv: 1101.0538 [hep-ph].

[141] J. Gao et al., *CT10 next-to-next-to-leading order global analysis of QCD*, Phys. Rev. **D89** (2014) 033009, arXiv: 1302.6246 [hep-ph].

[142] J. A. Aguilar-Saavedra, *PROTOS, a PROgram for TOp Simulations*, http://jaguilar.web.cern.ch/jaguilar/protos/.

[143] ATLAS Collaboration, *ATLAS Pythia 8 tunes to 7 TeV data*, ATL-PHYS-PUB-2014-021 (2014), https://cds.cern.ch/record/1966419.

[144] M. Guchait, F. Mahmoudi and K. Sridhar, *Associated production of a Kaluza-Klein excitation of a gluon with a $t\bar{t}$ pair at the LHC*, Phys. Lett. B **666** (2008) 347, arXiv: 0710.2234 [hep-ph].

[145] J. Alwall et al., *MadGraph 5 : Going Beyond*, JHEP **1106** (2011) 128, arXiv: 1106.0522 [hep-ph].

[146] ATLAS Collaboration, *ATLAS Pythia 8 tunes to 7 TeV data*, ATL-PHYS-PUB-2014-021, 2014, URL: https://cds.cern.ch/record/1966419.

[147] P. Meade and M. Reece, *BRIDGE: Branching ratio inquiry / decay generated events*, (2007), arXiv: hep-ph/0703031.

[148] ATLAS Collaboration, *Comparison of Monte Carlo generator predictions to ATLAS measurements of top pair production at $\sqrt{s} = 7$TeV*, ATL-PHYS-PUB-2015-002 (2015), https://cds.cern.ch/record/1981319.

[149] J. Pumplin et al., *New generation of parton distributions with uncertainties from global QCD analysis*, JHEP **07** (2002) 012, arXiv: hep-ph/0201195 [hep-ph].

[150] P. Z. Skands, *Tuning Monte Carlo Generators: The Perugia Tunes*, Phys. Rev. D **82** (2010) 074018, arXiv: 1005.3457 [hep-ph].

[151] M. Czakon, D. Heymes and A. Mitov, *High-precision differential predictions for top-quark pairs at the LHC*, Phys. Rev. Lett. **116** (2016) 082003, arXiv: 1511.00549 [hep-ph].

[152] M. Czakon, D. Heymes and A. Mitov, *Dynamical scales for multi-TeV top-pair production at the LHC*, (2016), arXiv: 1606.03350 [hep-ph].

[153] F. Cascioli et al., *NLO matching for $t\bar{t}b\bar{b}$ production with massive b-quarks*, Phys. Lett. B **734** (2014) 210, arXiv: 1309.5912 [hep-ph].

[154] T. Gleisberg et al., *Event generation with SHERPA 1.1*, JHEP **0902** (2009) 007, arXiv: 0811.4622 [hep-ph].

[155] F. Cascioli, P. Maierhofer and S. Pozzorini, *Scattering Amplitudes with Open Loops*, Phys. Rev. Lett. **108** (2012) 111601, arXiv: 1111.5206 [hep-ph].

[156] T. Gleisberg and S. Höche, *Comix, a new matrix element generator*, JHEP **0812** (2008) 039, arXiv: 0808.3674 [hep-ph].

[157] S. Schumann and F. Krauss,
A Parton shower algorithm based on Catani-Seymour dipole factorisation,
JHEP **03** (2008) 038, arXiv: 0709.1027 [hep-ph].

[158] C. Anastasiou et al., *High precision QCD at hadron colliders: Electroweak gauge boson rapidity distributions at NNLO*, Phys. Rev. **D69** (2004) 094008,
arXiv: hep-ph/0312266 [hep-ph].

[159] S. Frixione et al., *Single-Top Production in MC@NLO*, JHEP **03** (2006) 092,
arXiv: hep-ph/0512250.

[160] N. Kidonakis, *Next-to-next-to-leading-order collinear and soft gluon corrections for t-channel single top quark production*, Phys. Rev. **D83** (2011) 091503,
arXiv: 1103.2792 [hep-ph].

[161] N. Kidonakis, *Two-loop soft anomalous dimensions for single top quark associated production with a W- or H-*, Phys. Rev. **D82** (2010) 054018, arXiv: 1005.4451 [hep-ph].

[162] N. Kidonakis, *NNLL resummation for s-channel single top quark production*,
Phys. Rev. **D81** (2010) 054028, arXiv: 1001.5034 [hep-ph].

[163] R. D. Ball et al., *Parton distributions for the LHC Run II*, JHEP **04** (2015) 040,
arXiv: 1410.8849 [hep-ph].

[164] R. Raitio and W. W. Wada,
Higgs Boson Production at Large Transverse Momentum in QCD,
Phys. Rev. D **19** (1979) 941.

[165] W. Beenakker et al., *NLO QCD corrections to $t\bar{t}H$ production in hadron collisions*,
Nucl. Phys. B **653** (2003) 151, arXiv: hep-ph/0211352 [hep-ph].

[166] S. Dawson et al., *Associated Higgs production with top quarks at the large hadron collider: NLO QCD corrections*, Phys. Rev. D **68** (2003) 034022,
arXiv: hep-ph/0305087 [hep-ph].

[167] Y. Zhang et al., *QCD NLO and EW NLO corrections to $t\bar{t}H$ production with top quark decays at hadron collider*, Phys. Lett. B **738** (2014) 1, arXiv: 1407.1110 [hep-ph].

[168] S. Frixione et al., *Electroweak and QCD corrections to top-pair hadroproduction in association with heavy bosons*, JHEP **1506** (2015) 184, arXiv: 1504.03446 [hep-ph].

[169] A. Djouadi, J. Kalinowski and M. Spira, *HDECAY: A Program for Higgs boson decays in the standard model and its supersymmetric extension*,
Comput. Phys. Commun. **108** (1998) 56, arXiv: hep-ph/9704448 [hep-ph].

[170] ATLAS Collaboration, *Measurement of the top quark-pair production cross section with ATLAS in pp collisions at $\sqrt{s}$ = 7 TeV*, Eur. Phys. J. C **71** (2011) 1577,
arXiv: 1012.1792 [hep-ex].

[171] P. Golonka and Z. Was,
PHOTOS Monte Carlo: A Precision tool for QED corrections in Z and W decays,
Eur. Phys. J. C **45** (2006) 97, arXiv: hep-ph/0506026.

[172] S. Jadach, J. H. Kuhn and Z. Was,
TAUOLA: A Library of Monte Carlo programs to simulate decays of polarized τ leptons,
Comput. Phys. Commun. **64** (1991) 275.

[173] D. J. Lange, *The EvtGen particle decay simulation package*, Nucl. Instrum. Meth. **A462** (2001) 152.

[174] B. DELAUNAY, *Sur la sphere vide*, Bulletin of the Academy of Sciences of the U. S. S. R. Classe des Sciences Mathematiques et Naturelles **7** (1934) 793.

[175] G. Aad et al., *Search for production of vector-like quark pairs and of four top quarks in the lepton-plus-jets final state in pp collisions at* $\sqrt{s} = 8$ *TeV with the ATLAS detector*, JHEP **08** (2015) 105, arXiv: 1505.04306 [hep-ex].

[176] ATLAS Collaboration, *Luminosity determination in pp collisions at* $\sqrt{s} = 8$ *TeV using the ATLAS detector at the LHC*, (2016), arXiv: 1608.03953 [hep-ex].

[177] ATLAS Collaboration, *Measurement of the Inelastic Proton–Proton Cross Section at* $\sqrt{s} = 13$ *TeV with the ATLAS Detector at the LHC*, (2016), arXiv: 1606.02625 [hep-ex].

[178] ATLAS Collaboration, *Performance of the ATLAS muon trigger in pp collisions at* $\sqrt{s} = 8$ *TeV*, Eur. Phys. J. C **75** (2015) 120, arXiv: 1408.3179 [hep-ex].

[179] ATLAS Collaboration, *Jet energy measurement and its systematic uncertainty in proton-proton collisions at* $\sqrt{s} = 7$ *TeV with the ATLAS detector*, Eur. Phys. J. C **75** (2015) 17, arXiv: 1406.0076 [hep-ex].

[180] G. Aad et al., *Performance of jet substructure techniques for large-R jets in proton-proton collisions at* $\sqrt{s} = 7$ *TeV using the ATLAS detector*, JHEP **09** (2013) 076, arXiv: 1306.4945 [hep-ex].

[181] ATLAS Collaboration, *Measurements of fiducial cross-sections for* $t\bar{t}$ *production with one or two additional b-jets in pp collisions at* $\sqrt{s} = 8$ *TeV using the ATLAS detector*, Eur. Phys. J. C **76** (2016) 11, arXiv: 1508.06868 [hep-ex].

[182] CMS Collaboration, *Measurement of* $t\bar{t}$ *production with additional jet activity, including b quark jets, in the dilepton decay channel using pp collisions at* $\sqrt{s} = 8$ *TeV*, Eur. Phys. J. C **76** (2016) 379, arXiv: 1510.03072 [hep-ex].

[183] ATLAS Collaboration, *Search for the Standard Model Higgs boson produced in association with top quarks and decaying into* $b\bar{b}$ *in pp collisions at* $\sqrt{s} = 8$ *TeV with the ATLAS detector*, Eur. Phys. J. C **75** (2015) 349, arXiv: 1503.05066 [hep-ex].

[184] S. Frixione et al., *Single-top hadroproduction in association with a W boson*, JHEP **07** (2008) 029, arXiv: 0805.3067 [hep-ph].

[185] J. M. Campbell and R. K. Ellis, *An Update on vector boson pair production at hadron colliders*, Phys. Rev. D **60** (1999) 113006, arXiv: hep-ph/9905386.

[186] J. Alwall et al., *Comparative study of various algorithms for the merging of parton showers and matrix elements in hadronic collisions*, Eur. Phys. J. C **53** (2008) 473, arXiv: 0706.2569 [hep-ph].

[187] J. M. Campbell and R. K. Ellis, $t\bar{t}W^{+-}$ *production and decay at NLO*, JHEP **1207** (2012) 052, arXiv: 1204.5678 [hep-ph].

[188] M. V. Garzelli et al., *$t\bar{t}W^{+-}$ and $t\bar{t}Z$ Hadroproduction at NLO accuracy in QCD with Parton Shower and Hadronization effects*, JHEP **1211** (2012) 056, arXiv: 1208.2665 [hep-ph].

[189] LHC Higgs Cross Section Working Group, S. Dittmaier et al., *Handbook of LHC Higgs Cross Sections: 1. Inclusive Observables*, (2011), arXiv: 1101.0593 [hep-ph].

[190] J. Alwall et al., *The automated computation of tree-level and next-to-leading order differential cross sections, and their matching to parton shower simulations*, JHEP **07** (2014) 079, arXiv: 1405.0301 [hep-ph].

[191] A. Wald, *Tests of Statistical Hypotheses Concerning Several Parameters When the Number of Observations is Large*, Transactions of the American Mathematical Society **54** (1943) 426, ISSN: 00029947, URL: http://www.jstor.org/stable/1990256.

[192] G. Cowan et al., *Asymptotic formulae for likelihood-based tests of new physics*, Eur. Phys. J. **C71** (2011) 1554, [Erratum: Eur. Phys. J.C73,2501(2013)], arXiv: 1007.1727 [physics.data-an].

[193] T. Junk, *Confidence level computation for combining searches with small statistics*, Nucl. Instrum. Meth. **A434** (1999) 435, arXiv: hep-ex/9902006 [hep-ex].

[194] 'Variable Radius, Exclusive-k_T, and Center-of-Mass Subjet Reconstruction for Higgs($\to b\bar{b}$) Tagging in ATLAS', tech. rep. ATL-PHYS-PUB-2017-010, CERN, 2017, URL: https://cds.cern.ch/record/2268678.

[195] R. Brock et al., 'Planning the Future of U.S. Particle Physics (Snowmass 2013): Chapter 3: Energy Frontier', *Proceedings, 2013 Community Summer Study on the Future of U.S. Particle Physics: Snowmass on the Mississippi (CSS2013): Minneapolis, MN, USA, July 29-August 6, 2013*, 2014, arXiv: 1401.6081 [hep-ex], URL: https://inspirehep.net/record/1278569/files/arXiv:1401.6081.pdf.

[196] N. Arkani-Hamed et al., *Physics opportunities of a 100 TeV proton–proton collider*, Phys. Rept. **652** (2016) 1, arXiv: 1511.06495 [hep-ph].